Journal of Engineering for Power (ISSN 0022-0825) is edited and published quarterly at the offices of The American Society of Mechanical Engineers, United Engineering Center, 345 E. 47th St., New York, N. Y. 10017. ASME-TWX No. 710-581-5267, New York. Second Class postage paid at New York, N.Y., and at additional mailing offices.

CHANGES OF ADDRESS must be received at Society headquarters seven weeks before they are to be effective. Please send old label and new address.

PRICES: To members, $36.00, annually; to nonmembers, $72.00. Single copies, $24.00 each. Add $5.00 for postage to countries outside the United States and Canada.

INDEXED by the Engineering Index, Inc.

Journal of Engineering for Power

Published Quarterly by The American Society of Mechanical Engineers

VOLUME 105 • NUMBER 1 • JANUARY 1983

TECHNICAL PAPERS

(Contents continued on p. 32)

(Contents Continued)

Investigation of the Tip Clearance Flow Inside and at the Exit of a Compressor Rotor Passage—Part I: Mean Velocity Field

A. Pandya[1]
Graduate Assistant.

B. Lakshminarayana
Director of Computational Fluid Dynamics Studies and Professor of Aerospace Engineering. Fellow ASME

Department of Aerospace Engineering, The Pennsylvania State University, University Park, Pa. 16802

This paper reports on an experimental study of the nature of the tip clearance flow in a moderately loaded compressor rotor. The measurements reported were obtained using a stationary two-sensor, hot-wire probe in combination with an ensemble averaging technique. The flow field was surveyed at various radial locations and at ten axial locations, four of which were inside the blade passage in the clearance region and the remaining six outside the passage. Variations of the mean flow properties in the tangential and the radial directions at various axial locations were derived from the data. Variation of leakage velocity at different axial stations and the annulus-wall boundary layer profiles from passage-averaged mean velocities were also estimated. The results indicate that there exists a region of strong interaction of the leakage flow with the annulus-wall boundary layer at half-chord. The profiles are well-behaved beyond this point. The rotor exit flow is found to be uniform beyond 3/4 blade chord downstream of the rotor trailing edge.

Introduction

The design of energy-efficient engines has received considerable attention in recent years. Important gains in the efficiency can be made by minimizing the aerodynamic losses in various components of the engine, especially in a compressor rotor, which is one of the least efficient components in the engine. Even marginal gains in the efficiency through reduction of these losses could substantially reduce the fuel requirement for the engine. It is well-known that the end-wall flow losses comprise a substantial proportion of the total losses, and a significant fraction of end-wall losses is attributed to the tip leakage flow and its interaction with the secondary flow, blade boundary layer, annulus-wall boundary layer, and the scraping vortex. Further improvements in design, performance, and prediction of the flow field in this region demand a better understanding of the complex flow structure which results from these interactions in the vicinity of the annulus wall.

Experimental investigations related to the tip-leakage flow have been limited to flow field measurements in straight cascades with tip clearance [1, 2, 3]. These studies, however, do not yield any information regarding the effect of rotation and curvature on the tip leakage flow. On the other hand, flow visualization experiments [4, 5, 6] provide only qualitative information regarding the flow. There have also been attempts to derive some information on leakage flow indirectly via flow field measurements downstream of the rotor [7, 8] and inside the passage near the tip region [9, 10]. Due to limitations imposed by measurement techniques, no measurements were made beyond 96 percent of the blade span and inside the clearance region. Thus, the need to study the flow in close proximity of the annulus wall and inside the tip clearance region becomes evident.

The objective of this investigation is to measure the flow in the tip clearance region of a compressor rotor with special emphasis on the leakage flow development in the tip clearance region and the exit of the rotor.

Only the mean properties of the flow at design conditions are discussed in this paper. Presentation and discussion of turbulence quantities at both the design and the off-design conditions as well as the mean flow field at off-design conditions are included in reference [11].

The data reported in this paper were taken only inside the gap region in the vicinity of the blade tip and the annulus wall. The three-dimensional flow field further down the blade tip from 4 to 20 percent of the span from the tip is reported in references [9] and [10]. These were taken with a rotating hot-wire probe. There are no measurements available in the outer 4 percent of the blade tip.

Experimental Facility, Instrumentation, and Program

Axial Flow Compressor Facility. A general description of the compressor stage is given by Smith [12], and a detailed discussion of the facility is given by Lakshminarayana [13]. Good peak efficiencies are exhibited by the rotor. The hub/annulus wall diameter ratio of the facility is 0.5, with the diameter of the annulus wall equal to 0.932 m. The inlet guide vane row, which consists of 45 blades, is followed by the 21-bladed rotor. The rotor is driven by a 37.29 kw variable-speed motor through a belt-and-pulley system. The rotor is followed

[1] Presently at Memorex Corporation, RTC Division, Santa Clara, California.

Contributed by the Gas Turbine Division of THE AMERICAN SOCIETY OF MECHANICAL ENGINEERS and presented at the 27th International Gas Turbine Conference and Exhibit, London, England, April 18–22, 1982, manuscript received at ASME Headquarters November 19, 1981. Paper No. 82-GT-12.

by a stator vane row of 25 blades. Downstream of the stator is located an axial flow fan with variable blade setting for the variation of pressure rise and mass flow. The facility is terminated downstream by an aerodynamically designed throttle which provides additional control of the stage operating characteristics. Some of the other operating conditions and rotor specifications are as follows: inlet velocity, 28.37 m/s; flow coefficient based on tip speed, 0.56; stage loading coefficient based on tip speed, 0.4864; speed of rotor, 1100 rpm. Blade element data at the tip are NASA 65 series, chord 15.41 cm, spacing 14.12 cm, maximum thickness 5.10 percent of chord, stagger angle 45.0 deg, and a maximum camber height of 8 percent chord. The blade profile near the tip section is given in references [12] and [13].

Instrumentation and Traverse Mechanism. All the flow-field measurements reported in this paper were carried out using a stationary probe in combination with the ensemble-averaging technique. The stationary-probe technique adopted for the present investigation was originally developed by Poncet and Lakshminarayana [14] for the study of the three-dimensional nature of rotor wakes.

The two-sensor, hot-wire probe used for the flow-field measurement is shown in Fig. 1(*a*). Unlike the conventional two-sensor, hot-wire probe (x-configuration), both the sensors are in the same plane, and the included angle between the two sensors is 90 deg. With this arrangement, it was possible to measure two components of the velocity at the same radial location with the least spatial error. The micrometer-type, probe-traverse mechanism designed for this study is shown in Fig. 1(*b*). It has an accuracy of ± .002 cm and can be easily mounted on the Lucite window on the casing of the compressor rotor.

The instrumentation used to record and process signals from the two-sensor, hot-wire probe in the stationary frame of reference is illustrated in Fig. 2. The sensors were connected to two DISA 55M010 constant-temperature anemometer units. The d-c components of the anemometer signals were measured with an integrating digital voltmeter. The fluctuating components of these signals were amplified and recorded with a SAVRE IV FM signal recorder/reproducer at the tape speed of 15 ips. The rpm of the rotor was monitored by a photocell circuit which used a 60-slot calibrated disk mounted on the rotor shaft. The output of the photocell circuit was displayed on a digital counter. The photocell circuit also provided one sharp pulse for each revolution of the rotor. This pulse was also recorded along with the a-c signals to identify a specific blade passage. The instantaneous signals from the anemometer and the pulse

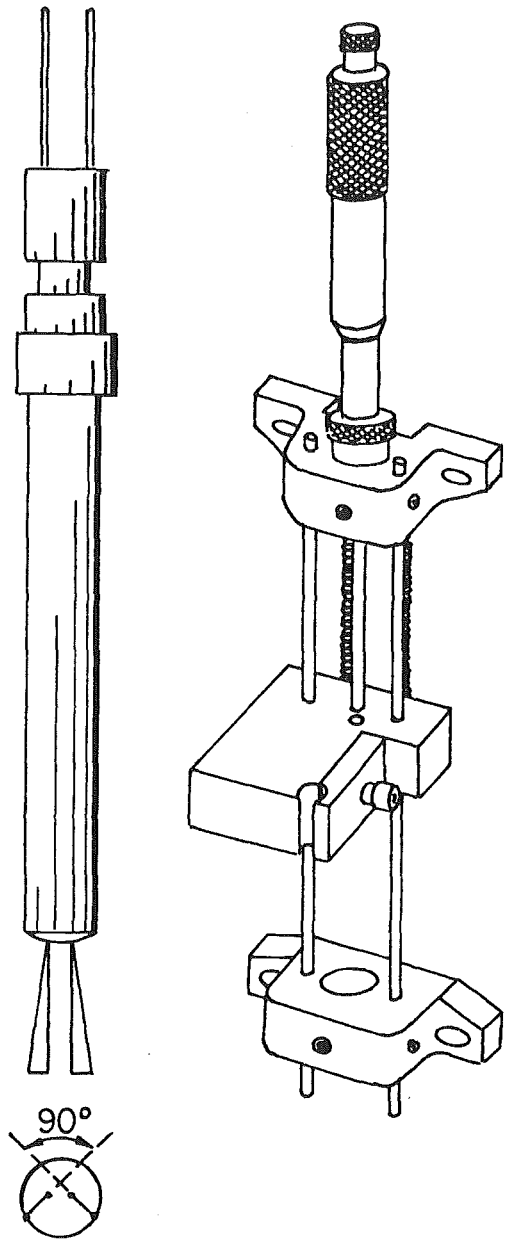

Fig. 1 Two-sensor, hot-wire probe and probe-traverse mechanism

Nomenclature

LE = leading edge
PS = pressure surface
$\bar{R}$ = distance from the annulus wall in the radial direction normalized by clearance at the LE
$\bar{r}$ = distance from the annulus wall normalized by (*a*) clearance at LE for rotor inlet flow, (*b*) local clearance for flow inside the passage, and (*c*) clearance at TE for rotor exit flow
S = blade spacing
SS = suction surface
TE = trailing edge
U = rotational velocity Ωx radius
V = velocity in stationary frame of reference
$\bar{V}$ = passage-averaged velocity in stationary frame of reference normalized by U_{tip}
W = velocity in relative frame of reference
$\bar{W}$ = passage-averaged velocity in relative frame of reference normalized by U_{tip}
W_N = leakage velocity, normalized by U_{tip}
W_{N_0} = W_N at the inlet of the rotor normalized by U_{tip}
$\bar{Y}$ = distance from the fixed line 0.0 in the tangential direction normalized by the blade spacing (Fig. 3)
z = axial coordinate direction corresponding to the axis of the compressor
Z = axial distance from the rotor blade leading edge normalized, by the axial chord (Fig. 3)
β = relative flow angle
Ω = rotational speed rpm
θ = tangential direction
ϕ = mass-averaged flow coefficient
τ = distance from the annulus wall in radial direction

Subscripts

max = maximum value in the passage
tip = value at the tip of the rotor blade
z = value in axial direction
θ = value in tangential direction

Table 1 Axial and radial locations for leakage flowfield measurements

	Z	τ^{**}	10	15	20	25	30	35	40	45	50	60	75	100	125	150	175	180	80	Clearance for the blade under investigation, in inches
Rotor inlet flow	−0.012	$\phi = .55$	*	–	*	*	*	*	–	*	*	–	*	*	*	*	–	–	–	—
		$\phi = .60$	*	–	*	*	*	*	–	*	*	–	*	*	*	*	–	–	–	
Leakage flow	0.003	$\phi = .55$	*	*	*	*	*	*	*	*	*	–	–	–	–	–	–	–	–	0.081
		$\phi = .60$	*	*	*	*	*	*	*	*	*	–	–	–	–	–	–	–	–	
	0.50	$\phi = .55$	*	*	*	*	*	*	*	*	*	–	–	–	–	–	–	–	–	0.087
		$\phi = .60$	*	*	*	*	*	*	*	*	*	–	–	–	–	–	–	–	–	
	0.75	$\phi = .55$	*	*	–	*	*	*	*	–	–	–	–	–	–	–	–	–	–	0.060
		$\phi = .60$	*	*	–	*	*	*	*	–	–	–	–	–	–	–	–	–	–	
	0.979	$\phi = .55$	*	*	*	*	*	*	–	–	–	–	–	–	–	–	–	–	–	0.061
		$\phi = .60$	*	*	*	*	*	*	–	–	–	–	–	–	–	–	–	–	–	
Rotor exit flow	1.055	$\phi = .55$	*	*	*	*	–	*	*	*	*	–	–	–	–	–	–	–	–	—
		$\phi = .60$	*	*	*	*	–	*	*	*	*	–	–	–	–	–	–	–	–	
	1.179	$\phi = .55$	–	–	*	–	*	–	*	–	*	–	*	*	*	*	–	*	–	—
		$\phi = .60$	–	–	*	–	*	–	*	–	*	–	*	*	*	*	–	*	–	
	1.440	$\phi = .55$	–	–	*	–	*	–	*	–	–	*	–	*	*	*	–	*	*	—
		$\phi = .60$	–	–	*	–	*	–	*	–	–	*	–	*	*	*	–	*	*	
	1.593	$\phi = .55$	–	–	*	–	*	–	*	–	*	–	*	*	*	*	–	*	–	—
		$\phi = .60$	–	–	*	–	*	–	*	–	*	–	*	*	*	*	–	*	–	
	1.731	$\phi = .55$	*	–	*	–	*	*	*	–	*	–	*	*	*	–	–	–	–	—
		$\phi = .60$	*	–	*	–	*	*	*	–	*	–	*	–	*	–	–	–	–	

τ^{**} is the distance in thousandths of an inch from the annulus wall.
* indicates the measuring location

were displayed on a Tektronix type RM561A storage oscilloscope.

Measurement Program. Experimental measurements consisted of two parts: (a) clearance measurements and (b) flow field measurements. An accurate measurement of the clearance for all the 21 rotor blades at various axial locations was necessary in order to acquire data as near the blade tip as possible. The measurement of clearance was carried out with a photonic sensor at four axial stations listed in Table 1. There was no appreciable difference between the static and dynamic clearance for the same blade, even though the clearance varied from blade to blade at all the axial stations.

The radial and axial locations at which the flow field measurements were carried out are listed in Table 1. The axial stations of measurement and the definition of the tangential distance $\bar{Y}$ are schematically shown in Fig. 3. The two-sensor, hot-wire probe was calibrated using an open-jet, low-turbulence calibration tunnel. The probe was also calibrated for the wall proximity effects. These are discussed in detail in reference [11]. Since the probe was introduced in the flow field through a series of holes in the Lucite window, care was taken to avoid a sudden step at the point of insertion in the flow field by making the probe flush with the annulus wall. Only the prongs and the sensors were protruding out to the desired radial location.

Data Processing. Major steps involved in the data processing are as follows:

1 Identifying the specific blade passage and digitizing only that part of the analog signal to give approximately 360 data points in a prescribed passage. An analog-to-digital conversion unit manufactured by DATEL was used for this phase of data processing.

2 Translating the digitized data for IBM/370 systems

3 Converting the voltages into velocities using hot-wire equations. The ensemble-averaging was carried out over 240 revolutions, one prescribed passage in each revolution, to calculate mean velocities and turbulent quantities. Therefore, the data includes 360 points in each passage, and 240 samples were used at each tangential location of the blade passage.

Experimental Results

Velocity Profiles and Angles Inside the Tip Clearance Region. Although the measurements were made at all the locations listed in Table 1, the discussion in this paper is limited to only four representative radial locations for some selected axial stations.[2] In addition, the blade static pressure near the tip of the blade, the inlet annulus-wall boundary layer profile, and the flow data below 4 percent of the span presented in reference [9] are extremely useful in the interpretation of the data presented in this paper. The variations of the mean axial velocity, W_z, and the mean tangential velocity in a stationary frame of reference, V_θ, and the relative flow angle (β) for each of the axial stations at four different radial locations are shown in Figs. 4–7 and 9(a), 9(b), and 9(c). In these figures, the blade locations are marked by dotted lines on the $\bar{Y}$-axis. Figure 3 also shows the blade locations on the $\bar{Y}$-axis for all the axial locations. The velocities W_z and V_θ are normalized by the local maximum axial velocity $(W_z)_{\max}$. Variations of $(W_z)_{\max}$ and $(V_\theta)_{\max}$ with radial distance at each axial location is shown in Figs. 4(d), 5(d), 6(d), 7(d), and 9(d).

The decreasing trend in W_z and V_θ, and the increasing absolute value of relative flow angle β near $\bar{Y} = 0.7$ in Fig. 4, reflect the effect of the unsteady flow field due to the rotor on the incoming flow upstream of the rotor. It is important, however, to note that these variations are rather small in magnitude and that the flow closer to the wall shows a greater degree of uniformity compared to that in the vicinity of the blade tip. The variation in the relative flow angle is less than 7 deg. The variation of maximum velocity shows unusual behavior, with a rapid increase in velocity up to $\bar{r} = 0.15$, beyond which the increase is gradual. That $\bar{r} = 1.88$ is well within the annulus-wall boundary layer profile is indicated in Fig. 2 of [9].

[2] The entire data set will be available from Dr. B. Lakshminarayana on request.

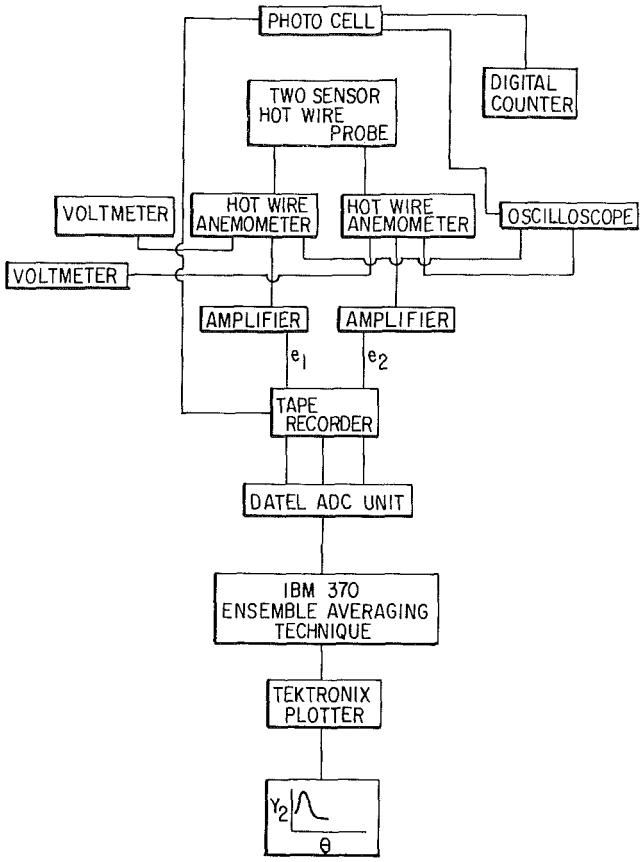

Fig. 2 Instrumentation for stationary, two-sensor, hot-wire probe

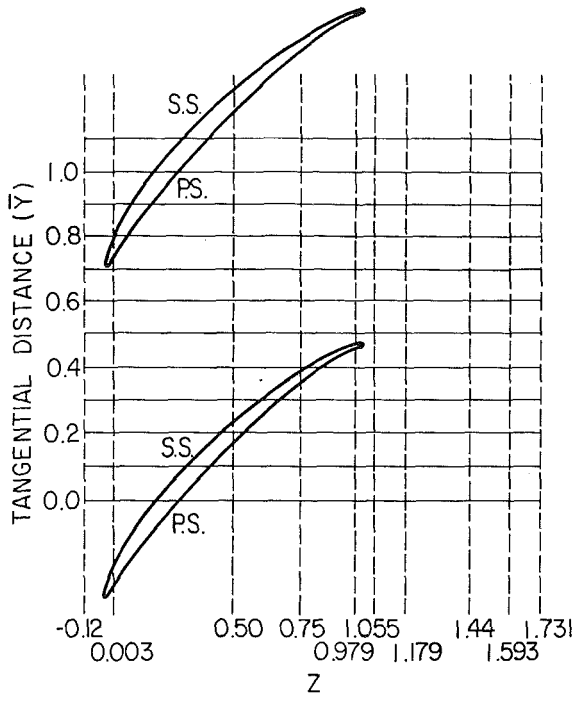

Fig. 3 Axial stations of measurement and definitions of $\bar{Y}$

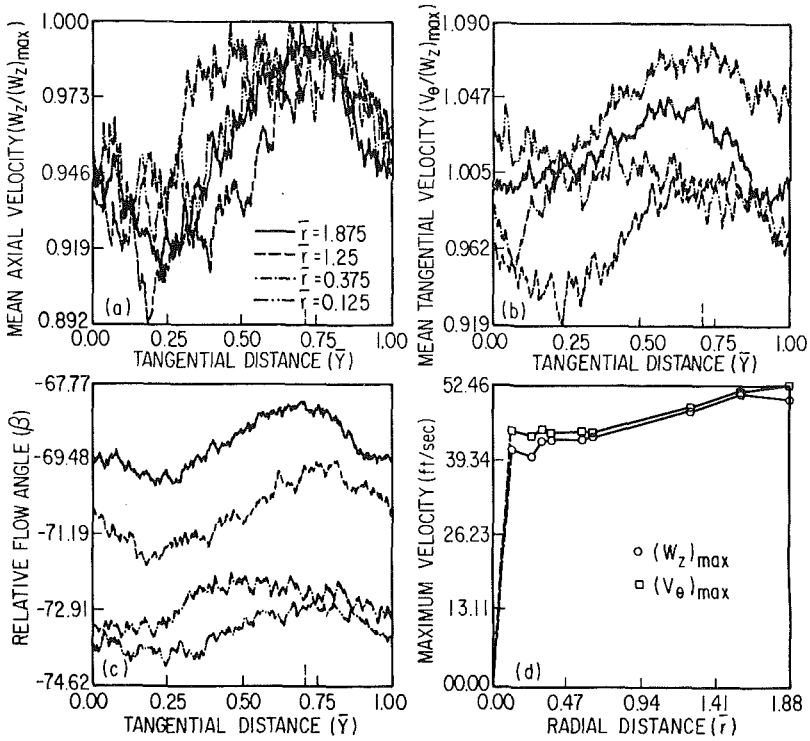

Fig. 4 Variation of mean flow properties at the inlet of the rotor ($Z = -0.012$)

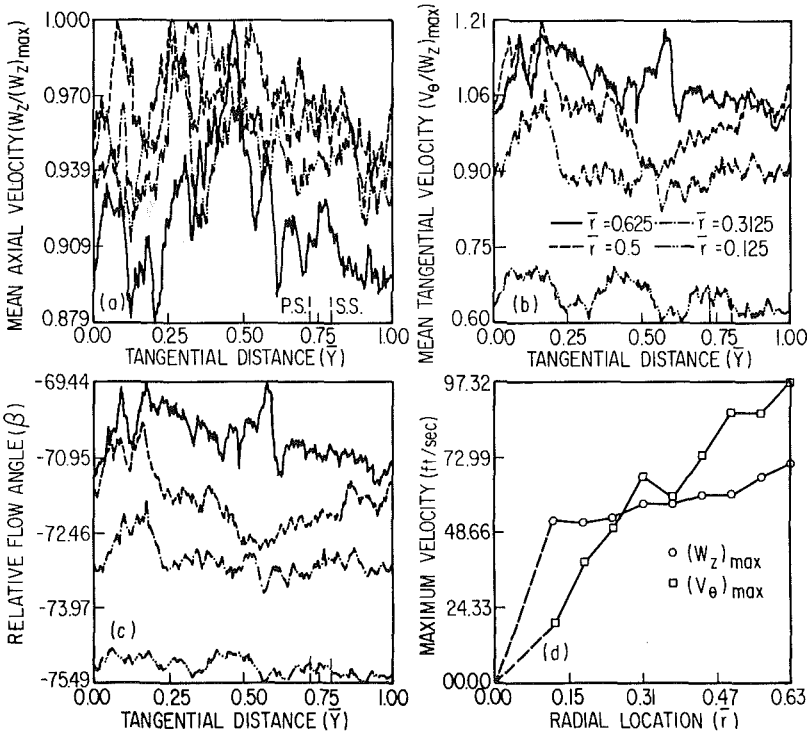

Fig. 5 Variation of mean flow properties at the leading edge ($Z = 0.003$)

At $Z=0.003$, the pressure difference across the blade is not large enough to induce a strong leakage flow. However, a noticeable dragging effect of the blade on the flow can be observed as evidenced by a considerable increase in the tangential velocity. Variation of the mean axial velocity (Fig. 5(*a*)) shows a peak near $\bar{Y} = 0.49$. As can be seen from this figure, a large change in W_z takes place over a small distance approximately midway between the passage, indicating possible flow separation regions near the blade surfaces and the presence of a scraping effect. Both of these effects tend to decrease the velocity components near the blade surfaces and increase it near the mid-passage. The variation in the relative flow angle shows a trend similar to the incoming flow at $Z = -0.12$. A dramatic decrease in the tangential velocity from the blade tip to the annulus-wall region is evident from Fig. 5(*b*). The radial variation of the maximum tangential velocity and the axial velocity at this location indicate a dramatic change from those at $Z = -0.12$. The axial velocity profile at

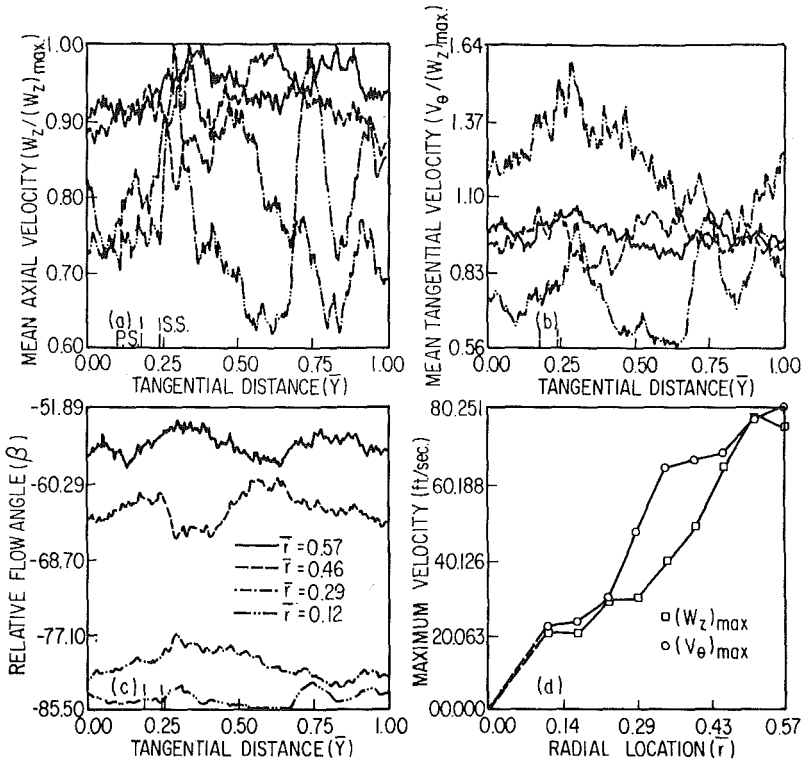

Fig. 6 Variation of mean flow properties at 1/2 chord (Z = 0.50)

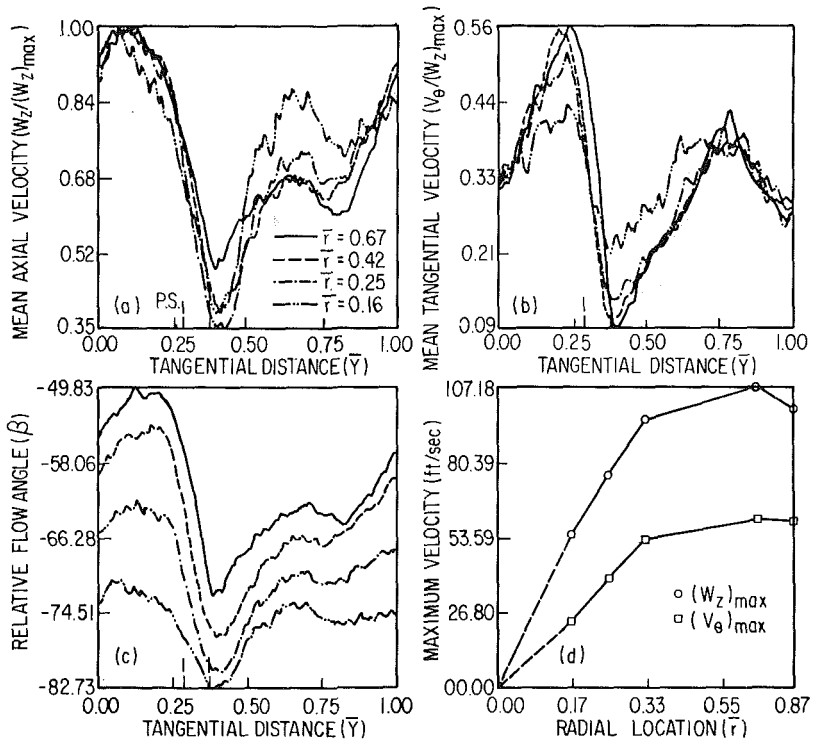

Fig. 7 Variation of mean flow properties at 3/4 chord (Z = 0.75)

this location shows an increase in axial velocity, but the tangential velocity distribution shows a large gradient near the annulus wall, decreasing drastically beyond $\bar{r} = 0.15$. The maximum values of tangential and axial velocities have increased slightly from their inlet values for $\bar{r} > 0.3$.

The flow field at $Z = 0.5$, shown in Fig. 6, is very complex. Such a behavior could result from the interaction of the leakage flow with other features present in this region. These features may include secondary flow, annulus-wall boundary layer, the rolling up of the leakage flow to form a vortex, and the presence of a vortex generated by the scraping of the annulus-wall boundary layer by the blade. Because the pressure difference across the blade at this station is quite high, one might even expect a washing away of the boundary layer leading to the above complex flow behavior.

The axial velocity profile at $Z = 0.5$ (Fig. 6) shows low velocities on either side of the blade near the annulus wall, while the velocities in the clearance region are quite high. This again may have been caused by the leakage flow which has a "blowing" effect on the annulus-wall boundary layer in this

region. The axial velocities near the blade tip are nearly uniform. The tangential velocity also shows a similar trend, with large values near the suction side of the blade near the annulus wall. The blade motion augments the leakage flow and tends to move it farther away from the suction side. The low velocity region observed at $\bar{Y} = 0.85$ for two radial locations near the annulus wall ($\bar{r} = 0.29, 0.12$) may have been caused by the roll up of the leakage flow in this region. The tangential velocities in this region are lower than those observed at $Z = -0.003$, an indication that the flow in this region proceeds through the blade row from $Z = 0.003$ to $Z = 0.5$, with a change in energy level or tangential momentum

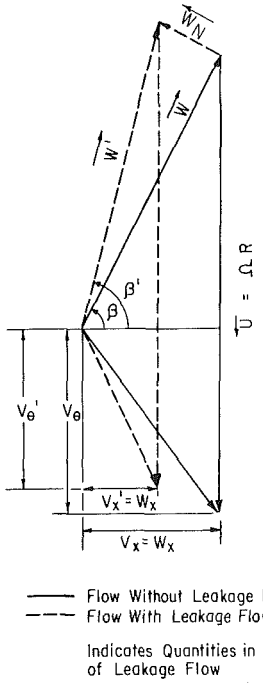

—— Flow Without Leakage Flow
– – – Flow With Leakage Flow

Indicates Quantities in Presence of Leakage Flow

Fig. 8 Velocity triangles with and without the leakage flow

opposite those of the free stream. The relative flow angles show the usual trend, with large angles near the annulus wall. The angle changes from $Z = 0.003$ to $Z = 0.5$ are small. The maximum axial and tangential velocities shown in Figure 6(*d*) at this location indicate very little change in radial variation of the maximum axial velocity from the previous axial location. The maximum tangential velocity is decreased at most radial locations, with the exception of the blade tip region. The radial variation of both velocities is found to be gradual.

At $Z = 0.75$, a clearly defined leakage flow can be seen from Fig. 7. In Fig. 7(*a*), a sudden decrease in the mean axial velocity takes place just before the pressure side at $\bar{Y} = 0.20$ over a very small distance. A similar trend in V_θ is also observed in Fig. 7(*b*). Figure 7(*c*) shows the sudden increase in the absolute value of the relative flow angle, β, in the same region. All three facts together indicate a very clearly defined leakage flow in this region. The significance of these features is better explained in Fig. 8, where a vector diagram of the flow velocities with and without the leakage flow is shown. As can be seen from this figure, the leakage velocity, which is defined as the component of the relative velocity normal to the blade surface, tends to turn the flow away from the blade. This causes an increase in the absolute value of β and a decrease in the axial and the absolute tangential velocities. This trend is clear from Fig. 7.

In Fig. 7(*a*), another peak in W_z occurs at $\bar{Y} = 0.70$. A similar peak in V_θ occurs at $\bar{Y} = 0.75$, but a similar peak in β is not very clearly defined. This phenomenon clearly indicates the presence of the tip-leakage vortex and/or scraping vortex. The most interesting feature of the flow field at this axial location is that though the variations in W_z, V_θ and β are comparatively very large for a particular radial location, the variation from one radial location to another is very small. All the nondimensionalized profiles nearly collapse into a single curve, indicating the similarity in the velocity profiles. It is thus clear that the leakage flow is the most predominant flow in the clearance region at this location.

Figure 7(*d*), showing the variation of $(W_z)_{max}$ and $(V_\theta)_{max}$, indicates a gradual increase in both the velocities away from

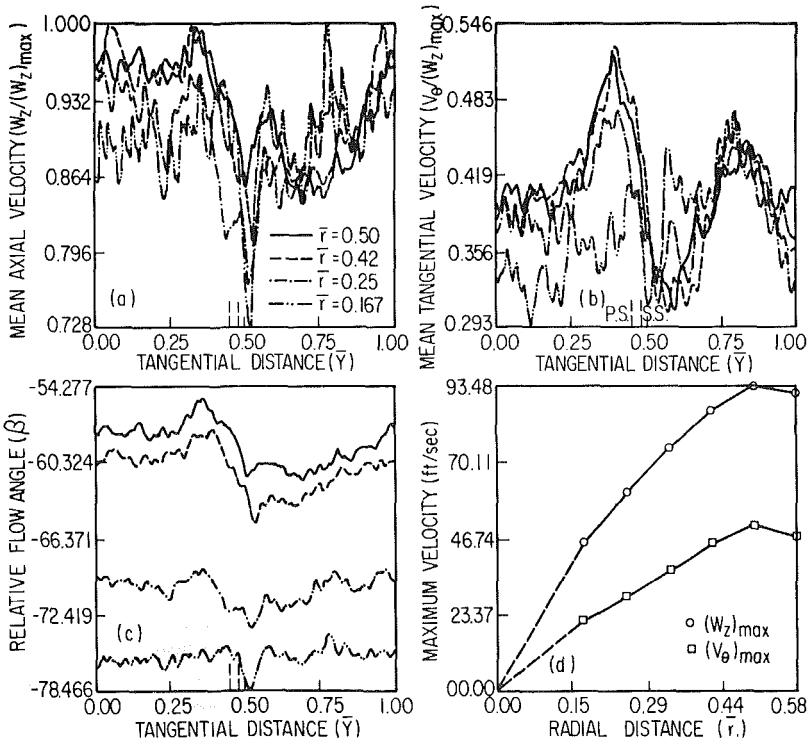

Fig. 9 Variation of mean flow properties at the trailing edge (Z = 0.979)

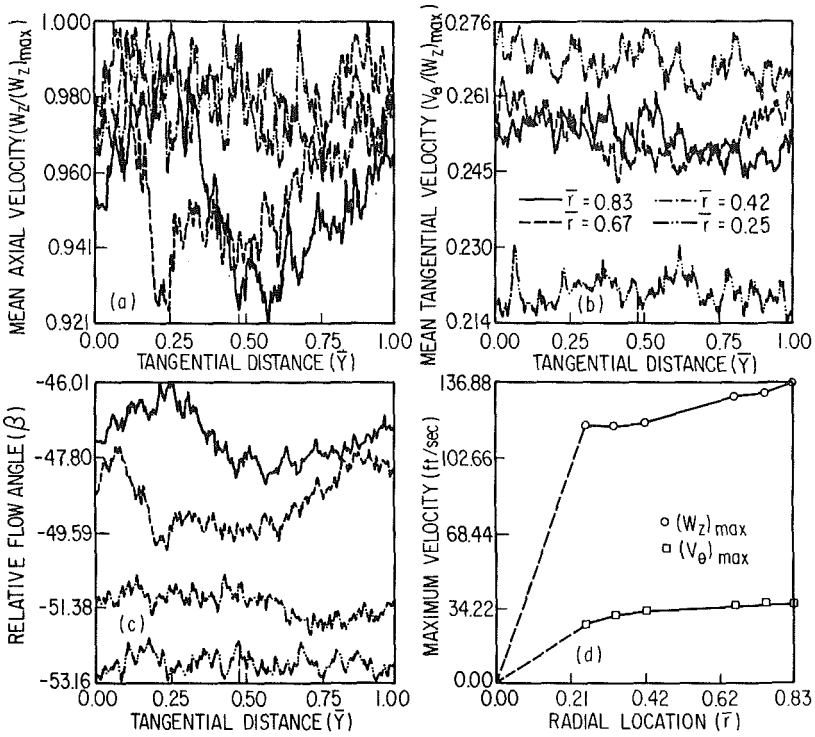

Fig. 10 Variation of mean flow properties at $Z = 1.055$

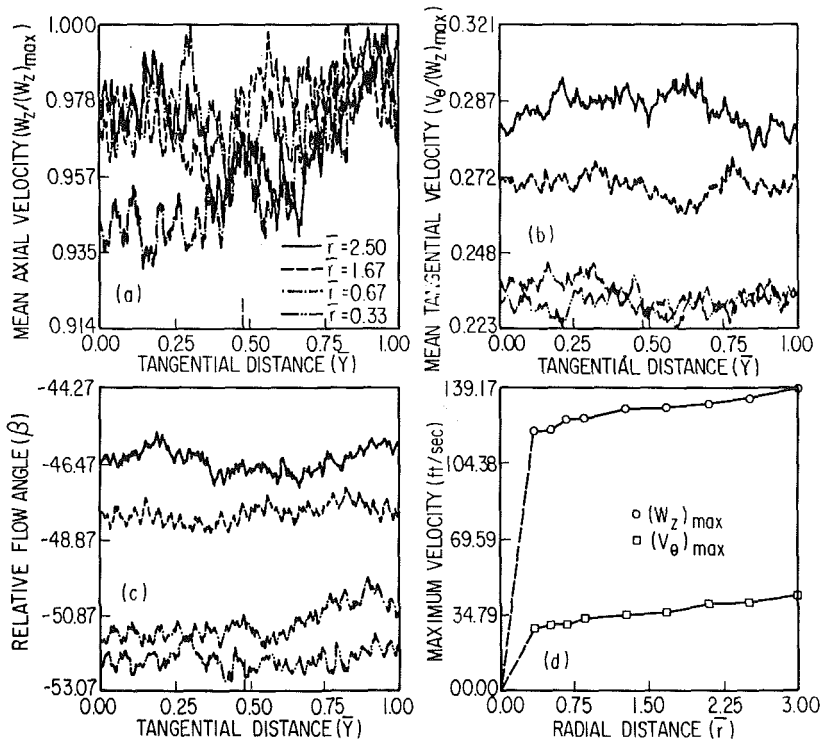

Fig. 11 Variation of mean flow properties at $Z = 1.179$

the wall. A maximum occurs at approximately 57 percent of the clearance height from the wall.

The flow field at the next axial station at $Z = 0.979$ (Fig. 9) has features similar to the previous axial station, only it is less pronounced. This may be due to a rather small blade-pressure difference and/or due to the fact that the thickness of the blade is quite small at this location and a clearly defined clearance region does not exist. The presence of a leakage vortex, characterized by low axial velocity and low tangential velocity, is evident near the suction surface of the blade. The relative flow angles are also large in this region, indicating a large region of underturning. A defect in W_z is observed near $\bar{y} = 0.250$ at $\bar{r} = 0.167$ and may indicate the presence of a scraping vortex. The maximum axial and tangential velocities plotted in Fig. 9 indicates that these are substantially the same as those at $Z = 0.75$. The axial velocity variation across the passage shows near uniform flow, except at the tip vortex region. This seems to indicate that the separated region observed near the suction side at $z = 0.75$ has been reduced.

A comparison of Figs. 6(*c*), 7(*c*), and 9(*c*) shows that there

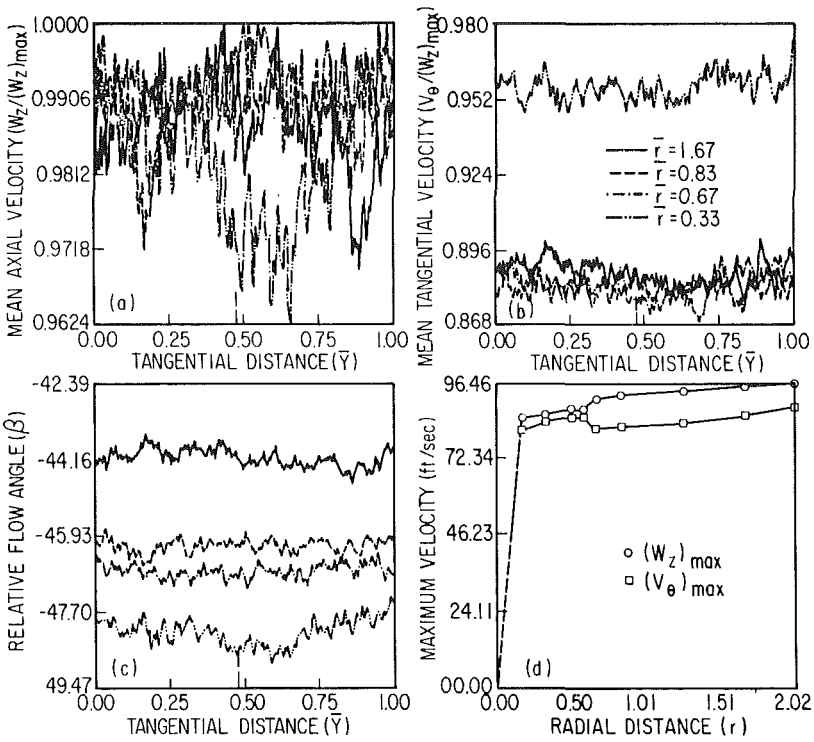

Fig. 12 Variation of mean flow properties at $Z = 1.731$

is a considerable variation of the relative flow angle with the radius. This seems to indicate a large underturning of the flow near the annulus wall.

Velocity Profiles and Angles at the Exit of the Rotor. Figures 10–12 provide information regarding the rotor exit flow. Figure 10 shows the variation of mean properties at $Z = 1.055$. From Fig. 10(*a*), it can be observed that the mean axial velocity variation shows a trend similar to that of a wake at the radial station very near the blade tip ($\bar{r} = 0.83$). This wake profile is marked by a minimum in the velocity at $\bar{Y} = 0.60$. The wake width is large. The blade wake may have moved towards the wall at the trailing region due to the radial outward transport inside the blade boundary layer. The suction side again shows the presence of separated regions. At $\bar{r} = 0.67$, this wake seems to be spreading, and instead of a sharp minimum as observed at $\bar{r} = 0.83$, the velocity remains minimum from $\bar{y} = 0.2$ to 0.55. However, the defect in velocity is small. This implies that there is a strong interaction between the exit flow and the annulus-wall boundary layer. The presence of a leakage vortex is not evident at these two radial locations, indicating the radially downward movement or dissipation of the vortex. At the last two radial stations near the wall ($\bar{r} = 0.47, 0.25$), the mean axial velocity seems to be fairly uniform. Compared to the variations in the axial velocity at the trailing edge, W_z variations at this station are very small.

The variation of V_θ in Fig. 10(*b*) shows a uniform distribution of the velocity across the passage for all the radial locations. Variation of β also shows a similar behavior. The variations in β from one radial location to the other are not very large (7 deg), indicating a uniform turning of the flow at all the radial locations.

Figure 10(*d*) shows a very interesting feature. The maximum axial velocities are very high compared to the maximum tangential velocities at all the radial locations. There is a sudden jump in the axial velocity from those measured at the previous axial station (trailing edge). This may be attributed partly to the absence of the blockage effect of the blade present inside the passage.

The next axial location ($Z = 1.179$) was farther from the blade and it was possible to probe the flow field within 4 percent of the blade span from the tip. Consequently, it was possible to capture the details of the wake near the blade. Figure 11(*a*) shows that at $\bar{r} = 2.5$, the mean axial velocity is minimum between $\bar{Y} = 0.4$ to $\bar{Y} = 0.7$. A similar profile exists for $\bar{r} = 1.67$. The actual variations in the velocity, however, are quite small, indicating a rapid decay of the wake. At $\bar{r} = 0.67$, the velocity remains uniform through most of the passage, with a rapid increase at $\bar{Y} = 0.70$. At $\bar{r} = 0.33$, W_z is fairly uniform.

Tangential velocity variations shown in Fig. 11(*b*) indicate a fairly uniform flow at all the radial locations. The variation of the V_θ in radial direction is not very large (6 percent). The same is true for β also. The maximum velocity variations shown in Fig. 11(*b*) do not reveal any remarkable change in the behavior from the previous axial station except for the fact that the difference in the two velocity components is decreasing continuously.

The measurements at the two subsequent axial stations ($Z = 1.44$ and 1.593) are not reported here, as they indicated that the flow field was becoming more or less uniform and had reached near equilibrium conditions. However, the tangential velocities were considerably smaller than the axial velocities at these locations. Figure 12 shows that at $Z = 1.731$, both the components of the velocity and the relative flow angle are uniform in the tangential direction, and the difference between the two components of the velocity is very small.

Leakage Velocity. In the absence of any clearance between the rotor blade and the annulus wall, the flow should follow the blade contours near the blade surfaces and the velocity component in the direction normal to the blade should be zero. Any deviation of the flow from the blade contour in the tip-clearance region will give rise to a component normal to the blade, which is termed as the leakage velocity in this paper. A true representation of the leakage flow should take into account the normal component of the velocity at the inlet (W_{N_0}). The change in the velocity triangle due to leakage flow

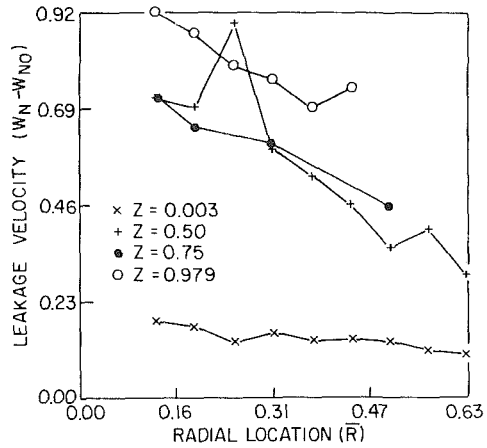

Fig. 13 Variation of the leakage velocity at the suction surface

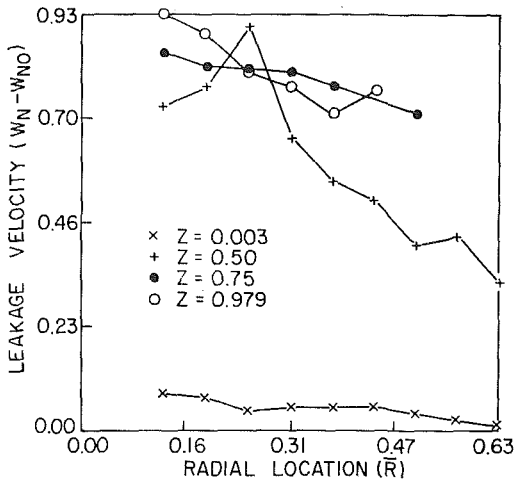

Fig. 14 Variation of the leakage velocity at the pressure surface

is shown in Fig. 8. W_N is the leakage velocity in the terminology adopted in this paper. In deriving the values of W_N near the blade surfaces, the value of β in Fig. 8 is taken to be respective blade surface angles.

Figures 13 shows the variation of the leakage velocity at the suction surface ($W_N - W_{N_0}$) in the radial direction for four axial locations inside the passage. The velocities are normalized by the blade-tip speed and the inlet component subtracted from it. At the leading edge, the leakage velocity is very small, which is in accordance with the fact that the pressure gradient across the blade is very small in this region. A considerable jump in the leakage velocity at $Z = 0.50$ is due to the existence of a large pressure gradient across the blade. There is no appreciable change in ($W_N - W_{N_0}$) from $Z = 0.50$ to $Z = 0.75$. The leakage velocity at the trailing edge is larger than that at $Z = 0.50$, which does not seem to follow from the argument based on pressure gradient alone. This may result from the formulation of the leakage vortex, and the consequent entrailment by the vortex. It is also evident that the leakage velocities are maximum away from the annulus wall and the blade tip. A plot of these velocities (Fig. 14) near the pressure surfaces shows a similar trend.

Velocity Vector Plots. Figures 15 and 16 show the relative velocity vectors in the z-θ plane at two different radii. At $\bar{R} = 0.3125$, as indicated in Fig. 15, the flow follows the blade contour at the leading edge, implying the absence of any leakage flow. This agrees well with the expected trend. At $Z = 0.5$, the flow has turned towards the tangential direction, giving rise to a substantial leakage velocity as shown in Fig.

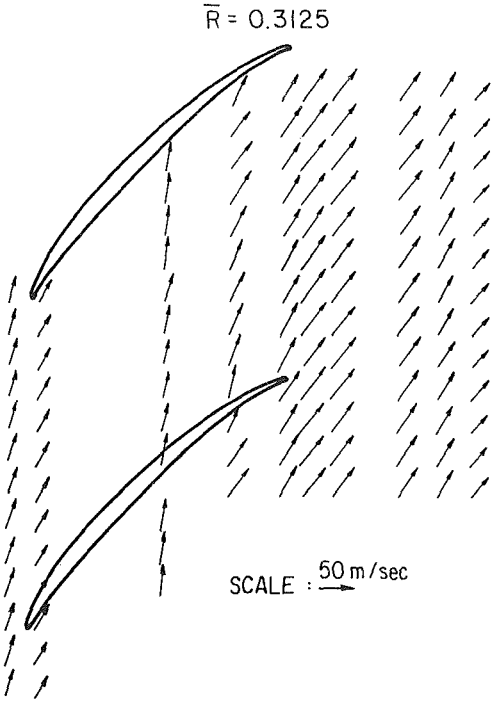

Fig. 15 Relative velocity vectors (W) inside the clearance region at $\bar{R}$ = .3125

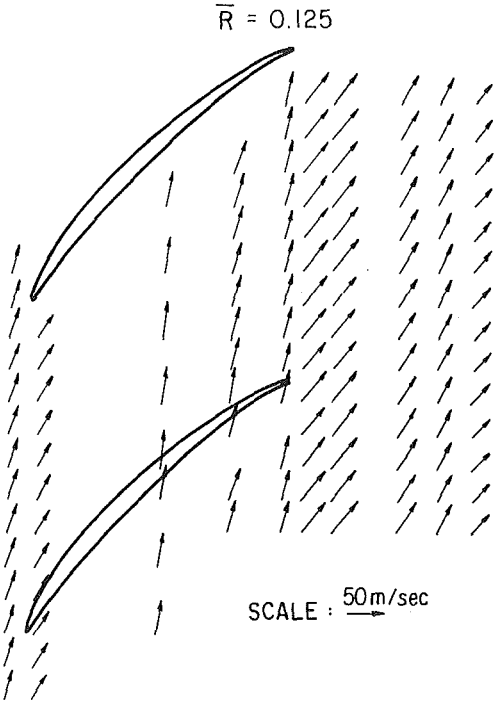

Fig. 16 Relative velocity vectors (W) inside the clearance region at $\bar{R}$ = .125

13. An abrupt change in the flow angle approximately at the middle of the passage can be attributed to the rolling of the leakage flow as discussed earlier and in reference [9]. At $Z = 0.75$, a large change in the flow angle from the pressure surface to the suction surface observed experimentally shows the effect of a predominant leakage flow in this region. A similar change is evident at $Z = 0.979$. A similar vector diagram at $\bar{R} = 0.125$ (Fig. 16) shows all the features mentioned above, but the main difference is in the relative flow angle, which is more inclined toward a tangential direction at the radial location nearer to the annulus wall. In both the

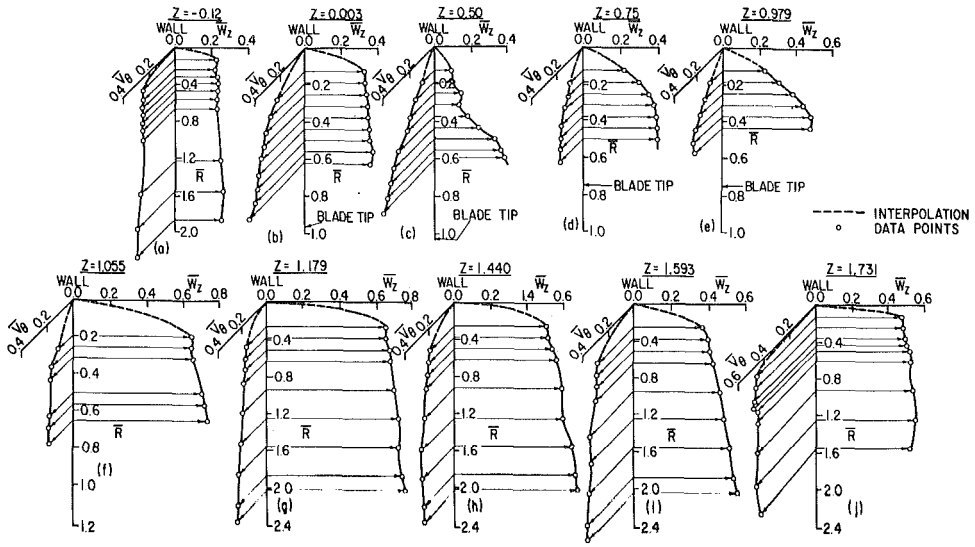

Fig. 17 Measured development of the annulus-wall boundary layer ($\bar{W}_z$ and $\bar{V}_\theta$ are passage-averaged values)

cases, the flow near the wall is nearly axisymmetric at the exit, indicating that the leakage flow and the vortex may have moved downward.

Annulus-Wall Boundary Layer Profile. The radial variation of the axial and absolute tangential velocities averaged over the passage at various axial locations is plotted in Fig. 17. The annulus-wall boundary layer profile within the passage, from 4 to 22 percent span, is given in [9]. Figure 17 gives an overall picture of the boundary layer growth as the flow proceeds from the inlet to the rotor and then downstream, where the flow has become nearly uniform across the passage.

At $Z = -0.012$, the radial gradient in velocity is very sharp near the wall. This indicates that the shear stresses in this region should be large. The tangential and axial velocities are of the same order of magnitude, even though the axial velocity is found to be nearly twice as much as the tangential velocity [9] in the free stream. As the flow approaches the leading edge ($Z = 0.003$), these large velocity gradients are reduced, and both axial and tangential velocities increase away from the wall. The axial velocity undergoes a dramatic change from $Z = 0.003$ to $Z = 0.5$, with considerable reduction in its magnitude at most clearance locations. The tangential velocity profile undergoes a very small change from $Z = 0.003$, to $Z = 0.5$, indicating little or no energy transfer from blade to blade flow. The effect of the leakage flow and its interaction with the annulus-wall boundary layer can be clearly seen at $Z = 0.5$. As indicated earlier, the boundary layer may be getting washed off by a strong leakage jet, resulting in such an unconventional boundary layer. The annulus-wall boundary layer profile in the clearance region from $Z = 0.75$ to 0.979 (Fig. 17(*d*) and 17(*e*)) indicate that the leakage flow has either reached an equilibrium stage or has moved downward along the radius, providing a rather smooth profile with very little variation from $Z = 0.75$ to 0.979, even though there is a slight increase in the axial velocity towards the trailing edge.

A dramatic change occurs as the flow leaves the blade trailing edge. The axial velocity increases by almost 50 percent and tangential velocities decrease only slightly. The change in profile from trailing edge to $z = 1.731$ indicates that the flow redistribution occurs continuously downstream, even though the flow is nearly uniform from blade to blade.

Conclusions

The following conclusions can be drawn from the detailed measurements carried out inside the tip clearance region of the rotor passage as well as the exit.

1 The flow very near the leading edge shows the usual features of the annulus-wall boundary layer, with perturbations caused by the scraping effect.

2 The presence and interaction of leakage flow, annulus-wall boundary layer, and the scraping vortex is the dominant feature at mid-chord position. The rotation of the blade augments the leakage flow, resulting in the movement of the leakage jet towards the mid-passage. This feature is observed from the measurement.

3 The blade-to-blade distribution of properties is highly nonuniform, except in the downstream and upstream regions.

4 The leakage flow develops considerably at 75 percent chord length. Leakage flow is the most predominant feature at this location, and the rolling up of the leakage flow takes place approximately midway between the passage. The flow at the trailing edge shows a similar trend. The measurements indicate the presence of separated regions near the suction side at mid-chord and the trailing edge locations.

5 A marked increase in the axial velocity and a considerable decrease in the tangential velocity characterizes the flow leaving the rotor blade passage in the annulus-wall region. A weak wake profile in the axial velocity is observed near the blade tip, but it rapidly decays as the flow approaches the annulus wall.

6 A rapid decay of the wake profile takes place in the axial direction downstream of the blade and the flow becomes nearly uniform after 20 percent of the chord downstream of the rotor. A large difference between the values of the two components of the velocity still exists beyond 20 percent chord downstream. A continuous redistribution of the flow takes place up to 75 percent of the chord downstream where both the components of the velocity are found to be of the same order of magnitude.

7 Leakage velocity measurements derived from the data show that it is very small at the leading edge and increases at mid-chord. At 75 percent chord, the leakage velocity is slightly less than that at mid-chord, but it is maximum at the trailing edge.

8 The vector plot indicates the flow is underturned in most regions inside the passage. This underturning decreases drastically as the flow leaves the blade trailing edge.

9 The annulus-wall boundary layer profile, based on the passage-averaged mean velocity, indicates substantial changes in the mid-chord and the exit regions.

Acknowledgments

This work was supported by the National Aeronautics and Space Administration through Grant No. NSG 3212, with P. M. Sockol as the project monitor.

References

1 Dean, R. C., "Influence of Tip Clearance on Boundary Layer Characteristics in a Rectilinear Cascade," M.I.T., G.T.L. Report No. 27-3, 1954.

2 Lakshminarayana, B. and Horlock, J. H., "Leakage and Secondary Flows in Compressor Cascades," British ARC R and M 3483, Her Majesty's Stationary Office, London, 1967, pp. 1-58.

3 Lakshminarayana, B., "Methods of Predicting the Tip Clearance Effects in Axial Flow Turbomachinery," *Journal of Basic Engineering*, Vol. D92, Sept. 1970, pp. 467-482.

4 Phillips, W. R. C. and Head, M. R., "Flow Visualization in the Tip Region of a Rotating Blade Row," *International Journal of Mechanical Science*, Vol. 22, Jan. 1980, pp. 495-521.

5 Booth, T. C., Dodge, P. R., and Hepworth, H. R., "Rotor Tip Leakage Part I—Basic Methodology," JOURNAL OF ENGINEERING FOR POWER, Vol. 104, No. 1, Jan. 1982, pp. 154-161.

6 Herzig, H. A., Hansen, A. G., and Costello, G. R., "A Visualization Study of Secondary Flows in Cascades," NACA T R 1163, 1953.

7 Davino, R. and Lakshminarayana, B., "Characteristics of Mean Velocity in the Annulus Wall Region at the Exit of Turbomachinery Rotor Passage," *AIAA Journal*, Vol. 20, No. 4, Mar. 1982, pp. 528-535.

8 Ravindranath, A., "Three-Dimensional Mean and Turbulence Characteristics of the Near Wake of a Compressor Rotor Blade," M.S. thesis, Department of Aerospace Engineering, The Pennsylvania State University, 1979.

9 Lakshminarayana, B., Pouagare, M., and Davino, R., "Three-Dimensional Flow Field in the Tip Region of a Compressor Rotor Passage—Part 1: Mean Velocity Profiles and Annulus Wall Boundary Layer," JOURNAL OF ENGINEERING FOR POWER, Vol. 104, No. 4, Oct. 1982, pp. 760-771.

10 Lakshminarayana, B., Davino, R., and Pouagare, M., "Three-Dimensional Flow Field in the Tip Region of a Compressor Rotor Passage—Part II: Turbulence Properties," JOURNAL OF ENGINEERING FOR POWER, Vol. 104, No. 4, Oct. 1982, pp. 772-781.

11 Pandya, A., "Investigation of the Tip-Clearance Flow Inside a Compressor Rotor Passage and at the Exit of the Rotor," M.S. thesis, Department of Aerospace Engineering, The Pennsylvania State University, Mar. 1982.

12 Smith, L. H., "Three-Dimensional Flow in an Axial Flow Turbomachinery," WADC Technical Report 55-348, Vol. 2, John Hopkins University, 1956.

13 Lakshminarayana, B., "An Axial Flow Research Compressor Facility Designed for Flow Measurement in Rotor Passages," ASME *Journal of Fluids Engineering*, Vol. 102, No. 4, Dec. 1980, pp. 402-411.

14 Poncet, A. and Lakshminarayana, B., "Three-Dimensional Analysis and Measurement of the Flow in a Three-Bladed Rocket Pump Inducer," NACA CR-2290, 1973, pp. 1-126.

Investigation of the Tip Clearance Flow Inside and at the Exit of a Compressor Rotor Passage—Part II: Turbulence Properties[1]

A. Pandya[2]
Graduate Assistant.

B. Lakshminarayana
Director of Computational Fluid Dynamics Studies and Professor of Aerospace Engineering.
Fellow ASME

Department of Aerospace Engineering,
The Pennsylvania State University,
University Park, Pa. 16802

The flow in the tip clearance region of a compressor rotor is highly turbulent due to the strong interaction of the leakage flow with the annulus wall boundary layer. This paper deals with the turbulence properties of the flow in the tip clearance region of a moderately loaded compressor rotor. The experimental results reported in this paper were obtained using a two-sensor hot-wire probe in combination with an ensemble averaging technique. Blade-to-blade distribution of the axial and tangential turbulence intensities at various radial locations and ten axial locations (four inside the blade passage and the remaining six outside the passage) were derived from this data. Isointensity contours in the clearance region at various radial locations were also obtained from the experimental data. A region of very high turbulence intensities was indicated at the half-chord location from these results. The turbulence intensity profiles also indicated that the leakage flow travels toward the midpassage before rolling up. The turbulence is almost isotropic beyond three-quarter chord downstream of the trailing edge.

Introduction

This paper is concerned with an experimental investigation of the flow field inside the tip clearance region of a compressor rotor. The mean velocity data in this region was presented in [1]. The turbulence data in this region is presented and interpreted in this paper. The major objective of this investigation is to get a deeper understanding of the flow field for future modeling/analysis/computation of the tip clearance flow. Furthermore, the turbulence influences the losses in this region; hence, this study should help in the development of a tip clearance loss model. The companion paper [1] has a listing of various measurements taken in regions away from the blade tip.

It is important to note that the experimental results presented in this paper are obtained using a two-sensor hot-wire probe. Hence, only the axial and the tangential components of the flow field properties are obtained. Near the end wall, the streamlines are expected to be almost parallel to the wall, and hence the velocity component in the radial direction should be very small. However, the turbulence intensity in the radial direction would introduce an error in the calculation of the axial and tangential turbulence intensities. A detailed discussion of the errors involved is given in [2]. Nevertheless, in view of the fact that no flow field measurements are available in this region, the relative levels of the turbulence intensities do provide important information regarding the nature of interaction among the various flow structures present in the annulus wall region.

The measurements reported in this paper were made in the axial flow compressor facility located in the turbomachinery laboratory at The Pennsylvania State University using a two-sensor hot-wire probe in combination with an ensemble averaging technique. The flow field was surveyed at various radial locations and at ten axial locations, four of which were inside the blade passage in the clearance region and the remaining six outside the passage. A detailed description of the experimental set-up, instrumentation, measurement technique, and data processing is given in the companion paper [1].

Experimental Results

Turbulence Intensity Profiles. Blade-to-blade distributions of the axial and the tangential turbulence intensities at various radial and axial locations are shown in Figs. 1–8. The blade locations are marked by broken lines on the $\bar{Y}$-axis. Both the turbulence intensity components are normalized by the local maximum total velocity (maximum at any given radial and axial location), since the turbulence is dependent upon the local flow conditions. The normalizing velocities are listed in Table 1.

Figure 1 shows the axial and the tangential turbulence intensity profiles at the inlet of the rotor. It is evident from

[1] This is a companion paper to reference [1]. Mean flow properties are presented in reference [1]; this paper deals with the corresponding turbulence properties.

[2] Presently at Memorex Corporation, RTC Division, Santa Clara, California.

Contributed by the Gas Turbine Division for publication in the JOURNAL OF ENGINEERING FOR POWER. Manuscript received by the Gas Turbine Division November 3, 1982.

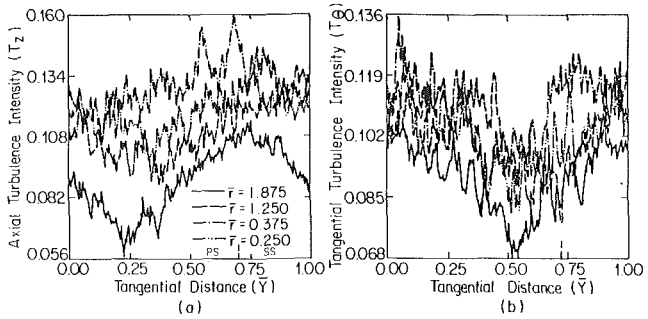

Fig. 1 Variation of turbulence intensities at the inlet of the rotor (Z = −0.012)

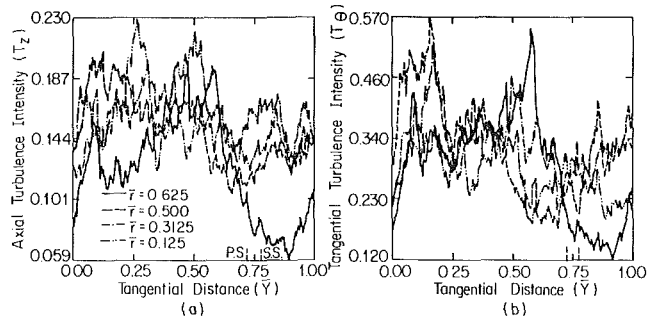

Fig. 2 Variation of turbulence intensities at the leading edge (Z = 0.003)

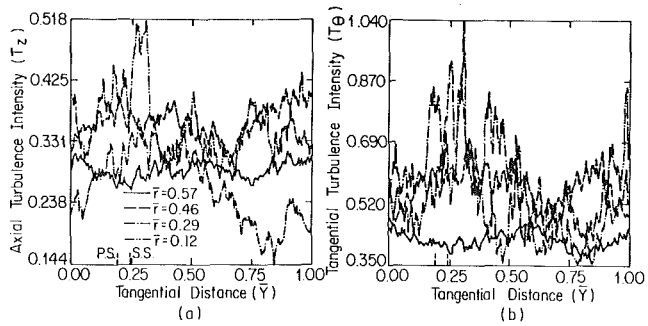

Fig. 3 Variation of turbulence intensities at 1/2 chord (Z = 0.50)

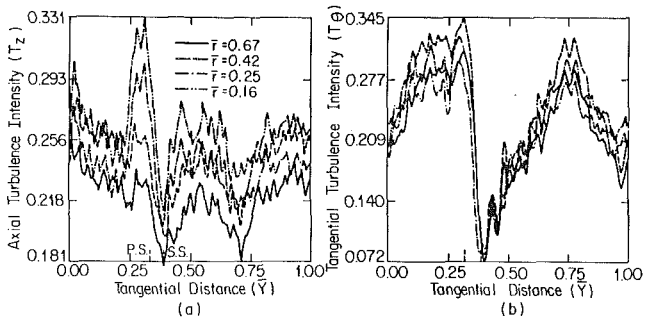

Fig. 4 Variation of turbulence intensities at 3/4 chord (Z = 0.75)

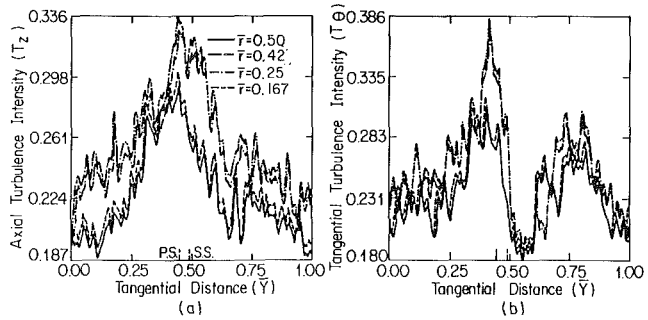

Fig. 5 Variation of turbulence intensities at the trailing edge (Z = 0.979)

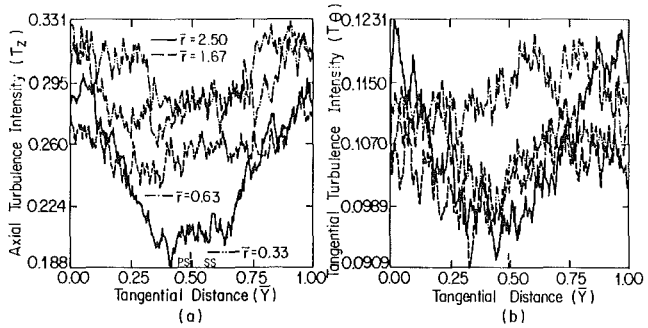

Fig. 6 Variation of turbulence intensities at Z = 1.055

Nomenclature

L.E. = leading edge
P.S. = pressure surface
$\bar{r}$ = distance from the annulus wall normalized by (*i*) clearance at L.E. for rotor inlet flow, (*ii*) local clearance for flow inside the passage, and (*iii*) clearance at T.E. for rotor exit flow
S.S. = suction surface
T = turbulence intensity normalized by local maximum mean total velocity $[(\overline{w^2})/(W_z^2 + V_\theta^2)_{\max}]^{1/2}$
T.E. = trailing edge
U = rotational velocity Ωx radius
V = mean velocity in stationary frame of reference
W = mean velocity in relative frame of reference
w = fluctuations in the relative mean velocity
$\bar{Y}$ = distance from the fixed line 0-0 in the tangential direction normalized by the blade spacing (Fig. 3, [1])
z = axial coordinate direction corresponding to the axis of the compressor
Z = axial distance from the rotor blade leading edge normalized by the axial chord (Fig. 3, [1])
Ω = rotational speed rpm
τ = distance from the annulus wall in radial direction
ϕ = mass-averaged flow coefficient for the stage

Subscripts

max, MAX = maximum value in the passage
tip = value at the tip of the rotor blade
z,θ,r = values in axial, tangential, and radial directions, respectively

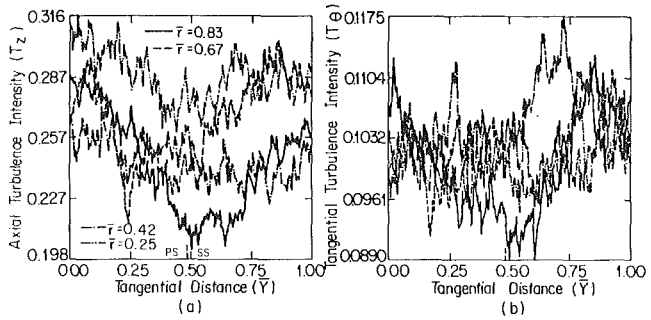

Fig. 7 Variation of turbulence intensities at $Z = 1.179$

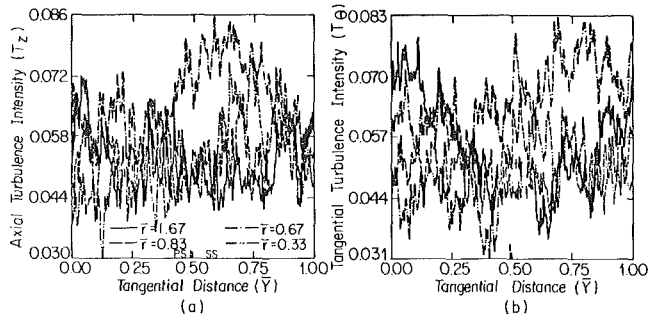

Fig. 8 Variation of turbulence intensities at $Z = 1.731$

Table 1 Maximum total velocities [a] at radial and axial stations of measurement at $\phi = 0.55$

$\bar{r}$ \ Z	−0.012	0.003	0.50	0.75	0.979	1.055	1.179	1.440	1.593	1.731
1.875	0.409	–	–	–	–	–	0.772	0.714	0.660	–
1.5625	0.390	–	–	–	–	–	0.765	0.693	0.638	0.697
1.25	0.377	–	–	–	–	–	0.750	0.650	0.597	0.723
1.0	–	–	–	–	–	–	–	0.629	–	–
0.9375	–	–	–	–	–	–	0.718	–	0.546	0.703
0.75	–	–	–	–	–	–	–	0.615	–	–
0.625	0.337	0.613	0.604	–	–	0.800	0.709	–	0.517	0.693
0.5625	0.348	–	–	–	–	0.740	–	–	–	–
0.5	–	0.493	0.436	0.551	–	0.716	0.687	0.575	0.496	0.683
0.4375	–	–	–	–	0.516	–	–	–	–	0.698
0.375	0.342	–	–	–	0.530	0.687	0.662	0.553	0.489	0.682
0.3125	0.345	0.460	0.300	0.539	0.484	–	–	–	–	–
0.25	0.322	–	–	–	0.420	0.674	0.667	0.538	0.462	0.667
0.1875	–	–	–	0.426	0.343	0.660	–	–	–	–
0.125	0.340	0.386	0.160	0.305	0.256	–	–	–	–	–

[a] All the velocities are normalized by the blade tip speed U_{tip} (53.50 ms)

this figure that both components of intensities increase as the annulus wall is approached. The intensities have peaks at $\bar{r} = 0.375$ and decrease continuously away from the wall. The velocity gradients are high near the wall because of the annulus wall boundary layer, which implies greater mixing. Hence higher turbulence intensities near the annulus was are expected. However, as the viscous sublayer approaches, the turbulence intensities decrease considerably. This explains the slight decrease in the intensities at $\bar{r} = 0.25$. Blade-to-blade variation of the axial and tangential turbulence intensities (Fig. 1) show some effects of the unsteady flow field downstream. The turbulence intensities vary as much as 50 percent in tangential direction.

Figure 2 shows the variation of T_z and T_θ inside the passage at the leading edge ($Z = 0.003$). A noticeable dragging effect of the blade on the flow can be evidenced by a considerable increase in the tangential velocity. The drastic increase in the tangential turbulence intensities from $Z = -0.012$ to $Z = 0.003$ support the above conclusion. Also, the decrease in T_θ near the blade surface and its increasing trend towards the middle of the passage supports the conclusions drawn from mean velocity profiles in [1] that the flow separates near the blade surface. The presence of the blade scraping effect is clearly evident at this location. An increase in T_z is also observed at this station, but this increase is quite small compared to the increase in T_θ. It is interesting to note that the blade-to-blade distributions of both T_z and T_θ show a large variation at the radial locations close to the blade tip. However, the radial stations close to the annulus wall show more uniform distribution of T_z and T_θ, though the level of intensities is higher at these stations compared to the stations near the blade tip. This implies that the effect of flow separation and dragging diminishes near the annulus wall. The dominant effect in this region is that caused by the shear gradient due to the annulus wall boundary layer.

Figure 3 shows blade-to-blade variation of T_θ and T_z for four radial locations at midchord position ($Z = 0.50$). As discussed in the case of mean velocity profiles, the flow at this axial station is quite complicated. A very high level of interaction of the leakage flow with the annulus wall boundary layer, secondary flow, and vortex generated by the scraping of the annulus wall boundary layer is indicated by the presence of very high turbulence intensities in the tangential direction. In contrast to the flow behavior at the leading edge, the blade-to-blade distribution of T_z and T_θ at radial locations close to the tip of the blade is nearly uniform, while the two stations ($\bar{r} = 0.29$ and 0.12) near the annulus wall show large variation in the tangential direction. The variation in T_θ at $\bar{r} = 0.12$ is nearly 65 percent, while at $\bar{r} = 0.29$ it is approximately 55 percent. The T_z variation in both the cases is about 20 percent. This trend in the flow behavior indicates the presence of a strong leakage jet which washes away the annulus wall boundary layer, causing a very high level of mixing in the region close to the annulus wall. This is in agreement with the similar inference derived from the mean velocity data in [1].

For $\bar{r} = 0.29$ and 0.12, Fig. 3(*b*) indicates a low turbulence region near $\bar{y} = 0.80$; and on either side of this low turbulence region, T_θ increase. The vortex generated due to the rolling up of the leakage flow is indicated in this region. The vortex formation is closer to the pressure surface of the blade. The pressure difference across the blade tip is high at $Z = 0.5$; hence, the leakage flow velocity is expected to be high. A high leakage velocity is further augmented by the blade rotation. Hence, as pointed out above, the leakage flow should travel further away from the suction surface before rolling up. However, it should be noted here that the axial and tangential

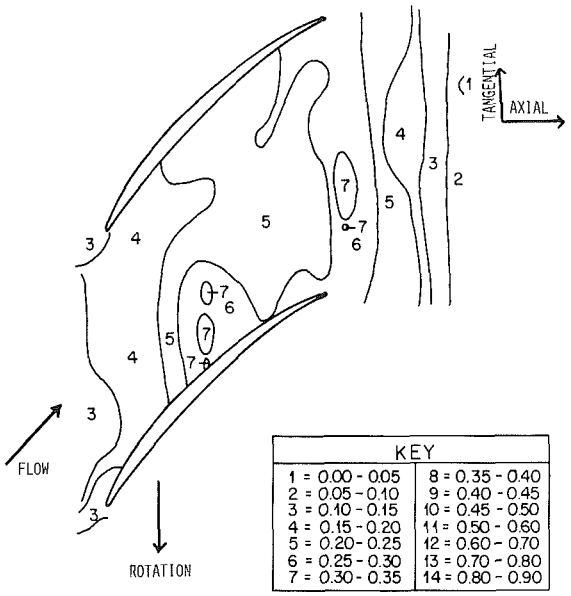

Fig. 9 Isocontours for axial turbulence intensity at $\bar{R} = 0.3125$

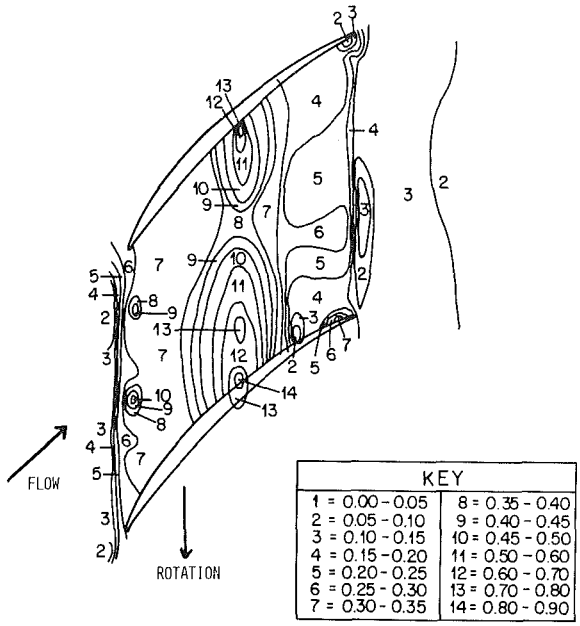

Fig. 11 Isocontours for tangential turbulence intensity at $\bar{R} = 0.3125$

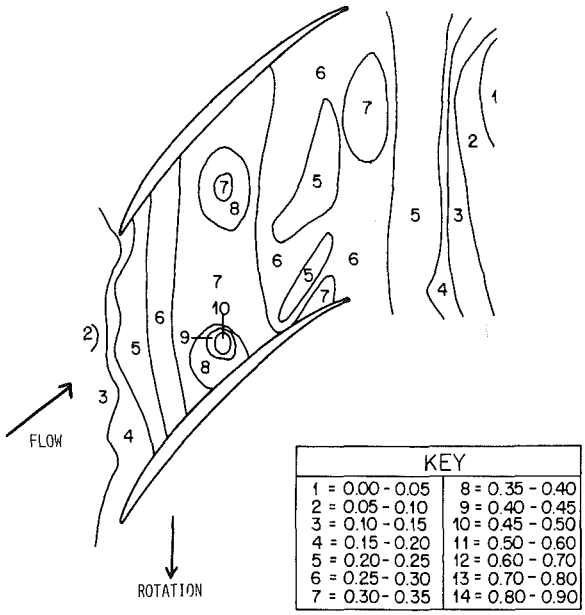

Fig. 10 Isocontours for axial turbulence intensity at $\bar{R} = 0.125$

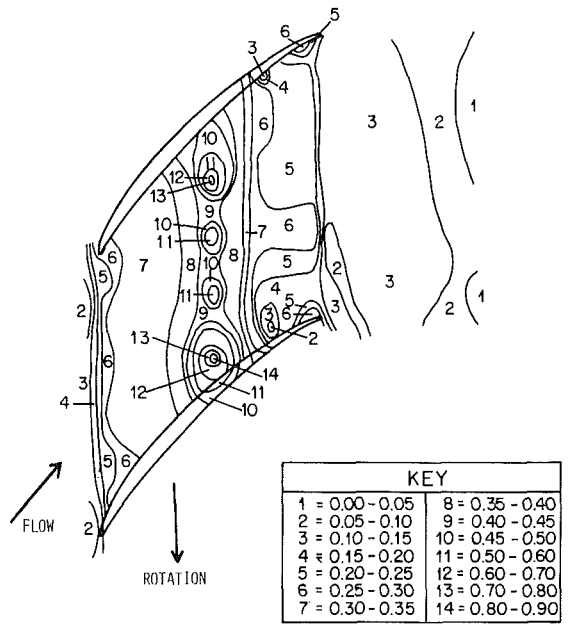

Fig. 12 Isocontours for tangential turbulence intensity at $\bar{R} = 0.125$

components of the mean velocity and the turbulence intensities by themselves are insufficient to predict the exact nature of the interaction among the various flows present in the end wall region and the exact nature of mixing. Additional information on the variation of the radial component of the mean velocity and the radial turbulence intensity is needed for interpreting the above data in further detail.

Variations of T_z and T_θ at three-quarter-chord location ($Z = 0.75$) are shown in Fig. 4. A well-defined behavior of the flow inside the tip clearance is evident. As can be seen from this figure, there is a sudden decrease in both T_z and T_θ inside the tip clearance region. The narrow passage formed between the blade tip and the annulus wall tends to channelize the leakage flow which results in reduced turbulence intensities. The blade-to-blade distribution of T_θ, as shown in Fig. 4(b), is very similar to that of $V_\theta/(W_z)_{\max}$, shown in Fig. 7 of [1]. The former shows a peak at $\bar{y} = 0.75$ for all the radial locations, after which T_θ starts decreasing. This clearly indicates the presence of a vortex due to rolling up of the leakage flow or scraping of the boundary layer. The variation of mean axial velocity $W_z/(W_z)_{\max}$ is also in agreement with the T_θ variation. The local minima in $W_z/(W_z)_{\max}$ at $\bar{Y} = 0.75$ corresponds to the maxima in T_θ at the location for all the radial stations.

Figure 4(a) shows a local minima near $\bar{r} = 0.67$ for all the four radial locations. This, accompanied with the radial velocity distribution, should indicate the presence of a leakage vortex. However, the radial velocity measurements are not available in this region, making it difficult to interpret the data completely. Comparing the T_θ and T_z distributions at this location ($Z = 0.75$), several interesting features of the flow field can be observed. In the case of the T_θ distribution, the four curves at different radial stations nearly overlap each other, while the T_z distribution for different radial locations shows four distinct curves, even though the profiles are

similar. It can be inferred from this behavior that in the tangential direction the leakage flow is very prominent and the effect of the annulus wall boundary layer on the turbulence is very weak. However, in the axial direction, the effect of the annulus wall boundary layer is noticeable in the form of increasing intensity towards the annulus wall. The axial turbulence intensity shows a decrease of about 20 percent from the previous axial station at $Z = 0.5$. The decrease in the tangential turbulence intensity is very large, indicating a stabilized leakage flow.

The T_θ distribution at $Z = 0.979$, as shown in Fig. 5(*b*), is very similar to that at $Z = 0.75$. One noticeable difference is in the magnitude and location of the local maxima, which is smaller and has shifted slightly towards the suction surface. Since the pressure drop across the blade is very small, the leakage flow starts rolling up closer to the suction surface, as indicated by the position of the local maxima in T_θ. T_z distribution, as illustrated in Fig. 5(*a*), shows a peak near the pressure side of the blade, decreases continuously till the middle of the passage, and then increases again. There is no appreciable difference in the level of T_θ and T_z from that at $Z = 0.75$.

The flow at the exit of the rotor in close proximity to the annulus wall is characterized by low turbulence intensity in the tangential direction. Figure 6 shows T_θ and T_z distributions at $Z = 1.055$. The tangential turbulence intensity distribution in Fig. 6(*b*) is almost uniform for all the radial locations. Also, the T_θ values are very much lower than those at the last station inside the rotor passage. The leakage flow effects vanish very rapidly outside the passage. Figure 6(*a*) shows that T_z decreases near the blade surface and increases towards the middle of the passage for two radial locations near the blade tip, while the stations closer to the wall show more or less uniform mixing. The turbulence characteristics of the flow at $Z = 1.179$, as shown in Fig. 7, are very similar to those at $Z = 1.055$.

At $Z = 1.440$ and $Z = 1.593$, the blade-to-blade variations of T_θ and T_z are almost uniform at all the radial locations. However, the T_z component is nearly twice as large as the T_θ component at $Z = 1.440$. The trend towards achieving an isotropic flow condition is reflected is the slowly decreasing axial turbulence intensity level. At $Z = 1.73$ (Fig. 8), both components of the turbulence intensities are of the same order, and the blade-to-blade variation of these components is nearly uniform at all the radial locations. The turbulence intensities vary from 3 percent to 8.5 percent.

Isoturbulence Intensity Contours in the Z-θ Plane. The contours of equal intensities in the clearance region at $\bar{r} = 0.3125$ and $\bar{r} = 0.125$ are shown in Figs. 9–12. Figures 9 and 10 show the isocontours for axial turbulence intensity. The overall level of turbulence is slightly higher at $\bar{r} = 0.125$ than that at $\bar{r} = 0.3125$. In both cases, peak intensities occur slightly away from the suction surface at $Z = 0.50$. Figures 11 and 12 show the isocontours for tangential turbulence intensity for the same radial locations mentioned above. It can be observed from these figures that maximum flow interaction takes place in the tangential direction. Over a small axial distance from $Z = -0.012$ to $Z = 0.003$, a rapid change in the tangential turbulence intensity level is observed at $\bar{r} = 0.3125$, as shown in Fig. 12. Two pockets of high intensity are observed at approximately one-third and two-thirds of the passage near the leading edge. At $\bar{r} = 0.125$, a similar rapid increase from $Z = -0.012$ to $Z = 0.003$ is observed, but two small regions of high intensity are absent. At $Z = 0.5$, an overall increase in the level of turbulence intensities is observed. As explained earlier in this chapter, maximum leakage velocities and a high level of mixing occur at $Z = 0.5$. At $\bar{r} = 0.125$, peak intensities occur slightly away from the suction surface; while at $\bar{r} = 0.3125$, the peak intensity level is observed very near the clearance region. The level of turbulence decreases as soon as the flow leaves the rotor passage.

Conclusions

The following conclusions can be drawn from the experimental results:

1 The turbulence intensities increase towards the annulus wall because the mean velocity gradients are high near the wall.

2 The turbulence intensity profiles at $Z = 0.003$ indicate the scraping effect of the blade on the flow. The flow separation near the blade surface and the presence of the blade boundary layer scraping are also evident from these profiles.

3 The presence of a high level of turbulence intensities at $Z = 0.50$ indicates a strong interaction of the leakage flow with the annulus wall boundary layer, secondary flow, and vortex generated by the scraping of the annulus wall boundary layer. Both the mean velocity profiles reported in [1] and the turbulence intensity distribution reported in this paper indicate the presence of a strong leakage flow jet which mixes with the annulus wall boundary layer, causing regions of high turbulence intensities.

4 At $Z = 0.75$ and 0.979, turbulence intensities drop suddenly in the tip clearance region.

5 The flow at the exit of the rotor is characterized by low turbulence in the tangential direction. A continuous redistribution of turbulent energy takes place up to 70 percent chord downstream of the rotor trailing edge.

6 The turbulence far downstream of the clearance region is nearly isotropic.

Acknowledgments

This work was supported by the National Aeronautics and Space Administration through contract No. NSG 3212, with P. M. Sockol as the project monitor.

References

1 Pandya, A., and Lakshminarayana, B., "Investigation of the Tip Clearance Flow Inside and at the Exit of a Compressor Rotor Passage, Part I: Mean Velocity Field," ASME Paper 82-GT-12, JOURNAL OF ENGINEERING FOR POWER, Vol. 105, No. 1, 1983, pp. 1–12

2 Pandya, A., "Investigation of the Tip Clearance Flow Inside and at the Exit of a Compressor Rotor Passage," M. S. thesis, Department of Aerospace Engineering, The Pennsylvania State University, Mar. 1982.

D. W. Naegeli
Senior Research Scientist.

C. A. Moses
Manager,
Combustion Technology.

Southwest Research Institute,
San Antonio, Texas 78284

Fuel Microemulsions for Jet Engine Smoke Reduction

The concept of water and alcohol/fuel microemulsions for the purpose of reducing smoke emissions from jet engine test cells was studied in a T-63 gas turbine combustor. Several ethanol/fuel, methanol/fuel, and water/fuel microemulsions were prepared with JP-4 and JP-8 base fuels and the appropriate surfactants; anhydrous ethanol was miscible in both base fuels. These blends reduced radiation and exhaust smoke, increased CO and total hydrocarbon emissions, and decreased combustion efficiency. NO_x was reduced when the surfactant did not contain nitrogen. The reductions in smoke and radiation correlated with changes in the H/C ratio of the fuel blends. Anhydrous ethanol/fuel solutions were most effective in reducing smoke from the standpoint of cost, operational, and systems effects.

Introduction

Soot formation in gas turbine engines continues to be a threat to the operation and performance of military and commercial aircraft. Exhaust smoke forms obvious signatures and is an environmental nuisance, while the flame radiation from incandescent soot particles reduces the life of combustor liners. A recent problem that has arisen is the control of smoke emissions from jet engine test cell facilities.

While it is not legally clear that jet engine test cells are subject to stationary source performance standards, the fact remains that Navy test cells have been cited by state air pollution control officials for violations of plume opacity regulations justifying concern by the Air Force. This situation threatens to worsen as premium petroleum fuels become less available and force the use of jet fuels with lower hydrogen content (higher aromatics) which have a greater propensity to soot.

A concept of water-in-fuel emulsions for the purpose of reducing smoke emissions from jet engine test cells was developed for the U.S. Naval Air Engineering Center. Both T-63 combustor rig tests [1] and a full-scale J-79 engine test [2] were used to confirm the effectiveness of the concept, e.g., in the J-79 testing, a concentration of 15 percent water reduced the observed Ringleman Number from 2.5 to less than 1.

These water-in-fuel macroemulsions were opaque, milky liquids that were formed by homogenization of a water/fuel/surfactant mixture. The water in a macroemulsion is in the form of microdroplets 1–3 microns in diameter dispersed in the fuel and stabilized by a surfactant which reduces the rate of coalescence. Coalescence will eventually cause the water in a macroemulsion to separate from the fuel because the dispersion is not thermodynamically stable but depends on a very low settling rate for stability. The basic problems that were encountered with the water-in-fuel macroemulsions were: (*i*) an energy-intensive mechanical device such as a homogenizer was required for their formation; (*ii*) they had a limited stability because the dispersed phase tends to coalesce, and; (*iii*) it was necessary to account for their decreased energy density when calibrating the engine.

Recently, methods for creating "microemulsions" of water-in-fuel and of alcohol-in-fuel were developed at Southwest Research Institute [3]. Microemulsified fuels form spontaneously by simple mixing of fuel, surfactant, and dispersed phase. Microemulsions may be characterized as a dispersion with a particle size ranging from 0.01 to 0.2 microns that is opically clear or opalescent and, when spun in a laboratory centrifuge for 5 min at 100 G's, will not separate. This class of emulsions then offers a distinct potential for eliminating the first two disadvantages. Alcohol-in-fuel emulsions offer the possibility of at least alleviating the third disadvantage since the energy density would not be reduced as much as with water addition.

The purpose of this work was to determine if the microemulsion concept could be used as a viable method to reduce exhaust smoke from gas turbine engines.

Experimental Program

Several fuel blends of both JP-4 and JP-8 with ethanol, methanol, and water were prepared. All of these fuel blends were microemulsions except the fuels containing anhydrous ethanol, which was soluble and did not require a surfactant. The fuels were burned in a T-63 combustor at realistic operating conditions. Combustion performance measurements included flame radiation, exhaust smoke, gaseous emissions (THC, CO, and NO_x) and combustion efficiency.

Combustor Facilities

This work was performed in the U.S. Army Fuels and Lubricants Research Laboratory (AFLRL) located at the Southwest Research Institute with the Army's permission. This facility was specially designed to study fuel-related problems in the operation of turbine engines. The air supply

Contributed by the Gas Turbine Division of THE AMERICAN SOCIETY OF MECHANICAL ENGINEERS and presented at the 27th International Gas Turbine Conference and Exhibit, London, England, April 18–22, 1982. Manuscript received at ASME Headquarters November 25, 1981. Paper No. 82-GT-33.

Table 1 T-63 combustor rig operating conditions

Mode	Full % power	BIP (psia)	BIT (°F)	*Wa* (lb/s)	*Wf* (lb/m)	*F/A*
Ground idle	10	33.4	300	1.40	0.92	0.0109
Cruise	55	53.6	430	2.06	1.79	0.0145
Climb	75	60.7	472	2.24	2.23	0.0166
Takeoff	100	69.2	524	2.42	2.87	0.0198

Table 2 Summary of fuel properties for JP-4 and JP-8

	JP-4	JP-8
Heat of combustion, Net (Btu/lb)	18,359	18,390
Carbon, % by weight	86.45	86.34
Hydrogen, % by weight	13.54	13.64
Aromatic ring carbon by UV		
Single ring, % by weight	17.2	19.5
Double ring, % by weight	1.1	0.4
Triple ring, % by weight	0.0	0.0
HPLC analysis		
Saturated, % by weight	---	77.4
Aromatics, % by weight	---	22.6
FIA analysis		
Aromatics, % by volume	23.1	23.6
Olefins, % by volume	0.6	2.8
Saturates, % by volume	76.3	73.6
Viscosity at 40°C, (cSt)	0.60	0.96
Flash point, °F	---	106
Freeze point, °C	−72	−67
Specific gravity at 60°F	0.7640	0.7941
Smoke point, mm	53.7	46.7
Aniline point, °C	34.8	50.0
Final boiling point, °C	194	256
H/C atom ratio	1.879	1.896

Table 3 Physical and chemical properties of surfactants

Gross	SOA	Clindrol 100 CG	Clindrol 101 CG
Heat of combustion (Btu/lb)	15,680	14,025	14,405
Hydrogen, wt%	11.73	11.2	11.2
Carbon, wt%	71.49	58.9	59.3
Oxygen, wt%	12.99	25.53	25.13
Nitrogen, wt%	3.79	4.37	4.37
Specific gravity	0.9539	0.9985	0.9896

system provides a clean, smooth flow of air to the combustion test cell at rates up to 1.1 kg/s at pressures to 1620 kPa (16 atm) and temperatures to 1100K (unvitiated). Turbine flow meters and strain-gage pressure transducers are used to measure flow properties of the air and fuel. Thermocouples are referenced to a 339K (150°F) oven. Data reduction is performed on-line with test summaries available immediately; these summaries provide average flow data as well as standard deviations (typically less than 1 percent of average values), exhaust temperature profiles, emissions data, and combustion efficiency.

Combustor Rig. The combustor rig is based on engine hardware from the Allison T-63 engine [4, 5]. The burner is a single-can type with a dual-orifice pressure atomizer centered in the dome. At the burner exit there is a centerbody that directs the flow into an annulus where the nozzles and turbine blades are normally located. Gas-sampling probes, pressure probes, and thermocouples are arranged circumferentially in one plane of this annulus at various radial positions. Table 1 presents the air flow and fuel flow conditions that were established to correspond with various power points following the guidelines of the manufacturer.

Exhaust smoke number was measured in accordance with SAE-ARP1179, and flame radiation from the primary zone was measured with a water-cooled bolometer-type radiation sensor attached to the side of the liner. The sensor had a sapphire window and a viewing angle of 150 deg. Gaseous emissions (CO, CO_2, NO, NO_2, O_2, and THC) were also measured, and combustion efficiency was calculated from the exhaust gas analysis.

Test Fuels. The objective in formulating the test fuels were (*i*) to evaluate several microemulsions of water in JP-4 and JP-8 and alcohols in JP-4 and JP-8 using surfactants that had previously shown promise in earlier fuel preparation studies, and (*ii*) to select the most favorable formulations from each of these four categories for combustor testing.

The JP-4 and JP-8 base fuels meeting ASTM specifications were obtained from Howell Hydrocarbons, Inc., San Antonio, Texas. The JP-4 and JP-8 as received had somewhat low aromatic contents, 15 and 8 percent, respectively. For this work, aromatics of an appropriate boiling range were added to the fuels to assure smoke numbers above 30 in the combustor tests. A summary of the fuel properties of JP-4 and JP-8 used in blending the microemulsified fuels is given in Table 2.

Based on previous experience in formulating microemulsions of water, methanol, and ethanol with diesel fuels, eighteen different surfactants were selected as being

Nomenclature

BIP = burner inlet pressure
BIT = burner inlet temperature
F/A = fuel/air ratio
THC = total hydrocarbons
Wa = air flow rate
Wf = fuel flow rate

potentially successful for JP-4 and JP-8. Of these, the most appropriate surfactants were selected by evaluating about fifty test formulations for each JP-4 and JP-8.

It was found that anhydrous ethanol (200 proof) was miscible in JP-4 and JP-8 and did not require a surfactant. The surfactant with the trade name Schercomid (SO-A) from Scher Chemical Co. was selected for the preparation of the aqueous methanol and ethanol (190 proof) and the anhydrous methanol (200 proof) in JP-4 and JP-8 microemulsions. Stabilization of microemulsions of JP-4 containing up to 20 percent aqueous ethanol and anhydrous methanol was achieved with about 3 percent SO-A. Much higher concentrations of SO-A were required in the stabilization of aqueous methanol/JP-4 microemulsions; equal amounts of SO-A and alcohol were used in these blends.

The JP-8 blends required concentrations of SO-A 1 to 2 percent more than the corresponding JP-4 blends. In preparing the water/fuel microemulsions, two surfactants with the trade names Clindrol 100 CG and Clindrol 101 CG from Clintwood Chemical Co. were selected for the respective JP-4 and JP-8 blends. For these emulsions, equal amounts of water and surfactant were used. The pertinent properties of the surfactants are given below in Table 3.

Results and Discussion

The main emphasis in combustor testing was to determine the potential of the fuel blends to reduce exhaust smoke. The testing was carried out in two phases. In the first phase, the fuel blends of JP-4 and JP-8 containing 10 and 20 percent of the dispersed phase (water, anhydrous and aqueous ethanol and methanol) were tested at the takeoff operating condition to determine if significant reductions in exhaust smoke could be achieved; this operating condition was selected because it gave the highest smoke emissions. A 40-percent reduction in smoke number was considered significant since in the earlier Navy work [1, 2] this value corresponded to a reduction in the J-79 plume visibility from Ringleman 2.5 to 1.

All three of the dispersants gave significant reductions in smoke number. Based on their concentration, the effectiveness in reducing smoke number was in the order water > methanol > ethanol. There are two reasons for this: (*i*) the amount of surfactant required, since the surfactant alone was found to reduce smoke a little; and (*ii*) the relative effects of water and the alcohols on the hydrogen-carbon ratio of the fuel, as will be discussed later.

In the second phase of the work, water and one of the alcohols were selected for comprehensive combustor testing which included all the operating conditions given in Table 1 and a complete combustion performance analysis. Two criteria were used to select the alcohol form to be used in the comprehensive combustor testing: (*i*) the fuel cost effectiveness in reducing smoke; and (*ii*) the increase in fuel flow rate associated with the reduction in smoke for the reasons discussed earlier. In comparing the fuel costs and their respective abilities to reduce smoke in the first phase of testing, it became apparent that the anhydrous ethanol solutions were most attractive. The aqueous methanol microemulsion cost the most, whereas the other microemulsions made with anhydrous methanol, aqueous ethanol, and water were about the same.

In comparing the relative increase in fuel flow rate associated with a reduction in smoke number, there was very little difference among the test fuels. The JP-4 and JP-8/anhydrous methanol blends showed only a slight advantage over the respective anhydrous ethanol blends. This is discussed in more detail later in the paper.

In considering both of the criteria given above, fuels blended with anhydrous ethanol were selected for comprehensive testing: the slightly higher penalty in fuel flow rate is more than offset by the significantly lower relative cost. Anhydrous ethanol solutions also have the advantage of being two component systems, which simplifies the blending of fuels for engine testing.

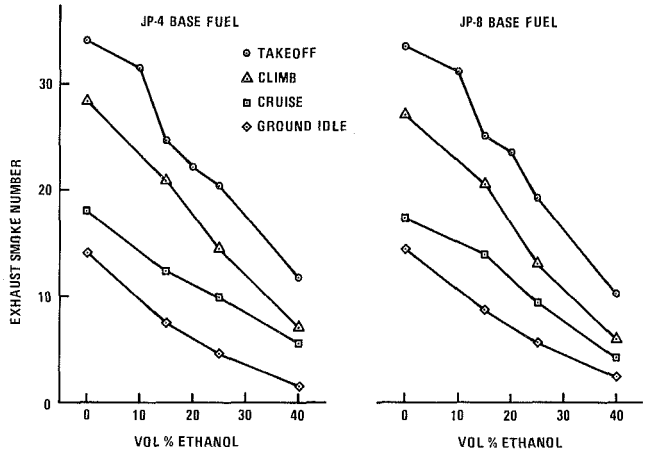

Fig. 1 Effect of ethanol concentration on exhaust smoke

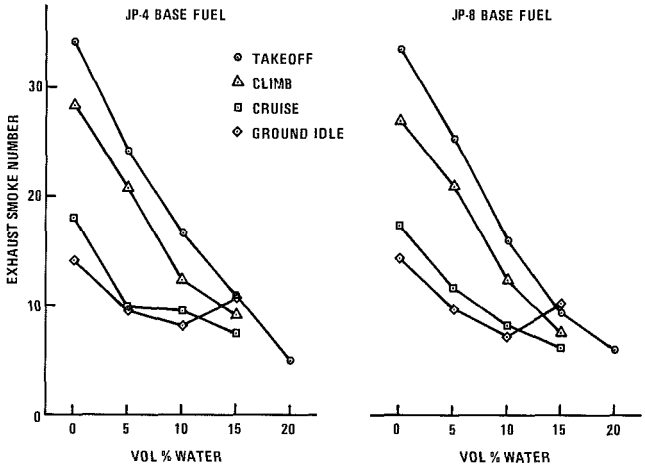

Fig. 2 Effect of water concentration on exhaust smoke

Comprehensive Combustion Performance Testing.

General Results. The ethanol/fuel and water/fuel blends were tested at the four combustor operating conditions shown in Table 1 ranging from idle to full power. The effects of ethanol and water on exhaust smoke and flame radiation are shown in Figs. 1–4; the effects on combustion efficiency are shown in Fig. 5. In general, the exhaust smoke and flame radiation were reduced by the added water and ethanol, but the carbon monoxide and total hydrocarbon emissions increased, thus decreasing the combustion efficiency. Figure 6 presents the NO_x emissions for the two fuel concepts for the anhydrous ethanol/fuel blends; the NO_x levels were reduced but they were higher for the water/fuel emulsions. This increase was due to the nitrogen content of the surfactant; if the surfactant had been more judiciously selected, the NO_x levels would have been lower for these fuels also.

Water and ethanol were both very effective in reducing soot formation. The most significant reductions in exhaust smoke and flame radiation were at the full power condition; changes in combustion efficiency, i.e., total hydrocarbon and carbon monoxide emissions, were very modest at this condition. As the power was reduced, the effect on smoke and radiation became less dramatic and the combustion efficiency decreased.

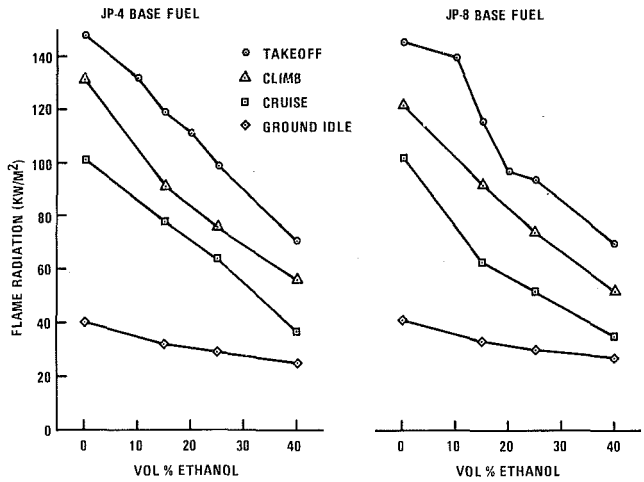

Fig. 3 Effect of ethanol concentration on flame radiation

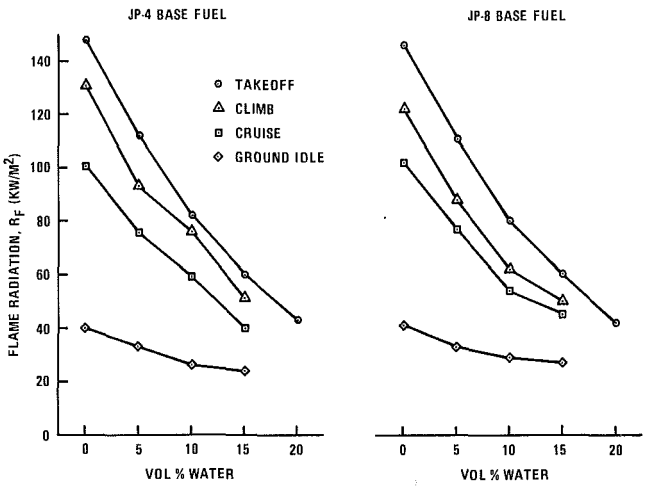

Fig. 4 Effect of water concentration on flame radiation

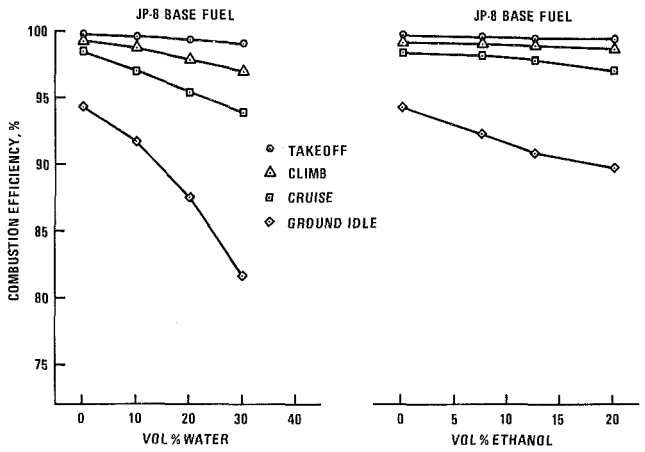

Fig. 5 Effect of ethanol and water on combustion efficiency: JP-8

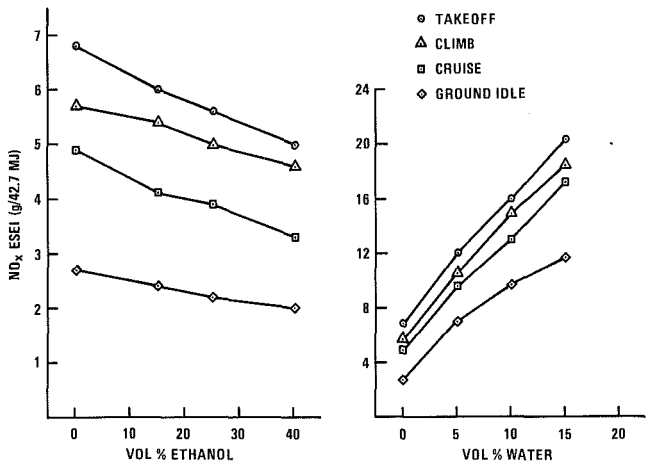

Fig. 6 Effect of ethanol and water on exhaust NO_x: JP-8 (energy specific emissions index)

Flame Radiation and Smoke. The reductions in soot formation by water and alcohols appears to be determined by the degree with which they increase the hydrogen/carbon ratio of the fuel blend. Several studies (4, 6–8) have shown that hydrogen/carbon ratio is a good correlating parameter for soot formation in gas turbine engines. Recent work [5] has shown that this correlation can be extended to hydrocarbon fuels containing oxygenates and dispersed water. In this case, the hydrogen and carbon contained in the water and alcohol are also included in calculating the H/C ratio. The purpose of those studies was to determine the fuel property that correlates most favorably with the tendency of a fuel to soot. The fuel properties examined were aromatic content, aromatic-ring-carbon content, H/C ratio, viscosity, and final boiling point. The correlation of aromatic content and aromatic-ring-carbon content was favorable for petroleum-base fuels consisting mainly of paraffins and aromatics but was invalid for fuel blends containing alcohols and water. On the other hand, the H/C ratio correlation was valid for all of the fuel blends examined. Since the properties, viscosity, and final boiling point, which determine droplet lifetime did not affect the correlation of H/C ratio with radiation and smoke, it was concluded that liquid-phase pyrolysis was not significant and that soot production was due to gas-phase reactions.

The correlations of smoke number and radiation with H/C atom ratio in Fig. 7 include two sets of data. The open symbols represent an earlier study [5], mentioned above which included six JP-5 petroleum fuels; three JP-5 fuels derived from coal, oil shale, and tar sands; seven fuels blended from JP-5 and diesel marine; six water-in-fuel macroemulsions; and two methanol-in-fuel (high aromatic fuel) solutions. The closed symbols represent the fuel microemulsions and solutions from the work presented here. It is apparent that the microemulsions and ethanol solutions correlate with H/C atom ratio in the same way as the other fuels and that the hydrogen contributed by the water and alcohol is chemically active in the reactions that consume soot precursors. Muller-Dethlefs and Schlader [9] have examined the effects of water on carbon formation in premixed flames and suggest that increased OH radical concentrations enhance the rate of oxidation of free carbon.

Combustion Efficiency. The reductions in combustion efficiency shown in Fig. 5 were considerably greater in the case of the water/fuel microemulsions than the ethanol/fuel solutions. In earlier work with water/fuel macroemulsions, it was also found that combustion efficiency decreased dramatically at the ground idle operating condition. In fuel blends containing only the surfactant (Clindrol 100 CG), the combustion efficiencies were about the same as the neat fuel, indicating these higher boiling point materials were not the cause. The effect would therefore appear to be differences in fuel atomization and vaporization rates because, at low power conditions, combustion is controlled largely by the fuel vaporization process. The fuel properties that affect atomization and droplet vaporization are viscosity and boiling point distribution, respectively. The viscosity of the

water/fuel microemulsion was much higher than that of the ethanol/fuel blend. This would result in a significant increase in the Sauter mean diameter of the fuel droplets in the sprays. In addition, recognizing the d^2 law for evaporation [10], a corresponding difference would result in the rates of vaporization.

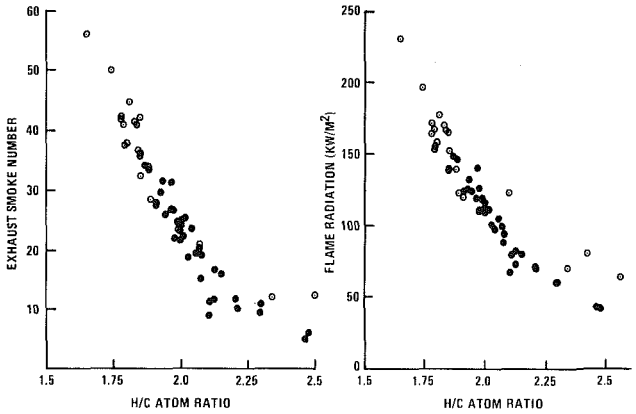

Fig. 7 Correlation of exhaust smoke and flame radiation with hydrogen/carbon ratio

The effect of boiling point distribution is speculative because of the complex nature of the vaporization process for immiscible systems (emulsions) and nonideal solutions such as alcohol/fuel blends. The temperature of a vaporizing droplet is approximately equal to the boiling point of the most volatile component in the fuel; for JP-8 there is little doubt that water and ethanol are the lowest boiling point components. In JP-4 there are some hydrocarbons in the same boiling point range as ethanol and water, but they are probably in relatively low concentration. Thus, in either case of JP-4 and JP-8, the rate of vaporization of a droplet containing ethanol would be slower than that of the neat fuel droplet because the temperature of the droplet would be depressed by the presence of ethanol. This may account for the decreased combustion efficiency found for the ethanol/fuel blends. It appears that this effect would be greater for water even though its boiling point is higher than that of ethanol. Ethanol is able to burn and thereby transfer heat back to the droplet, whereas the vaporization of the water-containing droplet is more dependent on convective heat transfer from the surrounding gas. Because of the immiscible nature of the water/fuel emulsion, the water evaporates much more freely; this suggests the possibility that the fuel droplet may not ignite until most of the water has evaporated. The water with its relatively high enthalpy of vaporization evaporates

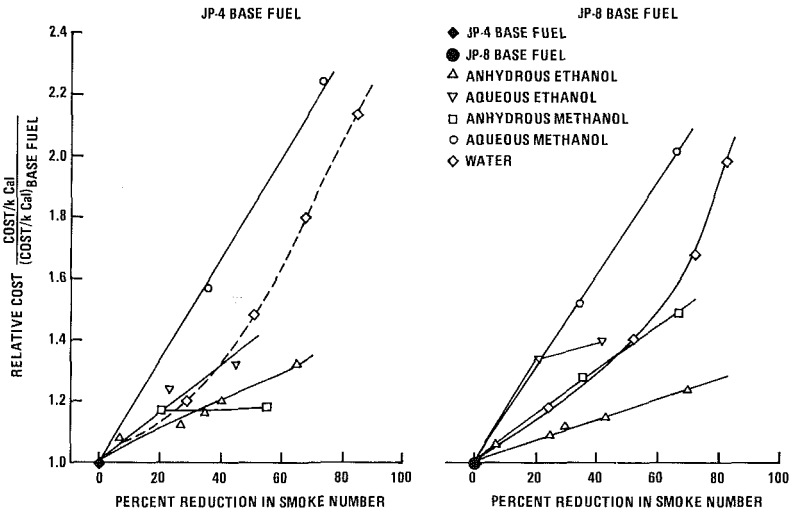

Fig. 8 Relative cost to reduce exhaust smoke take-off condition

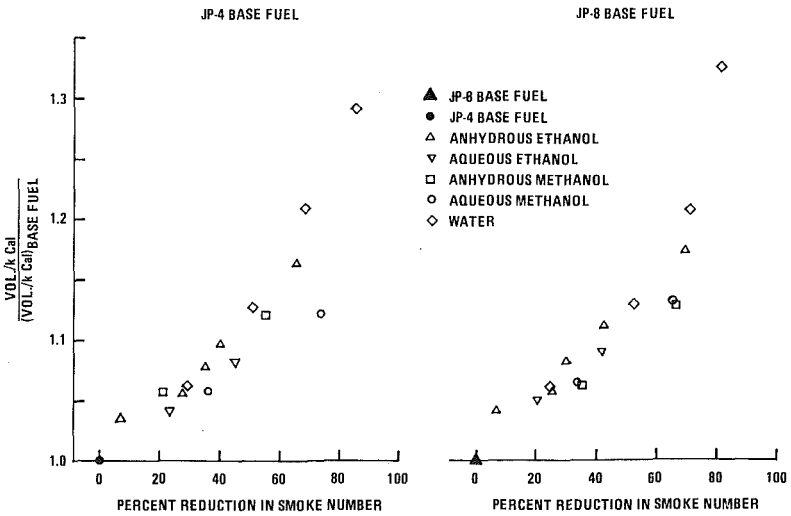

Fig. 9 Increase in fuel flow rate associated with reductions in exhaust smoke: takeoff condition

preferentially and suppresses the volatilization of combustible components. This cooling effect combined with the relatively high viscosity of the water/fuel microemulsions may account for the substantial decrease in combustion efficiency that is observed.

NO_x Emissions. Figure 6 shows the effects of ethanol and water in JP-8 on the NO_x energy specific emissions index (ESEI). For this study, the emissions were normalized in this manner to account for the variations in heat of combustion among the test fuels. While the ethanol blends reduced the oxides of nitrogen, the water-in-fuel microemulsions increased them significantly because the surfactant contained nitrogen. It was not possible to calculate the conversion of fuel-bound nitrogen to NO_x relative to that produced by the Zeldovich mechanism (thermal NO_x) [10], because the effect of water was not known. In the earlier work with macroemulsified fuels where the surfactant was free of nitrogen, the NO_x was reduced significantly by the presence of water and undoubtedly would have been here also.

Fuel blends of JP-4 and JP-8 containing 10 percent surfactant were tested at all four operating conditions. In these experiments, it was possible to determine the conversion of fuel-bound nitrogen to NO_x by simply comparing the NO_x produced by the surfactant-containing fuel with that of the neat fuel. It was found that the conversion efficiencies (78 and 63 percent for JP-4 and JP-8, respectively) were essentially the same at all operating conditions. These fuel blends contained 0.437 percent nitrogen; according to Blazowski [11], the percent conversion to NO_x decreases as the concentration of fuel-bound nitrogen is increased.

Cost Effectiveness. Figure 8 shows the relative cost to reduce the smoke number of the base fuel by adding water and alcohols. The relative fuel cost per kcal is plotted against the percent reduction in exhaust smoke number because it is the heat input rate required to maintain a specific combustor operating condition that is important. In comparing the slopes of the curves shown in Fig. 8, it is apparent that the anhydrous ethanol solutions are the most cost effective. It is clear that the microemulsions made with aqueous methanol cost the most whereas the others made with anhydrous methanol, aqueous ethanol, and water are similar. The costs (in dollars/lb) of the fuel components were JP-4 (0.15), JP-8 (0.17), anhydrous ethanol (0.21), 190 proof ethanol (0.19), anhydrous methanol (0.09), methanol (0.08), and surfactants (0.80).

Flow Rate Penalty. When a component such as water is blended with fuel, the energy density of the fuel is reduced so that it is necessary to increase the fuel flow rate to the engine in order to sustain the same power output. Figure 9 shows the increase in fuel flow rate associated with reductions in smoke. From an energy density standpoint alone, alcohols should reduce this penalty because they contribute to the heat of combustion of the fuel blend. However, of some surprise, the results indicate that the smoke reduction is accompanied by about the same flow rate penalty for all the fuel blends. This seems to be due to the fact that while the smoke reducing order is water > methanol > ethanol, the order of increasing energy density is ethanol > methanol > water.

Summary

- Microemulsions or water, methanol, and ethanol (aqueous) in JP-4 and JP-8 can be formulated.
- Ethanol (anhydrous) is soluble in JP-4 and JP-8.
- These blends affected combustion performance as follows:
  - Reduced soot formation
  - Reduced exhaust smoke
  - Reduced oxides of nitrogen (Increased NO_x when surfactant contains nitrogen)
  - Increased CO
  - Increased total hydrocarbons
  - Decreased combustion efficiency
- The last three detrimental effects are only important at low power operating conditions such as ground idle where smoke is low and the smoke reduction concepts would not be necessary.
- Smoke and radiation reductions from the addition of water and alcohol correlated with changes in hydrogen/carbon ratio.
- Ethanol (dry) solutions appear to be the most effective from the standpoint of cost, operational, and system effects.

Acknowledgments

The authors wish to thank Messrs. R. C. Haufler and F. H. Lessing for their excellent work in conducting the combustor experiments. Special thanks is given to Dr. G. E. Fodor for formulating the microemulsified fuels used in this study. This work was conducted under Contract No. F08635-79-C-0213 under the technical management of Major Joseph A. Martone, Environmental Sciences Branch, Air Force Engineering and Services Center, Tyndall Air Force Base, Florida.

The work was performed at the U.S. Army Fuels and Lubricants Research Laboratory located at the Southwest Research Institute with the permission of the U.S. Army Mobility Equipment Research and Development Command, Energy and Water Resources Laboratory (DRDME-GL), Fort Belvoir, Virginia.

References

1 Moses, C. A., "Reduction of Exhaust Smoke From Gas Turbine Engines by Using Fuel Emulsions-II," presented at the Western States Section of the Combustion Institute, University of California, La Jolla, Calif., Oct. 18, 1976.

2 Klarman, A. F., Rollo, A. J., and Scott, H. C., "Evaluation of Water/Fuel Emulsion Concept for Test Cell Smoke Abatement," Naval Air Propulsion Center, Trenton, N.J., Report No. NAPC-PE-7, Mar. 1978.

3 Weatherford, W. D., Jr., Fodor, G. E., Naegeli, D. W., Owens, E. C., Wright, B. R., and Schaekel, F. W., "Army Fire-Resistant Diesel Fuel," SAE Paper No. 790926, Oct. 1979; G. E. Fodor, et al., "Fire-Safe Hydrocarbon Fuels," USA Patent No. 4,173, 455, 1979.

4 Moses, C. A., and Naegeli, D. W., "Fuel Property Effects on Combustor Performance," ASME Paper No. 79-GT-178.

5 Naegeli, D. W., and Moses, C. A., "Effects of Fuel Properties on Soot Formation in Turbine Combustors," SAE Paper No. 781026, 1978 SAE Aerospace Meeting, San Diego, Calif., Nov. 22-30, 1978.

6 Blazowski, W. S., "Dependence of Soot Production on Fuel Blend Characteristics and Combustion Conditions," ASME Paper No. 79-GT-155.

7 Jackson, T. A., and Blazowski, W. S., "Fuel Hydrogen Content as an Indicator of Radiative Heat Transfer in an Aircraft Gas Turbine Combustor," Technical Report AFAPL-TR-79-2014, (see also AFAPL-TR-77-93).

8 Friswell, N. J., "The Influence of Fuel Composition on Smoke Emissions from Gas-Turbine-Type Combustors: Effect of Combustor Design and Operating Conditions," *Combustion Science and Technology*, Vol. 19, 1979, p. 119.

9 Muller-Dethlefs, K., and Schlader, A. F., "The Effects of Steam on Flame Temperature, Burning Velocity, and Carbon Formation in Hydrocarbon Flames," *Comb. and Flame*, Vol. 27, 1976, p. 205.

10 Glassman, I., *Combustion*, Academic Press, New York, 1977.

11 Blazowski, W. S., "Combustion Considerations for Future Jets Fuels," *Proceedings of the Sixteenth Symposium (International) on Combustion*, 1976, p. 1631.

Secondary Flow Mixing Losses in a Centrifugal Impeller

M. W. Johnson
Department of Mechanical Engineering,
The University of Liverpool,
Liverpool, U.K.

J. Moore
Department of Mechanical Engineering,
Virginia Polytechnic Institute,
Blacksburg, Va. 24061

Detailed flow measurements made in a 1-m dia shrouded centrifugal impeller running at 500 rpm are presented. All three mutually perpendicular components of relative velocity and rotary stagnation pressures were measured on five cross-sectional planes between the inlet and the outlet, using probes which were traversed within the rotating impeller passage. The reduced static pressures were also calculated from these flow measurements. The measurements were made for an impeller flow rate corresponding to approximately zero incidence at the blade leading edges. Shroud boundary layer separation and secondary flow were observed to lead to the formation of a wake in the suction-side/shroud corner region. It is concluded that the turbulent mixing associated with the shroud boundary layer separation and the strength of the secondary flow strongly influence the size and location of the wake, respectively.

Introduction

Many research workers, for example [1, 2, 3], have studied the outlet flows from centrifugal impellers and most have observed a "jet-wake" pattern. Eckardt [4] was able to show that potential flow theory was capable of describing the jet flow, which he measured in some detail. However, although impeller geometry, flow rate and operating speed are known to influence the size and position of the wake, wake flows cannot be predicted reliably by current design methods. An improvement in our understanding of the wake flow could therefore help in optimizing the performance of centrifugal compressors.

In order to predict the development of the wake it is necessary to investigate in detail the secondary flows which contribute to the thickening of the boundary layers on the suction and shroud walls.

Objective. The principal objective of this work was to determine the flow phenomena which influence the development of the wake and its size and location in the impeller discharge flow. To this end, the authors measured all three mutually perpendicular velocity components and the rotary stagnation pressure, $p^* = p + 1/2\ \rho(W^2 - \omega^2 r^2)$, on five cross-sectional planes between the inlet and outlet of the impeller.

Secondary Flow. Let us now consider how secondary flow develops in centrifugal impellers.

The generation of streamwise vorticity along a streamline in inviscid, incompressible flow in a rotor is governed by an equation derived by Smith [5], but more recently presented by Hawthorne [6] in the following simple form:

$$\frac{\partial}{\partial s}\left(\frac{\Omega_s}{W}\right) = \frac{2}{\rho W^2}\left(\frac{1}{R_n}\frac{\partial p^*}{\partial b} + \frac{\omega}{W}\frac{\partial p^*}{\partial z'}\right) \qquad (1)$$

where $p^* = p + 1/2\rho(W^2 - \omega^2 r^2)$ is the rotary stagnation pressure, W is the fluid velocity relative to the rotor and ωr is the rotor tangential velocity. The equation is expressed in streamwise coordinates where s is the streamwise direction, n the normal direction, and b the binormal direction. The two terms contributing to the generation of streamwise vorticity, Ω_s, are due to curvature of the streamlines with radius R_n and to rotation with angular velocity ω about the axis z'. These contributions are due to gradients of p^* in the binormal and axial directions, respectively.

Rotary Stagnation Pressure p^*. The rotary stagnation pressure, p^*, is conserved along a streamline in steady, inviscid, incompressible flow in a rotor. Viscosity reduces p^*, but for small distances along streamlines one may identify a fluid particle by its value of p^*. This is particularly useful as it offers a method of following the development of the flow by tracking fluid particles. The migration and accumulation of low p^* fluid which will be found in the boundary layers and the wake, can thus be observed directly. The large gradients of p^* which will occur in boundary layers will give rise to secondary flows as indicated by equation [1].

Stable Locations for Low p^* Fluid. Low p^* fluid will migrate under the influence of secondary flows towards regions of low reduced static pressure, which Johnson [7] has termed "stable locations." However, the low p^* fluid will not necessarily accumulate at these stable locations because, as discussed by Johnson, the inertia of the secondary flow may carry this fluid beyond the stable location. Nonetheless, the stable location for each cross section of the impeller passage, is the approximate position where the wake flow should develop.

Secondary Flow in Centrifugal Impellers. The Ghost impeller and Eckardt's impeller have similar geometries [8] and both have two bends, the inducer bend and the axial-to-radial bend. In the inducer bend, secondary flow develops

Contributed by the Gas Turbine Division of THE AMERICAN SOCIETY OF MECHANICAL ENGINEERS and presented at the 27th International Gas Turbine Conference and Exhibit, London, England, April 18–22, 1982, Manuscript received at ASME Headquarters December 2, 1981. Paper No. 82-GT-44.

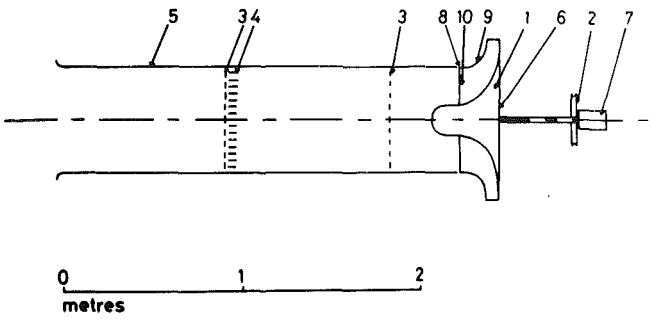

Fig. 1 Schematic of test rig:
(1) Impeller roating at 500 r.p.m.
(2) Pulley driven by motor
(3) Screens (30 mesh, 27 gauge)
(4) Honeycomb
(5) Inlet duct
(6) Pressure transducers and amplifiers
(7) Slip rings
(8) Seal
(9) Shroud attached to impeller
(10) Boundary layer trips

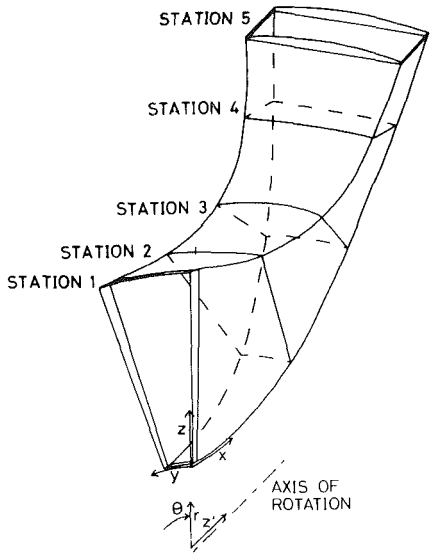

Fig. 2 Impeller passage with measurement planes

which convects fluid with low p^* from the shroud and hub surfaces towards the suction surface. Secondary flow in the axial-to-radial bend moves low p^* fluid towards the shroud from the suction and pressure surface boundary layers.

Rotation also induces a streamwise component of vorticity whenever a gradient of p^* exists in the axial direction. Such gradients occur on the blade surfaces in the inducer of the centrifugal impeller and also on the shroud and hub surfaces once the flow has a radial component of velocity in the later part of the passage. Anand and Lakshminarayana [9] have investigated inducer flow and observed the convection of low momentum boundary layer fluid towards the shroud on both the suction and pressure surfaces of their axial inducer blades. The migration of low p^* fluid towards the suction surface in the radial part of an impeller passage was studied by Moore [10], who used a rotating radial flow channel.

It is interesting to note that in the axial-to-radial bend, the rotation and the curvature do not produce similar three-dimensional flows, but compete for the dominating influence on the stable location of low p^* fluid. This competition must contribute to the observed differences in wake location in the discharge flow from different centrifugal impellers. From equation (1) it can be seen that the Rossby number, $W/\omega R_n$, is a measure of the relative influence of curvature and rotation. For impellers operating with a low Rossby number for the axial-to-radial bend, rotation effects will dominate and the wake fluid will most likely be found on the suction surface. However, if the Rossby Number is high, the wake fluid may be expected on the shroud wall at the impeller exit as the bend's curvature will dominate the flow.

The axial-to-radial bend of both the Ghost and Eckardt's impeller have Rossby numbers close to unity and so in these impellers, curvature and rotation are likely to be of approximately equal importance and so the wake might be expected close to the suction-side/shroud corner region, as was indeed observed by Eckardt.

Turbulent Mixing. Just as rotation and curvature can influence large scale secondary flow in centrifugal impellers through processes described by equation (1), so small scale fluid motions can be modified also. Turbulence modifications by curvature and rotation has been studied in detail by Johnston [11], but here we simply note a rule for determining whether turbulent mixing is suppressed or enhanced. If, in a boundary layer or shear layer, the cross-stream gradient of rotary stagnation pressure, p^*, is in the same direction as the gradient of reduced static pressure, p_r, then turbulent mixing will be suppressed. However, if the gradients are in opposite directions, turbulent mixing will be enhanced. In the centrifugal compressor impeller this will mean that, in general, mixing will be suppressed in the boundary layer close to the stable location for low p^* fluid.

The Test Rig

The centrifugal impeller rig, as described in Johnson and Moore [12] and Johnson [13], is shown in a schematic diagram (see Fig. 1). Measurements were made on five cross-sectional planes as shown in Fig. 2, using probes which rotated with the impeller.

The three mutually perpendicular components of relative velocity were measured using a five-hole pressure probe. The probe was calibrated for flow direction and velocity and the

Nomenclature

p = static pressure
p_r = reduced static pressure, $p_r = p - \frac{1}{2}\rho\omega^2 r^2$
p^* = rotary stagnation pressure, $p^* = p + \frac{1}{2}\rho W^2 - \frac{1}{2}\rho\omega^2 r^2$
P_r = dimensionless reduced static pressure, equation (2)
P^* = dimensionless rotary stagnation pressure, equation (3)
r,θ,z' = cylindrical polar coordinates
R_n = radius of curvature of streamline
s,n,b = streamwise, normal and bi-normal directions – streamline coordinates
W = relative velocity
x/x_o = meridional inlet to outlet coordinate, measured along the shroud
y/y_o = pressure-side to suction-side coordinate
z/z_o = hub to shroud coordinate
ω = angular velocity
Ω_s = component of absolute vorticity along streamline
ρ = fluid density

Subscripts

min = minimum value
max = maximum value

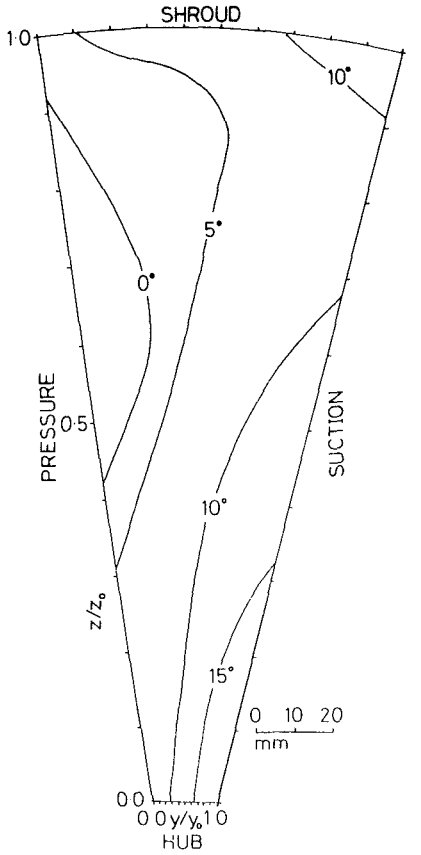

Fig. 3 Incidence angles at impeller inlet

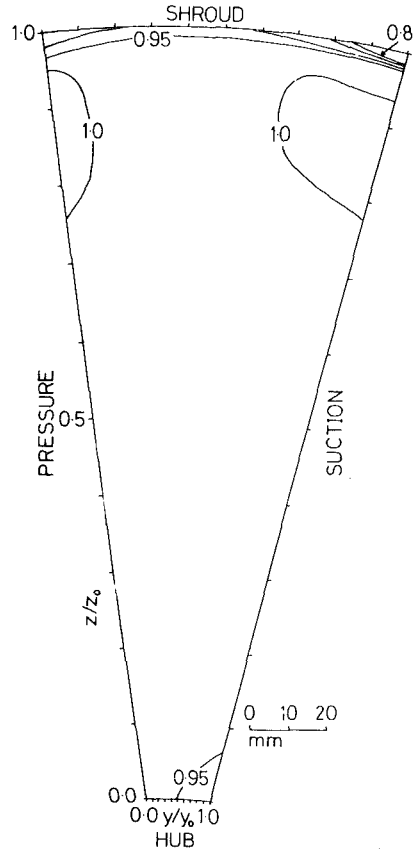

Fig. 4 Station 1: dimensionless rotary stagnation pressure P^*

estimated accuracies were ± 1 m/s and ± 5 deg for a typical velocity reading of 10 m/s.

A Kiel probe was used to measure the rotary stagnation pressure, p^*, and the estimated accuracy here was ± 10 N/m^2. The reduced static pressure, p_r, is calculated from the measured values of p^* and relative velocity and the estimated accuracy of p_r is ± 40 N/m^2 in the wake region and ± 20 N/m^2 elsewhere.

Experimental Results

The results presented show details of the flow development in one of the nineteen impeller passages for a design flow rate corresponding to approximately zero incidence angle at the inducer leading edge. The mass flow rate through the passage was 0.14 (±0.01) kg/s.

Limiting Values of p^*. The uniform axial inlet flow gave a flow with an approximately uniform value of $p^* = -270$ N/m^2 (± 10 N/m^2) gauge. This was the highest value of p^* measured in the impeller flow and is subsequently referred to as p^*_{max}. p^*_{max} was less than atmospheric because of stagnation pressure drops through the screens and the honeycomb in the inlet duct, which correspond to the pressure rise achieved in the impeller and in the diffusion beyond the impeller outlet.

The lowest values of p^* in the impeller flow occur in regions of low reduced static pressure close to wall where the relative velocity is also low. Such regions are to be found near the shroud in the inducer, and a value of $p^*_{min} = -600$ (± 30)N/m^2 gauge was estimated here. $p^*_{max} - p^*_{min}$ corresponds to the maximum dynamic pressure of the potential flow, which is often used to characterise pressure recovery in centrifugal impellers.

A dimensionless rotary stagnation pressure, p^*, and a dimensionless reduced static pressure, p_r, are defined using the limiting values of p^*, such that

$$P_r = \frac{p_r - p^*_{min}}{p^*_{max} - p^*_{min}} \tag{2}$$

and

$$P^* = \frac{p^* - p^*_{min}}{p^*_{max} - p^*_{min}} \tag{3}$$

A value of one for p^* occurs in the inviscid potential flow and $P_r = 1$ is associated with stagnation of the potential flow, at the blade leading edges for example.

Presentation of the Relative Velocity Results. The passage direction is defined as the direction in which the ratio of the distances from each pair of walls remains constant. The relative velocity is then resolved into two parts; the component in the passage direction and the remaining component perpendicular to this, that is, in the cross-passage direction. The velocity in the passage direction is represented by contours in the results, whereas the cross-passage component is represented by an arrow at each measurement point. These arrows therefore indicate the combined effects of diffusion and secondary flow.

Discussion

Station 1. The flow angles at Station 1 (approximately 6-mm downstream of the blade leading edge show that the incidence is relatively small (see Fig. 3). The blade leading edges present a blockage for the inlet flow, and this varies from 46 percent at the hub to 1 percent at the tip. Thus, there is an elliptical flow, in the blade-to-blade plane, around the blade leading edge and the incidence angles, relative to the

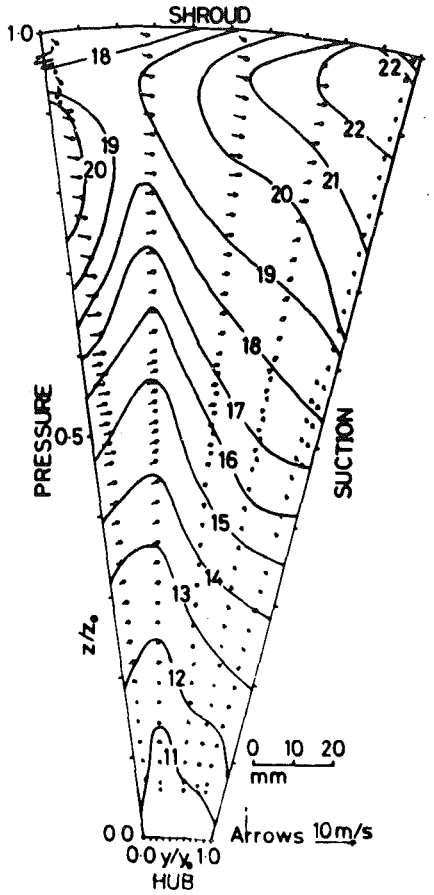

Fig. 5 Station 1: relative velocities – contours in *m/s*

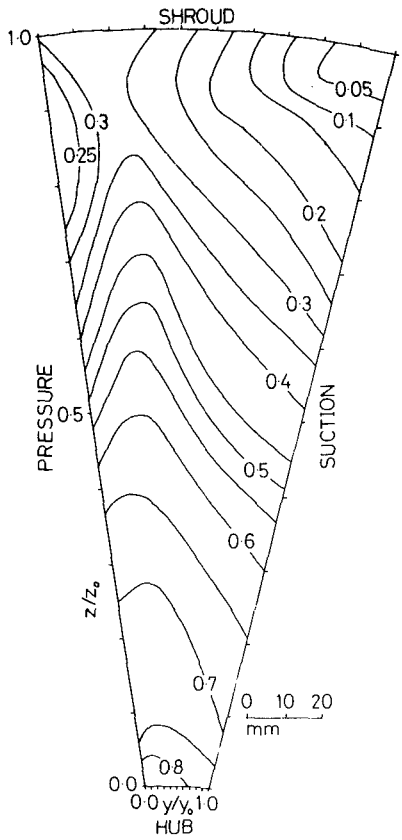

Fig. 6 Station 1: dimensionless reduced static pressure P_r

blade camber line, are therefore positive on the suction side and predominantly negative on the pressure side.

The velocity contours in Fig. 5 represent contours of relative velocity at Station 1. These show that the fluid near the shroud has developed a higher axial velocity than the fluid near the hub. This is probably an upstream effect of the axial-to-radial bend. The velocity vectors show fluid in the lower half of the passage moving in the hub-to-shroud direction to make up the increased flow.

The reduced static pressure (Fig. 6) shows a gradient of p_r in the hub-to-shroud direction due to the centrifugal acceleration. The pressure is also slightly higher on the pressure side than on the suction side, so the blades are only lightly loaded. The minimum p_r occurs in the shroud/suction-side corner region ($p_r < 0.05$ at $y/y_o = 1.0$, $z/z_o = 1.0$). Within this region at the wall, fluid with the lowest p^* ($p^* < 0.05$) at Station 1 will occur. This does not appear on the p^* diagram (Fig. 4), however, as the Kiel probe could not be brought close enough to the wall to measure p^* within the thin boundary layer. Figure 4 also shows little or no losses have occurred, and the flow is therefore essentially a potential flow.

Hot wire measurements indicate that the r.m.s. turbulence level is about 1.5 to 2.5 percent within the potential flow region at Station 1.

Station 2. Close to the shroud there is a large adverse pressure gradient of reduced static pressure, particularly between Stations 2 and 3, as shown by the minimum values of P_r (0.05 and 0.3, respectively) in the two reduced static pressure diagrams (Figs. 9 and 12). This pressure rise occurs as the fluid reduces its tangential velocity, and hence its relative velocity, as it turns through the inducer bend.

Due to the adverse pressure gradient, low velocity fluid in

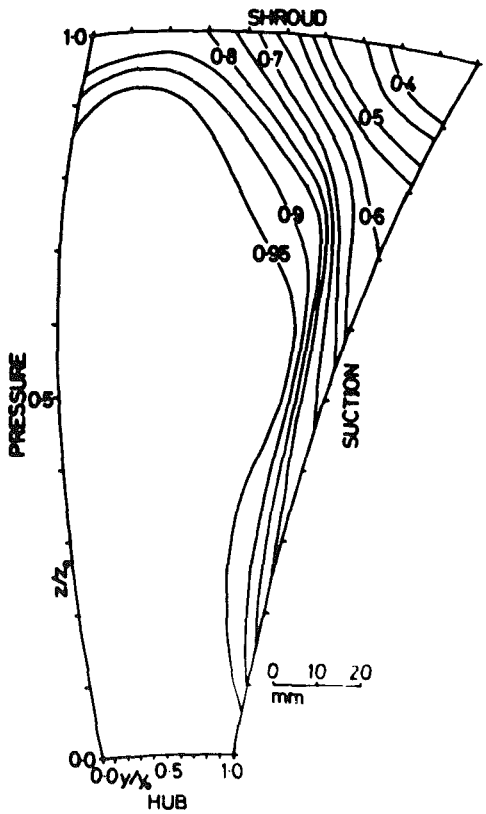

Fig. 7 Station 2: dimensionless reduced static pressure P^*

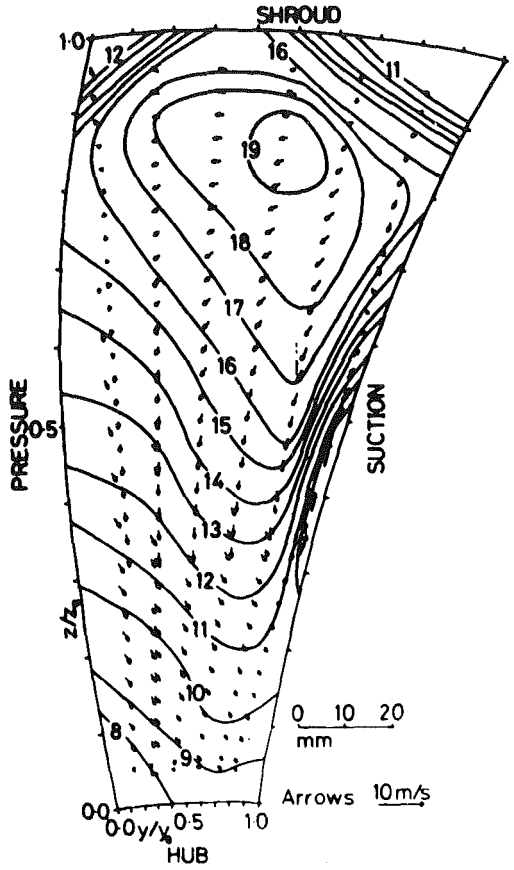

Fig. 8 Station 2: relative velocities – contours in m/s

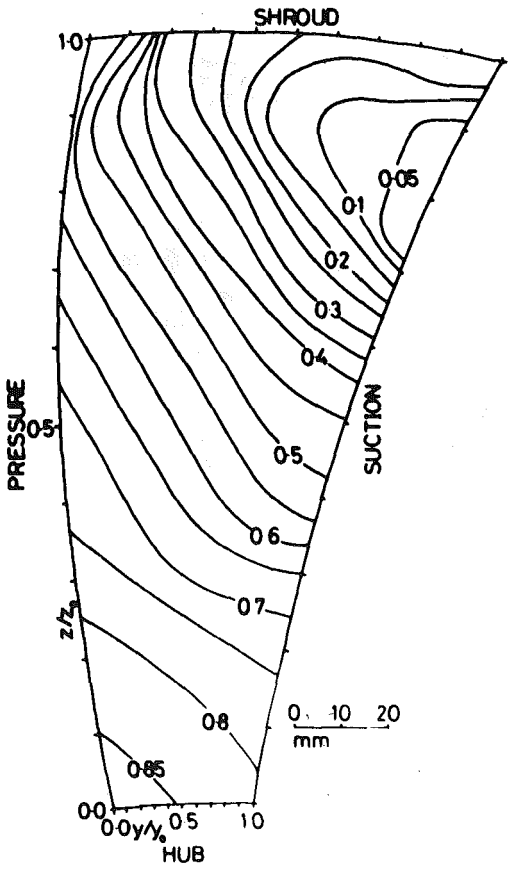

Fig. 9 Station 2: dimensionless reduced static pressure P_r

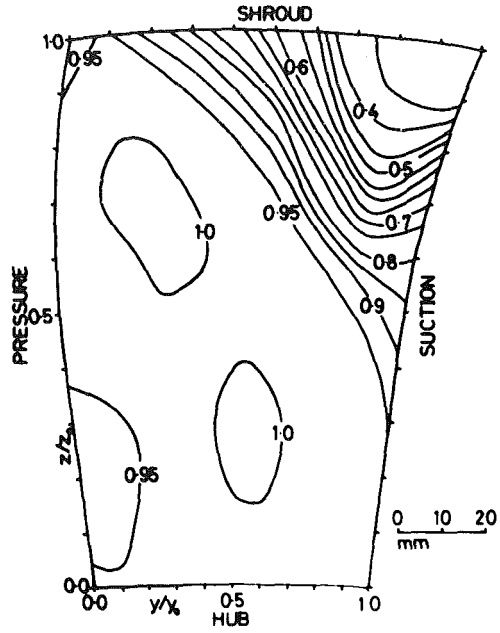

Fig. 10 Station 3: dimensionless rotary stagnation pressure P^*

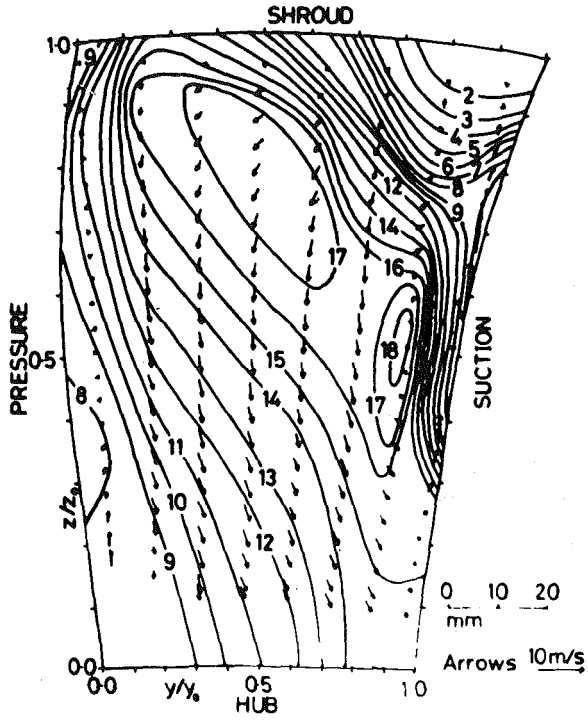

Fig. 11 Station 3: relative velocities – contours in m/s

the boundary layers close to the suction-side/shroud corner region at Station 2 will possess insufficient rotary stagnation pressure ($P^* < 0.3$) to reach Station 3. Consequently, this fluid must mix with higher p^* fluid in order that it may increase its momentum and proceed to Station 3. However, turbulent mixing will be suppressed by the pressure gradients induced by the curvatures in the inducer and axial-to-radial bends. The measured pressures in this region at Stations 2 and 3 were observed to be very unsteady, and it therefore seems probable that the mixing, which must occur in this region, was associated with some unsteady flow separation. This may also be associated with periodic reversed flow.

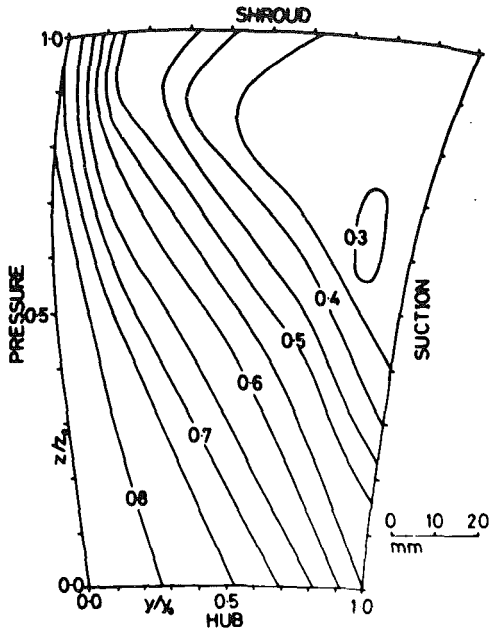

Fig. 12 Station 3: dimensionless reduced static pressure, P_r

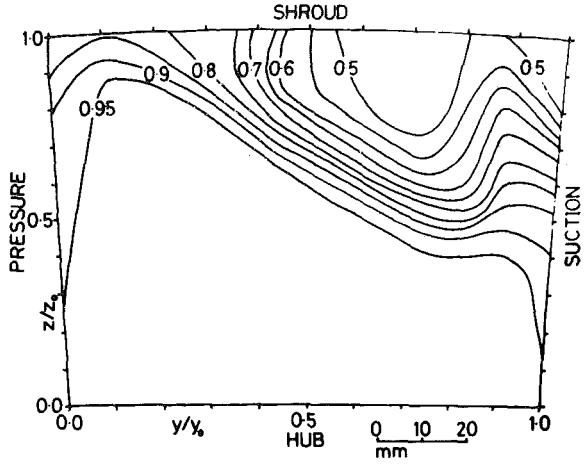

Fig. 13 Station 4: dimensionless rotary stagnation pressure, P^*

On the hub surface, the boundary layer experiences little or no pressure rise in the streamwise direction. In addition, secondary flows cause boundary layer fluid to move from the hub wall onto the suction and pressure surfaces as shown in Figs. 8 and 11. The region of low p^* fluid observed on the suction side wall in Fig. 7 is due to the thickening of the boundary layer caused by these secondary flows. Figure 8 shows that this low p^* fluid is moving up the suction side wall to a point at approximately $z/z_0 = 0.65$.

The stable location for this low p^* fluid is close to the suction-side/shroud corner, where the reduced static pressure is lowest. However, as P_r is increasing in the streamwise direction in this corner region, the flow here is decelerating and diverging. Hence cross velocities are induced, away from the corner, which oppose the secondary flow up the suction surface and so prevent to low p^* fluid from reaching the corner region.

It is interesting that the large change in the distribution of P^* between Stations 1 and 2 is not reflected in a similar change in the velocity distributions as shown in Fig. 8. This is because there has been no significant rise in P_r in the suction-side/shroud corner region between Stations 1 and 2 (see Figs. 6 and 9) as the blades have loaded.

The blade-to-blade pressure gradient for the inducer bend can be approximately modeled by the streamline curvature equation

$$\frac{\partial p}{\partial r} = \frac{\rho W^2}{R_n} \tag{4}$$

Taking R_n for the inducer bend at Station 2 as 200 mm and $W = 15$ m/s, the calculated value for the blade-to-blade pressure difference at about midheight is $\Delta P_r = 0.25$, which is of the same magnitude as the measured value. This pressure difference is larger near the shroud, where the relative velocities are higher ($W \simeq 17$ m/s) and the blade-to-blade distance is larger. The calculated value is $\Delta P_r = 0.48$, which again compares well with the measurements.

Station 3. Station 3 is approximately halfway along the passage and the flow has turned through 58 deg of the axial-to-radial bend.

The reduced static pressure gradient required to turn the flow around the axial-to-radial bend can again be calculated from the streamline curvature equation (4). For the axial-to-radial bend, $R_n \simeq 200$ mm and $W \simeq 12$ m/s, which gives a calculated hub-to-shroud pressure difference of $\Delta P_r = 0.34$, close to the measured value in most of the potential flow region (see Fig. 12).

The velocity diagram (Fig. 11) shows that the axial-to-radial bend is dominating the secondary flow pattern. The passage is occupied by two opposing vortices; an anticlockwise vortex on the suction side, and a second, weaker, clockwise vortex on the pressure side of the passage near the hub. This is the pattern which is characteristic of a stationary axial-to-radial bend, but here there is evidence of a secondary flow along the shroud towards the suction side corner, which is generated by Coriolis forces due to the passage rotation. This flow along the shroud, together with the flow up the suction side, has convected the low p^* fluid on these two walls at Station 2 into the shroud/suction side corner region, as shown in Fig. 10.

The flow now has a jet-wake flow pattern. In the jet, where P^* is approximately unity (see Fig. 10), the potential flow has changed very little between Station 2 and 3, as can be seen from the velocity and pressure diagrams (Figs. 8, 9, 11, and 12). But a wake has formed as the low p^* fluid has accumulated and slowed down. This gives the first indication in the velocity diagram of a large-scale departure from a potential flow and as such, it corresponds remarkably closely with Eckardt's first observation of the wake, in his impeller, at his operating condition and his Station 3. In this study, however, the thickening of the suction side and shroud wall boundary layers has already been observed in the p^* diagram at Station 2 (Fig. 7) and the subsequent migration of this low p^* fluid between Stations 2 and 3.

Station 4. At Station 4, the passage is almost radial. The reduced static pressure distribution is therefore dominated by the tangential blade-to-blade gradient of pressure due to the Coriolis acceleration. This is seen in Fig. 15, where the static pressure falls almost linearly from the pressure side to the suction side near the hub. Near the shroud, however, the pattern is broken by a uniform pressure region in the wake.

This pressure gradient can be modeled fairly simply as due to a radial flow with a mean velocity $W = 12$ m/s. The tangential pressure gradient is then given by the simple expression:

$$\frac{1}{r}\frac{\partial p}{\partial \theta} = 2\rho\omega W \tag{5}$$

In the impeller at Station 4, the tangential distance between the suction and pressure wall is about 0.11 m. Hence, we

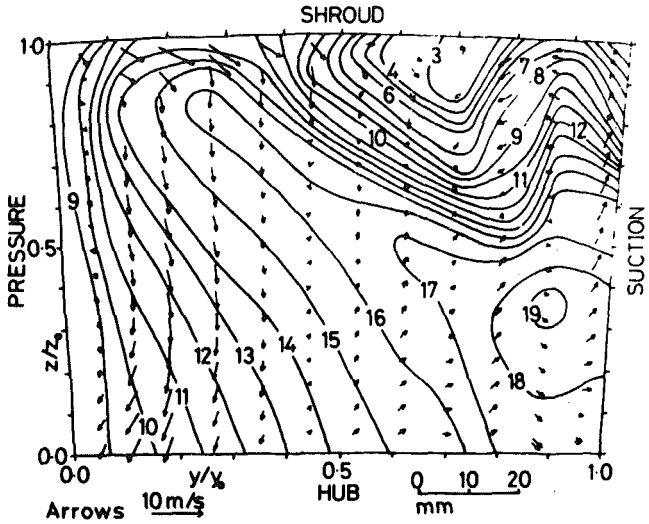

Fig. 14 Station 4: relative velocities – contours in m/s

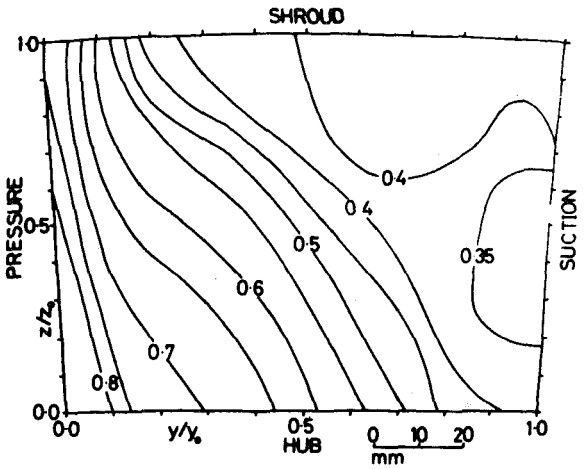

Fig. 15 Station 4: dimensionless reduced static pressure, P_r

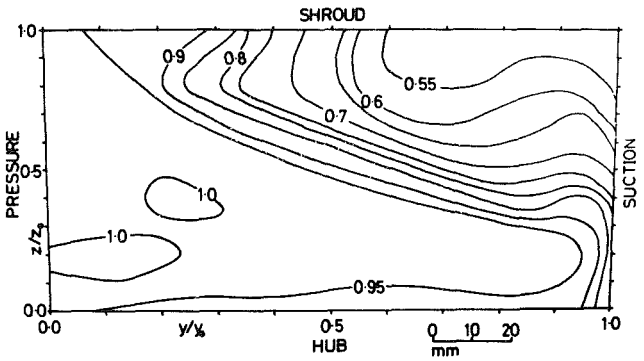

Fig. 16 Station 5: dimensionless rotary stagnation pressure, P^*

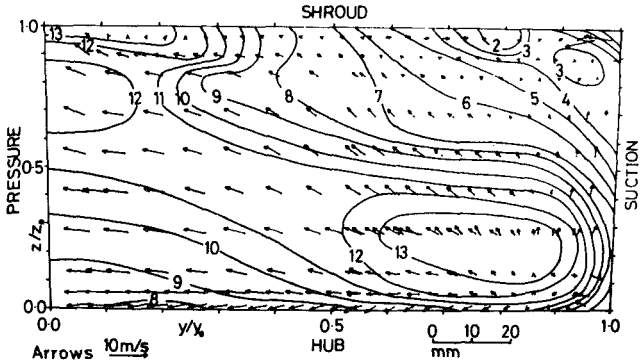

Fig. 17 Station 5: relative velocities – contours in m/s

obtain a simple estimate for the pressure difference between the blade surfaces of 0.51. This agrees well with the measured static pressure difference of about 0.50.

The stable location for low p^* fluid in the radial section of the passage is the suction side, which is also the position of the lowest reduced static pressure (see Fig. 15), as would be predicted for a straight rotating channel. However, although the axial-to-radial bend has a small influence on the p_r distribution, its influence remains in the inertia of the twin secondary flow vortices observed at Station 3 (see Fig. 14). The flow up the suction and pressure surfaces to the shroud has weakened considerably, but low p^* fluid is still being convected up the suction surface to the shroud. As illustrated by the velocities (Fig. 14) and the p^* contours (Fig. 13), the wake has moved further along the shroud, its core now being at $y/y_o = 0.7$, even though the stable location for low p^* fluid has moved the other way! This movement must be attributed to the inertia of the anticlockwise vortex on the suction side of the passage. The second vortex, the clockwise one on the pressure side of the passage, has been greatly augmented along the shroud by the action of Coriolis forces. The low p^* fluid from the secondary flows up the suction side and along the shroud collide on the shroud at $y/y_o \simeq 0.7$ and this causes low energy fluid to move away from the wall.

In the strong shear layer between the wake and the potential flow region at Station 4 turbulent mixing is probably suppressed by the action of curvature and Coriolis forces.

Station 5. Station 5 is close to the impeller exit and the passage is still radial as shown in Fig. 2.

The p^* contours (Fig. 16) show that the wake area had increased considerably between Stations 4 and 5. The minimum value of P^* at Station 5 is higher than that obtained at Station 4 ($P^* = 0.51$ compared with $P^* = 0.46$). The only way the rotary stagnation pressure of a fluid particle can increase along a streamline is by mixing with neighboring fluid with a higher value of p^*. Therefore, the lowest p^* fluid at Station 4 must have mixed with higher p^* fluid.

Mixing was suppressed at Station 4 by the strength of the Coriolis forces but, as can be seen from the p_r diagram (Fig. 18), these forces have weakened as the static pressure gradient has reduced, due to the blades unloading close to the impeller discharge. The reduced static pressure on the suction side has risen while that on the pressure side has dropped only slightly. This has been achieved in the wake region by mixing, as no further diffusion was possible with the very low momentum of the wake fluid. However, fluid in the suction side hub quarter of the passage has diffused considerably, decelerating from 18 to 13 m/s, while the fluid in the pressure-side/shroud corner region has accelerated to take the excess flow from the suction side.

The secondary velocities (Fig. 17) show the divergence of the highest velocity fluid, and this fluid is the most likely source of the high p^* fluid required to mix out with the wake fluid. The cross velocities also show that the flow up the suction side is carrying this high p^* fluid into the wake region, and a flow from the centre of the high velocity zone at $y/y_o = 0.8$, $z/z_o = 0.25$ is carrying similar fluid to the other side of the wake ($y/y_o = 0.4$, $z/z_o = 0.9$). The general trend in the cross velocities from the suction to the pressure side of the

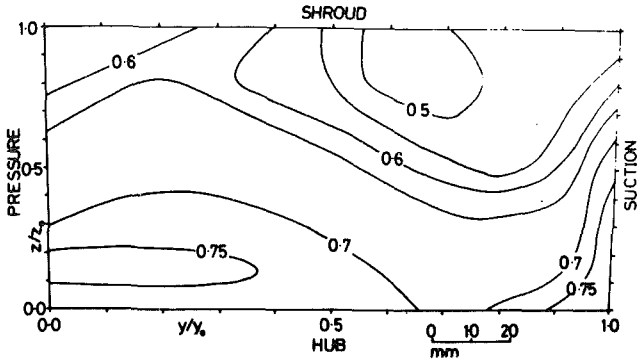

Fig. 18 Station 5: dimensionless reduced static pressure, P_r

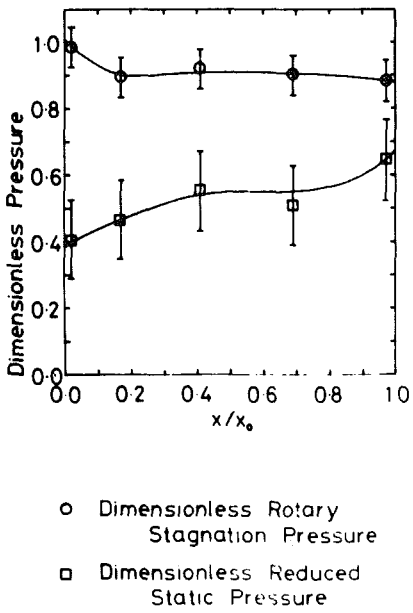

Fig. 19 Mass-averaged dimensionless pressures

passage is due to the slip of the flow near the outlet. This is most marked on the pressure side of the flow near the outlet. There is some evidence of the secondary flow along the shroud, due to the Coriolis forces, which has not been entirely effaced by the slip.

The wake has moved closer to the suction-side/shroud corner, so the secondary flow along the shroud must have been stronger than the flow up the suction surface between Stations 4 and 5. However, the wake is still some distance from its stable location on the suction side of the passage.

The dimensionless reduced static pressure, p_r, corresponds to the pressure coefficient of potential flow which has diffused from the maximum relative velocity in the inducer. This pressure coefficient is used by many designers as a simple criterion for two-dimensional boundary layer growth in a diffusing impeller flow. Clearly, the boundary layer flow in this study is not two-dimensional but nevertheless, it is interesting that the value of 0.5 for the wake is representative of the pressure coefficient necessary to cause separation of a two-dimensional turbulent boundary layer.

Mass-Averaged Pressures. The mass-averaged P^* (Fig. 19) shows that the main loss occurs between Stations 1 and 2, and this must be attributed to the boundary layer separation and associated mixing which takes place in this region. Figure 19 also shows that the diffusion of the flow through the impeller achieves a fairly steady rise in the mass-averaged P_r.

Conclusions

1 The wake flow observed in the present study is an accumulation of fluid with a low rotary stagnation pressure, p^*, which forms in the suction-side/shroud corner region of the impeller passage. The major flow phenomena which contribute to the formation and development of the wake are:

(*a*) The adverse gradient of reduced static pressure between Stations 2 and 3 near the shroud/suction-side corner, which results in a substantial increase in the quantity of low p^* fluid in this region at Station 2; and

(*b*) the convection of low p^* fluid by the secondary flows, which are generated in the boundary layers due to the curvature and rotation of the impeller passage.

2 The adverse gradient of reduced static pressure between Stations 2 and 3 causes the separation of the shroud boundary layer and also substantial turbulent mixing, which accounts for approximately two-thirds of the total loss in the impeller. The magnitude of this separation will therefore, to a large extent, determine the size of the wake in the discharge flow. The authors consider the separation to be an unsteady phenomenon which may exhibit periodic reversed flow.

3 The results show the build up of low p^* fluid upstream of the point where the first large-scale departures from potential flow are observed in the contours of relative velocity. Low p^* fluid from the boundary layer is observed to migrate to the shroud/suction-side corner region, where the wake is formed. It is therefore concluded that secondary flow contributes to the formation of the wake.

4 The axial-to-radial bend dominates the secondary flow pattern through most of the impeller. Two opposing passage vortices are induced, one on the suction side and one on the pressure side of the passage. On the suction side, low p^* fluid is carried by the vortex along the wall to the wake region. The passage vortex on the pressure side creates a secondary flow along the shroud towards the suction surface. This flow is enhanced by the action of Coriolis forces due to the passage rotation. The low p^* fluid in these two flows collides in the wake region and moves away from the shroud wall.

5 The inertia of the suction side passage vortex, induced in the axial to radial bend, prevents the wake from moving from the shroud to its stable location on the suction surface at the outlet. The authors therefore conclude that the secondary flows strongly influence the position of the wake in the outlet plane of a centrifugal impeller.

Acknowledgments

The authors wish to thank Rolls Royce Limited for their financial support of this project and especially Mr. P. H. Timmis of the Rolls Royce Helicopter Engine Group and Mr. P. Clark of Rolls Royce, Bristol, for their encouragement.

References

1 Cheshire, L. J., "Centrifugal Compressors for Aircraft Gas Turbines," *Proceedings of the Institution of Mechanical Engineers*, Vol. 153, 1945, p. 440.

2 Hamrick, J. T., Mizisin, J., and Michel, D. J., "Study of Three-Dimensional Flow Distribution Based on Measurements in a 48-Inch Radial-Inlet Centrifugal Impeller," NACA TN 3101, 1954.

3 Olivari, D., and Salaspini, A., "Measurement of Velocity Distribution at the Impeller Exit of a Radial Compressor," Technical Note 106, Mar. 1975, Von Kármán Institute, Belgium.

4 Eckardt, D., "Detailed Flow Investigations Within a High-Speed Centrifugal Compressor Impeller," *Journal of Fluids Engineering*, Vol. 98, 1976, pp. 390–402.

5 Smith, A. G., "On the Generation of the Streamwise Component of Vorticity for Flows in a Rotating Passage," *Aeronautical Quarterly*, Vol. 8, 1957, pp. 369–383.

6 Hawthorne, W. R., "Secondary Vorticity in Stratified Compressible Fluids in Rotating Systems," A-Turbo/TR63, Cambridge University Engineering Department, Cambridge, U.K., 1974.

7 Johnson, M. W., "Secondary Flow in Rotating Bends," JOURNAL OF ENGINEERING FOR POWER, Vol. 100, Oct. 1978, pp. 553–560.

8 Moore, J., "Eckardt's Impeller—A Ghost from Ages Past," A-Turbo/TR83, Cambridge University Engineering Department, Cambridge, U.K., 1976.

9 Anand, A. K., and Lakshminarayana, B., "An Experimental Study of Three-Dimensional Turbulent Boundary Layer and Turbulence Characteristics Inside a Turbomachinery Rotor Passage," JOURNAL OF ENGINEERING FOR POWER, Vol. 100, Oct. 1978, pp. 676–690.

10 Moore, J., "A Wake and an Eddy in a Rotating Radial-Flow Passage," JOURNAL OF ENGINEERING FOR POWER, Vol. 95, July 1937, pp. 205–219.

11 Johnston, J. P., "The Effects of Rotation on Boundary Layers in Turbomachinery Rotors," *Fluid Mechanics, Acoustics and Design of Turbomachinery*, NASA sp-304, part 1, 1974, pp. 207–249.

12 Johnson, M. W., and Moore, J., "The Development of Wake Flow in a Centrifugal Impeller," JOURNAL OF ENGINEERING FOR POWER, Vol. 102, Apr. 1980, pp. 382–390.

13 Johnson, M. W., "Secondary Flows in Centrifugal Compressor Impellers," Ph.D thesis, Cambridge University, Cambridge, U.K. May 1979.

The Influence of Flow Rate on the Wake in a Centrifugal Impeller

M. W. Johnson
Department of Mechanical Engineering,
The University of Liverpool,
Liverpool, U.K.

J. Moore
Department of Mechanical Engineering,
Virginia Polytechnic Institute,
Blacksburg, Va. 24061

Three-dimensional flows and their influence on the stagnation pressure losses in a centrifugal compressor impeller have been studied. All three mutually perpendicular components of relative velocity and stagnation pressure on five cross-sectional planes, between the inlet and outlet of a 1-m dia shrouded impeller running at 500 rpm were measured. Comparisons were made between results for a flow rate corresponding to nearly zero incidence angle and two other flows, with increased and reduced flow rates. These detailed measurements show how the position of separation of the shroud boundary layer moved downstream and the wake's size decreased, as the flow rate was increased. The wake's location, at the outlet of the impeller, was also observed to move from the suction surface at the lowest flow rate, to the shroud at higher flow rates.

Introduction

A "jet-wake" flow pattern has been observed in the discharge flow of a centrifugal compressor impeller by many researchers (e.g, [1,2,3]). However, the wake has been detected at different positions in the outlet plane. For example, Fowler [4] has located a wake on the suction surface at the outlet of his shrouded impeller (running with zero tip clearance), whereas Eckardt [5] observed his wake on the shroud. The location of the wake is known to be influenced by flow rate and running speed as well as impeller geometry, but even today design techniques cannot predict accurately either the wake's size or its location. This shortcoming must not only influence the resulting impeller performance, but also the efficiency of the diffuser which must accept the impeller discharge flow.

Objective. In this paper, results of measurements made in a de Havilland Ghost centrifugal impeller running at low speed (500 rpm) are presented. The authors' aim was to determine the main flow phenomena influencing the formation and development of the wake and how these phenomena are modified by changes in the flow rate. Accordingly, in the present study all three mutually perpendicular components of relative velocity and the rotary stagnation pressure were measured on five cross-sectional planes between the inlet and the outlet of the impeller for three different flow rates.

Secondary Flow. In all types of turbomachines secondary flows develop in the boundary layers, and it is therefore fruitful to consider the secondary flow pattern we might expect to develop in a centrifugal impeller. Johnson and Moore [6] discussed this in some detail, and here we note their salient points.

1 The centrifugal and Coriolis forces associated with the impeller passage curvature and rotation induce gradients of reduced static pressure ($p_r = p - \frac{1}{2}\rho\omega^2 r^2$) across the impeller passage. Frequently, in turbomachines pressure gradients due to both curvature and rotation occur simultaneously and here the Rossby number $\mathrm{Ro} = W/\omega R_n$ gives an indication of the relative magnitudes of these two effects.

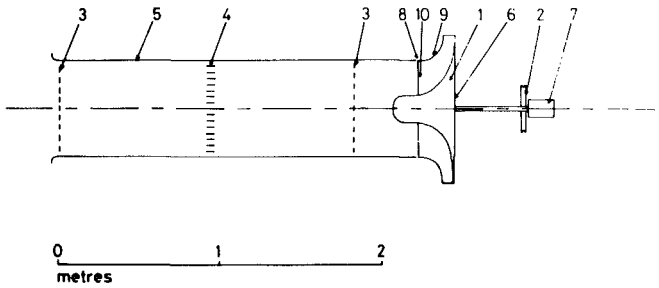

Fig. 1 Schematic of test rig:
(1) Impeller
(2) Pulley driven by motor
(3) Screens
(4) Honeycomb
(5) Inlet duct
(6) Pressure transducers and amplifiers
(7) Slip rings
(8) Seal
(9) Shroud attached to impeller
(10) Boundary layer trips

2 Fluid with a low rotary stagnation pressure ($p^* = p + \frac{1}{2}\rho W^2 - \frac{1}{2}\rho\omega^2 r^2$) is found in the boundary layers. This fluid tends to migrate under the influence of secondary flows to regions of low reduced static pressure. These regions have been termed "stable locations" by Johnson [7]. Johnson also discussed how low p^* fluid may not necessary accumulate at its stable location, as it may be carried beyond this point by the inertia of the secondary flows. Nevertheless, the stable location still gives a good indication of where a wake might be expected to form.

3 The centrifugal compressor impeller has two bends, the inducer bend and the axial-to-radial bend and these will both induce secondary flows. Rotation will modify these secondary flows wherever the flow has a nonaxial component of velocity. This occurs in the early part of the inducer, in the later part of the axial-to-radial bend and in the radial outlet

Contributed by the Gas Turbine Division of THE AMERICAN SOCIETY OF MECHANICAL ENGINEERS and presented at the 27th International Gas Turbine Conference and Exhibit, London, England, April 18-22, 1982, Manuscript received at ASME Headquarters December 2, 1981. Paper No. 82-GT-45.

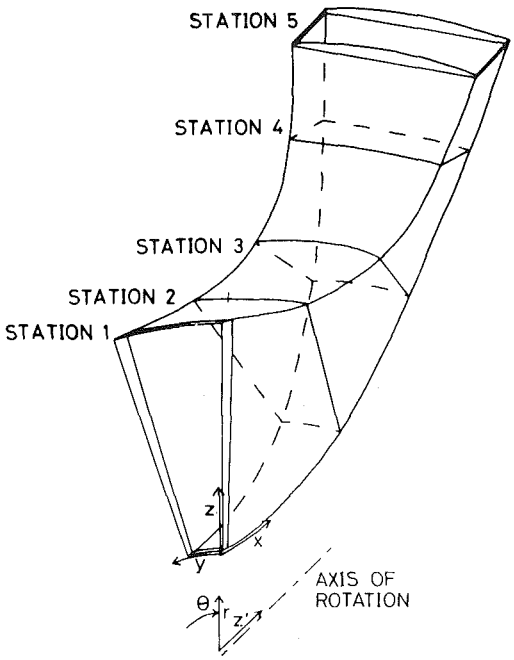

Fig. 2 Impeller passage with measurement planes

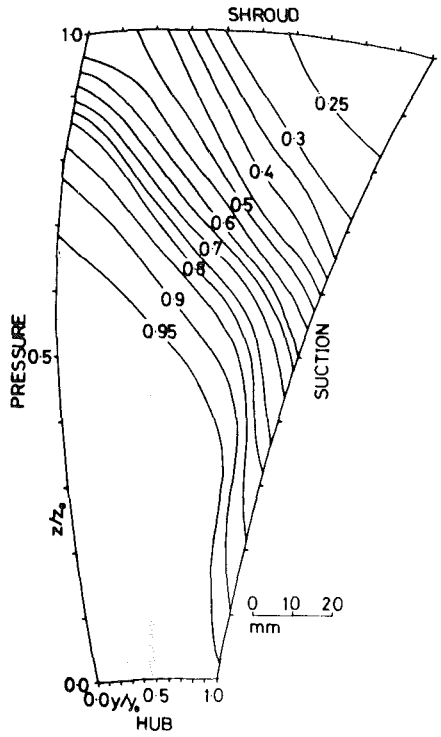

Fig. 3 "Below design" flow: Station 2 – dimensionless rotary stagnation pressure, P^*

section. Johnson and Moore therefore concluded that the stable location for low p^* fluid would move from the suction-side/shroud corner in the inducer to the shroud in the early part of the axial-to-radial bend and then pass back through the corner region to a point on the suction surface at the outlet.

Turbulent Mixing. Curvature and rotation modify the turbulent mixing which occurs in the boundary layers and in other regions of high shear. Johnston [8] and Bradshaw [9] have studied these modifications extensively, but here it is only necessary to note a simple rule for determining how mixing is modified. If in a region of high shear the cross-stream gradients of rotary stagnation pressure, p^*, and reduced static pressure, p_r, are in the same direction, turbulent mixing will be suppressed. However, if the gradients are in opposite directions, mixing will be enhanced. In general, this means that mixing is suppressed significantly in the boundary layer close to the stable location for low p^* fluid.

The Test Rig

The test rig, which is described by Johnson [10] and Johnson and Moore [6], is shown in a schematic diagram (Fig. 1). The impeller, which rotates at 500 rpm, is from a de Havilland Ghost engine. A shroud is attached to, and therefore rotates with, the impeller. Measurements were made on five cross-sectional planes (see Fig. 2), using probes which rotate with the impeller. A five-hole probe was used to measure all three mutually perpendicular components of relative velocity with an estimated accuracy of ± 1 m/s and ± 5 deg for a typical reading of 10 m/s. A Kiel probe was used to measure the rotary stagnation pressure relative to atmospheric pressure with an estimated accuracy of ± 10 N/m^2.

Experimental Results

The results presented are for three flow rates. The first corresponds to approximately zero incidence angle at the blade leading edge and is therefore referred to as the 'design' flow rate. The other two flows are 'below design' and 'above design' and are for flow rates of 85% and 121% of the 'design' flow rate respectively. The mass flow rates for the three flows are given in Table 1.

Presentation of Results.

Rotary Stagnation Pressures. The limiting values of rotary stagnation pressure (p^*_{max} and p^*_{min}) are determined by consideration of the impeller flow. At each flow rate, the approximately uniform axial inlet flow gave a uniform value of p^* at the impeller inlet. This was the highest value of p^* measured anywhere in the impeller flow and is therefore referred to as p^*_{max}. The lowest values of p^* in the impeller flow occur where fluid with low velocity is found in regions of low static pressure. p^*_{min} was therefore estimated from the measurements made in the boundary layer near the shroud surface in the inducer. The values of p^*_{min} and p^*_{max} for each flow rate are listed in Table 1.

Nomenclature

p = static pressure
p_r = reduced static pressure, $p_r = p - \frac{1}{2}\rho\omega^2 r^2$
p^* = rotary stagnation pressure, $p^* = p + \frac{1}{2}\rho W^2 - \frac{1}{2}\rho\omega^2 r^2$
P_r = dimensionless reduced static pressure, equation (2)
P^* = dimensionless rotary stagnation pressure, equation (1)
R_n = radius of curvature of bend
W = relative velocity
x/x_o = meriodional inlet-to-outlet coordinate measured along the shroud
y/y_o = pressure-side to suction-side coordinate
z/z_o = hub-to-shroud coordinate
ω = angular velocity
ρ = fluid density

Subscripts

min = minimum value
max = maximum value

Table 1 Impeller flow rates and limiting values of p^*

	Below design	Design	Above design
Measured mass flow rate (kg/s) in one impeller passage	0.121 (±.007)	0.142 (±.009)	0.172 (±.008)
Equivalent total mass flow rate (kg/s) through impeller	2.30 (±.13)	2.71 (±.17)	3.27 (±.15)
p^*_{max} (N/m^2 gauge)	−275 (±20)	−270 (±20)	−250 (±20)
p^*_{min} (N/m^2 gauge)	−565 (±30)	−600 (±30)	−650 (±30)
Mean incidence angle at blade leading edge	7° (±1°)	3° (±1°)	−2° (±1°)

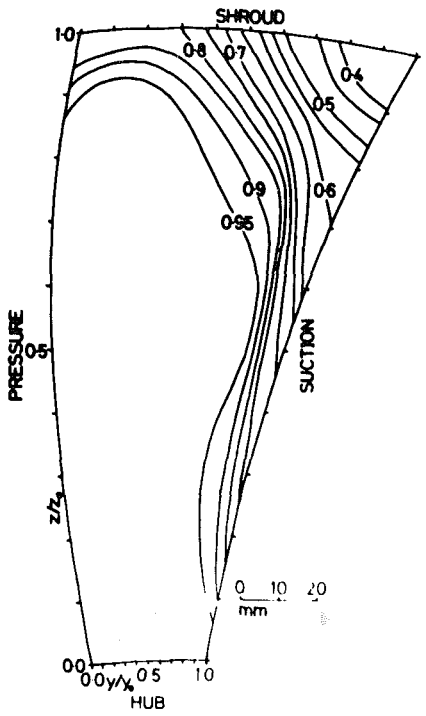

Fig. 4 "Design" flow: Station 2 – dimensionless rotary stagnation pressure, P^*

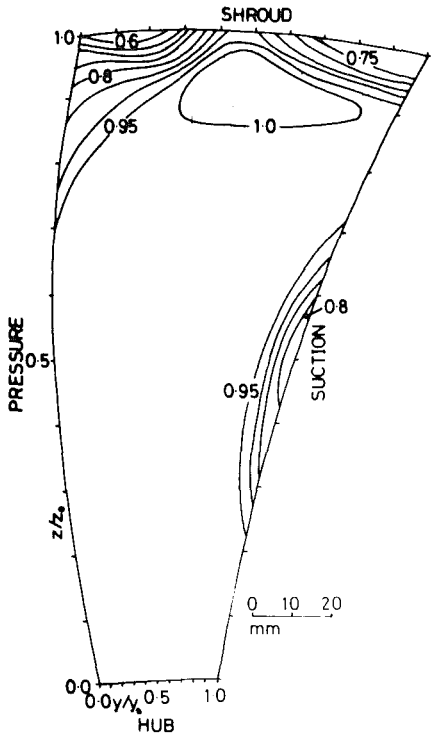

Fig. 5 "Above design" flow: Station 2 – dimensionless rotary stagnation pressure, P^*

The pressure difference $p^*_{max} - p^*_{min}$ is used to define a dimensionless rotary stagnation pressure, P^*, such that

$$P^* = \frac{p^* - p^*_{min}}{p^*_{max} - p^*_{min}} \quad (1)$$

Clearly, P^* can only vary between zero and one in the impeller and is equal to one anywhere within the inviscid potential flow region.

A dimensionless reduced static presure, P_r, is also defined such that

$$P_r = \frac{p_r - p^*_{min}}{p^*_{max} - p^*_{min}} \quad (2)$$

Relative Velocities. A "passage direction" is defined such that in this direction the ratio of the distances from each pair of walls remains constant. The relative velocities are then resolved into two components; a component in the passage direction and a component perpendicular to this, that is, in the cross-passage direction. In the diagrams, the velocity component in the passage direction is represented by contours and the cross-passage velocity component by an arrow at each measurement point. These arrows will therefore give an indication of the combined effects of flow diffusion and secondary flow.

Discussion

The Inducer Flow. At Station 2, which is close to the exit of the inducer, there are substantial differences between the P^* contours for the three flow rates (Figs. 3, 4, and 5). The loss close to the pressure-side/shroud corner at the "above design" flow rate (see Fig. 5) is probably due to a local separation induced by the high incidence angles at the blade leading edge (up to 20 deg). However, in order to understand how much larger losses occurred at the lower flow rates, the flow in the suction-side/shroud corner region must be studied.

At each station, the lowest measured value of P^*, which always occurred near the suction-side/shroud corner, together with the reduced static pressure at the same measurement point are plotted in Fig. 6. This diagram then shows that an adverse pressure gradient in the streamwise direction occurs in this region at some point in the impeller for each of the three flow rates. This adverse pressure gradient will induce the separation of the boundary layer in this region. Let us define the probable location of this separation as the point where flow with a relative velocity less than 20 percent of the maximum relative velocity in the inlet plane was first observed (that is, where $P^* - P_r < 0.04$). Figure 6 then indicates that

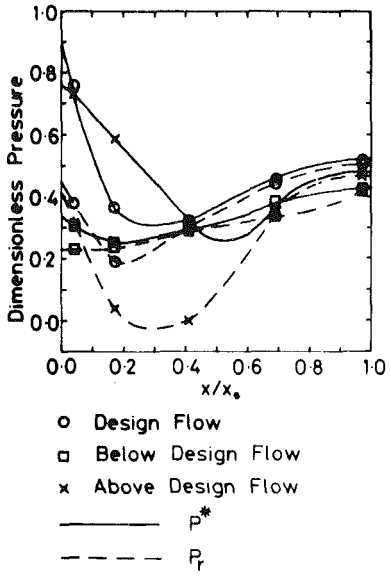

Fig. 6 Dimensionless pressures in the wake region

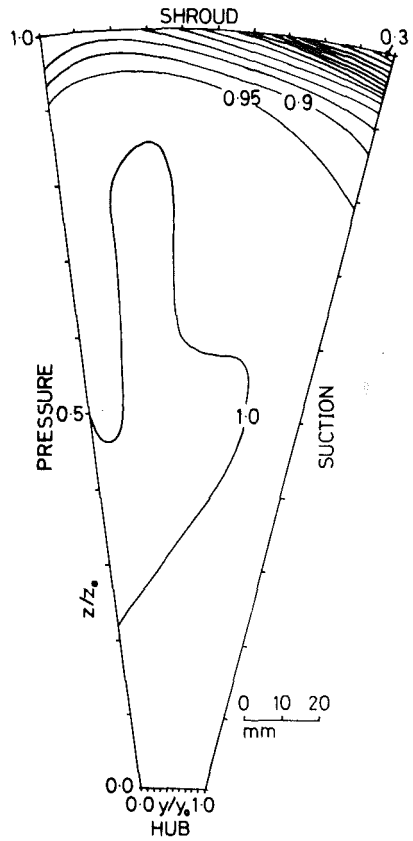

Fig. 7 "Below design" flow: Station 1 – dimensionless rotary stagnation pressure, P^*

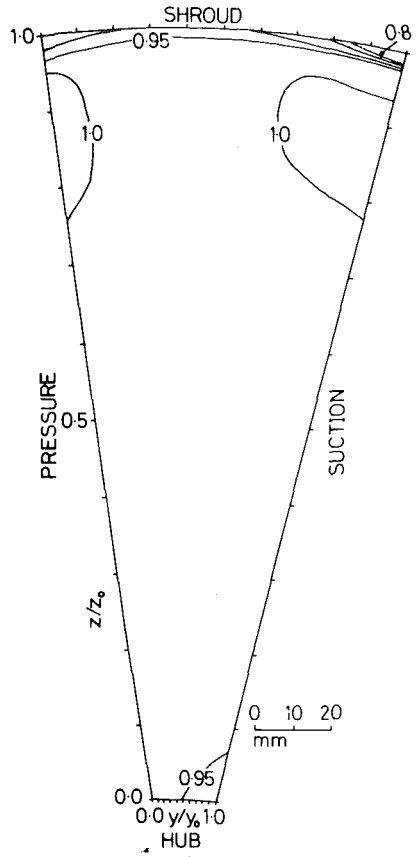

Fig. 8 "Design" flow: Station 1 – dimensionless rotary stagnation pressure, P^*

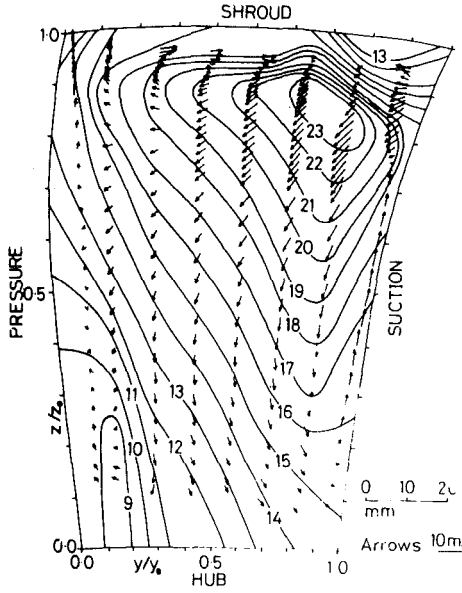

Fig. 9 "Above design" flow: Station 3 – relative velocities-contours in m/s

separation occurs near Station 2 in the "below design" flow, near Station 3 in the "design" flow and near Station 4 in the "above design" flow.

The P^* contours at Station 1 in the "below design" flow (Fig. 7) and at Station 1 (Fig. 8) and Station 2 (Fig. 4) in the "design' flow show that substantial p^* losses occur upstream of the point of separation. The loss mechanism responsible can perhaps be best understood by considering the plight of low p^* fluid in the shroud boundary layer at Station 1. Regions with P^* as low as zero are present here, but they do not appear in the figures because the measurement probes could not be brought close enough to the shroud wall. Such low energy fluid must mix with fluid with a higher p^* value in order to avoid being brought to rest by the adverse pressure gradient. The P^* plot in Fig. 6 suggests that fluid particles in the suction-side/shroud corner region mix with lower p* fluid until their momentum is depleted at which point they start mixing with higher p^* fluid, thus maintaining a small, but positive, velocity in the streamwise direction.

It is perhaps surprising that large mixing losses occur in the inducer as turbulent mixing is suppressed in the suction-side/shroud corner region by both Coriolis and centrifugal

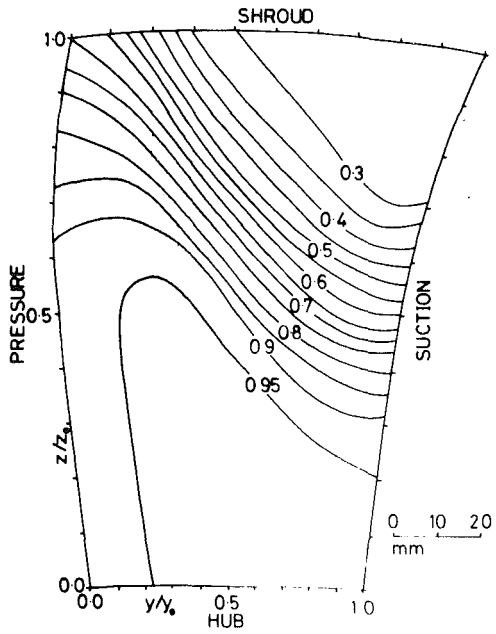

Fig. 10 "Below design" flow: Station 3 – dimensionless rotary stagnation pressure, P^*

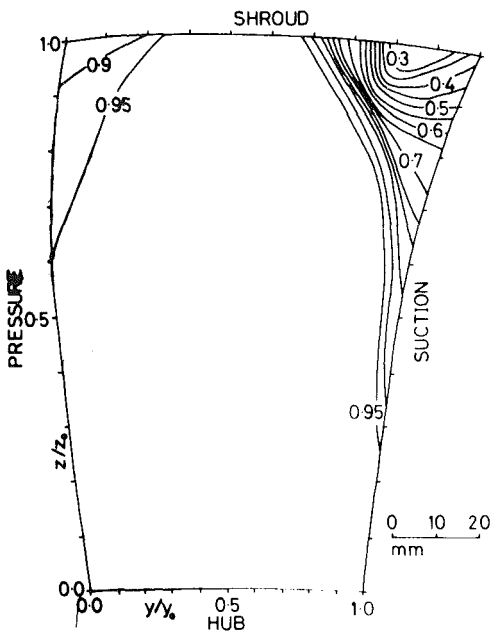

Fig. 12 "Above design" flow: Station 3 – dimensionless rotary stagnation pressure, P^*

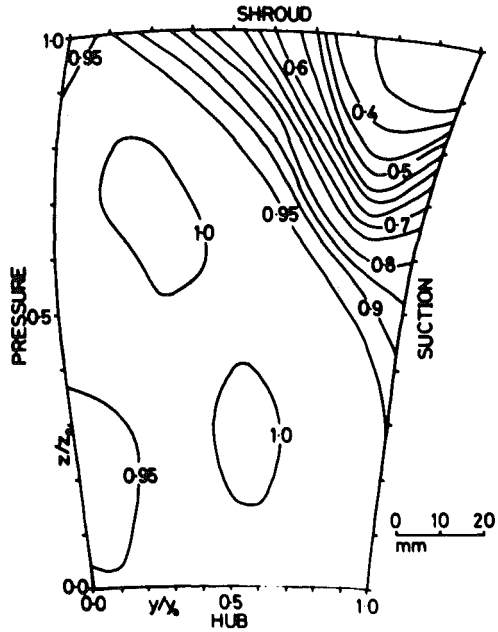

Fig. 11 "Design" flow: Station 3 – dimensionless rotary stagnation pressure, P^*

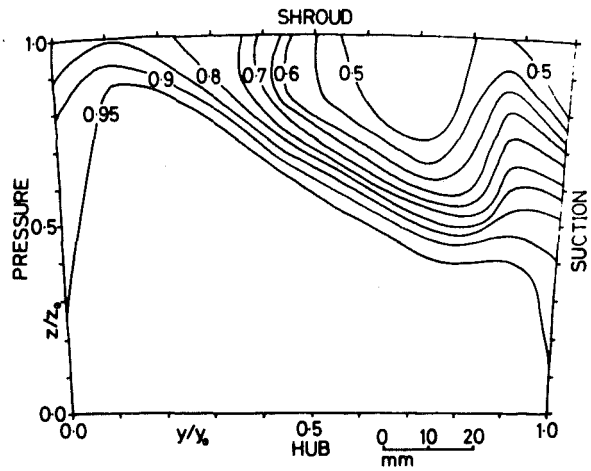

Fig. 13 "Design" flow: Station 4 – dimensionless rotary stagnation pressure, P^*

forces. However, at Station 2 in both the "design" and "below design" flows, the measured pressures in this corner region were found to be very unsteady. The authors therefore believe that the separation of the shroud boundary layer is probably an unsteady flow phenomenon and that periodic reversed flow may occur in this region.

The Axial-to-Radial Bend. Station 3 is about halfway through the impeller and the axial-to-radial bend has turned the flow through about 58 deg. The velocity diagram for the "above design" flow (see Fig. 9) is typical of the flow pattern at all three flow rates. The arrows in this diagram indicate that the curvature of the axial-to-radial bend has induced significant secondary flows. These secondary flows, which move low p^* fluid from the suction and pressure side boundary layers towards the shroud, can be clearly seen. The secondary flow on the suction surface is stronger as there is more low p^* fluid present in this boundary layer. The overall secondary flow pattern is dominated by two opposing passage vortices; an anticlockwise one on the suction side of the passage and a clockwise one on the pressure side. This twin vortex pattern is similar to that observed in a stationary bend by Hawthorne [11] and therefore the curvature of the axial-to-radial bend can be considered to dominate the secondary flow pattern. However, close to the shroud the affects of Coriolis acceleration are noticeable. A secondary flow which transports low p^* fluid from the shroud boundary layer towards the suction-side corner region has developed. This secondary flow is of similar strength to that on the suction surface as might be expected as the Rossby number for the axial-to-radial bend is approximately one.

At all three flow rates an accumulation of low p^* fluid occurs in the suction-side/shroud corner region. The size of this wake region is larger in the "below design" case (Fig. 10) and smaller in the "above design" case (Fig. 12) than for the "design" flow rate (Fig. 11) as might be predicted from the differing losses which occured in the inducer.

The passage is almost radial at Station 4 and therefore the

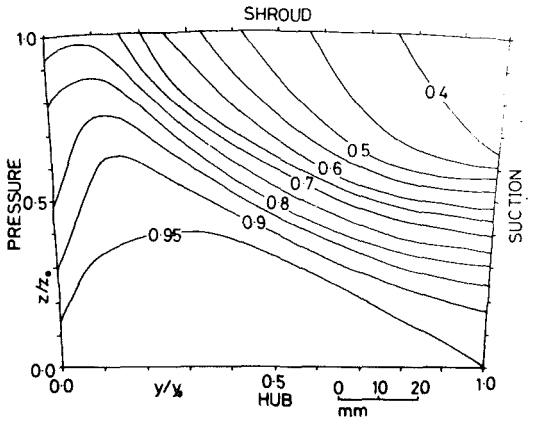

Fig. 14 "Below design" flow: Station 4 – dimensionless rotary stagnation pressure, P^*

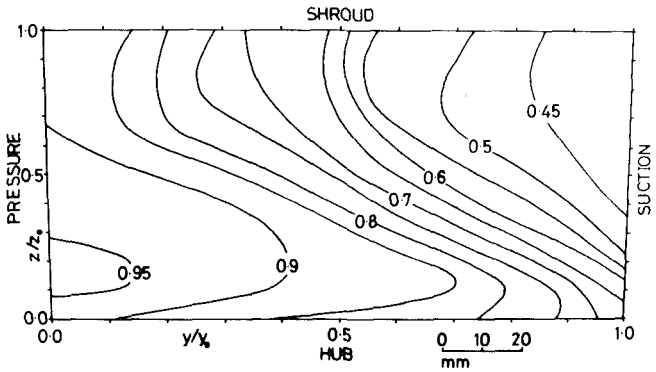

Fig. 15 "Below design" flow: Station 5 – dimensionless rotary stagnation pressure, P^*

stable location for the wake fluid will be on the suction surface. It is perhaps surprising therefore to find in the "design" flow that the wake has moved the other way to a position on the shroud! (see Fig. 13). The migration is due to the inertia of the suction-side passage vortex which developed in the axial-to-radial bend. Again, the flow pattern is similar in the "above design" flow, but in the "below design" flow the secondary flows generated by the curvature of the axial-to-radial bend are weaker (Rossby number smaller) and so the wake remains in the corner region (see Fig. 14).

The Radial Section. At the outlet of the impeller, the passage is radial, and therefore the stable location for low p^* fluid will be on the suction surface. However, the wake is only found here at the "below design" flow rate (see Figs. 15 and 16). The wake's position is found to be strongly influenced by any increase in flow rate and hence Rossby number (see Figs. 17 and 18). At these higher flow rates, the inertia of the vortex on the suction side of the passage prevents the wake from moving to its stable location. This vortex can still be seen at Station 5 in the relative velocity diagram at the "above design" flow rate (Fig. 19, $y/y_o = 0.6$ to 1.0, $z/z_o = 0.6$ to 1.0). The overall cross flow from the suction to pressure side is due to slip, as Station 5 is only about 5 mm from the impeller outlet.

Turbulent mixing is suppressed on the suction surface by Coriolis forces in the radial section of the passage. Therefore, it might be expected that more mixing will occur in the radial outlet section between the wake and the jet at the two higher flow rates.

The total pressure plots (Figs. 15, 17, and 18) show that the size of the wake increases with a decrease in flow rate. The jet and the wake are quite distinct at the two higher flow rates, but in the "below design" flow the two regions are less well

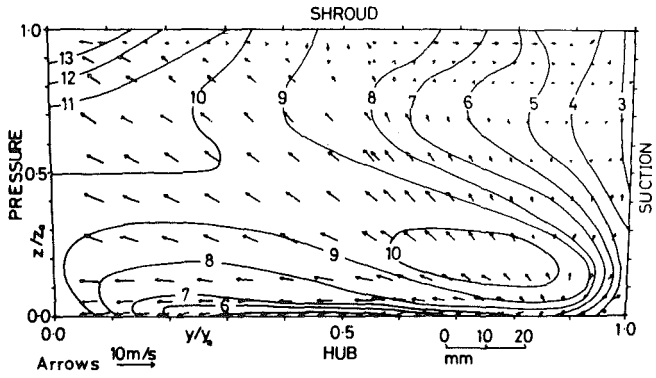

Fig. 16 "Below design" flow: Station 5 – relative velocities, contours in m/s

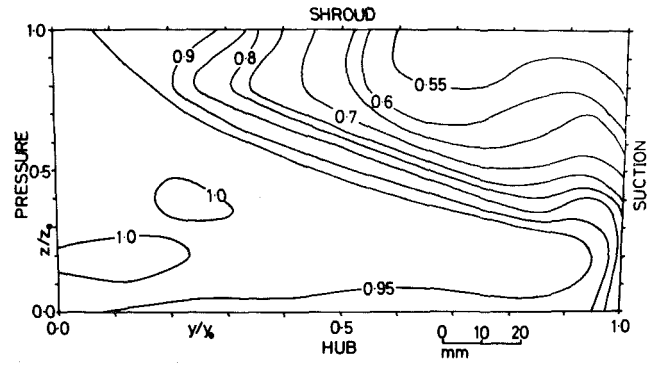

Fig. 17 "Design" flow: Station 5 – dimensionless rotary stagnation pressure, P^*

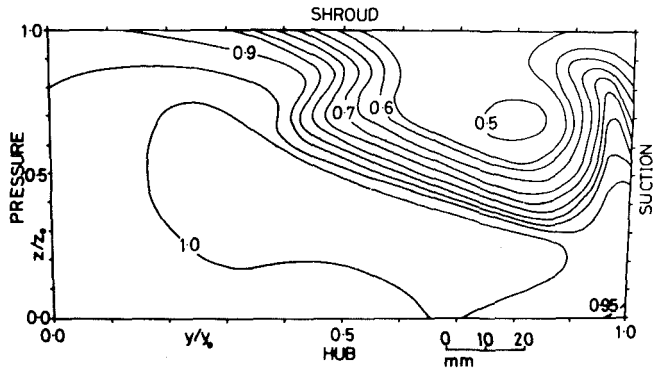

Fig. 18 "Above design" flow: Station 5 – dimensionless stagnation pressure, P^*

defined. This merging of the jet and wake may be due to the upstream influence of rapid mixing at the outlet. This is likely to occur between the wake fluid on the suction side of one passage with the fluid on the pressure side of the neighbouring passage in the "below design" flow. Such rapid mixing will be less significant at the two higher flow rates where the rotary stagnation pressures near the suction and pressure surfaces are more nearly equal.

Mass-Averaged Pressures. Mass-averaged reduced static pressures and rotary stagnation pressures for each of the three flow rates are presented in Fig. 20. The p^* curves show that there are two sections of the impeller where major losses occur. The first is in the inducer where the shroud boundary layer separated at the two lower flow rates. The severity of this separation and hence the loss increases with a reduction in the flow rate. The second region of loss occurs in the radial section between Stations 4 and 5. As already discussed, the upstream influence of rapid mixing at the impeller exit is

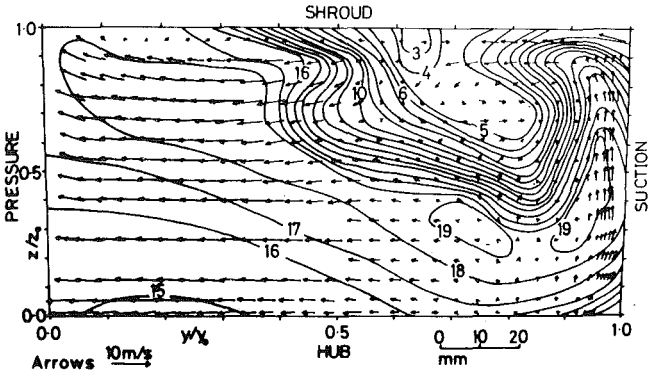

Fig. 19 "Above design" flow: Station 5 – relative velocities, contours in m/s

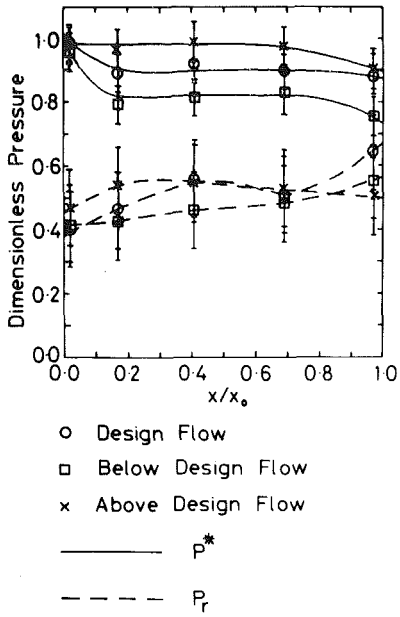

Fig. 20 Mass-averaged dimensionless pressures

believed to be responsible for the mixing losses at the "below design" flow rate. The smaller losses at the two higher flow rates are attributed to mixing between the jet and the wake which is not suppressed near the shroud in these flows. It should be noted that downstream of the impeller the discharge flow must eventually mix out to a uniform flow. Large mixing losses are therefore likely to result in the diffuser at the higher flow rates where the impeller outlet flow is very nonuniform.

The reduced static pressure curves (Fig. 20) show where diffusion took place in the impeller. It is clear therefore that most diffusion occurred in the impeller at the "design" flow rate. The diffusion is reduced in the "below design" flow by the high mixing losses in the inducer and is smaller in the "above design" flow because of the highly nonuniform flow in the axial-to-radial bend and outlet section of the impeller.

Conclusions

1 Significant total pressure losses occur in two regions of the impeller:

(*a*) In the suction-side/shroud corner region in the inducer at both the "below design" and "design" flow rates; and

(*b*) in the final radial section of the impeller at all three flow rates.

2 The losses in the inducer are the result of an adverse pressure gradient in the streamwise direction in the suction-side/shroud corner region which causes the separation of the boundary layer. The separation point moves downstream as the flow rate is increased until, at the "above design" flow rate, separation losses are entirely avoided in the inducer.

3 Secondary flows develop in the axial-to-radial bend of the impeller, and these transport low p^* fluid from the boundary layers towards the stable location near the shroud/suction-side corner. A wake forms in this region at all three flow rates. Turbulent mixing is suppressed close to the stable location and normally therefore little mixing between the wake and jet fluid occurs.

4 The losses which result in the final radial section of the impeller occur for two different reasons. In the "below design" flow rapid mixing is believed to take place downstream of the outlet between the wake from one passage and the jet from the neighbouring passage. This mixing may then influence the flow in the radial section of the impeller and induce the stagnation pressure losses observed in the results. At higher flow rates, losses are induced by the inertia of the secondary flows developed in the axial-to-radial bend. The secondary flow up the suction surface directs the wake away from its stable location on the suction side to a position on the shroud. Here, turbulent mixing between the jet and wake is not suppressed and therefore some mixing losses occur. At the below design flow rate, this secondary flow is much weaker and the wake remains close to its stable location.

5 At the outlet, the wake is located on the suction surface in the "below design" flow, near the suction-surface/shroud corner in the "design" flow and on the shroud in the "above design" flow. It is concluded that the relative magnitudes of the secondary flows due to curvature and due to rotation generated in the axial-to-radial bend are responsible for the wake's position. The Rossby number associated with this bend, therefore, gives a useful indication of where the wake is likely to reside in the discharge flow.

Acknowledgments

The authors wish to thank Rolls-Royce Limited for their financial support of this project and especially Mr. P. H. Timmis of the Rolls-Royce Helicopter Engine Group and Mr. P. Clarks of Rolls-Royce, Bristol, for their encouragement.

References

1 McDonald, G. B., Lennemann, E., and Howard, J. M. G., "Measured and Predicted Flow Near the Exit of a Radial-Flow Impeller," ASME JOURNAL OF ENGINEERING FOR POWER, Vol. 93, No. 4, Oct. 1971.

2 Mizuki, S., Ariga, I., and Watanabe., "A Study on the Flow Mechanism within Centrifugal Impeller Channels," ASME Paper No. 75-GT-14, Mar. 1975.

3 Olivari, D., and Salaspini, A., "Measurement of Velocity Distribution at the Impeller Exit of a Radial Compressor," Technical Note 106, Von Kármán Institute, Belgium, Mar. 1975.

4 Fowler, H. S., "An Investigation of the Flow Processes in a Centrifugal Compressor Impeller," ME-220, National Research Council of Canada, July 1966.

5 Eckardt, D., "Detailed Flow Investigations Within a High-Speed Centrifugal Compressor Impeller," ASME *Journal of Fluids Engineering*, Vol. 98, 1976, pp. 390–402.

6 Johnson, M. W., and Moore, J., "The Development of Wake Flow in a Centrifugal Impeller," ASME JOURNAL OF ENGINEERING FOR POWER, Vol. 102, 1980, pp. 382–390.

7 Johnson, M. W., "Secondary Flows in Rotating Bends," ASME JOURNAL OF ENGINEERING FOR POWER, Vol. 100, No. 4, Oct. 1978, pp. 553–560.

8 Johnston, J. P., "The Suppression of Shear Layer Turbulence in Rotating Systems," Fluid Mechanics, Acoustics and Design of Turbomachinery Rotors, NASA SP-304, 1974, pp. 207–250.

9 Bradshaw, P., "Effects of Streamline Curvature on Turbulent Flow," AGARDograph 169, 1973.

10 Johnson, M. W., "Secondary Flows in Centrifugal Compressor Impellers," Ph.D. thesis, Cambridge University Engineering Department, Cambridge, U.K. May 1979.

11 Hawthorne, W. H., "Secondary Circulation in Fluid Flow," Gas Turbine Report, Massachusetts Institute of Technology, Cambridge, Mass., May 1950.

Secondary Flow Effects and Mixing of the Wake Behind a Turbine Stator

A. Binder

R. Romey

Research Engineers,
DFVLR Propulsion Institut,
Cologne, West Germany

In highly loaded turbines with large hub/tip ratios there is a marked increase in secondary flow effects. The optimization of the turbine flow requires detailed knowledge both of three-dimensional cascade flow and of the wake impinging on the downstream rows of airfoils. Therefore, in the DFVLR, thorough investigations of a single-stage turbine with cold air flow were performed. The stator of this turbine was designed for transonic flow and has a hub/tip ratio of 0.756 and an aspect ratio of 0.56. First, measurements were taken without the rotor in several sections behind the turbine stator with special regard to the mixing of the wakes and secondary vortices. Distributions of total pressure loss coefficient and flow direction give the order of magnitude of the mixing losses. Also, position, intensity, structure, and development of secondary vortices are shown. Some complementary measurements were carried out using five-hole probes. They confirm the above described results from two-dimensional measurements.

Introduction

In turbines of low aspect ratio (h/c) secondary losses form a significant part of total losses, and their reduction would offer a substantial potential to improve efficiency.

In recent years many experimental and theoretical studies on secondary flow effects have been presented. These papers describe the effects of secondary flow and also methods of calculating the secondary losses. Those publications testing the development of secondary flow within the blade passage [9–12], are of special importance. The papers of Langston [9] and Marchal and Sieverding [11] very clearly express the relations in plane turbine cascades. Langston [9] carried out detailed measurements in the boundary layer on the side wall and gives simple empirical correlations.

In the DFVLR an experimental investigation of secondary flow effects was conducted with a single stage cold air turbine. Before carrying out complete stage tests, there was an opportunity to take detailed measurements from a circular turbine stator with realistic three dimensional flow effects.

In the present work, the flow behind the turbine stator (without rotor) is described with special regard to mixing of the wake and following the secondary vortex flow. An attempt was made to locate the vortices by means of the yaw angle distribution by interpretations based on relations shown in the appendix.

The mixing of the wake behind the turbine stator results in an increase of losses, which are called mixing losses. At those positions, where the measurements of mixing losses were taken, the rotor is normally mounted. In further tests, run with the complete stage, the measured mixing losses downstream of the stator would be included in measured rotor losses although they are not produced within the rotor.

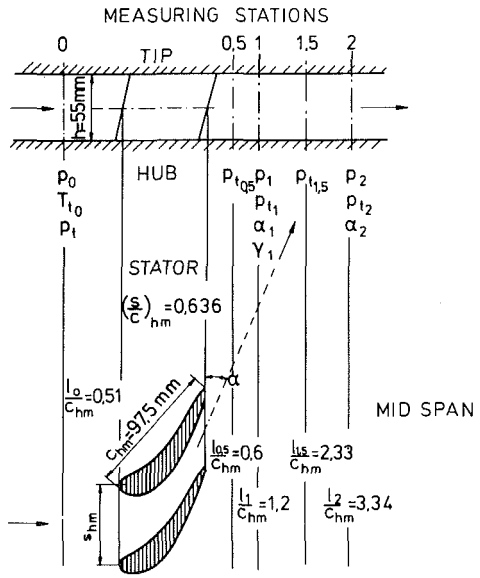

Fig. 1 Stator geometry and measuring planes

Experimental Apparatus

Testing was conducted in a turbine stator with low aspect ratio and high hub-to-tip ratio. Higher secondary flows will be produced by the low aspect ratio and the long chord.

Contributed by the Gas Turbine Division of THE AMERICAN SOCIETY OF MECHANICAL ENGINEERS and presented at the 27th International Gas Turbine Conference and Exhibit, London, England, April 18–22, 1982, Manuscript received at ASME Headquarters December 2, 1981. Paper No. 82-GT-46.

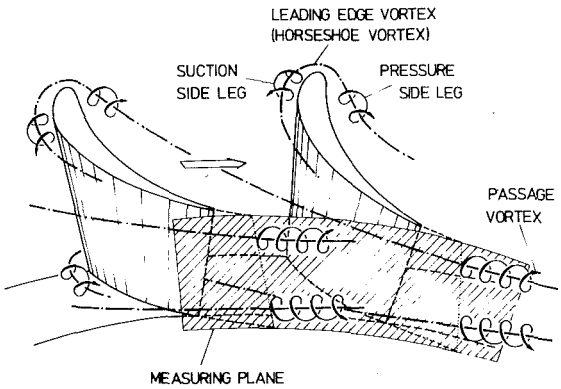

Fig. 2 Vortex systems within blade passages

The stator geometry is as follows:

Tip diameter	$d_G = 0.45$ m
Span	$h = 0.055$ m
Chord (mid-span)	$c_{hm} = 0.0975$ m
Blade spacing (mid-span)	$s_{hm} = 0.062$ m
Aspect ratio (mid-span)	$h/c_{hm} = 0.56$
Hub-to-tip ratio	$r_N/r_G = 0.756$
stagger angle (mid-span)	$\beta = 46$ deg
flow angle at inlet (mid-span, designed)	$(\alpha_{in})_{hm} = 90$ deg
flow angle at exit (mid-span, designed)	$(\alpha_{ex})_{hm} = 21.1$ deg

The tests described were the first measurements in the turbine, and were taken without the rotor. They were performed to obtain some information on losses, stream angles, and secondary flows behind the stator. The measurements were taken in one plane before and four planes behind the stator (Fig. 1). The distances of the measuring planes from trailing edge were measured in the streamwise direction (mid-span) normalized on the chord in mid-span. In one plane behind the stator, additional five-hole probe measurements were conducted to obtain information on static pressure and radial components. Because of the high test costs, measurements were performed only at one low Mach number.

The quantities measured are shown in Fig. 1. The air inlet angle was not recorded in all tests, because controls always gave an axial flow direction.

The static pressure on the walls (hub and casing) was taken in planes 0, 1, and 2. Only in plane 1 (five-hole probe measurements) was it measured in the flow field.

For technical reasons in planes 0.5 and 1.5, only total pressure could be taken. The total pressure has been measured by Kiel type probes, the yaw angle by wedge type probes and the total temperature by a thermocouple probe.

In the five-hole probe tests, the total pressure, yaw angle, slope angle, and static pressure were obtained with one probe. All probes had a tip diameter of 1.8 mm. Measurements at thirteen positions in the spanwise direction and sixteen positions in the circumferential direction were taken in each plane, of which twelve positions in the circumferential direction were in one channel.

Test Conditions

All tests were run with axial flow at inlet. The test conditions wer as follows:

$$\bar{\bar{p}}_0 = 2.346 \text{ bar}$$
$$\bar{\bar{T}}_{t0} = 321.7 \text{ K}$$
$$\bar{\bar{M}}_1 = 0.74$$

The mass flow rate for this case was $m = 12.3$ kg/s. The Reynolds number in plane 1, referred to the chord at mid-span and the averaged values, was $\text{Re}_1 = 2.6 \times 10^6$.

The five-hole probe was used at the following conditions:

$$\bar{\bar{p}}_0 = 2.1697 \text{ bar}$$
$$\bar{\bar{T}}_{t0} = 321.0 \text{ K}$$
$$\bar{\bar{M}}_1 = 0.503$$

The mass flow rate was $m = 9.8$ kg/s, the Reynolds number $\text{Re}_1 = 1.83 \times 10^6$.

Experimental Results

Firstly, the results of measurements taken in the four planes behind stator are given.

Plane 0.5 The distribution of the total loss coefficient in plane 0.5 is shown in Fig. 3. The region showing high loss is the wake. It is inclined to the radial direction due to the radial yaw angle distribution behind stator and the different axial distances between measuring plane and trailing edge. The two regions of high loss, A and B, are not caused by the wake; they are the result of secondary flows within the blade passage. The development of such loss regions is described in the works of Langston, Nice and Hooper [10] and Marchal and Sieverding [11].

At the walls, both casing and hub, the inlet boundary layer separates near the leading edge and forms a leading edge vortex called a horseshoe vortex with one leg in one blade passage (see Fig. 2) and the other leg in the adjacent passage.

Nomenclature

c = chord
d = diameter
h = blade height
l = distance from trailing edge in streamwise direction
M = Mach number
m = mass flow rate
p = pressure
q = dynamic head, $q = (\rho \cdot v_s^2/2)_{hm}$
Re = Reynolds number
r = radius
s = blade spacing
T = temperature
v = velocity
x = coordinate
y = coordinate
z = coordinate
α = yaw angle (angle between absolute velocity and a plane perpendicular to the axis)
β = stagger angle with respect to axial direction
γ = slope angle, $\sin\gamma = v_r/v_{abs}$ (positive to hub)
ζ = total pressure loss coefficient $(\zeta_i = (\bar{p}_{t0}(r) - p_{ti}(r,\varphi))/q_i$
ρ = density
φ = coordinate in circumferential direction

Subscripts

i = 0, 0.5, 1, 1.5, 2 = numbers of measuring planes
abs = absolute
hm = mid span
G = tip
N = hub
s = isentropic
t = total
stat = static
u = tangential
x = in x-direction
y = in y-direction
z = in z-direction
in = inlet
ex = exit

Superscripts

$-$ = pitchwise averaged value
$=$ = average over the entire measuring plane.

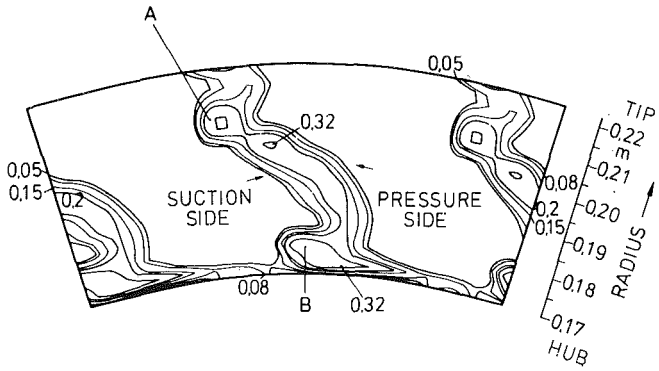

Fig. 3 Isobar plot of total pressure loss coefficients in plane 0.5

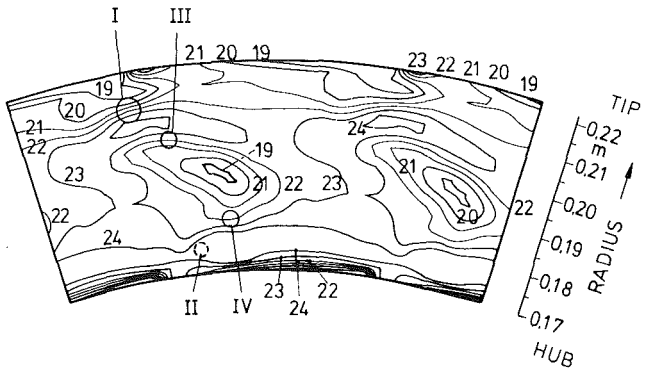

Fig. 5 Isoclinal plot of yaw angles (α = constant) in plane 1

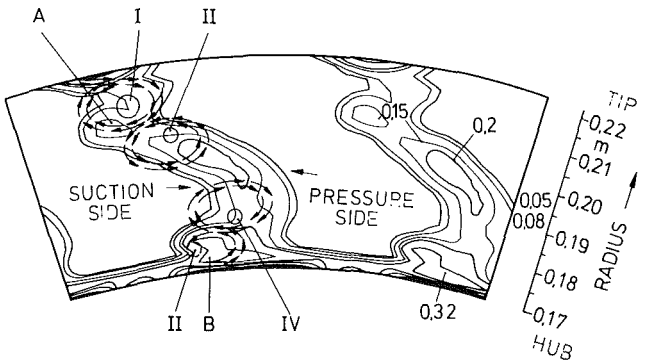

Fig. 4 Isobar plot of total pressure loss coefficients in plane 1

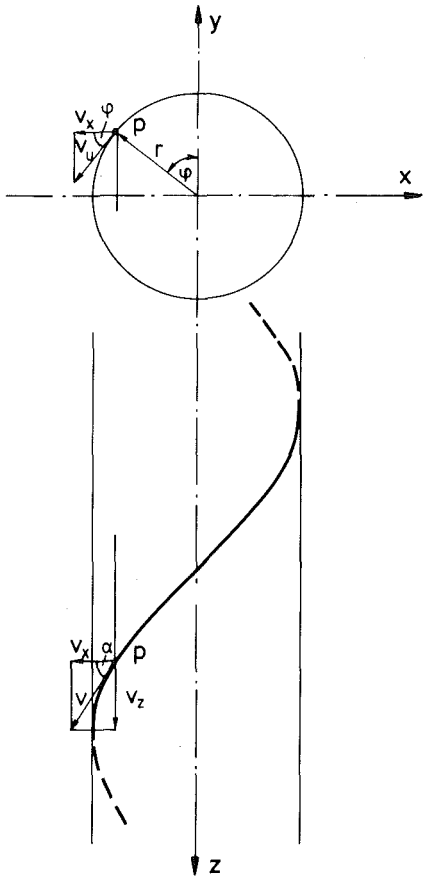

Fig. 6 Spiral motion around the z-axis

The pressure side leg of the leading edge vortex initiates a flow, on the wall, from the pressure surface to the suction surface within passage [11]. The pressure gradient between pressure and suction surface also leads to flow from the pressure to suction surface in the boundary layer on the wall. This flow reinforces the pressure side leg of the leading edge vortex and both form the passage vortex. Due to this flow on the wall, low energy material accumulates near the wall on the suction surface. The accumulation of this "high loss" material considerably disturbs the suction surface boundary layer and this results in additional losses.

Behind the stator, the passage vortex comprises the low energy material which has accumulated near the suction surface. So the approximate positions of the passage vortices can be recognized by the loss distribution. The rotation of the suction side leg of the leading edge of vortex (Langston labeled it "counter vortex") rotates in the opposite sense to the passage vortex. It is much smaller than the passage vortex, and it probably dissipates because of viscous effects and the remainder of it passes into the wake region behind the blade (see [11]).

The high loss region A is at a distinct distance from the casing, while the region B is close to the hub (Fig. 3). This is the consequence of the radial pressure gradient due to the centrifugal forces (higher pressure on the casing). This pressure gradient is built up by deflection within the turbine stator. Reduction of this gradient, behind the stator, requires a radial flow towards the hub. This radial flow moves the region B to the hub and separates the region A from the casing. Within the wake, there is a stronger flow towards the hub, because the tangential velocity is lower. As a consequence, low energy material from the wake migrates to the hub and thus increases the loss regions near the hub.

Plane 1. In plane 1 (Fig. 4), the wake is more inclined to the radial direction than in plane 0.5. However the wake region near the hub is less inclined or not inclined at all. This is a result of the design geometry (see chapter 1, "Experimental Apparatus"). The qualitative loss distribution is according to that in Fig. 3.

The relations, derived in the appendix are taken to locate the centers of vortices. If a vortical flow is centered on the z-axis (Fig. 6), the direction of flow is measured in a plane perpendicular to the z-axis, and the distribution of lines of constant yaw angle can be used to give a rough interpretation of the vortex types. The parallel lines in Fig. 7 are the isoclinal lines of a solid body vortex, and they are lines parallel to the plane $(x-z)$ in which the angle (α) was measured. The corresponding isoclinal lines of a free vortex are a pair of enclosing circles touching each other at one point, the center of the vortex (Fig. 8).

In the case of real measurements, however, the measuring planes are not perpendicular to the vortex axes, so that constant yaw angle distributions may appear as ellipses in-

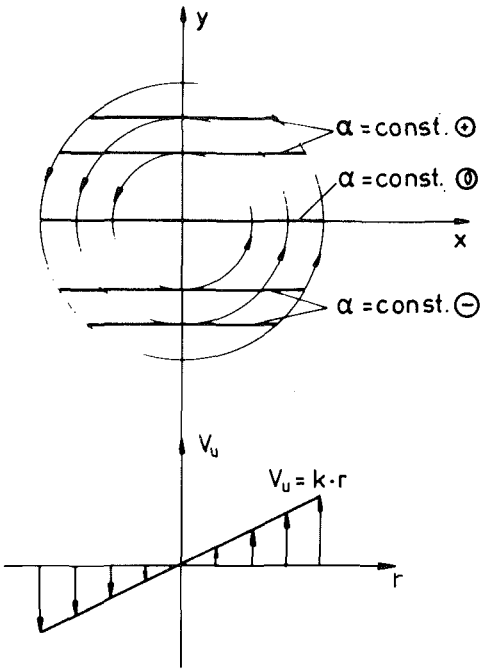

Fig. 7 Isoclinal plot of yaw angles (α = constant) of a solid body vortex

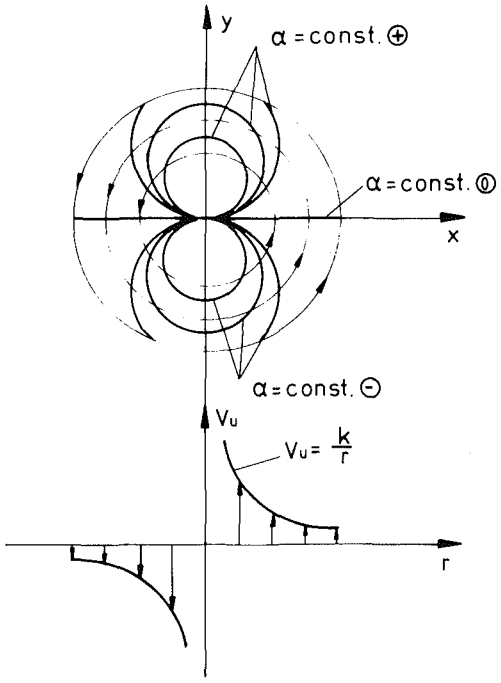

Fig. 8 Isoclinal plot of yaw angles (α = constant) of a free vortex

stead of circles. In the graphs showing isoclinal lines, the long axes of the ellipses (in the case of a free vortex flow field) and the parallels (in the case of a solid body vortex) must be perpendicular to the radial direction if no radial motion of the vortex axis exists.

Figure 5 shows the constant yaw-angle distribution from measuring plane 1. By means of the foregoing explanation it is possible to locate the center of the passage vortex I near the casing (Fig. 5). The position of the vortex center is assumed to be between the overturning region ($\alpha = 19$ deg) on the casing and the underturning region ($\alpha = 24$ deg), therefore between lines 21 and 22 deg. Near the vortex center the lines are nearly straight. This indicates a solid body rotation in the vortex

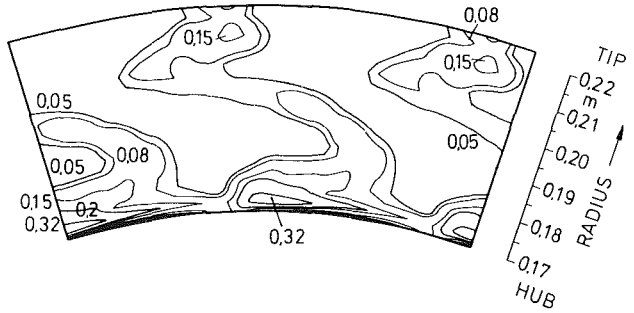

Fig. 9 Isobar plot to total pressure loss coefficients in plane 1.5

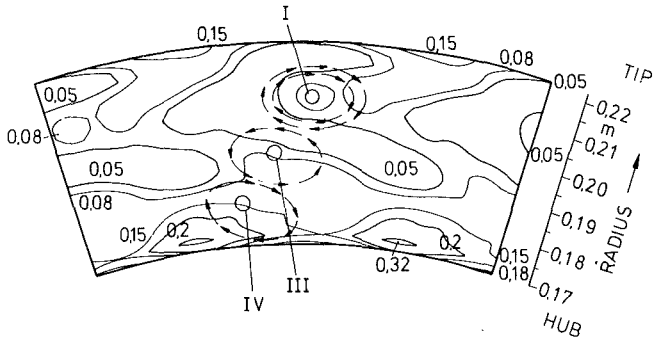

Fig. 10 Isobar plot to total pressure loss coefficients in plane 2

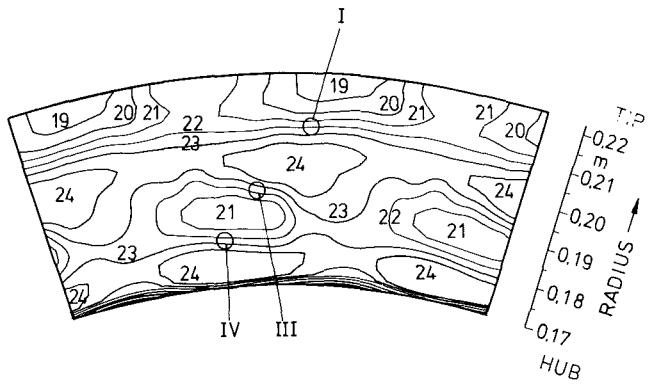

Fig. 11 Isoclinal plot of yaw angles (α = constant) in plane 2

center. At a greater distance from the center, the curves are oval, indicating a free vortex motion. There are no closed curves at the casing, and this is because the wall disturbs the rotation of the vortex. The passage vortex II near the hub is not visible in the flow angle distribution. Either there is no closed vortex rotation or this vortex has disappeared.

Other vortices exist in the wake, and their direction of rotation is shown in Fig. 4. Such vortices are described in publications by Hawthorne [4], Marchal and Sieverding [11] and Traupel [15]. They are associated both with trailing shed vorticity and vorticity remaining from the suction side leg of the leading edge vortex. This is over and above the influence that varying blade circulation along the blade height may have on this process. The overturning region in the wake (Fig. 5) is an oval with its long axis inclined to the tangential direction. This indicates a radial component of the vortex center motion.

Plane 1.5 The loss distribution (Fig. 9) shows increasing inclination of the wake, except in the vicinity of the hub similar to plane 1.

The deformation of the wake, near the casing, is caused by the passage vortex I. Both mixing of the wake and radial flow

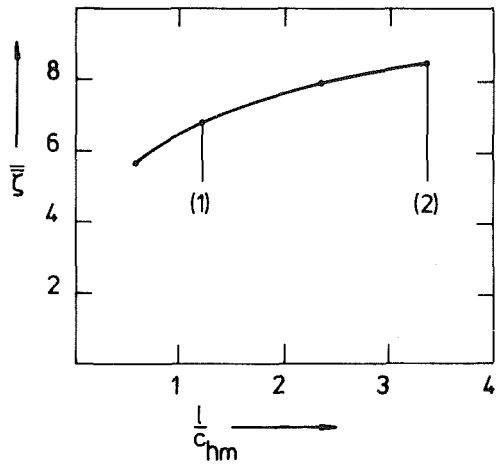

Fig. 12 Growth of losses behind the stator

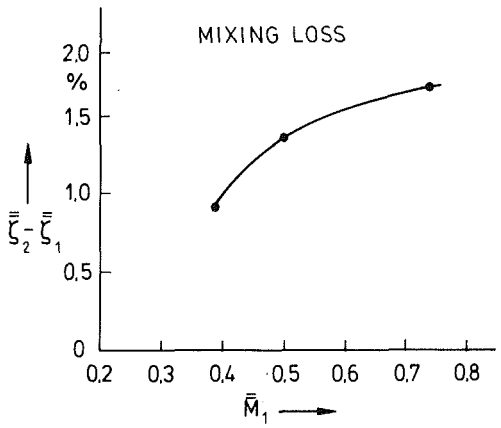

Fig. 13 Mixing losses against the Mach number

of the low energy material towards the hub may cause lower losses within the wake in plane 1.5 than in plane 1. The loss regions near the hub are more extended but their intensity is reduced.

Plane 2. In plane 2 the discrete regions of high losses have disappeared because of mixing (Fig. 10) Due to the nearly uniform stream and the strong inclination of the wake, the wake itself is scarcely visible.

In order to locate the vortices, the distribution of measured yaw angles is much more sensitive (Fig. 11). The passage vortex I is moved towards the hub, rotating nearly free from wall influences. In the center of the vortex there is a solid body vortex (see yaw angle distribution and the above mentioned relations), but at a certain distance from the center it changes to a free vortex flow. In this plane there is no passage vortex near the hub; however, the vortices III and IV in the wake still exist. These two wake vortices III and IV (belonging to wake to the left) can be located by regions of parallel isoclinal lines in the graph. The centers of the vortices in the wake move more towards the hub than the passage vortex I, because within the wake there is a stronger radial motion towards the hub.

Due to the mixing of the wake and the motion of vortices there is an increase in losses downstream of the blade row. Figure 12 shows the development of such losses, called mixing losses, behind stator in the stream wise direction. This result may be of special interest, because in plane turbine cascades Came [2] observed mixing losses only up to $l/c = 1.35$, while the present measurements were taken in an annular turbine stator.

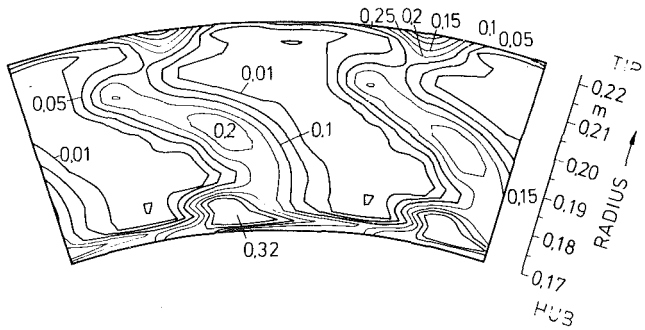

Fig. 14 Isobar plot of total pressure loss coefficients in plane 1 (measured with five hole probe)

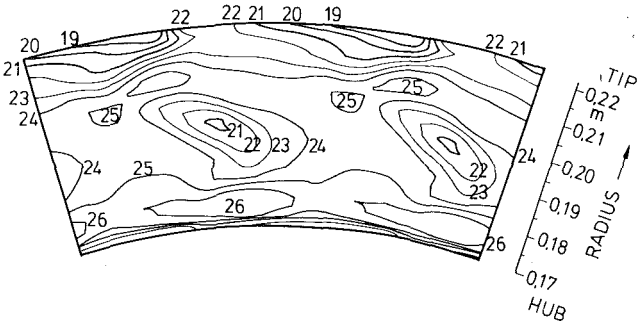

Fig. 15 Isoclinal plot of yaw angles (α = constant) in plane 1 (measured with five hole probe)

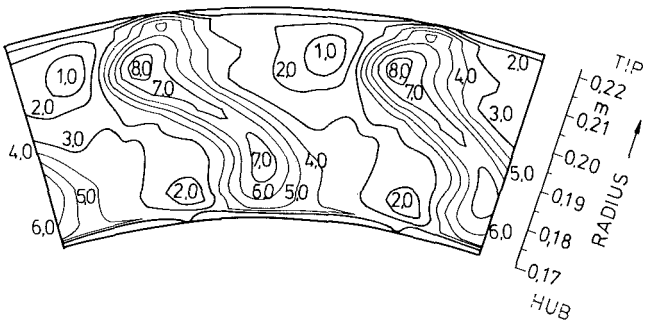

Fig. 16 Isoclinal plot of slope angles (γ = constant) in plane 1 (measured with five hole probe)

In Fig. 13 the difference in the losses between planes 2 and 1 are plotted against Mach number. In the referred case, the total losses in plane 2 are 6.86 percent and the additional losses of 1.68 percent may be caused by mixing. This result would emphasize that a substantial part of the total losses in plane 2 consists of mixing losses.

In order to confirm the aforementioned results taken with two-dimensional measurement as in plane 1, additional five-hole probe measurements were conducted. Described in the section concerning the experimental apparatus, only one test with a Mach number of $\bar{M}_1 = 0.503$ was run, but there were no substantial differences in the flow field to the previously described measurements (Figs. 14, 15), although the tests were conducted at lower Mach number.

The slope angle distribution can be seen in Fig. 16. Within the total flow field, the radial velocity vector was directed towards the hub. Due to the radial pressure gradient and low tangential velocity in the wake, greater slope angles occur there. The centrifugal force and the pressure gradient are unbalanced, because the tangential velocity is low.

Low slope angles exist on the left-hand side of the wake near the casing and near hub, indicating there are regions of

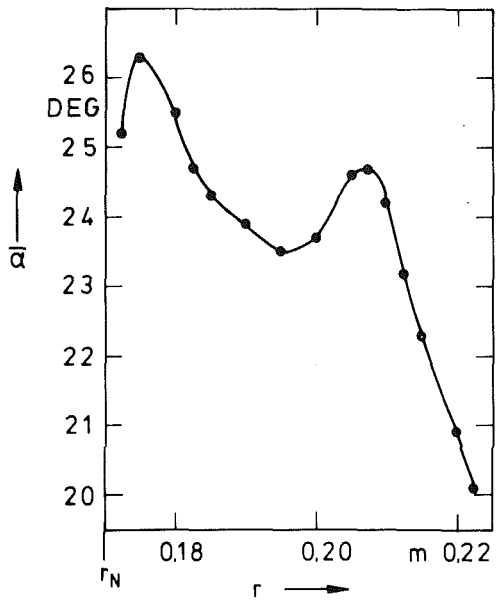

Fig. 17 Pitchwise averaged yaw angle ($\bar{\alpha}$) of plane 1

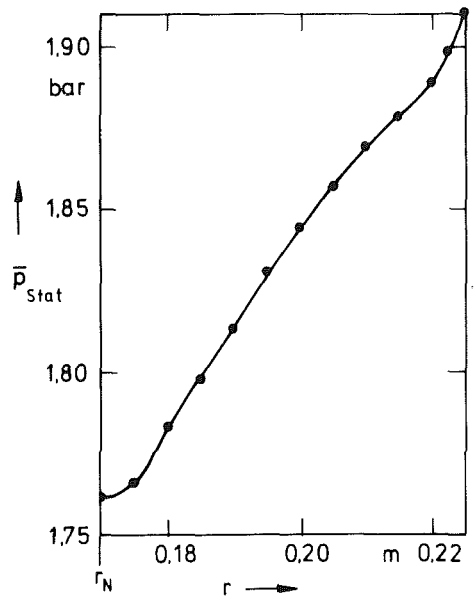

Fig. 19 Pitchwise averaged static pressure of plane 1

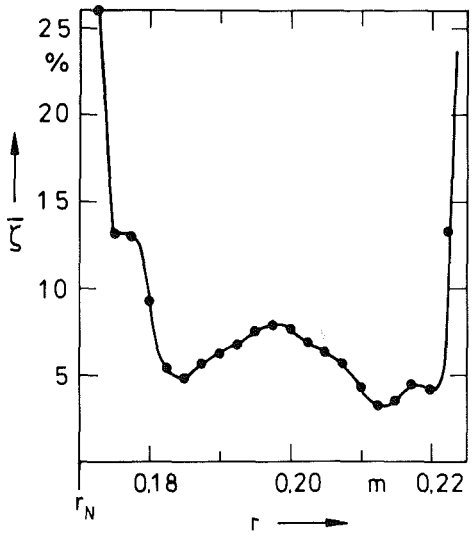

Fig. 18 Pitchwise averaged total pressure loss of plane 1

the passage vortices where the component of vortex rotation is directed toward the casing. But in this case the rotational speed is insufficient to cancel the overall movement toward the hub. On the opposite side of the vortex center (near the casing) the rotational component has an additional effect, increasing the slope angle.

In plane 1 (Fig. 15), the regions of nearly parallel isoclinal lines near the casing, with the lines 22 and 23 deg in the middle, clearly indicate that the center of the outer passage vortex is situated at a radius of $r=0.215$ m. The pitchwise averaged radial yaw angle distribution in plane 1 (Fig. 17) clearly indicates the effect of this passage vortex. In the immediate vicinity of the casing there is an overturning region (lower $\bar{\alpha}$), while on the other side of the vortex centre there is an underturning region. This high underturning region near the hub is a result both of the vortex motion near the hub and the design of the turbine stator.

The corresponding pitchwise averaged radial loss distribution can be seen in Fig. 18. In addition to profile losses, there are high losses near the wall caused by wall effects which are stronger near the hub. The weak peaks in the loss-distribution near the walls outside the region of wall effects are produced by the passage vortices, and the peak near mid-span may be assumed to be the result of interference between vortices within the wake and the wake itself.

In Fig. 19 the static pressure distribution measured by means of a five-hole probe and wall taps, averaged in pitchwise direction, is plotted against radius. As a known result there is a steady increase in static pressure from hub to tip caused by the tangential velocity distribution. The pressure tap values and the wall near probe values are in a good agreement.

Conclusions

Summarizing the results of experimental measurements presented herein, the following description of the flow behind the turbine stator emerges:

(*i*) The loss distributions behind the stator, measured at four different axial locations, give an idea of the mixing of the wake and the increase of losses due to that mixing. Even far downstream from the trailing edge (until $l/c=3.34$), mixing losses were still measured.

(*ii*) With the help of the yaw angle distributions, vortices could be located which strongly influenced the distribution of flow direction and mixing behind the stator. The measurements implied that some vortices exist even far downstream of the trailing edge.

(*iii*) Five-hole probe measurements gave insight into both radial components of the flow and the static pressure distribution. One could see that in all parts of the flow field the velocity vectors were inclined towards the hub, especially in the wake regions.

Acknowledgments

The authors wish to express their gratitude to Dr. Kruse for the discussions of the results, H. Rogge who supervised the test work and W. Karnatschke who calibrated the five hole probe.

References

1 Armstrong, W. D., "The Secondary Flow in a Cascade of Turbine Blades," A.R.C. Rep. Ser. No. 2979, 1957.

2 Came, P. M., "Secondary Loss Measurements in a Cascade of Turbine Blades," *Institute of Mechanical Engineering Conference*, Publ. 3, 1973, pp. 75–83.

3 Dunham, J., "A Review of Cascade Data and Secondary Losses,"

Journal of Mechanical Engineering Science, Vol. 12, No. 1, 1970, pp. 48–59.

4 Hawthorne, W. R., "Rotational Flow Through Cascades, Part I: The Components of Vorticity," *Q. Jl Mech. app. Math.*, Vol. 8, 1955, pp. 266–279.

5 Herzig, H. Z., and Hansen, A. G., "Visualization Studies of Secondary Flow With Applications to Turbomachines," *Transactions American Society of Mechanical Engineers*, Vol. 77, 1955.

6 Hultsch, M., and Sauer, H., "Sekundär strömungen in Beschaufelungen axialer Turbomaschinen," *Maschinenbautechnik* Vol 28, 1979 H1.

7 Klein, A., "Untersuchungen über den Einfluß der Zuströmgrenzschicht auf die Sekundärströmugen in den Beschaufelungen von Axialturbinen," *Forsch. Ing.* Wesen 32, No. 6, 1966.

8 Kruse, H., "ZTL-Erfolgsbericht 4. 3. 8, 1979."

9 Langston, L. S., "Crossflows in a Turbine Cascade Passage," ASME JOURNAL OF ENGINEERING FOR POWER, Vol. 102, No. 4, 1980, pp. 866–874.

10 Langston, L. S., Nice, M. L., and Hooper, R. M., "Three-Dimensional Flow Within a Turbine Cascade Passage," ASME Paper No. 76-GT-50.

11 Marchal, Ph., and Sieverding, C. H., "Secondary Flow Within Turbomachinery Bladings," *Secondary Flows in Turbomachines*, AGARD-CPP-214 (Netherlands), Mar. 1977.

12 Sjolander, S. A., "The Endwall Boundary Layer in an Annular Cascade of Turbine Nozzle Guide Vanes," Tech. Report No. ME/a 75-4, Department of Mechanical Aerospace Engineering, Carleton University, Ottawa, Canada, Dec. 1975.

13 Squire, H. B., and Winter, K. G., "The Secondary Flow in a Cascade of AirFoils in a Nonuniform Stream," *Journal Aeron. Science*, Apr. 1951, pp. 271–277.

14 Taylor, E. S., "Boundary Layers, Wakes and Losses in Turbomaschines," GTL-Report 105, Apr. 1971.

15 Traupel, W., "Wirbelsysteme in Schaufelgittern und Turbinen," VDI-Bericht, Bd. 3, 1955.

16 Wolf, H., "Die Randverluste in geraden Schaufelgittern," Wiss. Z. Techn. Hochschule Dresden, 1961, 10, pp. 352–364.

APPENDIX

It is difficult to locate a vortex motion behind or within a turbine stator, because the velocity components of secondary flows cannot be easily separated from the other velocity components. With the help of measurements of yaw angle distribution, an attempt was made to get more information of the vortex motions.

If one looks at a small portion of a fluid moving in a vortex, it is moving along a spiral line shown in Fig. 6 with its central axis z. If v is the absolute velocity, the components of that motion are an axial component v_z and a tangential component v_u. In the following derivations of the velocity, v_z is assumed to be constant. In order to use the yaw angle distribution for characterizing the vortex type the component v_x is defined as a component in a plane parallel to the plane $x-z$, in which the yaw angle α is measured. If φ, r are the polar coordinates of the fluid portion under consideration one can write from Fig. 6:

$$\cos\varphi = \frac{v_x}{v_u} \tag{A1}$$

$$\cos\varphi = \pm\frac{y}{r} \tag{A2}$$

$$\tan\alpha = \frac{v_z}{v_x} \tag{A3}$$

With constant axial velocity component, v_z, it can be seen from equation (A3), that along an isoclinal line, that means $\alpha = \text{const}$, v_x is also constant.

Solid Body Vortex (Fig. 7)

Looking at a solid body vortex the distribution of the tangential velocity component is

$$v_u = k \bullet r \tag{A4}$$

with $k = \text{constant}$.
Using now the equations (A1) and (A2) one gets

$$y = \pm\frac{v_x \bullet r}{v_u}$$

using (4) this leads to

$$y = \pm\frac{v_x}{k} \tag{A5}$$

i.e., lines with the same velocity, v_x, that means isoclinal lines with $\alpha = \text{constant}$, are straight lines parallel to the x-axis (Fig. 7).

Free Vortex

For the free vortex motion around the z-axis, the distribution of the tangential velocity is

$$v_u = \frac{k}{r} \tag{A6}$$

with $k = \text{constant}$.
Using again the equations (A1), (A2), and (A6) one can write

$$y = \pm\frac{v_x \bullet r^2}{k}$$

Substituting r^2 by $x^2 + y^2$ it follows

$$y = \frac{k}{2 \bullet v_x} \pm\sqrt{\left(\frac{k}{2 \bullet v_x}\right)^2 - x^2} \tag{A7}$$

i.e., lines with the same velocity, v_x, and $\alpha = \text{constant}$, are a pair of enclosing circles touching in the vortex center (Fig. 8).

L. S. Han
Professor.
Mem. ASME

W. R. Cox
Capt. USAF, AEDC,
Arnold Airforce Station.

Mechanical Engineering Department,
The Ohio State University,
Columbus, Ohio 43210

A Visual Study of Turbine Blade Pressure-Side Boundary Layers

Boundary layer characteristics on the pressure-side of a turbine airfoil were investigated experimentally in a three-blade cascade tunnel. The blades had a chord length of 21 in. to facilitate flow visualization and high-speed photography. The investigation revealed the existence of the Gortler's vortices appearing in spurts in regions of severe curvature. In the trailing edge region, Karman vortices were detected and found to interact strongly with the Gortler's vortices convected thereto.

Introduction

Over the years, turbine inlet temperatures have been steadily rising, and the capability of material developments to cope with high temperature environments has been outstripped. Cooling of gas turbine vanes becomes, therefore, increasingly demanding for more refined estimates as to where and the amount of cooling needed in order to achieve economical use of the available cooling air supply. Simultaneously, there is a trend towards higher output per stage, necessitating larger turning angles and mixed flow regimes in cascades, and the fluid dynamics associated with turbine cascades is no longer a simple application of the well-developed classical theories.

Designers therefore look more into the boundary layers on turbine airfoils to garner as much information as possible in order to understand and mitigate frictional losses and heat transfer because of the presence of boundary layers. A typical gas turbine engine environment represents a combination of conditions operating simultaneously. Their combined effect is invariably not the same as the sum of their individual effects when each operating condition is considered alone. Factors characterizing turbine airfoil flow are pressure gradient, streamwise curvature, secondary flow, surface roughness and free-stream turbulence, to name but a few. These factors control laminar-to-turbulent transition of the boundary layers. In gas turbine applications, the transition phenomenon is, therefore, not an academic curiosity, for turbine cascades are noted to operate in the vicinity of the transition Reynolds number, which in turn influences the surface heat transfer.

Consequently then, heat transfer analysis on turbine airfoil surfaces is indeed a complex process, the various ramifications of which have been recently reviewed in a comprehensive publication by Graham [1].

To be sure, there have been numerous investigations on turbine airfoil heat transfer which resulted in experimental and theoretical data on actual blade surfaces or their geometric models under various conditions. In general, these data are, however, not consistent among themselves. The sheer volume of the works precludes a comprehensive discussion; hence, a few selected studies are cited to highlight their uncertain and incomplete nature. A representative work is that of Cumsty [2], who studied the pressure-side transition on a turbine airfoil. Boundary layer transition was observed to take place over a region extending from the midchord position to almost the trailing edge of the airfoil for a chord Reynolds number of 2×10^5, a typical value for an aircraft gas turbine airfoil. Such a relatively large extent of the transitional boundary layer would make the classical prediction formulas rather uncertain indeed. Walker and Markland [3, 4] were able to predict successfully the suction-side heat transfer but not the pressure side. This state of uncertainty is not unique in the works cited but is also found in other investigations.

Despite extensive basic heat transfer research on clearly defined problems, the task of determining quantitative answers is still vexing. An underlying reason for this uncertainty is that past research efforts were directed at the pertinent boundary layer environmental factors one at a time. Such an approach was born out of necessity in order to pursue the investigations in a systematic fashion. Thus, the pressure gradient effect was investigated in the absence of the curvature effect and vice versa. Similarly, the roughness effect was studied in isolation from others, and so on. Much understanding has been achieved on each of the phenomena related to the boundary layer development and transition, but the mutual synergistic effects in combined operation are poorly understood and will probably remain so for some time to come.

Of course, a turbine blade cascade capable of replicating all operational factors is most ideal but is practically unattainable. A cascade with simulation of a few important environment features becomes, therefore, a practical necessity. The investigation reported herein represents such a step by experimentally observing, through a smoke visualization technique and other means, the fluid dynamic behaviors surrounding a turbine blade in a three-blade static cascade. The experimentation blade is scaled up from a practical working chord dimension of 3 or 4 in. to a dimension of 21 in., thus permitting a more detailed examination of the flow characteristics. Two principal parts are involved in this investigation: the first one concerns the trailing edge vortex

Contributed by the Gas Turbine Division of THE AMERICAN SOCIETY OF MECHANICAL ENGINEERS and presented at the 27th International Gas Turbine Conference and Exhibit, London, England, April 18–22, 1982. Manuscript received at ASME Headquarters December 2, 1981. Paper No. 82-GT-47.

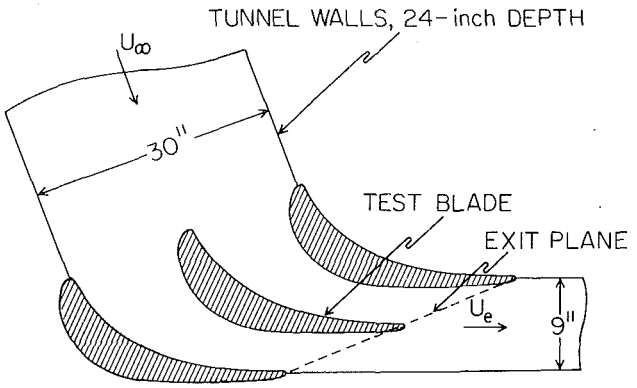

Fig. 1 Three-blade static cascade

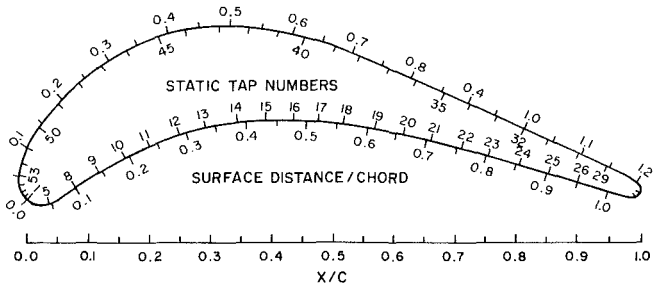

Fig. 2 Airfoil profile with static tap locations and surface distances

shedding phenomenon; the second part concerns laminar-to-turbulent transition on the pressure side of the blade.

Cascade and Instrumentation

The cascade tunnel is an open-circuit design with ambient air drawn from the laboratory space through a bell-mouth entrance section which contains a honeycomb and six five-mesh screens to stabilize the flow and reduce the freestream turbulence to about 0.6 percent. The test section has three blades, with two forming the outside turning walls and the center one serving as the test blade. The blade has a chord dimension of 21 in. and a span of 24 in. The blade spacing is 15 in. and the flow turning angle is 72.5 deg. Figure 1 depicts schematically the cascade arrangement. Details of the experimental apparatus and accessories can be found in reference [5], from which a portion of the material in this paper is excerpted.

Airfoil Characteristics. The blade profile used in the investigation is that previously studied by Cox and Han [6]. It is typical of those used in modern gas turbine engines. The profile is shown in Fig. 2, and its coordinates are given in Table 1. Inside the contour are shown the locations of static pressure holes, chronologically numbered starting from the tap at the frontal stagnation point. Outside the contour are labeled the surface distances reckoned from the stagnation point, with the latter somewhat arbitrarily assigned as the tangent point of the circle of curvature. The nondimensionalizing length is the chord length, c.

The blade was "checked out" by running a static pressure test under a normal air flow run. The static pressure

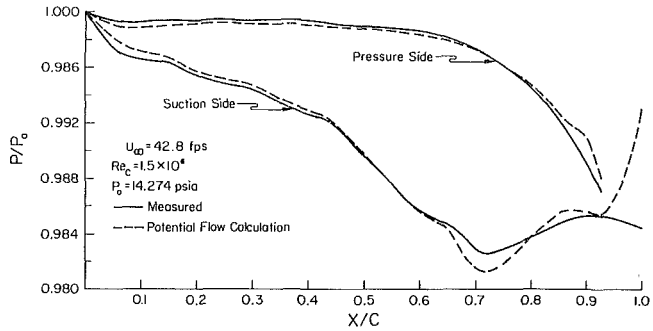

Fig. 3 Airfoil static pressure distribution

distribution on the airfoil was compared with that calculated on the basis of potential flow[1]. Figure 3 shows the pressure distributions on both surfaces of the test blade. The nondimensional pressure distributions (p/p_o) form the tests, and from the calculations show good agreement, except near the trailing edge, where a small change in the rear stagnation point location is known to have large effects on the pressure distribution. Additionally, the blade surface curvature in terms of a local radius to the chord, c, is displayed in Fig. 4, along with the Görtler parameter $G(\delta_2)$, where δ_2 is the calculated momentum thickness. The blade profile used has a rather severe curvature of $R = c/2$ occurring near the quarter-chord position. The radius of curvature at the stagnation region is determined to be 0.78 inch or 0.037c.

Instrumentation. Principally, flow visualization by means of introducing kerosene smoke into the airstream was used to study the flow features around the airfoil. The cascade tunnel has plexiglass walls which permit the use of high-speed stroboscopic lighting to illuminate the smoke of kerosene vapor. Smoke patterns with various features of interest were photographed by a 35-mm camera and a 16-mm Fastex high-speed movie camera at film speeds up to 4000 frames/s. The majority of the test runs was conducted with air inlet velocities (upstream of cascade) between 22 and 43 fps, corresponding to chord Reynolds numbers between 8×10^5 to 1.5×10^6.

Results

Trailing Edge Vortex Study. Kerosene vapor was injected in the entrance section of the cascade tunnel in the midspan plane of the test blade. After impinging the stagnation point, the smoke stream followed the contours of the pressure-side and suction-side surfaces and merged in the trailing-edge region. Figure 5 illustrates the path of the smoke stream and the two areas in which visual studies were conducted; i.e., the concave side of the blade for boundary layer visualization and the trailing edge plane for vortex study. Static photographs with strobolight and high-speed movies at 1500–4000 frames/s were taken of the smoke stream in the midspan plane of Fig. 5. Figures 6 and 7 are examples of those still records.

[1] Program originated from Pratt and Whitney and was supplied by Dr. Kervyn Mach of AFAPL.

Nomenclature

a = arc length of a constant curvature surface, or longitudinal spacing of trailing edge vortices
c = chord length of airfoil
d = diameter of curvature
f = frequency, Hz.
$G(\delta_2)$ = Görtler parameter $(U\delta_2/\nu)\sqrt{\delta_2/R}$
h = transverse spacing of trailing edge vortices
p = pressure
p_o = stagnation pressure $(p_\infty + \frac{1}{2}\rho U_\infty^2)$
p_∞ = free stream pressure
R = radius of curvature
Re_c = chord Reynolds number $(U_e c/\nu)$
U = local boundary layer edge velocity
U_e = average velocity in the trailing edge section, cascade exit

Table 1 Airfoil coordinates (dimensions in inches)

X	Y	X	Y	X	Y
0.000	0.000	12.000	2.340	9.000	5.670
0.300	−0.180	13.500	2.025	6.900	5.880
0.600	−0.222	15.000	1.650	4.500	5.550
1.200	0.000	16.500	1.200	3.000	4.830
1.800	0.390	18.000	0.750	2.250	4.320
3.000	1.140	19.300	0.355	1.500	3.690
4.500	1.890	19.500	0.315	0.750	2.880
6.000	2.400	21.000	0.300	0.000	1.680
7.500	2.640	19.500	1.200	−0.220	1.050
8.400	2.685	16.500	2.580	−0.240	0.660
9.000	2.670	13.500	3.960	−0.165	0.300
10.000	2.550	10.500	5.220	−0.027	0.030

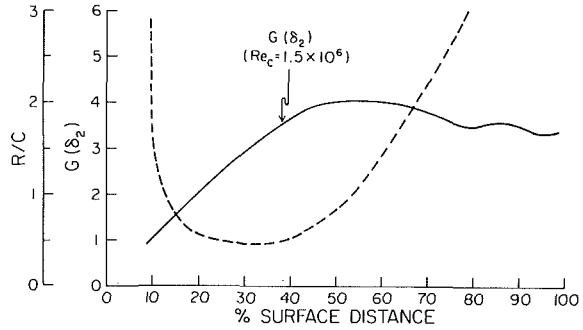

Fig. 4 Curvature distribution and the Görtler parameter on pressure-side of airfoil

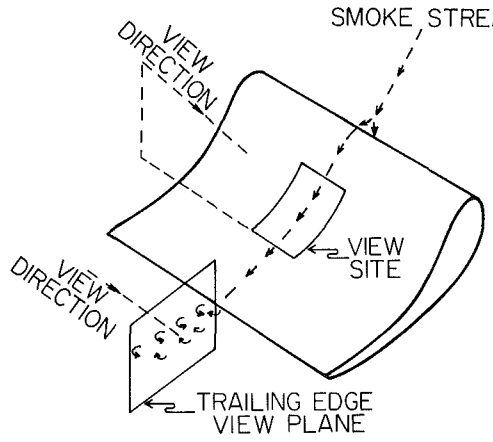

Fig. 5 View directions and sites on test blade

Quantitative Deductions. From the photographic and movie records, transverse and longitudinal vortex spacings were determined. With the trailing edge cross-sectional velocity varying from 75 to 140 fps, the longitudinal spacing was found to have an average value of 1.9 in. with a scatter of ±10 percent. The vortex distribution appeared stretching and spreading with increasing distance from the trailing edge at a fixed velocity. At lower speeds near 74 fps, the spacing ratio (h/a) (i.e., transverse-to-longitudinal pitch ratio) agreed reasonably with Karman's stability value of 0.281 [7]. At higher speeds, however, the data points presented in Fig. 8(a) indicated considerable scatter.

The vortex frequency was measured by two different methods: one was to examine and analyze the movie film taken at a speed of 1500 frames/s. By a frame-by-frame analysis, the frequency of these visible vortices can be inferred. A second method employed a hot-wire probe embedded in the wake axis. A spectrum analysis of the hotwire signals revealed the principal vortex frequency. These two independent measurements corroborated each other within 5 percent.

Because of the enormous labor required for these procedures, only a few runs were analyzed; the results are shown in Fig. 8(b), with the measured frequency plotted

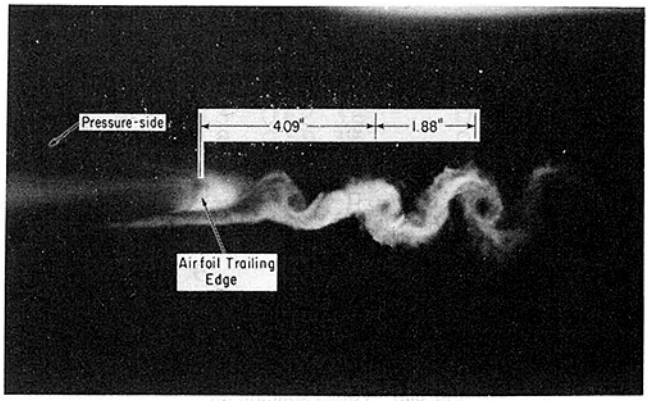

Fig. 6 Cascade wake vortex street, $Re_c = 7.9 \times 10^5$

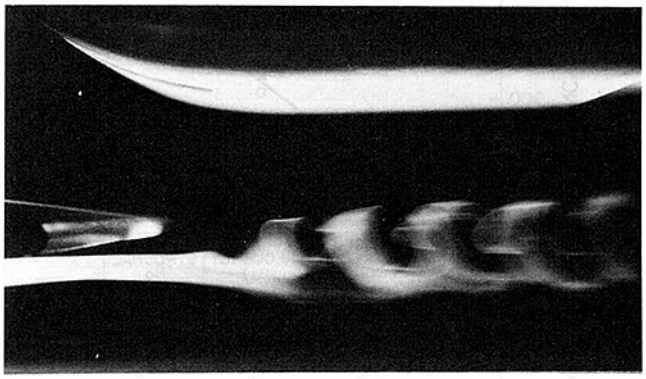

Fig. 7 Cascade wake vortex street, $Re_c = 7.4 \times 10^4$

against the trailing edge cross-sectional velocity. Linearity of the data points implied a constant Strouhal number. In order to contrast and compare with the phenomenon of vortex shedding from a circular cylinder, a Strouhal number based on (fd/U_e) is formulated. A trailing edge diameter of curvature (0.56 in.)[2] was used. This resulted in a value of 0.36, a value in considerable excess of that for a circular cylinder. To forestall any doubt as to the validity of the measurements reported here, a cylinder was mounted in the upstream section of the cascade tunnel. The measurements resulted in a Strouhal number of 0.23, which is in line with the copious amount of data available in the literature.

It is of interest to note the similarities and differences between these two configurations – cylinder and trailing edge with a finite curvature. Vortex shedding in both cases is governed by a periodic separation of the flow. Hence, the local transverse dimension should characterize the Strouhal number. In the cylinder case, the boundary layer at the separation point is solely affected by the cylinder diameter; whereas in the present case the boundary layer reaching the separation point is governed by its prior history. The dominant factor in this regard is, of course, the distance or the chord length over which a boundary layer has evolved. In other words, vortex shedding at the trailing edge of an airfoil has one more geometrical parameter, perhaps (d/c), affecting the Strouhal number.

The same cascade arrangement has been used in an earlier work [5] by the authors in which the wake velocity profiles were surveyed. It was conducted along the exit plane, indicated by the dashed line in Fig. 1, with a hot-wire probe. The time-averaged velocity distributions at successive downstream positions are typified by those shown in Fig. 9. Of course, the discrete influence of the vortex system on the order of 1 kHz in affecting the wake velocity distributions is

[2] Measured value. Reference [5] reported a value of 0.73 in. calculated from smoothed coordinates.

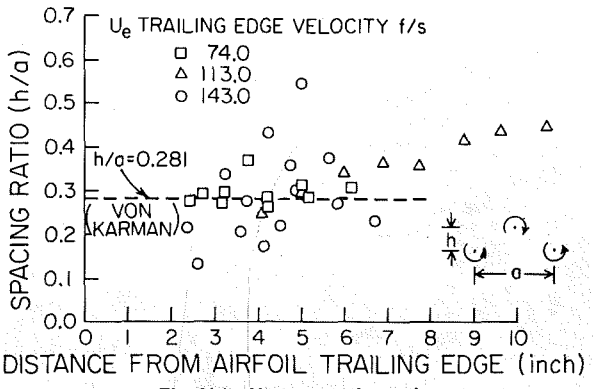

Fig. 8(*a*) Vortex spacing ratio

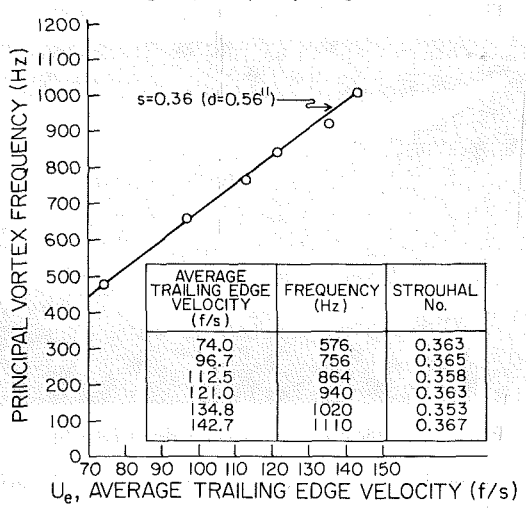

AVERAGE TRAILING EDGE VELOCITY (f/s)	FREQUENCY (Hz)	STROUHAL No.
74.0	576	0.363
96.7	756	0.365
112.5	864	0.358
121.0	940	0.363
134.8	1020	0.353
142.7	1110	0.367

Fig. 8(*b*) Airfoil wake vortex shedding frequencies

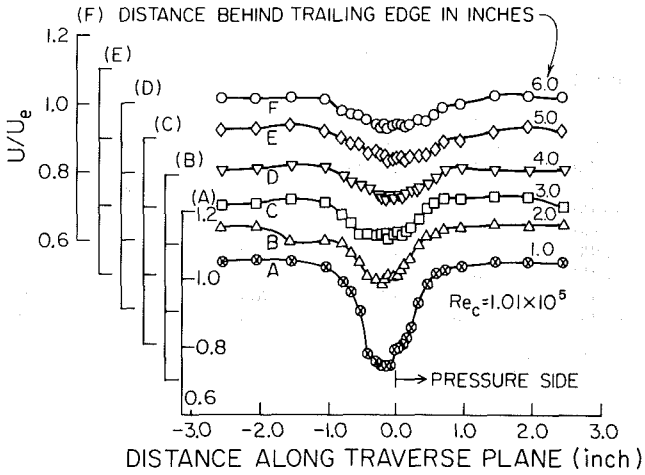

Fig. 9 Airfoil wake velocity distributions

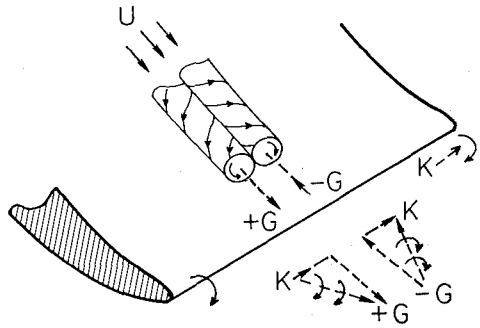

Fig. 10 Interaction of vortices in the trailing edge zone

not discernible but must have been instrumental in the wake development. The influence of the vortices in the wake upon heat transfer on the downstream blades can therefore be hardly ignored in its final reckoning. Additionally, gradual filling of the wake deficit is accountable for the longitudinal stretching of vortex spacing, as mentioned earlier.

Qualitative Observations. Based on the visual records, some qualitative remarks can be made. First, the vortex contours of those shed from the pressure side were much sharper and more well defined than those emanating from the suction side. The authors inferred from this observation as evidence of stronger vortex shedding from the pressure side, which the classical lift theory would require. Secondly, the smoke-stream traces, as exemplified by Fig. 7, showed an interesting interaction phenomenon between the Görtler vortices and the Karman vortices in the trailing edge zone. At the risk of being, perhaps, overly suggestive, the smoke traces in Fig. 7 resembled two oppositely curled ribbons being stretched axially. A close scrutiny of the smoke paths indicated two adjacent streams, both of which rotated about a common axis transverse to the main flow. Simultaneously, both streams counter-rotated about an axis parallel to the main flow. It should be pointed out that such a flow structure was visible only in the region occupied by the smoke. Elsewhere in the span direction, similar flow structure was most likely to occur, not necessarily in unison with that in the smoke zone.

Events described in the preceding section are pictorially illustrated in Fig. 10 where two counter-rotating Görtler cells are represented by $\pm$G vectors. Upon emerging into the trailing edge zone, these Görtler vectors interacted with the Karman vortical vector, K, resulting in two skew vectors, K $\pm$ G. The latter resulted in the smoke traces shown in Fig. 7. Thus, it becomes plausible that the ideal linear Karman vector, K, is given a three-dimensional characteristic which becomes one of the many mechanisms rendering a highly turbulent wake flow.

It must be emphasized that the flow interaction as depicted had not been observed as a steady phenomenon owing, chiefly, to the intermittent nature of the Görtler vortices, as will be discussed in the next section. During the period when Görtler votices were absent in the wake region, the flow picture was observed to be quite similar to that described by Morkovin [8] in his excellent review of the subject matter.

The Boundary Layer on the Pressure Side. Under steady-state lighting, smoke traces on the concave side of the blade revealed conventional characteristics without any unusual features. When Strobolight was directed to the region marked in Fig. 5, scenes of observable disorder were visible. Aside from the unsteady characteristics, smoke traces were observed to resemble two counter-rotating corkscrews advancing along the blade surface. Naturally, this was only confined to the extent of the smoke introduced. And within this width, usually two cells adjacent to one another were visually quite discernible. Illustrated pictorially in Fig. 10 as the Görtler vortices, such a still photographic record of the motion described is contained in Fig. 11, typical of the records obtained in this investigation.

In that figure, Tap 16, as defined in Fig. 2, is located at a surface distance of about 0.5 of the chord length where the local curvature is very near the most severe value. High-speed movies were also taken of these events and analyses of the movie frames were performed to obtain quantitative information.

Qualitative Observations. Generally speaking, one tends to term these counter-rotating pairs as the Görtler vortices, since they appear to possess the essential features attributed to

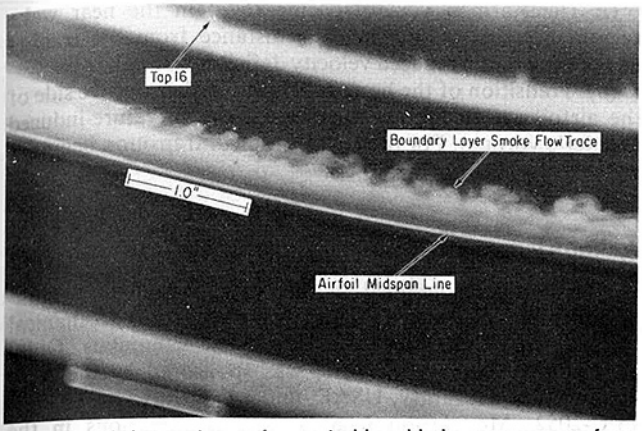

Fig. 11 Görtler vortex pair on turbine blade pressure surface, $Re_c = 1.03 \times 10^6$

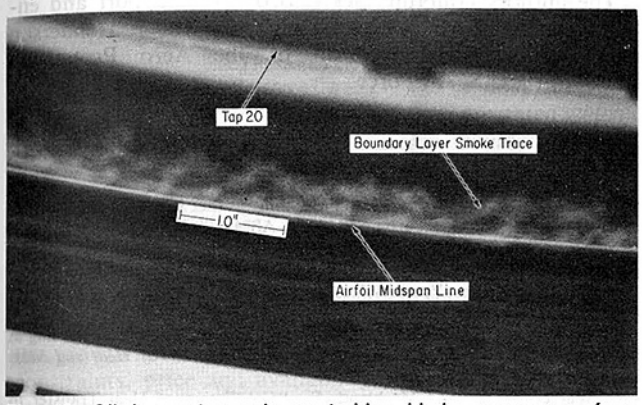

Fig. 12 Görtler vortex pair on turbine blade pressure surface, $Re_c = 7.9 \times 10^5$

them. Usually, the locations at which these vortices became sharply observable were at positions of 0.3 to 0.4 of the chord length where the curvature was severe. From there, these counter-rotating cells were convected downstream with an increasingly less distinct outline and were eventually diffused into a cloud. These are all quite discernible in Fig. 11. As a fixed site, however, Görtler vortices emerged in spurts, interposed by a long period of quiescence. Not infrequently, two successive groups of Görtler vortices emerged from approximately the same spot with little intervening time in between. Each group contained ten or more visible cells in the main flow direction and the two groups were identifiable in some of the high-speed movie records at two different sites with a quiet space gap in between. Far more flow details were revealed in frame-by-frame analyses of these movie records.

Not only were the Görtler vortices identifiable, but also packets of superimposed traveling waves with features similar to the Tollmien-Schlichting type were observed in the course of examining the movie films. Pictorially, the existence of the T-S type waves is evidenced in Figs. 11 and 12 where the smoke stream appeared to have regularly spaced crests.

Further downstream, the interaction of the T-S waves with the Görtler vortices led to complete transition into turbulent flow. The entire transition process, although a complex event, consisted mainly of intermittent appearances of transverse waves of the Tollmien-Schlichting type superimposed on the Görtler vortices with their resultant deformation and decomposition. In Fig. 11, the two Görtler vortices visible in the photo are being deformed through the action of traveling waves which appear as two rows of sawteeth. Analysis of the high-speed motion pictures on a frame-by-frame basis showed that a group of these waves numbering from three to fifteen would become visible at a surface distance between 0.3 and 0.5 of the chord length. This group of waves would proceed

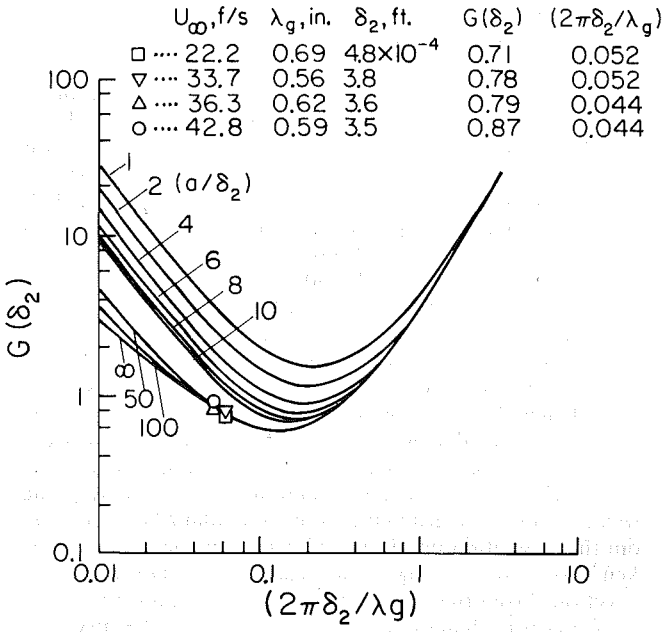

Fig. 13 Comparison of Görtler wavelengths with stability theory due to Tobak [16]

downstream, grow, and eventually break down into complete turbulence. Another group of waves did not form until a brief period of time passed during which no traveling waves were observed. Although these wave groups emerged at relatively random time intervals, approximately thirty occurrences could be observed each second at $Re_c = 7.0 \times 10^5$.

The sequence of events just described for the traveling waves bears a remarkable resemblance to the events described by Knapp and Roache [17] for Tollmien-Schlichting transition along an ogive-nosed circular cylinder. They reported a sequence in which a group of amplified Tollmien-Schlichting waves proceeds downstream and eventually breaks up into fully turbulent flow, followed by a period of time during which the transition region is essentially laminar prior to the emergence of the next group of vortices. However, none of the prediction methods reviewed in [14] indicated that Tollmien-Schlichting instability would occur along the airfoil pressure surface in absence of Görtler vortices. Thus, it can be concluded that traveling waves are part of the breakdown process for the Görtler vortices, and not just superimposed. Because Bippes and Görtler [18] also observed traveling waves accompanying Görtler vortex deformation in hydrodynamic flows, it can be further concluded that this occurrence is not unique to the present test configuration.

Returning to the Görtler vortices and their observed existence on the turbine airfoil, it is difficult to ascertain their origin. Morkovin [9] reported that even along a constant-pressure flat plate it is not unusual to observe transition initiated by counter-rotating vortices. Another possible origin lies in the stagnation region where the transverse vortical lines inherent in the on-coming stream are deformed and bent as the main flow encounters the stagnation region of an obstacle – in this case, the turbine airfoil. Analytically, this phenomenon was studied by Kestin and Wood [10] on the basis of vortex amplification. Their thesis was subsequently corroborated by a thorough experimental study by Sadeh et al. [11]. On the other hand, it is widely known that the concavity of a surface gives rise to the Görtler vortices which would cause instability of the main flow, and would subsequently lead to transition. The experimental work of Wortman [12] amply demonstrated the phenomenon discussed.

Quantitative Observations. Transition from a laminar

boundary layer to a turbulent one is naturally a topic of acute interest in turbine blade cooling analysis. In an earlier work [14], major factors influencing the transition process have been summarized for turbine blade applications. Instability due to Görtler vortices has, of course, been studied extensively, particularly by the detailed computations of Smith [15] for surfaces with uniform curvature. For turbine airfoils, however, surface curvature varies and the analysis by Tobak [16] appears more appropriate. His calculated stability curves are for concave surfaces of a finite extent bounded by surfaces of zero curvature on both sides. This finite nature is characterized by a parametric ratio (a/δ_2) where a is the arc length and δ_2 is the momentum thickness.

To ascertain the transition possibility on the concave side of the airfoil in this study, parameters used in Tobak's work were calculated at the commencing section of concave curvature where Görtler vortices were first observed. This occurred at a surface position about 0.1 of the chord length. The momentum thickness, δ_2, was obtained by calculating the developing two-dimensional laminar boundary layer starting from the stagnation point. The Görtler wave length, λ_g, was taken from the photographic records by photogrametric projection. From these sources, the Görtler parameter $G(\delta_2)$, the Görtler wave length number $(2\pi\delta_2/\lambda_g)$, and the curvature number (a/δ_2) were obtained. For the four sets of processed data, the points are shown in Fig. 13. The fact that these four points all lie within the neutral stability envelope lends credence to the argument that incipient transition commences at that location. Indeed, by a detailed examination of the movie frames, the breakdown of the vortical structure downstream from that location was quite visually prominent.

As to how the Görtler vortices originated in the present study, it appeared that those vortices were caused by concavity of the surface. The Görtler wave length, λ_g, (defined as the repeating length) was measured photogrametrically in this study. For chord Reynolds numbers of 1.5×10^6 and 8×10^5, wavelength values of 0.59 and 0.7 in., respectively, were obtained from the photographic records. According to the criterion of Kestin and Wood [10], the calculated wavelengths turned out to be 0.07 and 0.1 in. This disparity tends to suggest that the observed Görtler vortices were not those originating in the stagnation region. On the other hand, it is quite likely that the spacing or wavelength of the Görtler vortices tends to increase as the vortices travel downstream along the blade surface, as suggested by Martin and Brown [13], thus partially accounting for the differences noted above.

Concluding Remarks

The complexity of turbine airfoil aerodynamics is of course well recognized; the research reported herein represents one of the few efforts, to the author's knowledge, to observe experimentally the phenomena of Görtler's vortices on the pressure-side and Karman's vortices in the trailing edge region. The latter has, of course, important bearings on the downstream cascade as it traverses through the wakes. Two general observations appear warranted:

First, the transition process on the pressure-side of a turbine airfoil seems to be more governed by the breakdown of the Görtler's vortical cells with the Tollmien-Schlichting waves as a superimposed influence. Secondly, the Karman vortices in the trailing-edge region, which in their ideal form are two-dimensional, are given a three-dimensional structure by the convected Görtler's vortices. More specifically:

(*i*) The Karman vortex spacing (h/a) in the near wake region increases with increasing distance from the trailing edge owing to the reduced velocity deficit in the wake.

(*ii*) Transition of the boundary layer on the concave side of the airfoil are strongly influenced by the curvature-induced Görtler's vortices. For the airfoil studied, transition begins at $s/c=0.1$ at which $G(\delta_2)\geq0.58$.

Acknowledgments

The material contained in this paper resulted from investigations performed in the Department of Mechanical Engineering, The Ohio State University, Columbus, Ohio. This work, along with others, was sponsored by the Aero Propulsion Laboratory, USAF, under Contract No. F33615-75-C-2052. Mr. Arnon Chait's able contributions in the experimental work are hereby recognized.

The authors gratefully acknowledge the support and encouragement of Mr. Charles Benz, Mr. Robert Henderson and Dr. Kervyn Mach, all of the Aero Propulsion Laboratory, U.S. Air Force.

References

1 Graham, R. W., "Fundamental Mechanisms that Influence the Estimate of Heat Transfer to Gas Turbine Blades," ASME 79-HT-43. *Heat Transfer Engineering*, Vol. 2, No. 1, July 1980, pp. 39–47.

2 Cunsty, R., "Boundary Layer Development on Turbine Blades in the Presence of Görtler Vorticity," Gas Turbine Laboratory, Cambridge University, Cambridge, England.

3 Walker, L. A., and Markland, E., "Heat Transfer to Turbine Blading in the Presence of Secondary Flow," *International Journal of Heat and Mass Transfer*, Vol. 8, 1965, pp. 729–748.

4 Walker, L. A., and Markland, E., "Calculation of Heat Transfer to Turbine Blading in the Presence of Secondary Flow," *International Journal of Heat and Mass Transfer*, Vol. 10, 1967, pp. 499–518.

5 Han, L. S., Cox, W. R., and Chait, A., "Investigation of the Boundary Layer Behavior on Turbine Airfoils," AFAPL-TR-79-2011, Dec. 1978.

6 Cox, W. R., and Han, L. S., "An Experimental Study of Turbine Airfoil Wakes," AFAPL-TR-76-2, Nov. 1975.

7 von Karman, Th., "Über den Mechanismus des Flussigkeits und Luftwiderstandes," *Phys. Z.*, Vol. 13, 1912, pp. 49–59.

8 Morkovin, M. V., "Flow Around Circular Cylinder—A Kaleidoscope of Challenging Fluid Phenomena," Symposium on Fully Separated Flows, ASME, New York, 1964, pp. 102–118.

9 Morkovin, M. V., "Observations on Streamwise Vortices in Laminar and Turbulent Boundary Layers," NASA-CR-159061, 1979.

10 Kestin, J., and Wood, R. T., "On the Stability of Two-Dimensional Stagnation Flow," *Journal of Fluid Mechanics*, Vol. 44, pt. 3, 1970, pp. 461–479.

11 Sadeh, W. Z., Brauer, H. J., and Garrison, J. A., "Visualization Study of Vorticity Amplification in Stagnation Flow," Project SQUID Technical Report CSU-1-PU, 1977.

12 Wortman, F. X., "Visualization of Transition," *Journal of Fluid Mechanics*, Vol. 38, pt. 3, 1969, pp. 473–480.

13 Martin, B. W., and Brown, A., "Factors Influencing Heat Transfer to the Pressure Surfaces of Gas Turbine Blades," *Journal of Heat and Fluid Flow*, Vol. 1, No. 3, 1979, p. 107.

14 Cox, W. R., and Han, L. S., "Prediction of Transition Region Location and Extent for the Effects of Surface Curvature, Free-Stream Turbulence, Pressure Gradients, Wall Temperature, and Unit Reynolds Number," U.S. Air Force Aero Propulsion Laboratory, Technical Report AFAPL-TR-76-2, pt. III, Sept. 1975.

15 Smith, A. M. O., "On the Growth of Taylor-Görtler Vortices Along Highly Concave Walls," *Quart. Appl. Math.*, Vol. 13, 1955, pp. 233–262.

16 Tobak, M., "On Local Görtler Instability," ZAMP (Zeitschrift fur Agnewandte Mathematik und Physik), Vol. 22, 1971, pp. 130–143.

17 Knapp, D. F., and Roache, P. J., "Combined Visual and Hot-Wire Anemometer Investigation of Boundary-Layer Transition," *AIAA Journal*, Vol. 6, No. 1, 1968, pp. 29–36.

18 Bippes, H., and Görtler, H., "Dreidimensionale Storungen in der Grenzschicht an einer konkaven Wand," *Acta Mechanica*, Vol. 14, 1972, pp. 251–267.

G. Brunton
Principal Engineer.

R. R. Willcock

M. A. Voisey
Shell Research Ltd.,
Thornton Research Center,
Chester, England

The Low-Temperature Properties of Aviation Fuels

A review is presented of work on the low-temperature properties of aviation turbine fuels that has been carried out in recent years at Thornton Research Centre. Details of both simulated full-scale aircraft tank tests and laboratory evaluations are included. Zero holdup is considered as a low-temperature specification parameter and a novel method for measuring its value is described. Experimental results are presented which demonstrate that a change from a freezing point to a flow criterion could provide an increase in fuel availability without prejudicing flight safety.

Introduction

The aviation fuel market is one of the few areas in the petroleum industry where an increase in future demand can be predicted with a reasonable degree of certainty [1]. However, this growth in demand is likely to be influenced by two major constraints, price and availability. At present aviation fuel represents only a relatively small portion of the barrel, but any increase in this fraction is limited by the need to meet specification requirements and competition from other products. The changing pattern in product demand is focusing attention on secondary refinery processes to maximize output of distillate fractions and on the use of alternative non-petroleum sources of fuel. In both of these approaches, significant upgrading of the initial product, involving both large capital outlay and high operating costs, may be necessary to produce final products within current specification limits. Under these conditions it is desirable to identify ways of easing specification requirements that will increase flexibility, but at the same time maintain product quality [2].

One of the important specification requirements that can constrain fuel availability is the freezing point. For Jet A-1 fuels this limit has been relaxed recently from $-50°C$ to $-47°C$. Analysis of a broad spectrum of in-flight fuel temperatures indicates that this relaxation corresponds to the maximum freezing point permissible before the temperatures experienced by the fuel could closely approach its freezing point [3]. Potential problems could be overcome by changes in fuel management procedures or modifications to aircraft fuel systems [4–7]. However, these approaches are not without their drawbacks. While they will certainly feature in scenarios for future utilization of higher freezing point fuels, they will in no way invalidate efforts directed at understanding the low-temperature behavior of the fuels themselves.

Research into the low-temperature properties of aviation fuels has been carried out by several organizations for more than three decades. This paper presents an overview of research carried out at Shell Research Ltd.'s Thornton Research Center and highlights the consequences that the results have for future considerations of the low-temperature specification requirement.

The Need to Redefine the Low-Temperature Specification Requirement

Currently the low-temperature specification requirement for an aviation turbine fuel is defined by its freezing point. The advantages of using this parameter include the relative ease with which it can be measured for conventional fuels, the reasonable degree of repeatability and reproducibility, and the margin of safety it ensures. This last factor is a consequence of the definition of freezing point. The ASTM D2386/IP 16 method that is currently used determines the

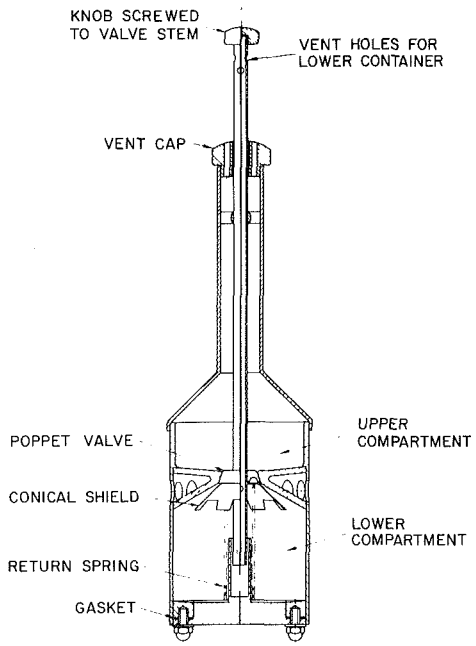

Fig. 1 Shell cold-flow tester – sectional elevation

Contributed by the Gas Turbine Division of THE AMERICAN SOCIETY OF MECHANICAL ENGINEERS and presented at the 27th International Gas Turbine Conference and Exhibit, London, England, April 18–22, 1982. Manuscript received at ASME Headquarters December 3, 1981. Paper No. 82-GT-48.

Table 1 Shell cold-flow rig studies: Features of test tanks

Tank	Type	Baffled	Capacity	Booster pump		
				Type	Mounting	Protecting filter
1	Ex-BAC lightning	Yes	~100 gal.	BP 18 Mk 1	Tank base	15 mesh gauge
2	Ex-BAC lightning	Yes	~100 gal.	BP 18 Mk 1	Tank base	15 mesh gauge
3	Rectangular	No	~100 gal.	SPE 15160/AC	Underside	20 mesh gauge cap

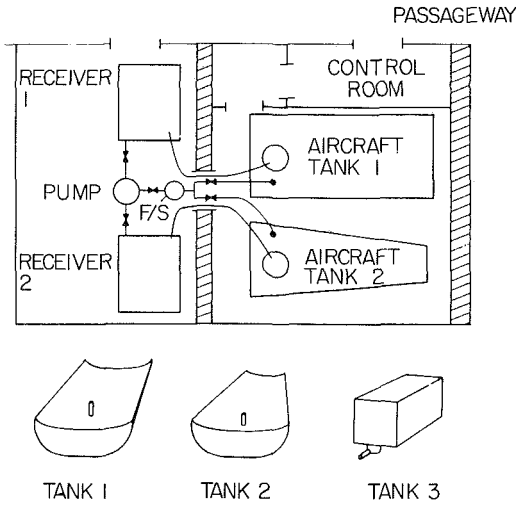

Fig. 2 Schematic layout of aircraft tanks in the cold room for pumpability tests F/S = filter separator

temperature at which crystals disappear when a sample is allowed to warm up from low temperature under controlled conditions. The major disadvantage of the use of a freezing point specification is that it bears little relation to the property that actually limits fuel usage under operating conditions, namely its ability to flow [8, 9]. A cold-flow property limit could reflect the practical low-temperature flight conditions more accurately than the established freezing point limit.

Past Shell Studies of the Low-Temperature Behavior of Aviation Turbine Fuels

Laboratory tests. The Shell Cold-Flow Test was developed as a result of early studies [8–10] that identified the need for a suitable procedure to characterize the low-temperature flow behavior of aviation turbine fuels. The procedure does not measure any fundamental rheological property, although the test conditions have been designed to represent as closely as possible those to which the fuel is subjected while flowing within a fuel tank towards the booster pump. The apparatus comprises two cylindrical chambers connected by a spring-loaded puppet valve (Fig. 1). The fuel sample is introduced into the upper chamber and the apparatus is immersed in a closely controlled low-temperature bath until the fuel and bath temperatures equilibrate. The poppet valve is then opened for a specified time, after which it is closed and the apparatus is removed from the bath. The volume of fuel remaining in the upper container is measured after the apparatus has warmed up to assess the flow characteristic of the fuel at the test temperature. (The poppet valve orifice is reasonably large; this ensures that the result obtained depends principally upon the rigidity of the fuel and to only a minor degree on the flow rate.)

The Cold-Flow Test was evaluated in some detail during an Institute of Petroleum program, and the method was adopted as a standard procedure (IP 217/66T) [11]. The method was withdrawn after 1972, owing to lack of interest in the need for a change in the low-temperature specification. However, more recent events have refocused attention on the influence

Table 2 Low-temperature properties of jet A/A-1 fuels

Fuel	Freezing point, °C	Tank test zero hold-up temperature, °C	Cold-Flow Test zero hold-up temperature, °C
1	−48	−48	−48
2	−51	−50	< −51
3	−51	−52	−50
4	−51.5	−55	−52
5	−52.5	−50	−50
6	−51.5	−50	−50
7	−50.5	−50	−50
8	−50	−51	−50
9	−60	−60	−60
10	−45	−47	−45

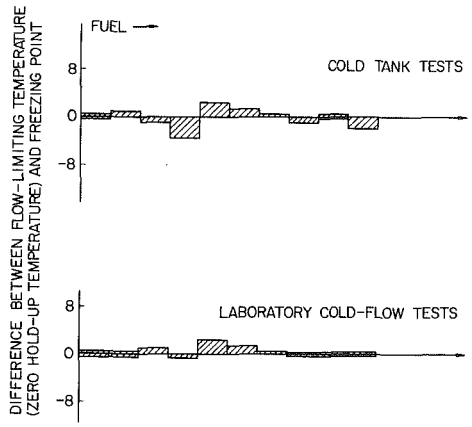

Fig. 3 Cold-flow studies: difference between flow-limiting temperature (zero hold-up temperature) and freezing point for a series of jet A/A – 1 fuels

of specification requirements on aviation turbine fuel availability, and the Cold-Flow Test has been used increasingly during the past few years to complement the results of tank studies carried out at Thornton Research Center and elsewhere.

Tank Studies. Tank studies started at Thornton Research Center in the mid-1950s; this work became part of an Institute of Petroleum program, and the results are discussed in detail elsewhere [12]. Most of the I.P. work was concerned with determining the accuracy of laboratory tests and their correlation with rig tests. It was considered that a 30 percent fuel hold-up in rig testing would best define the aircraft pumpability temperature limit and that the Shell Cold-Flow Test (30 percent hold-up) was the preferred method for determining this limit. A 30 percent hold-up condition means that almost one-third of the fuel is unable to flow from the tank. Irrespective of the time that such a condition prevails, the fuel would be unusable for that period, and the chances of experiencing operation problems would increase markedly. A more realistic criterion than the 30 percent hold-up condition would be the 'zero hold-up' temperature, even though it is more difficult to measure experimentally. This temperature represents the lowest temperature at which *all* the fuel can be recovered, i.e., a flow-limiting temperature and is obtained by extrapolation. For this reason, later tank tests and related laboratory studies have focused on the 'zero hold-up' temperature and the variation of this parameter with the nature of the fuel.

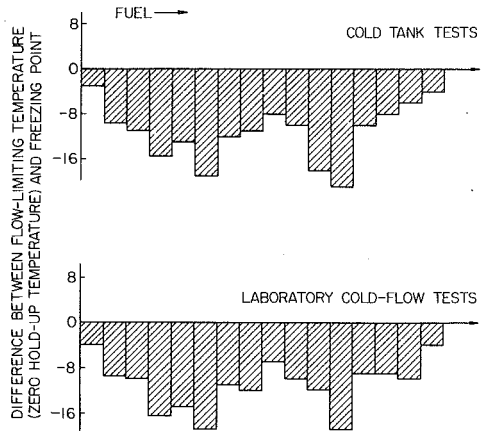

Fig. 4 Cold-flow studies: difference between flow-limiting temperature (zero hold-up temperature) and freezing point for a series of experimental extended fuel blends

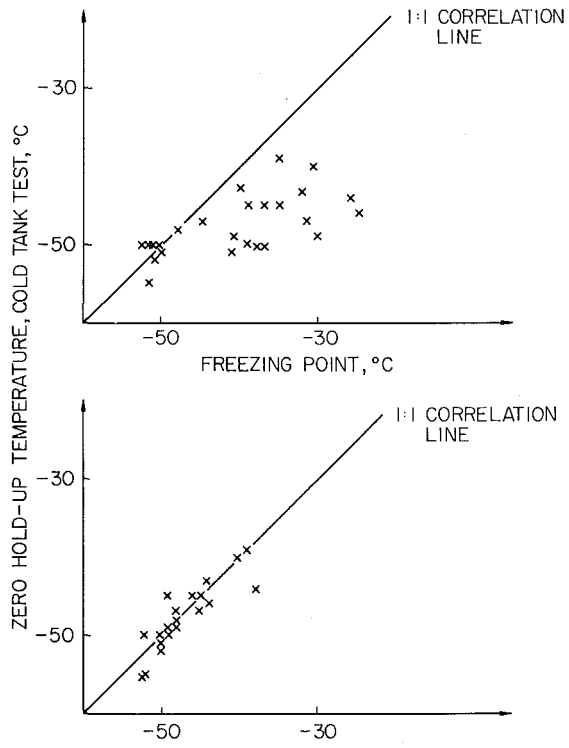

Fig. 5 Correlation between cold tank test, zero hold-up temperature and (*a*) Freezing point, (*b*) Laboratory cold-flow test zero hold-up temperature

More recent studies have been carried out using one of three tanks (Table 1) placed in a cold room capable of operating down to −60°C (Fig. 2) [13]. After filling the test tanks with fuel (via a coalescer to ensure the removal of free water) the cold-room temperature was reduced to the required value. Conditions were controlled to maintain the desired test temperature throughout the fuel (the time taken to reach these conditions varied between 36 and 72 hrs, depending on the degree of approach to the cold-room limiting temperature). Upon reaching the required test temperature, the boost pump was operated to empty the test tank and the fuel was collected. Conditions were arranged so that cavitation occurred at the boost pump, and the variation of this condition with temperature was measured allowing the zero hold-up temperature to be determined.

Tests have been carried out on a range of conventional aviation turbine fuels with specifications within the limits for

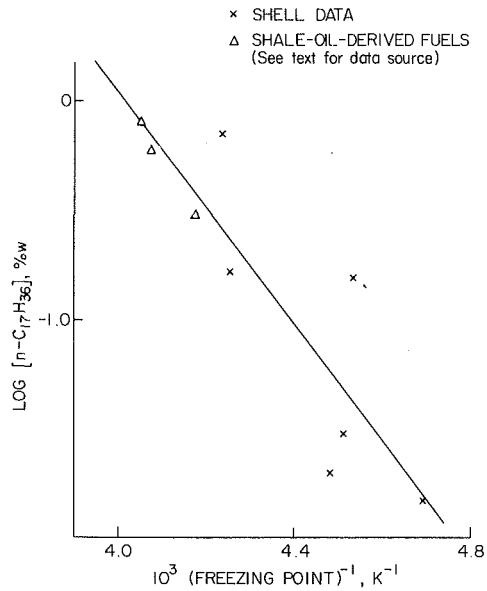

Fig. 6 Correlation between concentration of the last member of straight-chain paraffin series for kerosines and the measured freezing point

Jet A/A-1 fuels. Comparison has been made between the freezing point (ASTM D2386/IP 16), cold-flow test zero hold-up temperature, and the tank test zero hold-up temperature (Table 2). There is good agreement between the zero hold-up temperature determined in both the tank tests and the Cold-Flow Test. In addition these results agree well with the freezing point, the difference being within experimental error (Fig. 3). The results establish that for most purposes either of the two criteria (i.e., freezing point or flow-limiting temperature) could be used to define the low-temperature specification requirement for these fuels.

However, in order to identify the most significant parameter that controls fuel behavior at low temperature it was important to study fuels for which the freezing and flow-limiting temperatures were well separated. This separation was achieved by a series of "experimental high density" fuels, prepared by blending varying quantities of heavier components into the kerosine fraction. The results of extensive tests with these experimental fuel blends established that the zero hold-up temperature obtained from both tank and laboratory tests were in good agreement and that these temperatures do *not* correlate with the freezing point (Table 3), but that the former temperature can be as much as 20°C below the freezing point (Fig. 4). Over the full range of fuels studied, only the cold-flow test results show a good correlation with the tank tests (Fig. 5), demonstrating that the zero hold-up temperature provides a more realistic indication of the limiting temperature for unrestricted flow of the fuel under severe low-temperature conditions than does the freezing point.

Effect of Fuel Composition on Low-Temperature Properties

Support for the above conclusion and insight into the factors influencing the observed results can be gained from closer examination of the relationship between fuel composition and performance in both freezing point and flow-related tests. It is known that of the molecular structures present in kerosine, the straight-chain paraffins, and in particular the least soluble paraffins (i.e., the longest-chain components) strongly influence the measured "freezing point" [13]. From a simplistic viewpoint of solubility, the concentration of these paraffins will be related to the observed "freezing point" according to the relationship:

$$\ln(\text{concentration} \propto (\text{freezing point})^{-1}$$

This relationship is supported experimentally, as shown in Fig. 6, for fuels in which n-heptadecane is the longest straight-chain paraffin present. There is good agreement between the Shell results and other available data for three jet fuels derived from shale oil [13], providing further support for the validity of this approach. Such evidence suggests that the "freezing point" is related to a solubility characteristic of the fuel (in fact the term "low-temperature solubility point" would be more correct than freezing point), and it is not perhaps surprising that a parameter that depends on the solubility of components present in low concentration in the fuel does not necessarily reflect the bulk performance of the fuel.

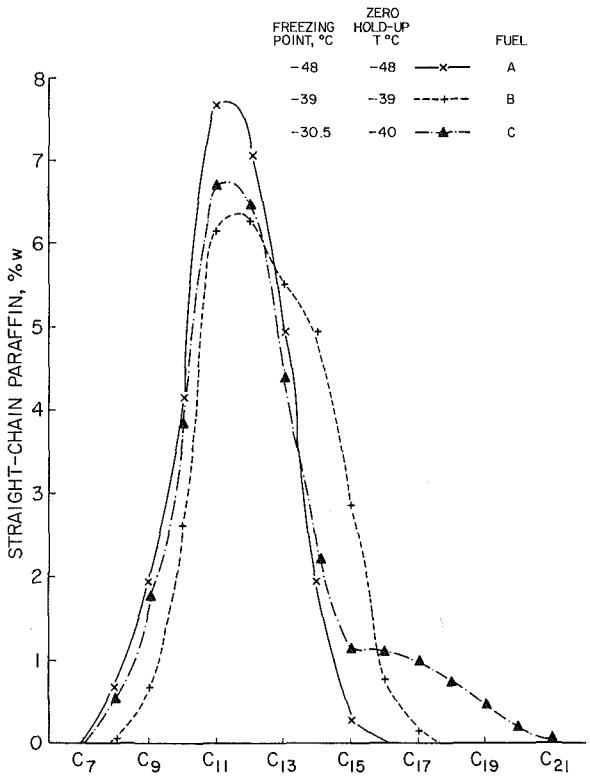

Fig. 7 Effect of straight-chain paraffin content on freezing point/no flow-limiting temperature

The shape of the straight-chain paraffin distribution for a fuel with similar freezing point and flow-limiting temperatures differs markedly from that for a fuel for which the parameters are dissimilar (Fig. 7). The flow characteristics of fuels are also influenced by the straight-chain paraffins present. Typically, extraction of these components from a sample of kerosine reduces its flow-limiting temperature from in the region of −50°C to values below those that can be determined experimentally. This suggests that the flow-limiting temperature is determined by the formation of a gel between the paraffin crystals and the remaining liquid, and offers an explanation for the observed differences between the freezing point and the flow-limiting temperature in some fuels but not others. Gel formation would be expected to be associated with a higher concentration of straight-chain paraffin crystals than would the freezing point. For fuels in which the slope of the straight-chain paraffin profile is steep, precipitation of a significant quantity of crystals would be expected to occur close to the freezing point temperature (Fuels A and B, Fig. 7), whereas for fuels with the asymmetrical profile, precipitation of sufficient crystals to induce gel formation would not be expected until the fuel was cooled significantly below the freezing point (Fuel C, Fig. 7). Efforts are still continuing in this area to clarify the role of other components which may influence performance. Nevertheless, the results already obtained provide considerable insight into

Table 3 Low-temperature properties of 'experimental high-density fuel' blends

Fuel	Freezing point, °C	Tank test zero hold-up temperature, °C	Cold-Flow Test zero hold-up temperature, °C
11	−40	−43	−46
12	−30.5	−40	−40
13	−39	−50	−49
14	−31.5	−47	−48
15	−37	−50	−52
16	−30	−49	−49
17	−38	−50	−49
18	−32	−43	−44
19	−41	−49	−48
20	−35	−45	−45
21	−26	−44	−38
22	−25	−46	−44
23	−15	–	−30
24	−41	−51	−50
25	−37	−45	−46
26	−39	−45	−49
27	−25	−39	−39

Table 4 Determination of the no-flow temperature of fuels using the Air Probe Flow Monitor and comparison with other low-temperature characteristics of the fuels

Fuel	APFM no-flow T., °C	ASTM D2386/IP 16 freezing pt., °C	Cold-Flow Test zero hold-up T., °C	Setapoint no-flow T., °C
n-decane	−29.2	−29.7[a]	–	–
tetradecane	+5.7	+6[a]	–	–
n-nonane	−52.5	−51[a]	–	–
Jet A-1	−52.8	−51	−51	−51.6
Jet A-1	−49.4	−50.5	−50	−53.9 (−51.9)[b]
Jet A-1	−51.5	−51	−52	−52.1
Jet A-1	−53.3	−50	−50	−51.5
EHDF[c]	−49.0	−39	−49	−48.7
EHDF[c]	−49.1	−35	−45	−48.5
EHDF[c]	−42.0	−26	−38	−48.2 (−43.9)[b]
EHDF[c]	−52.9	−37	−52	−53.3
EHDF	−51.9	−30	−49	−49.8
ERBS[d]	−33.6	−26.0	–	−34.1
ERBS[d]	−33.9	−24.5	–	−31.8
ERBS[d]	−33.7	−25.0	–	−33.2

[a]literature freezing point
[b]400 mesh filter; all other values of Setapoint, no-flow temperature obtained with 325 mesh filter.
[c]EHDF-experimental high density fuel
[d]ERBS-experimental referee broadened specification fuel

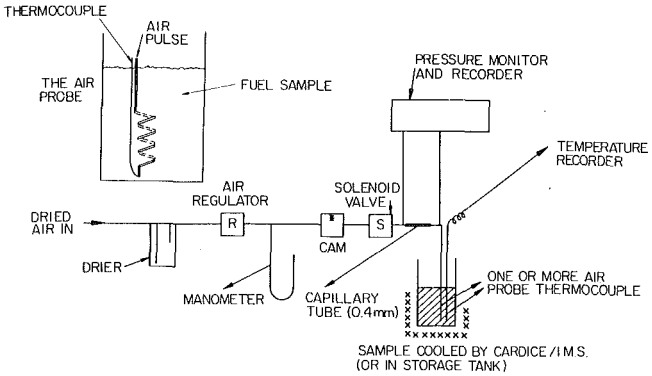

Fig. 8 Layout of the air probe flow monitor (*Allows the use of more than one probe)

the nature of the measured performance criteria and the reasons underlying the advantages of using a flow-related measurement rather than freezing point as an indicator of low-temperature performance.

Current Efforts

A drawback of the Cold-Flow Test is that the zero hold-up temperature cannot be determined directly; the usual procedure is to plot the temperature dependence of the hold-up factor over a range of readily determined values (typically between 10–90% hold-up) and to extrapolate to zero hold-up to obtain the corresponding zero hold-up temperature. To minimize errors in the measurement of the zero hold-up temperature several determinations are necessary, particularly in the region of low hold-up factors. Ideally, it would be far better to characterize directly the temperature at which fuel will cease to flow. This objective has been achieved using a newly developed technique – the Air Probe Flow Monitor (APFM). The APFM is based on pulsing a small bubble of air through a sample of the fuel, which is cooled at a constant rate (Fig. 8). The uniform fluctuations of air pressure upstream and downstream of a glass capillary are monitored, the capillary acting as a fine control on the air pulse pressure. A change in the observed pressure profiles (Fig. 9) is observed when the air ceases to flow through the sample, and the temperature at which this occurs is recorded as the no-flow temperature. The inability of air to flow through the sample is a direct indication to the loss of sample fluidity.

Initial evaluation of the APFM indicates that the results relate closely to those from other more laborious and less versatile flow tests, and that this flow monitor provides a straightforward and rapid method for characterizing a wide range of distillate fuels (typical results are shown in Table 4). Several features emerge from the results to date. There is good agreement between the APFM no-flow temperature and the literature freezing point for pure straight-chain paraffins. This demonstrates that the APFM provides a sound measurement of the no-flow temperature, since for a pure material the freezing point and the no-flow temperature would be expected to be indistinguishable. For conventional Jet A-1 fuels the APFM results are reasonably close to the measured freezing points. This observation is consistent with the results of the past work described above, and provides further support for the practice of describing the low-temperature behavior of conventional fuels by either a flow-related criterion or freezing point. For "experimental high-density fuel" blends the APFM results bear no relation to the freezing points (an observation that is also consistent with past work), but there is reasonable agreement between the APFM no-flow temperature and the zero hold-up temperature for both conventional and experimental fuels (Fig. 10). Thus the APFM achieves one of the major requirements of any new

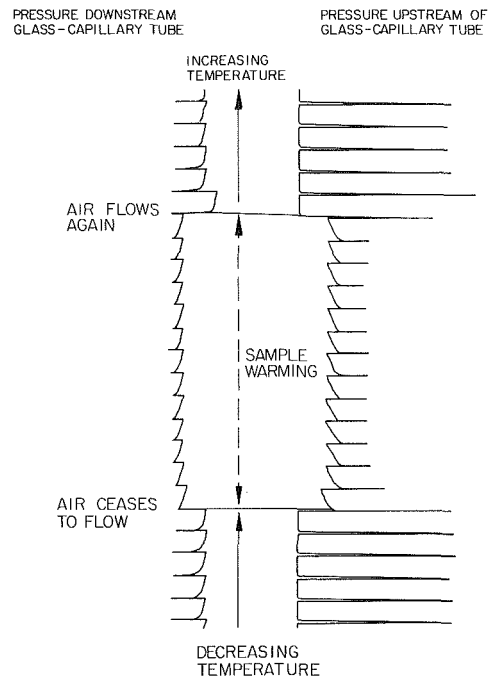

Fig. 9 Typical pressure trace of air probe flow monitor

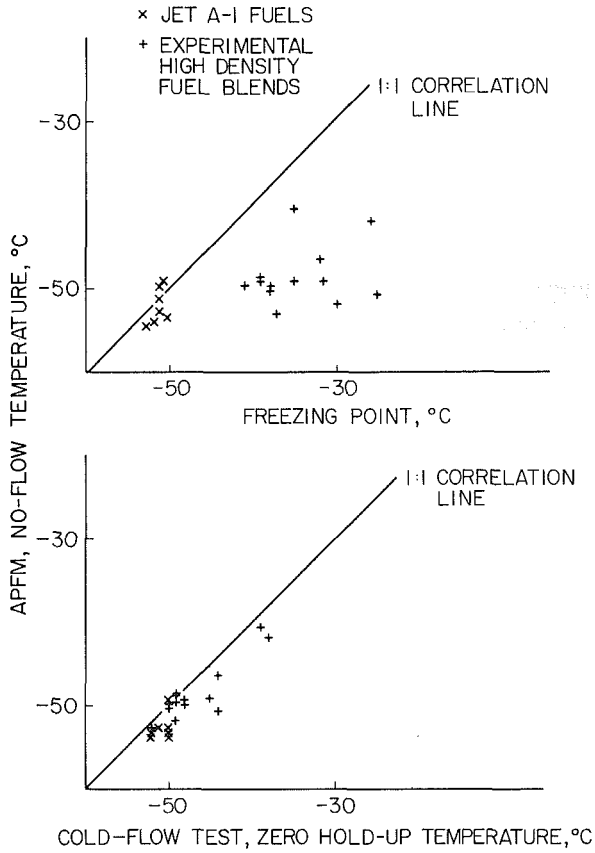

Fig. 10 Correlation between APFM no-flow temperature and (*a*) freezing point, (*b*) Shell Cold-Flow Test, zero hold-up temperature

flow test – viz., the ability to measure the flow-limiting temperature directly.

The no-flow temperatures of samples of experimental referee broadened specification (ERBS) fuels have been determined, and the results are included in Table 4. It is of interest to note that the freezing point and no-flow temperatures are well separated, and the results indicate that these

fuels remain fluid at temperatures significantly below the freezing point.

Stanhope-Seta, Ltd. have recently developed an instrument, the Setapoint detector, that measures a similar characteristic to the APFM, but by means of an entirely different principle of operation [14]. Table 4 compares the no-flow temperatures measured by the two devices. Although the agreement is reasonable it should be interpreted with caution. The Setapoint technique involves cooling a sample of fuel while at the same time forcing the fuel forwards and backwards through a filter. The pressure developed across the filter is sensed, and when it exceeds a predetermined value the temperature is recorded as the no-flow temperature. The presence of the filter in the system introduces an additional complication, in that the pore size can influence the observed result. Thus the Setapoint measurement may not be solely a flow-related measurement, but may also be influenced by the filter-plugging characteristics of the fuel.

In addition to its use as a laboratory method to characterize the low-temperature behavior of fuels, the APFM shows considerable potential for studying in-situ the flow characteristics of fuels in tank tests (a situation that cannot be achieved with other flow tests currently available). Recent tank tests designed to simulated temperature profiles experienced in flight [15] have highlighted the need to be able to make this type of measurement during the test cycle. The Cold-Flow Test was designed to evaluate bulk flow characteristics of the fuel under isothermal conditions and cannot cope satisfactorily when temperature gradients have been established in the tank. The APFM on the other hand offers the capability of monitoring fluidity at various locations subjected to different local temperature regimes. In the longer term it may be possible to adapt the APFM to provide a means of monitoring the condition of the fuel in aircraft tanks during flight.

Consequences of Utilizing a Flow-Related Low-Temperature Specification Requirement

The results of the research program described above question the validity of using a freezing point requirement to specify the low-temperature performance of jet fuels. The extensive laboratory and tank tests support the premise that a flow-related measurement would be a more realistic criterion than freezing point. It is important that the specification requirements reflect as closely as possible the desired performance characteristics, in order to maintain optimum fuel quality and avoid any confusion in the future. For conventional fuels the use of freezing point or a flow-related criterion would be equally applicable. However, for less conventional fuels the freezing point could be unnecessarily restrictive as evidenced by fuels used in the present studies that have satisfactory flow characteristics at temperatures well below their freezing point. (It should be noted that the use of heated filters downstream of the fuel tank avoids problems related to filter-blocking by any crystals present in fuels.) For such fuels (perhaps representing future products) a no-flow specification requirement (possibly based on a technique such as the air probe flow monitor) would allow significant increases in the jet fuel yield to be obtained from refineries otherwise restricted by the need to meet a freezing point requirement.

Acknowledgments

The authors wish to acknowledge the valuable contributions made by colleagues at Thornton Research Centre, and in particular those of P. T. Ford. In addition, the gift of samples of ERBS fuels by NASA is gratefully acknowledged.

References

1 Lewis, A., "Future Aviation Fuels: The Petroleum Industry Responds to the Challenge," SAE paper 800769, 1980.

2 Robertson, A. G., and Williams, R. E., "Jet Fuel Specifications: the Need for a Change," *Shell Aviation News*, No. 435, 1976, pp. 10–13.

3 Pasion, A. J., "In-Flight Fuel Tank Temperature Survey Data," D6-48611, Boeing Commercial Airplane Co., Seattle, Wash., May 1979, (NASA CR-159569).

4 Barr, N. M. et al., "Boeing Airplane Fuel Systems at Low Temperatures," Document D6-42386, Boeing Commercial Airplane Co., Seattle, Wash., 1975.

5 Pasion, A. J., and Thomas, I., "Preliminary Analysis of Aircraft Fuel Systems for Use With Broadened Specification Jet Fuels," D6-44538, Boeing Commercial Airplane Co., Seattle, Wash., (NASA CR-135198).

6 Longwell, J. P., and Grobman, J., "Alternative Aircraft Fuels," ASME ENGINEERING FOR POWER, Vol. 101, 1979, pp. 155–161.

7 Friedman, R., "High-Freezing-Point Fuels Used for Aviation Turbine Engines," ASME Paper No. 79-6-7-141, Mar. 1979.

8 Strawson, H., "Using Turbine Fuels at Low Temperatures," *Shell Aviation News*, No. 210, Dec., 1955, pp. 8–12.

9 Strawson, H., "The Pumpability of Aviation Turbine Fuels at Low Temperature," *J. Inst. Petrol.*, Vol. 45 (425), 1959, pp. 129–146.

10 Hutton, J. F., "Flow Properties of Distillates at Low Temperatures. A Review," *J. Inst. Petrol.*, Vol. 45 (425), 1959, pp. 123–129.

11 "Proposed IP Standard Method for Cold Flow Test of Aviation Turbine Fuels," *J. Inst. Petrol.*, Vol. 48 (467), 1962, pp. 388–390.

12 "Low Temperature Flow Characteristics of Aviation Turbine Fuel," Report of Panel ST-B-6 of the Institute of Petroleum, Sept., 1960.

13 Solash, J., et al., "Relation Between Fuel Properties and Chemical Composition, Part 1: Jet Fuels from Coal, Oil Shale and Tar Sands," *Fuel*, Vol. 57, 1978, pp. 521–528.

14 UK Patent Application 2 043 246 A, Oct. 1980.

15 Friedman, R., and Stockemer, F. J., "Temperature and Flow Measurements on Near-Freezing Aviation Fuels in a Wing-Tank Model," ASME Paper No. 80-GT-63, Mar. 1980.

Deposit Formation in Hydrocarbon Fuels

R. Roback

E. J. Szetela

L. J. Spadaccini

United Technologies
Research Center,
East Hartford, Conn. 06108

A high-pressure fuel coking test apparatus was designed and developed and was used to evaluate thermal decomposition (coking) limits and carbon deposition rates in heated copper tubes for two hydrocarbon fuels, RP-1 and commercial-grade propane. Tests were also conducted using JP-7 and chemically-pure propane as being representative of more refined cuts of the baseline fuels. A parametric evaluation of fuel thermal stability was performed at pressures of 136 atm to 340 atm, bulk fuel velocities in the range 6–30 m/s and tube wall temperatures in the range 422–811 K. In addition, the effect of the inside wall material on deposit formation was evaluated in selected tests which were conducted using nickel-plated tubes. The results of the tests indicated that substantial deposit formation occurs with RP-1 fuel at wall temperatures between 600 and 800 K, with peak deposit formation occurring near 700 K. No improvements were obtained when deoxygenated JP-7 fuel was substituted for RP-1. The carbon deposition rates for the propane fuels were generally higher than those obtained for either of the kerosene fuels at any given wall temperature. Finally, plating the inside wall of the tubes with nickel was found to significantly reduce carbon deposition rates for RP-1 fuel.

Introduction

The performance characteristics of advanced technology hydrocarbon-fueled rocket and gas turbine engines may be enhanced by operating at higher combustion pressures and utilizing more of the heat sink capability of the fuel to accommodate the increased heat fluxes that result from high-pressure operation. Regenerative cooling with hydrocarbon fuels is feasible up to a point where the coolant wall temperature reaches a limit defined by a thermal decomposition or "coking" temperature. Deposit formation on the coolant wall surface, which usually occurs when the thermal decomposition temperature is reached, causes an increased thermal resistance, a progressively increasing wall temperature and, ultimately, failure. Therefore, it is desirable to establish (*i*) the maximum heat fluxes that can be accommodated by determining the minimum wall temperature limits for incipient deposit formation under a variety of coolant flow conditions, (*ii*) what rates of formation will prevail, and (*iii*) the nature of the deposit, as it affects the heat transfer limits.

Hydrocarbon fuel stability and deposit formation (coking) has been a subject of investigation for many years and the results of many of these previous studies have been summarized in [1, 2]. The rates of fuel decomposition and deposit formation have been found to be functions of the temperature, pressure, velocity, composition and physical state of the fuel. Although the exact mechanism of deposit formation has not been clearly defined, it usually results from the pyrolysis of organic molecules which make up the fuel. Free radicals are generated thermally and, because of their affinity for atoms such as nitrogen, oxygen, and sulfur which might be in the fuel, stable complex solids are formed. Studies have shown that additional processing of the fuel to remove these deposit forming precursors has improved thermal stability and decreased deposit formation [3].

Because of its superior thermal conductivity, copper has been the preferred material for forming the regenerative cooling passages in the high heat-flux regions of high-pressure rocket thrust chambers. However, studies of the effect of wall materials on deposit formation [4, 5, 6] have indicated that deposit rates on copper can be very high, although no data was available for the particular fuels and test conditions of interest. Therefore, to permit more accurate determinations of the maximum allowable wall temperatures, a fuel coking

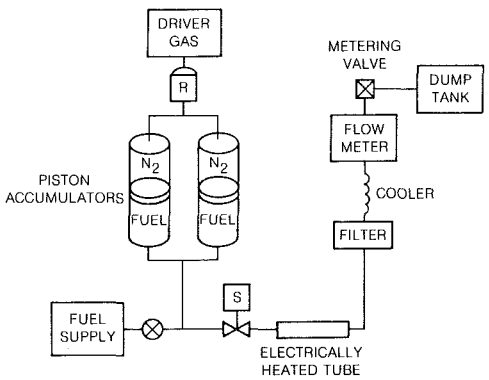

Fig. 1 Fuel deposit test apparatus

Contributed by the Gas Turbine Division of THE AMERICAN SOCIETY OF MECHANICAL ENGINEERS and presented at the 27th International Gas Turbine Conference and Exhibit, London, England, April 18–22, 1982. Manuscript received at ASME Headquarters December 3, 1981. Paper No. 82-GT-49.

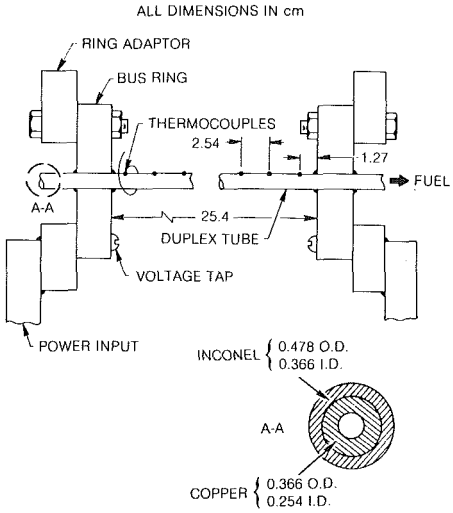

Fig. 2 Test tube assembly

test apparatus was designed and developed and was used in experiments directed toward (*i*) evaluating the thermal decomposition (coking) limits and rates of deposition in heated copper tubes for two hydrocarbon fuels, RP-1, and propane, and (*ii*) investigating the effect of further refining of these fuels, to reduce the concentration levels of deposit-forming precursors, on improving their thermal stability [7]. Tests were conducted using RP-1 and commercial-grade propane as the standard hydrocarbon fuels and deoxygenated JP-7 and chemically pure propane (99.4 percent pure) as being representative of more refined cuts of these fuels. A parametric evaluation of fuel thermal stability was performed at pressures of 136 atm to 340 atm, bulk fuel velocities in the range 6 to 30 m/s, and tube wall temperatures in the range 422 to 811 K. In addition, the effect of the inside wall material on deposit formation was evaluated in selected comparative tests which were conducted using nickel-plated tubes.

Test Facility and Test Hardware

The test apparatus, shown schematically in Fig. 1, consisted of: (*i*) a fuel supply tank, including a porous metal nitrogen sparger and a zeolite-type molecular sieve for removing dissolved oxygen and water from the JP-7 fuel; (*ii*) a fuel delivery system consisting of two piston-type accumulators which were pressurized with nitrogen and used to drive fuel through the test section; (*iii*) a resistance-heated test tube connected to a 40-kVA high-amperage a-c power supply; (*iv*) an in-line filter for collecting any solid particles which might form in the bulk flow or break off from the test tube wall during test; (*v*) a fuel cooler; (*vi*) a turbine-type flowmeter; (*vii*) an electrically-driven metering valve which was used to control the fuel flow through the test section; and (*viii*) a fuel dump tank.

To permit testing at pressures up to 340 atm and tube wall temperatures up to 1000 K, a duplex tube wall configuration, shown schematically in Fig. 2, was selected. In the duplex tube configuration, an inner wall of an oxygen-free, high-conductivity copper (No. 102; 99.95 percent pure; electrical conductivity = 0.0586 Megmho-cm) provided the desired test surface for studying the rates of deposit formation on copper while an outer wall of Inconel 600 provided the necessary high-temperature tensile strength. The duplex tube was manufactured by threading a 0.254-cm i.d. × 0.366-cm o.d. copper tube into an oversized Inconel outer sheath, and subsequently drawing the Inconel tube through a die to obtain a sheath thickness of 0.056 cm and an overall duplex tube o.d. of 0.478 cm. This configuration had the advantage that, while the structural load was carried by the outer sheath, the majority of the power (~95 percent) was conducted through the copper and, as a result, the tube radial temperature gradient was small.

To verify the condition that no significant electrical or thermal resistance at the interface of the two metals, stemming from oxidation, contamination or local separation, had developed, tube samples were subjected to various tests which included: metallographic examination using a scanning electron microscope and microprobe, shear tests, and thermal cycling in a high-temperature oven. The results indicated that the copper closely followed the contour of the Inconel surface and the interface was free of contamination and/or air gaps. In addition, any tendency for separation at the copper/Inconel interface would be opposed during testing by the combined action of internal pressure forces and the higher rate of thermal expansion of copper relative to Inconel.

The test tube assembly is also shown schematically in Fig. 2. The test tube was silver soldered to a copper bus ring which in turn was bolted to copper ring adaptors. Ten thermocouples were spotwelded to the outer Inconel wall at equal spacings of 2.54 cm starting at a location 1.27 cm from the bus ring. The surface of the tube was coated with Sauereisen cement at the thermocouple junctions to electrically insulate the thermocouple wire from the tube, and the wire was wrapped once around the tube and coated with additional Sauereisen cement to insure good thermal contact and minimize conduction losses. By use of an a-c power supply, thermocouple errors resulting from a voltage drop across the thermocouple bead were minimized. The test tube assembly was supported on teflon lined cradles that were designed to accommodate the bus rings and to permit thermal expansion by providing a low coefficient of sliding friction. The teflon also acted as an electrical insulator and prevented grounding of the test tube. In addition, nonconductive flexible hose was installed at the entrance and exit of the test tube assembly to allow thermal expansion and to electrically isolate the tube from the other components of test apparatus.

Experimental Results and Discussion

Prior to actual testing, the test tube inner wall temperatures were calculated from outer wall temperatures using a computerized, multielement heat transfer analysis (TCAL) in which a finite difference representation of the heat conduction equation is solved by a relaxation technique. The calculated differences between the inner and outer wall temperatures of the duplex tube ranged from approximately 1 to 15 K over the entire range of test conditions. These temperature differences were, for the most part, within the expected experimental accuracy of the temperature measurement and, therefore, the measured outer (Inconel) wall temperature was considered representative of the inner (copper) wall temperature.

The experimental program began with a sequence of calibration tests to corroborate the results of the heat transfer analysis and to verify the absence of a significant thermal resistance at the Inconel-copper interface. Tests were performed with a specially instrumented test tube which allowed direct measurement of the temperature at the Inconel/copper interface as well as at the Inconel outer wall. The results of these tests indicated that there was excellent agreement between the two wall temperature distributions. The largest temperature difference measured was only 10 K, thereby verifying (in a general sense) the temperature predictions as well as confirming the absence of a significant resistance at the interface between the two metals.

Kerosene Fuel Tests. Testing began with RP-1 fuel at a fluid velocity of 6.1 m/s and a wall temperature of 422 K. No significant temperature rise was observed along the tube

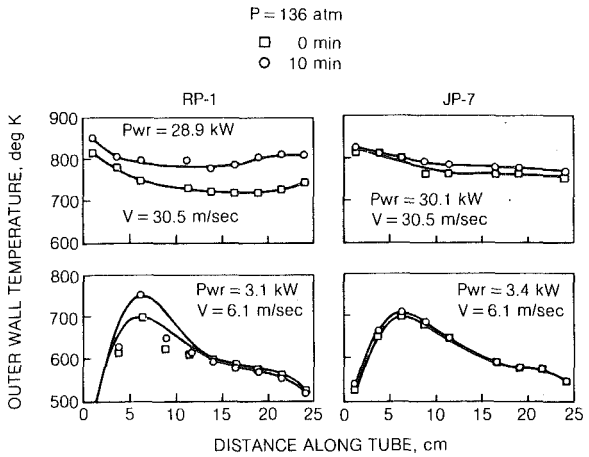

Fig. 3 Comparison of temperature distributions for RP-1 and JP-7

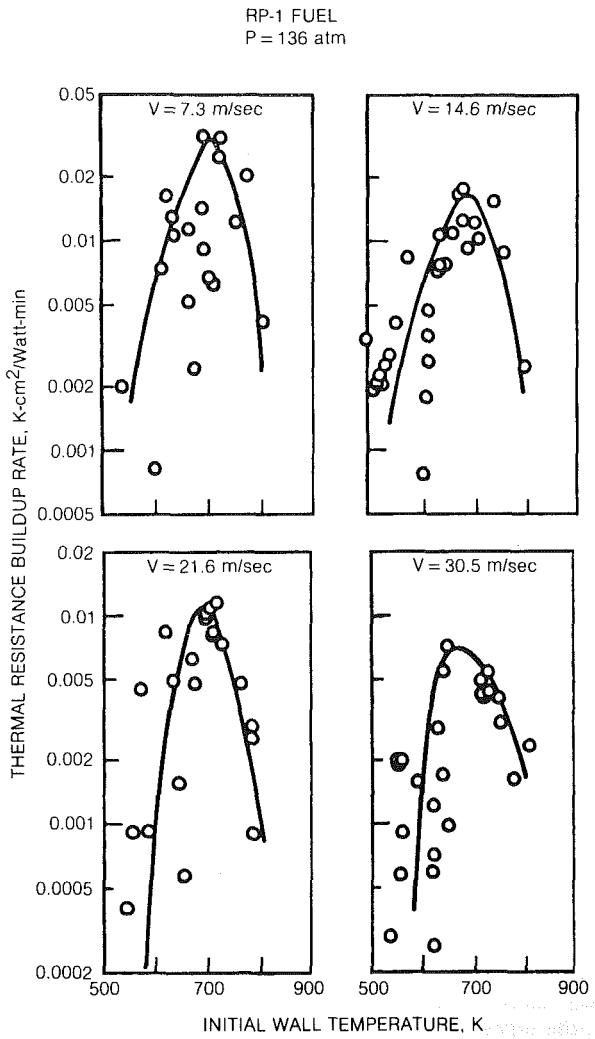

Fig. 4 Variation of thermal resistance buildup rate with wall temperature

during the 10 min test duration, suggesting the absence of significant deposit formation. Subsequent sectioning of the tube and microscopic inspection of the inner copper surface confirmed that deposits had not been formed; therefore, no additional testing was done at a wall temperature of 422 K. The remaining tests with RP-1 fuel were conducted at wall temperatures between 589 and 811 K, at a pressure of 136 atm, and for fluid velocities ranging from 6.1 to 30.5 m/s. The input heat flux to the tube was varied between 173 and 1460 W/cm^2, in order to achieve the desired wall temperature. In addition, selected tests with deoxygenated JP-7 fuel were also conducted at test conditions which indicated significant deposit formation with RP-1 fuel.

Typical temperature distributions obtained with the kerosene type fuels at the maximum and minimum test velocities (i.e., 6.1 and 30.5 m/s) are shown in Fig. 3. These results indicated that substantial changes in the heat transfer processes were incurred as the flow, power, and wall temperature were varied. As can be seen in the figure, the highest wall temperatures occur near the tube entrance, and the wall temperature decreases along the length of the tube. This seemingly anomalous trend stems from the variation of bulk fuel properties with temperature, and results in a local heat transfer coefficient which is lowest at the tube entrance, where the fuel is cold, and increases as the fuel is heated. At low velocity conditions, and particularly at high power, the wall temperature increased with length near the tube entrance, reached a maximum value, and thereafter decreased continuously to the end of the tube. The wall temperature distribution noted at low velocity appears to indicate laminar-like flow at the tube entrance followed by a transition to turbulent flow. This entrance effect could be expected to be minimized at the higher Reynolds numbers associated with the higher flow rates. It can also be seen that over the 10 min duration, significant wall temperature rises occurred during the RP-1 fuel tests while smaller increases in wall temperatures were observed with the JP-7 fuel. This trend was generally observed over the entire range of test conditions. The results indicated that the maximum temperature rises that were measured during the 10 min tests occurred at tube locations where the wall temperatures were initially between 700 K and 750 K. There appeared to be no significant effect of fluid velocity on the magnitude of the peak temperature rise.

A measure of the rate of carbon deposition which occurred during a test is the deposit thermal resistance buildup rate (R_c), which is defined as:

$$R_c = \frac{\Delta T_w}{(Q/A)\,(t)}$$

where ΔT_w is the wall temperature rise (deg K) observed during the test, Q/A is the heat flux (W/cm^2) maintained during the test, and t is the test duration (min). The thermal resistance buildup rates calculated for tube sections which exhibited temperature rises during testing with RP-1 fuel are shown in Fig. 4. It can be seen that the thermal resistance buildup rate reached a maximum at tube locations where the initial wall temperature was approximately 700 K. In addition, as the fluid velocity was increased, the magnitude of the peak thermal resistance buildup rate appeared to decrease. The magnitude of the rates obtained for a fluid velocity of 30.5 m/s are in good agreement with experimental data obtained by other investigators [8] for RP-1 at velocities in the range 46 to 76 m/s.

During testing, deposit formation was indicated by a significant change in the tube axial wall-temperature distribution when the system pressure, fluid velocity, and tube heating rate were held constant. After each test in which there was a positive indication of coking, the test tube was sectioned and prepared for microscopic examination and deposit analysis. Inspection of the inside surfaces of longitudinal sections of the tubes tested with RP-1 fuel revealed that the deposit coverage was generally very nonuniform and ranged from specks, to connected islands of deposits, to essentially full coverage. No particular pattern could be established with test conditions and the nonuniform deposit coverage made a determination of the point of incipient deposit formation impossible. Also, the deposits observed were multicolored

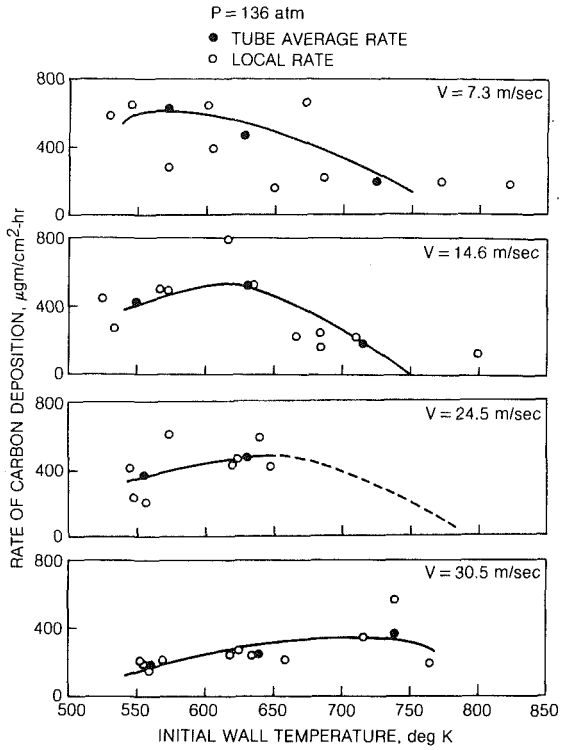

Fig. 5 Rate of carbon deposition for RP-1 fuel

and took on various shades of red, black, and sometimes gray. All three colors could sometimes be seen on samples taken from a single tube; however, it was difficult to associate color with a particular run condition or wall temperature. The deposits appeared to vary in degree of roughness but were generally hard and did not break loose from the tube surface very easily. From the general appearance of the inner surfaces of the tubes, it was concluded that the formation of deposits on copper is a very complex process, leading to various intermediate compounds which can take on various colors and textures and which will likely affect the local heat transfer processes.

The primary measure of the deposit formation rate with the various test operating conditions was made by burning off the tube deposits and measuring the quantity of CO_2 evolved. A special laboratory bench-type apparatus was employed for this task, wherein a metered flow of air was passed at a constant rate through heated sections of the test tube. The product gases resulting from the burnoff were subsequently passed through a nondispersive infrared analyzer which provided a continuous measurement and record of the concentration of CO_2 in the effluent gas. Integration of the data over the total burnoff time gave the total volume of CO_2 evolved, from which a carbon weight and deposition rate were calculated.

The rates of carbon deposition determined for RP-1 are presented in Fig. 5 as functions of the average initial wall temperatures. The open symbols represent data obtained from 3.8-cm-long tube sections while the closed symbols represent a composite of the smaller sections, or a tube average value. Although there is considerable scatter in the data, believed to result from the combined effects of experimental error and the nonuniformity of the deposits on the tubes, some general trends can be observed. The deposit rate data appear to substantiate the conclusions drawn previously from the deposit thermal resistance buildup rates (see Fig. 4); i.e., the rate of carbon deposition increases with increasing temperature, reaches a maximum at an initial wall temperature of approximately 600 to 700 K, and then falls off as temperature is increased further. Also, the carbon deposition rates decrease with increasing fluid velocity.

Deposit burnoff tests were also conducted on the tube sections obtained from the deoxygenated JP-7 tests. Since only a limited number of tests were performed with JP-7, not enough test data was acquired to graphically indicate the trends with test conditions. However, the data do indicate that the deposit formation rates are generally of the same magnitude as was determined for RP-1. Since JP-7 typically has an order of magnitude lower sulfur content than RP-1 and because it must meet a stringent thermal stability specification, it was assumed that JP-7 would be a good simulator of refined quality RP-1 and demonstrate improved thermal stability. Also, since the dissolved oxygen concentration in the JP-7 was reduced to less than 5 ppm by sparging with nitrogen, and because the temperature rises obtained with JP-7 were generally lower than those obtained with RP-1, it was expected that less deposit would be found with JP-7. However, when the tubes used in the JP-7 tests were sectioned, microscopic examination revealed that there was significant deposit formation and that the deposits appeared darker and more uniform than the RP-1 deposits. A diagnostic test was conducted with unsparged JP-7 fuel to determine if the presence of antioxidant and lubricity improving additives, in the absence of dissolved oxygen in the sparged JP-7 fuel, might have promoted higher rates of deposit formation. When the results of this test indicated similar deposit formation, additional testing with JP-7 was suspended because the JP-7 did not appear to offer any benefit in terms of increased thermal stability. A measurement of the actual difference in the thermal stability between the two fuels (i.e., the breakpoint temperatures) was made in a series of tests using a Jet Fuel Thermal Oxidation Tester (JFTOT). The results of this evaluation revealed that both the JP-7 and RP-1 met the thermal stability requirement for JP-7, but the RP-1 was even more stable than the nominally higher quality JP-7. Also, a comparison of certified analyses of the compositions of the two fuels indicated that the actual difference in sulfur contents was only a factor of 2.3, and not the order of magnitude expected. Therefore, it can be concluded that there is little difference in carbon deposition rates and probably no particular advantage in using JP-7.

A limited number of tests were conducted with RP-1 fuel at pressures up to 340 atm. The results indicated that there was no significant change in the tube wall temperature distributions as a consequence of increasing pressure, suggesting that the rate of deposit formation is relatively independent of pressure over the pressure range of 136 to 340 atm. Microscopic examination of the deposits obtained from these tests also revealed that there was no substantial difference in the deposit appearance. The rates of carbon deposition determined from deposit burnoff tests showed the usual data scatter; however, the overall deposition rates fell within a relatively narrow band and indicated that the deposit formation rate increased slightly with pressure.

Propane Tests. All deposit formation tests with commercial-grade and chemically pure propane were conducted at a pressure of 136 atm. Test data was obtained at fluid velocities ranging from 6.1 to 36.6 m/s and for tube wall temperatures ranging from 422 to 811 K. Most of the tests at the higher temperatures (700 to 811 K) had to be terminated prematurely; i.e., before the full 10 min test time was achieved, because the wall temperature fluctuated excessively and eventually exceeded the maximum allowable level (866 K). The erratic wall temperature behavior was repeatable and was observed in tests where the initial wall temperature was set at 700 or 811 K. Minor temperature fluctuations were also observed during many of the tests which were conducted at

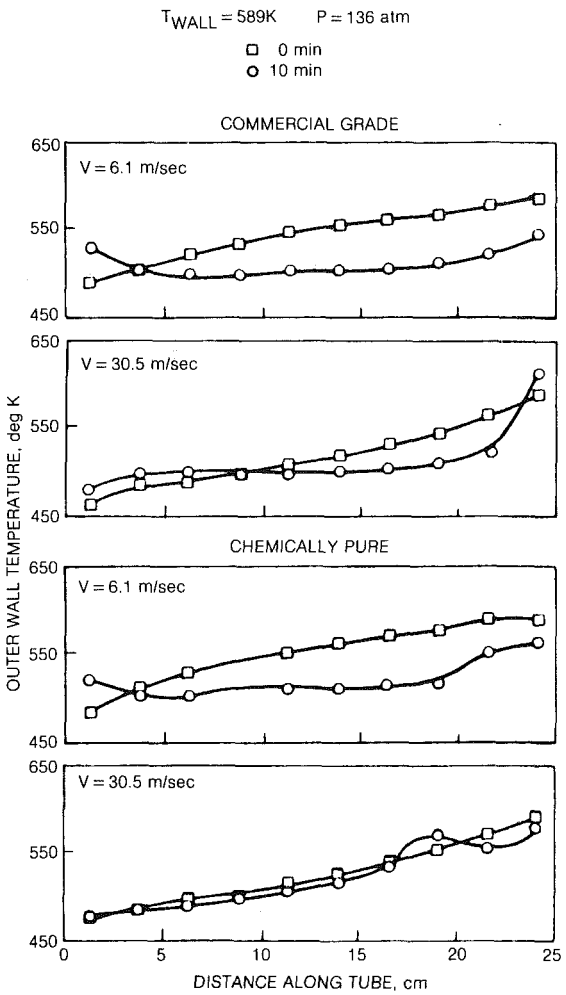

Fig. 6 Comparison of temperature distributions for propane

wall temperatures of 589 K; however, they were not severe enough to necessitate premature shutdown. It should be noted that at the higher tube wall temperatures, the bulk temperature of the propane exceeded the critical point (366 K), suggesting that the temperature fluctuations may be due to a change in character of the propane when the critical temperature is exceeded. Moreover, when severe temperature instabilities were observed, the measured bulk fluid temperature was generally between 400 and 500 K, a temperature range in which the specific heat of propane at 136 atm pressure changes very rapidly and passes through a maximum [9]. Therefore, it would appear likely that other transport properties of propane (such as density, viscosity, and thermal conductivity) may also be changing very rapidly and that these properties changes could lead to the unusual heat transfer characteristics that were observed.

The wall temperature distributions obtained for both grades of propane are not appreciably different and are compared in Fig. 6. It can be seen that unlike the results obtained for the distillate fuels RP-1 and JP-7, the wall temperatures observed in the propane tests at the start of the test run exhibited a more or less monotonic increase in temperature from the inlet end to the exit end of the heated tube. This behavior is to be expected from a fluid whose local heat transfer coefficient is nearly constant over the tube length. In contrast to the test runs conducted with the kerosene fuels, a continuous drop in local wall temperature with increasing test time is shown in the figure. This behavior was noted with the propane fuels at most of the test conditions, suggesting that deposit formation may have significantly increased the turbulence level in the flow, and thereby, increased the heat transfer rates.

Microscopic examination of the deposits obtained with both types of propane indicated heavier, blacker and more uniform deposits than those observed with the kerosene-type fuels, especially at the higher tube temperatures. The carbon deposition rates determined for propane in the burnoff tests confirmed this observation, and the deposit levels were generally higher than those obtained for either of the kerosene fuels at any given tube wall temperature. An interesting phenomenon that was observed in many of the higher wall temperature propane tests was the appearance of dendritic or tree-like formations in which the deposits appeared to grow out from the copper surface as filaments. Scanning electron microprobe analysis (discussed below) revealed that the filament composition was primarily copper, with some carbon concentrated at the base of the tree-like structure. The presence of copper in the deposit may have also contributed to the enhancement of the heat transfer with increasing test time.

Since most of the high wall temperature (> 589 K) tests with propane were terminated prematurely, the deposit burnoff data for propane could not be used in a graphical presentation of the dependence of the rates of carbon deposition on wall temperature. The rate data for wall temperatures of 422 and 589 K indicated that the deposit rates for both grades of propane fell in the range 400 to 600 $\mu g/cm^2$-hr, and generally overlapped. Although there was some scatter in the data, the carbon deposition rate for propane fuel appeared to decrease slightly with increasing fluid velocity for each tube wall temperature condition.

Nickel-Plated Tube Tests. The results of the experiments for kerosene and propane fuels appear to corroborate and extend the findings of earlier experimental studies which indicated that deposit rates on copper can be very high. Furthermore, it would appear that a copper surface probably promotes deposit formation to as great an extent as any deposit forming precursor contained in the fuels. Therefore, in order to obtain an indication of the importance of the tube wall material on deposit formation, tests were conducted using tubes in which the inside (copper) surface had been plated with nickel by means of an electroless process. All of the tests were run using RP-1 fuel at conditions which resulted in high rates of carbon deposition on copper. The tube wall temperature distributions obtained with the nickel-plated tubes were very similar to those obtained with the copper tubes; however, the temperature rises obtained with the nickel-plated tubes were significantly lower than those obtained with copper, suggesting a substantial decrease in deposit formation. A scanning electron microprobe analysis of the inner surfaces of representative tube sections revealed little or no deposits (1600X magnification), and an elemental analysis indicated the presence of nickel and phosphorous (the major constituents in the electroless plating solution) but no copper, carbon, oxygen, or sulfur. Also, the results of deposit burnoff tests indicated that very little carbonaceous material was deposited on the nickel surface during testing. The average rates of carbon deposition were approximately 50 $\mu g/cm^2$-hr, an order-of-magnitude lower than corresponding rates on copper. Therefore, it can be concluded that a substantial decrease in deposit formation occurred when the copper tubes were replaced with nickel-plated tubes.

Deposit Morphology

In order to characterize the complex structure of the deposits observed, a scanning-electron microscope (SEM) was used to study the deposits. The SEM is particularly useful for examining solid specimens whose surface structures are

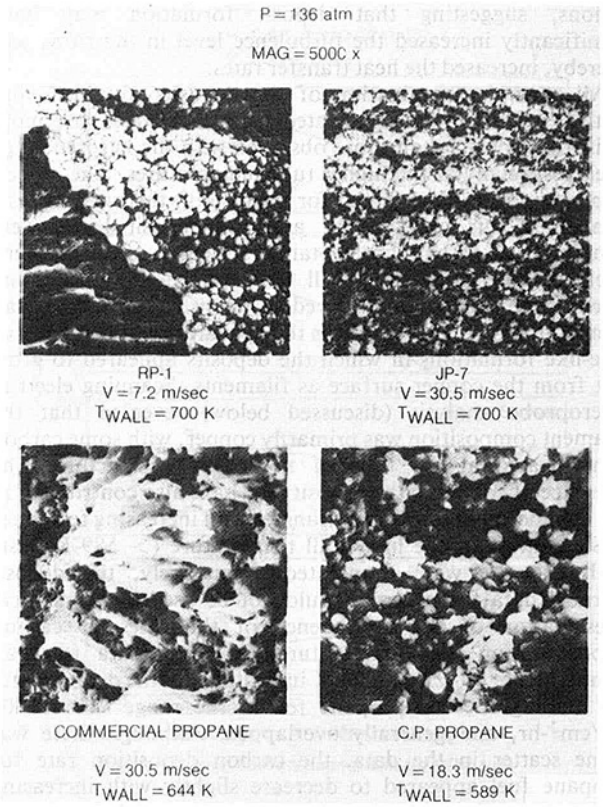

Fig. 7 Microstructure of fuel deposits on copper

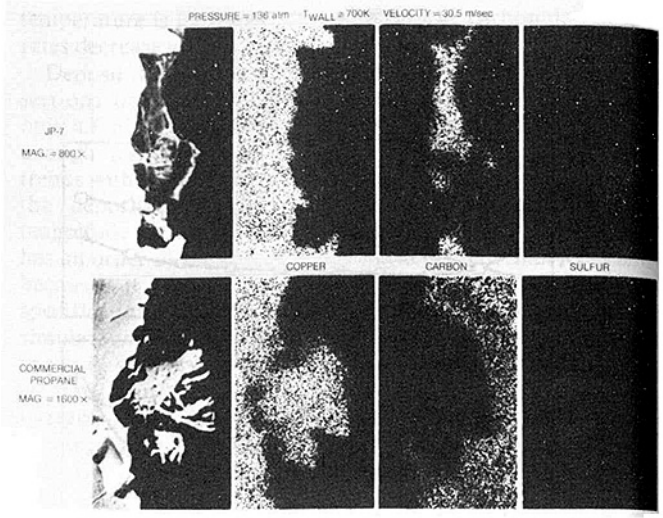

Fig. 8 Scanning electron microprobe analysis of deposits

rough, because it has a considerably greater depth of focus compared to a conventional reflected-light microscope. When viewed with a SEM, amorphous materials (such as asphalt) show no particular form, crystalline materials (such as graphite) have sharp geometric outlines, and carbonized materials (such as coke) tend to group together in tightly packed aggregates of spherical particles.

SEM analyses were performed on four deposit samples, one for each fuel, which were obtained from tests conducted with copper tubes. The photomicrographs, shown in Fig. 7, were taken at a magnification equal to 5000X and reveal the deposit microstructures. The RP-1 deposit (shown in the upper left) comprises a large number of spherically shaped agglomerated particles which are approximately 0.5 μm diameter. It appears that the top film of deposit fractured, exposing a highly fused substrate which has been overlayed with the tightly packed spherical agglomerates. Photomicrographs taken near the exit of the tube revealed a type of microstructure that had a more vitreous and amorphous appearance. The SEM photographs of JP-7 fuel deposits (shown in the upper right) again indicate a microstructure of tightly packed spherical agglomerates typical of coke deposits. Compared to the RP-1 deposits, the JP-7 deposits appear to be more uniform and there is not much evidence of deposit fracturing. Photographs taken at other tube locations indicated that there were areas where the deposits appeared to be more flocculent and porous, and areas where the particles appeared to have fused together, forming a knobby surface. The microstructure of commercial-grade propane deposits (shown in the lower left) reveals typical dendritic formations which were dispersed randomly along the entire length of the tube. The photograph does not show the aggregates of spherical particles that were observed with the kerosene type fuels and that are characteristic of coke formation, but instead shows distinctly smooth, finger-like structures. The microstructure of deposits obtained with chemically pure propane is shown in the lower right side of the figure. It can be seen that the dendritic formation is not as obvious at this lower wall temperature condition (589 K) and that clusters of packed particles are spread across the length of the tube. These clusters appear to overlay a fused layer of deposits and consist of packed spherical particles that are similar to those observed in the kerosene fuel deposits.

The photomicrographs shown in Fig. 7 indicate that the deposits accumulated on the tube surfaces are generally not smooth, continuous films of uniform structure and composition. Instead, they indicate that discrete particles, spherical or dendritic in shape, accumulate over a fused substrate to produce a highly variable three-dimensional structure. The deposit surface appears to be sufficiently rough to significantly increase turbulence and thereby affect heat transfer. However, there also appears to be areas on the tube where the surface appears smoother after deposit formation. From the SEM photomicrographs, it is obvious that surface roughness and deposit homogeneity can be expected to change along the length of a test tube and may significantly affect the local heat transfer characteristics.

A limited qualitative elemental analysis of the deposits was made utilizing a Scanning Electron Microprobe (SEMP). The SEMP incorporates an X-ray energy-dispersive spectrometer, to identify elements which are present in the deposit, and a selective wavelength spectrometer, for X-ray mapping of selected elements. The presence of the selected element is indicated by clusters of white dots on a dark background that matches the standard photomicrograph of the sample and allows easy identification of the areas of local concentration of the particular element. The results of the selected wavelength analysis made with the SEMP are shown in Fig. 8. In the figure, the upper series of photographs correspond to a tube deposit obtained with JP-7 fuel. The first photograph shows a SEM photomicrograph of the deposit sample. This region was selectively scanned for the presence of copper, carbon, oxygen, and sulfur, and, if present, these elements would be indicated by an agglomeration of white dots against the dark background. It can be seen that the copper surface of the tube is clearly outlined but that no significant copper is contained in the area occupied by the deposit. The deposit, however, contains a heavy concentration of carbon and a smaller concentration of sulfur. The SEMP analysis of RP-1 fuel deposits gave essentially the same result as the JP-7 analysis, except that a small concentration of oxygen was also present.

The bottom set of photographs represent a SEMP analysis of the microstructure of deposits obtained with propane at a

high tube wall temperature (~700 K) condition and show a typical dendritic formation. It can be seen that the dendrite contains a high concentration of copper, suggesting that tube material was forced up and away from the surface. Most of the carbon image results from the composition of the potting material, but some carbon is also evident at the base of the treelike deposit structure. A very small concentration of sulfur is also indicated in the deposit but no oxygen was observed. Analysis of a tube deposit obtained with chemically pure propane at a lower wall temperature (~589 K) revealed no obvious dendritic formations; however, the deposit material contained significant amounts of copper and substantially more carbon than was found in the dendritic structure.

Concluding Remarks

The thermal decomposition (coking) limits and rates of carbon deposition in heated copper tubes were investigated for two standard hydrocarbon fuels, RP-1 and commercial-grade propane. In addition, tests were conducted using deoxygenated JP-7 and chemically pure propane as being representative of more refined cuts of the standard fuels. The apparatus developed for these tests permitted independent variation and control of tube wall temperature, fluid pressure, and fluid velocity in order that the effects of each parameter could be investigated independently.

The results of the experiments with RP-1 fuel were as expected, in that there was previous evidence that copper promotes deposit formation in kerosene-type fuels. However, the relatively high deposition rates of between 400 and 600 $\mu g/cm^2$-hr at wall temperatures of 500 and 800 K for only a 10 min test duration were not anticipated. Peak deposit formation occurred at tube wall temperatures near 700 K, which is consistent with results obtained with kerosene-type aviation fuels. The deposit coverage was generally nonuniform and ranged from specks, to connected islands of deposits, to essentially full coverage. No particular pattern could be established with test conditions, and the nonuniformity of deposit coverage made a determination of the point of incipient deposit formation impossible. Plating the inside wall of the tubes with nickel was found to significantly reduce carbon deposition rates for RP-1 fuel.

It was believed that JP-7, which has a lower sulfur content (typically an order of magnitude lower) and meets a stringent thermal stability specification, would be a good simulator of refined quality RP-1 and demonstrate improved thermal stability. However, no benefit in terms of increased stability was realized with JP-7.

Deposits obtained with propane fuels were heavier, blacker and more uniform than those observed with the kerosene-type fuels and there appeared to be little difference between commercial-grade and chemically pure propane with regard to type and quantity of deposit. The carbon deposition rates for the propane fuels were generally higher than those obtained for either of the kerosene fuels at any given wall temperature. An interesting phenomenon observed in the deposits formed from propane was the appearance of dendritic or treelike formations which seemed to grow out from the copper surface as filaments. The filament composition was primarily copper, with some carbon concentrated at the base of the treelike structure.

Post-test photomicrographic examination of the tube surfaces indicated that the deposits were generally not formed as smooth, continuous films of uniform structure and composition. Instead, discrete particles, spherical or dendritic in shape, accumulated over a fused substrate to produce a highly variable three-dimensional microstructure. The deposit surface appeared to be sufficiently rough to significantly increase turbulence and thereby affect heat transfer. However, there were instances where the surface became smoother during deposit formation. It was obvious from the photomicrographic analysis of the deposits that surface roughness and deposit homogeneity can be expected to change along the length of a test tube and may significantly affect the local heat transfer characteristics. Finally, deposition rate appeared to change with time and, therefore, test duration is an important factor to consider in deposit rate correlations.

Acknowledgment

This work was performed with the support of the NASA-Lewis Research Center, under Contract NAS3-22277, P. A. Masters, Project Manager.

References

1 Szetela, E. J., "External Fuel Vaporization Study, Phase I Report," NASA Contractor Report CR-159850, June 1980.

2 Hazlett, R. N., ed., "Coordinating Research Council (CRC) Literature Survey: Thermal Oxidation Stability of Jet Fuels," CRC Report 50-9, Apr. 1979.

3 Lander, H. R., and Martel, C. R., "Jet Fuel Thermal Stability Improvements through Fuel Processing," Air Force Aero Propulsion Laboratory Report AFAPL TR-74-35, Aug. 1974.

4 Faith, L. E., Ackerman, G. H., and Henderson, H. T., "Heat Sink Capability of Jet A Fuel: Heat Transfer and Coking Studies," NASA Contractor Report CR-72951, July 1971.

5 Taylor, W. F., "The Study of Hydrocarbon Fuel Vapor Deposits," Air Force Aero Propulsion Laboratory Report AFAPL-TR-69-77, Sept. 1969.

6 Smith, J. D., "Fuel for the Supersonic Transport," *Industrial and Engineering Chemistry—Process Design and Development*, Vol. 8, No. 3, July 1969, p. 229-308.

7 Roback, R., Szetela, E. J., and Spadaccini, L. J., "Deposit Formation in Hydrocarbon Rocket Fuels," NASA Contractor Report CR-165405, Aug. 1981.

8 Wagner, W. R., and Shoji, J. M., "Advanced Regenerative Cooling Techniques for Future Space Transportation Systems," AIAA Paper No. 75-1247, AIAA/SAE 11th Propulsion Conference, Anaheim, Calif., Sept. 29-Oct. 1, 1975.

9 Goodwin, R. D., "Provisional Thermodynamic Functions of Propane from 85 to 700K at Pressures to 700 Bar," National Bureau of Standards Report NBSIR 77-860, July 1972.

Effects of Unsteady Free-Stream Velocity and Free-Stream Turbulence at a Stagnation Point

R. S. R. Gorla
Professor,
Department of Mechanical Engineering,
Cleveland State University,
Cleveland, Ohio 44115
Mem. ASME

An analysis is presented to investigate the combined effects of transient free-stream velocity and free-stream turbulence at a stagnation point on a cylinder situated in a crossflow. A model has been successfully formulated for the eddy diffusivity induced by the free-stream turbulence. The governing momentum equation has been integrated by the steepest descent method. Numerical solutions are provided for the unsteady wall shear stress function for specific free-stream transients. The results are correlated by a new turbulence parameter. It has been found that the wall friction increases with increasing free-stream turbulence intensity. In the case of flows involving unsteady free-stream velocity, the friction factor increases with increasing values of the reduced frequency of oscillations.

Introduction

There exists a need for a systematic and detailed theoretical and experimental study of the effects of the upstream flow disturbances on the flow and heat-transfer characteristics of a gas turbine blade. The flow disturbances at the exit of the stationary vanes are pulsatile in character and so the velocity and temperature distribution as well as the local skin friction and heat-transfer coefficients become transient.

It is known that free-stream turbulence augments the friction factor significantly in flows with large streamwise pressure gradients. Sutera et al. [1] and Sutera [2] simulated the free-stream turbulence by a distributed vorticity in the free stream and showed that the stretching of the vorticity component parallel to the surface caused a substantial increase in the heat-transfer rate, while the increase in the wall shear was relatively small. This theory provides a qualitative explanation of the phenomenon; but, because the free-stream vorticity was not related to the turbulence intensity, it does not enable an independent prediction of the wall shear stress augmentation. Smith and Kuethe [3] employed a more direct approach and postulated an expression for the eddy diffusivity induced by the free-stream turbulence. Their model of the eddy diffusivity involves an unknown constant, which was determined from their experimental data. Galloway [4] attempted to provide a rationale for Smith and Kueth's eddy diffusivity model. Recently, Traci and Wilcox [5] presented a two-equation model of turbulence along with the other conservation equations. In order to complete the analysis, use was made of empirical information from the experiments of Smith and Kuethe [3]. By means of a similarity type solution, they evaluated the friction factor at the stagnation point of a cylinder in a uniform crossflow.

Early theoretical investigators [6, 7] predicted that free stream oscillations would have little or no effect on the mean boundary layer heat-transfer or shear stress. These studies resulted in a good qualitative understanding of the flow mechanisms involved, but they do not provide a capability for quantitative predictions.

Junkhan and Serovy [8] reported experimental data concerning the effects of free-stream turbulence intensity on the flow and heat transfer from an isothermal flat plate with a favorable pressure gradient. Their data indicates that there is no effect of free-stream turbulence intensity on heat transfer through a laminar boundary layer with zero pressure gradient.

There exist several practical applications in which wakes evolve in the presence of free-stream turbulence. One such situation exists in multistage turbomachinery, in which the wake of a blade following the first row of blades always evolves under the influence of the turbulence present in the wake of the previous row of blades. An extensive search of literature on general two and three-dimensional wakes is reported by Raj [9]. Pal and Raj [10] have investigated the effect of free-stream turbulence on the characteristics of a turbulent wake developed from the trailing edge of a thin and smooth flat plate both analytically and experimentally. They found that the free-stream turbulence increases the wake recovery and growth rates.

No analyses have been reported in the literature to study the combined effects of free-stream turbulence and transient free-stream velocity on the unsteady flow behavior on a body. The proposed study has been undertaken in order to investigate the combined effects of free-stream turbulence and time dependent free-stream velocity on the unsteady flow characteristics of a stagnation point on a circular cylinder. The basic study is expected to enable understanding the complex flow phenomenon in the real turbomachinery environment to a first degree of approximation. No such analyses have been reported in the literature so far.

Analysis

Assuming an incompressible flow with constant properties

Contributed by the Gas Turbine Division of THE AMERICAN SOCIETY OF MECHANICAL ENGINEERS and presented at the 27th International Gas Turbine Conference and Exhibit, London, England, April 18-22, 1982. Manuscript received at ASME Headquarters December 4, 1981. Paper No. 82-GT-69.

and negligible dissipation, the governing boundary layer equations may be written as:
mass,

$$\frac{\partial u}{\partial x} + \frac{\partial v}{\partial y} = 0 \tag{1}$$

momentum,

$$\frac{\partial u}{\partial t} + u\frac{\partial u}{\partial x} + v\frac{\partial u}{\partial y} = -\frac{1}{\rho}\frac{\partial P}{\partial x} + \frac{1\partial \sigma}{\rho \partial y} \tag{2}$$

In the above equations, x and y represent the distances along the streamwise direction and normal direction, u and v the velocity components in x and y-directions, t the time, and ρ the density of the fluid. The shear stress term in equation (2) may be written as

$$\sigma = \rho(\nu + \epsilon_m)\cdot\frac{\partial u}{\partial y} \tag{3}$$

In equation (2) P is for pressure.

In the present problem, the fluid transients are assumed to arise from a free stream velocity U_e which is initially steady but at some instant of time begins to undergo continuous change in magnitude with time. That is, the free-stream velocity is assumed to be of the form

$$U_e(x,t) = Kx\cdot G(t)$$

where $G(t)$ represents unsteadiness of the free stream. It must be noted that K is a proportionality constant and is equal to $2u\infty/R$ for a cylinder, where $u\infty$ is the reference velocity and R the radius. It is assumed that $G(t) = 1$ for $t<0$. The initial and boundary conditions for equations (1) and (2) are

$$\begin{aligned} u(x,0,t) &= v(x,0,t) = 0 \\ u(x,\infty,t) &= u\infty(x,t) \end{aligned} \tag{4}$$

Proceeding with the analysis we define $u = \partial\psi/\partial y$ and $v = -\partial\psi/\partial x$. It may be verified that the continuity equation is automatically satisfied.

We introduce the following transformations:

$$\begin{aligned} \tau &= K\cdot t \\ \eta &= y\sqrt{KG/\nu} \\ \psi &= x\sqrt{KG}\nu\cdot f(\tau,\eta) \end{aligned} \tag{5}$$

Substituting the expressions in (5) into the momentum equation we may write the transformed momentum equation as follows:

$$f''' + \left(\frac{1}{1+s}\right)\cdot\left(s' + f - \frac{\eta}{2}\frac{\dot{G}}{G^2}\right)f'' = \frac{1}{1+s}\cdot\left\{\frac{\dot{G}}{G^2}(f'-1) + \frac{\dot{f}'}{G} + (f')^2 - 1\right\} \tag{6}$$

where

$$S = \frac{\epsilon_m}{\nu}$$

The transformed boundary conditions are

$$\begin{aligned} f'(\tau,0) &= f(\tau,0) = 0 \\ f'(\tau,\infty) &= 1 \end{aligned} \tag{7}$$

In the above equations, primes indicate differentiation with respect to η and the dot with respect to τ.

Eddy Diffusivity Formulation

It must be noted that by substituting $\partial/\partial\tau = 0$ amd $G = 1$ into equation (6) and solving it, one obtains the steady-state velocity field. The momentum equation for the steady-state problem is given by

$$[(1+s)f'']' + ff'' + [1-(f')^2] = 0 \tag{8}$$

It must be noted that $f = f(\eta)$ only in equation (8). The appropriate boundary conditions are given by

$$f(0) = f'(0) = 0 \text{ and } f'(\infty) = 1 \tag{9}$$

The steady-state friction factor becomes

$$c_f = \frac{\sigma w}{(\frac{1}{2}\rho u\infty^2)} = 13.838\,\frac{x}{D}\cdot \mathrm{Re}^{-\frac{1}{2}} f''(0) \tag{10}$$

where

$$\mathrm{Re} = \text{Reynolds number } \left(\frac{u\infty D}{\nu}\right)$$

Equation (8) is solved on a computer using the fourth-order, Runge-Kutta numerical procedure. The double precision arithmetic was used in all the computations. The selection of the integration step size depends upon the desired level of accuracy. After some computational trials, a step size of $\eta = 0.001$ was chosen.

In the present paper, we restrict ourselves to the case of homogeneous and isotropic free-stream turbulence. This will be realized in the turbulence produced by grids at locations sufficiently downstream from the turbulence promoters. We have assumed the following expression for the eddy diffusivity in the present work.

$$\frac{\epsilon_m}{\nu} = s_1(\eta + \eta^2) \tag{11}$$

where

s_1 = constant proportional to the turbulence intensity

and

η = dimensionless distance normal to the surface.

A review of the literature suggests that there are several uncertainties in the published experimental data including tunnel blockage, variation of physical properties, effect of turbulence scale, and inaccuracies in the measurement of turbulent intensity. Restricting the discussion to the

Nomenclature

$a_2(\tau)$ = transient wall shear function
c_f = skin friction coefficient $\sigma w/(\frac{1}{2}\rho u\infty^2)$
D = diameter of cylinder
$G(t)$ = time variation of free-stream velocity
K = proportionality constant
R = radius of cylinder
Re = Reynolds number $(u\infty D/\nu)$
t = time
Tu = turbulence intensity $(u'/u\infty)$
u,v = velocity components
u' = rms velocity fluctuation
U_e = free-stream velocity
x,y = coordinates
ρ = density
ϵm = momentum eddy diffusivity
τ = dimensionless time
σ = shear stress
Ω = dimensionless frequency of free-stream oscillations

Subscripts

w = wall conditions
∞ = ambient conditions

stagnation point, it has been found convenient to use the single correlation parameter ($Tu \cdot Re^{1/2}$). This parameter has also been suggested by Smith and Kuethe [3] on the basis of a semi-empirical theory.

Figure 1 shows the results for the steady-state friction coefficient as a function of the correlation parameter ($Tu \cdot Re^{1/2}$). The constant s_1 in the present eddy diffusivity model has been adjusted so as to have a best fit of the present numerical predictions with experimental data available in the literature. It has been found that the following expression for s_1 makes the predictions of the present analysis to be in good agreement with the published data over the entire range of ($Tu \cdot Re^{1/2}$) within 15 percent error:

$$s_1 = 0.018(Tu \cdot Re^{1/2}) \tag{12}$$

The results from the present analysis are seen to agree with the experimental data of Smith and Kuethe [3] within 15 percent. In addition to the data of Smith and Kuethe, the predictive curves of Smith and Kuethe [3], Galloway [4] and Traci and Wilcox [5] are also shown in Fig. 1.

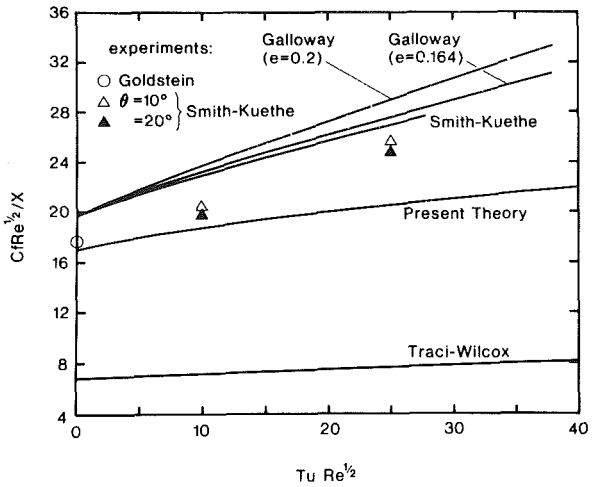

Fig. 1 Effect of turbulence intensity on friction factor

Solution

The governing momentum equation (6) for the unsteady problem will now be integrated by the steepest decent method. Toward this end, we let

$$f(\tau,\eta) = \sum_{n=2}^{\infty} a_n(\tau) \cdot \frac{\eta^n}{n!} \tag{13}$$

Substituting the expression for $f(\tau,\eta)$ into equation (6) and collecting coefficients of like powers of η, we find that

$$\begin{aligned}
a_3 &= -\left(s_1 a_2 + 1 + \frac{\dot{G}}{G^2}\right) \\
a_4 &= \frac{\dot{a}_2}{G} + \frac{3}{2}\frac{\dot{G}}{G^2} \cdot a_2 + 2{s_1}^2 a_2 + 2s_1 \cdot \left(1 + \frac{\dot{G}}{G^2}\right) \\
a_5 &= -3s_1 a_4 + a_2 + \frac{2\dot{G}a_3}{G^2} + \frac{\dot{a}_3}{G} \\
a_6 &= -4s_1 a_5 + \frac{5}{2}\frac{\dot{G}}{G^2} a_4 + \frac{\dot{a}_4}{G} + 2a_2 a_3
\end{aligned} \tag{14}$$

etc.

The unknown coefficient $a_2(\tau)$ is determined through the use of boundary and initial conditions. When once $a_2(\tau)$ is determined, the remaining features of the flow field such as the transient velocity profiles may be readily evaluated. The time-dependent wall shear stress and friction factor may be written as

$$\begin{aligned}
\sigma_w &= \mu\left(\frac{\partial u}{\partial y}\right) x,0,t \\
&= \mu \cdot KxG\sqrt{\frac{KG}{\nu}} \cdot a_2(\tau) \\
c_f &= \frac{\sigma w}{\left(\frac{\rho u \infty^2}{2}\right)} = \frac{2}{x}\sqrt{\frac{\nu}{KG}} \cdot a_2(\tau)
\end{aligned} \tag{15}$$

We now define an integrating factor: $e^{I(\tau,\eta)}$

where

$$I = \int_0^{\eta} \left(\frac{1}{1+s}\right)\left(s' + f - \frac{\eta}{2}\frac{\dot{G}}{G^2}\right) d\eta \tag{16}$$

Momentum equation then becomes upon integration

$$f'' = e^{-I} \cdot \alpha(\tau,\eta)$$

where

$$\alpha = a_2(\tau) + \int_0^{\eta} \frac{e^I}{1+s} \cdot \left[\frac{\dot{G}}{G^2}(f'-1) + \frac{\dot{f}'}{G} + (f')^2 - 1\right] d\eta$$

In order to arrive at the boundary condition at the outer edge of the boundary layer, momentum equation is integrated from $\eta = 0$ to ∞.

Thus

$$1 = \int_0^{\infty} f'' \, d\eta = \int_0^{\infty} e^{-I(\tau,\eta)} \cdot \alpha(\tau,\eta) d\eta \tag{17}$$

We observe that the integrand of equation (17) for all values of time is proportional to the shear stress within the boundary layer. Under the boundary layer approximation it is a rapidly decreasing function of η. This implies that the main contribution to the integral in equation (17) comes from the region close to the wall. Thus the finite radius of convergence of the series for $f(\tau,\eta)$ is not important.

To evaluate the integral in equation (17), the series for $f(\tau,\eta)$ is to be inverted. We now define a new variable γ such that

$$\begin{aligned}
\gamma = \mathrm{I}(\tau,\eta) &+ \frac{\dot{G}}{G^2}\left[\frac{\eta^2}{4} - \frac{s_1\eta^3}{6} + \frac{{s_1}^2\eta^5}{10}\right] - s_1\eta \\
&- \left(\frac{2s_1 - s_1^2}{2}\right) \cdot \eta^2 = \sum_{\eta=0}^{\infty} \mathrm{Cn} \cdot \eta^{n+3}
\end{aligned} \tag{18}$$

where

$$\begin{aligned}
C_0 &= \frac{a_2}{3!} - \frac{2}{3}{s_1}^2 \\
C_1 &= \frac{a_3}{4!} - \frac{s_1 a_2}{8} + \frac{{s_1}^3}{4} \\
C_2 &= \frac{a_4}{5!} - \frac{s_1 a_3}{30} + \frac{2}{5}{s_1}^3 + \frac{2}{5}{s_1}^4 + \frac{{s_1}^5}{5} \\
C_3 &= \frac{1}{6} \cdot \left[\frac{-s_1 a_4}{4!} + \frac{{s_1}^2 a_2}{2!} + ({s_1}^4 - 2{s_1}^3)\left(2s_1 - \frac{\dot{G}}{2G^2}\right)\right]
\end{aligned}$$

Inversion of series for γ in equation (18) is given by

$$\eta = \sum_{m=0}^{\infty} \frac{Am}{m+1} \cdot \gamma^{(m+1)/3} \tag{19}$$

Upon applying Cauchy's residue theorem, we get

$$Am = \frac{1}{2\pi i}\int \gamma^{-(m+1)/3} d\eta$$

where $i=\sqrt{-1}$. The integrations are carried out three times in the γ plane to dispose of the fractional powers of γ once in the η plane. We now have

$$1=\int_0^\infty f''\,d\eta=\int_0^\infty e^{-\gamma}\cdot\psi(\eta,\tau)\cdot\frac{d\eta}{d\gamma}\cdot d\gamma \tag{20}$$

where

$$\psi=\sum_{n=0}^{\infty}\frac{Bn}{n!}\cdot\eta^n$$

$$B_0=a_2$$

$$B_1=-\left(\frac{1+\dot{G}}{G^2}\right)\left(1+s_1-\frac{\dot{G}}{4G^2}\right)-s_1a_2$$

$$B_2=\left(1+s_1-\frac{\dot{G}}{4G^2}\right)\cdot\left(\frac{\dot{G}}{G^2}a_2+\frac{\dot{a}^2}{G}\right)$$

$$+2s_1\left(1+\frac{\dot{G}}{G^2}\right)\left(1+s_1-\frac{\dot{G}}{4G^2}\right)$$

$$+2a_2\left(\frac{\dot{G}}{4G^2}-s_1+{s_1}^2\right)$$

$$B_3=2\left(1+s_1-\frac{\dot{G}}{4G^2}\right)\left(\frac{\dot{G}a_3}{2G^2}+\frac{\dot{a}_3}{2G}+{a_2}^2\right)$$

$$-3s_1\left(1+s_1-\frac{\dot{G}}{4G^2}\right)\left(\frac{\dot{G}}{G^2}\cdot a_2+\frac{\dot{a}_2}{G}\right)$$

$$-6\left(1+\frac{\dot{G}}{G^2}\right)\left(1+s_1-\frac{\dot{G}}{4G^2}\right)\left(\frac{\dot{G}}{4G^2}-s_1+{s_1}^2\right)$$

$$+6a_2\left(\frac{{s_1}^2}{2}-\frac{7}{24}\frac{s_1\dot{G}}{G^2}-\frac{5}{12}{s_1}^3\right) \tag{21}$$

etc.

From equation (20) we recall that

$$\psi(\eta,\tau)\cdot\frac{d\eta}{d\gamma}=\gamma^{-2/3}\sum_{n=0}^{\infty}dm\cdot\gamma^{m/3}$$

where

$$d_0=\frac{B_0}{3}\cdot{C_0}^{-\frac{1}{3}}$$

$$d_1=\frac{1}{3}\cdot{C_0}^{-\frac{2}{3}}\cdot\left(B_1-\frac{2}{3}B_0\frac{C_1}{C_0}\right)$$

$$d_2=\frac{1}{3}\left[-B_0C_2{C_0}^{-2}+B_0{C_1}^2{C_0}^{-3}\right.$$

$$\left.-B_1C_1{C_0}^{-2}+\frac{B_2}{2}{C_0}^{-1}\right]$$

$$d_3=\frac{1}{3}\left[\frac{4}{3}B_0C_3{C_0}^{-\frac{7}{3}}+\frac{28}{9}B_0C_1C_2{C_0}^{-\frac{10}{3}}\right.$$

$$-\frac{140}{181}{C_1}^3B_0{C_0}^{-\frac{13}{3}}-\frac{4}{3}B_1C_2{C_0}^{-\frac{7}{3}}$$

$$\left.+\frac{14}{9}B_1{C_1}^2{C_0}^{-\frac{10}{3}}-\frac{2}{3}B_2C_1{C_0}^{-\frac{7}{3}}+\frac{B_3}{6}{C_0}^{-\frac{4}{3}}\right]$$

etc.

Equation (20) will now be integrated in terms of the complete gamma functions to yield

$$\frac{\partial f}{\partial\eta}(\tau,\infty)=\sum_{m=0}^{\infty}dm\cdot\Gamma\left(\frac{m+1}{3}\right)=1 \tag{23}$$

Upon applying Euler's summation procedure to the above series, we have

$$1=\frac{15}{16}\cdot\Gamma\left(\frac{1}{3}\right)\cdot d_0(\tau)+\frac{11}{16}\cdot\Gamma\left(\frac{2}{3}\right)\cdot d_1(\tau)$$

$$+\frac{5}{16}\cdot d_2(\tau)+\frac{1}{16}\cdot\Gamma\left(\frac{4}{3}\right)\cdot d_3(\tau) \tag{24}$$

After substituting expressions for d_0, d_1, d_2 and d_3 into the above equation, we obtain a first-order ordinary differential equation for $a_2(\tau)$. Equation (24) has been integrated numerically by means of a fourth-order, Runge-Kutta procedure. A discussion of the results will be presented in the next section.

It should be noted that the transient velocity profiles may be determined when once $a_2(\tau)$ is determined. The velocity profiles are given by the equation

$$\frac{\partial f}{\partial\eta}=\sum_{j=0}^{\infty}d_j\Gamma\gamma\left(\frac{j+1}{3}\right) \tag{25}$$

where $\Gamma\gamma$ is the incomplete gamma function. The friction factor is given by equation (15).

Discussion

It must be noted that the analysis is performed for predicting the transient response behavior at the stagnation point due to the combined effects of an arbitrary time dependent free-stream velocity and free-stream turbulence. No assumption has been made for $G(\tau)$ that represents the unsteadiness of the free stream. In fact, the present analysis is valid for any arbitrarily varying continuous $G(\tau)$. There exist in the literature some experimental data and some predictive methods to analyze separately the wall shear factor at a stagnation point under steady-state conditions in the presence of free-stream turbulence and the friction factor due to transient free-stream velocity with no free-stream turbulence. Neither experimental nor analytical work has been reported to investigate the combined effects of unsteady free-stream velocity and free-stream turbulence at a stagnation point.

Many modern turbine blade sections, even at the high Reynolds numbers at which they operate, manifest considerable areas over which the boundary layer remains laminar. The superimposition of mainstream velocity fluctuations associated with artificially induced mainstream turbulence is known to affect dramatically the fluid flow and performance characteristics. Clearly such effects can be important in turbine blade design for, as rotor speed changes, so will the frequency of the perturbations in flow velocity which the blades experience.

In order to illustrate the application of the present analysis to investigate the title problem and also to assess its accuracy, we have chosen two different cases of time-dependent, free-stream velocity.

The first case corresponds to $G(\tau)=(1+\tau)$ with no free-stream turbulence present. Physically, this implies that at time $\tau=0$ the inviscid flow begins to change with constant positive temporal acceleration. Yang [11] investigated this problem by approximate integral methods. The results for $a_2(\tau)$ from the present analysis are compared with those of Yang [11] in Fig. 2. The quasi-steady solution given by Yang incorrectly predicts a discontinuity in the wall shear at $\tau=0$. The results from the present analysis start at $a_2(0)=1.23259$. After reaching a maximum value of a_2 initially as τ increases, a_2 decreases with increasing τ towards the quasi-steady solution. The present analysis is seen to yield physically more realistic results than Yang's integral analysis for $\tau<1$, during which time the flow is experiencing its greatest unsteadiness. The agreement between the present results and those of Yang is within 2 percent for $\tau>1.0$.

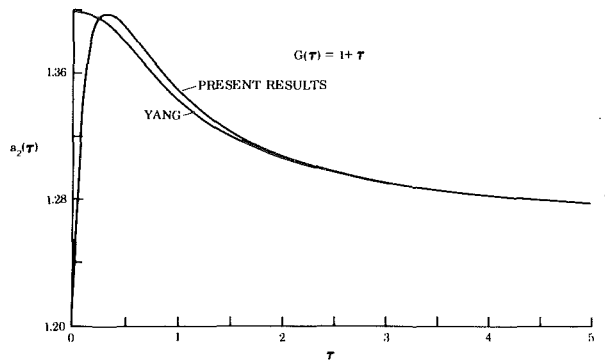

Fig. 2 Shear stress function versus τ for $G(\tau) = 1 + \tau$

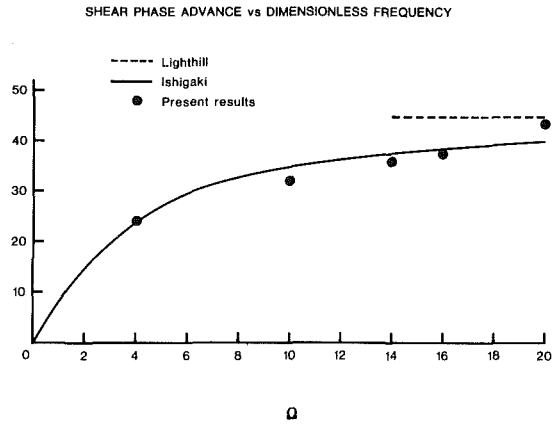

Fig. 3 Shear phase advance versus dimensionless frequency for $G(\tau) = 1 + A\sin(\Omega\tau)$

The second case corresponds to $G(\tau) = 1 + A\sin(\Omega\tau)$. This represents a stagnation point flow in which the free-stream oscillates with amplitude A and dimensionless frequency Ω about a mean velocity. Lighthill [6] studied this problem using a perturbation method and integral approach. Lighthill's analysis was valid for $\Omega \to \infty$. Ishigaki [7] studies the same problem retaining second-order terms in the perturbation analysis. The results from the present analysis for the shear phase advance are compared with those of Ishigaki and Lighthill in Fig. 3. The agreement between the present results and those of Ishigaki was seen to be within 5 percent. Lighthill's asymptotic result as $\Omega \to \infty$ is also in Fig. 3.

Figures 4 and 5 illustrate variation of the shear stress function $a_2(\tau)$ under the combined effect of transient free-stream velocity and free-stream turbulence. For the sake of illustration, $G(\tau) = 1 + A \sin(\Omega\tau)$ only was chosen. It is seen that any existing transients die out within 1 oscillation of the free stream. After about 1 oscillation, the shear stress function $a_2(\tau)$ assumes a periodic shape. The amplitude of the oscillations is a strong function of the turbulence parameter $(\mathrm{Tu} \cdot \mathrm{Re}^{1/2})$. It must be noted that $a_2(\tau)$ increases substantially from the steady-state solution for wall shear stress. Physically, $a_2(\tau)$ corresponds to the wall shear stress at given instant of time as given by equation (15). It may be observed that even after all starting transients have died out the wall shear does not fluctuate with equal amplitude about the steady-state value. This nonsymmetric fluctuation of the wall shear is the result of acoustic streaming near the wall.

It must be noted that the dimensionless frequency parameter Ω may be written as $(\pi f R/u\infty)$ where f is the frequency of disturbance, R the cylinder radius and $u\infty$ the free stream velocity. The grouping $(fR/u\infty)$ is the Strouhal number. Ishigaki [12] dervied from his theoretical analysis that the parameter $\Omega^{1/2}\mathrm{Tu}^{1/2}$ is a controlling parameter to

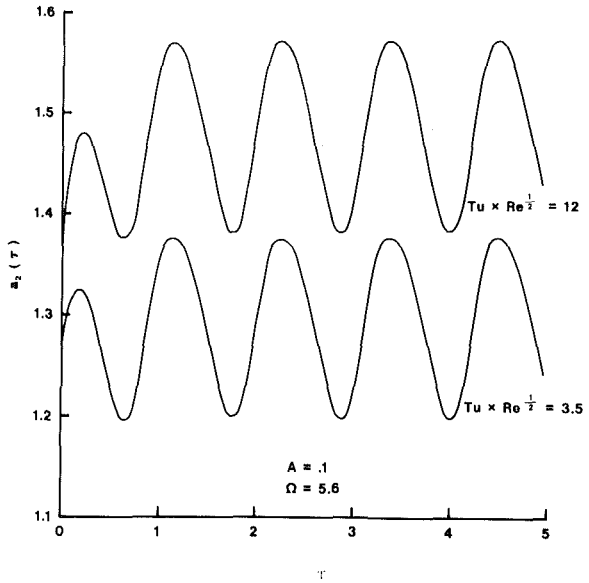

Fig. 4 Shear stress function versus τ for $G(\tau) = 1 + A\sin(\Omega\tau)$

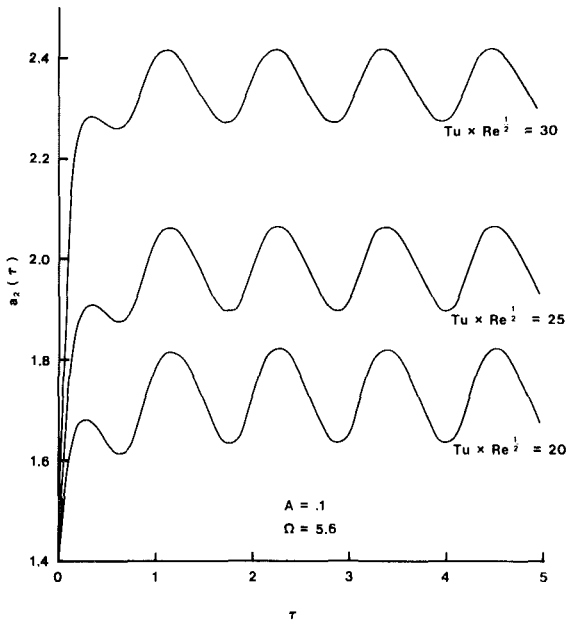

Fig. 5 Shear stress function versus τ for $G(\tau) = 1 + A\sin(\Omega\tau)$

describe heat transfer in turbulent oscillating flows. Bayley and Priddy [13] reported heat-transfer measurements around a gas turbine blade by controlling the frequency and amplitude of turbulence. The Nusselt number data was correlated by then in terms of a parameter $(fC/u\infty)^{1/2}$. $\mathrm{Tu}^2 \cdot \mathrm{Re}$ where C was the chord length of the blade. For the title problem including both unsteady free-stream velocity and free-stream turbulence, $a_2(\tau)$ could not correlate well with the parameter $(\mathrm{Tu} \cdot \mathrm{Re}^{1/2})$. It may be recalled that the steady-state friction factor data has been successfully correlated by the parameter $(\mathrm{Tu} \cdot \mathrm{Re}^{1/2})$ as shown in Fig. 1. Utilizing the analogy between heat and momentum transfer mechanisms, it was hypothesized that $(\Omega^{1/2}\mathrm{Tu}^2\mathrm{Re})$ may be a suitable correlation parameter. Figure 6 illustrates variation of the maximum value of $a_2(\tau)$ and $\bar{a}_2(\tau)0$ may be successfully correlated in terms of $(\Omega^{1/2}\mathrm{Tu}^2\mathrm{Re})$ within an error of 5 percent. The recommended correlations are as follows:

$$\bar{a}_2(\tau) = 0.005(\Omega^{1/2}\mathrm{Tu}^2\mathrm{Re}) + 1.28$$

$$\mathrm{Max} \cdot a_2(\tau) = 0.005(\Omega^{1/2}\mathrm{Tu}^2\mathrm{Re}) + 1.34$$

Concluding Remarks

The method of approach used in this paper to the analysis of the combined effects of free-stream transient velocity and free-stream turbulence at a stagnation point reduces the governing equations to a single first-order ordinary differential equation. The method is capable of yielding results for any arbitrary time-dependent nature of the free stream velocity. The solutions are not restricted by small perturbation assumptions. A successful formulation has been performed to obtain an expression for the eddy diffusivity induced by the free-stream turbulence intensity. The solution of the governing unsteady momentum equation with the proposed eddy diffusivity model yielded predictions for the skin friction coefficient in the presence of the combined action of free-stream turbulence and transient free-stream velocity. A new correlation parameter is suggested to correlate the friction factor results for the title problem. It has been found that the wall friction increases with increasing free-stream turbulence intensity. In the case of flows involving unsteady free-stream velocity, the friction factor increases with increasing values of the reduced frequency of oscillations.

Acknowledgments

This work has been supported through the cooperative agreement No. NCC3-3 by NASA Lewis Research Center. The author is grateful to Dr. Robert J. Simoneau and Dr. Robert W. Graham of the NASA Lewis Research Center for their interest and encouragement. Thanks are due to the reviewers and to Dr. Ted Okiishi for their valuable suggestion that helped to considerably improve the form and quality of the paper.

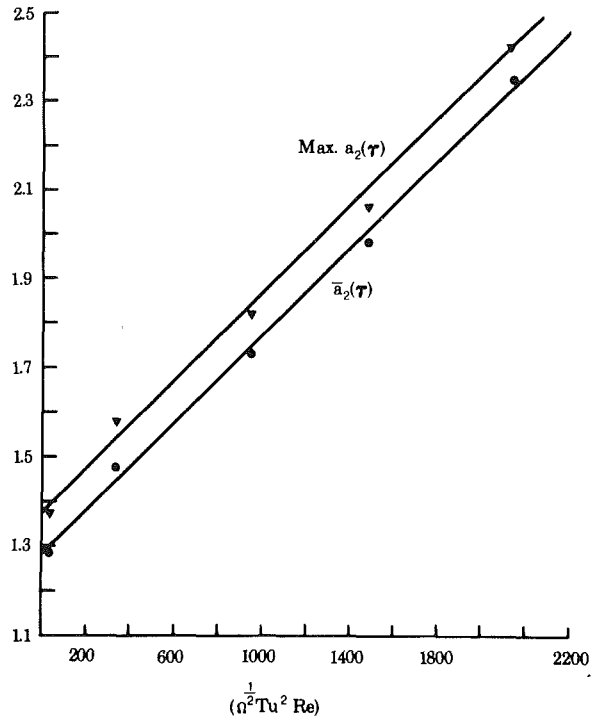

Fig. 6 Correlation of the magnitude of shear stress function

References

1 Sutera, S. P., Meader, P. F., and Kestin, J., "On the Sensivity of Heat Transfer in the Stagnation Boundary Layer to Free Stream Vorticity," ASME *Journal of Fluids Mechanics*, Vol. 16, 1963, pp. 497-520.

2 Sutera, S. P., "Vorticity Amplification in Stagnation Point Flow and Its Effect on Heat Transfer," ASME *Journal of Fluid Mechanics*, Vol. 21, 1965, pp. 513-534.

3 Smith, M. C. and Kuethe, A. M., "Effects Turbulence on Laminar Skin Friction and Heat Transfer," *Physics of Fluids*, Vol. 9, 1966, pp. 2337-2344.

4 Galloway, T. R., "Enhancement of Stagnation Flow Heat and Mass Transfer through Interactions of Free Stream Turbulence," *AIChE Journal*, Vol. 19, 1973, pp. 608-617.

5 Traci, R. M. and Wilcox, D. C., "Free Stream Turbulence Effects on Stagnation Point Heat Transfer," *AIAA Journal*, Vol. 13, 1975, pp. 890-896.

6 Lighthill, M. J., "Contributions to the Theory of Heat Transfer through a Laminar Boundary Layer," *Proc. Roy. Soc.*, A202, pp. 359.

7 Ishigaki, H., "Heat Transfer in a Periodic Boundary Layer near a Two-Dimensional Stagnation Point," ASME *Journal of Fluid Mechanics*, Vol. 56, 1972, pp. 619-627.

8 Junkhan, G. H. and Serovy, G. K., "Effects of Free Stream Turbulence and Pressure Gradient on Flat Plate Boundary Layer Velocity Profiles and on Heat Transfer," ASME *Journal of Heat Transfer*, Vol. 89, 1967, pp. 169-176.

9 Raj, R., "On the Investigation of Cascade and Turbomachinery Rotor Wake Characteristics," Ph.D. thesis, Department of Aerospace Engineering, The Pennsylvania State University, Nov. 1974.

10 Pal, S. and Raj, R., "Wake Behavior in the Presence of Free Stream Turbulence," ASME JOURNAL OF ENGINEERING FOR POWER, Vol. 103, 1981, pp. 490-498.

11 Yang, K. T., "Unsteady Laminar Boundary Layers in an Imcompressible Stagnation Flow," ASME *Journal of Applied Mechanics*, Vol. 25, 1958, pp. 421-427.

12 Ishigaki, H., "The Effect of Oscillation on Flat Plate Heat Transfer," *Journal of Fluid Mechanics*, Vol. 47, 1971, pp. 537-549.

13 Bayley, F. J. and Priddy, W. J., "Effects of Free Stream Turbulence Intensity and Frequency on Heat Transfer to Turbine Blading," ASME JOURNAL OF ENGINEERING FOR POWER, Vol. 103, 1981, pp. 60-64.

14 Meksyn, D., *New Methods in Laminar Boundary Layer Theory*, Pergamon Press, Oxford, England, 1961.

Gas Turbine Airflow Control for Optimum Heat Recovery

W. I. Rowen
Gas Turbine Division.

R. L. Van Housen
Industrial Sales Division.

General Electric Company,
Schenectady, N. Y. 12345
Mems. ASME

Gas turbines furnished with heat recovery equipment generally have maximum cycle efficiency when the gas turbine is operated at its ambient capability. At reduced gas turbine output the cycle performance can fall off rapidly as gas turbine exhaust temperature drops, which reduces the heat recovery equipment performance. This paper reviews the economic gains which can be realized through use of several control modes which are currently available to optimize the cycle efficiency at part load operation. These include variable inlet guide vane (VIGV) control for single-shaft units, and combined VIGV and variable high-pressure set (compressor) speed control for two-shaft units. In addition to the normal control optimization mode to maintain the maximum exhaust temperature, a new control mode is discussed which allows airflow to be modulated in response to a process signal while at constant part load. This control feature is desirable for gas turbines which supply preheated combustion air to fired process heaters.

Introduction[1]

Integration of gas turbines into industrial plant energy supply systems is not a new concept. It is a practice which has been used by many industrial operators within the past quarter century as an economic method of meeting their energy requirements.

The use of gas turbines in the process industries has increased primarily because, in addition to shaft power, the process plant designer has found economic uses for energy in the gas turbine exhaust gases. For exhaust heat recovery applications, the ability to control gas turbine airflow may offer significant advantages at gas turbine part load conditions.

Maximum Airflow Control

Providing no design or application limitation exists, maximum gas turbine airflow and power generation capability vary directly with ambient air temperature as shown in Fig. 1. Maximum airflow control is normally used for simple cycle gas turbines or gas turbines operated at their ambient capability. A typical gas turbine fuel control system for a gas turbine operating on maximum airflow control is shown in Fig. 2. The control system performs startup (shutdown), speed control and temperature override functions. The speed control employs magnetic pickups on the

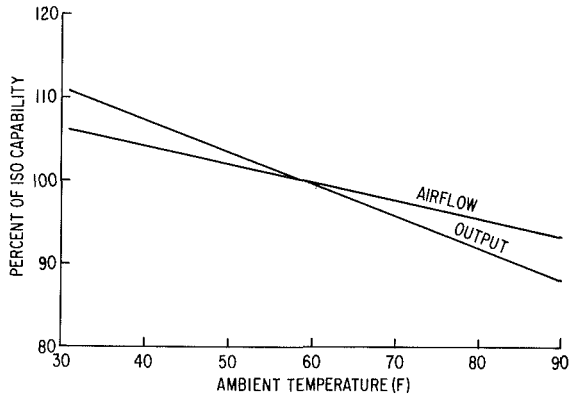

Fig. 1 Typical gas turbine maximum airflow and output capability versus ambient temperature

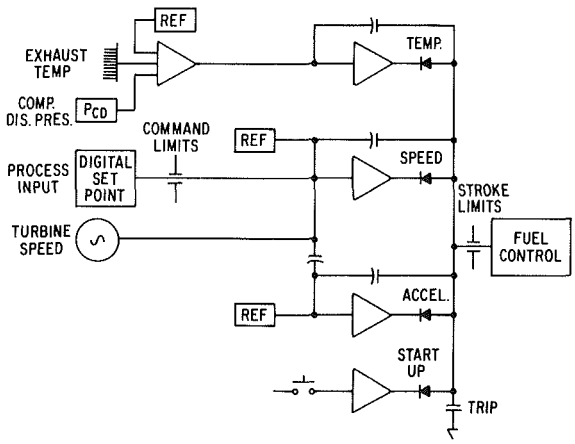

Fig. 2 Fuel control system for single shaft gas turbine, maximum airflow control

[1] Conversion factors for tables and figures
kW = hp × .7457
kg/hr = lbs/hr × .4536
°C = (°F − 32) × 5/9
kj/hr = Btu/hr × 1.055
kPa = in. H_2O × .2488
kPa = (psig + 14.7) × 6.895

Contributed by the Gas Turbine Division of THE AMERICAN SOCIETY OF MECHANICAL ENGINEERS and presented at the 27th International Gas Turbine Conference and Exhibit, London, England, April 18–22, 1982. Manuscript received at ASME Headquarters December 7, 1982. Paper No. 82-GT-83.

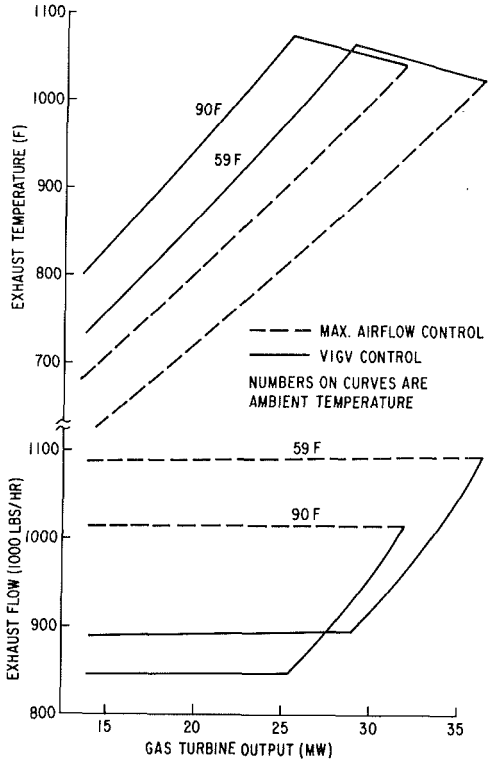

Fig. 3 Gas turbine exhaust characteristics MS6001(B), 37,500-kW ISO, single shaft gas turbine. Basis: (*i*) natural gas fuel; (*ii*) 4 in. H_2O inlet ΔP; (*iii*) 10 in. H_2O exhaust ΔP; (*iv*) sea level.

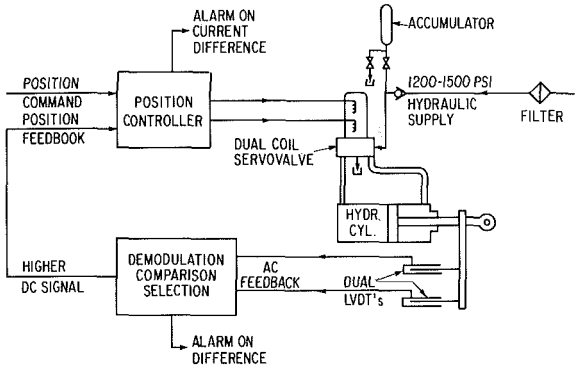

Fig. 4 Gas turbine position control system used for fuel control and VIGV control and turbine nozzle control

machine to produce an a-c voltage signal with frequency proportional to shaft speed. The temperature control loop limits the startup and operating temperature to safe values by sensing exhaust temperature. Variable angle inlet guide vanes are furnished on those machines that require them to ensure that the gas turbine compressor does not enter the surge or pulsation region during gas turbine starting conditions. This region of unstable flow typically commences about 55 percent corrected compressor speed and extends up to about 80 percent corrected compressor speed. Intermediate stage bleeds to atmosphere are also used to assist in increasing flow through the early stages of the compressor that are most susceptible to surge and rotating stall.

Inlet guide vanes are normally held in the partially closed position until normal operating speeds of about 92 to 95 percent are attained. On shutdown, the inlet guide vanes are closed prior to the gas turbine dropping through the 88 to 90 percent speed range, and are kept closed until the previously mentioned conditions are again reached on the subsequent

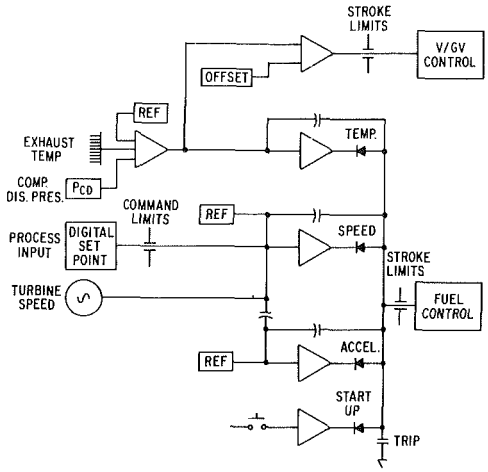

Fig. 5 Fuel and air flow control system for single shaft gas turbine, maximum exhaust temperature control

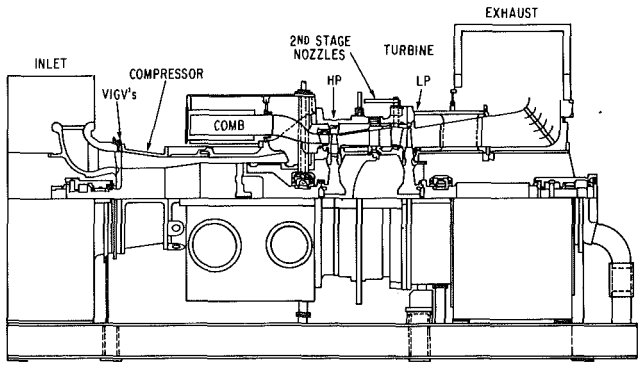

Fig. 6 MS5002(B) cross section

startup. This relatively simple two-position mode of operation is achieved using a four-way solenoid actuated, double acting hydraulic cylinder, with one or two limit switches as checks, to insure that the appropriate position has been achieved.

Maximum Exhaust Temperature Control

For exhaust heat recovery applications where the gas turbine will be operated at less than its ambient capability, there is an economic advantage in maintaining part load exhaust temperatures at the highest possible levels. This is accomplished by varying airflow, within a given operating range, as the required load varies.

Single-Shaft Gas Turbine. For single-shaft gas turbines, airflow control is accomplished by modulating the variable inlet guide vanes (VIGV). The exhaust characteristics for a single-shaft gas turbine based on maximum airflow control or VIGV control are shown in Fig. 3. These data are based on a 37,500-kW, ISO rated gas turbine, General Electric Company model MS6001(B). At a given ambient temperature, the gas turbine output can be reduced to about 80 percent of its ambient capability by reducing airflow (i.e., maintaining the design gas turbine firing temperature). Further reductions in output would require a reduction in gas turbine firing temperature. The higher exhaust temperatures available with VIGV control are readily apparent from Fig. 3. For example, Fig. 3 shows the MS6001(B) gas turbine, at an output of 25,000 kW on a 90°F (32.2°C) ambient day, would have an exhaust temperature of about 1065°F (574°C) with VIGV control compared to 900°F (482°C) if the turbine is operated with maximum airflow.

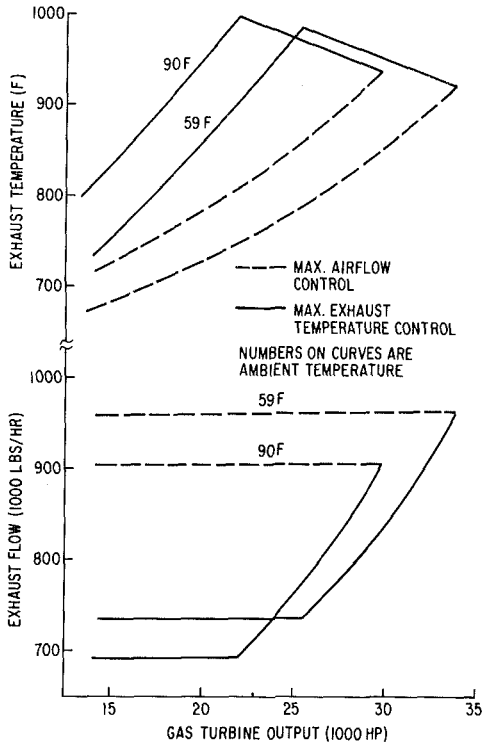

Basis: Same as Fig. 3

Fig. 7 Gas turbine exhaust characteristics MS5002(B), 35,000-hp ISO two-shaft gas turbine, 100 percent speed

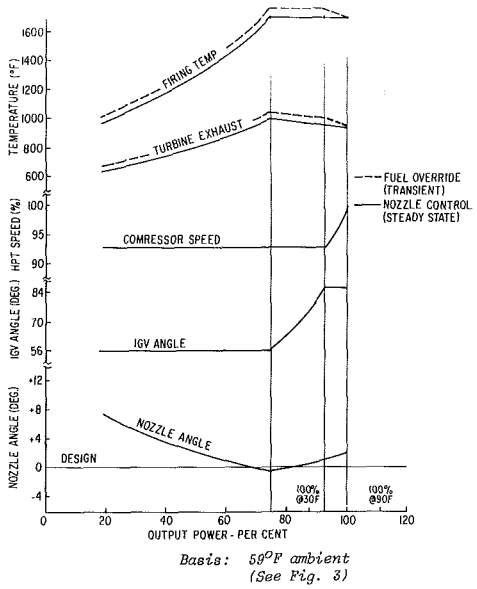

Basis: 59°F ambient (See Fig. 3)

Fig. 8 Part load performance MS5002(B) two-shaft gas turbine

To allow inlet guide vane modulation to occur, the four-way solenoid value mentioned earlier is replaced by a servovalve, and position feedback is added to the hydraulic actuator. This position feedback is most usually in the form of linear variable differential transformers (LVDT's), in a dual configuration for added reliability. The dual coil servovalve and dual LVDT feedback provide the added feature of being able to maintain control in spite of a single failure, and even alarm on a difference of signals to provide self-

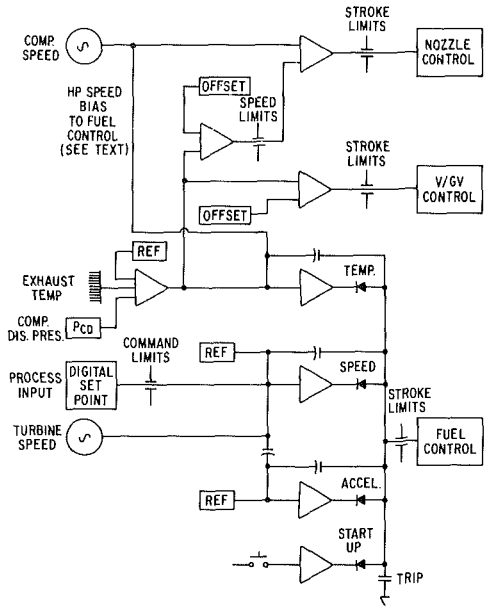

Fig. 9 Fuel and airflow control system for two-shaft gas turbine, maximum exhaust temperature control

monitoring of potential problems. This arrangement is shown in Fig. 4.

The command signal for the inlet guide vane position control loop is derived from the same exhaust temperature control signal that is used to limit fuel flow to the gas turbine to prevent excessive firing temperatures. In the case of inlet guide vane control, the circuits are designed to close the inlet guide vanes until the rated exhaust temperature, less an appropriate offset, is reached. Independent electronic stroke limits on the position command signal prevent this system from calling for inlet guide vane positions beyond the normal operating range. This arrangement is shown schematically in Fig. 5.

Two-Shaft Gas Turbine. Two-shaft gas turbines make use of a first stage, or high-pressure turbine to drive the gas turbine's axial flow compressor, and an independent power turbine or second stage turbine that drives the load equipment connected to the output shaft. In this type of arrangement, it is common for the axial flow compressor to vary in speed as output power varies. Many industrial General Electric two-shaft gas turbines also incorporate variable area second stage turbine nozzles in the hot gas path ahead of the second stage load turbine wheel. By varying the area of the second stage nozzle, the pressure ratio across the high-pressure and low-pressure turbines, and therefore the division of available energy between the two turbine stages, can be varied independently. This provides a means of controlling compressor speed independently of output shaft speed over a limited range of operation. The variable inlet guide vanes and variable area second stage nozzles are shown for a model MS5002(B) gas turbine in Fig. 6.

By using a combination of reduced high-pressure set (compressor) speed and variable inlet guide vane control, gas turbine airflow can be controlled over a wider range of turbine output than with a single-shaft gas turbine with VIGV control only. This can be seen by comparing Fig. 7, the exhaust characteristics for the two-shaft, 35,000 hp, ISO, General Electric Company model MS5002(B) gas turbine with the single-shaft unit characteristics shown in Fig. 3. Variable airflow control for the two-shaft unit is available from about 75 percent site capability, or 25,500 hp at 59°F (19.0 MW at 15.0°C), to 100 percent site capability or 33,800 hp at 59°F

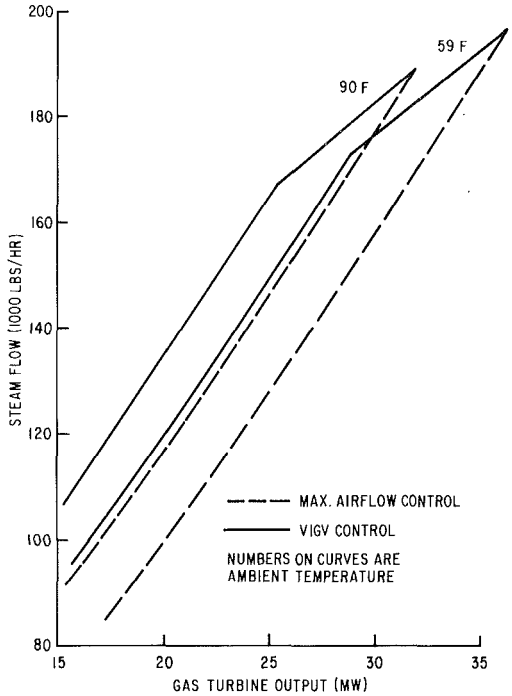

Basis: Same as Fig. 3

Fig. 10 Unfired HRSG performance 250 psig/saturated steam MS6001(B), 37,500-kW ISO single-shaft gas turbine

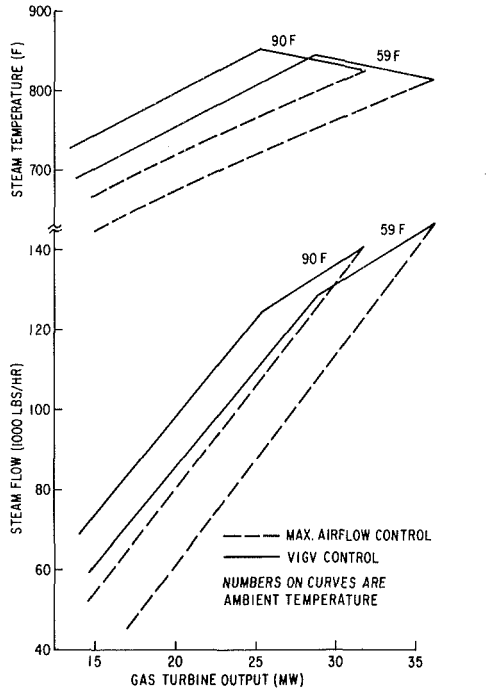

Basis: Same as Fig. 3

Fig. 11 Unfired HRSG performance 850 psig/825 F steam MS6001(B), 37,500-kW ISO single-shaft gas turbine

(25.2 MW at 15°C). As with the single-shaft gas turbine, variable airflow (maximum exhaust temperature) control results in significantly higher exhaust temperatures than with maximum airflow operation as shown on the upper part of Fig. 7.

Figure 8 shows the relationship of turbine firing temperature, compressor speed, VIGV angle, and second stage turbine nozzle angle to turbine output with variable airflow (maximum exhaust temperature) control on the two-shaft MS5002(B) gas turbine. The basis shown in Fig. 8 is 59°F (15°C) ambient temperature. In general, the effect of ambient temperature on the part load characteristics shown in Fig. 8 is to expand or contract the abscissa, relative to the curves, by 0.4 percent/°F (.72 percent/°C) of ambient temperature change. This scaling of the abscissa is indicated for two additional temperatures, 30°F (−1°C) and 90°F (32.2°C) on Fig. 8.

The second stage nozzle position control is functionally equivalent to that for the variable inlet guide vanes (see Fig. 4), except that hydraulic cylinders and servovalves are larger to better match the higher aerodynamic force levels encountered.

Control of the variable area second stage nozzles for two-shaft gas turbines is accomplished through use of a compressor speed governing loop, in which nozzle position is used to maintain the compressor speed at a predetermined setpoint. This setpoint is generated as a function of the exhaust temperature control signal in much the same way as is the command signal for variable inlet guide vane position. The compressor speed setpoint uses a different offset than that of the variable inlet guide vane control so as to insure that the compressor speed is held at its minimum value until after the inlet guide vanes are fully open.

Upper and lower speed limits are imposed on the output of the speed setpoint generator to insure that the control does not call for compressor speeds that are outside the normal operating range. Since the gas turbine, at part load conditions, is operating at the designed maximum steady state exhaust temperature while on active nozzle control, it is necessary to transiently offset the fuel control exhaust temperature limit to allow the extra power required to accelerate the compressor to a higher speed, upon an increase in power output demand. This is accomplished by biasing the exhaust temperature setpoint for fuel control upwards by 4°F (2.2°C) for each percent that the compressor speed is below its design speed. The net result is a maximum transient increase in exhaust temperature of 30°F (16.7°C), and in firing temperature of 50°F (27.8°C) above the normal steady-state values when the compressor is at its 92.5 percent minimum running speed as shown in Fig. 8. It is not necessary to provide a similar bias to the inlet guide vane system, since

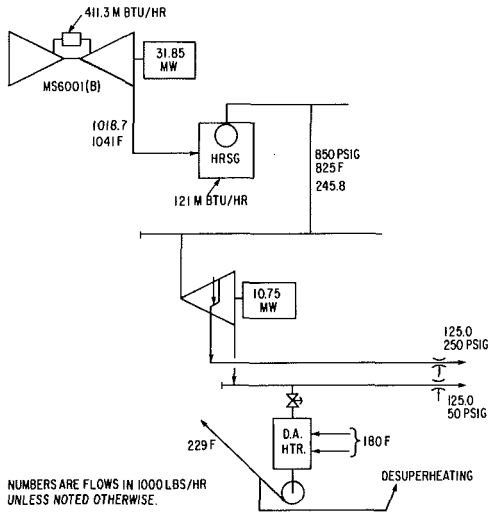

Fig. 12 Estimated schematic MS6001(B) gas turbine combined cycle. Basis: (*i*) 90°F ambient, sea level; (*ii*) natural gas fuel; (*iii*) 4 in. H_2O inlet ΔP; (*iv*) 10 in. H_2O exhaust ΔP; (*v*) power generated 42.6 MW; (*vi*) fuel 532.3 M Btu/hr HHV.

Table 1 Gas turbine, heat recovery steam generator example, assumed energy system requirements

Process heat required	
@ 250 psig, 406°F	125,000 lbs/hr, 132 M Btu/hr
@ 50 psig, 298°F	125,000 lbs/hr, 129 M Btu/hr
Power required	
Minimum	30,000 kW
Maximum	46,000 kW
Fuel	natural gas

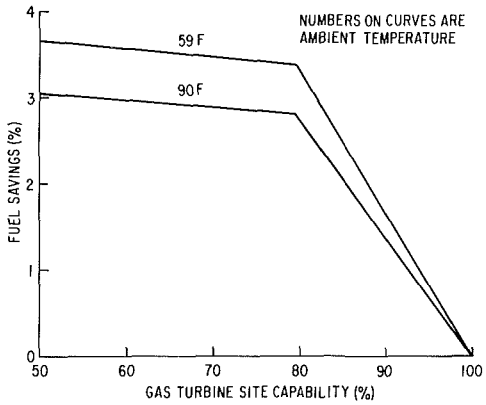

Fig. 13 Savings in system fuel with gas turbine VIGV control, MS6001(B) single-shaft gas turbine. Basis: see Fig. 3 and Table 1.

opening the inlet guide vanes increases airflow through the machine and transiently lowers exhaust temperature, thus allowing an increase in fuel flow. A functional schematic of the complete two-shaft control system is shown in Fig. 9.

Economics of Maximum Exhaust Temperature Control. The economics of gas turbines in process applications usually depend on effective use of the exhaust energy. The most common use of this energy is for steam generation in heat recovery steam generators (HRSG), unfired as well as fired designs. However, the gas turbine exhaust gases can also be used as a source of energy for unfired and fired process fluid heaters as well as for combustion air for power boilers.

Unfired HRSG. Figure 10 shows the performance of an unfired HRSG generating 250 psig (1825 kPa) saturated steam using the exhaust of the MS6001(B) gas turbine. Steam production rates available with and without VIGV control at ambient temperatures of 59°F (15°C) and 90°F (32.2°C) are shown. If we assume that the turbine will be operated at 25 MW on a 90°F (32.2°C) ambient day, VIGV control will result in 19,000 lbs/hr (8618 kg/hr) additional steam production compared to operating without VIGV. If the additional steam production is displacing a similar amount of steam being produced in an 84 percent efficient fuel fired boiler using natural gas at 5 dollars/M Btu, VIGV control will reduce boiler fuel costs 114 dollars/hour. Using the same gas turbine output at 59°F (15°C) ambient temperature, fuel savings would be 126 dollars/hour. Figure 11 shows unfired HRSG steam production at 850 psig/825°F (5962 kPa/441°C) using the same MS6001(B) gas turbine-generator. Notice how the use of VIGV gas turbine control results, in addition to higher steam production rates, in significantly higher superheated steam temperature at reduced gas turbine loads than does the conventional maximum airflow operation.

Combined Cycle Example. To demonstrate the potential economic benefits of variable inlet guide vane control in a combined gas and steam turbine cycle, plant energy requirements as shown in Table 1 were assumed. A simplified

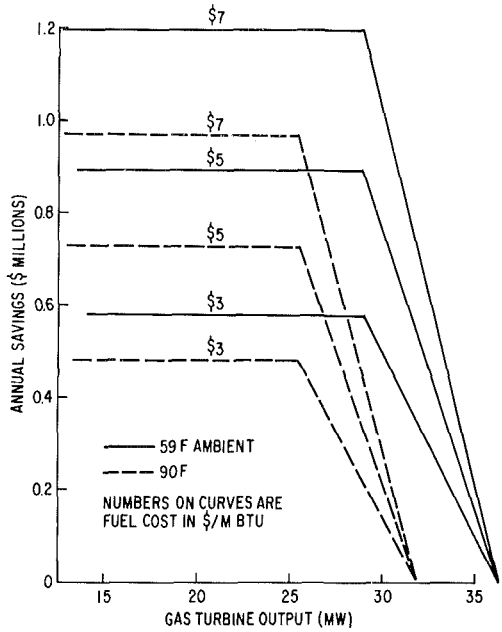

Fig. 14 Annual savings in energy costs with gas turbine VIGV control MS6001(B) single-shaft gas turbine. Basis: *(i)* 8400 hr/yr operation; *(ii)* incremental power credited at 4¢/kWh (see Fig. 3 and Table 1).

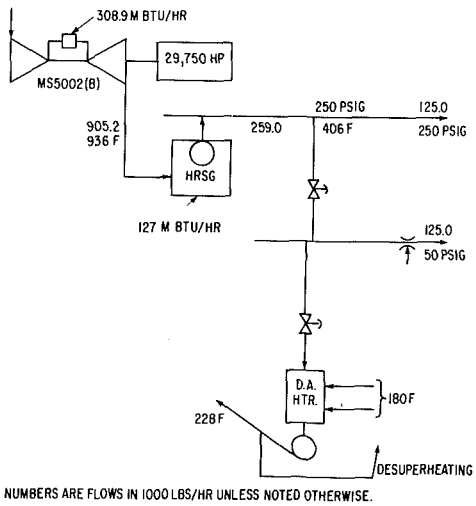

Fig. 15 Estimated schematic MS5002(B) gas turbine HRSG cycle. Basis: *(i)* 90°F ambient, sea level; *(ii)* natural gas fuel; *(iii)* 4 in. H_2O inlet ΔP; *(iv)* 10 in. H_2O exhaust ΔP; *(v)* power generated 29,750 hp; *(vi)* fuel 435.9 M Btu/hr HHV.

schematic of the combined cycle system at the design condition of 90°F (32.2°C) ambient temperature is shown in Fig. 12. For this energy supply system, the supplementary fired, convective type HRSG has a firing temperature of about 1400°F (760°C) at the design condition which is shown on Fig. 12.

The fuel savings in the gas turbine and HRSG if this combined cycle system is operated with maximum gas turbine exhaust temperature (reduced airflow) control, compared to maximum airflow control, is indicated on Fig. 13. Figure 13 shows that at gas turbine outputs of 80 percent of site capability, or less, system fuel savings of 3 to 4 percent are available with maximum exhaust temperature control when compared to maximum airflow control. At part loads greater than 80 percent, fuel savings range from 3 to 4 percent down to zero at site capability. The annual (8400 hr) savings in energy costs for this combined cycle system with the gas turbine operating on maximum exhaust temperature control is

Table 2 Annual fuel savings with maximum exhaust temperature control, gas turbine-HRSG example

G.T. horsepower	20,000		24,000		28,000		32,000	
Ambient temp – °F	59	90	59	90	59	90	59	90
Annual savings ($1000)								
Fuel cost								
$3/M Btu	480	380	460	280	310	90	100	–
$5	800	630	770	470	520	150	170	–
$7	1120	890	1070	650	720	210	230	–

Basis:
(*i*) Model MS5002(B) gas turbine, 35,000 hp ISO
(*ii*) Sea level
(*iii*) Natural gas fuel
(*iv*) 4 in. H_2O inlet ΔP
(*v*) 10 in. H_2O exhaust ΔP
(*vi*) 8400 hr/yr operation
(*vii*) See Fig. 15 for schematic

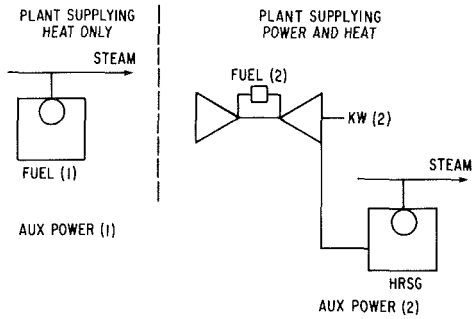

Fig. 16 Fuel chargeable to power

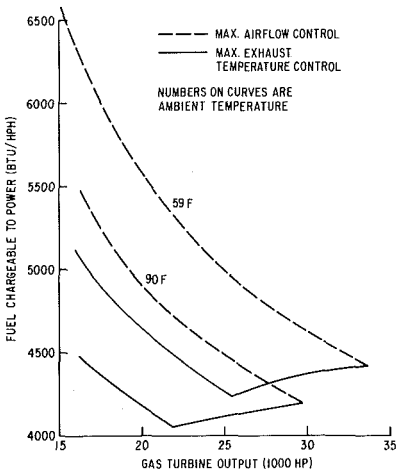

(See Fig. 15 for schematic)

Fig. 17 Fuel chargeable to power MS5002(B) two-shaft gas turbine

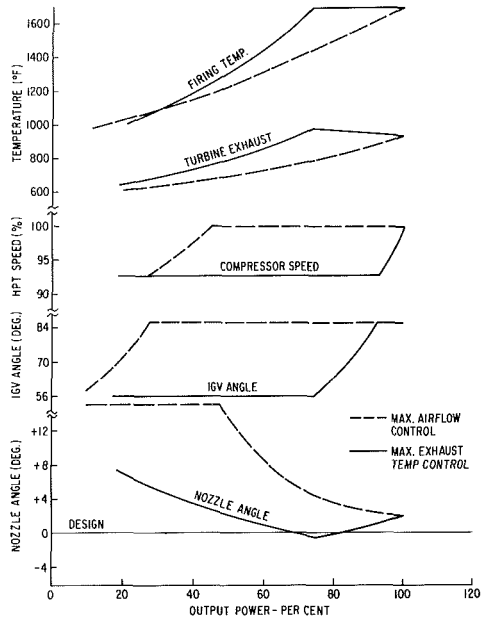

Basis: 59°F ambient (See Fig. 3)

Fig. 18 Part load performance MS5002(B) two-shaft gas turbine

shown on Fig. 14. If the average annual gas turbine output required is 27,000 kW, Fig. 14 shows that annual energy cost savings with VIGV control is about 540,000 dollars if the average ambient temperature is 90°F (32.2°C) and natural gas fuel is valued at 5 dollars/M Btu. If the average ambient temperature is 59°F (15°C) at the same conditions, the annual savings would increase to 890,000 dollars.

Gas Turbine-HRSG Cycle Example. Using the same process heat requirements listed in Table 1, Fig. 15 shows a model MS5002(B) two-shaft gas turbine exhausting into a fired HRSG generating saturated steam at 250 psig (1825 kPa) to supply process requirements at 250 psig (1825 kPa) and 50 psig (446 kPa). Gas turbine capability at 90°F (32.2°C) ambient temperature and sea level is 29,750 hp (22,180 kW).

The relative efficiency of cycles which supply both process heat and power can be measured using a yardstick called Fuel Chargeable to Power (FCP). This parameter, illustrated in Fig. 16, is the extra increment of fuel required for the plant supplying process heat and power versus the fuel required for process heat only. These performance data should include all energy related factors, such as boiler efficiency, boiler blowdown, and auxiliary power requirements.

The FCP in Btu/hph, for the MS5002(B) gas turbine HRSG example is plotted in Fig. 17 for both maximum exhaust temperature control (solid lines) and maximum airflow control (dashed lines). The favorable FCP with maximum exhaust temperature control is apparent. At a gas turbine output of 25,000 hp (18,640 kW) and 59°F (15°C) ambient, the FCP is about 5000 Btu/hph (7074 kj/kWh) if the gas turbine is on maximum airflow control or 4270 Btu/hph (6041 kj/kWh) for the reduced airflow controlled gas turbine-HRSG system. The 730 Btu/hph (1033 kj/kWh) improvement represents a savings of about 14.5 percent in the FCP.

Table 3 Use of gas turbine exhaust as preheated combustion air, assumptions and economic results

Gas turbine		MS5002(B)
Avg. output (hp)		27,000
Exhaust		
Flow (1000 lbs/hr)		768.5
Temperature (°F)		973
Fuel (M Btu/hr HHV)		
Gas turbine		284.6
Incremental furnace		−164.9
Total incremental fuel		119.7
Annual savings in energy costs with gas turbines ($ Million/year)		
Purchased power	Fuel	
4¢/kWh	$4/M Btu	$3.5
4¢	$5	2.5
4¢	$6	1.5
5¢	$5	4.4
5¢	$6	3.4
5¢	$7	2.4

Basis: (*i*) 59°F ambient temperature, sea level
(*ii*) Natural gas fuel
(*iii*) 4 in. H_2O inlet ΔP
(*iv*) 10 in. H_2O exhaust ΔP
(*v*) 8400 hrs/year operation
(*vi*) 90% electrical system transmission and distribution efficiency

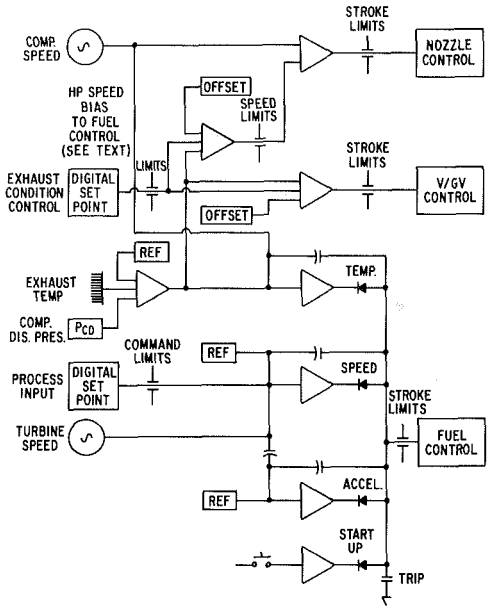

Fig. 19 Fuel and airflow control sytem for two-shaft gas turbine, variable exhaust condition control

Annual savings in fuel cost for the reduced airflow control versus maximum airflow controlled cycle is shown in Table 2. At an average annual gas turbine output of 28,000 hp (20,880 kW) at 59°F (15°C) ambient, savings in fuel costs if natural gas costs 5 dollars/M Btu, is about 520,000 dollars.

Variable Exhaust Condition Control

In the airflow control system examples discussed so far, comparisons have been made with the gas turbine operated either on maximum airflow control or maximum exhaust temperature control and exhausting into a HRSG supplying steam for process use. The primary control input for these systems is a power command which is entered via a setting on the digital setpoint as shown on Figs. 2, 5, and 9. There are, however, some processes that have a requirement for heated air, and therefore can make direct use of the gas turbine exhaust. These include, but are not limited to, drying processes, unfired process fluid heaters and fired heaters such as reformers. In this type of situation, the digital setpoint could be responsive to the air requirements of the process rather than a power output demand. If the power excess or deficiency cannot be absorbed by additional connected sources of electrical power, then a scheme of combined power output control and exhaust condition control may be required.

This is exactly the situation that arises in most two-shaft applications, since the two-shaft gas turbines are almost always applied to mechanical drive equipment where process drive requirements change independently of the process thermal loads. The balance of this discussion will concentrate on the two-shaft gas turbine; however, it should be remembered that the same concept of combined control can be accomplished with the single-shaft gas turbine, with the proviso that the range of airflow control is somewhat less, since the gas turbine compressor speed is constant.

As a matter of simplicity, simple cycle gas turbines operate at essentially constant airflow over the load range. As mentioned previously, for single-shaft gas turbines, inlet guide vanes are opened to the full position prior to reaching operating speed. In the case of the two-shaft gas turbine, inlet guide vanes are opened, and the compressor speed is brought to 100 percent as soon as load demand is sufficient to support full compressor airflow with an acceptable combustor temperature rise. If the part load characteristics of this simple cycle (maximum airflow) control scheme are overlaid on those of the maximum exhaust temperature control scheme shown in Fig. 8, the two sets of operating lines form the boundaries of a set of operating regions, which are shown in Fig. 18. Since the same gas turbine design can be operated on either of the two sets of lines shown in this figure, it can also be operated at any single point within the regions defined between the two sets of lines.

In terms of the control implementation of this scheme, this is accomplished by providing a second offset to the temperature control setpoints for both nozzle control and variable inlet guide vane control. By providing this second offset from a digitally driven setpoint control, similar to that for the fuel control speed governor, all of the advantages such

as local/remote and auto control are also obtained. This system is shown schematically in Fig. 19. In essence, this system provides independent control of power output and exhaust temperature or exhaust flow within the limits shown in Fig. 18. It should be remembered that the range of variable exhaust conditions for the two-shaft turbine decreases from a maximum at approximately 75 percent of rated output power, to essentially zero at 100 percent of output power.

Gas Turbine Exhaust as Preheated Combustion Air Example. The use of gas turbine exhaust as preheated combustion air may result in favorable economics compared to conventional ambient air-fired furnaces and purchased power. Table 3 lists the annual savings in energy costs which can result from using the MS5002(B) gas turbine exhaust as preheated combustion air for a fired heater. For the specific operating point listed, annual (8400 hr) savings in fuel and purchased power costs range from 1.5 million dollars with 4¢/kWh purchased power and 6 dollars/M Btu fuel, to 3.5 million dollars with 4¢ power and 4 dollars/M Btu fuel.

Other Considerations

There are some situations in which the use of reduced airflow control systems may be overridden by other considerations. The most notable of these is the existence of a system requirement for rapid load pickup capability in isolated generator drive applications. The load pickup capability of a gas turbine is greatest when operating in the maximum airflow mode of operation since this results in the lowest part load exhaust temperature and therefore the greatest allowable fuel increase, before being limited by temperature control. Therefore, if rapid increases in power output are a requirement of a specific application, this fact must be taken into consideration in choosing the method of exhaust condition control.

Also, in HRSG applications the maximum allowable level of HRSG firing temperature for a particular design may limit the reduction of gas turbine airflow for a given steam production requirement. If, for example, an application required a HRSG firing temperature of, say, 1500°F (816°C) with the part-loaded gas turbine operating on maximum exhaust flow, use of maximum exhaust temperature (reduced airflow) control would result in a higher HRSG firing temperature and may dictate a change in HRSG design from a convective type heat exchanger to a primarily radiant heat exchanger. The annualized added cost of the HRSG in this particular case might offset the fuel advantage of the reduced airflow control.

Summary

This paper has discussed the performance, economics, and control flexibility of single-shaft and two-shaft gas turbines in industrial heat recovery applications. Three modes of part load operation have been discussed, including maximum exhaust temperature control, maximum airflow control, and a new combined mode of control. This latter mode of operation is unique in that simultaneous dual control of both power output and exhaust flow or exhaust temperature is achievable under part load conditions. This again points up the flexibility and adaptability of gas turbines in meeting unique industrial process requirements.

Liquid Particle Dynamics and Rate of Evaporation in the Rotating Field of Centrifugal Compressors

O. Pinkus
Consulting Engineer,
Mechanical Technology Incorporated,
Latham, N.Y. 12110

A model is presented which consists of injecting a liquid coolant into the gas or superheated vapor of centrifugal compressors via slots in the rotating blades. The aim of the injection is minimization of required compression work. The three-dimensional analysis determines the relative velocities and trajectories of the liquid particles, and their rate of vaporization as a function of the prevailing flow field and inlet conditions. Inertia, viscous drag, centrifugal and Coriolis forces are all included. The analysis rests on the assumption of low volumetric liquid/gas ratios so that the aerodynamics of the flow is not appreciably disturbed. The computer-obtained results show that for optimum conditions, and to avoid collision with the blades, it is desirable that injection occur at the suction side of the blades and close to the hub, that low rather than high initial particle velocities are preferred, and that small droplet sizes are required both to avoid blade erosion and to assure the highest rate of vaporization.

Background

Improvement in the performance of compression cycles is usually achieved by discrete interstage cooling which is a stepwise approximation to an isothermal process. Of course, the larger the number of cooling stages, the closer the approximation to isothermal compression. In actuality, however, it is impractical and even unprofitable to have a large number of stages. A more direct method of achieving isothermal conditions would be a quasi-continuous cooling by the injection of a coolant from the rotating blades along the path of compression. By full or partial vaporization, the injected liquid would cool the gas, or superheated vapor, and keep it below adiabatic compression temperatures.

The particular attraction of such an injection system in centrifugal compressors is that no special equipment is needed for the delivery and compression of the coolant. As shown in Fig. 1, the liquid admitted at atmospheric conditions to the rotating shaft is pumped by centrifugal force outward along channels cut in the blades or the other adjacent surfaces. Due to high speeds of rotation, the liquid can be raised to considerable pressures so that the dimensions of the channels and discharge orifices can be kept extremely small.

The process of liquid injection into the compression path involves at least four areas of investigation, as follows:

(*a*) Liquid Injection. This relates to the centrifugally generated pressures and flow of the liquid in terms of the radial spokes of the rotating system and the orifice restriction at the discharge end. A good treatment of this subject is given in [1]. However, this region is of little interest for our purposes. Given a predetermined rate of injection, together with slot dimensions, this flow will determine the required pumping pressure, p_o, at the inlet to the compression path.

(*b*) Particle Dynamics. This relates to the relative velocities and trajectories of the liquid particles in the rotating field. The flow map of these particles is a function of many variables: the initial conditions, that is, point of injection, particle size, velocity, etc.; the flow field of the gas into which the droplets are injected; the geometry of the blades; and on the angular velocity of the rotor which imparts (via the rotating fluid) centrifugal and Coriolis forces on the particles.

(*c*) Rate of Vaporization. Since the aim is to reduce the temperature by particle evaporation, the expected rate of vaporization must be determined as a function of particle dynamics and the state of the gas. In turn, particle vaporization, which brings about a variation in particle size, has a direct bearing on particle dynamics.

(*d*) Two-Phase Flow. As mentioned in parts (*b*) and (*c*), the underlying flow map has an important bearing on particle trajectory and rate of vaporization. While this flow map, i.e., velocities, pressures, temperatures, etc., can initially be taken from an aerothermodynamic analysis applied to the gas alone, the presence of droplets will tend to alter this map. Should the volumetric liquid/gas ratio be very high, a new map of pressures and velocities must subsequently be obtained on the basis of a two-phase flow system.

There are a number of referenced works dealing with gas-particle flows, but these contain only elements of the problem under study here. Perhaps the closest in subject matter and scope is the work of [2] which is concerned with the trajectories of entrapped solid particles in turbine cascades, the emphasis being on minimizing collision with the stationary and moving surfaces. The present case, of course, deals in-

Contributed by the Gas Turbine Division of THE AMERICAN SOCIETY OF MECHANICAL ENGINEERS and presented at the 27th International Gas Turbine Conference and Exhibit, London, England, April 18-22, 1982. Manuscript received at ASME Headquarters December 7, 1981. Paper No. 82-GT-86.

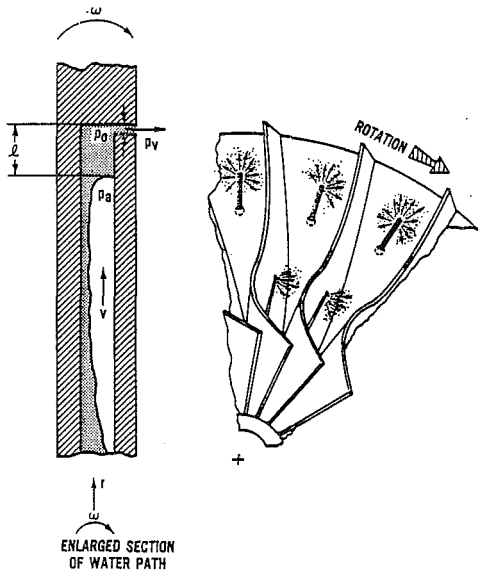

Fig. 1 Water injection in centrifugal compressor

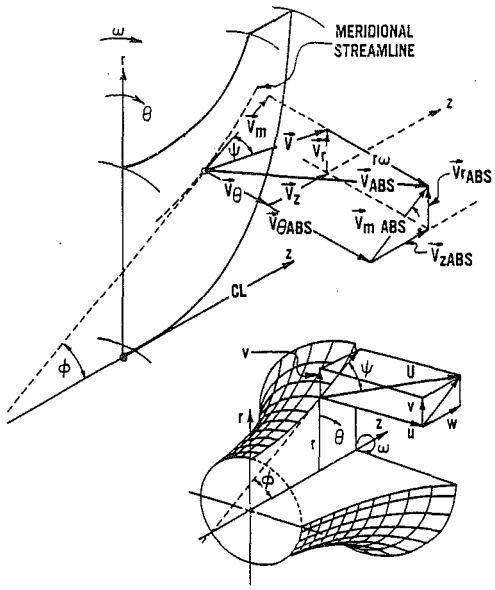

Fig. 2 Coordinate system and velocities

stead with deliberate particle injection, and instead of solids it deals with liquid particles which, due to evaporation, undergo continuous variation in size. The particular system studied here deals with water droplets injected into the field of superheated steam, and it is confined to cases where the volumetric (droplet/steam) ratios remain sufficiently low so as not to alter appreciably the aerodynamics of compression. The emphasis here is on droplet dynamics aimed at providing guidelines for the optimum positioning, sizing, and metering of the required injection system.

Equations for Particle Dynamics

Particle Flow in a Rotating Fluid. To account for the spatial configuration of a centrifugal compressor, the equations will be written in three dimensions of a cylindrical coordinate system. The coordinates are fixed in the rotating system, with z along the axis of rotation and constant θ representing a meridional plane as shown in Fig. 2. All velocities are relative to the rotating blades and the other bounding surfaces. However, as is clear from Fig. 2, the radial and axial velocities are also absolute velocities, whereas the relative circumferential velocity, u, differs from the absolute circumferential velocity by the quantity $r\omega$.

In this scheme the three relevant momentum equations are

$$\rho V r \frac{d^2\theta}{dt^2} = F_\theta - 2\rho V\left(\omega + \frac{d\theta}{dt}\right)\frac{dr}{dt} \tag{1a}$$

$$\rho V \frac{d^2 r}{dt^2} = F_r + \rho V r\left(\omega + \frac{d\theta}{dt}\right)^2 \tag{1b}$$

$$\rho V \frac{d^2 z}{dt^2} = F_z \tag{1c}$$

Above, F is the viscous drag force, the last term in equation (1a) is the Coriolis force, and the last term in equation (1b) is the centrifugal force, both imparted on the particle by the drag of the rotating fluid. No pressure forces are included

Nomenclature

A = area
C_D = viscous drag coefficient
D = diameter of particle
D_o = particle diameter at point of injection
E = denotes particle exit
F = drag force
I = denotes particle impact with wall
I_θ = impact with θ wall
I_z = impact with z wall
N = revolutions for unit time
R = radius of particle
$\bar{R}$ = (R/R_o)
R_o = radius of particle at point of injection
Re = Reynolds number, $(DU_R/\nu_v) = \mathrm{Re}_o \bar{U}_R \bar{R}$
Re_o = reference Reynolds Number, $(D_o r_2\omega/\nu_v)$
S = denotes particle stagnation
T = absolute temperature
T_{sat} = saturation temperature
U = particle velocity relative to blade
U_R = particle velocity relative to vapor
$\bar{U}$ = $U/r_2\omega$
V = volume
W = work
c = specific heat
g = gravitational constant
h = enthalpy
h_{fg} = heat of vaporization
k = heat conductivity
l = height of full water column
m = mass; meters
p = pressure
q = heat
r = radial coordinate
r_2 = blade outer radius
$\bar{r}$ = (r/r_2)
s = entropy
t = time
u = circumferential velocity relative to blade
$\bar{u}$ = $(u/r_2\omega)$
v = radial velocity relative to blade
$\bar{v}$ = $(v/r_2\omega)$
w = axial velocity relative to blade
$\bar{w}$ = $(w/r_2\omega)$
z = axial coordinate
$\bar{z}$ = (z/r_2)
α = angular distance between blades
β = $\frac{3}{2}(\rho_v/\rho)(r_2/R_o)$
γ = $0.74\ \mathrm{k}/\rho g D_o^2 \omega h_{fg}$
θ = angular coordinate
λ = film heat transfer coefficient
μ = absolute viscosity
μm = microns, 10^{-6} m
ν = kinematic viscosity
ρ = density
τ = dimensionless time, $t\omega$
$\Delta\tau$ = residence time of droplet until exit or impact
ϕ = angle between z-axis and streamline
ω = angular velocity

because these are small by comparison, as can be seen from the following:

$$\frac{dp}{dr} = \frac{dp}{dR} = 0\left(\frac{1}{2}\frac{\rho U^2}{r_2}\right) (0 \equiv \text{order of})$$

so that the pressure force acting on a particle is

$$F_p = \Delta p \cdot A = \frac{1}{2}\frac{\rho U^2}{r_2} \cdot R \cdot \pi R^2 \tag{2}$$

The viscous drag force on a spherical particle is [3]

$$F_\mu = 6\pi\mu R U$$

Thus

$$\frac{F_p}{F_\mu} = \frac{\frac{1}{2}\left(\frac{\rho U^2}{2}\right)\pi R^3}{6\pi\mu R U} = \frac{1}{12}\frac{\rho U R}{\mu}\left(\frac{R}{r_2}\right) = \frac{\text{Re}}{12}\left(\frac{R}{r_2}\right) \tag{3}$$

Now the Reynolds number is of the order 1 to 100 whereas R, the particle radius, is of the order of 1 to 100 microns, yielding for the (F_p/F_μ) ratio values anywhere from 10^{-2} to 10^{-6}.

The viscous force F can in general be represented by

$$F = C_D \cdot \frac{1}{2}\rho A U_R^2$$

where the coefficient C_D is a function of the Reynolds number

$$\text{Re} = \frac{\rho_v D U_R}{\mu_v}$$

and U_R, the relative velocity between the vapor and particle, is given by

$$U_R = \left\{\left(u_v - r\frac{d\theta}{dt}\right)^2 + \left(v_v - \frac{dr}{dt}\right)^2 + \left(w_v - \frac{dz}{dt}\right)^2\right\}^{1/2}$$

$$= [U_{R\theta}{}^2 + U_{Rr}{}^2 + U_{Rz}{}^2]^{1/2} \tag{4}$$

The component drag forces in equations (1) thus become

$$F_\theta = (U_{r\theta}/U_R)F \tag{5a}$$

$$F_r = (U_{Rr}/U_R)F \tag{5b}$$

$$F_z = (U_{Rz}/U_R)F \tag{5c}$$

Normalizing all velocities by $r_2\omega$; all distances by r_2; and writing

$$\bar{F} = \frac{F}{\frac{1}{2}\rho r_2 \omega^2} = 3C_D\left(\frac{\rho_v}{\rho}\right)\left(\frac{r_2}{R_o}\right)\bar{U}_R^2$$

$$\tau = t\omega$$

we obtain the normalized form of equations (1)

$$\bar{r}\left(\frac{d^2\theta}{d\tau^2}\right) = \frac{\beta\bar{U}_R C_D}{\bar{R}}(\bar{u}_v - \bar{u}) - 2\left(1 + \frac{d\theta}{d\tau}\right)\bar{v} \tag{6a}$$

$$\frac{d^2\bar{r}}{d\tau^2} = \frac{\beta\bar{U}_R C_D}{\bar{R}}(\bar{v}_v - \bar{v}) + \bar{r}\left(1 + \frac{d\theta}{d\tau}\right)^2 \tag{6b}$$

$$\frac{d^2\bar{z}}{d\tau^2} = \frac{\beta\bar{U}_R C_D}{\bar{R}}(\bar{w}_v - \bar{w}) \tag{6c}$$

where

$$\bar{U}_R = [(\bar{u}_v - \bar{u})^2 + (\bar{v}_v - \bar{v})^2 + (\bar{w}_v - \bar{w})^2]^{1/2}$$

$$\beta = \frac{3}{2}\left(\frac{\rho_v}{\rho}\right)\left(\frac{r_2}{R_o}\right)$$

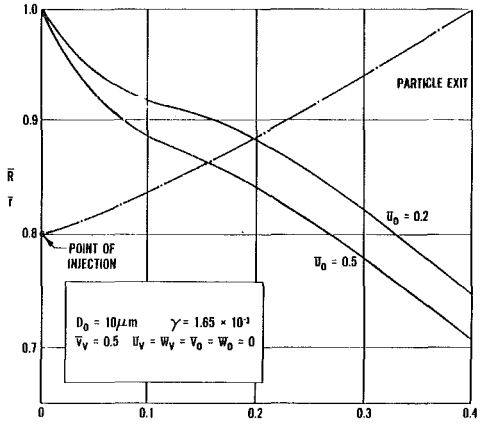

Fig. 3 Rate of droplet vaporization

In equation (6), $\bar{R} = (R/R_o)$ where R_o is the particle size at point of injection, and C_D is a function of the Reynolds number $(U_R D/\nu_v)$. All subscripts v refer to the superheated vapor, whereas the unsubscripted quantities refer to the droplets. The trajectory coordinates θ, $\bar{r}$, $\bar{z}$ and velocities $\bar{u} = \bar{r}\ d\theta/d\tau$, $\bar{v} = d\bar{r}/d\tau$, $w = d\bar{z}/d\tau$ are the unknowns to be solved, for all relative to the rotating blades. For purposes of numerical evaluation the dependence of C_D on Re was put in equation form, as follows

$$C_D = \begin{cases} \dfrac{24}{\text{Re}} \text{ for } \le 0.6 \\ 0.05 \exp\,[6.193\ \text{Re}^{-0.1496}] \text{ for } 0.6 < \text{Re} < 1500 \\ 0.398 \text{ for Re} > 1500 \end{cases} \tag{7}$$

which is a close representation of C_D as given in [3].

Evaporation of Liquid Particle. In all the previous equations the size of the droplet, R, is a variable and a function of time. The evaporation of the particle is in fact the main objective of this injection scheme. The variation in droplet size can be obtained from a heat balance between the heat required for evaporation and the rate of heat transfer occurring between the superheated vapor and droplet. The amount of heat required to induce a given rate of vaporization is

$$\frac{dq}{dt} = h_{fg}\frac{dm}{dt} = (g\rho)h_{fg}\frac{dV}{dt} \tag{8}$$

Above, it is assumed that the liquid injected into the vapor is at a temperature corresponding to the saturation temperature of the local pressure, and the only heat required is the vaporization enthalpy, h_{fg}. If the liquid is below that temperature, it would first have to be heated requiring

$$\frac{dq_s}{dt} = cm\frac{dT}{dt}$$

with T going from T_o to T_s, T_o being the inlet temperature. This quantity, however, is bound to be small as compared with that given by equation (8).

The heat required for vaporization has to be transferred from the superheated vapor to the liquid particle by conduction, or

$$\frac{dq}{dt} = \lambda A(T_v - T_s) \tag{9}$$

Writing $A = 4\pi R^2$, $V = 4/3\ R^3$ and equating the two rates of heat transfer, we obtain

$$\frac{dR}{dt} = \frac{\lambda(T_v - T_s)}{g\rho h_{fg}} \tag{10}$$

Now the film coefficient, λ, can be related to the heat conductivity between the vapor and water droplet, via [4]

$$\frac{\lambda D}{k} = 0.37\ \mathrm{Re}^{0.6}$$

The above inserted into equation (10) and properly normalized, yields

$$\bar{R}\frac{d\bar{R}}{d\tau} = -\gamma \mathrm{Re}^{0.6}[T_v - T_s] \tag{11}$$

where

$$\gamma = \frac{0.74\,k}{g\rho D_o^2 \omega h_{fg}}$$

If the variation in T_v is not very large then γ is approximately constant, with only Re and ΔT varying. If ΔT_v varies over a wide range then certainly h_{fg}, and to some degree also k, would vary and equation (11) should more properly be written as

$$\bar{R}\frac{d\bar{R}}{d\tau} = -\frac{0.74}{g\rho D_o^2 \omega}\left[\frac{k\mathrm{Re}^{0.6}(T_v - T_s)}{h_{fg}}\right]$$

$$= -\frac{0.74}{g\rho D_o^2 \omega} F(\theta, r, z) \tag{12}$$

The above differential equation for $R(\tau)$ must be added to the set of equations (6) for a complete solution of the problem of evaporating droplets moving in a rotating high-speed fluid.

Method of Solution. As derived in the previous section, we have a set of four differential equations to solve, namely

$$\bar{r}\frac{(d^2\theta)}{d\tau^2} = \frac{\beta \bar{U}_R C_D}{\bar{R}}\left(\bar{u}_v - \bar{r}\frac{d\theta}{d\tau}\right) - 2\left(1 - \frac{d\theta}{d\tau}\right)\frac{d\bar{r}}{d\tau} \tag{13a}$$

$$\frac{d^2\bar{r}}{d\tau^2} = \frac{\beta \bar{U}_R C_D}{\bar{R}}\left(\bar{v}_v - \frac{d\bar{r}}{d\tau}\right) + \bar{r}\left(1 + \frac{d\theta}{d\tau}\right)^2 \tag{13b}$$

$$\frac{d^2\bar{z}}{d\tau^2} = \frac{\beta \bar{U}_R C_D}{\bar{R}}\left(\bar{w}_v - \frac{d\bar{z}}{d\tau}\right) \tag{13c}$$

$$\bar{R}\frac{d\bar{R}}{d\tau} = -\gamma \mathrm{Re}^{0.6}[T_v - T_s] \tag{14}$$

As indicated above, $\bar{U}_R$, C_D, and Re are functions of τ since they all depend on particle velocity. The solution sought is of course the position of the particle $P(\theta,r,z)$, and its radius R as a function of time, which would, via the time derivatives, also provide the particle velocities u, v, and w relative to the blade. The history of particle flow, in particular its trajectory and rate of vaporization, can then be mapped in detail.

Equations (13) and (14) contain as parameters u_v, v_v, w_v and T_v. These are the characteristics of the superheated vapor which represent input data to be taken either from equations, tables, graphs or any other available separate solution. In most cases the presence of droplets should not influence the underlying flow so as to affect droplet dynamics too much, even though they may modify to some degree the vapor flow itself. However, should the resulting two-phase flow modify the original flow in a substantial way, some iteration between the particle equations and the pure vapor solutions may be required.

Equations (13) and (14) constitute an initial value problem and we need starting conditions in order to proceed. These conditions are supplied by the mode of injection, namely.

$\tau = 0$

Point of injection θ_o, r_o, z_o
Velocity of injection u_o, v_o, w_o
Particle size $\bar{R}_o = 1$
Relevant constants Re_o, β, γ

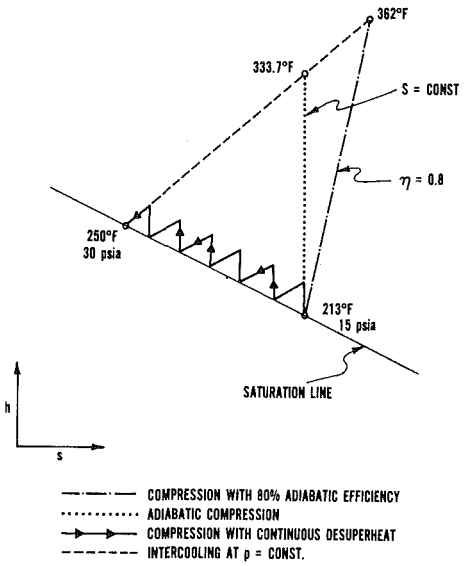

Fig. 4 Path of continuous desuperheat

With $\mathrm{Re} = \mathrm{Re}_o\ \bar{U}_R\bar{R}$ and C_D, as given by equation (7) evaluated at each point in time, the solution can then proceed in such time intervals $\Delta\tau$ as to provide solutions of sufficient accuracy. The equations were solved on a computer using a fourth order Runge-Kutta method. For particles in the range of 50–100μm, time intervals of $\Delta\tau = 0.01$ gave sufficiently accurate results. However, as particle sizes of the order of 1 μm were approached, a finer time mesh was required, in which case $\Delta\tau$'s of the order of 0.001 were used.

Parametric Solutions

Two sets of solutions will be presented here. The first serves as a brief introductory survey of the basic behavior of droplet flow in a rotating system. The second and main series deals with an actual compressor whose characteristics are described in detail in [5], along with its aerothermodynamic flow conditions. All cases deal with water being injected into centrifugally compressed superheated steam.

Preliminary Runs. In order to bring out some of the basic features of droplet behavior, a few preliminary runs were made under the following conditions:

- $\bar{u}_v = \bar{v}_v = \bar{w}_v = 0$
- $\bar{v}_v = 0.5; \bar{u}_v = \bar{w}_v = 0$

The first represents a case where the gas moves integrally with the blades. The results show that the drag imposed on the droplet tends to keep it at a nearly constant radius, in phase with the gas. Thus, the Coriolis and centrifugal forces seem to play a small part as compared to the viscous drag, at least for the 10 μm particle considered in this example. The second set of conditions represents a situation of constant gas velocity in the radial direction only. Small particles are completely dominated by the viscous drag; however 30 μm particles have sufficient inertia to remain in the flow field until they are caught up and struck by the upstream blade.

The rate of change in particle diameter due to evaporation, as shown in Fig. 3, seems to go through three stages. It is high at the beginning of injection, probably because at that point the relative velocity is high; it then tapers off, to increase again toward the end of the path. The latter increase is due to the decrease of particle size, which, as will be seen later on, yields higher rates of evaporation. Since the variation in mass is proportional to $(1 - \bar{R})^3$, the above variation in slope will be even more pronounced for the particle's rate of change of mass.

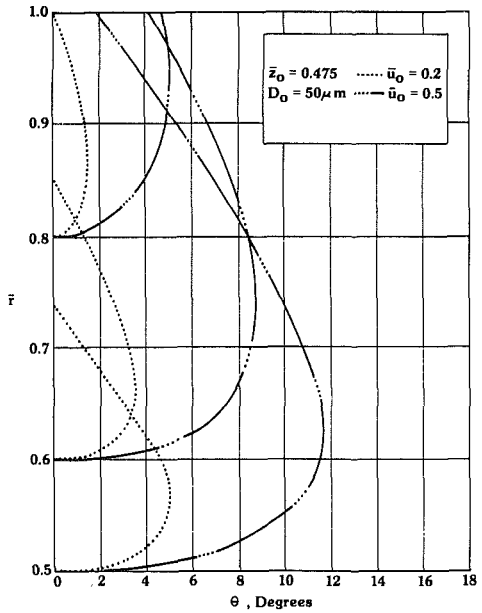

Fig. 5 Particle trajectories for injection from pressure side

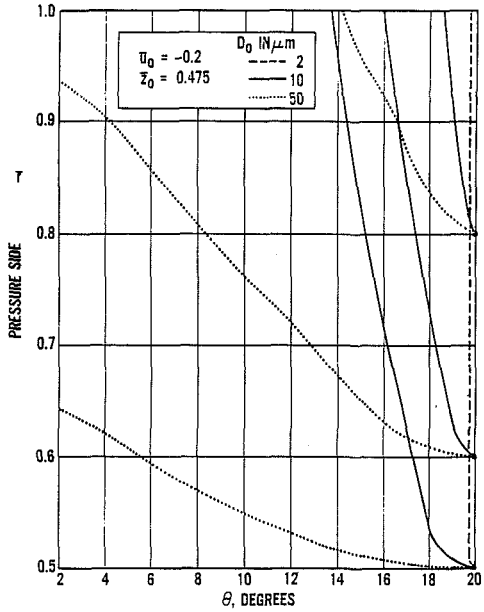

Fig. 6 Trajectories for different particle sizes

Centrifugal Compressor.

Compressor Characteristics. The required performance of the centrifugal compressor under consideration here is mapped out in Fig. 4. Other relevant data are as follows:

Mass of vapor flow - 0.9 kg/s (2 lb/s)
Angular speed - 3142 rad/s (30,000 rpm)
Maximum blade radius - $r_2 = 0.14$ m (0.455 ft)
Tip speed - 437 m/s (1433 ft/s)
Number of blades - 17 or $\alpha \simeq 20$ deg

Values of the velocities, pressures, and temperature throughout the flow field are documented in some detail in [5]. In summary fashion, their main characteristics are as follows:

- The static pressure rise in the compressor is 60 percent, yielding maximum superheat temperatures of the order of 28°C (50°F).
- Most of the compression occurs in the outer reaches of the blade, so that in the present context the inner half of the blade is of little interest.

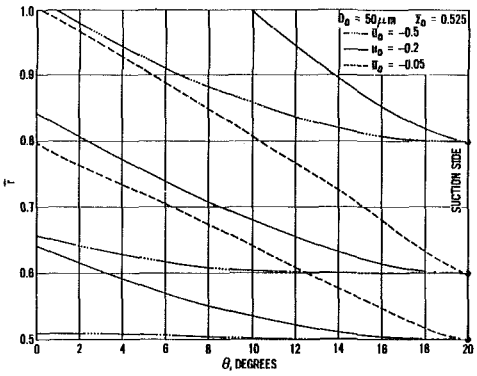

Fig. 7 Effect of varying u_o on particle trajectory

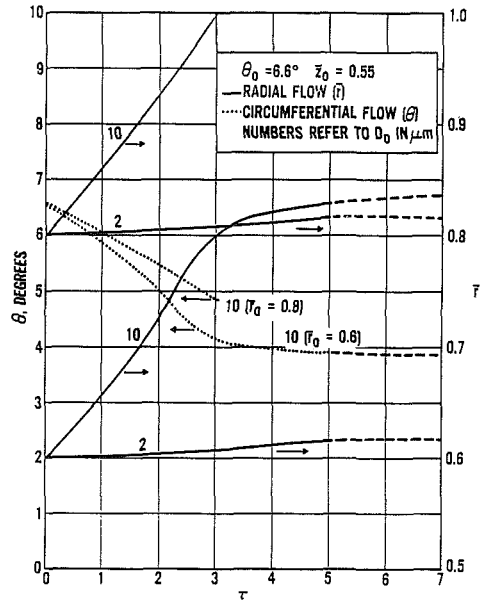

Fig. 8 Time history of particles for injection from hub wall

- In the outer half of the blade, the circumferential vapor velocities vanish and both the radial and axial components reach values equal to blade tip velocity.
- Velocities are higher on the suction side than on the pressure side; and higher near the shroud than near the hub.
- The circumferential velocities (u_v) are all negative; that is, they are all directed toward the pressure side of the blade. They decay rapidly as the straight radial portion of the passage is approached, so that they vanish at $\bar{r} > 0.55$. The radial velocities (v_v), on the other hand, are low in the curved portion and approach a maximum at about $\bar{r} = 0.8$.

Particle Trajectory and Evaporation. Solutions were obtained for particle injection at three different planes: on the pressure side with injection in the direction of rotation ($\theta = 0$); at the suction side with injection against the rotation ($\theta = 20$ deg); and from the hub surface ($z = 0.55$). Several injection radii were examined. The advantage of a low radius is that it provides the droplet with a longer trajectory in the channel and thus higher evaporation; however, it also increases the likelihood of collision with the walls, which is to be avoided. For the higher radius the conditions are reversed. Then, too, at any given radius the particle can be injected closer to the hub or to the shroud, that is at various values of $\bar{z}_o$.

Aside from the location of injection point, the next parameters of importance are the injection velocity and direction. Two velocities, 20 and 50 percent of tip velocity, were chosen which correspond to the pressure differentials that the centrifugal forces are likely to generate in the water

column. Finally, three particles sizes were examined: 2, 10, and 50 microns in diameter.

A summary of the more relevant results is contained in Figs. 5 through 8. The particle dynamics tied to the prevailing vapor velocities suggests the following:

• Injection from Pressure Side. Physically this mode of injection means that the particle has little opportunity to move away from the plane of injection. As a result, small particles whose inertia is low are, in most cases, struck by the pressure side of the blade. Thus no results are offered for particle sizes of 2–10 μm. Increasing the $\bar{u}_o$ velocity from 0.2 to 0.5 did not seem to make much difference. Likewise, runs in which the angle of injection was varied from 90 to 45 deg, i.e., with $v_o = \pm u_o$, did not improve the exiting chances, and in some cases made the situation worse .

• Injection from Suction Side. Injection against rotation, i.e., with the injection plane moving away from the particle, provides satisfactory trajectories, enabling the particles in most cases to exit from the chamber. Here, as seen from Fig. 6, lighter particles are preferred, as with the $D_o = 50$ μm particles the vapor does not succeed in sweeping them out the channel before they are struck by the approaching upstream blade. The very light particles are swept out of the channel along a path nearly parallel and very close to the injection plane ($\theta_o = 20$ deg). Here, in contrast to the situation with $\theta_o = 0$, the lower the injection velocity the better the exiting chances. Thus, as seen in Fig. 7, by reducing the injection velocity to nearly zero, and placing the injection point at $\bar{z}_o = 0.55$ even the $D_o = 50$ μm particles succeed in exiting. For the large particles collision with the pressure side of the blade occur whenever $|u_o| > 0.55$.

• Injection from the Hub Wall. Here injection near the pressure side of the blade ($\theta_o = 6\text{-}1/2$ deg) results in unsatisfactory trajectories due to the stagnant flow pockets prevailing there; injection near the suction side ($\theta_o = 13$ deg) improves the chances of particle exit. As shown in Fig. 8, the small particles tend to be lodged in stagnant pockets of vapor and remain there. A radius of injection higher than $\bar{r}_o = 0.5$ and particle sizes larger than $D_o = 10$ μm are required to assure particle exit, provided its injection is near the suction side of the blade.

• Particle Vaporization. Overall levels of vaporization are low for all cases, less than 5 percent. This is due primarily to the low levels of ΔT available, ($\sim$ 50°F). The smaller particles yield higher percentage levels of vaporization. Even though the actual mass of vaporization per particle is a product of the percentage Δm and m_o, still for a fixed rate of water injection the number of smaller particles present will be correspondingly higher. Consequently, the percentages represent the total mass of vaporization. For suction side injection the highest values are of the order of 4 percent; for hub wall injection (excluding the stagnant particle data which are meaningless) the highest values are of the order of 5 percent.

Optimum Injection System. Based on the results of the parametric study the design of the injection system for the prototype compressor could then proceed subject to the following considerations:

• The lower the injection point in the compression passage, the longer the droplet residence time, and thus better vaporization. However, low injection points raise the risk of droplet collision with, and erosion of, the passage walls.

• A large number and dispersion of orifices are desirable in order to maximize the spatial distribution of the droplet sprays within the compression passage. But here again, good dispersion of the droplet spray increases the risks of wall impingement; in addition, many orifices require a large number of radial channels in the blade, which the blade may not be able to accommodate.

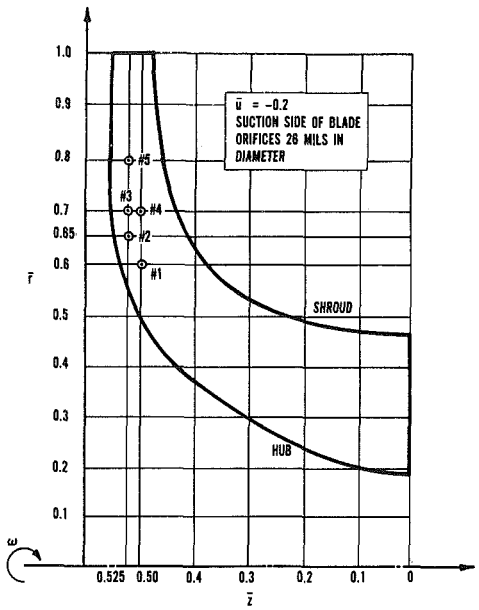

Fig. 9 Location of orifices

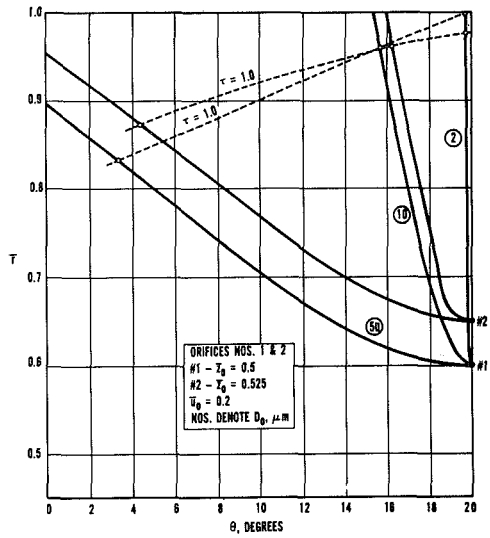

Fig. 10 Particle trajectories for orifices No. 1 and No. 2

• Higher injection velocities yield better atomization, higher evaporation rates, and better chances of traversing stagnant flow pockets; however, they also increase chances of collision and require more input power for centrifugal pressurization.

Based on the above, five injection ports were selected at the locations and initial conditions as shown in Fig. 9. This arrangement yields the following flow characteristics:

• As seen in Fig. 10, the heaviest particles in orifices 1 and 2 just impinge on the upper tip of the pressure side of the blade. This was done intentionally in order to extend the droplet fan over the widest possible area. For all other cases the droplets succeed in emerging from the passage without colliding with any of the surfaces.

• The smallest particles, $D_o \leq 2$ μm, are swept out of the channel along a path nearly parallel and close to the injection surface. The heaviest particles, due to their larger inertia, penetrate the deepest in the blade passage.

• For trajectories of the particle in the $\bar{z}$-plane, i.e., in plane at the blade (the previous plots were in the plane of rotation $\theta\bar{z}$), there is no variation in the axial excursion between the large and small particles.

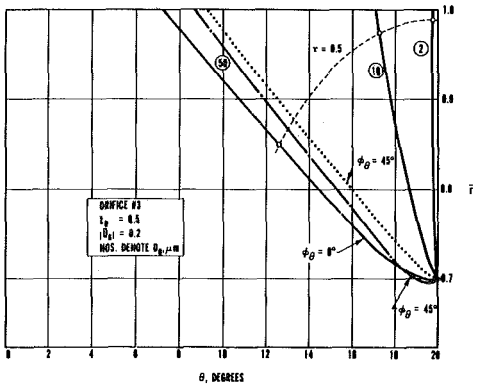

Fig. 11 Particle trajectory for orifice No. 3

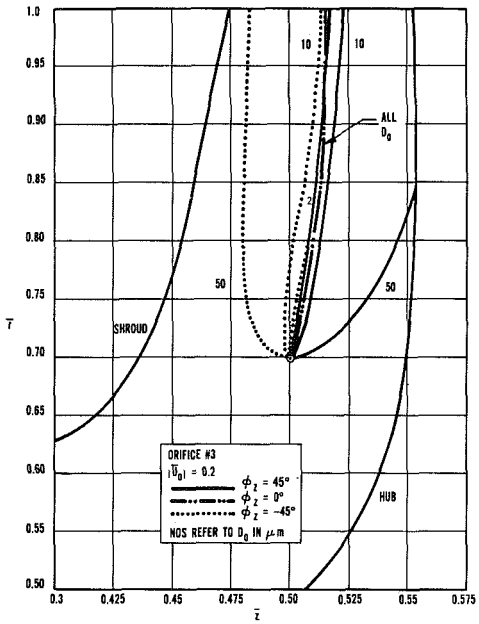

Fig. 12 Effect of varying ϕ_z on particle trajectory, orifice No. 3

• The residence time of the particles decreases with an increase in injection radius, $\bar{r}$, as expected. Also, the heavier particles have a longer residence period, as can be surmised from the τ = constant plots in Figs. 10 and 11. The residence times range from about $\tau = 0.5$ to $\tau = 1.3$ which for $\omega = 3152$ rad/s yields

$$0.16 \times 10^{-3} \text{ s} < t < 0.37 \times 10^{-3} \text{ s}$$

• Near the exit from the path, the small particles, 2 μm < D_o <10 μm, have a nearly zero relative circumferential velocity ($u_f \sim 0$); whereas the particles in the 50 μm range have relative velocities of the order of 30 percent. This is of some significance from the standpoint of erosion as the smaller particles, even where they impinge on the blade, would do so carrying negligible momentum and thus cause no damage. This once again emphasizes the great importance of obtaining small particle sizes.

Effect of Injection Angle. We shall consider the effects of varying the injection angle, while keeping the total velocity constant, i.e.,

$$\bar{U}_o = [\bar{u}_o{}^2 + \bar{v}_o^2 + w_o^2]^{1/2} = 0.2$$

In discussing the results for various injection angles we shall maintain the following convention:

• $\phi_\theta = 0$ is the injection normal to the suction plane or $\bar{U}_o = -0.2$

• $\phi_\theta = 45$ deg refers to a velocity vector tilted in the $r\theta$-plane 45 deg toward the exit, i.e., toward positive $\bar{r}$

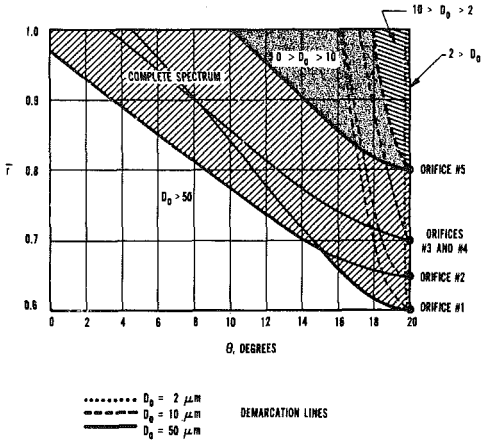

Fig. 13 Domains of droplet sizes

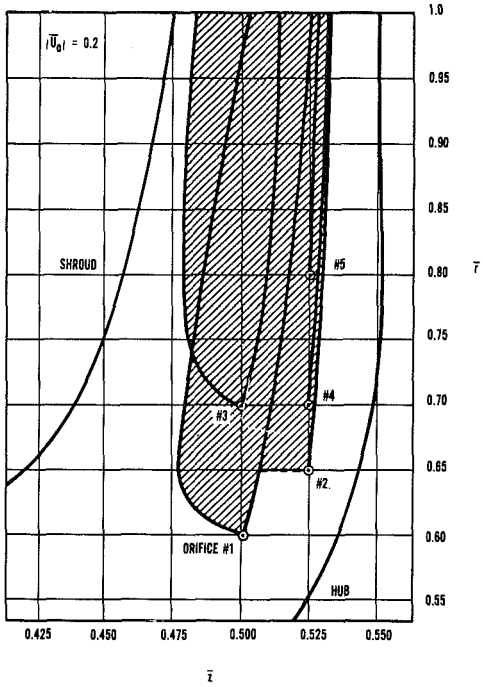

Fig. 14 Domain of droplet flow in blade plane

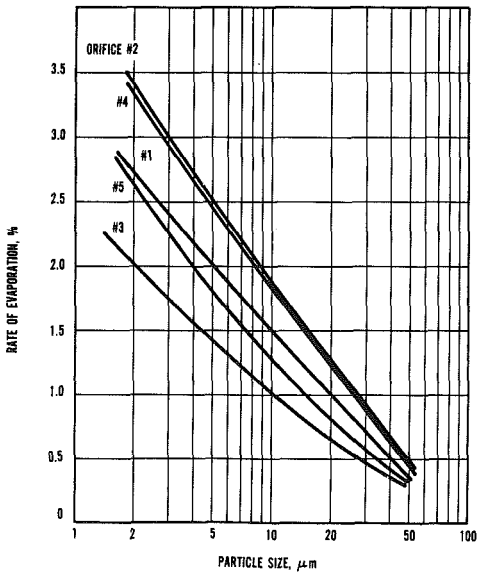

Fig. 15 Rate of droplet evaporation

• $\phi_\theta = -45$ deg is the same as above but with a tilt away from the exit ($-\bar{r}$)

• $\phi_z = 45$ deg refers to a velocity vector tilted in the (θz)-plane 45 deg toward the hub ($+z$)

• $\phi_z = -45$ deg is the same as above with a tilt toward the shroud ($-z$)

For small particles $D_o \simeq 2$ μm, varying the injection angle has no effect whatsoever. Also the vaporization rates are little affected by varying the orientation of the velocity vector. Furthermore, as shown in Fig. 11, the effect of varying ϕ_θ on the droplet trajectories are also minor. Thus the only area of possible interest is that pertaining to the effect of varying the angle ϕ_z on the behavior of the larger droplets.

The effects of orienting the flow 45 deg either towards the hub or towards the shroud are shown in Fig. 12. First, it will be noted that for either plus or minus values of ϕ_z the trajectories of the particles below 10 μm are very close to that of normal injection. However, there are important effects on the trajectories of the heavier particles. For $\phi_z = +45$ deg the result is that the larger particles collide with the wall of the hub. However directing the flow toward the shroud, $\phi_z = -45$ deg, produces in both orifices #1 and #3 a significant excursion away from the $\phi = 0$ solution.

Comparing the results of Figs. 11 and 12 with the results for normal injection, the conclusion is reached that orienting the water jet towards the shroud ($\phi_z = 45$ deg) can at times be extremely useful for the following reasons:

• Whereas normal injection produces sheetlike sprays in the rz-plane, that is, particles of various sizes follow the same trajectory, orientation towards the shroud produces a wide and satisfactory fanlike spray also in the plane of the blade. This, of course, is of importance in that such a fanlike distribution inundates the maximum space with liquid droplets and maximizes vaporization.

• Whereas in orifice #1 normal injection led to collision with the pressure side of the blade for $D_0 = 50$ μm, an angle of $\phi_z = -45$ deg eliminates that danger yielding a trajectory in which even the heaviest particles exit the chamber with ease.

To give a comprehensive view of the spatial domain that the sprays from the five orifices are expected to cover, the trajectories from all the orifices were superimposed on each other. Figure 13 gives the expected domain of various particle spectrums in the plane of rotation ($r\theta$); while Fig. 14 gives the expected domains in a plane passing through the axis of rotation ($z\theta$). Finally, Fig. 15 gives the expected rates of droplet vaporization as a function of size for the various orifices.

Conclusions

Injection System.

• Orifices. A large number should be used, so that their diameter is as small as possible while their length/diameter ratio is high. The orifices, barring other considerations, should be located at points of high gas velocity.

• State of the Injected Coolant. Liquids of low viscosity and at the highest possible temperature should be used. It should have high enthalpy of vaporization and low surface tension. The lowest possible ratio of (liquid/gas) flows should be aimed for.

Mode of Injection.

• Injection from the pressure side nearly always leads to collision with the injection surface and is not recommended.

• Injection from the hub wall leads to particle arrest due to stagnant velocity pockets and is also not recommended.

• Injection from the suction side at $\bar{r}_o \geq 0.5$ is the most satisfactory mode.

• Angles of injection slanted towards the shroud are useful in widening the spray in the meridional plane and in reducing the chances of collision for larger drops.

• High injection velocities do not change substantially the particle trajectory for large particles; lower injection velocities are, in fact, preferable.

• Small size particles, below 10 μm in diameter, increase the chances of particle exit.

Evaporation and Particle Size.

• Droplet size is probably the most crucial parameter in a liquid injection system. Smaller particles have the highest rates of vaporization, whereas large drops are also more likely to collide with walls.

• For a $\Delta T = 28°C$ (50°F) and $D_o = 2$ μm the maximum values obtained (for particles with assured exit from the channel) were 4 percent of the original mass; for $\Delta T = 280°C$ (500°F) evaporation of the order of 20 to 30 percent of original mass can be realized.

Acknowledgments

This research was performed under Subcontract No. 36X-24713C with Mechanical Technology Incorporated under Union Carbide Corporation Contract W-7405-eng-26 with the U.S. Department of Energy.

Credit is due to Mr. Andrew Tuzinkiewicz of MTI who provided the input material on the aerodynamics and thermodynamics of the steam flow, and to Mr. Herman Leibowitz of MTI for his interest and support in carrying out the program.

References

1 Dakin, J. T., "Viscous Liquid Films in Nonradial Rotating Tubes," GE Report No. 77CR133.

2 Hussein, M. F., and Tabakoff, W., "Computation and Plotting of Solid Particle Flow in Rotating Cascades," *Computer and Fluids*, Vol. 2, No. 1-A, Pergamon Press, 1974, pp. 1-55.

3 Schlichting, H., *Boundary Layer Theory*, McGraw-Hill, 1955.

4 McAdams, W. H., *Heat Transmission*, 3d ed., McGraw-Hill, 1954.

5 Pinkus, O., "Particle Dynamics in a Rotating High-Speed Vapor," MTI Report No. 80TR19, Mar. 1980.

G. A. Whitlow
Mem. ASME

S. Y. Lee
Mem. ASME

P. R. Mulik

R. A. Wenglarz
Mem. ASME

Westinghouse Research and Development Center, Pittsburgh, Pa. 15235

T. P. Sherlock
Westinghouse Combustion Turbine Systems, Concordville, Pa.

A. Cohn
Electric Power Research Institute, Palo Alto, Calif.
Mem. ASME

Combustion Turbine Deposition Observations From Residual and Simulated Residual Oil Studies

Burning residual oil in utility combustion turbines and the consequent deposition on blades and vanes may adversely affect reliability and operation. Corrosion and deposition data for combustion turbine materials have been obtained through dynamic testing in pressurized passages. The deposition produced by the 1900°F (1038°C) combustion gases from a simulated and a real residual oil on cooled Udimet 500 surfaces is described. Higher deposition rates for the doped fuel than for the real residual oil raised questions of whether true simulation with this approach can be achieved. Particles 4-8 μm in diameter predominated in the gas stream, with some fraction in the 0.1 - 12 μm range. Deposition rates seemed to be influenced by thermophoretic delivery of small molten particles, tentatively identified as magnesium pyro and metavanadates and free vanadium pentoxide, which may act to bond the larger solid particles arriving by inertial impaction to turbine surfaces. Estimated maintenance intervals for current utility turbines operating with washed and treated residual oil agreed well with field experience.

Introduction

The fuels traditionally used to power utility combustion turbines, natural gas and distillate oil, are becoming less desirable because of rising costs and governmental restrictions on their use. In the future, crude and residual oils and coal-derived liquids and gases will probably fuel combustion turbines. These fuels will contain elements that can affect the reliable operation of the combustion turbine by causing corrosion of the turbine hot parts and/or by leading to increased deposition of combustion products on the turbine vanes and blades, resulting in lower efficiency and power output.

To understand better the problems associated with burning lower-grade fuels, Westinghouse and the Electric Power Research Institute (EPRI) developed a program to obtain deposition and corrosion data for combustion turbine materials through dynamic testing in pressurized passages. The threefold objective of this research was to:

- Optimize metal component temperatures based on corrosion/deposition considerations
- Establish trade-offs between metal temperature, performance, maintenance, and reliability
- Develop a predictive model for deposition rates in combustion turbines burning low-grade, ash-bearing fuels that is capable of integrating laboratory data and field experience

Results from initial, short-term tests with washed and unwashed residual oil, describing deposition and corrosion screening studies, were the subject of a previous paper [1]. The second test series, described in this paper, covers particulates in the gas stream and the resulting deposits from the 1900°F (1038°C) combustion gases produced in the combustion of simulated and real residual oil. A deposition modeling approach has enabled turbine maintenance intervals to be estimated from these deposition data and to be compared with current operating experience.

Two additional, long-term tests ($\geq$150 h) burning residual oil at gas temperatures of 2300°F (1260°C) have recently been completed and the resulting deposition information analyzed [2].

Background on Residual Fuel Combustion and Usage

A recent survey conducted with users of over 100 combustion turbines burning residual or crude oil [3] concluded that improperly washed or inhibited fuel or impurities in the inlet air were responsible for the limited hot gas path

Contributed by the Gas Turbine Division of THE AMERICAN SOCIETY OF MECHANICAL ENGINEERS and presented at the 27th International Gas Turbine Conference and Exhibit, London, England, April 18-22, 1982. Manuscript received at ASME Headquarters December 7, 1981. Paper No. 82-GT-87.

Table 1 Fuel types and trace element analyses (ppm)

Fuel	Mg	Ca	V	Pb	Na	K	S[a]
Washed residual oil with KI-16 magnesium additive Simulated residual oil	255	0.9	85.0	0.5	3.0	0.2	0.66
No. 2 distillate oil plus the standard dopant	171.9	5.7	57.3	-	0.6	-	0.33
No. 2 distillate oil plus the zero Ca containing dopant	171.9	0	57.3	-	0.6	-	0.33

[a]weight percent

corrosion observed. Of the many problems that were presented, however, deposition was a prime concern.

Much of the available data in the open literature on the effects of residual fuel oil combustion on deposition consists of field experience from utility operation [5-7]. Controlled experiments have been performed by several companies using simulated residual oil in the form of a doped No. 2 distillate oil [8-9], but there is some question on the direct comparison between data obtained in this way and that from testing residual oil. Parametric studies oriented to gas turbine rather than boiler applications are not readily available. One example is the General Electric study on a deposition comparison of synthetic and real residual oil [10] which was for real residual fuel, unfortunately limited to firing temperatures of 1800°F (982°C). Another example is the work of Nomura et al. [11] in which deposition from unwashed, untreated residual fuel oil was examined. Deposits were found to be principally sodium-vanadium-containing compounds. The current study, therefore, is designed to satisfy some of the deficiencies in the data base regarding the effects of the combustion of residual fuel oil. Some of the initial data were very encouraging [1] in that corrosion was not evident with treated fuel, but deposition from treated residual oil was such that a better understanding is required if reliable, continuous turbine operation is to be attained.

Currently, Florida Power and Light (FPL) is burning washed residual oil in their 500-MW combined-cycle plant located in Palatka. An evaluation [5,12] of corrosion and deposition on various components from this plant concluded that the combination of fuel treatment, corrosion inhibitors, and metal surface temperature control can effectively inhibit vanadium-induced corrosion. Deposition of magnesium vanadate and sulfate was not excessive, and, indeed, FPL has now converted all four units to residual oil operation. The combustion turbines are operated at full power, and high starting reliability and overall availability have been achieved.

Although confidence has been generated through thousands of hours of successful operation with Westinghouse turbines, deposition will always be a concern when residual fuels are burned because of the high ash concentration in the fuel and the magnesium added to control vanadium corrosion. The deposits formed can be removed by water washing the turbine, but only with the unit off line and with consequently reduced unit availability. On-line cleaning techniques, such as nutshell injection and thermal cycling, have not been as effective as water washing in removing deposits, but they will continue to be developed to avoid the loss of availability.

Currently, burning residual fuels may generate problems in corrosion, deposition, fuel handling, and combustion, for which there are or will be solutions, but the decision to burn residual oil will probably be dictated by economic considerations.

Materials and Experimental Techniques

The washed residual oil obtained from the Putnam station of FPL was treated with KI-16 magnesium additive (supplied by the Tretolite Division of Petrolite) to inhibit vanadium corrosion. The magnesium-to-vanadium ratio was three on a weight basis. The two doped distillate fuels used were prepared by blending given quantities of dopant (supplied by Tretolite) and No. 2 diesel fuel. The dopant was supplied with a magnesium-to-vanadium ratio of three on a weight basis. Trace element analyses for both fuels are detailed in Table 1.

These fuels were burned in the Westinghouse Research and Development Center pressurized-turbine test passage (303.9 kPa [3 atm]), which utilizes preheated compressed air in 6-in. (15.24-cm) dia, film-cooled combustor. Fuel is injected into the primary combustion zone and burned with compressed air. Combustion gases are then mixed with secondary cooling air to attain the desired turbine inlet temperature. Downstream of the combustor exit thermocouples, the flow area is reduced and the gas velocity increased to ~600 fps (~183 m/s). At this location, ~24 in (61 cm) from the combustor outlet, duplicate test specimens are exposed to the combustion gases. These cylindrical Udimet 500 (54Ni, 18Cr, 18.5Co, 4Mo, 3Al, 3Ti) alloy specimens (2-in. [5.1-cm] long × 1-in. [2.5-cm] dia × 1/8-in. [3.2-mm] wall thickness) were cooled with ambient compressed air introduced from the top and instrumented with thermocouples in the specimen wall that measured metal temperature.

Typically, the test passage was fired up with the desired fuel while the specimens were held in a retracted position from the gas stream. When test conditions were reached, the specimens were lowered into the gas stream. The procedure was reversed during a shutdown. The number of shutdowns within a given test was a function of factors such as fuel mixing and equipment maintenance. The overall average metal temperature was maintained constant by adjusting the cooling airflow rate, but the temperature distribution external to the specimen was dependent on the gas temperature pattern factor.

A water-cooled, isokinetic, retractable sampling probe provided information on particulates in the gas stream. It consisted of inner and outer tubes with cooling water circulating in the annular region. A ceramic sampling substrate supported on a perforated stainless steel disk was contained in a cavity at one end of the probe body. During operation, the probe was inserted directly into the hot, pressurized test passage and the appropriate sampling volumetric flow rate for isokinetic conditions established on a rotameter in the sampling train. Exposure periods were varied from 15 to 45 min and a minimum of three samples procured per test series.

Great care was necessary in evaluating the Udimet 500 specimens because of the fragility and tenuous adherence of the deposition products. After determining weight change, we measured deposit thicknesses at different locations on the specimens to relate deposition-to-gas impingement and flow perturbations. Both X-ray diffraction and scanning electron metallography were used to provide information on deposit chemistry and morphology. Selected specimens were examined metallographically for corrosion and deposition using a kerosene lubricant in the sample preparation to prevent loss of water/alcohol soluble components from the

Table 2 Deposition characteristics for Udimet 500 specimens exposed to the combustion of washed residual oil and doped no. 2 distillate oil

Test No.	Gas temp., °F(°C)	Metal temp., °F(°C)	Exposure time, h	Deposition rate, mg/h	Maximum deposit thickness, mils(μm)
Washed residual fuel oil (with KI-16 Mg additive)					
6	1900(1038)	1350(732)	17.5	15	8(200)
7	1900(1038)	1350(732)	20	25	9(225)
Doped No. 2 distillate fuel oil					
5 Std. dopant	1900(1038)	1250(677)	20	60	26(650)
8 Zero Ca dopant	1900(1038)	1350(732)	20	23 28	25(625)[a] 56(1400)[a]

[a]These represent high points in the deposit; typical thicknesses were 1 to 5 mils (25 to 125 μm).

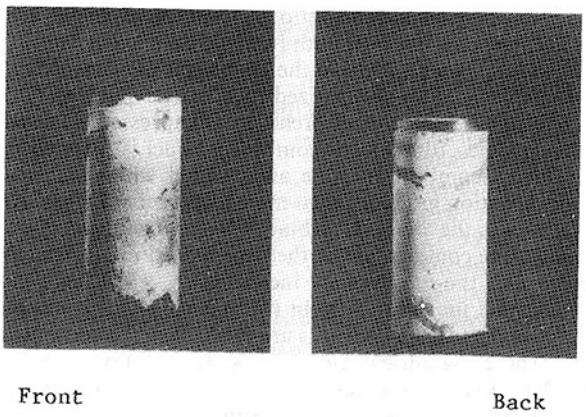

Fig. 1 Surface appearance of Udimet 500 specimens after exposure to hot combustion gases generated from the combustion of a washed residual fuel (KI-16 Mg additive) in test 7 (Max. deposit thickness: 8.2 mils; T_{gas} = 1900°F (1038°C); T_{metal} = 1350°F (732°C) 29.1 mg/h)

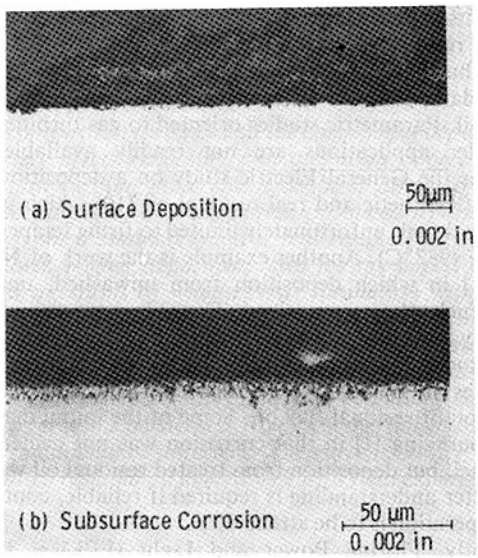

Fig. 2 Cross-sectional micrographs of a Udimet 500 specimen exposed to hot combustion gases in test 7 (washed residual with KI-16 Mg additive). Section taken ~3/4 in (~ 2 cm) from bottom of sample at the front impingement region.

deposit. These experimental data on deposition were compared with theoretical predictions to permit calculation of turbine maintenance intervals and comparison to field experience.

Results

The deposition characteristics for both types of fuels examined in this study are summarized in Table 2.

Washed Residual Oil. For tests 6 and 7, generated at 1900°F (1038°C) gas temperature and 1350°F (732°C) metal temperature, deposition rates of 15 to 25 mg/h, obtained from weight change determinations, were comparable to those obtained in our previous studies [1]. The buildup of deposit on the leading edge of the specimens reached a maximum, as shown in Table 2, but it was typically 3 to 6 mils (75 to 150 μm) for the residual oil tests.

Visual examination of the deposition revealed colors varying from white to yellow-brown to greenish yellow, and reference to Fig. 1 clearly shows their fragility and tenuous adherence to the substrate. The deposits have apparently flaked during either the test, the thermal cycle, or the disassembly. Any interpretation of significant differences in deposition values, therefore, must take this into consideration.

In typical cross-sectional photomicrographs taken close to the bottom end of a specimen shown in Fig. 2, deposition is shown to be concentrated on the front or gas impingement face of the sample. Less deposition was observed in this test, however, than in test 5 for the No. 2 distillate fuel with standard dopant (i.e., simulated residual oil). Hot corrosion attack of the Udimet 500 substrate was also evident.

X-ray diffraction analyses of the deposits are summarized in Table 3. Principal constituents in deposits from test 7 were MgO, hydrated $MgSO_4$ and $Mg_3V_2O_8$, with the possibility of a calcium-containing vanadate. The previous test (No. 6), which burned the same residual fuel, resulted in comparable deposit chemistries, except that a V_2O_5 phase was present, and the calcium was found to be associated with the $MgSO_4$ phase rather than the $Mg_3V_2O_8$ phase.

Electron microprobe analyses performed on polished cross sections of deposits from these washed residual fuel tests confirmed the presence of magnesium, vanadium, sodium, nickel, and chromium as major constituents, together with significant quantities of oxygen, calcium, and sulfur. In test 6, a near-surface region of the deposit was found to exhibit a higher concentration of sulfur, silicon, calcium, and aluminum.

Simulated Residual Oil. For these doped No. 2 distillate fuel tests, apart from the dopant chemistry differences with respect to calcium, the metal temperature for the standard dopant test (No. 5) was 1250°F (667°C), versus 1350°F (732°C) for the zero calcium dopant test (No. 8). These differences are reflected in the much higher deposition rates

Table 3 X-ray diffraction analyses of deposits from specimens exposed to hot combustion gases in the pressurized test passage

Test No.	Temperature, °F(°C) Gas	Metal	Time (h)	Deposit chemistry Major	Minor
Residual fuel with KI-16 Mg additive					
[contains 255 Mg, 85V, 0.9 Ca (ppm) and 0.7 wt % S]					
6	1900 (1038)	1350 (732)	17.5	MgO $MgSO_4$ V_2O_5	$Mg_3V_2O_8$ $CaMg_3(SO_4)_4$
7	1900 (1038)	1350 (732)	20	$MgSO_4 7H_2O$ MgO	$Mg_3V_2O_8$ $CaZMgV_3O_{12}$ [a]
Doped No. 2 distillate fuel					
[5.7 Ca, 172 Mg, 57 ppm V, 0.33 wt % S]					
5 Std. dopant	1900 (1038)	1250 (677)	20	MgO, $MgSO_4$ $Mg_3(PO_4)_2$, V_2O_5	$Mg_3V_2O_8$ $CaMg_3(SO_4)_4$
8 Zero Ca dopant	1900 (1038)	1350 (732)	20	MgO $Mg_3V_2O_8$	$MgSO_4 \cdot 6H_2O$ $MgSO_4 \cdot 7H_2O$

[a] Z = Na or Li

Table 4 Summary of particulate probe deposit characterization [a] (gas temperature: 1900°F (1038°C)

Test	Fuel type	Particulate Size (μm)	Shape	Principal constituents
11	Residual oil with Mg additive	4-12	Spheres	Mg, S some V, K, Na, Ca
		1-3	Spheres	Mg, some Na
12	No. 2 distillate oil with zero Ca dopant	5-15	Platelets	Mg
		2-3	Spheres	Mg, V
13	No. 2 distillate oil with std. Ca dopant	Larger fused shapeless agglomerates		Mg
		1-3		Mg, V some S, Ca P, Cr Fe

[a] Data obtained from SEM/EDAX analyses – elements with atomic number less than Na (i.e., <11) such as O or C – may well be present but are not detected by this technique.

measured for the standard dopant (test 5), as detailed in Table 2.

The photographs of typical surface deposits from these tests, shown in Fig. 3, show that maximum deposition occurred at isolated points; frequently there was an air space between the raised, pimplelike deposit and the underlying metal substrate.

Colors varying from white to greenish yellow were evident on deposit surfaces, and from their fragility and tenuous adherence to the substrate seen in Fig. 3, it was apparent that the deposits flaked during either the test, the thermal cycle, or the disassembly.

X-ray diffraction analyses of the deposits obtained by scraping samples from selected areas and then grinding the powder into a composite sample are shown in Table 3. The same compounds were found in these samples as in those from the washed residual fuel tests. Reflecting the fuel-additive chemistry, there was no evidence of a calcium-containing phase in the test with zero calcium dopant. Additional evaluation of these deposits using the electron beam microprobe and the scanning electron microscope generally confirmed the X-ray diffraction data. A typical example of the range of elements found in a deposit from the standard dopant test (No. 5) is shown schematically in Fig. 4.

The presence of calcium in the deposits in test 5, together with higher deposition rates compared to the residual fuel and zero calcium dopant tests, suggests, as other workers have reported [9] that the sticking tendency of the deposited particles was enhanced.

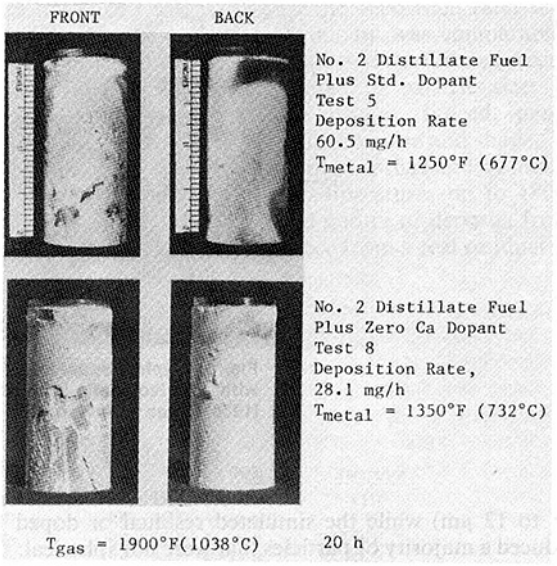

Fig. 3 Surface appearance of Udimet 500 specimens after exposure to hot combustion gases generated from the combustion of doped No. 2 distillate fuel oil in tests 5 and 8

Particulate Probe Data. From the summary of the sampling results presented in Table 4, one can see that burning of residual fuel produces essentially spherical particles

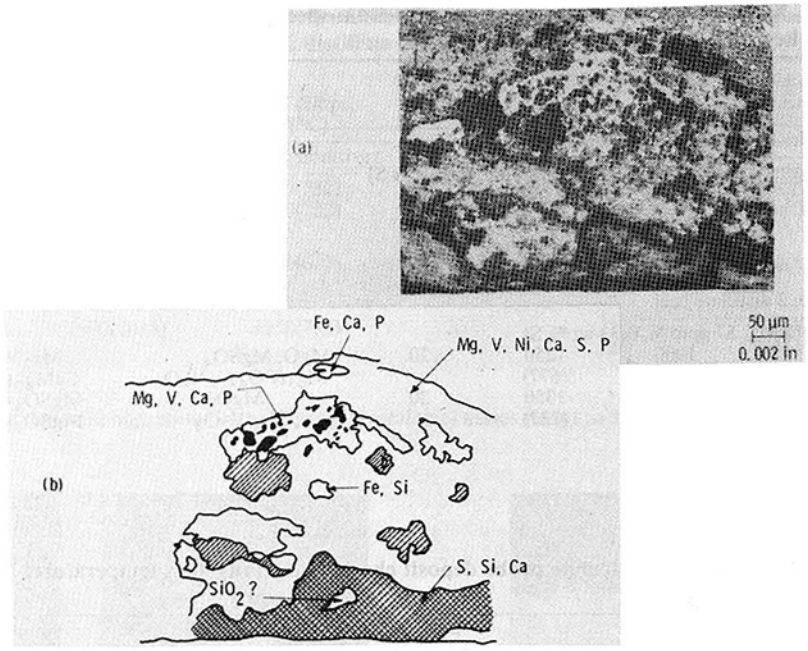

Fig. 4 Deposit on a Udimet 500 sample after exposure to hot combustion gases in test 5 (doped distillate fuel) (*a*) cross-sectional photomicrograph, and (*b*) schematic showing elemental distribution in deposit (from electron microprobe scans)

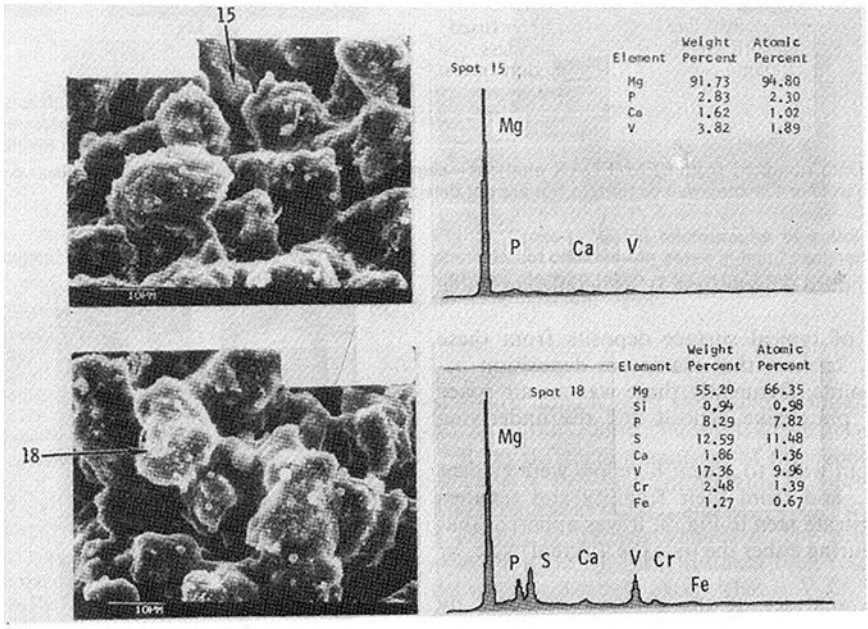

Fig. 5 Typical scanning electron micrographs of particles captured with the isokinetic sampling probe (doped distillate at a 1900°F [1038°C] gas temperature)

(<1 to 12 μm) while the simulated residual or doped fuels produced a majority of particles that were not spherical; those that were produced tended to be significantly smaller (1 to 3μm). In the case of the Ca-free fuel, 5 to 15 μm platelets were the "typical" particle size and shape, in contrast with the even larger and more irregular particles produced by the addition of Ca to the fuel. These are termed "fused shapeless masses" in Table 4, and based on these observations, it appears that calcium served as a binding agent that enhanced deposition. Figure 5 shows the appearance of the "fused shapeless masses" captured by the particulate probe when doped distillate containing calcium is burned. It is apparent from the figure that calcium, while not the principal element present, certainly plays a key role in the deposit chemistry.

The second observation that can be made from these data deals with a comparison of the deposit chemistry of the doped fuels and the residual oil. For the former, the larger particles were essentially MgO. On the other hand, the residual oil yielded a deposit consisting not only of magnesium oxides, but also of vanadates and sulfates.

Discussion of the Deposition Data

In the early formulation of this program, we emphasized deposition effects and assigned corrosion effects less importance. The data have confirmed this division, in that deposition was in all the tests a major consideration and corrosion of the test specimens was only of concern in the early, unwashed residual fuel test [1] and in a 300-h, higher temperature, long-term test reported elsewhere [2].

Deposition Rates. For tests involving the combustion of simulated residual oil, deposition rates were found to be dependent on the dopant chemistry. With the standard dopant (test 5), rates were approximately three times higher than for the zero calcium doped fuel (test 8). This increase is attributed to the 5.7 ppm calcium present in the fuel containing the standard dopant, increasing the sticking tendency for the particles deposited from the gas stream onto the specimen surface. Note that deposition rates for No. 2 distillate fuel containing the zero calcium dopant were comparable for the residual fuel (test 7), even though the former exhibited higher peak deposit thicknesses. This similarity may or may not have been fortuitous.

Deposit Characterization. The deposits in these short-term tests with both residual fuels were generally very loosely attached to the substrate. Although samples were examined metallographically, information on individual particle sizes in the deposits was not obtained. The presence of 5.7 ppm calcium in the No. 2 distillate fuel containing the standard dopant is thought to be responsible for the somewhat harder, more tenacious deposits observed on specimens from test 5. These observations were confirmed by the particulate probe findings of 1 to 3 μm dia spherical particles and fused masses of particles for this test. Urbas and Tomlinson [9] have reported that for both real and simulated residual oil, 1.3 ppm calcium in the fuel greatly enhanced the deposition rate and also promoted the formation of hard deposits. The data from tests 5 through 8 would, therefore, seem to be consistent with their observations, since reference to Table 3 shows that combustion of residual fuel containing 0.9 ppm calcium also resulted in a mixed sulfate phase containing both calcium and magnesium.

The combustion of residual fuel containing a magnesium additive produced both large (6–12 μm) and smaller (<2 μm) particulates in the gas stream at 1900°F (1038°C), and it is likely that many of these ended up in the deposits subsequently examined on the specimens from test 6 and 7.

Analyses of Deposits. The considerable volume of data collected on the chemistry of the deposits generally indicated MgO to be their major constituent, with $Mg_3V_2O_8$ and $MgSO_4$ also present. These compounds arose from the reaction between the magnesium additive, the combustion air, and the fuel impurities, vanadium and sulfur. Other compounds detected included vanadium pentoxide (V_2O_5), which has a relatively low melting point (1240°F [671°C]), and a magnesium phosphate (probably originating from impurities in the dopant and/or the distillate fuel).

Corrosion Observations. The Udimet 500 alloy exposed to hot combustion gases in these tests was not affected by corrosion when washed and treated residual fuel or the doped distillate fuel was used. In the initial tests with unwashed, untreated fuel, some corrosion was observed, caused by sodium sulfate attack, but no rapid corrosion was observed with metal temperature <1000°F (<538°C), even in the absence of the corrosion inhibitor, magnesium [1]. Additional studies may be necessary, however, to determine the effects of long-term continuous and intermittent operation on this phenomenon.

Fuel Chemistry Considerations. The observations that vanadium pentoxide may be present in the deposits/gas stream may cause concern about the suitability of the accepted Mg/V ratio of 3. Apparently, even though the magnesium is present in excess of that required to combine with the vanadium in the fuel, there is still vanadium pentoxide (and possibly Mg vanadates) formed that can act as binder phases in these deposits. If V_2O_5, a relatively low melting-point constituent of deposits, can be completely combined with magnesium in the form of a vanadate or maybe in some other preferred form, this so-called glue will be absent, and deposit buildup may be reduced.

Simulated Residual Fuel Oil Testing. Doped No. 2 distillate fuel tests simulating residual fuel oil were run in order that some comparison might be made with the results from a parallel EPRI program on doped distillate fuel containing calcium at Detroit Diesel Allison (DDA) [8]. Based on the deposition data discussed earlier, where considerable differences were noted in deposition behavior for simulated and real residual fuel, it would seem that a good simulation was not achieved with the DDA dopants. This may have been partially due to differences in trace element concentrations in the fuels. However, the fact that the deposition rate for the fuel containing the zero calcium dopant was comparable to that for the residual fuel is considered fortuitous, because significantly differences were noted in particle sizes and shapes in the particulate probe studies. Indeed, particle arrival rates are known to be sensitive to size and shape. This observation contrasts with the data of Urbas and Tomlinson [10], who found that at firing temperatures up to 1800°F (982°C) the chemical and physical nature of deposits from a synthetic fuel were the same as those from a real residual fuel oil.

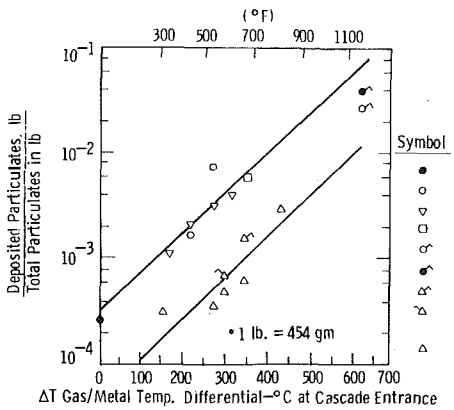

Symbol	Test	Inlet Temp. °C	Inlet Temp. °F	Fuel	Reference
●	Uncooled 15 MW Turbine	752	1385	Residual	(11)
○	Cooled Cascade	800	1472	Residual	(11)
▽	Cooled Cascade	900	1652	Residual	(11)
□	Cooled Cascade	1100	2012	Residual	(11)
◇	DDA Cascade	1037	1900	Doped Distillate	This Paper
◆	DDA Cascade (Adjusted)	1037	1900	Doped Distillate	This Paper
◇	Cooled Cylinder	1037	1900	Doped Distillate	This Paper
△	Cooled Cylinder	1037	1900	Doped Distillate (No Calcium)	This Paper
△	Cooled Cylinder	1093/1025	2000/1875	Residual	(1)

Fig. 6 Deposition results on cascades and cylinders

Extrapolation of Data to Utility Turbines

The data obtained during this test program, together with mechanistic evaluations of the dominant deposition mechanisms, have enabled us to make initial estimates of deposit buildup rates and maintenance intervals for turbines burning washed residual oil treated with a magnesium additive.

Deposition Mechanisms. Deposition buildup in combustion turbines depends on several types of mechanisms. These include those of:

- Particle delivery to turbine surfaces
- Adherence and removal of particles delivered to turbine surfaces
- Gross detachment (spallation) of previously built-up deposits

The primary mechanisms of particle delivery in turbines are inertial impaction, turbulent eddy diffusion, Brownian diffusion, and thermophoresis [13]. The dominant delivery mechanism depends on the sizes of the particles entrained in the turbine expansion gas. Inertial impaction dominates on vane and blade pressure surfaces for particle diameters larger than a few microns [14], but turbulent eddy diffusion tends to dominate for diameters of about 1 μm down to a diameter that depends on the degree of vane or blade cooling. For highly cooled surfaces, thermophoretic delivery (which increases with the temperature differential between the gas and surface) becomes important for particle diameters perhaps as large as 0.5 μm, while for uncooled surfaces Brownian diffusion begins to dominate in the 0.1 to 0.05 μm particle diameter range. Once particles arrive at a turbine surface, deposit buildup depends on the balance of adherence forces and removal forces on the particles at the surface. For hard particles, adherence forces tend to be weak. Molten or semimolten particles, however, can adhere to vane and blade surfaces with attachment forces and deposit growth rates much greater than for hard particles. Finally, even should removal forces be insufficient to prevent individual particles from remaining on turbine surfaces, forces and stresses can occur within the bulk deposit formed that can eventually result in spallation (gross deposit detachment), thereby restricting deposit net growth rates. These stresses can be caused by factors such as differential thermal expansion and chemical reactions producing volumetric changes in underlying deposit layers.

The above considerations suggest the difficulties in producing doped fuels to simulate deposition environments resulting from residual oils or other fuels. The elemental fractions of contaminants must be reproduced in the doped fuel, and the particles formed during combustion should have the same size distribution and chemical composition, with the same melting points, as the fuel being simulated. The differences in pin specimen deposition characteristics between the residual oil and simulated residual oil distillate tests discussed earlier are not surprising when one considers the differences in sizes, shapes, and chemistries of gas stream particles observed during the particulate probe tests.

Information from these particulate probe measurements and the delivery mechanism observations have helped to identify the primary modes of particle delivery to turbine surfaces for operation with residual oils. Measurements revealed particles predominantly 4 to 12 μm in diameter, with some particles ranging in diameter up to 15 μm and down to less than 0.1 μm. Since most of the particulate mass is above a few microns in diameter, the bulk of the particles is expected to arrive on turbine surfaces (and the pin specimens tested) by inertial impaction. The small mass fraction in the size range smaller than a few tenths of a micron, however, where thermophoretic effects are significant, appears to affect

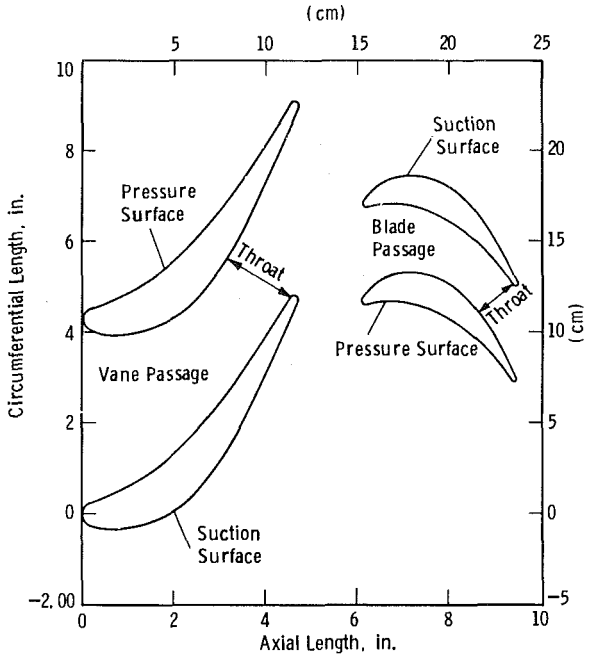

Fig. 7 Schematic showing vane and blade passage throats

deposition rates. Comparison of deposit buildup rates on the pin specimens for earlier tests in this program, at 1900 to 2000°F (1038 to 1093°C) gas temperatures, but with various specimen surface temperatures, shows that, at these gas temperatures, deposition increases with gas/metal surface temperature differentials [1, 4].

A plausible explanation may be that even though a small mass fraction of gas stream particles is in the few tenths of a micron and smaller size range, where thermophoretic effects are significant, the bulk of molten gas stream particles is in this size range. These smaller particles delivered by thermophoresis can then act as a molten glue to bond the larger, solid particles arriving by inertial impaction to test specimen (and turbine) surfaces. Apart from MgO, the major compound formed for residual fuels containing a magnesium inhibitor for vanadium is $Mg_3V_2O_8$, which has a melting point of about 2200°F (1024°C); smaller amounts of magnesium pyrovanadate ($Mg_2V_2O_7$) and magnesium metavanadate (MgV_2O_6) may be formed, with melting points of about 1700°F (927°C) and 1400°F (760°C), respectively [15]. A low melting-point calcium compound that may have resulted in the higher deposition rates observed for the fuels containing calcium is $CaO \cdot V_2O_5$ (1432°F [778°C] melting point) [16]. Low levels of V_2O_5 (1240°F [671°C] melting point) may also occur in the gas stream because of incomplete reaction of the available vanadium with the magnesium. Any of the above, and the Ca-based compounds detected in the deposits, could be the low mass fraction glues in the small size range where thermophoretic effects are significant. For the Ca-based compounds detected, however, the only melting point information available was for the $CaMg_3(SO_4)_4$ compound detected. Its melting point of 2192°F (1200°C) indicates that it did not act as a glue. Vanadium pentoxide was detected in deposits following tests in this program. Whether the deposit bonding glue was V_2O_5, $Mg_2V_2O_7$, MgV_2O_6, or a $CaO \cdot V_2O_5$ compound that decomposed during test cooldown, however, is uncertain. Further evidence for the above explanation is given in Fig. 6, which indicates that deposition on test cascades and cylindrical specimens is correlated with the gas/metal surface temperature differential for gas temperatures below 2000°F (1093°C).

The arrival of molten deposit bonding glues on specimen (and turbine airfoil) surfaces is affected by the degree of

cooling of those surfaces in addition to the melting point of gas stream particles. Solidification of molten gas stream particles in cooled surface boundary layers depends not only on the surface temperature but also on factors such as particle residence times in boundary layers and particle thermal inertias. Consequently, even though the melting points of several of the above potential deposit bounding glues are higher than the 1250–1350°F (677–732°C) specimen surface temperatures for the tests reported here, particles of some of these compounds could reach the specimen surface in a molten state. Furthermore, the melting point (1240°F [671°C]) of V_2O_5 is lower than the specimen surface temperature for any of these tests.

Deposition Modeling. A turbine deposition model was developed, using information such as that described above concerning dominant residual oil deposition mechanisms, to relate deposition on turbine airfoils to deposition on the circular, cylindrical specimens used in this experimental program. By this means, the deposit buildup rates measured on the specimens during the tests were extrapolated to obtain estimates of deposit buildup rates and deposit removal maintenance intervals for utility turbines.

Combustion turbine performance degradation is affected by rates of deposit buildup and also by the locations of deposit buildup on vanes and blades. While substantial deposits may be tolerated on vane and blade noses without a major effect on turbine performance, deposit buildup at vane and blade flow passage throats (indicated in Fig. 7) results in greater performance degradation because of flow blockage and, to a lesser extent, decrease in aerodynamic efficiency. In this case, deposit constriction of the throat by approximately 0.32 cm (1/8 in.) results in about a 10 percent drop in turbine power. Consequently, the critical locations for deposition are on the suction surface, past midchord, and the pressure surface tip regions that bound the passage throat.

Turbine power drops are related to flow passage blockage by considering that the turbine control system tends to maintain a constant rotation speed, which in turn tends to sustain a constant mass flow rate from the compressor. Consequently, as the expander flow passage area decreases because of deposition, the compressor pressure ratio increases to drive the same mass flow through a smaller flow area. An increasing fraction of the power generated by the expander is required to drive the compressor, resulting in decreasing turbine net output power.

For the particle sizes measured in this test program using the particulate probe, the bulk of particulate mass delivered to the critical suction surface locations is transported by turbulent eddy diffusion, and that delivered to the critical pressure surface locations is transported by inertial impaction. Because of higher transport rates for inertial impaction, the mass delivery to pressure surface locations is expected to be substantially greater than to suction surface locations.

The inertial impaction delivery to the circular front surfaces of the test specimens of this program and to the circular noses of turbine airfoils are similar. Consequently, with proper adjustment for physical scale differences and test pressure versus turbine passage pressure difference, the measured deposit buildup rates on the test specimens have been used to estimate deposit buildup rates at the nose of a turbine vane. Physical scale adjustments are necessary because tests and analyses have shown [17] that a larger fraction of approaching particles strike the cylinder with decreasing cylinder diameters. Pressure adjustments are necessary because particle arrival rates are proportional to the local particle concentration per unit volume of gas, which is proportional to gas pressure [18].

For any specific turbine airfoil passage geometry and particle size, the arrival rate at the airfoil pressure surface tip region (which bounds the passage throat) is related to the airfoil nose particle arrival rates. Particle equations of motion have been integrated to relate the tip arrival rates to nose arrival rates resulting from inertial impaction for the first stator (illustrated in Fig. 7) of a 10-to-1 pressure ratio turbine. Tip arrival rates were determined to be about one-fifth of nose arrival rates for the 4-to-6 μm particle size range, representing the bulk of gas stream particles measured with the particulate probe. Stator tip deposit buildup rates were determined by reducing projected nose deposit buildup rates by a factor of five.

Maintenance Interval Projections. The approach just outlined of relating measured deposit buildup rates on the circular pin specimens to turbine vane nose particle arrival rates and then to pressure surface tip arrival rates has been used to project turbine maintenance intervals to remove deposit blockage of the first stators of the 10-to-1 pressure ratio turbine. The much smaller deposit buildup rates on the suction surface side of the vane throats were obtained by approximate adjustments of the pin specimen back surface measured deposit buildup rates. Due to the much lower deposit buildup measured in the back surfaces than on the front surfaces of the pin specimens (and on turbine airfoil suction surfaces than on pressure surfaces for the particle sizes observed in the particle probe tests), the approximate adjustments to obtain suction surface deposit buildup rates did not substantially affect projected maintenance intervals.

Earlier deposition data for pin specimen tests at 1600°F (871°C) surface temperature and 2000°F (1093°C) gas temperature [1, 4] were used to check the modeling approach projection with field experience. For these conditions representative of current turbine operation, the projected maintenance interval of 580 h was in agreement with the range of water washing intervals from 200 to 1500 h determined in a survey [3] of turbine operators using residual and crude oils.

Projected maintenance intervals were 250 h, using deposition data from pin specimen tests representing current turbine inlet temperatures but greater surface cooling (1350°F [732°C]) based on short-term tests (20 h), the deposits formed on the cooler pin surfaces appeared to be more susceptible to spallation and may have reached a maximum steady-state thickness of about 250 μm (10 mils). If spallation at the lower surface temperatures does result in acceptable steady-state deposit thicknesses, increased vane cooling may offer an alternative to water washing for controlling deposition in turbines with inlet temperatures lower than 2000°F (1093°C). Longer duration tests are necessary, however, to determine whether lower surface temperatures do limit deposit growth to tolerable steady-state thicknesses and whether spallation occurs during operation or shutdown.

The above maintenance interval projections are based on test data using washed residual oils with KI-16 magnesium-based additive. Other residual oil treatments (such as additives containing silicon in addition to magnesium) may significantly affect deposit removal maintenance intervals. At their Putnam Station [12], however, FP&L were burning residual fuel oil containing only the KI-16 Mg additive used in this study. In peaking load operation they encountered no problems with deposit removal using periodic water washing of the turbine where the gas temperature was 2000°F. Likewise, Florida Power Corporation at their DeBary plant reported excellent service, with deposits spalling off during start-up, and the turbine thus requiring no water washing [19].

Conclusions

- At 1900°F (1038°C) gas temperatures deposition onto

cooled Udimet 500 specimens was greater for simulated than for real residual oil, probably because of greater fractions of molten particulates present in the gas stream.

- Deposition rates appeared to be influenced by thermophoretic delivery of small molten particles of magnesium and calcium vanadates and free vanadium pentoxide, which may act as a glue, bonding the larger solid MgO particles delivered by inertial impaction.
- Maintenance intervals estimated from these deposition data were in good agreement with field experience for current utility turbines operating with washed and treated residual oil.

Acknowledgments

This work was performed with the support of the Electric Power Research Institute, Contract No. RP 1345-1. Many people contributed to the success of this research effort and particular thanks are due to the technical staff of the Metallurgy and Chemical Engineering Research Departments of the Research and Development Center. The contributions of S. M. DeCorso, of the Westinghouse Combustion Turbine Systems Division, P. P. Singh and A. Y. Ranadive of the Chemical Engineering Research Department, and S. C. Singhal of the Metallurgy Research Department are especially gratefully acknowledged.

References

1 DeCorso, S. M., Vermes, G., Lee, S. Y., Singhal, S. C., and Cohn, A., "Combustion Turbine Design Guidelines Based on Deposition/Corrosion Considerations," ASME Paper 80 GT-72.

2 Whitlow, G. A., Lee, S. Y., Mulik, P. R., Wenglarz, R. A., Sherlock, T. P., and Cohn, A., "The High-Temperature Combustion of Residual Fuel Oil — Some Deposition Product Considerations," EPRI/DOE 2nd Conference on Advanced Materials for Alternative Fuel-Capable Heat Engines, Monterey, Calif., EPRI Report RD-2369-SR, May 1982, pp. 4-73 to 4-108.

3 "Worldwide Survey of Current Experience Burning Residual and Crude Oils in Gas Turbines," EPRI Report AF-1243, TPS 78-883, Dec. 1979.

4 Workshop Proceedings: Deposition in Utility Gas Turbines, EPRI Report WS-80-121, May 1981.

5 Strong, R. E., and Sherlock, T. P., "Residual Oil Operating Experience with Westinghouse Industrial Combustion Turbines," presented at the EPRI Combustion Turbine Residual Oil Workshop, Atlanta, Ga., July 1980.

6 Felix, P. C., "Practical Experience with Crude and Heavy Oil in Stationary Gas Turbines," BBC Report No. CH-T113333E, 1980; also ASME Paper 78-GT-103.

7 Hefner, W. J., and Lordi, F. D., "Progress in Heavy Fuels," General Electric Report GER-3110A, 1979.

8 Nealy, D. A., and Timmerman, W. H., "Investigation of the Influence of Contaminated Fuel on Turbine Vane Surface Deposition," Paper No. AIAA-80-1113, AIAA/SAE/ASME 16th Joint Propulsion Conference, Hartford, Conn., June 1980.

9 Urbas, T. A., and Tomlinson, L. H., "Part II, Formation and Removal of Residual Fuel Ash Deposits in Gas Turbines Formed at Firing Temperatures above 982°C (1800°F)," *Proceedings of International Conference on Ash Deposits and Corrosion from Impurities in Combustion Gases*, Engineering Foundation, Henniker, N.H., Hemisphere Publishing Corp., 1977.

10 Urbas, T. A., and Tomlinson, L. H., "Part I, Formation and Removal of Residual Fuel Ash Deposits in Gas Turbines Formed at Firing Temperatures Below 982°C (1800°F)," *Proceedings of International Conference on Ash Deposits and Corrosion from Impurities in Combustion Gases*, Engineering Foundation, Henniker, N.H., Hemisphere Publishing Corp., 1977.

11 Nomura, M., et al., "An Experiment on Deposit Formation on the Surface of an Air Cooled Gas Turbine Blade," Paper No. 69, Gas Turbine Soc. of Japan/The Japanese Soc. of Mech. Engineers/ASME: Tokyo, May 1977.

12 Vitello, J. J., and Scheirer, S. T., "Hot Component Corrosion Evaluation to Obtain Baseline Data for Utilization of Low Grade Fuels in Combustion Turbine Applications," Westinghouse Final Report on EPRI Research Project 1079-2, Sept., 1980.

13 Moore, M. J., and Crane, R. I., "Aerodynamic Aspects of Gas Turbine Blade Corrosion," from *Deposition and Corrosion in Gas Turbines*, edited by A. B. Hart, and A. J. B. Cutler, Halstead Press, New York, 1973.

14 Wenglarz, R. A., "An Assessment of Deposition in PFBC Power Plant Turbines," ASME Paper 80-WA/CD-1; also in ASME JOURNAL OF ENGINEERING FOR POWER, Vol. 103, July 1981, pp. 552-557.

15 Krulls, G. E., "Gas Turbine Vanadium Inhibition, ASME Paper 81-GT-187, 1981.

16 Barin, J., and Knacke, O., *Thermochemical Properties of Inorganic Substances*, Berlin, Springer-Verlag, 1973.

17 Hidy, G. M., and Brock, J. R., *The Dynamics of Aerocolloidal Systems*, Pergamon Press, Oxford, 1970.

18 Wenglarz, R. A., and Menguturk, M., "Use of Cascade and Small Turbine Tests to Determine Erosion of Utility Turbines," ASME Paper 81-GT-52, ASME JOURNAL OF ENGINEERING FOR POWER, Vol 104, Jan. 1982, pp. 58-63.

19 Allen, H. L., "Florida Power Corporation Experience Operating Gas Turbines on Residual Fuel," presented at the EPRI Combustion Turbine Residual Oil Workshop, Atlanta, Ga., July 1980.

Heavy Fuels Ash Deposit Formation and Removal in Water-Cooled High-Temperature Gas Turbines

J. C. Blanton
Corporate Research and Development.

G. A. Durgin

J. E. Palko
Gas Turbine Division.

General Electric Company,
Schenectady, N.Y. 12301

Experimental data obtained in heavy fuels operation of a gas turbine simulator with a water-cooled, transonic turbine nozzle cascade are presented. The ash fouling is characterized by the rate of decrease of the aerodynamic throat area. Particular attention is given to the cleanability of the ash deposits. A simple heat transfer analysis was performed to assist in evaluating the data. The rate of ash fouling in the water-cooled nozzle was found to be of the same order of magntude as for conventional air-cooled designs. Cleanability, both on and off-line, was found to be significantly enhanced, thus making the water-cooled gas turbine an attractive alternative for heavy fuels applications.

Introduction

The trends toward higher firing temperature and increased fuels flexibility for new-generation gas turbines has created an operational conflict. This has been found to be particularly true in applications involving the use of heavy liquid fuels, i.e., crudes, residuals, and blends. As the turbine inlet temperature is increased, the deleterious effects due to the fuel contaminants on the turbine hot gas patch become more pronounced. The major problems encountered involve hot corrosion and ash fouling. The corrosion problem has been minimized by the development of standardized fuel treatment techniques, but the ash deposit fouling problem remains a serious obstacle.

This report describes part of an ongoing investigation of gas turbine heavy fuels ash deposition. The particular work described herein was conducted as part of the Water-Cooled Gas Turbine Development Program[1] and the Advanced Cooling Full Scale Engine Demonstration Program[2] sponsored by the Electric Power Research Institute.

Objective

The objective of the experiments was to investigate the formation and removal of heavy fuels ash deposits in a water-cooled gas turbine nozzle. The effects of various operational parameters were to be studied, including turbine inlet temperature, gas path surface temperature, and fuel contaminant levels. Ash cleanability was of particular interest. The sample fuel chosen for the program was a washed and treated heavy residual petroleum distillate.

Background

A listing of some of the more important properties of typical gas tubine liquid fuels (taken from [1]) is given in Table 1. Note that the specific gravity and viscosity are higher and the heating value lower for the hevy residuals. Of particular interest are the high ash content and the high quantities of trace metal contaminants present in the heavy residual fuel. It is due to these properties that difficulties arise in maintaining high turbine efficiencies.

Corrosion in the turbine gas path is due primarily to the formation of vanadium pentoxide and sodium sulfate in the combustion products [2,3]. Successful inhibition of the corrosive contaminants has been accomplished by appropriate fuel treatment procedures [2,4]. The fuel is first water-washed and mechanically centrifuged to remove the water-soluble sodium contaminants. The vanadium cannot be removed in this manner, however, as it generally occurs in the fuel as so-called "porhyrin complexes" [3]. It has been discovered through operating experience that the formation of vanadium pentoxide in the combustion products can be successfully inhibited by the use of magnesium additives in the fuel. A weight ratio of 3 to 1 for magnesium to vanadium is generally used [2,4].

An unfortunate circumstance of the magnesium additive is that the ash content in the combustion products is substantially increased. The content of the ash is predominantly MgO and $MgSO_4$, with some occurrence of $Mg_3V_2O_8$ or other orthovanadates [4–7]. These observed species can be predicted from the equilibrium chemistry of the ash formation at the appropriate temperature and pressure [8]. The ash tends to adhere to the aerodynamic surfaces of the tur-

[1] Funding for this specific task was provided under EPRI Contract RP234-3, Task 6.0.

[2] Funding for this program was provided under EPRI Contract RP1319-1.

Contributed by the Gas Turbine Division of THE AMERICAN SOCIETY OF MECHANICAL ENGINEERS and presented at the 27th International Gas Turbine Conference and Exhibit, London, England, April 18–22, 1982. Manuscript received at ASME Headquarters December 7, 1981. Paper No. 82-GT-88.

Table 1 Typical properties of liquid fuels

	True distillates		Ash-bearing fuels	
Fuel type	Kerosene	No. 2 distillate	Blended residuals and crudes	Heavy residuals
Specific gravity, 100°F (38°C)	0.78/0.83	0.82/0.83	0.80/0.92	0.92/1.05
Viscosity, cSt, 100°F (38°C)	1.4/2.2	20./4.0	2/100	100/1800
Gross heating value, kcal/kg	10,700/10,950	10,500/10,950	10,500/10,900	10,150/10,500
Gross heating value, Btu/lb	19,300/19,700	19,000/19,600	19,000/19,400	18,300/18,900
Sulfur, %	0.01/0.1	0.1/0.8	0.2/3	0.5/4
Nitrogen, %	0.002/0.01	0.005/0.06	0.06/0.2	0.05/0.9
Hydrogen, %	12.8/14.5	12.2/13.2	12.0/13.2	10/12.5
Ash (fuel as delivered), ppm	1/5	2/50	25/200	100/1000
Ash (inhibited), ppm	–	–	25/250	100/7000
True metal contaminants (untreated)				
Sodium	0/0.5	0/1	1/100	1/350
Vanadium, ppm	0/0.1	0/0.1	0.1/80	5/400
Lead, ppm	0/0.5	0/1	0/1	0/25
Calcium, ppm	0/1	0/2	0/10	0/50

bine, resulting in a loss of power [2,3]. This deterioration eventually necessitates off-line maintenance for deposit removal.

The loss of power due to the ash deposits is the combined result of two effects. The first and most obvious is a reduction in the gas flow resulting from the physical and aerodynamic restriction imposed by the deposits on the gas path. This restriction is generally observed as an increase in the turbine inlet pressure and can be correlated in terms of a corrected mass flow parameter. Turbine simulator tests have been used extensively to study this phenomenon [6,7,9,10]. The second effect leading to a loss in net power output is the decrease in the specific work output of the turbine due to a decrease in the gas turning and the turbine efficiency [3,11]. This effect is difficult to study experimentally due to the extreme gas path conditions.

Experimental investigations of gas turbine ash deposition have been very helpful in the study of the fouling effects as well as of the ash character and morphology. Most of the investigations have been carried out in turbine simulators, designed to duplicate the hot gas path temperatures, pressures, and aerodynamics as closely as deemed necessary without the expense of using a full engine test. A description of some recent investigations involving the use of turbine simulators may be found in [4–7, 9, 10, 12]. The heavy liquid fuels used in these tests are also simulated by introducing additives to No. 2 distillate in the desired amounts. This enables accurate monitoring of the contaminant levels and eliminates the impracticality associated with storing and handling the many variations of research fuels [4]. Both water-soluble [4,6,7,9,10] and oil-soluble [5,12] additives have been used successfully in simulating turbine fuels.

In addition to the aerodynamic degradation of the turbine gas path by the ash deposits, there are other important effects which should be considered. One of these is the effect on the gas turbine heat transfer. As ash deposits form on the gas path surfaces, the heat transfer characteristics have been shown to change due to the roughness of the ash surface (tends to increase heat transfer) and its insulating properties (tend to decrease heat transfer). The overall trend between cleaning intervals is a net decrease in heat transfer and nozzle metal temperatures [9,12], although during the initial stages of ash formation the opposite has been observed [9]. These effects are important for several reasons. The life of the nozzle is very much dependent on the temperature history of the gas path surface. The lower temperatures experienced during much of the operational cycle on depositing fuels may allow increased component fatigue life, providing surface corrosion is controlled. Another aspect often overlooked in the ash thermal chemistry models is that, due to the thermal barrier effect of the ash deposit, the actual gas path surface temperature (that is, the deposit surface) will be much higher than at the metal surface of the vanes [9]. The reduction in gas side heat transfer in a water-cooled turbine with deposits will also have a beneficial effect on the simple cycle efficiency (heat rejection from the cycle will be diminished).

Operational considerations for industrial and utility applications of gas turbines burning heavy liquid fuels are likely to include: (*i*) the rate at which deposits accumulate in the turbine, and (*ii*) how well (and easily) the deposits can be removed. The rate of deposition affects both the rate of decrease in net power output of the turbine and the rate of increase in combustion chamber pressure. Control of the latter effect is essential to steady machine operation, since the surge margin is decreased by increased discharge pressure. Good correlation has been achieved between turbine simulator tests and field operation of gas turbines in this area [4].

Nomenclature

A = aerodynamic throat area
k_{gas} = thermal conductivity of combustion gas
L = airfoil chord length
m_{gas} = mass flow rate of combustion gas
NAIN = Nozzle Area Index Number [Equation (21)]
P = stagnation pressure
Q_{vane} = heat transfer rate for turbine vane
R = gas constant of combustion gas
Re = Reynolds number
T = stagnation temperature
V = velocity
Z = dimensionless heat transfer conductance [(Equation (4)]
γ = specific heat ratio of combustion gas
μ = absolute viscosity of combustion gas
ρ = static density of combustion gas

Subscripts

L = based on airfoil chord length
ti = turbine inlet condition
1,2,3 = stations of 1-D heat transfer network (Fig. 10)

Superscript

* = at the nozzle throat

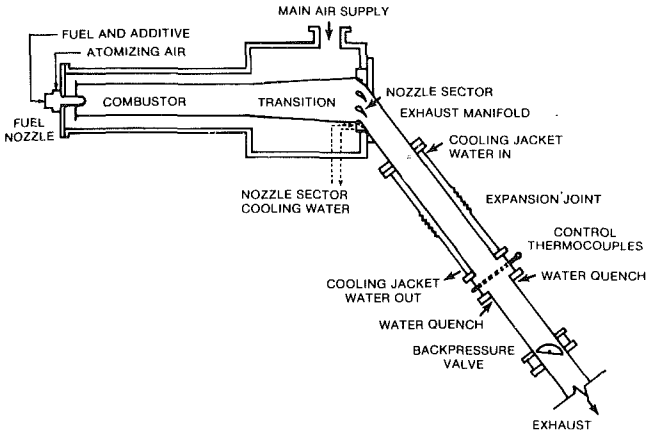

Fig. 1 Turbine simulator

Cleaning procedures for the ash deposits formed in gas turbines have been evaluated in two categories: (*i*) those performed on-line at simulated load, and (*ii*) those requiring a shutdown of the turbine engine. Obviously, the on-line procedures are preferred if they can be applied. These methods include injection of an abrasive material such as crushed nutshells or coke. Experiences using state-of-the-art air-cooled turbine vane designs indicate that on-line cleanability of ash deposits formed at firing temperatures below 1255 K is quite good [6]. Recoveries in effective blocked nozzle area of the order of 50 percent were achieved. At higher firing temperatures, however, on-line cleaning procedures attempted have shown a varied degree of success [7]. Off-line cleaning has shown consistent success at all firing temperatures (usually a water-wash, soak, and restart sequence), and standard procedures have been developed for implementing these techniques [4]. The removal of ash is accomplished off-line due to a softening of the water-soluble $MgSO_4$ ash component during the water-wash and soak sequence followed by a combustor refire. This procedure naturally results in an operational expense and a loss in availability during cleaning. The development of effective on-line techniques at higher firing temperatures is thus a high priority.

The trend toward higher firing temperature has aggravated the task of maintaining effective operation in heavy fuels applications. The ash deposits formed at higher temperatures tend to deposit at a higher rate, to be physically harder, and to be more difficult to remove than those formed at lower temperatures [6]. Of particular concern are the newer high-technology turbine designs being developed for the higher temperature applciations. A number of the more thermally efficient air-cooled nozzle designs contain a large number of film cooling holes, particularly in the critical leading edge region [12,13]. These holes are especially sensitive to plugging by the ash deposits [12]. A possible solution to the problem is a water-cooled gas turbine. An active development program in water-cooled gas turbine technology has been underway for some time by the General Electric Company [14]. Included in this program is a task involving the application of heavy liquid fuels to water-cooled turbines. Some preliminary work in this area has been presented previously [9,10]. The potential advantages of water cooling cover a broad spectrum of economic and technical objectives including: (*i*) fuels flexibility with uninterrupted growth in plant efficiency, (*ii*) improved reliability through reduced metal temperatures and increased corrosion resistance, and (*iii*) low temperature airfoil surfaces which have demonstrated total on-line ash cleanability at full-fired conditions. Analysis of ash samples removed from the water-cooled nozzle reflect a softer, more friable water-soluble ash than that recovered from similar air-cooled tests.

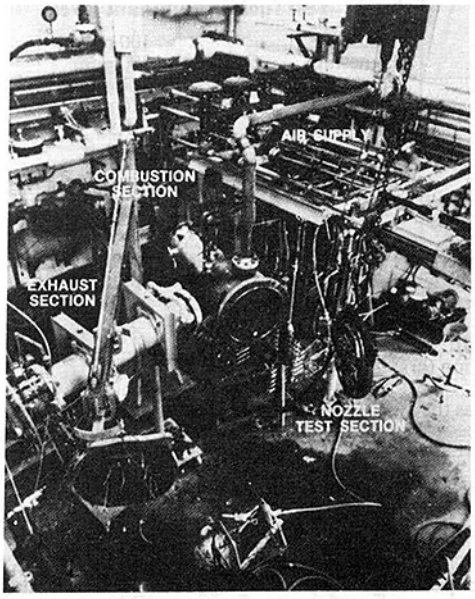

Fig. 2 Turbine simulator test cell

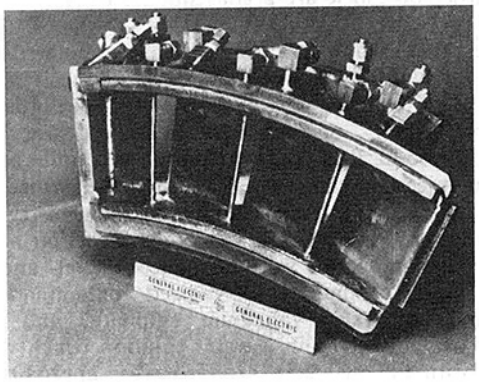

Fig. 3 Water-cooled turbine nozzle sector

Experiments

Test Systems and Apparatus. The primary research vehicle used for heavy fuels testing is a high-pressure high-temperature test rig known as a turbine simulator [6,9,10]. A schematic showing its principal features is shown in Fig. 1. The design philosophy of the turbine simulator is to simulate kinematically and dynamically as closely as possible, given the constraints of the test system, the hot gas path conditions of a prototype first-stage gas turbine nozzle. The simulator shown in Fig. 1 operates at a design pressure of 6 atm and has been operated at turbine inlet temperatures up to 1540 K. The main air enters the simulator at the top of the pressure vessel from a supply system at 6 atm pressure and 560 K temperature. The air supply system includes two 600 kW reciprocating air compressors and a nonvitiating gas-fired air preheater. An exhaust back-pressure valve allows control of the nozzle expansion ratio, which is generally set at about 2.0 to ensure sonic conditions at the nozzle throats. Figure 2 shows the turbine simulator test cell.

The turbine nozzle sectors used in simulator tests are four-vane, three-throat annular cascades, generally fabricated from cobalt-base alloy castings. For this program, a special sector of Inconel alloy 718 was cast, STEM-drilled, machined, and electron-beam welded to form a monolithic, water-cooled nozzle sector. The finished product is shown in Fig. 3. Figure 4 shows the mounting and cooling circuits at the nozzle sector. A design goal for this nozzle was to keep peak metal tem-

Table 2 Test fuel contaminant levels

Vanadium	100 ppm
Magnesium	300 ppm
Sodium	1 ppm
Calcium	10 ppm
Sulfur	0.5 %

Table 3 Nominal test conditions

Test designation	1	2	3	4
Program test	2	5	6	7
Firing temperature[a] (K)	1283	1394	1394	1394
Turbine inlet temperature (K)	1317	1428	1428	1428
Average metal temperature (K)	672	728	728	617
Reynold's number,[b] $Re^*L \times 10^{-6}$	1.9	1.7	1.7	0.8
Test duration (hrs)	64.7	48.4	22.3	61.5

[a]Defined as the average gas temperature leaving first-stage nozzle
[b]Using free-stream throat conditions and airfoil chord length

peratures below 810 K at the peak design turbine inlet temperature of 1420 K. By way of comparison, an air film-cooled nozzle used in tests at similar conditions experienced peak metal temperatures in excess of 1100 K. The vanes of the monolithic nozzle were cooled by radial, parallel-flow water channels. Spatial variations in the vane surface temperature of the order of 250 K are a consequence of the design and material properties.

The test fuel used in this program was a simulated residual oil specified by EPRI. The contaminate level specifications of this fuel are given in Table 2. Since the pressure in the turbine simulator is only one-half the rated pressure for the prototype, both the contaminant levels and corrosion inhibitor injection rates were adjusted to ensure proper simulation of the ash throughput and chemistry in the combustion products [15]. Distillate No. 2 fuel oil was used, and various compounds were introduced in oil- and water-soluble forms to simulate the desired contaminant levels. Magnesium sulphate, vanadium sulphate, and sodium chloride were dissolved in a water solution which was then blended with the fuel at a proportion of approximately 2 percent volume. Oil-soluble calcium naphthenate and carbon disulfide were added by separate metering pumps.

Test operation and data acquisition were performed by a computer-based test management system. This system allowed hands-off, around-the-clock operation of the test facility in addition to providing rapid data logging and on-line data reduction. The analyses of ash samples performed through wet chemistry, photomicrographs, and the scanning electron microscope have been integrated with test data and post-test observations to provide morphology as well as property data which support increased on-line cleanability experience on the water-cooled nozzle.

Results and Discussion

As noted previously, four turbine simulator tests have been performed to date using the water-cooled turbine sector, as shown in Table 3. Three different test conditions are represented. These are best expressed in an aerothermal sense by airfoil Reynolds numbers given in the table, calculated using the equation

$$Re_L^* = \rho^* V^* L / \mu^* \tag{1}$$

Since the turbine nozzle is operated in the choked (sonic) condition, the Reynolds number given by equation (1) is solely a function of the nozzle inlet temperature and pressure. The nozzle inlet temperature is calculated using the measured fuel and air flows to the rig and the combustor inlet condition. The calculated gas temperatures were independently verified by a nozzle inlet temperature traverse probe and through an analysis of the free oxygen content in the exhaust gases. The nozzle inlet total pressure was taken as equal to the measured static pressure in the combustor liner head end.

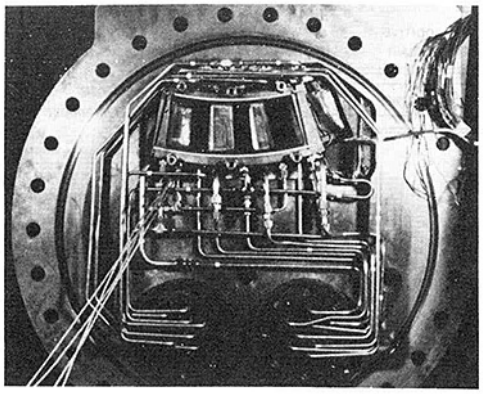

Fig. 4 Nozzle sector mounting and plumbing assembly

Ash deposit accumulation rates along the nozzle aerodynamic surfaces over the range of Reynolds numbers have been shown to be largely dependent on the ash flux and turbine firing temperature. Ash physical characteristics derived through post-test ash analysis and on-line heat transfer measurements correlate well with airfoil surface temperature and location. Inadvertent ash shedding and active on-line cleanability have shown a strong dependence on reduced surface temperatures achievable through water cooling [4,6,7,10]. As can be observed from Table 3, two different gas temperature and three different metal temperature levels were studied during the test series.

Throat Area Degradation and Recovery. The single most important result parameter characterizing ash accumulation is the mass flow capacity, sometimes referred to as the nozzle area index number (NAIN), and given by the equation

$$\text{NAIN} = \dot{m}_{\text{gas}} \sqrt{T_{ti}} / P_{ti} \tag{2}$$

Note that equation (2) is a simplified version of the equation giving the throat area for a sonic isentropic nozzle,

$$A^* = \frac{\dot{m}_{\text{gas}}}{P_{ti}} \left[\frac{RT_{ti}}{\gamma} \left(\frac{\gamma+1}{2} \right)^{\frac{\gamma+1}{\gamma-1}} \right]^{\frac{1}{2}} \tag{3}$$

In a turbine simulator test where ash deposits are fouling the gas path, a quantitative assessment of the degree and rate of blockage can be gained by observing changes in the above quantities. Either quantity may be used; however, in tests at significantly different gas temperatures, equation (3) is preferred as variation in gas properties may be properly accounted for through the specific heat ratio, γ. In addition, the "effective" area, A^*, is a meaningful physical parameter. For these reasons, the "effective" throat area, A^*, will be used in this report as the measure of ash deposit accumulation or flow blockage.

In similar turbine simulator tests involving air-cooled nozzles, the effective nozzle area has been found to decrease at a more or less constant rate [6,7]. In order to make an objective evaluation of the rate of ash accumulation, it has thus become the practice to fit a straight line through the data obtained during periods of steady ash deposition. The "ash deposition rate" is then expressed using the slope of this line. In this report, rates will be computed in terms of the percent decrease in the effective nozzle throat area per 100 hrs of testing. Removal of ash from the nozzle results in an effective increase in the throat area. The magnitude of the recovery will be expressed relative to the blocked area just prior to that point in the test. Straight-line correlation of the throat area data before and after the recovery event will be used primarily for ease in computation.

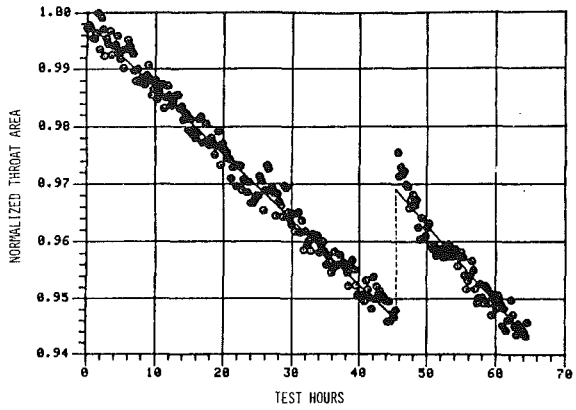

Fig. 5 Test 1 throat area history

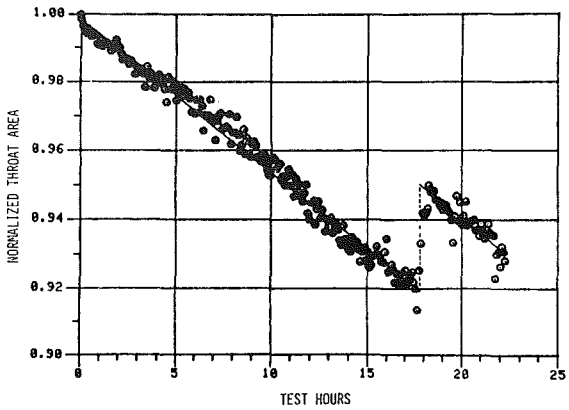

Fig. 7 Test 3 throat area history

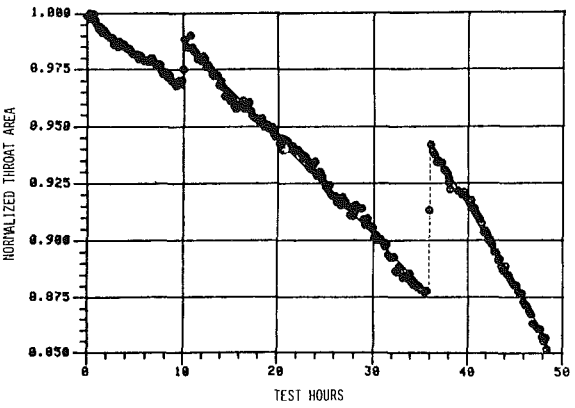

Fig. 6 Test 2 throat area history

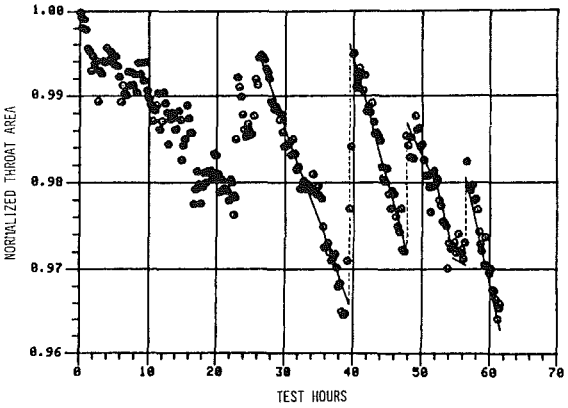

Fig. 8 Test 4 throat area history

The nozzle throat area histories for the four turbine simulator tests described previously are shown in Figs. 5–8. In each case, the area is normalized using the value for the clean nozzle.

Consider first Fig. 5, which shows the throat area history for the first of the four tests. From the plot, one observes two distinct periods of steady ash deposition separated by a pronounced throat area recovery. The effective area increase in this instance was due to a spalling of the ash deposit just after a sudden momentary increase in the turbine inlet temperature.

"Thermal excursions" are rare under computer-automated controlled operation; however, during manual control, when air flow and fuel flow rates are being adjusted by way of remote-controlled valving, the sequence may be somewhat out-of-phase, which produces a transient in gas temperature–in the case of the first test, an increase in temperature of approximately 75 K at the 45-hr point. A significant change in low temperature ash character relative to typical air-cooled nozzle testing was revealed and later supported by follow-on testing. Nozzle metal temperature data were used to identify particular locations where ash fracture and subsequent shedding occurred [9].

Using the least squares method of analysis, straight lines were fit through the data in the two steady periods of operation. These lines are plotted in Fig. 5. The throat area recovery, which occurred approximately 45.4 hrs into the test, is shown as a vertical broken line. Note that the recovery represented by the broken line is not as large in magnitude as the recovery to the largest effective throat area actually achieved after the thermal excursion. The local ash deposition rate immediately following the excursion is very high for a 4- to 6-hour period, followed by a rate very close to that originally observed. Flow distribution through the nozzle passage has undoubtedly been upset and is reflected in an abnormal local ash accumulation rate. For this reason, it is felt that the recovery represented by the broken line gives the best quantitative assessment of the throat area recovery. The ash deposition rates before and after the thermal excursions were calculated to be 11.4 and 13.6 percent, respectively, per 100 hrs. The throat area recovery due to the mild thermal excursion was an appreciable 43 percent.

The throat area history for the second of the four tests is shown in Fig. 6. Three periods of steady ash deposition and two area recovery events are shown. Ash removal was again due to thermal excursions. The nature of each excursion, however, was somewhat different. The first, which occurred approximately 9.9 hrs into the test, was similar to the event reported previously in the first test where air valve response lagged fuel flow to provide the increased fuel/air ratio, temperature, and pressure. The second excursion at the 35-hr point resulted from a momentary decrease in the combustion air flow, which resulted in a higher fuel/air ratio and thus higher temperatures. The actual temperature levels reached cannot be determined; however, in all likelihood, 1550 K gas temperatures were attained for a fraction of a second. This type of thermal excursion varies markedly from the previus type in that it was accompanied by an abrupt pressure decrease. In addition, the elapsed time was considerably less in the second case. A demonstration of low temperature ash deposit strength at the metal-ash bondline and within the ash layer at a firing temperature of 1394 K reveals a quality which will later be exploited to improve on-line cleanability.

The straight-line approximations for the throat area are shown in Fig. 6. The ash deposition rates for the three periods were 31.3, 42.5, and 69.9 percent, respectively, per 100 hrs, with intermediate throat area recoveries of 68 and 55 percent. Test data support the association of ash particle accumulation

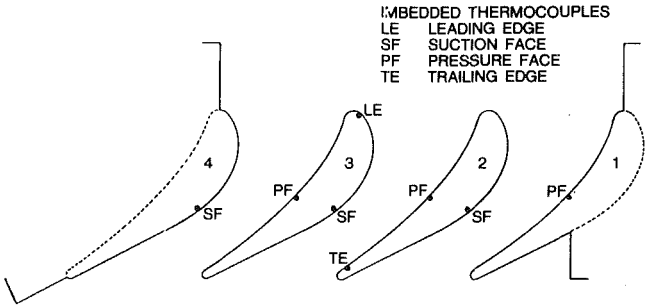

Fig. 9 Nozzle sector geometry and instrumentation

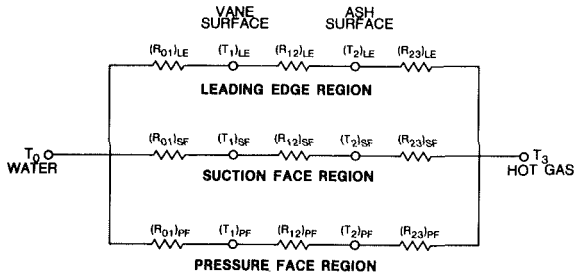

Fig. 10 One-dimensional heat transfer network

rates which change in passage aerodynamic behavior [17]. Redeposition rates on a partially cleaned surface reflect the importance of establishing on-line cleaning methods which alleviate major aerodynamic disturbances.

The actual objective of performing the first two tests was to establish ash deposition rate trends at two different firing conditions. In retrospect, much of the significant data was made available through computer data storage of system-excited events. Following each of the first two tests, the ash deposits were water-washed at low air flow in an unfired mode and allowed to soak for a period of approximately 30 min. The simulator was then refired to evaluate the ash removal. In each case, complete aerodynamic recovery was noted, and a visual inspection after shutdown revealed complete removal of ash. These results are somewhat more favorable than those obtained on more conventional air-cooled turbine nozzle designs [7].

In the third test, active on-line ash removal at full-fired conditions was attempted. The technique used was the injection of crushed walnut shells into the secondary zone of the combustor (see Fig. 1). Two charges (approximately 4 kg each) of No. 16 mesh shells were injected using compressed air with a 30-min interval between injections.

The ash deposition and on-line cleanability results during the third test may be seen in Fig. 7. The effective throat area recovery, as the result of nutshell injection 17.7 hrs into the test, is clearly evident. The ash deposition rates before and after the nutshelling were calculated to be 44.5 and 44.8 percent per 100 hrs, with a throat area recovery of 39 percent due to the cleaning. Comparable deposition rates before and after on-line cleaning attempts would appear to reflect an overall similarity in aerodynamic behavior with an increased passage area unlike the local ash fracture and shedding previously discussed. An improvement in area recovery beyond the 39 percent must certainly be maintained as an objective.

The fourth test in the program was planned with two objectives in mind. The first concern was to investigate the effect of reduced nozzle surface temperature on ash deposition. A lower nozzle surface temperature was attained by operating the turbine simulator at 3 atm pressure rather than the usual 6 atm. This effect could not be achieved simply by increasing the coolant flow rate because of the heat transfer characteristics of the nozzle and of the coolant (water). The reduced pressure resulted in lower nozzle heat flux and hence lower surface temperatures. The second major goal was a more extensive investigation of on-line cleanability at these lower ash temperatures.

The throat area history for the fourth test is shown in Fig. 8. The data during the first 26 hrs of testing reflect ash accumulation rates at a reduced ash loading level relative to the previous testing. Spontaneous shedding of a substantial portion of the accumulated deposit followed an increase in the ash loading rate at the 22-hr point. A search for the cause of the disbond in the data records was not rewarded, indicating a likely shift downward in ash bond strength and toughness at reduced surface temperaures.

Ash accumulation was allowed to proceed for 4 hrs, when an attempt was made to restore the effective nozzle area and to test for improved aerodynamic behavior. The same nutshell procedure used in the third test was employed. The nozzle throat area recovery was not complete, as can be seen in Fig. 8. At this point, 26 hrs into the test, the throat area was 0.5 percent less than that measured for the clean nozzle. From this point to the conclusion of the test, there are four distinct periods of ash deposition interrupted by three area recovery events.

The first two periods of ash deposition were of 13.0 and 7.3 hrs duration, respectively. At a point 39.4 hrs into the test, the deposit was nutshelled. A procedure similar to that described above was used, except that No. 4 mesh nutshells were used in place of the smaller No. 16 nutshells used previously. The deposit rates for the two periods were 21.6 and 28.4 percent per 100 hours, with an effective throat area recovery of 95 percent.

Ash flux levels were increased to 100 percent engine levels, adjusted for nozzle mass flow at 3 atm prior to the next on-line cleaning attempt.

The deposit was nutshelled 47.7 hrs into the test using the smaller No. 16 mesh shells. A throat area recovery of 58 percent was observed.

A comparison can be made between identical on-line cleaning attempts on partially blocked nozzle passages at 3 atm versus 6 atm pressure considering tests 3 and 4. Natural expectations were that nutshell acceleration and impact energy would be increased with increased drag capability at 6 atm, and yet it would appear that reduced ash strength in terms of hardness and ash-metal bonding at lower surface temperatures was an overriding variable.

Deposition testing continued to explore the influence of combustor operation on accumulation rates. This period was interrupted at 56 hrs by a partial shedding of the deposit caused by remote manual adjustments in fuel atomization. Despite a careful attempt to retain collected ash deposits intact on the nozzle surface during shutdown, fracture of the pressure side layer was evident during post-test inspection.

Heat Transfer Results. The monolithic water-cooled nozzle sector used in the test program was instrumented with a number of imbedded thermocouples which provided vane surface temperature histories. In addition, the water flows through the individual vanes were monitored to determine the heat loadings. These temperatures and heat loads provided input data for heat transfer analyses of the ash deposition process.

Figure 9 shows the nozzle sector geometry along with the thermocouple locations.

The general trends of nozzle temperatures during an ash deposition test were as follows:

1 During the initial stages of a test, the temperatures were observed to increase. This phenomenon has been attributed to the increased surface roughness of the developing deposit.

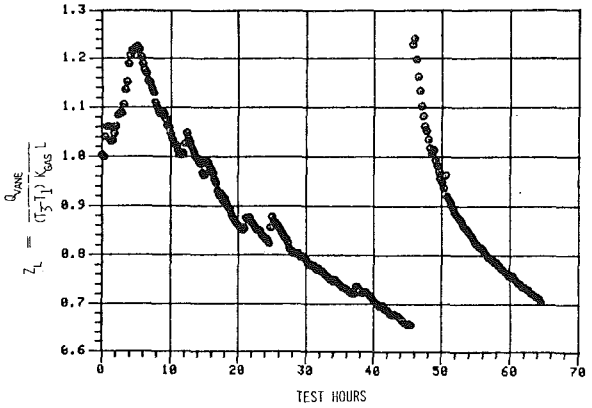

Fig. 11 Typical surface heat conductance history, vane 3 pressure surface

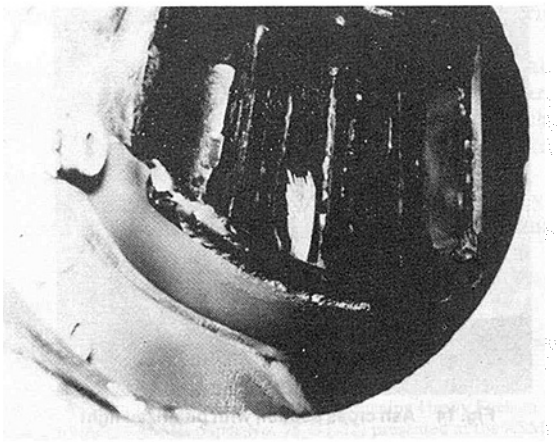

Fig. 12 Hydration of accumulated ash deposits

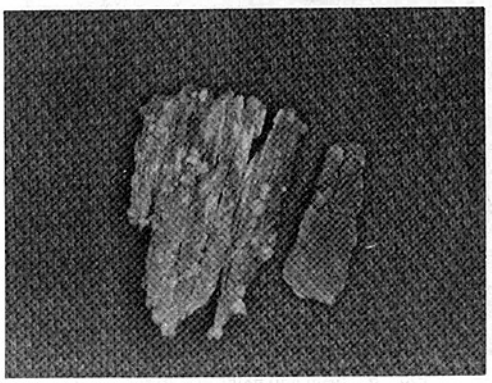

Fig. 13 Pressure side ash deposit, test 4

2 As the deposit became well developed, a decrease in temperatures was observed. This effect is clearly due to the thermal resistance of the ash layer.

3 Local shedding of the ash layer was noted to cause sharp increases in temperatures. Loss of the insulating layer is undoubtedly the major contributing factor; however, prominent flow disturbances are likely to cause increases in heat transfer.

A study of the temperature history at each of the various thermocouple locations has yielded insight into the local ash deposition behavior. In particular, the chronology of the ash formation may be observed, and the local effects of ash removal events are revealed.

In order to make objective quantitative evaluations of the heat transfer effects of ash deposition on nozzle heat transfer, a one-dimensional network analysis was employed, A schematic of this network is shown in Fig. 10. Surface effects were evaluated by changes in dimensionless circuit "conductance" defined by

$$Z_L = \frac{Q_{\text{vane}}}{(T_3 - T_1)k_{\text{gas}}L} \tag{4}$$

Note that no attempt is made to separate the heat flow in the individual network paths. The conductance value defined by equation (4), although not exact, provides a better relative measure of gas path surface effects than the surface temperature, T_1, alone. The value of the conductance is influenced by the gas path surface resistance and the thermal barrier of the deposit layer.

Typical behavior of the conductance variable in a test is shown in Fig. 11, taken from the first test. The data are normalized using the clean nozzle value. The typical trends noted previously are all apparent in the plot. Note the sharp increase in the pressure side heat transfer fuel to the thermal excursion induced fracture of ash-metal bond followed by the local, dramatic shift in heat flux.

Some of the more interesting heat transfer effects observed in the ash deposition tests are summarized below:

1 The trend of initially increased conductance and decrease was noted at all locations on the nozzle. The effect was much less pronounced, however, on the suction surfaces. The initial "peaking" of the conductance was observed to occur first on the suction surface, then on the pressure surface.

2 The relative reduction in conductance for a well-established ash deposit was somewhat greater for the suction surfaces than for the pressure surfaces.

3 Spontaneous increases in conductance were noted at several points, apparently indicating a localized removal of ash deposit. Many of these events were not sufficient to effect a noticeable increase in effective throat area for the three-passage nozzle.

4 Ash removal by nutshelling resulted in pronounced increases in conductances at all locations.

5 Ash removal due to thermal excursions resulted in conductance increases exceeding the increases observed during nutshelling.

6 For given levels of throat area plugging, the ash layer conductance for the second and third (higher firing temperature) tests was somewhat greater than for the first test. This would seem to indicate a higher ash conductivity, assuming a similar deposit thickness.

7 The trend of initially increasing conductance early in the tests was noticed to be occurring more quickly but to peak at lower magnitudes in the higher temperature tests.

Ash Sample Analysis

A number of ash samples are commonly taken at the conclusion of each test together with color photographs of the nozzle sector to aid in integrating the microscopic findings to the actual nozzle surface location. The history and analysis results of a particular ash sample taken during test 4 should illustrate the variety of analyses performed and lend an insight into the ash structure and properties.

The turbine simulator was shut down with approximately 4 percent of the effective throat area blocked. Nozzle high pressure cooling water circulation was stopped to prevent ash hydration prior to the deposit distribution and thickness inspection.

Figure 12 shows a view of the water-cooled nozzle throat region 20 min after an off-line hydration cleaning experiment was initiated. Note the pressure side section of ash which had

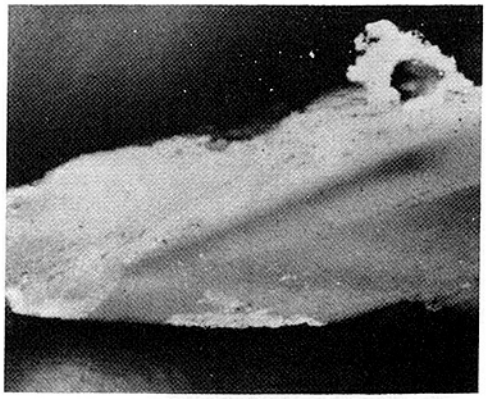

Fig. 14 Ash cross section with polarized light

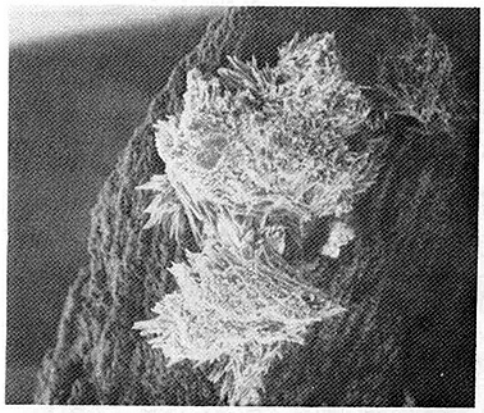

Fig. 15 SAM ash exterior surface (70X)

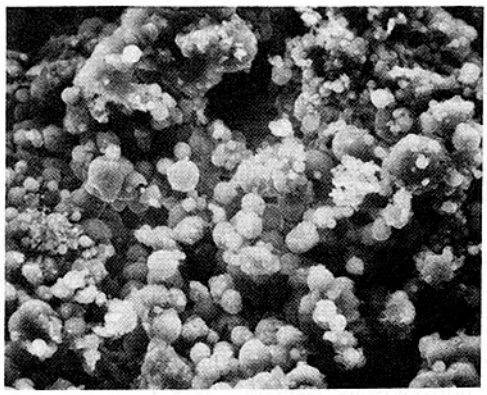

Fig. 16 SEM ash interior surface (1000X)

become disbonded from the wet nozzle surface. The renewed circulation of cooling water in the nozzle caused surface temperatures to drop below the dew point. Hydration of the water solubles is evident within minutes, particularly in the low ash density areas.

The disbonded section of ash was picked from the passage and retained for analysis. Figure 13 shows the outer surface of the dry ash sample just prior to the analysis. In appearance, the deposit outer surface was tan-brown while the interior surface had a distinct grey tinge. Small clusters of white crystals, 1 or 2 mm in diameter, were scattered on the outer surface. Three small powder samples were taken by scraping and subjected to x-ray diffraction for identification of compounds. Samples were as follows:

1 Small white crystals on exterior surface
2 Tan-brown powder on exterior surface

Table 4 Ash x-ray diffraction results pressure side sample—test 4

Amount of compounds detected	(1) White crystals	(2) Tan-brown exterior	(3) Grey interior
Major	$MgSO_4 \cdot 7H_2O$	MgO	MgO
Minor	---	---	---
Trace	MgO	$Mg_3V_2O_8$	$MgSO_4 \cdot 7H_2O$ $MgSO_4 \cdot 6H_2O$

3 Grey powder on interior surface

The results of the analysis are shown in Table 4, indicating that the bulk of the deposit was MgO with traces of $Mg_1V_2O_8$. The white magnesium sulfate crystals were likely caused by the hydration of $MgSO_4$ to form $MgSO_4 \cdot 6H_2O$, which moved through the ash deposit pores by capillary action. Evaporation of some of the water on the surface left $MgSO_1 \cdot 7H_2O$ crystals, which had carried a trace of MgO out of the structure. A typical cross section is shown in Fig. 14 using polarized light. At the bottom of the photograph is the grey interior surface of the deposit while the tan exterior and white crystal module is shown at the top. The probable porous path for the solution of $MgSO_4 \cdot 7H_2O$ is plainly seen from lower left to upper right. The structure is not uniform and contains many pores throughout.

An SEM photograph was taken of the outer surface at 70X (Fig. 15). The rough brown exterior relative to the smoother grey interior reflects the erosive relative to the smoother grey interior reflects the erosive nature of heavy fuels particle deposition along the leading edge and pressure surface of stage 1 nozzles. A 1000X SEM photograph of the grey interior surface which had disbonded from the nozzle pressure side is shown in Fig. 16 to contain a range of particles below 10 micrometers in diameter.

Discussion

The water-cooled nozzle throat area plugging rates observed have demonstrated the marked influence of increased combustor exit temperatures. Similar results have been shown on companion tests using an air-film cooled nozzle sector.

Ash cleanability characteristics observed in the water-cooled nozzle tests differ markedly from those of previous air-cooled tests. The ash deposits appeared to be much more sensitive to operational disturbances and were more easily removed, both off- and on-line, than deposits observed in air-cooled tests. The apparent explanation for this is that the lower metal surface temperature of the water-cooled nozzle results in the formation of ash with a lower bonding strength at the ash/metal interface. Stresses imposed by thermal shocks or impact of abrasive material are thus more likely to exceed this lower bonding strength and fracture the deposit.

Some of the heat transfer observations made during the tests were very intersting and, in addition, provided support for explanations of other phenomena. For instance, it was noted that the surface conductance of the vane increased initially due to roughness, and then decreased as an insulating ash layer formed. The heat transfer augmentation effect was not as pronounced, however, on the suction surfaces of the vanes. Physical observations of the ash deposit made after the tests revealed that the suction surface deposits were indeed much finer than those on the pressure surfaces and at the leading edge. The difference is somewhat due to erosion of the ash along areas where inertial impaction plays a strong role, while other mechanisms, such as diffusion or eddy impaction, may predominate along the suction surface [16,17]. In addition, physical observation of the ash layer thickness, along with the conductance calculations, allows one to estimate the

conductivity of the ash formed [9]. The conductivity for the suction surface ash was found to be much lower than for the inertial impaction region, indicating a less dense deposit.

The conductivity of the ash formed at the higher temperature was apparently greater than that formed in the first test. This may be due to the higher gas momentum resulting in a more densely packed deposit, or possibly to a change in the physical character of the ash at the higher temperature. The airfoil aerodynamic state certainly has been shown to play a major role in local ash accumulation rates.

Conclusions

From a preliminary assessment of the ash deposition rate data, on-line cleaning attempts, nozzle inspections, and ash analysis on the four water-cooled turbine nozzle tests performed thus far, the following conclusions are drawn:

1 Ash deposition rates increase with increasing turbine inlet temperatures.

2 The effect of airfoil surface temperature on net ash accumulation rate would appear quite narrow at present-day heavy fuels firing temperatures; however, at increased firing temperature, the variance is broadened.

3 Several important factors apparently affect the rate of ash deposition on a surface of given geometry aside from the ash species and loading. The gas and surface temperature effects have been discussed. Particular consideration must be given the aerodynamic state of the surfaces when incomplete cleaning or partial shedding has taken place.

4 Ash cleanability is dramatically enhanced by the lower surface temperatures at the ash/metal interface in the water-cooled turbine nozzle.

5 Alternative on-line cleaning techniques such as thermal excursions and nutshelling appear to offer promise for application in prototype water-cooled turbines using heavy fuels.

6 Use of a simple heat transfer model to assist in data reduction can lead to increased insight into the localized in-situ ash behavior during its formation and removal.

7 Ash analysis of samples removed from the nozzle after testing has determined that the composition contains magnesium compounds both water soluble and nonsoluble in a porous matrix of wide-ranging density. The presence of weaker bonded and more friable $MgSO_4$ found along the nozzle-ash interface supports the shedding sensitivity to thermal excursions, as well as a susceptibility to hydrate quickly upon shutdown.

Acknowledgments

The authors wish to express their appreciation to the Electric Power Research Institute, in particular Dr. A. Cohn, for the continued interest in the advancement of gas turbine availability and fuels flexibility. Recognition goes, as well, to D. P. Smith and his organization for management and technical support of fired testing, data collection, and processing.

Appreciation is also expressed for the excellent detailed advanced technology support provided by the following individuals from the Gas Turbine Engineering and Manufacturing Department:

Heavy fuels and corrosion	H. V. Doering R. Haskell
Mechanical design	K. P. Zeman A. J. Piekarski
Heat transfer	D. M. Kercher D. W. Geiling
Turbine aero-thermo	J. M. Hill T. K. Staley
Advanced programs management	A. Caruvana R. S. Rose

References

1 Foster, A. D., Doering, H. VonE., and Hickey, J. W., "Fuels Flexibility in GE Gas Turbines," Gas Turbine Reference Library publication No. GER-2222L, 1977, General Electric Company.

2 White, A. O., "Twenty Years' Experience Burning Heavy Fuels in Heavy Duty Gas Turbines," ASME paper No. 78-GT-22, presented at the ASME Gas Turbine Conference and Products Show, Washington, D.C., Apr. 8-12, 1973.

3 Frieder, A. J., Felix, P. C., and Hess, H. J., "Experiences with Gas Turbines Burning Nonrefined Fuels Oils and Related Theoretical Investigations," ASME paper No. 74-GT-12, presented at the ASME Gas Turbine *Conference and Products Show, Zurich, Switzerland, Mar. 30–Apr. 4, 1974.*

4 Hefner, W. J., and Lordi, F. D., "Progress in Heavy Fuels," Gas Turbine Refernce Library publication No. GET-3110A, 1979, General Electric Company.

5 Lee, S. Y., and Spengler, C. J., "Characterization of Corrosion and Deposits in the Laboratory Gas Turbine Simulator Burning Heavy Fuels with Additives," *Ash Deposits and Corrosion Due to Impurities in Combustion Gases*, edited by R. W. Bryers, Hemisphere Publishing Corp., 1977, pp. 285–308.

6 Urbas, T. A., and Tomlinson, L. H., "Part I: Formation and Removal of Residual Fuel Ash Deposits in Gas Turbines Formed at Firing Temperatures Below 982°C (1800°F)," *Ash Deposits and Corrosion Due to Impurities in Combustion Gases*, edited by R. W. Bryers, Hemisphere Publishing Corp., 1977, pp. 309–320.

7 Urbas, T. A., and Tomlinson, L. H., "Part II: Formation and Removal of Residual Fuel Ash Deposits in Gas Turbines Formed at Firing Temperatures Above 982°C (1800°F)," *Ash Deposits and Corrosion Due to Impurities in Combustion Gases*, edited by R. W. Bryers, Hemisphere Publishing Corp., 1977, pp. 321–333.

8 Lay, K. W., "Ash in Gas Turbines Burning Magnesium-Treated Residual Fuel," ASME JOURNAL OF ENGINEERING FOR POWER, Vol. 95, No. 2, Apr. 1974, pp. 134–137.

9 Blanton, J. C., and Durgin, G. A., "The Effect of Heavy Liquid Fuels Ash Deposition on Heat Transfer in a Water-Cooled Gas Turbine Nozzle Sector," ASME paper 80-HT-15, presented at the Joint ASME/AIChE National Heat Transfer Conference, July 27–30, 1980, Orlando, FL.

10 Horner, M. W., Caruvana, A., Cohn, A., and Smith, D. P., "Near Term Application of Water-Cooling," ASME paper No. 80-GT-159, presented at the ASME Gas Turbine Conferences and Products Show, Mar. 10–13, 1980, New Orleans, LA.

11 Pavri, R. E., and Hill, J. M., "Thermodynamics of Heavy Fuels Operation in Gas Turbine," ASME paper No. 80-GT-171, presented at the ASME Gas Turbine Conference and Products Show, Mar. 10–13, 1980, New Orleans, LA.

12 Nealy, D. A., Timmerman, W. H., and Cohn, A., "Investigation of the Influence of Contaminated Fuel on Turbine Vane Surface Deposition," Paper No. AIAA-80-113, presented at the AIAA/SAE/ASME 16th Joint Propulsion Conference, June 30–July 2, 1980, Hartford, CT.

13 Taylor, J. R., "Heat Transfer Phenomena in Gas Turbines," ASME Paper No. 80-GT-172, presented at the ASME Gas Turbine Conference and Products Show, Mar. 10–13, 1980, New Orleans, LA.

14 Caruvana, A., Day, W. H., Manning, G. B., and Sheldon, R. C., "Evaluation of a Water-Cooled Gas Trubine Combined Cycle Plant," ASME paper No. 78-GT-77, presented at the ASME Gas Turbine Conference and Products Show, April 9–13, 1978, London, England.

15 Halstead, W. K., "Calculations on the Effects of Pressure and Temperature on Gas Turbine Deposition," *Deposition and Corrosion in Gas Turbines*, edited by A. B. Hart and A. J. B. Cutler, John Wiley and Sons, 1973, pp. 22–23.

16 Moore, M. J., and Crane, R. I., "Aerodynamic Aspects of Gas Turbine Blade Corrosion," *Deposition and Corrosion in Gas Turbines*, edited by A. B. Hart and A. J. B. Cutler, John Wiley and Sons, 1973, pp. 34–57.

17 Rosner, D. E., "Mass Transfer from Combustion Gases," prepared for AIChE 73rd Annual Meeting, Nov. 16–20, 1980, Chicago, IL.

Two-Phase Transpiration Cooling

M. A. El-Masri
Assistant Professor.
Department of Mechanical Engineering,
Massachusetts Institute of Technology,
Cambridge, Mass. 02139

Two-phase transpiration is shown to possess considerable potential for gas turbine cooling. In this concept, water fed into a porous component boils within the wall. The resulting steam issues from the hot surface forming the transpiration film. A model for the performance of such a system is developed. Assuming constant properties and a linear reduction of Stanton number with transpiration rate, closed-form solutions are obtained. The governing dimensionless parameters are identified, the system behavior predicted, and the modes of operation delineated. Those are defined as two-phase, partially-flooded, and completely-flooded modes. At low values of a certain "modified Peclet number," the two-phase mode is unstable and the system tends to flood. Large values of this parameter indicate stable, well-regulated behavior. Discussions on gas turbine applications are presented. A typical numerical example is given in the Appendix.

Introduction

Historic Note. The concept of "sweat cooling", the use of a transpired evaporating liquid film to cool a surface is quite old. According to Grootenhuis [1], it was first proposed by H. Oberth in 1929 in connection with cooling rocket engines. Experiments on an oxygen sweat-cooled rocket nozzle were performed by Goddard who obtained a patent in 1928 [2]. Moore and Grootenhuis first suggested its use for gas turbine cooling in 1946 [3].

Historically, the gas turbine has been developed primarily for aircraft propulsion. As firing temperatures increased more sophisticated cooling technologies evolved. The requirements of simplicity and light weight made the use of compressor air as a cooling medium an obvious choice. This was first used as an internal convection coolant, followed by the development of state-of-the-art film injection cooling. To realize a more efficient use of compressor air, full-coverage film cooling and air transpiration using porous blades were proposed. The latter is currently under industrial development [4–6]. Although this effort is directed at utility-type turbines, it is the author's opinion that this technology may eventually be applied to aircraft gas turbines.

More recently, a need has arisen for durable, high-temperature gas turbines to operate in combined gas/steam cycle plants. Low metal temperatures are desirable to minimize corrosion due to sulfur and alkali metal compounds present in residual oil, coal, or coal-derived fuels. The requirement of increased gas and reduced metal temperatures necessitates more effective cooling systems. Water-cooling is one solution.

Since the 1940s a large variety of water-cooling schemes have been proposed and tested. They include closed forced convection, thermosyphons, and open-loop systems. References [7] and [8] provide a review of those schemes. A recent program to develop an open-loop water-cooled turbine is in progress [9,10].

Potential of Two-Phase Transpiration. Two-phase transpiration cooling, as this paper will show, offers considerable benefits. Compared to an equivalent air transpiration system, these are:

1 lower coolant transpiration rate which enhances blade aerodynamic performance as well as cut back on thermodynamic mixing losses;

2 less work lost to pump the liquid coolant than to compress air;

3 cooling water pressure is no longer limited by compressor delivery pressure and may be used to "wash" the porous surface and prevent ash deposition.

Comparing two-phase transpiration to open loop water-cooling reveals the following advantages:

1 Lower water requirements, typically less than 1/3 of that for an open loop system[1]

2 Smaller water pumping work penalty in the rotors

3 Substantial reduction of the "quenching" thermodynamic loss due to mixing coolant and hot gas. This loss may be considerable in an open-loop turbine [11]. Since in transpiration the coolant is discharged as superheated vapor at a lower flow rate this loss is cut drastically.

4 Freedom from critical heat flux constraints [12]

A major incentive to study two-phase transpiration cooling is the thermodynamic benefit if fuel could be used as the transpiration coolant. This avoids any gas quenching losses and enables the expansion to approach isothermicity. Moreover, the effectiveness of the cooling system allows the continuous reaction through such a turbine to be maintained at a very high temperature. The elevated temperature reduces the difference in Gibbs Free Energy between reactants and products associated with combustion at a lower temperature. In the limit where the combustion reaction is carried out near its equilibrium temperature, the turbine approaches the reversible conversion of fuel availability to mechanical work.

Contributed by the Gas Turbine Division of THE AMERICAN SOCIETY OF MECHANICAL ENGINEERS and presented at the 27th International Gas Turbine Conference and Exhibit, London, England, April 18–22, 1982. Manuscript received at ASME Headquarters December 7, 1981. Paper No. 82-GT-89.

[1] This is shown in Appendix C.

This limit can only be approached during part of the cycle and to a degree consistent with a realistic reaction rate. Considerable further study of this concept and its associated coupling of mechanical, thermodynamic, and kinetic constraints is required.

The primary disadvantages of two-phase transpiration are the structural difficulties due to the large differential pressure imposed upon the porous structure and the need for high-purity water to prevent mineral deposits from plugging the porous wall. The latter problem may be less severe if the system is operated in the partially-flooded mode as discussed later. Another major disadvantage is the uncertainty due to lack of data on this system, the potential for unstable operation particularly during transients, and the need to develop novel materials.

Perspective of Work. The heat transfer problem in a transpired wall is composed of two matched subproblems: the internal heat transfer between the coolant and the porous wall, and the interaction of the transpired stream with the external boundary layer.

The internal problem with a single-phase coolant is discussed in [1] and [13]. With a two-phase coolant, Koh and del Casal [14] presented internal temperature distributions for the case of a given external heat flux. Rubin and Schweitzer [15] solved the problem for a given external wall temperature or given external heat flux. They showed that the latter possesses three possible solutions, two stable and one unstable.

Considerable research has been done on the external heat transfer problem, the transpired boundary layer. An excellent comprehensive review is given by Jeromin [16].

In this paper the two problems are combined using a simple model to describe their interaction. The basic relations describing the performance of the composite problem are set forth. The operating regions and essential features of this system are defined and discussed.

Analysis

Model Physical Description. Figure 1 shows a section through the transpiration-cooled wall. A hot gas stream of adiabatic wall temperature, T_g, and static pressure, p_g, flows along its external surface at a moderate Mach Number. To cool the wall, subcooled liquid is provided at its internal surface from a reservoir at a pressure $p_o > p_g$. The coolant temperature is T_o at a large distance from the wall. The pressure difference drives coolant across the wall at a mass flux, G.

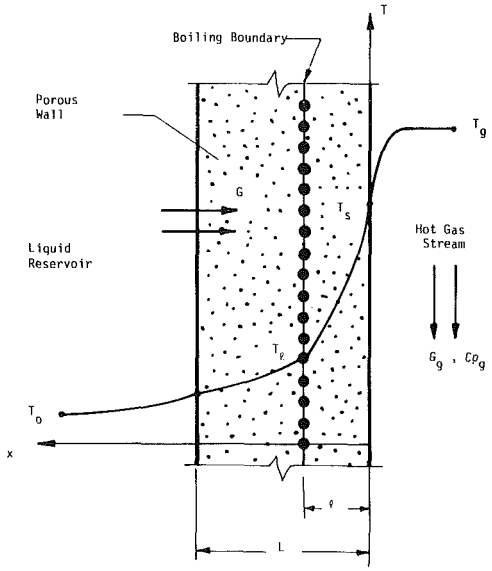

Fig. 1

Under certain conditions, discussed later in this paper, the situation depicted in Fig. 1 prevails. The liquid flowing into the wall boils at a certain location $x = l$. The vapor generated at the boiling plane continues across the wall and transpires through the hot surface.

In such a system, for a given set of physical dimensions and property values, the externally imposed parameters are the driving pressure difference $(p_o - p_g)$ and the hot gas stream conditions and temperature, T_g. The system responds to those parameters by having a certain coolant flow rate, G, and corresponding values of the boiling length, l, and the wall surface temperature, T_s.

The nonlinearity of the system, i.e., the possibility of

Nomenclature

a = permeability of prous matrix (s)
$\tilde{a}$ = ratio of vapor to liquid permeabilities
B = blowing ratio, defined in equation (12)
b = injection parameter, defined in equation (11)
Cp = constant pressure specific heat (J/kg-K)
G = mass flux (kg/m^2-s)
H = dimensionless pressure drop, defined in equation (22)
h = heat transfer coefficient (W/m^2-K)
i_{fg} = latent heat of vaporization (J/kg)
K = dimensionless pore-geometry constant
k = thermal conductivity (W/m-K)
L = thickness of porous wall (m)
l = boiling length (m)
$\tilde{l}$ = dimensionless boiling length = l/L
M = heat sink number, defined in equation (19)
m = dimensionless parameter, defined in equation (25)
p = pressure (N/m^2)
Δp = pressure drop across wall (N/m^2)
Pe = Peclet Number, defined in equation (7)
Pe′ = modified Peclet Number, defined in equation (23)
Pe″ = second modified Peclet Number, defined in equation (31)
r = characteristic pore radius (m)
S = boundary layer transpiration parameter, defined in equation (20)
St = Stanton Number = $h/G_g\, Cp_g$
St_o = Stanton Number in the absence of transpiration
T = temperature (K)
T_l = temperature at boiling plane (K)
x = length coordinate from surface (m)

Greek

θ_o = dimensionless reservoir subcooling, defined in equation (18)
θ_s = dimensionless surface temperature, defined in equation (17)
ν = kinematic viscosity (m^2/s)
ϕ = heat flux into wall surface

Subscripts

g = gas
l = liquid properties
o = reservoir
v = vapor

multiple internal solutions to the same set of externally imposed parameters, can be appreciated by noting that the solution results from the following physical interactions:

1 Due to the difference in hydraulic resistance of the porous matrix to liquid or vapor phase, a relationship between transpired mass flux, G, and boiling length, l, exists for a given pressure drop.

2 The internal "Peclet problem" in the porous wall relates wall temperature, T_s, saturation temperature, T_l, boiling length, l, transpired mass flux, G, and heat flux into the wall surface, ϕ. In addition, the Peclet problems for each phase should match at the boiling boundary.

3 The surface heat flux is determined by the gas-to-surface temperature difference and an appropriate external heat transfer coefficient. The latter, in turn, is a function of the transpired mass flux, G.

In what follows, an elementary model using constant properties and simplified relations describing those interactions is presented. This is thought to retain sufficient basic features as to shed light on the expected behavior of this system. More detailed analysis, including property variations and appropriate empirical results for the interaction relationships should be performed for any specific design situation.

Model Assumptions and Governing Equations.

1 The porous matrix is homogeneous.

2 The flow is steady and one-dimensional.

3 Properties for each phase are constant.

4 D'Arcy's law may be used to relate pressure gradient to flow rate through the porous matrix. If r characterizes pore size, this assumption would be valid if the Reynolds number $\mathrm{Gr}/\mu_v < 1$. This enables D'Arcy's law to be written in the form

$$\frac{dp}{dx} = -\frac{8\nu G}{Kr^2} \tag{1}$$

where the numerical constant, K, depends on porosity, pore geometry, and wetting characteristics of the porous body. Its value is unity for a single capillary if surface effects are neglected.

Defining the hydraulic permeability of the porous matrix to the liquid and vapor phases, respectively, as

$$a_l = \frac{Kr^2}{8\nu_l}$$

$$a_v = \frac{Kr^2}{8\nu_v} \tag{2}$$

allows the pressure drop across the slab for the case where K is assumed the same for both phases to be written as

$$\Delta p = \frac{G(L-l)}{a_l} + \frac{Gl}{a_v} \tag{3}$$

In equation (3) the pressure drop due to accelerating the coolant at the boiling boundary has been tacitly ignored. This may be shown to be valid provided $L/r >> \nu_v/\nu_l$ in addition to the previous assumption of small vapor pore Reynolds Number.

5 Changes in saturation temperature due to the pressure drop across the slab are small. Hence a constant saturation temperature corresponding to the system pressure is used.

6 The boiling boundary may be treated as a plane of negligible thickness rather than a zone of finite extent, probably covering a distance of many pore sizes. The influence of pore curvature on boiling is acknowledged by assigning a saturation temperature, T_l, to this hypothetical plane.

7 The temperature of the fluid at any point is identical to the local matrix temperature.

8 An effective thermal conductivity, k, assumed constant, can be assigned to the porous matrix/fluid combination.

With the above assumptions we may now solve the internal Peclet problem in the wall. For the vapor zone $l > x \geq 0$, the energy equation

$$-GCp_v \frac{dT}{dx} = k\frac{d^2T}{dx^2} \tag{4}$$

can be integrated with boundary conditions

$$\begin{aligned} T(0) &= T_s \\ T(l) &= T_l \end{aligned} \tag{5}$$

the resulting temperature distribution may be used to relate the wall heat flux, ϕ, to surface temperature, T_s, and boiling length, l:

$$\phi = -k\frac{dT}{dx}\bigg|_{x=0} = \frac{G\,Cp_v(T_s - T_l)}{1 - e^{-Pe\tilde{l}}} \tag{6}$$

where $\tilde{l}$ denotes the dimensionless boiling length l/L and Pe the Peclet Number,

$$\mathrm{Pe} = \frac{G\,Cp_v L}{k} \tag{7}$$

An energy balance between $x = 0$ and $x = \infty$ may be used in lieu of solving the Peclet problems in the liquid zone and reservoir and matching them to that for the vapor zone. The result is independent of T_L and yields

$$\phi = G[Cp_l(T_l - T_o) + i_{fg} + Cp_v(T_s - T_l)] \tag{8}$$

To close the system, we now focus on the external heat transfer

$$\phi = h(T_g - T_s) \tag{9}$$

where the heat transfer coefficient, h, depends on transpired mass flux

$$h = h(G) \tag{10}$$

The form of this dependence is discussed in Appendix I. Equations (3, 6, 8, 9, 10) are five equations in the five unknowns G, l, T_s, ϕ, h. Their simultaneous solution provide the model performance.

Dimensionless Relations and Results. We define an injection parameter, b, as the ratio between transpired and gas stream mass fluxes

$$b = \frac{G}{G_g} \tag{11}$$

Denoting by b_{cr} the injection parameter which just separates the gas stream boundary layer, we define a blowing ratio, B, as

$$B = \frac{b}{b_{cr}} = \frac{G}{G_{cr}} \tag{12}$$

The external heat transfer coefficient may be expressed in dimensionless form as the Stanton Number

$$h = \mathrm{St} \cdot G_g Cp_g \tag{13}$$

and, following the arguments presented in Appendix A, we assume a linearized relation between Stanton Number and blowing ratio[2]

$$\mathrm{St} = \mathrm{St}_o(1 - B) \tag{14}$$

Thus relations 13 and 14 are used to imply equation (10). This allows the elimination of the unknown heat transfer coefficient from equation (9) in favor of the blowing ratio giving

$$\phi = \mathrm{St}_o(1 - B)G_g Cp_g(T_g - T_s) \tag{15}$$

[2] Note that St_o and b_{cr} in this relation need not be the actual values, but suitable numbers to linearize the Stanton Number – Injection Rate relation around the projected operating point.

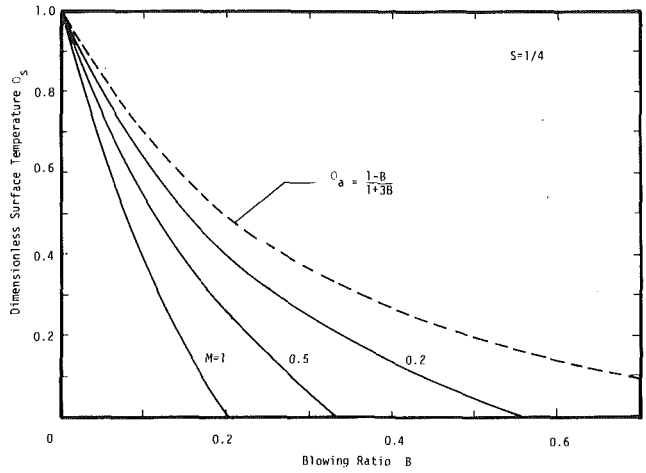

Fig. 2 Reduction of surface temperature by transpiration

Now the wall surface heat flux, ϕ, may be eliminated between equations (8) and (15) to yield a relation between the wall surface temperature and the blowing ratio

$$\theta_s = \frac{S(1-B)-MB}{S(1-B)+B} \tag{16}$$

where the dimensionless wall surface temperature, θ_s, reservoir subcooling, θ_o, "heat sink number," M, and boundary layer transpiration parameter, S, are defined as

$$\theta_s = \frac{T_s - T_l}{T_g - T_l} \tag{17}$$

$$\theta_o = \frac{T_l - T_o}{T_g - T_l} \tag{18}$$

$$M = \frac{Cp_l}{Cp_v}\theta_o + \frac{i_{fg}}{Cp_v(T_g - T_l)} \tag{19}$$

$$S = \frac{Cp_g}{Cp_v}\frac{\mathrm{St}_o}{b_{cr}} \tag{20}$$

Equation (16) shows the power of two-phase transpiration cooling. It is plotted on Fig. 2 for $S = 1/4$. Typical of water-transpired gas turbine conditions as discussed in Appendix I. For comparison, the dashed line represents air transpiration with $S = 1/4$ and $M = 0$, θ_s in this situation representing the "cooling effectiveness" defined by Bartle and Leadon [17] if the air were supplied at a temperature, T_l. It shows that for $M = 0.5$, $\theta_s = 0.2$, typical of high temperature water-cooled turbines[3], water transpiration requires less than half the blowing ratio, B. The injected mass flux for water would be still lower since b_{cr} is less for water vapor than for air. Moreover, the surface can be maintained at saturation temperature for any gas temperature without separating the boundary layer.

Now equation (16) and Fig. 2 present the wall temperature for a given blowing ratio, B. As discussed above, the latter is an internal variable, determined by the externally imposed parameters, physical dimensions, and properties. To investigate this relation some algebraic manipulation of equations (3, 6, 8, 15) is required to eliminate heat flux, surface temperature, and boiling length, leaving a relation between blowing ratio (or transpired mass flux) and given externally imposed quantities

$$B + \frac{Me^H}{1+M}\left[1 + \left(\frac{1-S}{S}\right)B\right]e^{-\mathrm{Pe}'B} = 1 \tag{21}$$

[3] A typical numerical example is given in Appendix B.

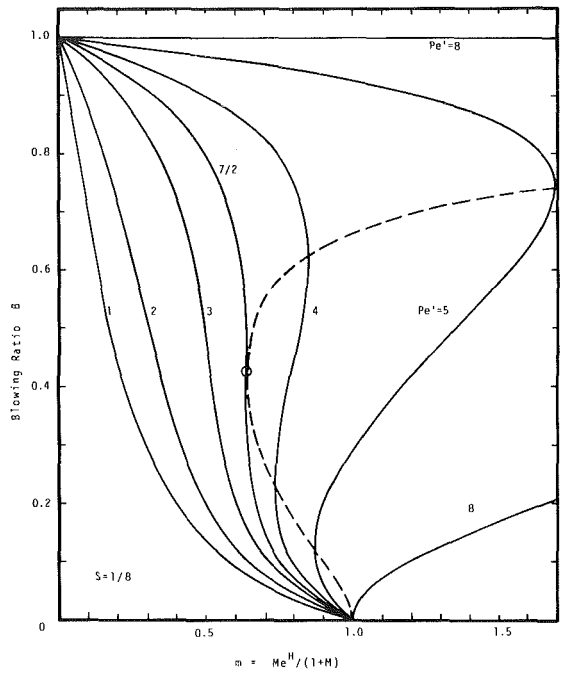

Fig. 3 System characteristics for $S = 1/8$

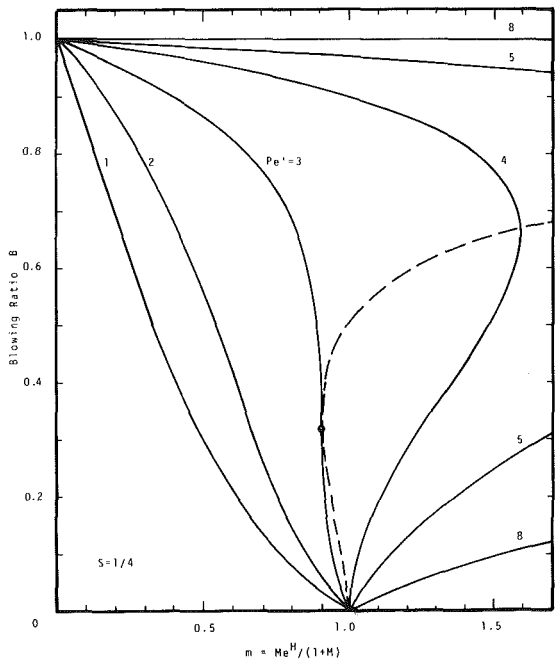

Fig. 4 System characteristics for $S = 1/4$

where H denotes a dimensionless pressure (or head) drop and P_e' a "modified Peclet Number,"

$$H = \frac{\Delta p Cp_v a_v}{k(1-\tilde{a})} \tag{22}$$

$$\mathrm{Pe}' = \frac{G_g Cp_v L}{k} \cdot b_{cr} \cdot \frac{\tilde{a}}{1-\tilde{a}} \tag{23}$$

$\tilde{a}$ denotes the ratio of hydraulic permeability for vapor to that for liquid, which, in view of equation (2) can be approximated by the kinematic viscosity ratio

$$\tilde{a} = \frac{a_v}{a_l} \simeq \frac{\nu_l}{\nu_v} \tag{24}$$

Equation (21) indicates that for a given value of S, the blowing ratio, B, is a function of Pe′ and a group, m,

$$m \equiv \frac{Me^H}{1+M} \tag{25}$$

this relation is plotted in Figs. 3 and 4 for values of S of 1/8 and 1/4, respectively.

Regimes and Modes of Operation. From Figs. 3 and 4, three regions may be discerned:

(*i*) $\text{Pe}' \leq 4(1-S)$: B is single-valued, moreover, $\partial B/\partial m < 0$ indicating a reduced pressure drop for increased blowing. This is unstable and the system would tend to flood itself.

(*ii*) $4(1-S) < \text{Pe}' \leq 1/S$: B is triple-valued, the intermediate value falls on a stable positive sloping characteristic whereas the upper and lower values are on an unstable negative-sloping portion.

(*iii*) $\text{Pe}' > 1/S$: B is double valued, with a stable lower and unstable upper value. In any practical case, however, the system would flood before the upper value is reached.

Setting $\partial m/\partial B = 0$ gives the equation for the envelope enclosing the positive-sloping characteristics shown by the dashed lines on Figs. 3 and 4

$$m = \frac{S(1-B)}{S+(1-S)B} \exp\left[\frac{B}{(1-B)[S+(1-S)B]}\right] \tag{26}$$

eliminating B from (21) and (26) numerically enables this zone to be defined on m versus Pe′ coordinates on Fig. 5.

Two-Phase Range, Flooding. Solving equations (3, 6, 8, 15) for $\tilde{l}$ gives

$$\tilde{l} = \frac{\tilde{a}}{(1-\tilde{a})}\left[\frac{H}{B\text{Pe}'} - 1\right] \tag{27}$$

If $l \geq 1$, boiling penetrates into the reservoir and this analysis ceases to be valid. The minimum blowing ratio, B_1, for the two-phase range is thus

$$B_1 = \tilde{a}H/\text{Pe}' \tag{28}$$

which, in view of equation (21), may be expressed from

$$\frac{1-\tilde{a}}{\tilde{a}}\text{Pe}'B_1 = ln\left[\frac{S(1+M)(1-B_1)}{M[S+(1-S)B_1]}\right] \tag{29}$$

On the other hand, the maximum blowing ratio for two-phase transpiration, B_2, occurs when $\tilde{l} = 0$.

$$B_2 = H/\text{Pe}' = S/(S+M) \tag{30}$$

Equations (29) and (30) are plotted on Fig. 6 for $S = 1/4$. They show that the width of the two-phase zone is governed by a second modified Peclet Number

$$\text{Pe}'' = (1-\tilde{a})\text{Pe}'/\tilde{a} = b_{cr} \cdot G_g Cp_v L/k \tag{31}$$

For $B > B_2$, the flow across the slab is single-phase liquid and the pressure drop -- flow rate relationship becomes

$$H = B\text{Pe}' \quad (B > B_2) \tag{32}$$

At blowing rates just above B_2, a highly complex situation develops. Portions of the transpired liquid may escape the wall without evaporation, wasting their latent heat. In this case, the boundary condition used at the wall in the preceding analysis cannot be satisfied. Partial loss of the evaporative heat sink for a given external heat transfer coefficient would result in raising the surface temperature above saturation. This would drive the boiling boundary back into the wall, resulting in recovery of the entire evaporative heat sink, lowering the surface temperature and re-expelling the boiling boundary. Hence, some unsteadiness is expected at those conditions with the boiling plane being bound to the wall outer surface. This condition is termed *partial flooding*.

At yet higher flow rates, a condition is eventually reached

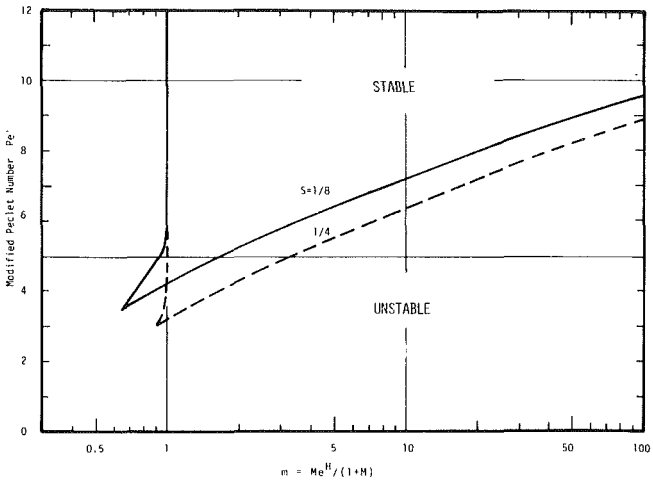

Fig. 5 Definition of unstable zone

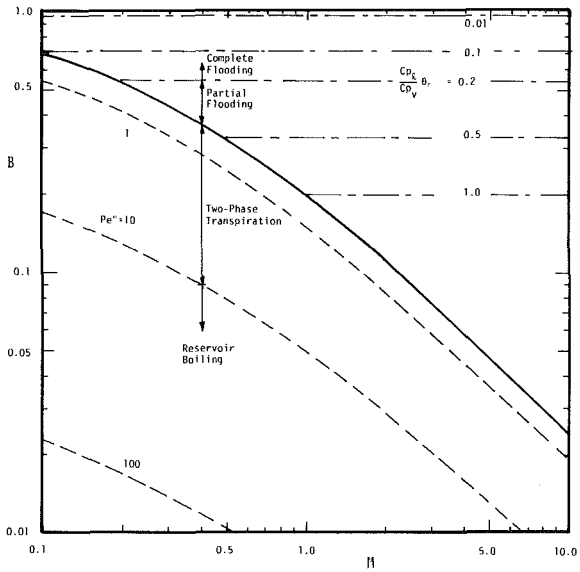

Fig. 6 Modes of system operation for $S = 1/4$

where sufficient liquid transpires through the wall to keep the surface at or below saturation temperatures even if the entire latent heat sink is lost to the gas stream away from the wall. This situation is termed *complete flooding* and in view of equation (30), prevails at blowing ratios above a certain value, B_3, defined by

$$B_3 = \frac{S}{S + \dfrac{Cp_l}{Cp_v}\theta_o} \tag{33}$$

In practice, equation (33) is expected to predict the upper bound for the onset of complete flooding, since there will always be some evaporative cooling in the gas boundary layer. The complete flooding lines are shown in Fig. 6 for different values of $Cp_l\theta_o/Cp_v$. After complete flooding, the system performance is expected to approximate continuous liquid film cooling provided the water remains attached to the surface [18].

An illustration of the system performance for $S = 1/4$. $M = 1/2$ is presented in Figs. 7, 8 and 9. The three internal variables B, θ_s, and l are plotted against H with Pe′ as parameter. For low values of Pe′, less than 3, the system

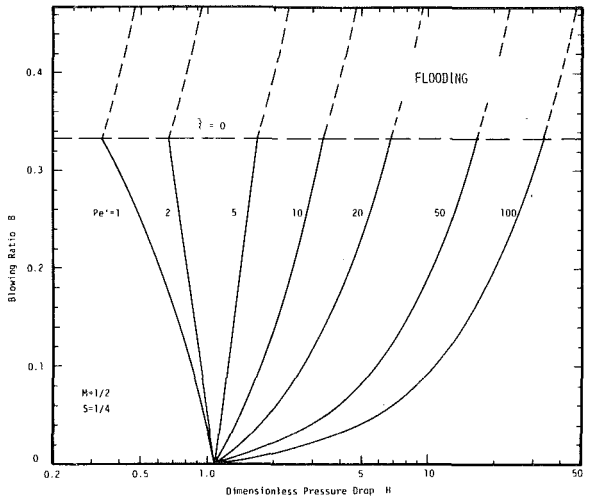

Fig. 7 Blowing ratio versus pressure drop for $M = 1/2$, $S = 1/4$

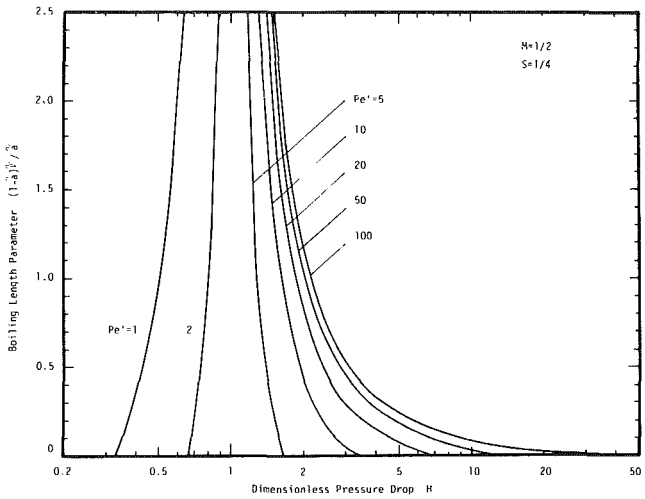

Fig. 9 Boiling length versus pressure drop for $M = 1/2$, $S = 1/4$

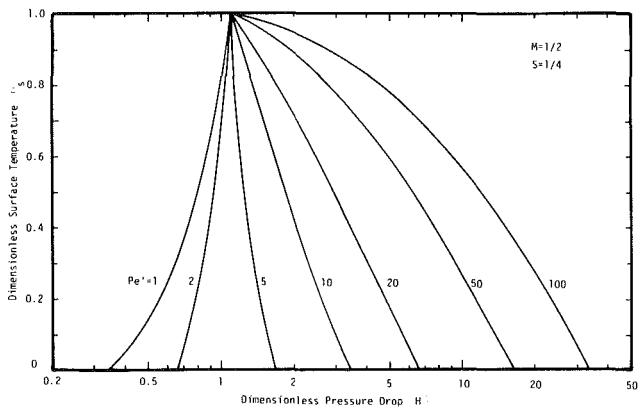

Fig. 8 Surface temperature versus pressure drop for $M = 1/2$, $S = 1/4$

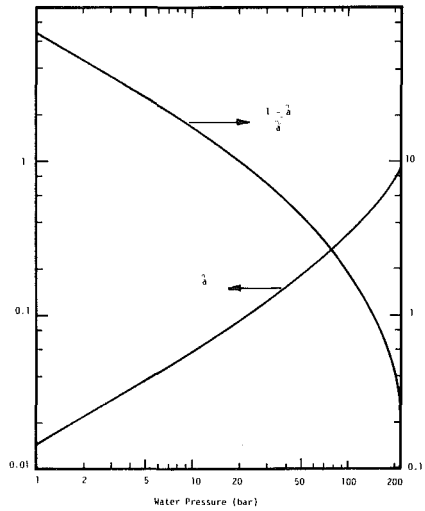

Fig. 10 Permeability ratio for water as a function of pressure

would suffer an excursion into the flooded mode. The blowing ratio would be set by the value of the pressure difference intersecting the dashed lines at the top of Fig. 7. Whether this is complete or partial flooding can be determined from Fig. 6 depending on the reservoir subcooling. Intermediate values of Pe′ indicate poor regulation due to the steepness of the curves. The larger values of Pe′ above 20, say, show regions where good regulation may be obtained. Those would require $(1-\tilde{a})\tilde{l}/\tilde{a}$ to be of the order unity or less. Figure 10 shows $(1-\tilde{a})/\tilde{a}$ for water as a function of system pressure. It shows that at typical gas turbine pressures, the well-regulated region prescribes values of $\tilde{l}$ on the order of 0.01.

It is recommended that gas turbine applications be designed to operate either partially flooded at low values of Pe′ or in the two-phase mode if sufficiently large Pe′ can be realized, on the order of 100 or more, say. The problem in achieving the latter may be that the necessary thickness, L, would be too large for thin blade profiles unless porous materials or very low conductivity are available.

In a gas turbine rotor, the reservoir within the blades would have a radial pressure gradient due to rotation, thus the pressure difference, Δp, and consequently, H, would vary along the blade length. To achieve uniform blowing the wall thickness can be tapered providing an increasing Pe′ with radius such that θ_s or B are maintained almost uniform along the blade. Figures 7 and 8 can be used to determine the necessary taper.

The problem of rotational pressure gradient may be ameliorated by running the reservoir at much higher pressure than the gas. Thus the percentage change in pressure difference may be kept quite moderate. At such conditions, the high reservoir pressure achieved by rotation is likely to be supercritical. Even then, the analysis presented here is thought to be representative. This is because in most practical cases the boiling length is so small that the saturation temperature is essentially determined by the gas-side pressure.

Conclusions

1 Two-phase transpiration has been identified as a potentially powerful cooling scheme for gas turbines. Moderate blade temperatures may be maintained in very high temperature gas streams without separating the boundary layer or incurring large aerodynamic or cooling penalties.

2 A stable well-regulated system is believed to be possible.

3 Considerable research and development is required to address all facets of this system. In view of its advantages this may be well justified.

References

1 Grootenhuis, P., "The Mechanism and Application of Effusion Cooling," *Journal of the Royal Aeronautical Society*, Vol. 63, 178, Feb. 1959, pp. 73–89.

2 Goddard, R. H., U.S. Patent 2,183, 313; 1938.

3 Moore, N. P. W., and Grootenhuis, P., U.K. Patent 619,634; 1946.

4 Wolf, J. C., Moskowitz, S., and Manning, G. B., "Development of a High-Temperature Turbine for Operation on Coal-Derived Fuel," ASME 80-GT-188.

5 Technical Progress Report, "High Temperature Turbine Technology Program Phase II," Curtiss-Wright Corp., Report No. FE-2291-58A, Woodridge, N.J., 1979.

6 "Turbine Spool Technology Rig Cascade Tests, High Temperature Turbine Technology Program, Phase II," Curtiss-Wright Corp., Report No. FD-2291-76A, Woodridge, N.J., June 1981

7 Bayley, F. J., and Martin, B. W., "A Review of Liquid Cooling of High-Temperature Gas-Turbine Rotor Blades," *Inst. Mech. Engrs. Proc.* Vol. 185, 1970-71, pp. 219–227.

8 Van Fossen, G. J., and Stepka, F. S., "Liquid Cooling Technology for Gas Turbines, Review and Status," NASA Tm-78906, 1978.

9 Caruvana, A., et al., "Design and Test of a 73-MW Water-Cooled Gas Turbine," ASME Paper No. 80-GT-112.

10 Caruvana, A., et al., "Evaluation of a Water-Cooled Gas Turbine Combined Plant," ASME Paper No. 78-GT-77.

11 El-Masri, M. A., Kobayashi, Y., and Louis, J. F., "A General Performance Model for the Open-Loop Water-Cooled Turbine," ASME Paper No. 82-GT-212.

12 El-Masri, M. A., and Louis, J. F., "On the Design of High-Temperature Gas Turbine Blade Water-Cooling Channels," ASME JOURNAL OF ENGINEERING FOR POWER, Vol. 100, Oct. 1978, pp. 586–591.

13 Koh, J. C. Y., and delCasal, E., "Heat and Mass Flow Through Porous Matrices for Transpiration Cooling," *Proceedings of the 1965 Heat Transfer and Fluid Mechanics Institute*, Vol. 16, Stanford, CA, 1965, pp. 263–281.

14 Koh, J. C. Y., and delCasal, E., "Two-Phase Flows in Porous Matrices for Transpiration Cooling," *Proceedings of the 10th Midwestern Mechanics Conference*, 1967.

15 Rubin, A., and Schweitzer, S., "Heat Transfer in Porous Media with Phase Change,' *International Journal of Heat and Mass Transfer*, Vol. 15, 1972, pp. 43–60.

16 Jeromin, L. F., "The Status of Research in Turbulent Boundary Layers with Fluid Injection," *Progress in Aeronautical Sciences*, Vol. 10, Pergamon Press, 1970, pp. 65–189.

17 Bartle, E. R., and Leadon, B. M., "The Effectiveness as a Universal Measure of Mass Transfer Cooling for a Turbulent Boundary Layer," *Proceedings of the 1962 Heat Transfer and Fluid Mechanics Institute*, Stanford, Calif., 1962, pp. 27–41.

18 Warner, C. F., and Emmons, D. L., "Effects of Selected Gas Stream Parameters and Coolant Properties on Liquid Film Cooling," ASME *Journal of Heat Transfer*, May 1964, pp. 271–278.

19 Kutateladze, S. S., and Leont ev, A. I., "Heat-Mass Transfer and Friction in a Turbulent Boundary Layer," NASA TT F-805, 1974.

20 Romanenko, P. N., and Karchenko, V. N., "The Effect of Transverse Mass Flow on Heat Transfer and Friction Drag in a Turbulent Flow of Compressible Gas Along an Arbitrarily Shaped Surface," *International Journal of Heat and Mass Transfer*, Vol. 6, 1963, pp. 727–738.

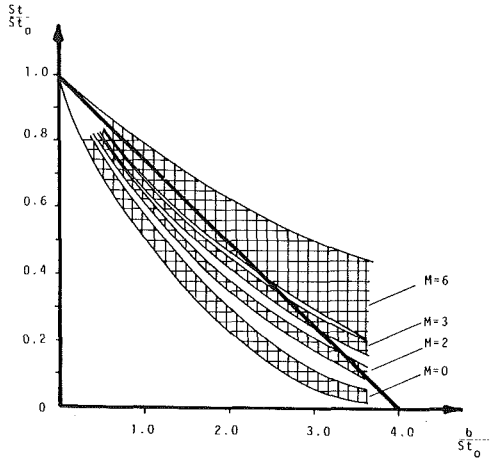

Fig. 11 Data compiled by Jeromin [16] from nine sources showing the reduction of Stanton Number by air transpiration into a turbulent airstream flowing at the indicated Mach Number

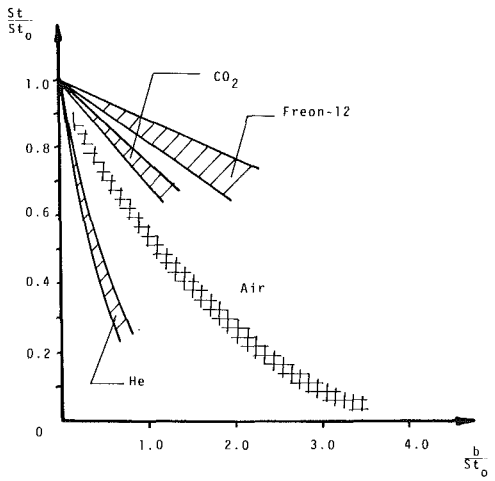

Fig. 12 Data on the reduction of Stanton Number due to transpiration of various gases into an airstream flowing at low Mach Number. After Romanenko and Karchenko [20]; comparison with air data by Jeromin [16].

APPENDIX A

The External Boundary Condition

The transpired turbulent boundary layer has been the subject of extensive research. A comprehensive review of the field has been given by L.O.F. Jeromin [16]. Figure 11, copied from that reference, shows data compiled from nine different sources. The shaded bands represent data scatter for each Mach Number range. The figure is for air transpiration from flat plates as well as cones.

In this paper, a linear reduction in Stanton Number with transpired flux will be assumed. This does not have to be regarded as covering the entire range, but may be thought of as a linearized portion of the curve near the operating point. In any case, a more accurate curve fit or numerical relation should be used for any specific situation. Thus, it is assumed that

$$\frac{\mathrm{St}}{\mathrm{St}_o} = 1 - \frac{b}{b_{cr}} = 1 - B \qquad \text{(A1)}$$

where b_{cr} is either the critical injection parameter or a suitable number to linearize the curve around a certain point. In the latter case St_o should be suitably changed from its true non-injection value. The solid line in the figure implies $b_{cr} = 4\ \mathrm{St}_o$, the theoretical value for an incompressible turbulent boundary layer as the Reynolds Number becomes infinite [19].

Where the transpired fluid is different from the mainstream the situation is considerably more complex. Generally, a lower molecular weight gas would have a smaller b_{cr} since its mass flux is smaller relative to its momentum flux. Figure 12 shows data for three different fluids as obtained by Romanenko and Karchenko [20]. The slopes of the data bands indicate values of b_{cr}/St_o of 1, 3.8 and 7.2 for He, CO_2, and Refrigerant 12, respectively.

Now we are interested in the value of the parameter, S. Using ideal gas laws for the specific heat ratio of equation (20) results in values of S of 0.19, 0.35 and 0.5 for He, CO_2, and Refrigerant-12, respectively. When tabulated values of the specific heats at room temperature are used in equation (20), the values of S obtained are 0.2, 0.3, and 0.23, respectively. Since the molecular weight of water vapor is about half way between He and CO_2, both the above approaches suggest $S = 0.25$ to be a reasonable expectation for steam transpiration into air or combustion gas.

APPENDIX B

Typical Numerical Example

Gas Stream Conditions		Saturated Water Properties @ 20 bars	
p	= 20 bars	T_l	= 485 K
T_g	= 2000 K	Cp_l	= 4.55 kJ/kg K
Cp_g	= 1.18 kJ/kg K	Cp_v	= 3.04 kJ/kg K
G_g	= 1672 kg/m^2 – s	i_{fg}	= 1901 kJ/kg

Assumptions

1 Boiling plane pressure same as gas side pressure
2 $S = 1/4$, as discussed in Appendix II
3 $St_o \simeq 0.005$, a typical value for turbine blades; thus $b_{cr} \cong 0.0078$ (from equation (20))

Design Decisions

1 $M = 0.5$, requiring a reservoir temperature of 397 K (88 K subcooling)
2 $\theta_s = 0.25$, which would maintain surface temperature $T_S = 864$ K, from equation (16) this requires $B = 0.2$
3 Wall thickness $L = 0.01$ m. This may be reasonable for large utility-size turbines where blades with chords of about 0.15 m are envisioned. The trailing edge would have a two-dimensional transpiration pattern that cannot be analyzed in a simple manner.
4 Pressure drop $\Delta p = 50$ bars. For a stationary component, this is fixed by the supply pressure; for rotating blades, by the radius of rotation; water feeding, and hydraulic resistance of feed channel.

Required Properties of Porous Structure

Selecting the high Pe′ range and using $B = 0.2$ in equation (21) gives

Pe′	100	50	20
H	20.4	10.4	4.41

Thus

$$\frac{H}{\text{Pe}'} = \frac{\Delta p a_l}{G_g L b_{cr}} \cong 0.2$$

and the required permeability is $a_l \cong 5.2 \times 10^{-9}$ s. Choosing Pe′ = 20 and noting from Fig. 10 that $(1-\tilde{a})/\tilde{a} \cong 10$ @ 20 bars gives the required thermal conductivity from equation (23) to be $k \cong 2$ W/m-K.

Equation (27) gives $\tilde{l} = 0.01$, corresponding to a boiling length l of 10^{-4} m (0.004 in.). If the boiling plane is to be kept several pores from the surface, the pore size should be of the order of 10^{-5} m. This is compatible with the low permeability required.

APPENDIX C

Comparison of Water Requirements with Open-Loop Water Cooling

In an open-loop water-cooling system, neglecting water subcooling relative to latent heat, a heat balance gives the coolant flow rate per unit of blade surface area as

$$\frac{\dot{m}_{\text{water}}}{A_{\text{blade}}} = \frac{St_o G_g Cp_g (T_g - T_s)}{X i_{fg}}$$

where X is the coolant quality at exit from the blade tip. The coolant required per unit area for two-phase transpiration cooling is G. Hence, the ratio of the latter to the former is

$$\frac{\dot{m}_{2-\phi\text{transp}}}{\dot{m}_{\text{open loop}}} = \frac{G X i_{fg}}{St_o G_g Cp_g (T_g - T_s)} = \frac{i_{fg} X}{Cp_v (T_g - T_s)} \frac{B}{S}$$

for the example of Appendix B, if the comparable open-loop system could operate with an exit quality of 0.5, this ratio is 0.22. At high gas temperatures and heat fluxes, the open-loop system is likely to operate at qualities below 0.5 due to critical heat flux constraints, and the advantage of two-phase transpiration would be greater still.

Development, Fabrication, and Testing of a Prototype Water-Cooled Gas Turbine Nozzle

M. F. Collins
Mem. ASME

M. C. Muth

W. F. Schilling

General Electric Company
Schenectady, N.Y. 12345

The design and development of a water-cooled high temperature gas turbine has been under active investigation by the General Electric Gas Turbine Division for the past 15 years. The transition from testing small scale, laboratory-size experimental hardware to full scale industrial gas turbine components was initiated in 1975 by General Electric and extended further under the U.S. Department of Energy's High Temperature Turbine Technology (HTTT) program. A key element in this transition was the identification of a composite (hybrid) design for the first stage nozzles. This design permits efficient heat transfer to the water-cooling passageways, thus lowering effective strains and increasing part life. This paper describes the metallurgical considerations and process technology required for such hardware. A review of the materials selection criteria utilized for the nozzle is presented, along with the results of several materials development programs aimed at determining metallurgical compatibility of the component materials, diffusion bonding behavior and both hot corrosion and aqueous corrosion performance of key materials. A brief description of the actual cascade testing of the part is given, along with results of a post-test metallurgical analysis of the tested hardware.

Introduction

Water cooling of industrial gas turbine hot gas path hardware is of considerable interest because it offers the opportunity for substantial increases in turbine firing temperature, lower metal operating temperatures, increased combined cycle efficiency, improved turbine reliability, and more fuel flexibility. The General Electric Company, through its Gas Turbine Division, has been actively involved in the design of a full-scale, water-cooled turbine and in the testing of key components in the U.S. Department of Energy-sponsored High Temperature Turbine Technology (HTTT) program.

A key development within the HTTT program has been the design and development of a first stage nozzle which is capable of surviving the high heat fluxes and thermal gradients associated with a 1427°C firing temperature while also meeting 80,000 hr part-life goals. A detailed description of the nozzle design is available in a forthcoming paper.[1] Basically it is a composite design consisting of a load-carrying spar surrounded by and bonded to a layer of high-strength, high thermal conductivity copper alloy in which are imbedded the water-carrying tubes. The entire hot gas path portion of the nozzle is then clad with a corrosion-resistant skin. The copper inner layer distributes the high heat fluxes to the water-carrying tubes while minimizing thermal gradients within the component.

The design, fabrication, and testing of a sub-scale composite water-cooled nozzle was undertaken to verify design and fabrication methodologies and confirm final materials selection. This paper describes the fabrication and cascade testing of a composite water-cooled nozzle which served as the precursor to a full-scale nozzle of similar construction.

Materials Selection

Nozzle Cladding. Early conceptual designs highlighted the need for a gas path cladding material which, at a thickness of 0.635 mm to 0.762 mm and operating at 538°C, could effectively resist the expected hot gas path corrosion and erosion for an intended life of 80,000 hrs.[2] Corrosion studies were conducted as part of an EPRI Water-Cooled Gas Turbine Development Program (Research Project 234-3) to assess this capability in a variety of materials.[3] The resultant data, summarized in Fig. 1, shows that:

- Hot corrosion is dramatically reduced when most materials are below a temperature range of 538-593°C.
- The alloys IN-671 and IN-617 have good corrosion resistance below 593°C.
- Corrosion life goals for the nozzle are based on 7000 hr tests.

Because the cladding was conceptualized as a sheet metal fabrication it was necessary to assess the two candidate alloys IN-617 and IN-671 in terms of :

[1] Muth, M., Klompas, N., "Design and Fabrication of Composite Water-Cooled Turbine Nozzles," ASME paper in preparation to be distributed at ASME Gas Turbine Conference, March 1982.

Contributed by the Gas Turbine Division of THE AMERICAN SOCIETY OF MECHANICAL ENGINEERS and presented at the 27th International Gas Turbine Conference and Exhibit, London, England, April 18-22, 1982. Manuscript received at ASME Headquarters December 7, 1981. Paper No. 81-GT-91.

[2] UHT Turbine Program, Contract RP234-2 Phase IA First Annual Report, February 28, 1976, made for Electric Power Research Institute, Palo Alto, California by the General Electric Co., Gas Turbine Products Division.

[3] EPRI AP-1889 Project 234-3 Volume 1 Final Report, June 1981.

Table 1 Copper alloy property goals

Property @427°C[a]	Goal[a]	Cu-MZC
Thermal conductivity	277 2/w•K	331 w/m•K
Coefficient of thermal expansion	17×10^{-6}cm/cm•K	16.4×10^{-6}cm/cm•K
Tensile strength	276 MPa	214 MPa
1000-hour rupture strength	172 MPa	103 MPa
Low cycle fatigue life	N_i = 3350 @ ϵ_T = 0.3% 2 min tensile hold	N_i = 3350 @ ϵ_T = 0.45% 2 min tensile hold

[a]Heat-treated properties after simulated diffusion-bonding cycle of 945°C/2 hours.

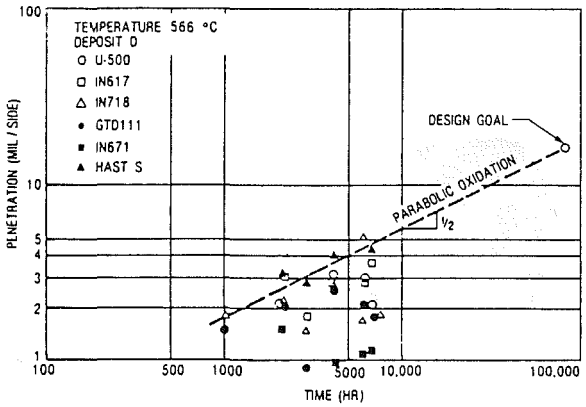

Fig. 1 Time dependence of penetration with Deposit D at 566°C; conversion factor: 1 mil = 2.54×10^{-5}m.

- formability with respect to processing schedules
- metallurgical phase stability as a function of thermal exposure
- weldability and weldment strengths

Low cost and dimensionally accurate shapes were believed possible using conventional cold forming methods. A three-piece cladding consisting of two endwalls plus airfoil shaped fillets and an airfoil covering piece was adopted. Concern existed, however, over the severe forming required in the airfoil-to-endwall fillets at the leading and trailing edge areas of the airfoil. Consequently, a sheet processing study was undertaken, utilizing various amounts of residual cold work from rolling and annealing temperatures. Based on the data generated, the following assessments were made:

- IN-617 has superior cold formability to IN-671
- air anneals impart substantial room temperature ductility recovery to IN-671 and IN-617
- IN-671 displays superior hot formability to IN-617

Good gas tungsten arc (GTA) weldability was confirmed for autogenous IN-617 welds and both autogenous IN-671 welds and those made with IN-72 filler wire. Cladding welds, both on the airfoil wrap and the airfoil-to-endwall fillets, were performed under argon cover and later inspected both visually and radiographically to a standard of no detectable indications.

Nozzle Components in Contact with Cooling Water. Endcaps, spar rods, manifolds, and water-carrying tubes of early designs specified 304L stainless steel. Later Nitronic 50 was adopted due to its high strength and much improved resistance to stress corrosion cracking. Moreover, based on extensive testing conducted by the Nuclear Energy Division of the General Electric Co., no water side problems were anticipated with this alloy.

An unknown was the ability of this material in small tubing form (nominally 3.18 mm o.d. × 0.25 mm wall) to survive

Table 2 Copper alloys evaluated

Alloy composition (w/o)	Strengthening mechanisms
Cu – 1.4 Al_2O_3	Dispersed fine (<1000 Å) Al_2O_3 + cold working
Cu – 0.17 Zr	Dispersed Cu_3Z_4, αZr + cold working
Cu – 5.0 Ni – 2.5 Ti	(Coherent?) Ni_3Ti, Ni_2Ti precipitation
Cu – 2.5 Co – 0.6 Be	Coherent αCo, αBe precipitation
Cu – 0.06 Mg – .15 Zr – .4 Cr	Dispersed Cu_3Zr, αZr, coherent αCr precipitation + cold working

expansion during the hot isostatic pressing (HIP) bonding operation without cracking. To assess this ability a bi-axial stress test was devised whereby tubes were subjected under controlled temperature and pressure conditions to various amounts of expansion. The diametral strain required is dictated by the machining and assembly tolerances necessary to drill the airfoil cooling holes and assemble the tubes therein. For this design the required diametral expansion is 0.20 mm. Testing conducted at 954°C and 996°C on 35 specimens showed no failures at 0.31 mm or less; all specimens which expanded 0.36 mm or more, failed. These results indicate that at the HIP temperature, ductility is sufficient to allow the full diametral expansion.

Copper Alloy Selection. It became apparent early in this program that the copper alloy selected for the heat conducting layer must be capable of maintaining or achieving mechanical property goals after a relatively severe diffusion bonding thermal cycle. These property goals are given in Table 1. A design limit of 427°C operating temperature was set for the copper inner layer. This was based on the fact that most age-hardenable copper alloys begin to lose strength rapidly through overaging at temperatures above 427°C and that little is known about the long time stability of these materials at elevated temperatures.

This application represents a major change in the way copper alloys have been used for structural components. Historically, high strength, high electrical and thermal conductivity copper alloys have been utilized for specialized electrical applications and derived their strength from a combination of age hardening and cold working. Typically, these alloy systems contain elements which have low solid solubility in copper at the use temperature in order to maintain high levels of electrical conductivity, and the mechanical properties of this class of materials decrease significantly with the increase of exposure temperature and time. Anticipated diffusion bonding cycles of 954–1010°C for 2-3 hrs for the composite nozzle represent severe exposure conditions for copper alloys.

Several types of copper alloys were considered for this application (see Table 2), including dispersion-strengthened materials, alloys strengthened by thermomechanical processing, and precipitation-hardenable alloys. Detailed

evaluations of the behavior of the candidate alloys were conducted after the bonding thermal cycle. Tensile and stress-rupture properties were evaluated as well as post-exposure microstructural stability.

Inspection of the data revealed some important trends. All of the age-hardenable alloys suffered a loss in tensile and yield strength as a result of the thermal exposure. The oxide dispersion-strengthened alloy AL-60 showed the highest resistance to the thermal exposure. Ductility was improved for all alloys after the simulated diffusion bonding thermal cycle. The Cu-Zr and Cu-MZC alloys displayed very high ductility levels, while the remaining alloys possessed elongations and reductions in area (RA's) in the 5–10 percent range. The stress-rupture strengths of the candidate alloys showed AL-60 to be superior, with Cu-MZC somewhat stronger than the other age-hardenable alloys at the higher Larson-Miller parameter values.

The Cu-MZC alloy was selected as the prime candidate for the composite nozzle on the basis of possessing the best overall combination of desired properties. Additional studies on the Cu-MZC alloy have yielded improvements in strength through modification of heat-treatment. Basically, higher solutioning temperatures and increased cooling rates resulted in more effective use of Cr in the aging reaction, thus increasing strength. Stress rupture strength was also similarly improved.

Final acceptance of the Cu-MZC alloy as the prime material for the composite nozzle was based on strain-controlled low cycle fatigue (LCF) testing. Figure 2 shows the LCF behavior of the Cu-MZC alloy and compares it to the design goal and to oxygen-free, high-conductivity (OFHC) copper. This alloy is the one used in wrought form for the airfoil copper in the HTTT first stage nozzle. A powder derivative is used for the endwalls to allow for more flexibility in tube location.

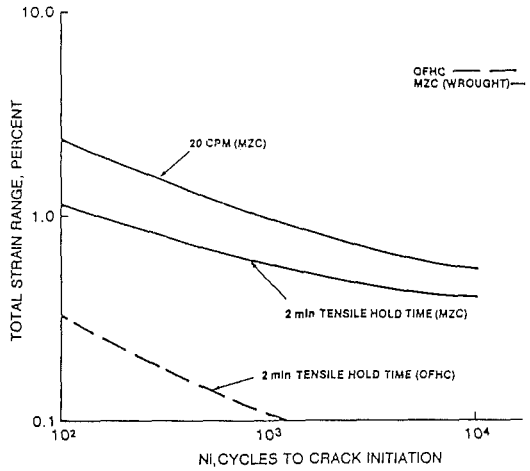

Fig. 2 LCF results for wrought Cu-MZC at 316°C

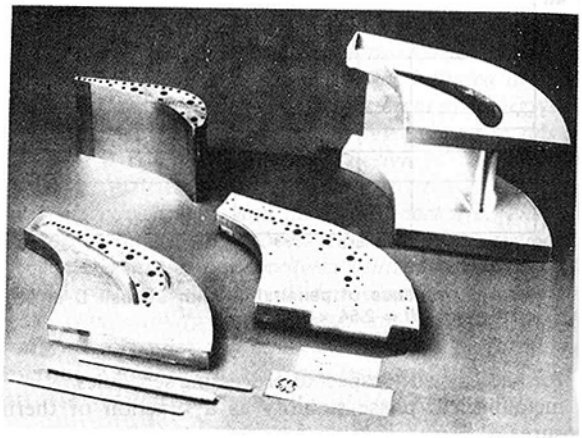

Fig. 3 Component pieces prior to assembly

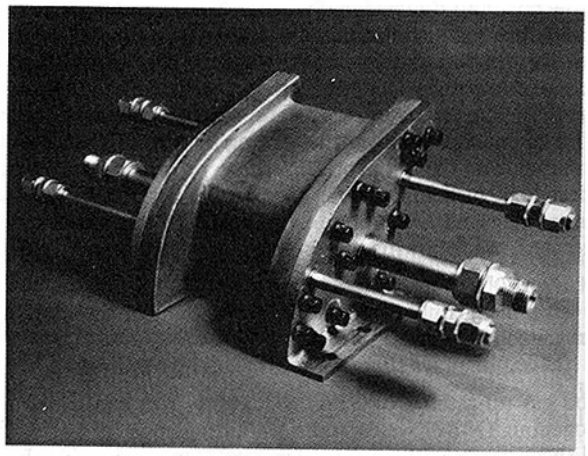

Fig. 4 Fully assembled nozzle segment

Fabrication Bonding

A three-piece construction technique was devised to fabricate the desired shape. The three pieces are a machined copper airfoil with drilled tube holes and two composite endwalls. The multialloy, composite structure of the part mandated that diffusion bonding be utilized for its fabrication. Because the complicated geometry normally associated with hardware of this type precludes uniaxial diffusion bonding, gas pressure bonding, utilizing a hot isostatic press, was the diffusion bonding technique selected.

The fabrication procedure is as follows. First, the composite endwalls are built up by using endwall plates to which circuitous cooling tubes are attached. Each entire endwall structure is fabricated separately and a container for powder consolidation is built up around the periphery of the endwall. Next, the endwall is filled with copper powder, evacuated, and then HIP-consolidated. This is followed by a machining step that defines the endwall gas path surfaces, the airfoil fillets, and the mating holes for the airfoil cooling tubes. A gas path cladding is also fabricated from cold-formed and welded sheet metal. (All these components can be seen in Fig. 3.) This assembly is then mated with appropriate airfoil cooling tubes and spar rods. The gas path cladding serves as a HIP container, and the structure is again evacuated and HIP-bonded. Manifolds for water delivery are added later.

A nozzle segment that was fabricated in this manner (see Fig. 4) was successfully tested as part of a General Electric turbine simulator test. (More information on the design and fabrication of these nozzles can be found in reference [1].) Three nozzle designs have been made and tested to date. They represent an obvious maturing of the overall design from one embodying a constant section airfoil, flat sidewalls, and nonoptimum materials to one incorporating a tapered airfoil, curved sidewalls, and acceptable material properties essentially ready for turbine insertion.

Cascade Testing of the Water-Cooled, Composite Deposition and Corrosion Nozzle

The objective of this test was to evaluate erosion, ash deposition, and corrosion characteristics of first stage water-cooled nozzles in an environment representative of a high temperature gas turbine burning coal-derived, low Btu gas fuel. Using a specially designed cascade rig, the test was conducted on a single vane, with endwalls approximating the two throats.

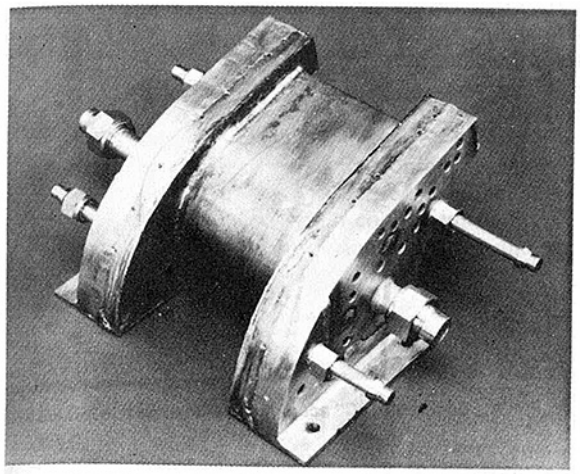

Fig. 5 Nozzle after deposition and corrosion testing

Low Btu gas was generated in an experimental GE gasifier, cleaned in a low-temperature chemical clean-up (Benfield) system, fired in a special combustor to 1427°C firing temperature, and directed onto the nozzle. The turbine simulator was operated for 70 hrs and 32 min. The full fired test conditions were:

Firing temperature	1427°C
Combustor shell pressure	1.18MPa
Compressor discharge air flow	2.54kg/s
LBtu gas fuel flow	0.68kg/s

Due to the actual heating value variation of the low Btu gas fuel, the water-cooled composite nozzle experienced several firing temperature excursions as high as 1649°C at the full 1.18 MPa pressure. The water-cooled composite nozzle also experienced a total of 32 thermal cycles of start-up and shutdown. About two-thirds of these shutdowns were severe transients from full flow conditions to flame-out.

Several unscheduled incidents resulted in some foreign objects impacting the water-cooled composite nozzle at full-fired conditions, and this included the impact of molten metals. The inspection of the nozzle after testing showed no apparent damage to the water-cooled composite nozzle (Fig. 5).

Post-Test Evaluation of Deposition and Corrosion Nozzle

A visual examination of the tested part showed that the nozzle has been subjected to extensive foreign object damage (FOD)—approximately 200 impacts—but there was no indication of penetration through the cladding. After removal of the manifold, all the water cooling passages were examined and found to be open. The composite nozzle test specimen was then ultrasonically inspected and no areas of disbond were detected either by immersion or contact scanning. For the immersion technique, a 15.0 MHz, 6.35 mm dia focused transducer was selected, while for the contact method, both a 20 MHz, 3.18 mm dia and a 10 MHz, 3.18 mm dia buff rod transducer were used.

Due to the curvature of the airfoil, several separate "C"[4] scans were made with the airfoil repositioned for each individual test. To obtain a series of positions, numerous props and shims were used to maintain the airfoil in an attitude fairly normal to the transducer. Five scans were made on the concave (pressure) side, and seven scans were made on the convex (suction) side. The cooling tubes were used as bench marks to ensure overlap coverage between the scans. The scanning sequence and the coverage are detailed in Fig. 6. The

[4] "C" scan is a semiquantitative display of echo intensity over an area of the surface of the test pieces.

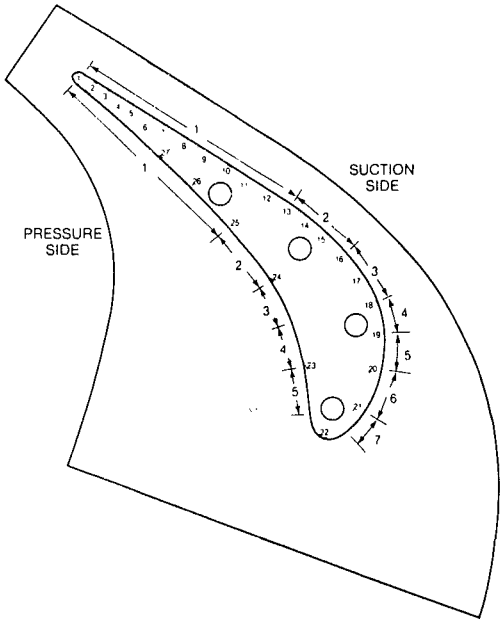

Fig. 6 Scan pattern of nozzle airfoil

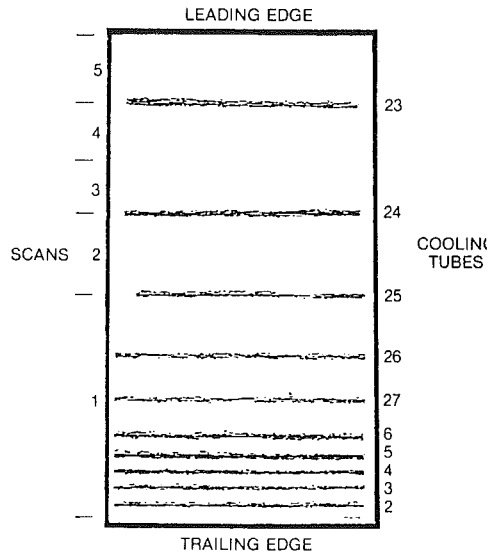

Fig. 7 Composite "C" scan of concave side of nozzle airfoil

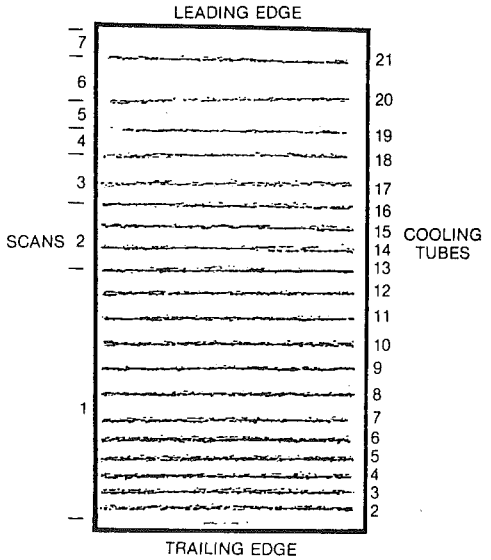

Fig. 8 Composite "C" scan of convex side of nozzle airfoil

composite "C" scans of the nozzle airfoil are shown in Figs. 7 and 8. The gas side of the end plates was immersion-tested in segments. Five separate scanning patterns were used. As with the airfoil, the "C" scans were composited and are shown in Figs. 9 and 10 with the remainder of the outline of the endwall shape sketched in to show the degree of coverage.

A manual contact method was used in those areas not covered by the immersion technique: specifically, the fillet area adjacent to the airfoil, that portion of the gas side of the end plates, and the seam area about the periphery of the end plates. The seam weld that traverses the concave side of the airfoil was retested as a double-check. Special attention was given to the leading edge of the airfoil.

In addition to the automated ultrasonic scan, a hand scan was done on the nozzle surfaces. Although the manual procedures employed could not duplicate the precision and sensitivity of an automated, focused, ultrasonic immersion scan, they did permit the evaluation of the overall integrity of the hardware after test. No areas of disbond were found during this inspection.

An eddy current examination was made on the airfoil cooling tubes of the composite nozzle specimen prior to welding of the water manifolds. The eddy current instrument used was a Nortec MTD6D featuring a frequency range through 2 MHz, amplified gain adjustable through 66 dB, 360 deg phase rotation, recorded outputs, and an X–Y storage display. The inspection procedure consisted of positioning the transport and the 500 kHz coil probe assembly so that the coil was within the airfoil cooling tube to be examined.

False indications are frequently generated when conducting eddy current examinations using hand-held probes. These indications can occur when there is a variation in the fill factor[5] or when the inspection speed is not kept uniform. In an attempt to reduce these effects, a transport mechanism was designed and built. The transport provided the eddy current probe with a linear-variable drive in two directions: single scan forward—reverse to start, and automatic continuous scan.

The eddy current instrument was balanced, and the impedance point positioned mid-screen on the X–Y display. The transport was then actuated, moving the coil through the axial length of the tube. The storage X–Y display of the eddy current instrument recorded the impedance plane profile of the tube. Whenever the impedance point moved into saturation, the transport was stopped and the eddy current instrument rebalanced.

Metallographic examination of the airfoil section confirmed complete bonding between the cladding, tubes, spars and copper. Areas of FOD were examined and although some penetrations extended to nearly 50 percent of the cladding thickness (~0.254 mm), the cladding-to-copper bonds were completely intact (Fig. 11).

The nickel plate in most areas was clearly observed. The two exceptions were the leading and trailing edges. It was known that the plating vendor had difficulty in plating regions of extreme curvature on the cladding. The plating thickness in these regions was approximately 2.54 μm versus 25.4 μm over the rest of the cladding. The bond between the IN-617 and the HIP densified MZC endwall was excellent. All areas except the corners at the leading and trailing edges of the endwall showed approximately 25.4 μm of nickel plate. There were small areas of apparent contamination between the cladding and nickel plate. This was probably the result of insufficient cleaning of the cladding prior to nickel deposition. The bondline between the HIP densified powder endwall and the wrought copper airfoil was free of contaminants and voids. Grain growth across the original interface confirmed the success of the assembly HIP cycle. All bonds between the powder MZC and Nitronic 50 endwall plates and spars were excellent. There was no indication of contamination or lack of bond. It was noted that the endwall plates had a very thin (~12.7 μm) layer of nickel plate versus the spar rods (~25.4 μm).

All endwall cooling tubes were fully bonded to the powder MZC. The tubes tended to flatten during the HIP process in such a way that the major axis was parallel to the Nitronic 50

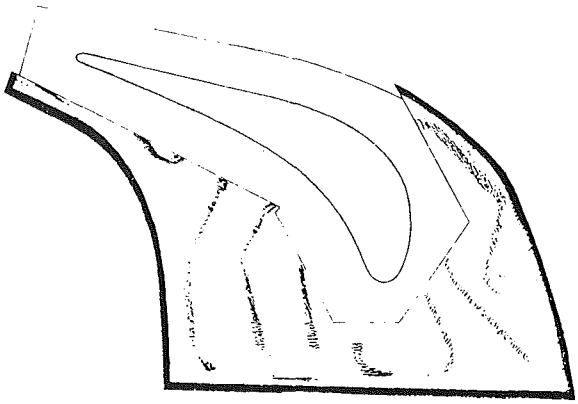

Fig. 9 Composite "C" scan of gas side of nozzle left endwall

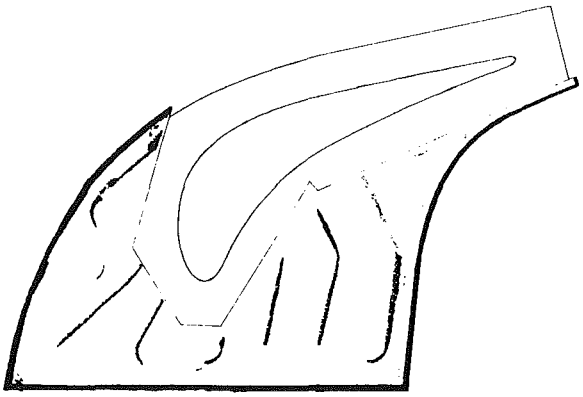

Fig. 10 Composite "C" scan of gas side of nozzle right endwall

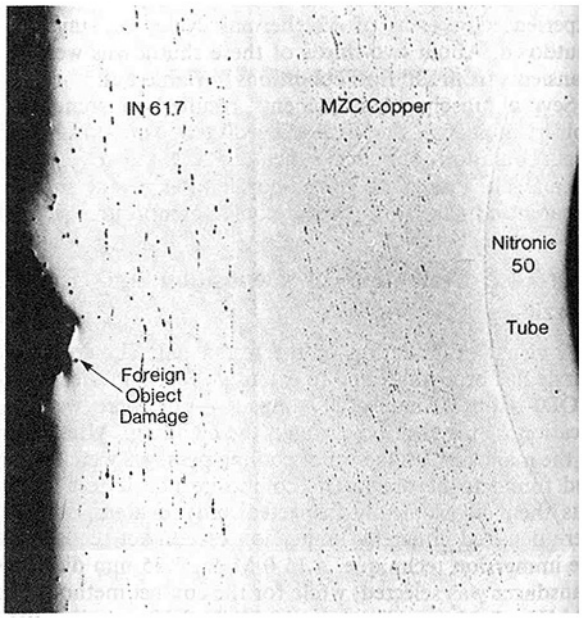

Fig. 11 Typical microstructure of deposition and corrosion nozzle

[5]The fill factor is related to the clearance between the probe and the tube inner surface.

plate. The average ratio of minor to major diameters was 0.51. The sides of the tubes with the smallest radius of curvature (greatest area of deformation) were depleted of nickel plate. The bond between the Nitronic 50 trailing edge tube and the IN-617 cladding was totally intact, with no indication of damage as a result of the severe testing cycle.

A microprobe examination of the composite nozzle concluded that the nickel layer provided an excellent interface between the copper and cladding or cooling tubes. Figures 12 and 13 show the typical distribution of nickel and copper throughout the nozzle.

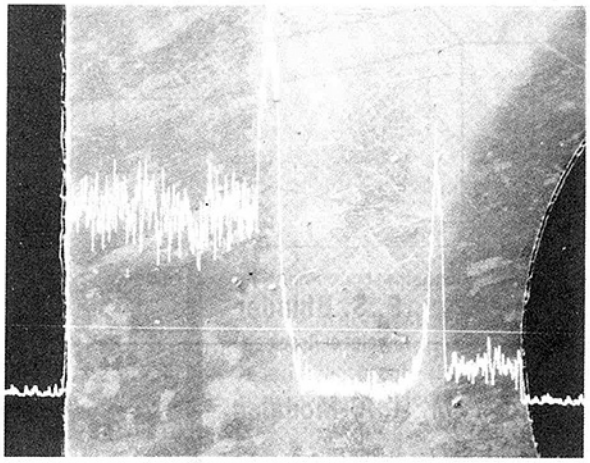

Fig. 12 Nickel scan

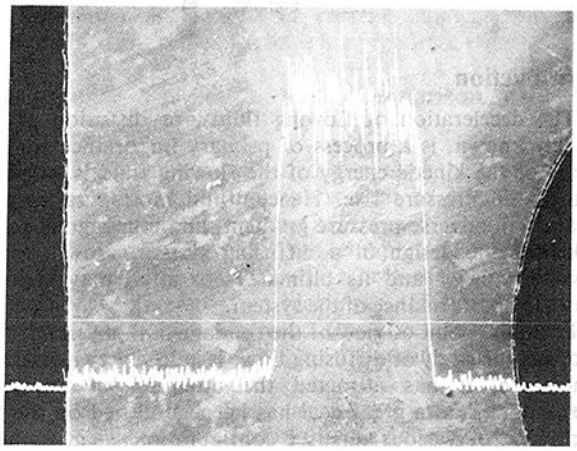

Fig. 13 Copper scan

Summary

Materials selection for a composite, water-cooled gas turbine nozzle has been described along with the fabrication techniques required for such hardware. Alloy IN-617 was selected as a prototype nozzle cladding based on formability, weldability, bonding capability, and low cycle fatigue strength. Nitronic 50 or XM-19 was selected as the material for water-side contact based on its excellent stress corrosion resistance and thermal expansion compatibility with the selected copper inner layer. The copper layer chosen was Cu-MZC, an age-hardenable copper alloy which can be produced in wrought or powder metallurgy (P/M) form.

Hot isostatic pressing was identified as the prime method for producing high integrity bondlines in a complex, composite structure. Metallographic evidence has verified the completeness and quality of bondlines produced in such a structure.

Actual deposition and corrosion testing of a prototypical nozzle was conducted as part of the DOE/HTTT Phase II program. This nozzle survived firing temperatures as high as 1649°C without any problems. Most significantly, a total of 32 thermal cycles and 70 operating hrs were accumulated along with important design data which permitted the construction of a full scale composite turbine nozzle.

Acknowledgments

The authors would like to acknowledge John Erickson, Robert Gilmore, Nick Klompas, Leo Willmott, Loyly Burnet and Robert Urich for their conscientious efforts on this program. The United States Department of Energy is recognized for sponsoring the HTTT Phase II program.

EPRI is acknowledged for their support of the early work in water-cooling technology.

F. S. Bhinder
Director of Research.

M. H. Al-Modafar

Mechanical and Aeronautical Engineering,
The Hatfield Polytechnic,
Hatfield, Hertfordshire AL 10 9AB,
England

Development and Application of a Performance Prediction Method for Straight Rectangular Diffusers

Introduction

The deceleration of flowing fluids, or diffusion as it is widely known, is a process of primary importance whereby some of the kinetic energy of the flowing fluid is converted into static pressure rise. Hence, fluid motion takes place against an adverse pressure gradient, and unless great care is taken in the design of a diffusing system, growth of the boundary layer and its ultimate separation may seriously upset the performance of the system.

From the point of view of the fundamental physics of fluid motion, the study of diffusing flows is indeed very interesting. Therefore, it has attracted the attention of many investigators, and a great deal has been published on the performance of various diffuser configurations, e.g., conical, annular, rectangular, radial, etc. However, performance prediction methods are still rather limited. Hence, in most cases, the designer has to rely on the available experimental data for general guidelines. In this connection, the data obtained by Sovran and Klomp [1], Reneau, Johnston, and Kline [2] and Runstadler and Dolan [3] are very comprehensive, and are widely used.

The aim of this paper is to describe a method which attempts to predict the performance of two-dimensional diffusers. The method has been tested against experimental data from two different sources [3, 4], and the results are very encouraging.

Theoretical Background

Flow in straight rectangular diffusers, particularly at high subsonic inlet Mach numbers, is known to be very complex. Therefore, it is necessary to make certain simplifying assumptions before attempting to model it theoretically. The model for the performance prediction method described in this paper is based on the following assumptions:

(a) the working fluid is a perfect gas
(b) the flow is adiabatic
(c) forces acting on the fluid are only those due to inertia and viscosity

Within the framework of these assumptions, the momentum integral equation may be used, together with the energy and continuity equations, to produce the following:

$$\left|\frac{\gamma f'(L)}{2}\cdot\frac{SdL}{dA}-\frac{1}{\bar{M}^2}\right|\frac{dA}{A}=\frac{(1-\bar{M}^2)d\bar{M}}{\bar{M}^2\left[1-\left(\frac{\gamma-1}{2}\right)\bar{M}^2\right]} \tag{1}$$

This is a general equation for one-dimensional compressible flow with area change, which may be solved analytically if it were permissible to assume that the first two terms in the square bracket on the left hand side were constant. Alternatively, f and S as functions of L must be known. The function $S = \phi(L)$ may be obtained quite simply from the known geometrical details of the flow channel, for example, for a rectangular diverging duct.

$$S\frac{\delta L}{\delta A}=\frac{2(b+W)}{b(W+2\delta W)}=\frac{\bar{A}S+1}{\bar{A}S}\cot\frac{\theta}{2} \tag{2}$$

where $\bar{A}S$ = mean aspect ratio $(b/\bar{w})$ for the short length δL. The overall friction coefficient would depend on the local Reynolds number and surface roughness of the enclosing walls. However, for a short duct, length δL, it may be assumed constant. Hence, equation (1) may be rewritten as follows:

$$\left|\sigma-\frac{1}{\bar{M}^2}\right|\frac{dA}{A}=\frac{(1+\bar{M}^2)d\bar{M}}{\bar{M}^2\left[1+\left(\frac{\gamma-1}{2}\right)\bar{M}^2\right]}$$

which on integration yields:

$$\frac{A}{A_1}=\frac{\bar{M}_1}{\bar{M}}\cdot\left|\frac{1-\sigma\bar{M}_1^2}{1-\sigma\bar{M}^2}\right|^{\frac{1-\sigma}{\gamma-1+2\sigma}}\left|\frac{1+\frac{\gamma-1}{2}\bar{M}^2}{1+\frac{\gamma-1}{2}\bar{M}_1^2}\right|^{\frac{\gamma+1}{2(\gamma-1+2\sigma)}} \tag{3}$$

where

$$\sigma=\frac{\gamma}{2}f'(L)\cdot\frac{\bar{A}S+1}{\bar{A}S}\cot\frac{\theta}{2}$$

and $f'(L)$ = means friction coefficient for the short length δL.

The friction coefficient, f, is a function of the surface properties and the flow parameters such as Re. Therefore, it is not constant but is calculated for every incremental length δL.

Contributed by the Gas Turbine Division of THE AMERICAN SOCIETY OF MECHANICAL ENGINEERS and presented at the 27th International Gas Turbine Conference and Exhibit, London, England, April 18–22, 1982. Manuscript received at ASME Headquarters December 10, 1981. Paper No. 82-GT-122.

Geometrical and Performance Parameters

The geometrical configuration of a straight rectangular diffuser is shown in Fig. 1, from which the following parameters can be defined:

$$\text{area ratio} \quad AR = 1 + 2L/W \tan\theta/2 \tag{4}$$

$$\text{aspect ratio} \quad AS = b/W \tag{5}$$

The performance of diffusers is usually given in terms of pressure recovery coefficient CP, which is defined as:

$$CP = \frac{P_2 - P_1}{P_{01} - P_1} \tag{6a}$$

This equation can be rewritten as:

$$CP = \frac{\left(1 - \frac{\Delta P_0}{P_{01}}\right)\left[1 + \left(\frac{\gamma-1}{2}\right)\bar{M}_1\right]^{\frac{\gamma}{\gamma-1}} - \left[1 + \left(\frac{\gamma-1}{2}\right)\bar{M}_2^2\right]^{\frac{\gamma}{\gamma-1}}}{\left[1 + \left(\frac{\gamma-1}{2}\right)\bar{M}_2^2\right]^{\frac{\gamma}{\gamma-1}} \left\{\left[1 + \frac{\gamma-1}{2}\bar{M}_1^2\right]^{\frac{\gamma}{\gamma-1}} - 1\right\}} \tag{6b}$$

where $\Delta P_0/P_0$ = loss of stagnation pressure in the diffuser.

The next major source of loss is the blockage at the entry of the diffuser. Sovran and Klomp [1] showed that complex inlet conditions could be easily modeled by means of a simple blockage parameter, which can be defined in terms of the geometric and effective areas as follows:

$$\text{Blockage factor } B = \frac{A_B}{A} = \frac{A - A_E}{A} = 1 - \frac{A_E}{A}$$

If the boundary layer displacement thickness on the diverging walls is δ^* and if the boundary layer on side walls is neglected, then:

$$B = \frac{Wb - (W - 2\delta^*)b}{Wb} = \frac{2\delta^*}{W}$$

Introducing aspect ratio:

$$B = \frac{2\delta^*}{A^*} \cdot \sqrt{AS} \tag{7}$$

However, if the same boundary layer thickness, δ^*, is assumed for the diverging as well as the parallel walls, equation (7) becomes:

$$B = \frac{2\delta^*}{\sqrt{A^*}} \cdot \frac{AS + 1}{\sqrt{AS}} \tag{7a}$$

Equations (3) to (7) may be used iteratively and in a step by step manner to calculate the performance of straight rectangular diffusers. However, in order to stop the calculations it is necessary to introduce some criterion such as the acceptable boundary layer displacement thickness or the minimum value of the mean velocity. Several criteria were carefully evaluated, but Townsend's criterion [5] for boundary layer separation was found to be most acceptable. This was suitably modified to fit experimental data. For the sake of brevity the details have been omitted but may be found in reference [6].

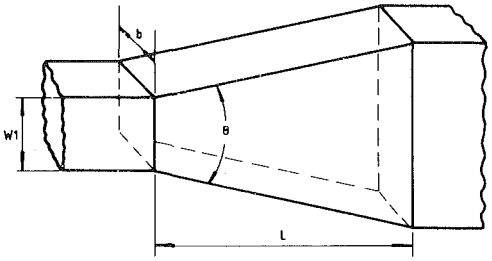

Fig. 1 Straight channel symmetrical rectangular diffuser

A computer programme in Fortran language has been written, the details of which have been reported elsewhere [7].

Performance Prediction and Comparison with Experimental Data

The analysis method was used to predict the performance of various diffuser configurations used by Runstadler and Dolan [3]. The results are shown in Figs. 2–5.

Figs. 2(a) and 2(b) show the comparisons between the predicted and experimental values for a range of values of divergence angles and two blockages. In both cases, the agreement is within ±4 percent. Pressure recovery increases with increasing diverging angle, the optimum in this case being 10 deg.

Figs. 3(a) and 3(b) show variations of pressure recovery coefficient against inlet Mach number M_1 for two values of inlet blockage. Other quantities such as θ, L/W_1, and AS_1 are constant. At low blockage, the calculated and measured results agree very closely, but at high blockage, the calculations tend to underestimate CP when $M_1 < 0.8$. For $M_1 > 0.8$, the trend is reversed. A refined model of blockage may produce closer agreement between the calculated and measured results.

The results given in Fig. 4 relate to a short diffuser, since L/W_1 has been reduced from 12 to 7, and the divergence angle increased from 8 to 16 deg. Even in this case, the calculated and measured results agree very closely.

Finally, the analysis was applied to calculate performances

Nomenclature

A, A^* = area of entry duct and diffuser throat, respectively, m^2
A_B, A_E = blocked, effective areas, respectively, m^2
AR = area ratio defined by equation (4)
AS = aspect ratio defined by equation (5)
b = diffuser depth, m
B = blockage factor defined by equation (7) or (7a)
Cp = specific heat at constant pressure kJ/kgK
CP = static pressure recovery coefficient defined by equation (6) or (6a)
D_h = hydraulic diameter defined by equation (9), m
f = friction coefficient
L = diffuser length, m
$\bar{M}$ = mean Mach number
P = static pressure, N/m^2
P_0 = total pressure, N/m^2
ΔP_0 = loss of stagnation pressure, N/m^2
Re = Reynolds number defined by equation (8) or (10)
S = perimeter of duct, m
W = diffuser width, m
α = ratio of specific heat = Cp/Cv
δ^* = boundary layer displacement thickness, m
θ = diffuser divergence angle degrees
μ = dynamic viscosity, Kg/ms
σ = constant defined by equation (3)
ρ = density, Kg/m^3

Subscripts

0 = total, stagnation
1 = at inlet
2 = at outlet

Superscript

* = at throat except for δ^*

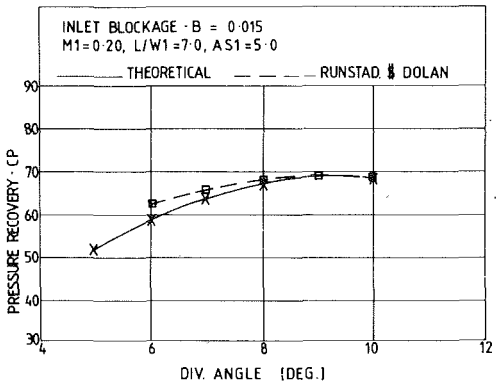

Fig. 2(*a*) Pressure recovery versus divergence angle for low blockage

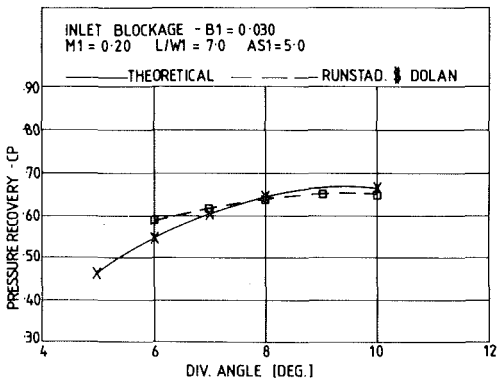

Fig. 2(*b*) Pressure recovery versus divergence angle for high blockage

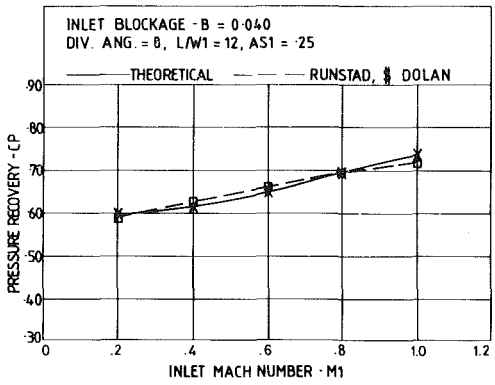

Fig. 3(*a*) Pressure recovery versus inlet mach number for low blockage

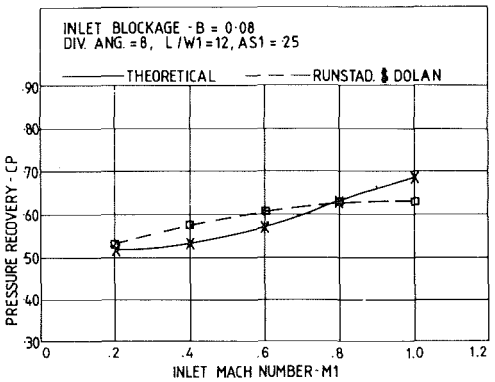

Fig. 3(*b*) Pressure recovery versus inlet mach number for high blockage

of various diffuser configurations used by Reneau et al. [2], and McMillan [4] in their experiments.

In this study, L/W_1, AS, $B1$, and Re were constant, but area ratio AR was varied. The results are given in Fig. 5. The calculated values lie well within the range of experimental data, but quantitatively, the agreement is not as good as has been in earlier diagrams.

It would be appropriate to mention at this juncture, that the experimental data in all cases were obtained laboriously from the figures given in the listed publications. In some cases, it was very difficult to read the values accurately. Probably closer agreement with the calculated results would have been achieved if actual experimental data were available.

Further Application of the Analysis

After having tested the validity of the analysis against available experimental data, it was felt necessary to apply it to a wide range of aspect ratios and entry Reynolds numbers. The results of these studies are given in Figs. 6–10.

Optimum Aspect Ratio. It is well known that the ideal section for a duct for fluid flow is circular. For a rectangular section duct of a given area, the perimeter would be minimum when the section is a square, i.e., the aspect ratio = 1.0. Hence, when $AS = 1$, the friction loss should be at its minimum value. This can be shown as follows:

$$\text{By definition Re} = \frac{\rho u D_h}{\mu} \tag{8}$$

From Fig. 1, it can be seen that:

$$D_h = \frac{2W_1 AS_1}{AS_1 + 1} \tag{9}$$

Hence, by substituting in (8) and simplifying, the following expression for Re is obtained:

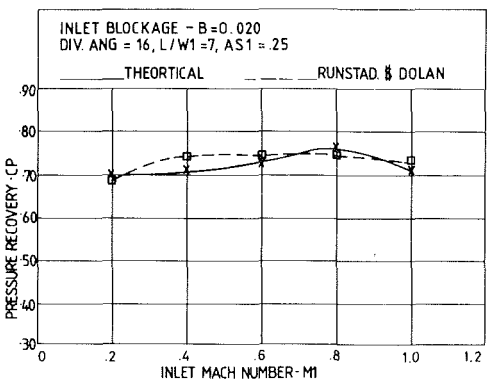

Fig. 4 Pressure recovery versus inlet mach number for large divergence angle

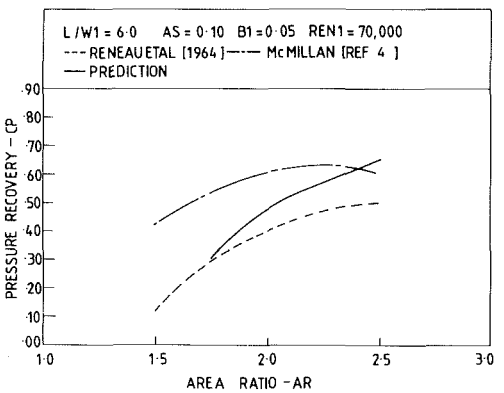

Fig. 5 Pressure recovery versus area ratio, further comparisons

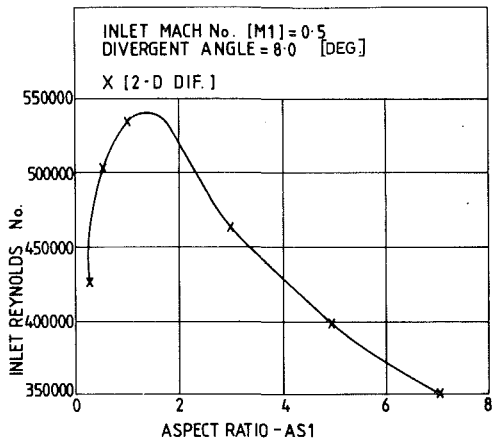

Fig. 6(*a*) The effect of aspect ratio on inlet Reynolds number

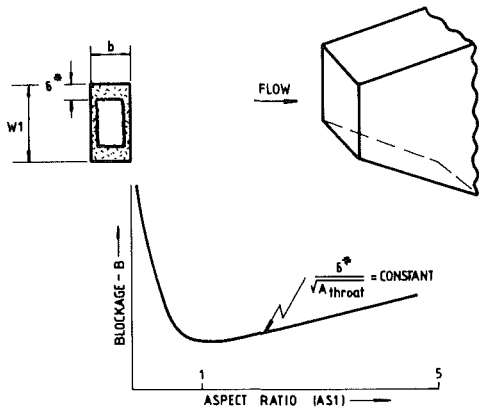

Fig. 6(*b*) The effect of aspect ratio on inlet blockage

$$\mathrm{Re} = \frac{\gamma}{\sqrt{C_p(\gamma-1)}} \cdot \frac{P_1}{\mu_1\sqrt{T_1}} \cdot \tilde{M}_1 W_1 \frac{2AS_1}{AS_1+1} \qquad (10)$$

The plot of equation (10) for $M_1 = 0.5$ is shown in Fig. 6(*a*). It is interesting to see that the Reynolds number attains a maximum value when aspect ratio is around unity. After that, the Reynolds number reduces sharply. At low values of Re, the losses would increase because the viscous forces would be more dominant than the inertia forces.

Another critical aspect of diffuser performance is the dependence on boundary layer blockage. The blockage parameter was defined in equation (7*a*). Figure 6(*b*) shows a graph of this equation for $\delta^*/(\sqrt{A_{\text{throat}}}) = \text{constant}$. It is interesting that minimum blockage occurs when the aspect ratio is around unity. Hence, maximum pressure recovery should be attained when the aspect ratio is unity. The same conclusion was drawn by Runstadler and Dolan [3] from the experimental data.

Figure 7 shows graphs of pressure recovery versus aspect ratio for three values of divergence angles. At $\theta = 8$ deg, as AS_1 is increased, CP first rises to a maximum value, remains constant around 1.0 to 3.0 for AS_1, and then starts to fall, but only slightly. At higher values of θ, pressure recovery reaches a clear maximum when AS_1 is around unity.

On Fig. 8, graphs of CP versus AS_1 for three values of inlet blockage are shown. As would be expected, the pressure recovery reduces over the entire range of aspect ratios quite significantly, as the blockage is increased.

From Figs. 7 and 8, it may be concluded that optimum entry aspect ratio is around 1.0 for high values of θ and extends from 1.0 to approximately 3.0 for low values.

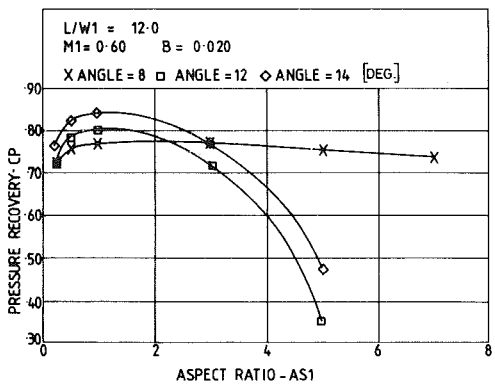

Fig. 7 Effect of aspect ratio and divergence angle on pressure recovery

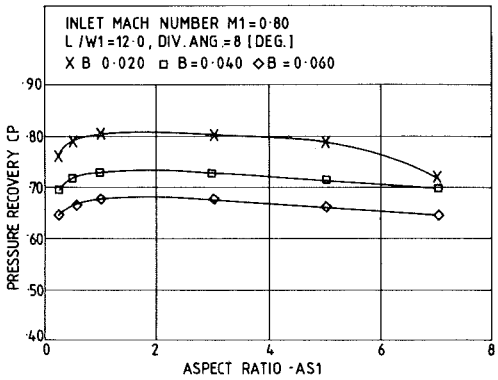

Fig. 8 Effect of aspect ratio and inlet blockage on pressure recovery

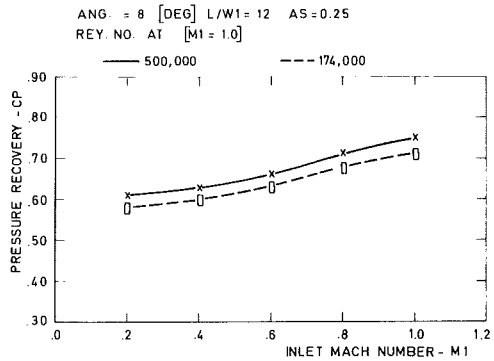

Fig. 9 Effect of inlet mach number and Reynolds number on pressure recovery, low aspect ratio

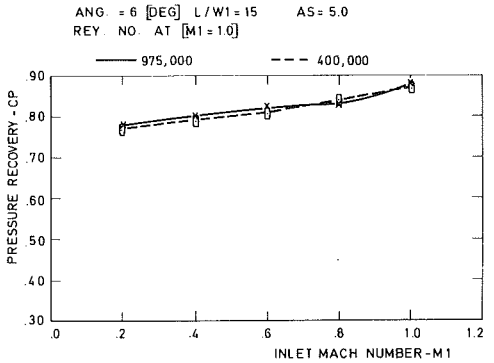

Fig. 10 Effect of inlet mach number and Reynolds number on pressure recovery, high aspect ratio

Effect of Entry Reynolds Number. Figures 9 and 10 show the graphs of CP versus M_1 for high and low values of entry Reynolds number. The aspect ratio in Fig. 9 is 0.25, and in Fig. 10 is 5.0. Increasing the Reynolds number at high aspect ratio has only a marginal influence on pressure recovery. However, at low aspect ratio, a small increase in CP over the entire range of M_1 may be achieved.

Conclusions

1 A brief description of a step by step method for predicting the performance of straight rectangular diffuser is given. The theory has been used to predict the performance of rectangular diffusers, for which the comprehensive experimental data is available.

2 The agreement between the experimental and the predicted results is very close, particularly bearing in mind the errors involved in extracting results mostly from published graphs.

3 The method has been shown to be applicable over a wide range inlet Mach numbers, aspect ratios, and Reynolds numbers.

4 For $\theta < 8$ deg, CP is only slightly dependent on AS_1, provided $AS_1 > 1$. However, for $\theta > 12$, the optimum entry aspect ratio is around unity.

5 Inlet blockage has a significant influence on pressure recovery for all geometrical configurations, entry Mach numbers and entry Reynolds numbers.

Acknowledgment

The authors wish to thank Rolls Royce Limited for support and helpful discussions, and the Hatfield Polytechnic for the use of computer and other facilities.

References

1 Sovran, G. and Klomp, E. D., "Experimentally Determined Optimum Geometries for Rectilinear Diffusers with Rectangular, Conical or Annular Cross-section," *Fluid Mech. of Internal Flow*, General Motors Research Laboratories, Warren, Mich., 1965.

2 Reneau, L. R., Johnston, J. P., and Kline, S. J., "Performance and Design of Straight, Two-Dimensional Diffusers," report PD-8, Sept. 1964, No. 533.697.3/HL.

3 Runstadler, P. W., Jr. and Dolan, F. X., "Further Data on the Pressure Recovery Performance of Straight Channel, Plane-Divergence Diffusers at High Subsonic Mach Number," ASME Paper No. 73-FE-S.

4 McMillan, O. J. and Johnston, J. P., "Performance of Low Aspect Ratio Diffusers with Fully Developed Turbulent Inlet Flows—Part 11—Development and Application of Performance Prediction Method," ASME Paper No. 73-FE-13.

5 Townsend, A. A., "The Behaviour of Turbulent Boundary Layer Near Separation," ASME JOURNAL OF FLUID MECHANICS, Vol. 12, 1962, pp. 536–554.

6 Al-Modafar, M. H., "Frotran Programme for Calculating the Performance Parameters in Two-Dimensional Diffusers," Hatfield Polytechnic, School of Engineering, Hatfield, England, Aug. 1981.

7 Al-Modafar, M. H., "Design and Performance of Two-Dimensional Diffusers," Ph.D. thesis. The Hatfield Polytechnic—to be submitted in April 1982.

Performance Analysis of the Test Results on a Two-Stage Transonic Fan

Chen Baoshi
Research Engineer.

Zhang Tianyi
Research Engineer.

Shenyang Aeroengine Research Institute,
People's Republic of China

Test results obtained from a two-stage fan are analysed and the reasons that caused the design performance target not to be attained are presented in this paper. Addition of a partspan shroud on rotor 1 caused higher losses and changed radial distribution of parameters. Modification on the flowpath and chord length of stator 1 resulted in excessively high inlet Mach number and flow separation in the hub region. The high load and high incidence at the hub of rotor 2 caused higher losses and reduced stall margin of the fan.

Introduction

Tests were conducted on a two-stage transonic fan with a stage 1 rotor tip-speed of 396m/s and a design pressure ratio of 2.15. It was demonstrated from tests that the design performance target was not attained for the fan. In order to find the causes of this poor performance, a test on the first stage and other two single-stage tests were conducted. Based on results of these tests, performance analyses of the two-stage fan were made. The analytical results are given in the paper. It is evident that these presented here are not successful experiences; however, some lessons could be drawn from these unfavorable results, and they are helpful for any future success.

A Brief Description of Fan Aerodynamic Design

The flowpath of the two-stage fan is shown in Fig. 1. The important design parameters are as following:

Pressure ratio of the fan (2.19 in calculation)	2.15
Efficiency of the fan	0.827
Weight flow per unit annular area 202kg/m^2	
Pressure ratio of stage 1	1.506
Efficiency of stage 1	0.841
Pressure ratio of stage 2	1.455
Efficiency of stage 2	0.832
Blades of rotor 1 – multicircular arc airfoil, aspect ratio	2.257
Vanes of stator 1 – BC-6 airfoil, aspect ratio	2.548
Blades of rotor 2 – multicircular arc airfoil, aspect ratio	2.372
Vanes of stator 2 – BC-6 airfoil, aspect ratio	2.314
Average Mach number at fan exit	0.5

Stage 1 of the fan was a modification of an existing single-stage transonic compressor (it was called original stage 1) from which the preliminary test results had been obtained. The modifications made on the original stage 1 were an addition of a partspan shroud to the rotor blades at 64.6 percent span from the hub (it was called shrouded rotor) and a reduction of 44 percent in the stator chord length with the solidity unchanged. At the same time, the flowpath at the stator exit was changed slightly (Fig. 2). This stator was called the modified stator. When the two-stage fan was designed, a reference design point of stage 1 was defined on the design speed line of the characteristic map obtained from the test results of the original stage 1. In order to take the effects of the preceding modification into account, the airflow, pressure ratio, and efficiency selected at this design point of stage 1 were correspondingly lower than those of the reference design point. Stage 2 was a new designed stage. A partspan shroud was also added to the rotor 2 blades at 60.5 percent span from the hub.

Test Results

Besides the test conducted on the two-stage fan, three single-stage tests shown in the following table were also conducted. The configurations of rotors and stators used for each test are also listed in the table.

The test facility and instrumentation can be seen from ASME Paper No. 81-GT-209.[1]

Name of test	Abbreviation	Configurations: Rotor	Configurations: Stator
First stage test	F.T	shrouded	modified
Calibration test	C.T	unshrouded (original),	original
Supplementary test	S.T	shrouded	original

Two-stage Fan Test. The overall performance of the two-stage fan is shown in Fig. 3. At design speed, the design pressure ratio was attained. But the peak efficiency was lower than the design value. The stall margin was only about 6 percent based on an operating point that was an intersection of the design speed line with a constant throttle line through

Contributed by the Gas Turbine Division of THE AMERICAN SOCIETY OF MECHANICAL ENGINEERS and presented at the 27th International Gas Turbine Conference and Exhibit, London, England, April 18–22, 1982, Manuscript received at ASME Headquarters December 10, 1981. Paper No. 82-GT-123.

[1] Wei Yubing, "Experimental Investigation of a Low Hub-to-Tip Ratio Single Stage Transonic Fan," ASME Paper No. 81-GT-209.

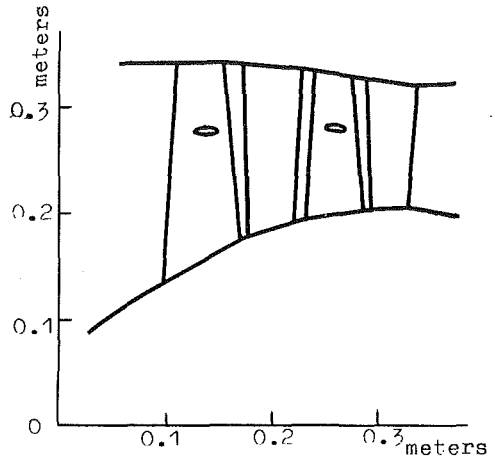

Fig. 1 Flowpath of two-stage fan

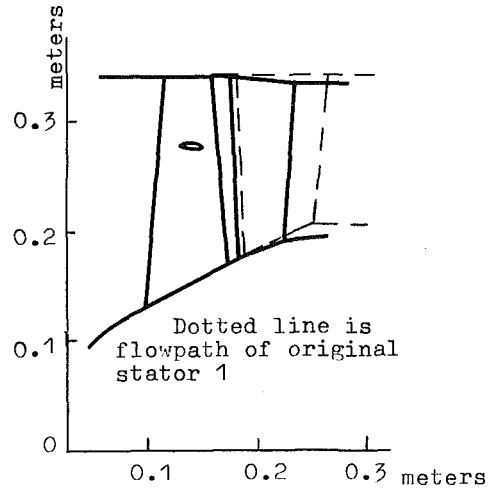

Fig. 2 Flowpath of first stage

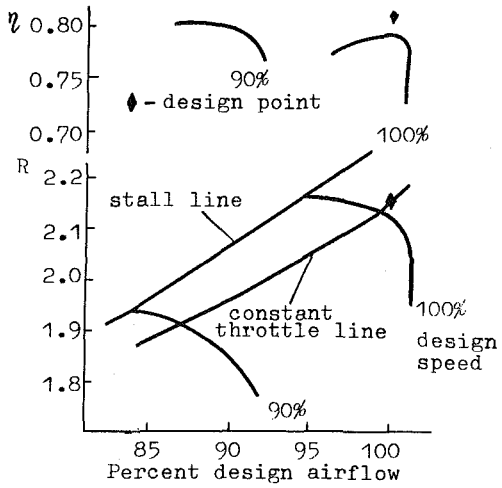

Fig. 3 Overall performance of two-stage fan

the design point. The blade element data at the near-design airflow point are shown in Fig. 4. The pressure ratio and

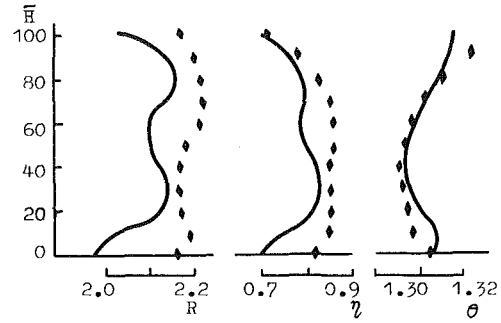

Fig. 4 Pressure ratio, efficiency, and total temperature ratio of the two-stage fan versus span at near-design airflow point: ♦ Design calculated value; – Test value

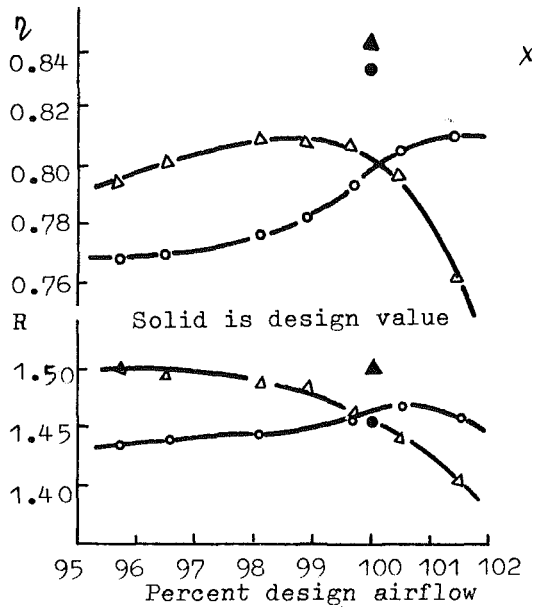

Fig. 5 Overall performances of stage 1 and stage 2 at design speed: – △ – Stage 1; – ○ – Stage 2

efficiency were lower than the design values along the whole span, especially in the hub and partspan shroud regions.

First Stage Test (F. T). The overall performance of stage 1 at design speed is shown in Fig. 5. Both the pressure ratio and efficiency were lower than the design values. But stall did not occur until very low airflow (below 80 percent design airflow). Figure 7 shows blade element data of stage 1 at the near-design airflow point. It was evident that the spanwise distributions of pressure ratio and efficiency were quite different from the design values (or the original test results). In the partspan shroud region the performance was even worse.

Second Stage Performance. The single-stage test could not be conducted on stage 2, and because there was not enough room for instrumentations between both stages, the performance of stage 2 could not be directly measured in the two-stage fan test. The performance of stage 2 was simply derived from the data obtained in the two-stage fan test and in the first stage test at the same airflow conditions. The derived

Nomenclature

A/A^* = ratio of channel actual area to critical area
D = diffusion factor
$\bar{H}$ = percent span
i = incidence angle, deg
M = Mach number
P = total pressure, kg/m^2
R = total pressure ratio
η = efficiency
θ = total temperature ratio
σ = stator total pressure recovery coefficient

overall performance and the blade element data at the near-design airflow point are shown in Fig. 5 and Fig. 6, respectively. The design pressure ratio of stage 2 was attained, but the efficiency was lower than the design value. In the midspan region the pressure ratio and efficiency were higher than (or near to) the design values. But the performance at the hub was rather poor.

Calibration Test (C.T). The original single-stage compressor, which was modified into stage 1 of the fan, was tested again to calibrate its performance. The test result showed that the performance in the calibration test was obviously worse than in the original test of the same single-stage compressor (Fig. 8 and Fig. 7). It seems that the performance obtained from the original test was too high.

Supplementary Test (S.T). Another single-stage test, i.e., the supplementary test, was conducted with the shrouded rotor and the original stator. It could be seen from the preceding table that the only difference in configurations between the supplementary test and the calibration test is with and without partspan shroud on the rotors. Therefore, the effect of the partspan shroud could be determined by comparing the results of both the tests, and the difference in configurations between the first stage test and the supplementary test is the only modification on the stator. Therefore, the effect of the modification on stator could be determined by comparing the results of both the tests (Fig. 8 and Fig. 7). Then, we can determine why the first stage performance was deteriorated from the performance of the original test. The comparisons are presented in the next section.

Analysis and Discussion

The data obtained from the preceding tests were put into a three-dimensional flow computer program. Based on the calculated results, the following analyses on the problems encountered in stage 1, stage 2, and on the match between them, are made.

First Stage. Overall performance at design speed of the three single-stage tests are shown in Fig. 8, while Fig. 7 shows their blade element data. These data points were intersections of their own design constant speed lines with a constant throttle line through the near-design airflow point of the first stage test. It could be seen that the following problems existed in stage 1:

The design performance parameters selected were too high. It was proved in the calibration test that the performance obtained from the original test was too high. Therefore, the design performance parameters for stage 1, which were based on the original test, were also too high.

Effect of partspan shroud on performance of rotor. Comparing the results from the supplementary test with the shrouded rotor and from the calibration test with the unshrouded rotor, it could be seen that adding a partspan shroud to the rotor caused characteristic lines to move leftward, and resulted in reductions of 1.5 percent in airflow, 1.8 percent in peak pressure ratio, and 0.016 in peak efficiency, respectively (Fig. 8). In the partspan shroud region which extended as much as 30 percent of the span on either sides of the partspan shroud, the pressure ratio and efficiency decreased markedly. However, the performance in this region for the calibration test with the unshrouded rotor was very good. Serious effect of the partspan shroud was attributed to the thick partspan shroud in the supersonic inlet flow. Moreover, the wake behind the partspan shroud was exaggerated by the radial flow caused by a steep hub conical angle (about 30 deg). In addition, because of the effects of choke and wake caused by

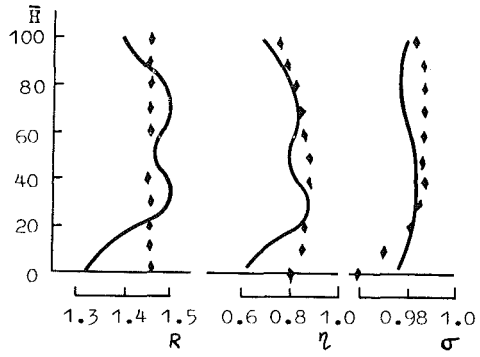

Fig. 6 Stage 2 pressure ratio, efficiency, and stator total pressure recovery versus span at near-design airflow point: ♦ Design value

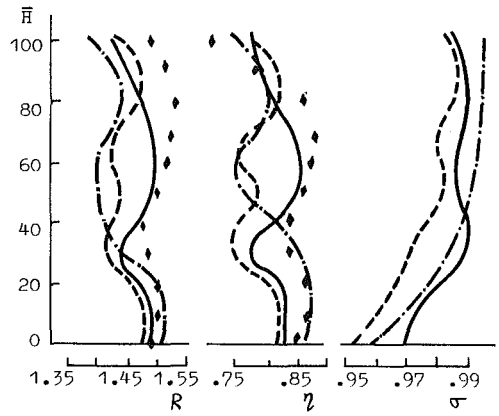

Fig. 7 Comparison of the pressure ratio, efficiency, and stator total pressure recovery of stage 1 at constant throttle condition: ♦ Design calculated value; – C.T: – • – S.T: ··· F.T

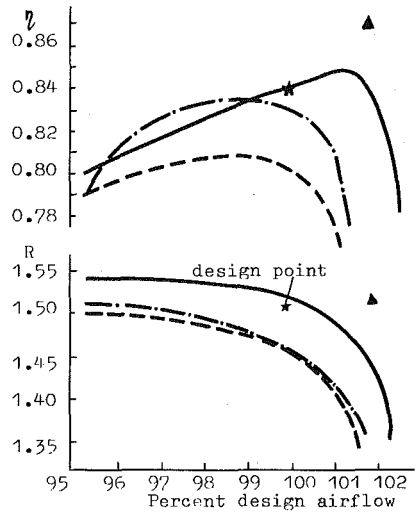

Fig. 8 Comparison of overall performance of stage 1 at design speed: ▲ reference design point; – C.T – • – S.T ··· F.T

the partspan shroud, the airflow through the midspan region reduced, but the airflow through the hub region increased. As a result, the air velocity in the hub region increased and the load decreased markedly. Consequently, the losses decreased, and the efficiency increased in the hub region. Therefore, addition of the partspan shroud not only caused higher losses, but also completely changed spanwise distributions of flow parameters. This is an important subject which is worth investigating in the design of the rotor with a partspan shroud.

Effect of stator modifications on performance. Comparing the results from the first stage test with the modified stator

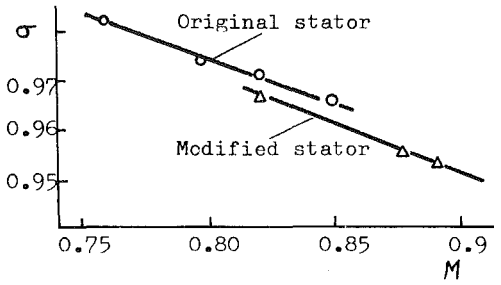

Fig. 9 Total pressure recovery coefficient versus inlet Mach number at stator 1 hub

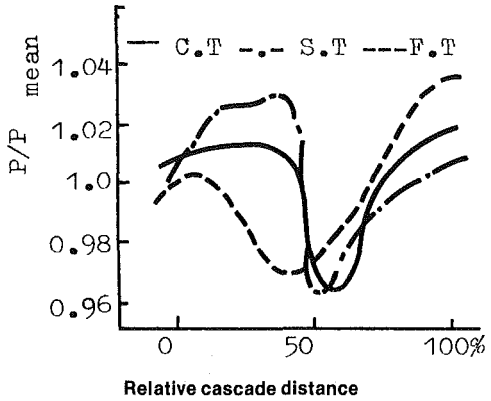

Fig. 10 Comparison of wakes behind stator 1 at hub

and from the supplementary test with the original stator, it could be seen that the characteristic lines of pressure ratio versus airflow for both cases agreed well. However, the modifications of the stator caused a reduction of 0.019 in peak efficiency. The total pressure recovery coefficient of the modified stator decreased considerably in its hub region. The inlet Mach number of 0.854 at the stator hub was obtained in the calibration test which was much higher than the critical Mach number. It increased to 0.881 in the supplementary test due to the effect of the partspan shroud. Because of the modification in flowpath of stator 1, such a curvature was formed that made the air accelerate at the hub of the stator 1 inlet and decelerate at the tip. This caused inlet Mach number at the hub of stator 1 to increase to 0.911. The airfoil of the stator 1 vane was BC-6, which is a subsonic airfoil. It can be seen from Fig. 9 that the higher the inlet Mach number, the more serious the losses. For comparison purposes, wakes at the hub of the stators for three single-stage tests are shown in Fig. 10. For the modified stator, the wake already extended in the complete channel. It meant that serious separation occurred in the vane channel. This separation, of course, was not only attributed to the high inlet Mach number, but also to marked decrease of stator vane chord length.

Second Stage and its Matching with First Stage. *Effect of first stage discharge flow field.* The higher velocity at first stage discharge due to its lower pressure ratio and airflow moving caused blockage margin A/A^* in the hub and tip regions of rotor 2 to decrease from 1.04 to 1.01 (Fig. 12). Although this could prevent the incidence from increasing further (Fig. 11), inadequate values of A/A^* resulted in an increase of the losses.

Matching with first stage. It could be seen from Fig. 5 that stage 2 was operating only on the left branch of its own characteristic line in the airflow range where the two-stage fan was tested. It seems that the maximum airflow of the two-stage fan was limited by stage 1. When stage 1 was operating

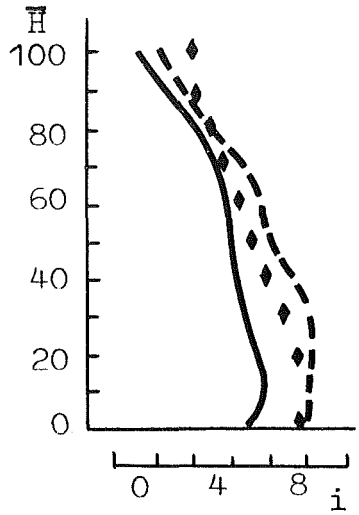

Fig. 11 Rotor 2 incidence versus span: ♦ design value; – near design airflow; ---near stall

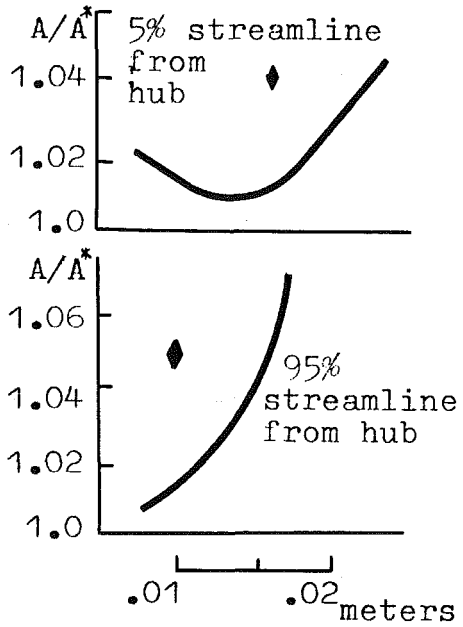

Fig. 12 Rotor 2 A/A* versus axial distance: ♦ design value

in its own high efficiency region, stage 2 ran in its own stall branch, where the performance was very poor. Therefore, stage 2 did not match well with stage 1. And the stall of the two-stage fan most likely originated from stage 2.

High load at hub of second stage rotor. It could be seen from Fig. 13 that the load at the hub of rotor 2 was high in all its operating range. The hub conical angle of rotor 2 selected was very small (about 10 deg), and it caused a high design load there. The flow with high velocity and separation from the stage 1 hub region caused serious diffusion at the hub of rotor 2. These were the main causes of high losses there.

Analysis on stall. J. Keenau and A. Burdsall pointed out[2] that a stall could occur when some elements of a blade row reached their critical load (usually, when diffusion factor was more than about 0.65). It can be seen from Fig. 13 that the diffusion factor at the hub of rotor 2 increased rapidly with the decrease of airflow. In the two-stage fan test, the diffusion factor at the hub of rotor 2 at a near-stall point was over 0.6, with rather high losses. At the same time, the incidence at this

[2] M. J. Keenan and E. A. Burdsall, "High Loading, Low Speed Fan Study, v final report," NASA CR-121148, 1973.

point was also high (Fig. 11). Therefore, it was considered that the stall in the two-stage fan originated from the hub of rotor 2. As regards the hub of Stator 2, there was no evidence of stall, although the diffusion factor was also more than 0.6 at the near-stall point (Fig. 13). For example, losses were not high and the wake in discharge flow was normal there. Stage 1 could not be considered as the source of the stall, because the spanwise load of rotor 1 at the near-stall point was not very high (Fig. 13), and there was considerable airflow margin in the first single-stage test.

Conclusions

The following conclusions could be obtained from the analyses on the test results of the two-stage fan:

1 The design airflow and pressure ratio of the fan were attained, but the efficiency and stall margin were far lower than the design values.

2 The problems existing in stage 1 were that the design performance parameters selected based on the original test were too high; that the partspan shroud added on the rotor deteriorated the performance and completely changed the spanwise flow field; and that the modifications on the flowpath and chord length of the stator caused a too high inlet Mach number at the stator hub, resulting in high losses and flow separation there.

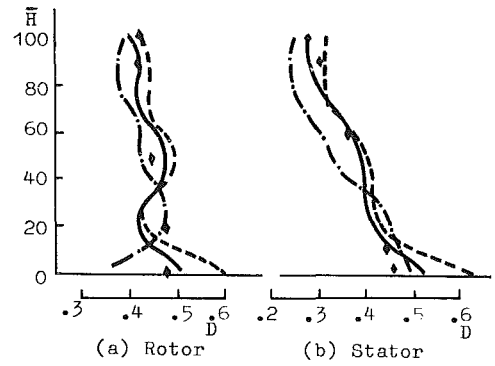

Fig. 13 Comparison of diffusion factor versus span: — stage 2 at near-design airflow; ---stage 2 at near-stall; ♦ stage 2 design value; — • — stage 1 at near-stall

3 The problems in stage 2 were that the load at the rotor hub was high; the blockage margins at the hub and tip of rotor 2 were inadequate due to effect of stage 1 discharge flow field; and the matching of stage 2 with stage 1 was not good.

4 It could be considered that the stall of the two-stage fan originated from the hub of rotor 2, because there were high load, high losses and high incidence at that region when the two-stage fan was operating at the near-stall point.

H. Pfeil
Professor.

R. Herbst
Research Engineer.

T. Schröder
Research Engineer.

Institute for Thermic Turbomachines,
Technical University of Darmstadt,
Darmstadt, West Germany

Investigation of the Laminar-Turbulent Transition of Boundary Layers Disturbed by Wakes

The boundary layer transition under instationary afflux conditions as present in the stages of turbomachines is investigated. A model for the transition process is introduced by means of time-space distributions of the turbulent spots during transition and schematic drawings of the instantaneous boundary layer thicknesses. To confirm this model, measurements of the transition with zero and favorable pressure gradient are performed.

Introduction

In the turbomachine, in which stationary and rotating blade cascades are successively arranged, unsteady flow to the following cascade is produced by the wakes of the previous one. In contrast to oscillating external flows, the periodical fluctuations of the mean velocity are superimposed here by the turbulent fluctuations caused by the mixing process in the wake. In this investigation the transition of a laminar boundary layer perturbed in this way is observed with the help of boundary layer measurements, in order to show the parameters responsible for the onset of transition.

The measurements were carried out in a low-velocity wind tunnel as already described by Pfeil and Herbst [1]. The unsteady flow to a plate is produced by means of a rotating cylinder cascade.

Former Investigations of Boundary Layer Transition in Instationary Flows

A fundamental assumption of the linear stability calculation as carried out by Tollmien [2] and Schlichting [3] is that the levels of the perturbations are small in comparison to the values of the basic flow. If the basic flow is superimposed by a periodically changed velocity, one must investigate whether the transition can be understood by means of the linear stability theory. Karlsson [4] performed preliminary experiments in this problem, in which he carrried out velocity and boundary layer measurements on a flat plate under oscillating external flow. With his results Karlsson showed that the average value of the local velocity was not influenced by the superimposing of an oscillating component in either laminar or turbulent boundary layers. The time-averaged velocity profile remains a solution of the Navier-Stokes equation, and the perturbation equations can also be treated as in the stationary case according to Tollmien and Schlichtings theory.

Greenspan and Benney [5] investigated the stability of the Tollmien-Schlichting flow, which is responsible for the high-frequency disturbances and breakdown into turbulence. They superimposed the Blasius profile with a time-dependent periodic shear flow of finite amplitude and established that at favoured locations a continuous production of local instabilities occurred at position and time of the most intense shear layer. The periodic turbulent spots created in this way spread downstream. If the amplitude of the external oscillating velocity is the same as or larger than that of a typical turbulent fluctuation, Miller and Fejer [6] as well as Obremski and Fejer [7] expect an agreement between the transition process within oscillating external flow and Greenspan and Benney's suggested model. The periodically changing external velocity is described by

$$U(t) = U_\infty \cdot (1 + N_A \cdot \sin\ \omega t) \tag{1}$$

where N_A represents the amplitude parameter.

$$N_A = \frac{\Delta U}{U_\infty} \tag{2}$$

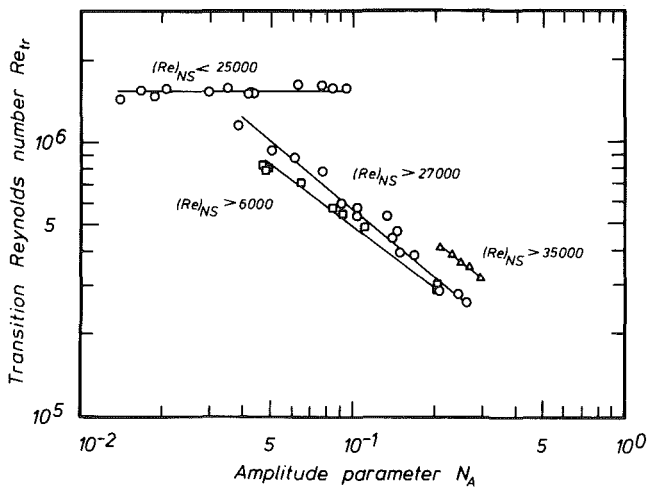

Fig. 1 Transition Reynolds number as a function of the amplitude parameter for three pressure gradients: ○, $dCp/dx = 0.004$/ft.; △, $dCp/dx = -0.081$/ft.; □, $dCp/dx = 0.045$/ft. (Obremski & Fejer [7])

Contributed by the Gas Turbine Division of THE AMERICAN SOCIETY OF MECHANICAL ENGINEERS and presented at the 27th International Gas Turbine Conference and Exhibit, London, England, April 18-22, 1982. Manuscript received at ASME Headquarters December 10, 1981. Paper No. 82-GT-124.

The evaluation of their measurements shows that with oscillating external flow the start of transition, especially with a zero pressure gradient, depends upon a certain nonsteady Re_{NS}-number, Fig. 1.

$$Re_{NS} = \frac{U_\infty}{\nu} \cdot \frac{\Delta U}{\omega} \tag{3}$$

If this Re_{NS}-number ($Re_{NS} \approx 27000$) is exceeded, the transition begins with turbulent spots which are periodically produced with the frequency of the outer flow. The Reynolds number Re_{tr} for the onset of transition is primarily dependent upon the amplitude of the external flow and not on the frequency.

Below a critical value of Re_{NS} ($Re_{NS} \approx 25{,}000$) the transition occurs at a relatively constant Reynolds number, which is not dependent upon the amplitude and frequency of the external flow. In this way the oscillation has lost its dominant role. However, Loehrke, Morkovin and Fejer [8] do not find the correlation just described as solely responsible for the correlation of the Re_{NS} number in their review of the transition of oscillating boundary layers. Morkovin et al. [9, 10] do succeed in explaining the above mentioned intermittent behaviour of the boundary layer in the transition region by means of a quasi-steady stability model.

Walker [11] investigated the transition of the boundary layer along the suction side of a stator blade in a single-stage axial-flow compressor. Corresponding to the model from Fejer et al., he regards the influence of the velocity oscillations caused by the wakes of previous rotor blades as responsible for the instability of the boundary layer.

In his considerations the relation of the instability length, i.e., distance between the point of instability and the turbulent breakdown, to local expansion of the wake on the blade surface represents an important parameter. If the instability length is large as a result of small or favourable pressure gradients, the turbulent breakdown can occur in the calmed region between two rotor wake disturbances. That assumes that the perturbations move more slowly than the wakes. When the instability length is small because of adverse pressure gradient the breakdown into turbulence can still take place in a wake area. The result of these considerations is that because of the importance of the instability length and therefore of the pressure gradient large velocity oscillations in the outer flow must not necessarily alter the transition region. However Walker does not make any statement about the influence on the transition of the stochastic turbulence in the wake.

Boundary layer measurements along stationary blades in the turbomachine cause great problems because of the small

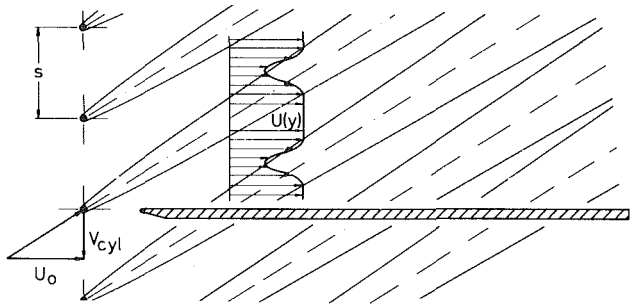

Fig. 2 Scheme of the unsteady flow produced by wakes

dimensions and the impossibility to be able to change only one of the various parameters alone which may influence transition in unsteady flow. For example, a variation of the circumferential velocity of the machine alters both disturbance frequency and Reynolds number simultaneously, while changing the throughflow coefficient alters both the disturbance amplitude and the mean streamwise pressure gradient over the transition region.

For this reason Pfeil and Pache [12] carried out boundary layer measurements on a 700-mm long plate. The unsteady flow was, as in [1], realized by a rotating cylinder cascade positioned in front of the plate. This test facility, which provides accurate measurements because of its large dimensions, allows the independent variation of the parameters influencing transition. Their measurements show that the perturbed flow in contrast to the stationary conditions involves large changes in the boundary layer development especially with favourable flows. In the case of undisturbed afflux and favourable basic flow, a laminar boundary layer develops along the entire plate length. In perturbed flow a laminar-turbulent transition occurred.

Comparisons of the transition obtained by measurements cannot be made to agree with Schlichtings stability theory and new empirical transition criteria such as those of Dunham [13], and Hall and Gibbings [14], which take the degree of turbulence in the external flow into account. It was presumed that the disturbances which consist of fluctuations and stochastic turbulence were so large that their influence on the transition can no longer be described by the linear stability theory, which is founded on small perturbations. In [12], the question was still open as to the effects of varied perturbation conditions on the temporary development of the instationary boundary layer. For this reason, in further investigations by Pfeil and Herbst [1, 15] the number of the cylinders in the rotating cascade was increased from zero upwards. The

Nomenclature

d = diameter
i = plate incidence angle
N_A = amplitude parameter of free-stream unsteadiness, $\Delta U/U_\infty$
Re_x = Reynolds number based on streamwise coordinate, $U_\infty \cdot x/\nu$
Re_{NS} = nonsteady Reynolds number, see equation (3)
Re_{tr} = transition Reynolds number, $U_\infty \cdot x_{tr}/\nu$
s = spacing of cylinder cascade
T = period, s/V_{cyl}
T-S = Tollmien-Schlichting
t = time
t_W = reference time value at half wake depth
U = longitudinal velocity component of mean flow
U_o = mean longitudinal velocity component in afflux
U_∞ = mean longitudinal velocity component in external flow
u = longitudinal fluctuation velocity
V_{cyl} = cross velocity of cylinder
v = transverse fluctuation velocity
x = coordinate along surface
y = coordinate normal to surface
δ = boundary layer thickness
ν = kinematic viscosity
ϕ = normalized velocity component in the wake in x-direction
ω = circular frequency

Subscripts

f = forced
LE = leading edge
lam = laminar
ns = neutral stability
0 = undisturbed
TE = trailing edge
Tr = end of transition
tr = start of transition, i.e., appearance of a turbulent spot
turb = turbulent

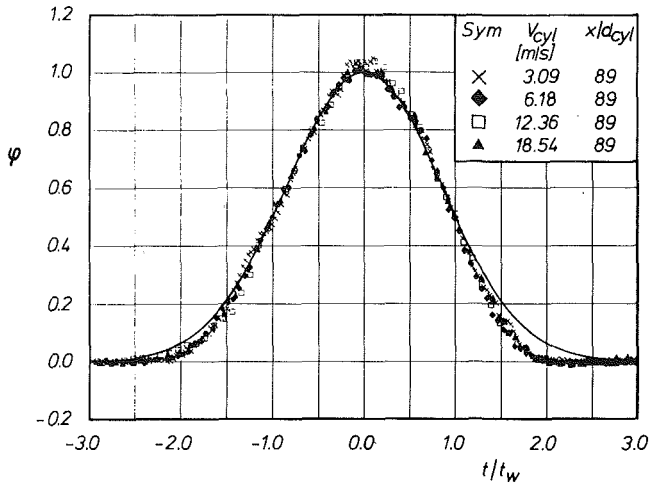

Fig. 3 Profiles of measured normalized velocities in the wake in x-direction compared with the Gaussian distribution curve (Pfeil & Schröder [16])

evaluations of the measurements led to a model which describes the temporary boundary layer development under these special conditions.

Model for Transition Behaviour Under Instationary Flow

Figure 2 shows according to the test conditions the flow behind a cylinder cascade crossing the flow direction. The wakes, whose slant results from the afflux velocity U_o and the cross velocity of the cylinder V_{cyl}, drift off along the plate surface and influence the boundary layer, and especially its transition behaviour, in a periodical intermittent way.

As an example, Fig. 3 presents measured temporal distributions of the ensemble-averaged wake velocities behind a moving cylinder, which crosses the flow with varied velocities V_{cyl}, (see Pfeil and Schröder [16]).

The time-space distributions, Fig. 4, are suitable to present the transition process, i.e., the formation and propagation of turbulent spots. The parallel lines to the x-axis reproduce the instantaneous flow conditions along the plate, while the vertical lines describe the change of the flow over the time at a fixed place. With undisturbed flow a laminar boundary layer forms along the plate, which undergoes natural transition after a certain flow distance according to the stability criteria from Tollmien and Schlichting, Fig. 4(a). The marked positions, the point of neutral stability, x_{ns}, the start, $x_{o,tr}$, and the end, $x_{o,Tr}$, of natural transition describe the transition process. Downstream from x_{ns} small disturbances of a defined area of wave length are stimulated (T-S-waves) and break off from $x_{o,tr}$ upwards in high-frequency irregular three-dimensional velocity fluctuations. The turbulent spots which are formed in this way cause an intermittently turbulent boundary layer. They propagate until they have merged at $x_{o,Tr}$ and the natural transition is ended. As the propagation velocity of two-dimensional waves (T-S-waves) is lower than that of the trailing edge of a turbulent spot (see Schubauer & Klebanoff [17]), a so-called "becalmed region" is formed at the trailing edge in which no further turbulent spot can arise. In Fig. 4 these regions are marked by hatching.

If a wake with its increased stochastic turbulence moves over the plate surface, the developing laminar boundary layer is already intensely disturbed. The perturbations are however subdued, i.e., are no longer stimulated. At first from the forced start of transition, $x_{f,tr}$, Fig. 4(b), the turbulent spots periodically produced by the wakes, spread and form an intermittent laminar-turbulent boundary layer. These turbulent spots are followed by becalmed regions of laminar

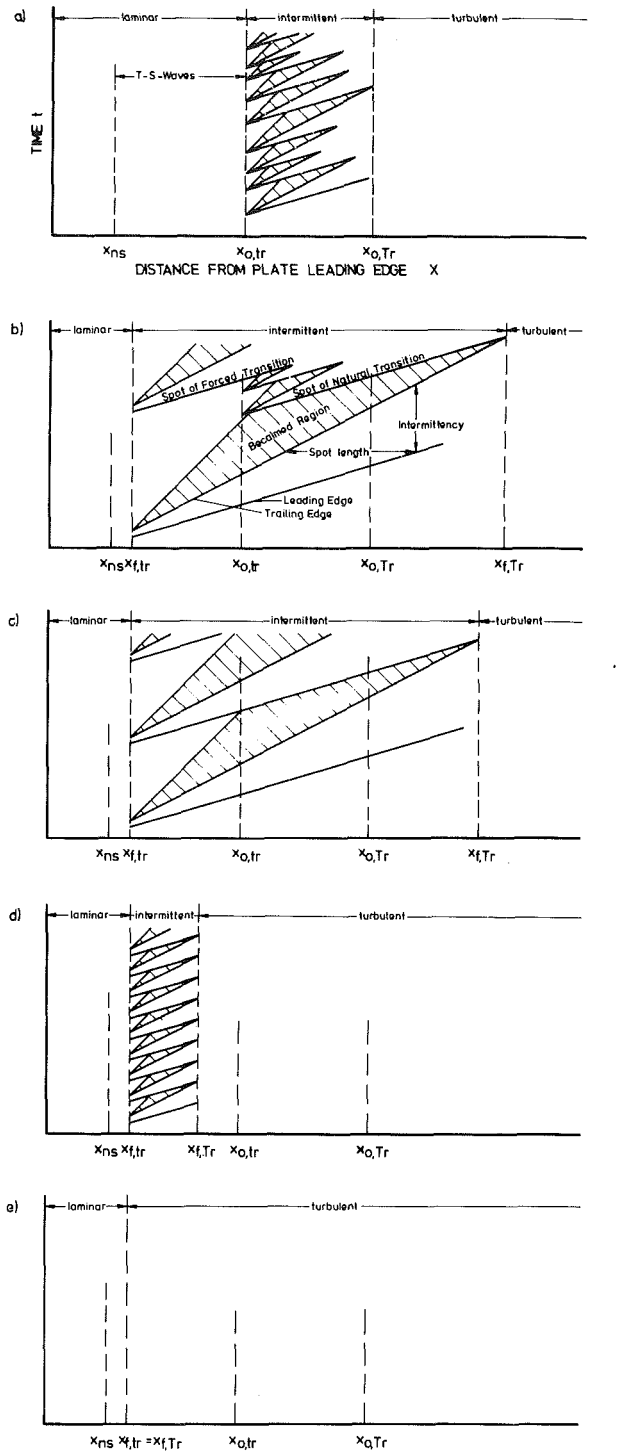

Fig. 4 Time-space distribution of the turbulent spots during transition

boundary layer in the same way as the turbulent spots of natural transition. If the spacing of the cylinder cascade is large, the turbulent spots of the natural transition are observed from $x_{o,tr}$ in the undisturbed areas between periodically produced turbulent spots and their becalmed regions. As a consequence of the large spacing and the becalmed regions of the forced turbulent spots the transition is not finished at $x_{o,Tr}$, but subsequently downstream at $x_{f,Tr}$, Fig. 4(b).

While other test parameters, such as constant cross velocity of the cylinder cascade, V_{cyl}, constant afflux velocity, U_o, as well as the positioning of the plate, remain unchanged, varied spacings show no influence on the position of $x_{f,tr}$. Only the

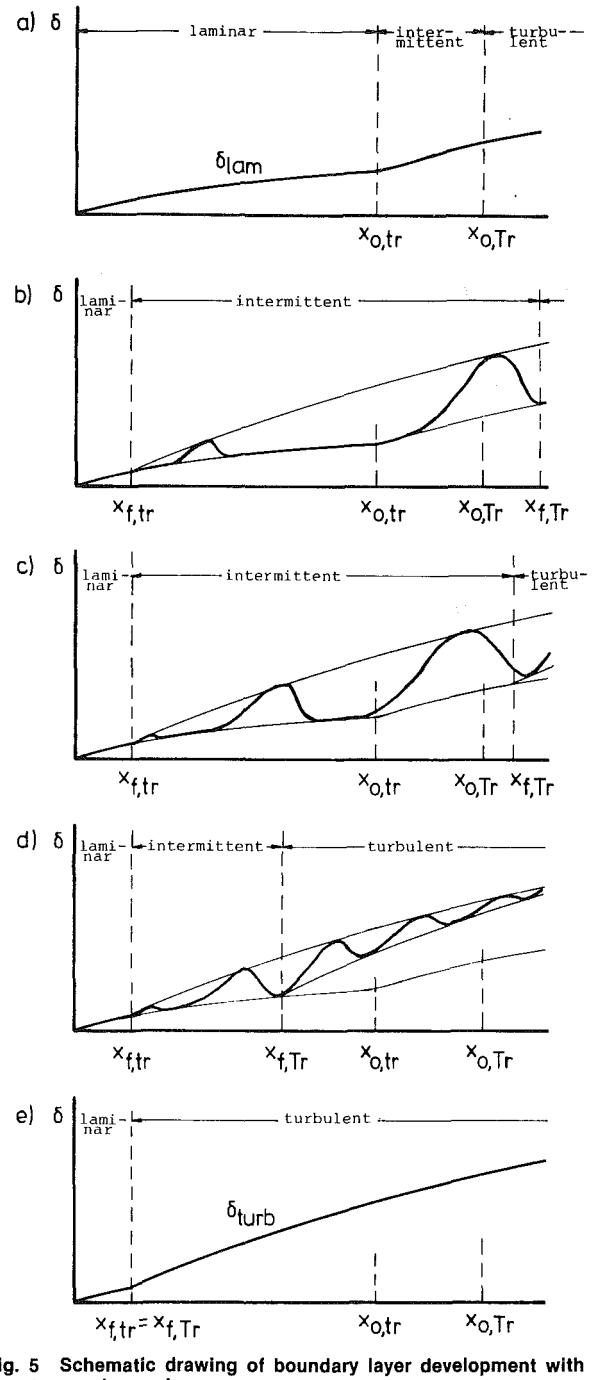

Fig. 5 Schematic drawing of boundary layer development with different cascade spacing

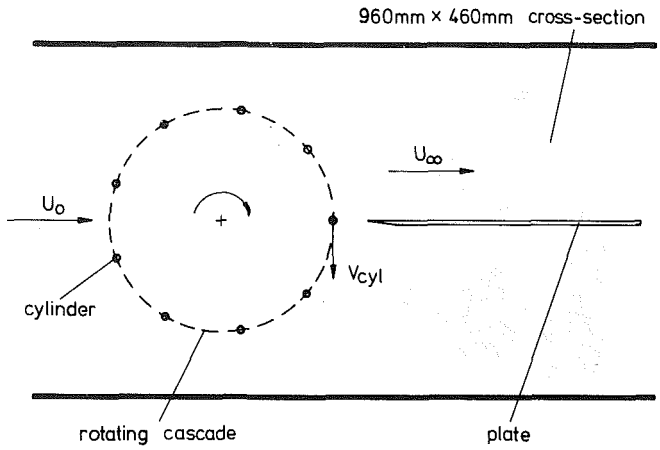

Fig. 6 Scheme of the test facility

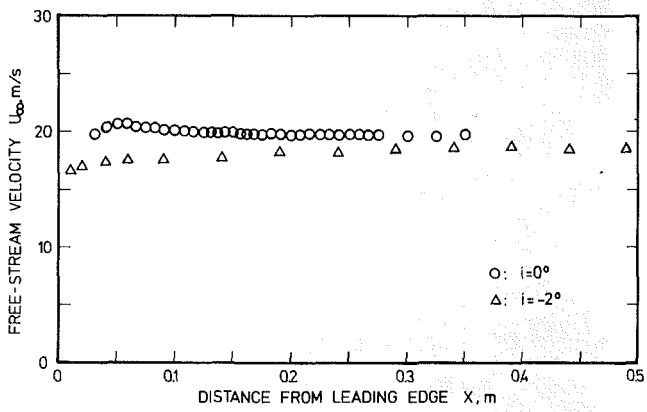

Fig. 7 Distributions of the free-stream velocity

number of periodic produced turbulent spots per unit of time increases inversely proportional to the spacing. With a certain spacing the creation of turbulent spots of natural transition is totally prevented by the becalmed regions of the forced turbulent spots, see Fig. 4(*c*). With this and smaller spacings, Fig. 4(*d*), the transition is only ended by the merging of the periodically produced turbulent spots at $x_{f,Tr}$.

If one reduces the spacing of the cylinder cascade down to a critical value, the wakes already merge in the afflux. Then at the point of the start of transition, $x_{f,tr}$, an almost uniform and still high turbulence level exists. Subsequently, the length of transition, $x_{f,Tr} - x_{f,tr}$, of the forced transition tends to zero, Fig. 4(*e*).

As can be seen from Fig. 4, besides the spacing one needs the other important parameters, the instability length and the spot propagation of the natural and the forced transition, in order to describe the entire transition process.

In analogy to Fig. 4 in Fig. 5 the boundary layer development is plotted. The forced turbulent spots of the disturbed flow can be recognized by a local thickening of the boundary layer, which moves downstream rising at the same time, as measured by Pfeil and Herbst [1]. As already shown in Fig. 4(*b*), the end of forced transition, $x_{f,Tr}$, is located downstream of the end of natural transition, Fig. 5(*b*). Smaller spacings affect a displacement of the end of forced transition in direction of the plate leading edge, Figs. 5(*c*) and 5(*d*), until, as in the case of critical small spacing, Fig. 5(*e*), the start and end of forced transition coincide. The then developing turbulent boundary layer δ_{turb}, represents a limiting curve for the growth of the thickness of the forced turbulent spots.

The conception described above should be employed as a model for further considerations in boundary layer transition under unsteady flow conditions. As the structure in the wake of a cylinder is almost the same as behind a blade, these relations can also be applied to a rotating blade cascade with the same C_D-value and spacing placed in front of the testing section. However the influence of the circulation of the previous cascade remains disregarded. It must be mentioned that in this investigation it was assumed that the periodic fluctuations of the static pressure caused by the wakes striking the plate are disregarded.

Measurement Results

The boundary layer measurements were carried out along a plate with zero pressure gradient, $i = 0$ deg, and a weak favourable pressure gradient, $i = -2$ deg. Figure 6 represents a scheme of the test facility.

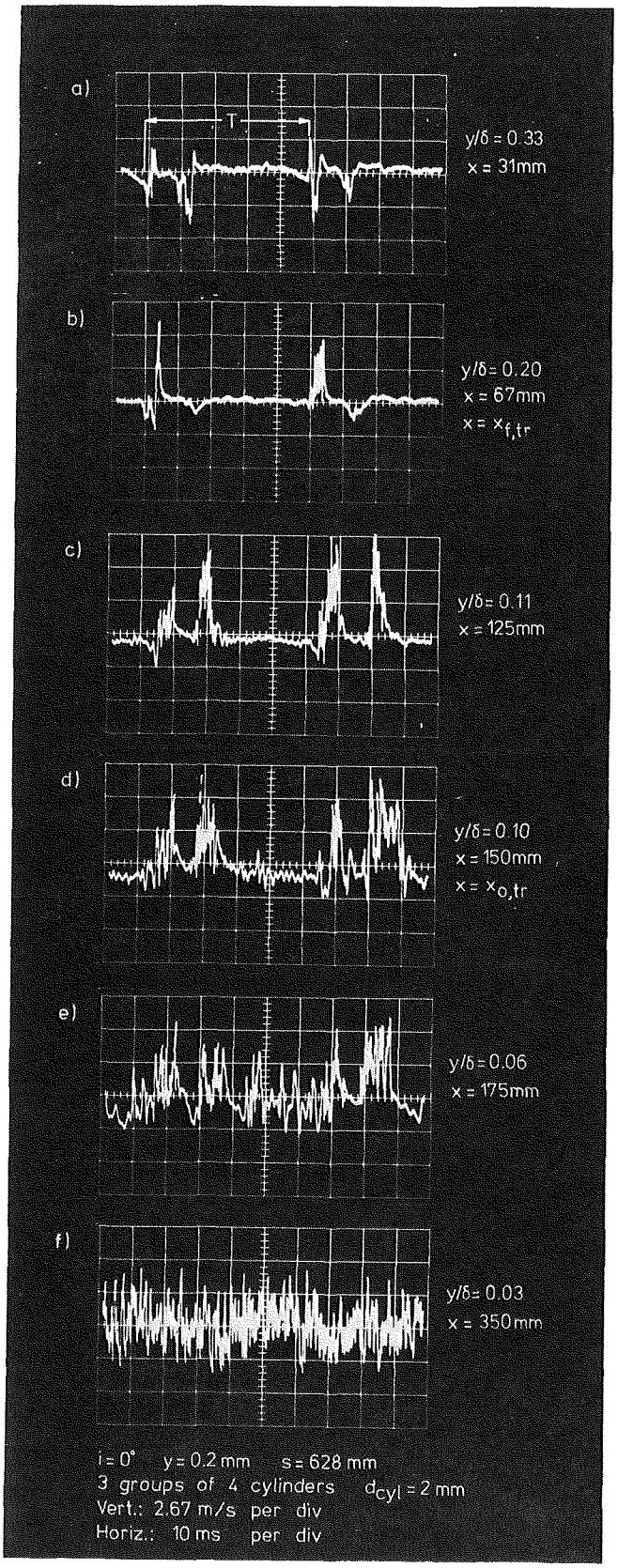

Fig. 8 Oscilloscope traces of the longitudinal velocity fluctuations in the perturbed boundary layer at constant wall distance, recorded at different x-stations

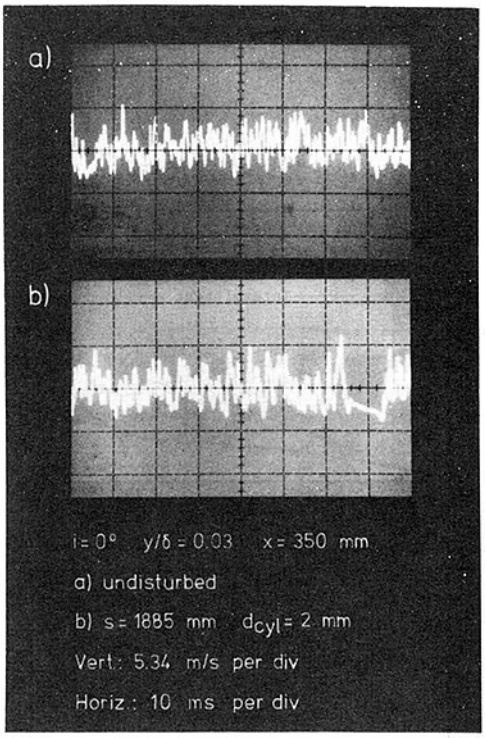

Fig. 9 Oscilloscope traces of the longitudinal velocity fluctuations in the perturbed boundary layer at constant wall distance, recorded at x = 350 mm

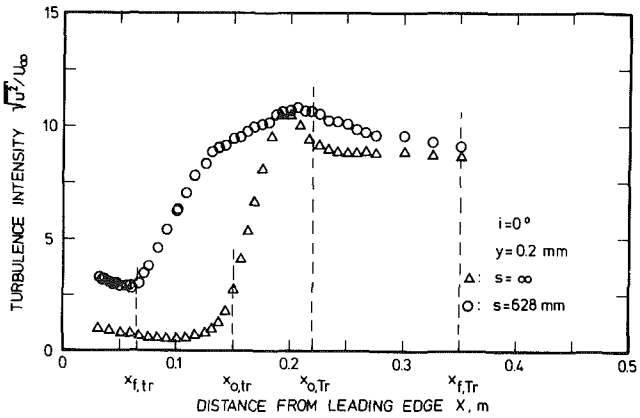

Fig. 10 Distribution of the nondimensional turbulence intensities along the plate at constant wall distance in undisturbed and disturbed boundary layer

The afflux velocity, U_o, amounted to approximately 20 m/s for all the measurements and the cross velocity, V_{cyl}, of the moved 2-mm wide cylinders to 12.6 m/s. The spacing of the cylinder cascade, which moves across the flow direction in an orbit with 0.6 m dia, can be altered.

During the zero pressure gradient measurements three groups of cylinders were mounted in the cascade with an individual displacement of 120 deg. Each of these groups of cylinders consists of four cylinders closely mounted in distances of 5 mm. In contrast to this, during the measurements with favourable pressure gradient the cylinders were placed individually.

The streamwise distributions of the free-stream velocity, U_∞, which belong to the two different plate incidences, are shown in Fig. 7.

Measurements with Zero Pressure Gradient. Figure 8 shows oscilloscope traces of the longitudinal velocity fluctuations in the boundary layer at a constant wall distance, y. Even from the leading edge of the plate the large perturbations periodically influence the boundary layer flow. As the cylinder twice crosses the middle of the channel in its orbit, in accordance with Fig. 6, two perturbations arise, one of which

is weaker, owing to the longer flow distance. It can be seen in Fig. 8(*a*) that when $x = 31$ mm the boundary layer reacts with high-frequency changes. The laminar boundary layer is however so stable further downstream that the perturbations are no longer stimulated but are even subdued, as is shown in Fig. 8(*b*) by the example of the perturbation of the upward moving cylinder.

After $x = 67$ mm a definite development also of the width of the periodically produced turbulent spots was established. In accordance with the introduced transition model, Figs. 4 and 5, the onset of forced boundary layer transition $x_{f,tr}$ is found at this x-wise position. The increase of the velocity in the turbulent spot is proof of the fact that the fluctuations of the wake are not carried into the boundary layer, but here a rapid change from the laminar to the turbulent velocity profile takes place in the boundary layer (see Pfeil and Herbst [1], Fig. 7). Even further downstream, Fig. 8(*c*), in the undisturbed area between the forced turbulent spots the typical T-S-waves of the natural transition are visible. The amplitude of the T-S-waves is increasingly stimulated until at $x_{o,tr}$. Fig. 8(*d*), the first turbulent spots of the natural transition appear. Further downstream these turbulent spots fill in the previously undisturbed area even more, Fig. 8(*e*), until, as in Fig. 8(*f*), only turbulent velocity fluctuations can be seen and the transition is ended. As in this record the periodically produced turbulent spots have just merged at their edges, an oscillation of the base flow with the frequency of the perturbation of the moving cylinder cascade is still observed in the turbulent boundary layer.

Due to the chosen spacing the becalmed regions occurring in the environment of turbulent spots are not clearly visible in the oscilloscope traces recorded in Fig. 8. The existence of the becalmed region is evident, if at a x-station downstream of $x_{o,Tr}$ with disturbed afflux an intermittent laminar-turbulent boundary layer is observed. Figure 9 shows oscilloscope traces of the longitudinal velocity fluctuations in the boundary layer, recorded at $x = 350$ mm.

Whereas with undisturbed afflux the boundary layer has undergone transition, Fig. 9(*a*), with disturbed afflux caused by a large spacing of the cylinder cascade portions of laminar boundary layer are clearly visible in the record, Fig. 9(*b*). That is, the end of forced transition $x_{f,Tr}$ is situated downstream of the end of natural transition, x_o, T_r.

The distribution of the fluctuation velocity at constant wall distance in streamwise direction is shown in Fig. 10.

The onset of the natural transition is identified by $x_{o,tr} = 150$ mm, whereby $x_{o,tr}$ was found with the help of oscilloscope traces. The increase of the fluctuation velocities in front of $x_{o,tr}$ can be explained by the appearance of T-S-waves. As with disturbed afflux, the superimposed perturbations in the stable laminar boundary layer are not stimulated, the fluctuation velocities decrease until the onset of transition at $x_{f,tr} \approx 67$ mm appears. The curve increases after $x_{f,tr}$ and bends in

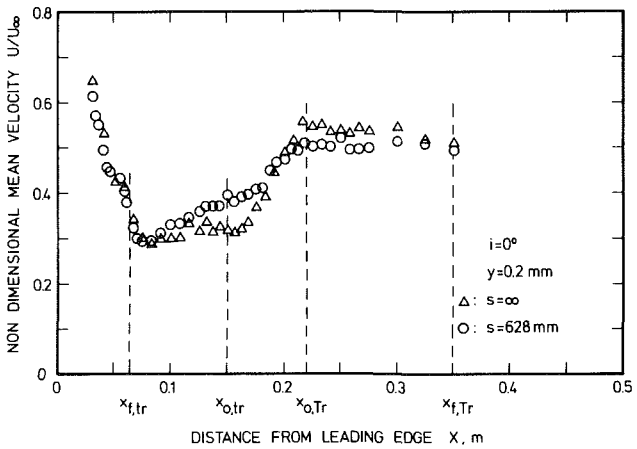

Fig. 11 Distribution of the nondimensional mean velocity along the plate at constant wall distance in undisturbed and disturbed boundary layer

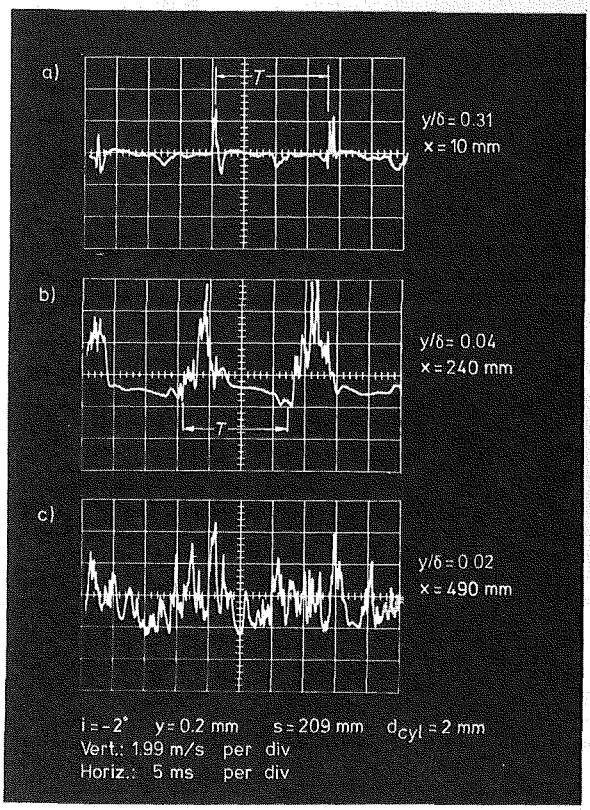

Fig. 12 Oscilloscope traces of the longitudinal velocity fluctuations in the perturbed boundary layer at constant wall distance, recorded at different x-stations

Table 1 Comparison of measured spot-velocities

Authors	U_{LE}	U_{TE}	Flow Conditions
Schubauer & Klebanoff [17]	0.88 U_∞	0.5 U_∞	flat plate, spark
Wygnanski, Sokolov & Friedman [18]	0.89 U_∞	0.5 U_∞	flat plate, spark
Obremski & Fejer [7]	0.88 U_∞	0.58 U_∞	flat plate, oscillating external flow
Houdeville, Cousteix & Desopper [19]	0.89 U_∞	0.48 U_∞	flat plate, oscillating external flow
Present results	0.75 U_∞	0.54 U_∞	favourable pressure gradient, i = -2°, wakes

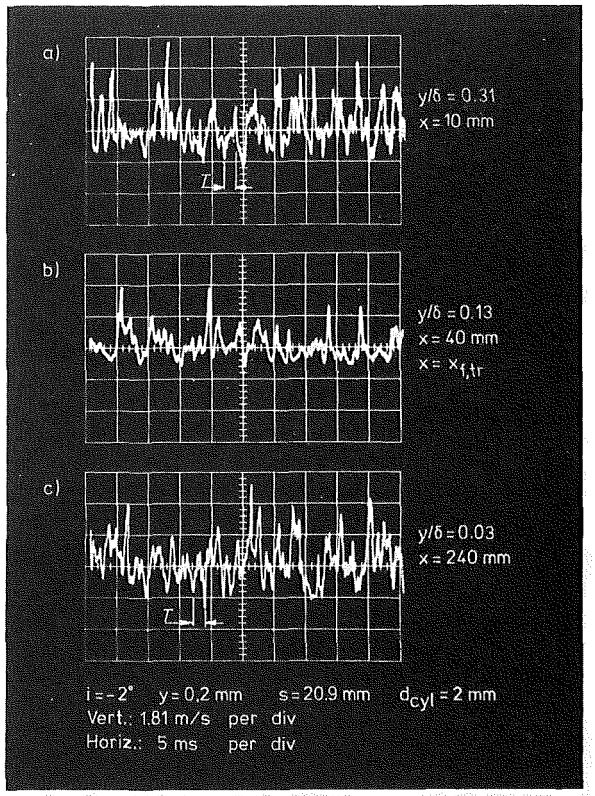

Fig. 13 Oscilloscope traces of the longitudinal velocity fluctuations in the perturbed boundary layer at constant wall distance, recorded at different *x*-stations

the area from $x_{o,tr}$, which could be attributed to the overlapping natural transition. The transition is ended when the turbulence intensity reaches a nearly constant level. The respective positions of the end of transition with undisturbed and disturbed afflux, $x_{o,Tr}$ and $x_{f,Tr}$, are stated in Fig. 10.

In Fig. 11 the distribution of the nondimensional mean velocity, U/U_∞, at constant wall distance was plotted. The alteration of the laminar into the turbulent velocity profile is to be recognized in this graph by an increase of the mean velocity close to the wall.

These measurements show that in the chosen experimental conditions the end of transition is found downstream of the end of natural transition (see Fig. 4(*b*)); the start of transition caused by large perturbations is located nearer to the plate leading edge, i.e., at smaller Re_x-numbers, as the start of natural transition.

Measurements with Favorable Pressure Gradient. Like Fig. 8, Fig. 12 shows a series of oscilloscope traces of velocity fluctuations in the boundary layer. In comparison to the measurements at zero pressure gradient, now nine single cylinders with the spacing of $s = 209$ mm are mounted in the rotating cascade. One can clearly recognize the turbulent spots, which are created by the wakes, Fig. 12(*b*). The time interval corresponds to the period, T, of the wakes, which successively strike the plate surface. As for the undisturbed flow, the boundary layer is stable laminar along the plate, no T-S-waves are observed in the undisturbed region between two spots in contrast to zero pressure gradient flow. From the oscilloscope traces, surprisingly, only the start of the forced transition, $x_{f,tr}$, can already be seen after a small distance from the plate leading edge. The turbulent spots merge at $x_{f,Tr} = 490$ mm as a result of the propagation of their leading and trailing edge, and the transition is terminated. It is then shown that the forced transition process was completed within the measured plate region before the natural transition had even begun (see Figs. 4(*d*) and 5(*d*)).

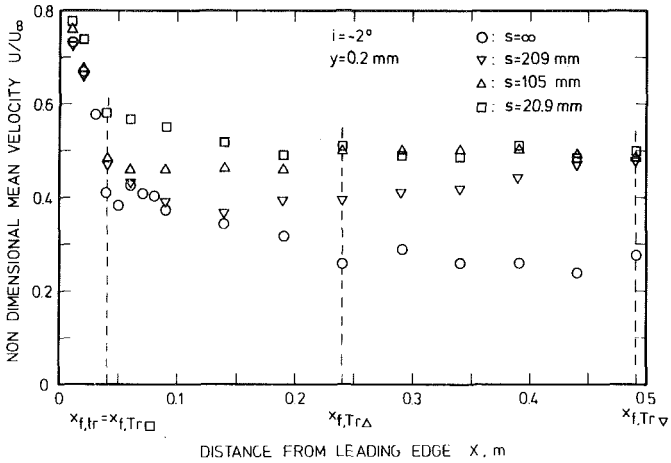

Fig. 14 Distribution of the nondimensional mean velocity along the plate at constant wall distance and varied cascade spacing

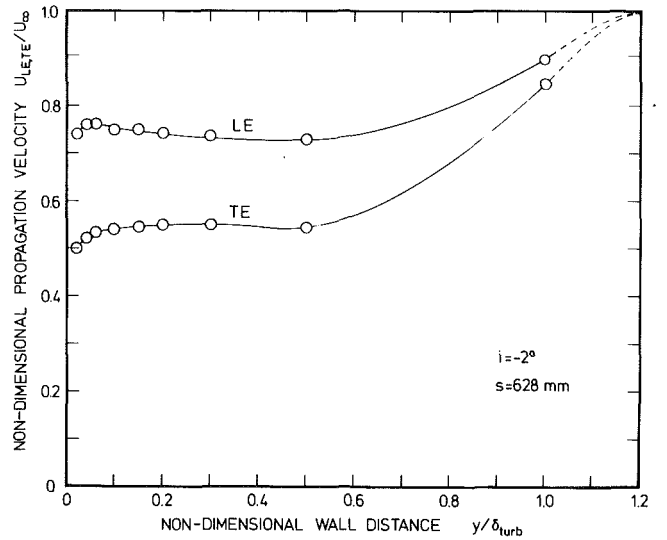

Fig. 15 Spot-velocities at incidence $i = -2$ deg as a function of the nondimensional wall distance

In Fig. 13 the velocity fluctuations in the boundary layer are shown with a cascade spacing of $s = 20.9$ mm. Due to this critical spacing and to all smaller spacings the wakes have already merged in the afflux. The comparison of the fluctuations where $x = 10$ mm, Fig. 13(*a*), and $x = 40$ mm, Fig. 13(*b*), shows that the perturbations, which can no longer be identified in their period, are primarily subdued downstream. From $x = 40$ mm this suppression was no longer to be seen. Therefore, the location of the beginning and end of transition was presumed to be in this position. Fig. 5(*e*) shows the expected distribution of the turbulent boundary layer δ_{turb}.

Figure 14 shows the plot of the nondimensional mean velocity, U/U_∞, at various cascade spacings and at constant wall distance.

The start of transition can be found at $x_{f,tr} = 40$ mm for all spacings except for undisturbed afflux ($s = \infty$). The end of transition, $x_{f,Tr}$, which at $s = 20.9$ mm is the same as the start of transition, is observed with larger spacing after larger distances from the plate leading edge.

Spot Propagation and Shape. In order to obtain the shape of the turbulent spot and the velocity with which it moves over the plate surface, the running time differences of the spots' leading and trailing edge between two stationary points were measured. The investigations were carried out at an incidence angle of -2 deg and a spacing of $s = 628$ mm. This incidence

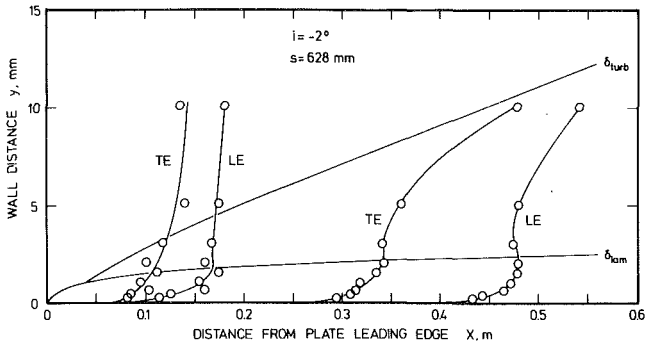

Fig. 16 Development of the turbulent spot along the plate at incidence $i = -2$ deg

angle was chosen as with favourable pressure gradient and no random turbulent spots of the natural transition occurred. The results of the measurements are presented in Fig. 15 as a function of the nondimensional wall distance y/δ_{turb}. Thus δ_{turb} is the defined boundary layer thickness according to Fig. 5(*e*), which was measured under the chosen test conditions at the critical cascade spacing $s = 20.9$ mm. As is seen from other authors' measurements, Table 1, which produced the turbulent spots in another way, a relation is determined between the external velocity, U_∞, and the velocity of the leading and trailing edge of the spot. Whereas the velocity of the trailing edge agrees with the other results, the measured leading edge velocity deviates to smaller values.

Figure 16 represents the shape of the turbulent spots and its change along the plate. The deformation of the turbulent region can be clearly recognized, which particularly close to the wall remains notably behind the wake in the outer flow. The curve of the undisturbed laminar boundary layer, δ_{lam}, was additionally drawn in the graph. As the laminar boundary layer which surrounds the spot has a subduing influence, the spot has its maximum width in the distance δ_{lam}. At the edge of the boundary layer the turbulent spot must change into the wake of the moving cylinder. This means that the spot velocity, as indicated in Fig. 15, also changes into the velocity of the external flow.

Conclusion

The boundary layer transition under instationary afflux conditions is investigated in this paper. In contrast to investigations by other authors [6, 7, 9], who researched the sole influence of the oscillating basic flow, an unsteady flow, as it occurs in the stages of turbomachines, is realized here by a moving cylinder cascade in front of a plate.

A model which describes the transition under these flow conditions is introduced with the aid of time-space distributions of the turbulent spots, Fig. 4, and schematic drawings of the instantaneous boundary layer thicknesses, Fig. 5. The spacing of the cascade in relation to the plate length represents an important parameter for the start and end of the transition. The cascade wakes force the onset of transition after a shorter flow distance than by undisturbed flow. The spacing of the cascade exerts no influence on the position of the forced start of transition. The end of forced transition does not depend on the end of natural transition and can occur due to the spacing downstream or upstream of the end or even upstream of the start of natural transition.

Measurements of the boundary layer transition taken by zero and favourable pressure gradient are referred to in order to confirm the model. Furthermore measurements of the shape and propagation of the turbulent spots in the disturbed boundary layer are introduced.

With the investigations so far carried out it could not be ascertained definitely if the stochastic fluctuations in the wake are responsible for transition. The influence on transition of the periodic fluctuations in the wake also cannot be excluded, as they produce periodic fluctuations of the static pressure on the plate surface. Subsequent investigations shall contribute to a further clarification.

Acknowledgment

As part of the research project "Transition Procedure of Instationary Boundary Layers" the investigation presented here has been supported by the Bundesministerium der Verteidigung (German Ministry of Defence). The authors are grateful for this support.

References

1 Pfeil, H., and Herbst, R., "Transition Procedure of Instationary Boundary Layers," ASME-Paper No. 79-GT-128, San Diego, Calif., 1979.

2 Tollmien, W., "Ein allgemeines Kriterium der Instabilität laminarer Geschwindigkeitsverteilungen," *Nachr. d. Ges. d. Wiss. zu Göttingen*, Math.-Phys. Klasse, Fachgruppe I, Band 1, 1935, pp. 79-114.

3 Schlichting, H., "Amplitudenverteilung und Energiebilanz der kleinen Störungen bei der Plattenströmung," *Nachr. d. Ges. d. Wiss. zu Göttingen*, Math.-Phys. Klasse, Fachgruppe I, Band 1, 1935, pp. 47-78.

4 Karlsson, S.K.F., "An Unsteady Turbulent Boundary Layer," *Journal of Fluid Mechanics*, Vol. 5, part. 4, 1959, pp. 622-636.

5 Greenspan, H.P., and Benney, D.J., "On Shear-Layer Instability, Breakdown and Transition," *Journal of Fluid Mechanics*, Vol. 15, 1963, pp. 133-153.

6 Miller, J.A., and Fejer, A.A., "Transition Phenomena in Oscillating Boundary-Layer Flows," *Journal of Fluid Mechanics*, Vol. 18, part. 3, 1964, pp. 438-448.

7 Obremski, H. J., and Fejer, A. A., "Transition in Oscillating Boundary Layer Flows," *Journal of Fluid Mechanics*, Vol. 29, part. 1, 1967, pp. 93-111.

8 Loehrke, R. I., Morkovin, M. V., and Fejer, A. A., "Review—Transition in Nonreversing Oscillating Boundary Layers," ASME *Journal of Fluids Engineering*, Vol. 97, 1975, pp. 534-549.

9 Obremski, H. J., and Morkovin, M. V., "Application of a Quasi-Steady Stability Model to Periodic Boundary-Layer Flows," *AIAA Journal*, Vol. 7, No. 7, 1969, pp. 1298-1301.

10 Obremski, H. J., Morkovin, M. V., and Landahl, M., "A Portfolio of Stability Characteristics of Incompressible Boundary Layers," AGARDograph No. 134, Paris, 1969.

11 Walker, G. J., "The Unsteady Nature of Boundary Layer Transition on an Axial-Flow Compressor Blade," ASME-Paper No. 74-GT-135, 1974.

12 Pfeil, H., and Pache, W., "Measurements of Flow Boundary Layers on Conditions of Turbomachines," *Journal of Flight Sciences and Space Research*, Vol. 1, No. 4, 1977, pp. 267-277.

13 Dunham, J., "Predictions of Boundary Layer Transition on Turbomachinery Blades," AGARDograph No. 164, 1972, pp. 55-71.

14 Hall, D. J., and Gibbings, J. C., "Influence of Stream Turbulence and Pressure Gradient upon Boundary Layer Transition," *Journal of Mechanical Engineering Science*, Vol. 14, No. 2, 1972, pp. 134-146.

15 Herbst, R., "Entwicklung von Grenzschichten bei instationärer Zuströmung," Ph.D. thesis, D 17, Technische Hochschule Darmstadt, 1980.

16 Pfeil, H., and Schröder, Th., "Decay of the Wake Behind a Cylinder Crossing Rapidly the Flow," AIAA Paper No. 81-0209, St. Louis, 1981.

17 Schubauer, G. B., and Klebanoff, P. S., "Contributions on the Mechanics of the Boundary-Layer Transition," NACA Report, No. 1289, 1956.

18 Wygnanski, I., Sokolov, M., and Friedman, D., "On a Turbulent Spot in a Laminar Boundary Layer," *Journal of Fluid Mechanics*, Vol. 78, part. 4, 1976, pp. 785-819.

19 Cousteix, J., Houdeville, R., and Desopper, A., "Transitione d'une couche limite soumise a une oscillation de l'écoulement exterieur," *Conference Proceedings* No. 224, Paper No. 17, Agard Fluid Dynamics Panel - Copenhagen, 1977.

Three-Dimensional Aerodynamic Characteristics of Oscillating Supersonic and Transonic Annular Cascades

M. Namba
Professor.

A. Ishikawa
Graduate Student.

Department of Aeronautical Engineering,
Kyushu University,
Fukuoka, Japan

A lifting surface theory is developed for unsteady three-dimensional flow in rotating subsonic, transonic and supersonic annular cascades with fluctuating blade loadings. Application of a finite radial eigenfunction series approximation not only affords a clear insight into the three-dimensional structures of acoustic fields but also provides mathematical expressions advantageous to numerical work. The theory is applied to oscillating blades. Numerical examples are presented to demonstrate three-dimensional effects on aerodynamic characteristics. Three-dimensional effects in supersonic cascades are generally small and strip theory predicts local aerodynamic forces as well as total aerodynamic forces with good accuracy. In transonic flow, however, the strip theory approximation breaks down near the sonic span station and three-dimensional effects are of primary importance.

Introduction

One of the most serious problems in the development of modern jet engines is the so-called supersonic cascade flutter, for which many authors have developed two-dimensional flow theories. Strictly speaking, however, axial fan and compressor stages in those engines usually operate in the transonic flow regime, where the inlet flow Mach number, relative to the rotating blades, varies from below unity at radii near the hub to values above unity at radii near the blade tips. Several authors have developed theories to predict three-dimensional effects on aerodynamic forces in a rotating annular cascade, as reviewed by Lordi and Homicz [1]. Most of them, however, are concerned with steady loadings in subsonic, transonic and supersonic flows or unsteady loadings in subsonic flows. Salaün has dealt with the problem of unsteady loadings in a supersonic annular cascade [2] and a transonic annular cascade [3]. However since his latter paper is written too briefly, one can neither trace details of his mathematical analysis nor obtain useful information on three-dimensional flow features in transonic compressors.

In this paper the unsteady lifting surface theory developed by one of the authors [4, 5] for a rotating subsonic annular cascade is extended so that it can be applied to a rotating transonic or supersonic annular cascade. In the present theory the method of finite radial acoustic eigenfunction series is employed, as was done in the previous theories by Namba [4–6]. This technique allows one to regard the disturbance pressure field in a transonic compressor as a superposition of acoustic modes of supersonic type consisting of a finite number of lower radial orders and those of subsonic type consisting of remaining higher radial orders. Owing to this method one can obtain not only a clear insight into the three-dimensional structure of the flow field, but also mathematical expressions appropriate for numerical work.

The theory is applied to predicting unsteady loadings on oscillating blades. Numerical examples of unsteady pressure distributions on blade surfaces and total unsteady works of the aerodynamic forces on blades are presented for some combinations of reduced frequency, interblade phase angle, modes of vibration and Mach number. All numerical results are graphically compared with results from strip theory to

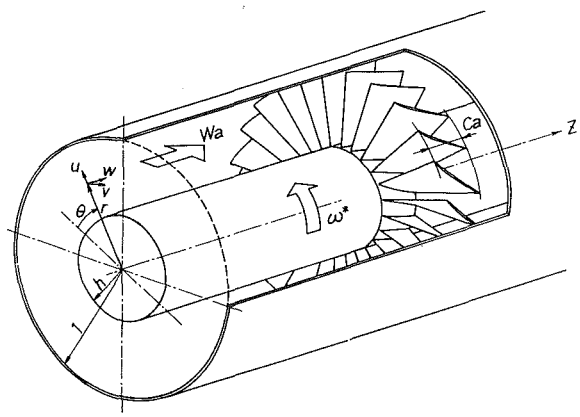

Fig. 1 Annular cascade and duct geometry

Contributed by the Gas Turbine Division of THE AMERICAN SOCIETY OF MECHANICAL ENGINEERS and presented at the 27th International Gas Turbine Conference and Exhibit, London, England, April 18–22, 1982. Manuscript received at ASME Headquarters December 10, 1981. Paper No. 82-GT-126.

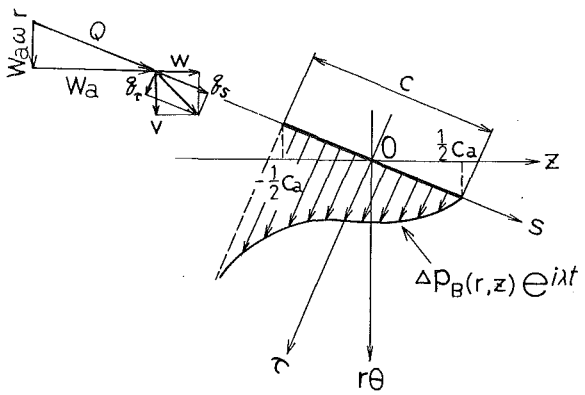

Fig. 2 Coordinates and velocity vectors

demonstrate the three-dimensional effects on unsteady aerodynamic characteristics.

Theoretical Model and Disturbance Pressure Field

Consider a single annular blade row with N blades rotating at a constant angular velocity ω^* in a solid-walled annular duct of infinite axial extent, where an inviscid perfect gas is flowing with uniform subsonic axial velocity, W_a, uniform entropy, and no preswirl. The disturbance caused by the blade row is assumed to be small and insentropic. Let (r,θ,z) be a cylindrical polar coordinate system fixed to the rotor as shown in Fig. 1, where the radial and axial coordinates, r and z, are normalized by the duct radius r_T^*. The dimensionless time coordinate, t, is correspondingly scaled with respect to r_T^*/W_a.

Let each blade have no steady loading and no thickness but an unsteady loading fluctuating with a local strength $\Delta p_B(r,z)$, an angular frequency, λ^*, and an interblade phase angle $\hat{\sigma}(=2\pi\sigma/N)$, as shown in Fig. 2. Then each blade can be represented by a lifting surface with lifting pressure distribution $\Delta p_B(r,z)\exp(i\lambda t+ik\hat{\sigma})$ located at a surface segment $\theta' = 2\pi k/N$ ($k = 0, 1, \ldots, N-1$), $-c_a/2 \le z \le c_a/2$ and $h \le r \le 1$. Here θ' is defined by $\theta' = \theta - \omega z$, ω is the dimensionless rotational speed of the rotor defined by $\omega = \omega^* r_T^*/W_a$, h denotes the hub to tip ratio, and c_a denotes the axial chord length, which is for simplicity assumed to be constant along the span. Furthermore, λ is the reduced frequency defined by $\lambda = \lambda^* r_T^*/W_a$. Then as shown in [5], the disturbance pressure field $p(r,\theta',z)e^{i\lambda t}$ can be expressed in the form

$$p(r,\theta',z)=\int_h^1 d\rho\int_{-c_a/2}^{c_a/2}\Delta p_B(\rho,\zeta)K_p(r,\theta',z-\zeta|\rho)\,d\zeta \qquad (1)$$

where

$$K_p(r,\theta',z-\zeta|\rho)=-\frac{N}{4\pi\beta_a^2}\sum_{\nu=-\infty}^{\infty}\sum_{l=0}^{\infty}R_l^{(n)}(r)R_l^{(n)}(\rho)$$
$$\times[i\{\rho\omega(n\omega+\lambda)M_a^2/\beta_a^2-n/\rho\}/\Omega_l^{(n)}-\rho\omega\,\mathrm{sgn}(z-\zeta)]$$
$$\times\exp(ig+in\phi+\Omega_l^{(n)}|z-\zeta|) \qquad (2)$$

$$\left.\begin{aligned}&\theta'=\theta-\omega z,\ g=(z-\zeta)\lambda M_a^2/\beta_a^2,\ \phi=\theta'+(z-\zeta)\omega/\beta_a^2,\\&\beta_a^2=1-M_a^2,\ n=\nu N+\sigma\end{aligned}\right\} \qquad (3)$$

and

$$\left.\begin{aligned}&\{\Omega_l^{(n)}\}^2=[\{k_l^{(n)}\}^2-(n\omega+\lambda)^2M_a^2/\beta_a^2]/\beta_a^2,\\&\Omega_l^{(n)}=|\Omega_l^{(n)}|\quad\text{for}\quad\{\Omega_l^{(n)}\}^2>0,\\&\Omega_l^{(n)}=i\,\mathrm{sgn}(n\omega+\lambda)\,|\Omega_l^{(n)}|\quad\text{for}\quad\{\Omega_l^{(n)}\}^2<0\end{aligned}\right\} \qquad (4)$$

Furthermore, M_a denotes the axial Mach number. $R_l^{(n)}(r)$ and $k_l^{(n)}$ are, respectively, the orthonormal radial eigenfunctions and corresponding eigenvalues as defined in [6], where $n\ (=\nu N+\sigma)$ and l denote, respectively, the circumferential wave number and the radial node number of an acoustic mode in the annular duct. One should note that in expressions corresponding to equation (1) in [3-5], $\Delta p_B(\rho,\zeta)$ is multiplied by a factor $1/\Lambda(\rho)$. As Lordi and Homicz [1] pointed out, $\Lambda(\rho)$ should be deleted. However, one should note also that the numerical results in references [4-6] are not affected by this mistake, since $\Delta p_B(\rho,\zeta)/\Lambda(\rho)$ is in fact treated as the lifting pressure.

Acoustic Field Expressed by Finite Radial Modes

As equation (2) shows, the disturbance pressure field is expressed as the sum of an infinite number of acoustic modes.

Nomenclature

A_l = defined by equation (27)
$a_j^{(b)}(r)$, $a_k^{(t)}(r)$ = spanwise mode shapes of the j-th order bending and k-th order torsional vibrations
$B_{lm}^{(n)}$ = coefficients of the finite series expansion of $R_l^{(n)}(r)$ in terms of $R_m^{(0)}(r)$, equation (5)
c_a = axial projection of the blade chord
$D_{lm}^{(n)}$ = defined by equation (16)
$G_m(\xi)$ = coefficients of expansion of $\Delta p_B(\rho,\zeta)$ in a series of functions $R_m^{(0)}(\rho)$, equation (39)
g = $(z-\zeta)\lambda M_a^2/\beta_a^2$
$H^{(N,\sigma)}(X)$ = special function defined by equation (29)
h = hub to tip ratio
i = $\sqrt{-1}$
K_p = pressure kernel function defined by equation (2)
K_τ = upwash kernel function defined by equation (21)
$K_\tau^{(SW)}$ = main vortical part of K_τ, defined by equation (23)
$K_{\tau b}^{(S)}$ = subsonic singular part of K_τ, defined by equation (24)
$K_{\tau p}^{(S)}$ = supersonic singular part of K_τ, defined by equation (25)
$K_\tau^{(R)}$ = regular part of K_τ, defined by equation (26)
$K_\tau^*, K_{\tau p}^{(S)*}$ = $K_\tau, K_{\tau p}^{(S)}$ substracted by the second term of the right hand-side of equation (25)
$K^{(N,\sigma)}(X)$ = special function defined by equation (30)
$k_l^{(n)}$ = radial eigenvalues
L = number of retained terms in the finite radial eigenfunction series
l = radial order of an acoustic mode
l_∞ = critical radial order defined by equation (14)
M_a = axial Mach number
N = number of blades
n = $\nu N+\sigma$ = circumferential wave number of an acoustic mode

[1] Lengths are scaled with respect to the radius of the blade tip r_T^*, and time with respect to r_T^* divided by the undisturbed axial velocity W_a.

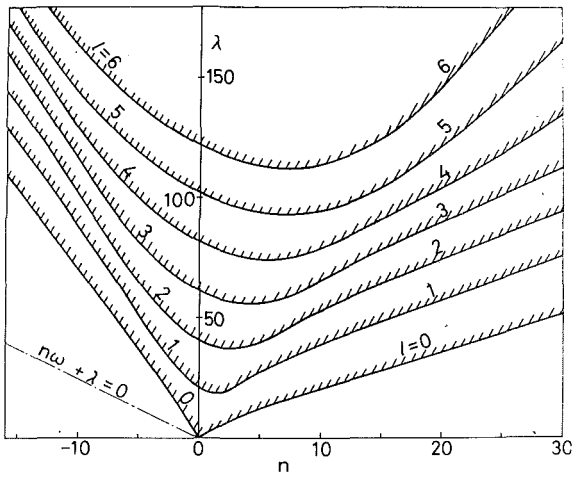

Fig. 3 Cutoff boundaries of acoustic modes in a subsonic flow: M_a = 0.25, h = 0.4, ω = 2.4744, L = 7. Hatched regions denote cut-on state.

Each acoustic mode will be referrred to by notation (n,l). One can easily see that acoustic modes for which the $\Omega_l^{(n)}$ defined by equation (4) are real are of cutoff state (i.e., decaying modes), while those with imaginary $\Omega_l^{(n)}$ are of cut-on state (i.e., propagating modes). One should note that the expression (2) is formally valid for all flow regimes i.e., subsonic, transonic, and supersonic flows. The factor $\Omega_l^{(n)}$, however, shows different behaviors for the three flow regimes as is clearly demonstrated by using the finite radial mode approximation.

The disturbance pressure field caused by rotor blades with no dihedral angle is expected to have a rather small radial variation. Therefore the contribution from acoustic modes of higher radial orders will be very small. Let the series expansion with respect to the radial order l in equation (2) be approximated by a finite series retained up to $l = L - 1$. Furthermore, let the radial eigenfuntion $R_l^{(n)}(r)$ of an aribitrary circumferential wave number n be expanded into a finite series in terms of $R_m^{(0)}(r)$ as follows

$$R_l^{(n)}(r) = \sum_{m=0}^{L-1} B_{lm}^{(n)} R_m^{(0)}(r), \tag{5}$$

Then, as shown in [5]

$$\sum_{m=0}^{L-1} B_{lm}^{(n)} [\{(\kappa_l^{(n)})^2 - (k_m^{(0)}/n)^2\}\delta_{jm} - R_{jm}] = 0; \tag{6}$$

$$[j = 0,1, \ldots, L-1],$$

where $\kappa_l^{(n)} = k_l^{(n)}/n$, and δ_{jm} is Kronecker delta, and

$$R_{jm} = \int_h^1 \frac{1}{r} R_j^{(0)}(r) R_m^{(0)}(r)\, dr \tag{7}$$

Equation (6) implies that $B_{lm}^{(n)}$ and $(\kappa_l^{(n)})^2$ can be determined as the eigenvectors and eigenvalues of a finite real symmetric matrix with elements $R_{jm} + \delta_{jm}(k_m^{(0)}/n)^2$. Owing to this finite series approximation, $B_{lm}^{(n)}$ and $\kappa_l^{(n)}$ possess definite limits as $n \to \pm\infty$, and one can write

$$B_{lm}^{(n)} = B_{lm}^{(\infty)} + 0(n^{-2}), \quad \kappa_l^{(n)} = \kappa_l^{(\infty)} + 0(n^{-2}) \tag{8}$$

for large $|n|$. It also holds that

$$1 < \kappa_0^{(\infty)} < \kappa_1^{(\infty)} < \ldots < \kappa_{L-1}^{(\infty)} < 1/h \tag{9}$$

Furthermore as $n \to \pm\infty$

$$\{\hat{\Omega}_l^{(n)}\}^2 \to \{\hat{\Omega}_l^{(\infty)}\}^2$$

$$= [1 - M_a^2\{1 + (\omega/\kappa_l^{(\infty)})^2\}](\kappa_l^{(\infty)}/\beta_a^2)^2 \tag{10}$$

where

$$\hat{\Omega}_l^{(n)} = \Omega_l^{(n)}/|n| \tag{11}$$

Taking into account these relations, let us see the structures of the acoustic fields for the three flow regimes:

(*i*) Entirely subsonic flow; $M_a^2(1+\omega^2) < 1$. It holds for all l $(= 0,1, \ldots, L-1)$ that

$$\{\hat{\Omega}_l^{(\infty)}\}^2 > \{1 - M_a^2(1+\omega^2)\}/\beta_a^4 > 0 \tag{12}$$

Acoustic modes of any radial order l become of cutoff state for large circumferential wave number, n, as shown in Fig. 3, where hatched regions denote cut-on state.

(*ii*) Entirely supersonic flow; $1 < M_a^2(1+\omega^2 h^2)$. For all l $(= 0,1, \ldots, L-1)$

$$\{\hat{\Omega}_l^{(\infty)}\}^2 < \{1 - M_a^2(1+\omega^2 h^2)\}/(h^2\beta_a^4) < 0 \tag{13}$$

Contrary to the case in subsonic flow, the circumferential

Nomenclature (cont.)

$p(r,\theta',z)e^{i\lambda t}$ = disturbance pressure
Q = $W_a\sqrt{1+\omega^2 r^2}$ = undisturbed fluid velocity relative to rotating blades
$q_\tau(r,\theta',z)e^{i\lambda t}$ = disturbance velocity component normal to blade surfaces
$R_l^{(n)}(r)$ = radial eigenfunctions
r_T^* = radius at the blade tip
(r,θ,z) = cylindrical coordinate system fixed to the rotor
$ST^{(N,\sigma)}(X)$ = special function defined by equation (31)
t = time
$\bar{W}_j^{(b)}$, $\bar{W}_k^{(t)}$ = dimensionless total aerodynamic work on a blade in the j-th order bending and k-th order torsional vibrations respectively
W_a = axial velocity of the undisturbed fluid
$Z_l^{(k)}(z,\theta')$ = defined by equation (36) and in Fig. 6
β_a^2 = $1 - M_a^2$
$\Delta p_B(r,z)e^{i\lambda t}$ = pressure difference across the reference blade
$\delta(X)$ = Dirac delta function
δ_{ij} = Kronecker delta
ζ = axial coordinate at a point on a blade surface
$\eta(r,z)e^{i\lambda t}$ = displacement of the reference blade normal to its surface
θ' = $\theta - \omega z$ = helical coordinate
$\kappa_l^{(n)}$ = $k_l^{(n)}/n$
λ = dimensionless angular frequency
ξ = Arccos $(-2\zeta/c_a)$
ρ = radial coordinate at a point on a blade surface
ρ_0 = undisturbed fluid density
$\hat{\sigma}$ = $2\pi\sigma/N$ = interblade phase angle
ϕ = $\theta' + (z-\zeta)\omega/\beta_a^2$
$\Omega_l^{(n)}$ = axial wave factor defined by equation (4)
$\hat{\Omega}_l^{(n)}$ = $\Omega_l^{(n)}/|n|$
ω = dimensionless angular velocity of the rotor

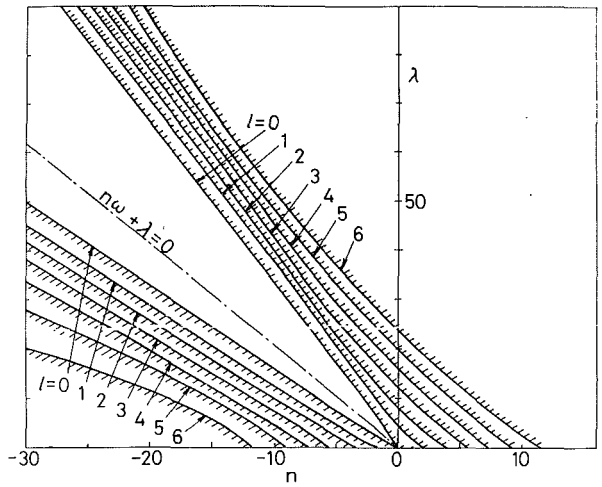

Fig. 4 Cutoff boundaries of acoustic modes in a supersonic flow: M_a = 0.8. Other conditions are same as in Fig. 3.

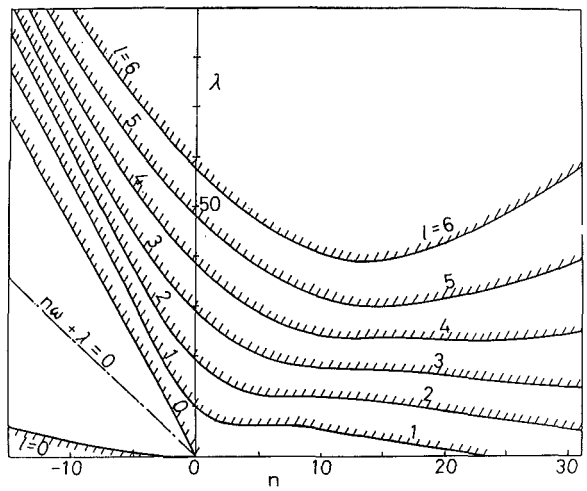

Fig. 5 Cutoff boundaries of acoustic modes in a transonic flow: M_a = 0.48. Other conditions are same as in Fig. 3.

wave number, n, of the cutoff modes are confined within a finite region for each radial order, l, as shown in Fig. 4.

(*iii*) Transonic flow; $M_a^2(1+\omega^2 h^2) < 1 < M_a^2(1+\omega^2)$. There is a critical radial order l_∞, such that

$$\left.\begin{aligned} \{\hat{\Omega}_l^{(\infty)}\}^2 &< 0 \quad \text{for} \quad 0 \le l \le l_\infty - 1 \\ \{\hat{\Omega}_l^{(\infty)}\}^2 &> 0 \quad \text{for} \quad l_\infty \le l \le L-1 \end{aligned}\right\} \tag{14}$$

One can see that the acoustic modes of lower radial order, l, in $0 \le l \le l_\infty - 1$ are of supersonic type, as shown in Fig. 5 for the case of $l_\infty = 3$.

Now one can rewrite equation (2) into a finite series form

$$K_p(r,\theta',z-\zeta|\rho) = -\frac{N}{4\pi\beta_a^2} e^{ig\rho} \sum_{m=0}^{L-1} R_m^{(0)}(\rho) \times \sum_{\nu=-\infty}^{\infty} e^{in\phi} \sum_{l=0}^{L-1} R_l^{(n)}(r) D_{lm}^{(n)} \exp[-\Omega_l^{(n)}|z-\zeta|] \tag{15}$$

where

$$D_{lm}^{(n)} = B_{lm}^{(n)} \left(i[(n\omega+\lambda)\omega M_a^2/\beta_a^2 - n\{(\kappa_l^{(n)})^2 - (k_m^{(0)}/n)^2\}] / \Omega_l^{(n)} - \omega \operatorname{sgn}(z-\zeta)\right) \tag{16}$$

and use is made of the relation

$$R_l^{(n)}(r)/r^2 = \sum_{m=0}^{L-1} B_{lm}^{(n)} \{(\kappa_l^{(n)})^2 - (k_m^{(0)}/n)^2\} R_m^{(0)}(r) \tag{17}$$

which can be derived from equations (5), (6), and (7). It is not difficult to show that K_p expressed by equation (15) has a singularity at each blade surface as follows

$$K_p \to \mp(1/2) e^{ik\hat{\sigma}} \delta(z-\zeta)\delta(r-\rho) + \text{finite value} \tag{18}$$

as $\theta' \to 2k\pi/N \pm 0$, where the formal relation

$$\delta(r-\rho) = \rho \sum_{l=0}^{L-1} R_l^{(n)}(r) R_l^{(n)}(\rho) \tag{19}$$

is used.

Upwash Velocity

As shown in reference [5], one can obtain the disturbance velocity by integrating the linearized equation of motion. Especially the upwash velocity $q_\tau(r,\theta',z)e^{i\lambda t}$, i.e., the velocity component normal to the blade surfaces, can be expressed in the form,

$$q_\tau(r,\theta',z) = \frac{1}{\rho_0 Q} \int_h^1 d\rho \int_{-c_a/2}^{c_a/2} \Delta p_B(\rho,\zeta) K_\tau(r,\theta',z-\zeta|\rho)\, d\zeta \tag{20}$$

where ρ_0 denotes the undisturbed fluid density, $Q = W_a(1+\omega^2 r^2)^{1/2}$ is the undisturbed local relative velocity and $K_\tau(r,\theta',z-\zeta|\rho)$ is the upwash kernel function given by

$$K_\tau(r,\theta',z-\zeta|\rho) = -e^{-i\lambda z} \int_{-\infty}^{z} e^{i\lambda z} \left[\left(\frac{1}{r}\frac{\partial}{\partial\theta} - \omega r \frac{\partial}{\partial z}\right) K_p\right]_{\theta=\theta'+\omega z} dz \tag{21}$$

Substituting equation (15) into (21) and performing the integration with respect to z, one obtains an expression for K_τ, which can be, for convenience, separated into four components as follows

$$K_\tau = K_\tau^{(SW)} + K_{\tau b}^{(S)} + K_{\tau p}^{(S)} + K_\tau^{(R)} \tag{22}$$

Here

$$K_\tau^{(SW)}(r,\theta',z-\zeta|\rho) = -\frac{N}{8\pi}\beta_a^2 \{1+\operatorname{sgn}(z-\zeta)\} e^{-i\lambda(z-\zeta)+i\sigma\theta'} \times \sum_{l=0}^{L-1} r\rho R_l^{(\infty)}(r) R_l^{(\infty)}(\rho) \{\hat{\Omega}_l^{(\infty)}\}^2 \tag{23}$$

$$\begin{aligned} K_{\tau b}^{(S)}(r,\theta',z-\zeta|\rho) = \frac{N}{4\pi\beta_a^2} e^{ig} \sum_{l=l_\infty}^{L-1} r\rho R_l^{(\infty)}(r) R_l^{(\infty)}(\rho) \\ \times [F_{l+} e^{V_l\lambda|z-\zeta|} H^{(N,\sigma)}(\hat{\Omega}_l^{(\infty)}|z-\zeta|-i\phi) \\ + F_{l-} e^{-V_l\lambda|z-\zeta|} H^{(N,-\sigma)}(\hat{\Omega}_l^{(\infty)}|z-\zeta|+i\phi) \\ - i\lambda\{(\kappa_l^{(\infty)})^2/\hat{\Omega}_l^{(\infty)}\}\{e^{V_l\lambda|z-\zeta|} K^{(N,\sigma)}(\hat{\Omega}_l^{(\infty)}|z-\zeta|-i\phi) \\ + e^{-V_l\lambda|z-\zeta|} K^{(N,-\sigma)}(\hat{\Omega}_l^{(\infty)}|z-\zeta|+i\phi)\}] \end{aligned} \tag{24}$$

$$\begin{aligned} K_{\tau p}^{(S)}(r,\theta',z-\zeta|\rho) = \frac{N}{4\pi\beta_a^2} e^{ig} \sum_{l=0}^{l_\infty-1} r\rho R_l^{(\infty)}(r) R_l^{(\infty)}(\rho) \\ \times \exp[-i\lambda|V_l(z-\zeta)| + i\sigma\{\theta' + (z-\zeta)A_l\}] \\ \times [\beta_a^2 |\hat{\Omega}_l^{(\infty)}| \{|\omega| - \operatorname{sgn}(z-\zeta)\beta_a^2 |\hat{\Omega}_l^{(\infty)}|\} \\ - \lambda(\kappa_l^{(\infty)})^2 \{\operatorname{sgn}(\omega)/|\hat{\Omega}_l^{(\infty)}|\}(i\pi/N) ST^{(N,\sigma)}(\theta' + (z-\zeta)A_l)] \\ - \frac{\beta_a^2}{2} \sum_{l=0}^{l_\infty-1} r\rho R_l^{(\infty)}(r) R_l^{(\infty)}(\rho) |\hat{\Omega}_l^{(\infty)}| \\ \times \sum_{k=-\infty}^{\infty} \delta(z-\zeta+(\theta'-2k\pi/N)/A_l) \end{aligned}$$

$$\times \exp(ik\hat{\sigma} - i\lambda S_l |\theta' - 2k\pi/N|) \tag{25}$$

$$K_\tau^{(R)}(r,\theta',z-\zeta|\rho) = \frac{N}{4\pi\beta_a^2} r\rho \sum_{m=0}^{L-1} R_m^{(0)}(\rho) \sum_{j=0}^{L-1} R_j^{(0)}(r)$$

$$\times (1/2)\{1+\mathrm{sgn}(z-\zeta)\} e^{-i\lambda(z-\zeta)} \sum_{\nu=-\infty}^{\infty} e^{in\theta'}$$

$$\times \sum_{l=0}^{L-1} \{M_{lmj}^{\{n\}-} - M_{lmj}^{\{n\}+} - 2(1-\delta_{\nu 0}) B_{lm}^{\{\infty\}} B_{lj}^{\{\infty\}} \beta_a^4 (\hat{\Omega}_l^{\{\infty\}})^2\}$$

$$+ \frac{N}{4\pi\beta_a^2} e^{ig} r\rho \sum_{m=0}^{L-1} R_m^{(0)}(\rho) \sum_{j=0}^{L-1} R_j^{(0)}(r) \sum_{\nu=-\infty}^{\infty} e^{in\phi}$$

$$\times \sum_{l=0}^{L-1} [M_{lmj}^{\{n\}} \exp(-\Omega_l^{\{n\}} |z-\zeta|)$$

$$- (1-\delta_{\nu 0}) B_{lm}^{\{\infty\}} B_{lj}^{\{\infty\}} \beta_a^2 \exp(-\psi_l^{\{n\}} |z-\zeta|)$$

$$\times \{\hat{\Omega}_l^{\{\infty\}} (i\omega\,\mathrm{sgn}(n) - \mathrm{sgn}(z-\zeta)\beta_a^2 \hat{\Omega}_l^{\{\infty\}})$$

$$- (i\lambda/|n|)(\kappa_l^{\{\infty\}}/\beta_a)^2/\hat{\Omega}_l^{\{\infty\}}\}] \tag{26}$$

$$\left.\begin{aligned}
F_{l\pm} &= \beta_a^2 \hat{\Omega}_l^{\{\infty\}} \{\pm i\omega - \mathrm{sgn}(z-\zeta)\beta_a^2 \hat{\Omega}_l^{\{\infty\}}\},\\
A_l &= \omega/\beta_a^2 - \mathrm{sgn}\{\omega(z-\zeta)\}|\hat{\Omega}_l^{\{\infty\}}|,\ S_l = M_a^2/(\beta_a^2|\hat{\Omega}_l^{\{\infty\}}|),\\
V_l &= \omega M_a^2/(\beta_a^4 \hat{\Omega}_l^{\{\infty\}}),\ \psi_l^{\{n\}} = \mathrm{sgn}(n)(n\hat{\Omega}_l^{\{\infty\}} - V_l\lambda),\\
M_{lmj}^{\{n\}} &= D_{lm}^{\{n\}} D_{lj}^{\{n\}} \Omega_l^{\{n\}} / \{\Omega_l^{\{n\}}\,\mathrm{sgn}(z-\zeta) - i(n\omega+\lambda)/\beta_a^2\},\\
M_{lmj}^{\{n\}\pm} &= D_{lm}^{\{n\}} D_{lj}^{\{n\}} \Omega_l^{\{n\}} / \{\pm\Omega_l^{\{n\}} - i(n\omega+\lambda)/\beta_a^2\}
\end{aligned}\right\} \tag{27}$$

$$\hat{\Omega}_l^{\{\infty\}} = \left\{\begin{aligned} &|\hat{\Omega}_l^{\{\infty\}}| : l_\infty \le l \le L-1,\\ &i\,\mathrm{sgn}(n\omega)|\hat{\Omega}_l^{\{\infty\}}| : 0 \le l \le l_\infty - 1 \end{aligned}\right\} \tag{28}$$

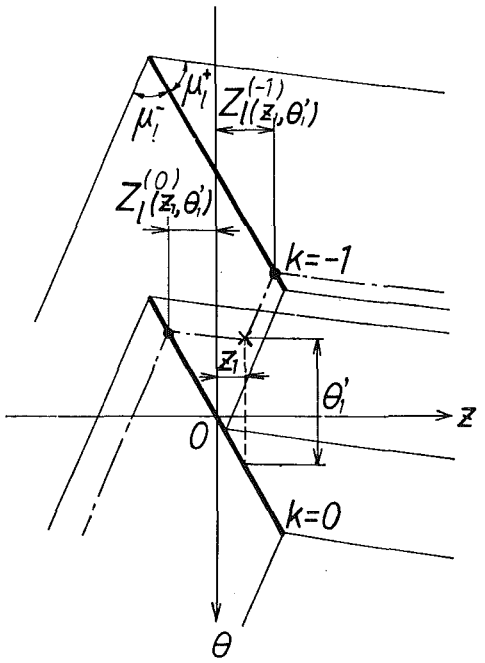

Fig. 6 Mach lines and definition of $Z_l^{(k)}(z,\theta')$

$$H^{(N,\sigma)}(X) = e^{-\sigma X}/(e^{NX}-1) \tag{29}$$

$$K^{(N,\sigma)}(X) = e^{-\sigma X}\{X - (1/N)\log_e(e^{NX}-1)\}$$

$$- \frac{\sigma}{N^2} e^{-\sigma X} \sum_{n=1}^{\infty} e^{-nNX}/\{n(n+\sigma/N)\} \tag{30}$$

$$ST^{(N,\sigma)}(X) = (2/\pi)\mathrm{Arctan}\{\cot(NX/2)\}$$

$$+ i\sigma/(\pi N) \sum_{\substack{n=-\infty \\ \neq 0}}^{\infty} e^{inNX}/\{n(n+\sigma/N)\} \tag{31}$$

The first component $K_\tau^{(SW)}$ given by equation (23) denotes the main part of the vortical disturbance contributed by trailing vorticities.

The second component $K_{\tau b}^{(S)}$ given by equation (24) denotes the subsonic singular part contributed by acoustic modes of subsonic type of radial order, l, from l_∞ to $L-1$. In fact, taking into account the behaviors of special functions $H^{(N,\sigma)}(X)$ and $K^{(N,\sigma)}(X)$ defined by equations (29) and (30), respectively, one can easily see that $K_{\tau b}^{(S)}$ possesses singularities of subsonic type at blade surfaces as follows

$$K_{\tau b}^{(S)} \to -\frac{1}{2\pi} r\rho \sum_{l=l_\infty}^{L-1} R_l^{\{\infty\}}(r) R_l^{\{\infty\}}(\rho)[\beta_a^2 \hat{\Omega}_l^{\{\infty\}}/(z-\zeta)$$

$$- i\lambda\{(\kappa_l^{\{\infty\}})^2/\hat{\Omega}_l^{\{\infty\}}\}\log_e|z-\zeta|] + \text{finite value} \tag{32}$$

as $\theta' \to 2k\pi/N \pm 0$.

On the other hand $K_{\tau p}^{(S)}$ given by equation (25) denotes the supersonic singular part contributed by acoustic modes of supersonic type of radial order, l, from 0 to $l_\infty - 1$. As the second term on the right-hand side of equation (25) shows, it possesses a singularity of delta function type along characteristic lines

$$z - \zeta + (\theta' - 2k\pi/N)/A_l = 0 : [l = 0,1,\ldots,l_\infty - 1] \tag{33}$$

in the (z,θ)-plane, which emanate from points denoted by $z = \zeta$, $\theta'(=\theta - \omega z) = 2k\pi/N$, $[k = 0,1,\ldots,N-1]$. One should note that there are as many characteristic lines as the number of supersonic orders l_∞. The characteristic line expressed by equation (33) will be referred to as the Mach line of the l-th radial order. One should note also that the first term on the right-hand side of equation (25) contains a singularity of finite discontinuity along the Mach lines due to the sawtooth function involved in the special function $ST^{(N,\sigma)}(X)$, which is defined by equation (31).

The last component $K_\tau^{(R)}$ given by equation (26) denotes the regular part bounded everywhere in the field.

Performing the integration with respect to ζ in equation (20) for delta function terms involved in $K_{\tau p}^{(S)}$, one obtains

$$q_\tau(r,\theta',z) = \frac{1}{\rho_0 Q} \int_h^1 d\rho \int_{-c_a/2}^{c_a/2} \Delta p_B(\rho,\zeta) K_\tau^*(r,\theta',z-\zeta|\rho)\, d\zeta$$

$$- \frac{1}{\rho_0 Q} \frac{1}{2} \beta_a^2 \int_h^1 \rho r \sum_{l=0}^{l_\infty - 1} R_l^{\{\infty\}}(\rho) R_l^{\{\infty\}}(r) |\hat{\Omega}_l^{\{\infty\}}|$$

$$\times \sum_{k=k^-}^{k} \exp(ik\hat{\sigma} - i2\pi|k|\lambda S_l/N)\, \Delta p_B(\rho, Z_l^{\{k\}}(z,\theta'))\, d\rho \tag{34}$$

where

$$K_\tau^* = K_\tau^{(SW)} + K_{\tau b}^{(S)} + K_{\tau p}^{(S)*} + K_\tau^{(R)} \tag{35}$$

and $K_{\tau b}^{(S)*}$ implies $K_{\tau p}^{(S)}$ without the second term on the right-hand side of equation (25). Furthermore

$$Z_l^{(k)}(z,\theta') = z + (\theta' - 2k\pi/N)/\{\omega/\beta_a^2 + \mathrm{sgn}(\theta' - 2k\pi/N)\,|\hat{\Omega}_l^{(\infty)}|\} \tag{36}$$

As shown in Fig. 6, it implies that the Mach line of the l-th radial order passing through a field point $z = z$, $\theta = \theta' + \omega z$ in (z, θ) plane starts from a point of z-wise coordinate equal to $Z_l^{(k)}(z,\theta')$ on the k-th blade surface. Moreover k^+ and k^- denote, respectively, the upper and lower limits of the integer k that satisfies

$$-c_a/2 \le Z_l^{(k)}(z,\theta') \le c_a/2 \tag{37}$$

Integral Equation for Oscillating Blades

Let the displacement of the k-th blade normal to its surface be denoted by $\eta(r,z)e^{i\lambda t + ik\hat{\sigma}}$. Then the flow tangency condition on the reference blade surface is represented by

$$q_\tau(r,0,z) = W_a(i\lambda + \partial/\partial z)\,\eta(r,z) \tag{38}$$

Combining equations (34) and (38), one obtains an integral equation for the lifting pressure $\Delta p_B(\rho,\zeta)$. In the present paper $\Delta p_B(\rho,\zeta)$ is expanded into a radial eigenfunction series of the form

$$\Delta p_B(\rho,\zeta) = \frac{2}{c_a \sin\xi} \sum_{m=0}^{L-1} G_m(\xi) R_m^{(0)}(\rho) \tag{39}$$

where

$$\xi = \mathrm{Arccos}(-2\zeta/c_a) \tag{40}$$

Then an integral equation for $G_m(\xi)$ is obtained as follows

$$\frac{1}{\rho_0 Q} \sum_{m=0}^{L-1} \int_0^\pi G_m(\xi) KT_m^*(r,0,z-\zeta)\,d\xi - \frac{1}{\rho_0 Q} \beta_a^2 r \sum_{m=0}^{L-1} \sum_{l=0}^{l_\infty - 1} R_l^{(\infty)}(r) B_{lm}^{(\infty)} |\hat{\Omega}_l^{(\infty)}| \times \sum_{k=k^-}^{k^+} G_m(X^{(k)}(z)) \exp(ik\hat{\sigma} - i\lambda S_l 2\pi |k|/N) / \{c_a \sin(X_l^{(k)}(z))\} = W_a(i\lambda + \partial/\partial z)\,\eta(r,z) \tag{41}$$

where

$$X_l^{(k)}(z) = \mathrm{Arccos}\{-2Z_l^{(k)}(z,0)/c_a\} \tag{42}$$

and

$$KT_m^*(r,\theta',z-\zeta) = \int_h^1 R_m^{(0)}(\rho) K_\tau^*(r,\theta',z-\zeta|\rho)\,d\rho \tag{43}$$

Integration with respect to ρ in equation (43) can be analytically performed, and the resulting expression, which is just a minor modification of the expression for K_τ^*, is given in Appendix.

Equation (41) can only be solved numerically. The method used in this paper is principally the same as that used in reference [6]. Namely $G_m(\xi_j)$ for $m = 0, 1, \ldots, L-1$; $j = 0,1, \ldots, I-1$ are determined so that equation (41) is satisfied at control points $r = r_\alpha$ $[\alpha = 0,1, \ldots, L-1]$, $z = z_i$ $(i = 0,1, \ldots, I-1]$. Special considerations are necessary in the treatment of the numerical integration with respect to ξ and the evaluation of $G_m(X_l^{(k)}(z_i))$ in equation (41).

The numerical integration formula applied to the first term of equation (41) should take into account the condition $G_m(\pi) = 0$, which is equivalent to the Kutta condition. One should note that this condition is not inconsistent with the possibility of finite pressure jump across the blade surface at the trailing edge in supersonic flow, since $\sin\xi$ in the denominator of equation (39) is zero at $\xi = \pi$.

The coordinate $X_l^{(k)}(z_i)$ is in general not equal to any of the ξ_j and hence $G_m(X_l^{(k)}(z_i))$ in the second term of equation (41) should be expressed in terms of $G_m(\xi_j)$ by using an interpolation method. In order to minimize the numerical error, however, interpolation across those points where $G_m(\xi)$ shows a very steep variation should be avoided, and, instead, extrapolation should be applied. In fact, $G_m(\xi)$ is expected to show a steep variation at those points where the Mach lines emanating from the leading and trailing edges of the adjacent blades reflect. The z-coordinates of the reflection points are given by

$$z_T^{(l)} = c_a/2 - s_z^{(l)-} \tag{44a}$$

$$z_{LDm}^{(l)} = -c_a/2 + m s_z^{(l)+} - (m-1) s_z^{(l)-} \tag{44b}$$

$$z_{LUm}^{(l)} = -c_a/2 + m(s_z^{(l)+} - s_z^{(l)-}) \tag{44c}$$

where

$$s_z^{(l)\pm} = (2\pi/N)(\omega/\beta_a^2 \mp |\hat{\Omega}_l^{(\infty)}|) \tag{45}$$

Here $z_T^{(l)}$ is the reflection point of the trailing edge Mach line of the l-th radial order, while $z_{LDm}^{(l)}$ and $z_{LUm}^{(l)}$ denote the m-th reflection points of the leading edge Mach line of the l-th radial order on the suction and pressure surfaces, respectively. One should note that Mach lines of different radial orders reflect at different points. This implies that the pressure variation across a Mach wave reflection in three-dimensional flow is less steep than that in two-dimensional flow.

In the present paper the chordwise control points z_j are taken so that they coincide with the coordinates corresponding to ξ_j, and further the ξ_j are selected as follows:

(*i*) The case of no trailing edge Mach line reflection.

$$\xi_j = (\pi/I)(j+1/2)\text{: } [j = 0,1, \ldots, I-1] \tag{46}$$

(*ii*) The case where only trailing edge Mach wave reflection occurs (as shown in Fig. 6).

$$\xi_j = \begin{cases} (2\xi^*/I)(j+1/2)\text{: } [j = 0,1, \ldots, (I/2)-1], \\ \xi^* + \{2(\pi - \xi^*)/I\}(j - I/2 + 1/2)\text{:} \\ \quad [j = (I/2), (I/2)+1, \ldots, I-1], \end{cases} \tag{47}$$

where $\xi^* = \mathrm{Arccos}(-2z_T^{(0)}/c_a)$.

The case where leading edge Mach wave reflection occurs is not treated in this paper. In order to deal with this case with satisfactory accuracy an improved computational scheme (which will be presented in future) should be employed.

Numerical Examples and Discussions

In this paper two types of vibrations are considered: the case of pure bending where the circumferential displacement of a reference blade is given by $Hc_a a_j^{(b)}(r)e^{i\lambda t}$, and hence

$$\eta(r,z) = Hc_a a_j^{(b)}(r)/(1+\omega^2 r^2)^{1/2} \tag{48}$$

and the case of pure torsion about the mid-chord axis where the twist angle of a reference blade is given by $\Theta a_k^{(t)}(r)e^{i\lambda t}$, and hence

$$\eta(r,z) = \Theta a_k^{(t)}(r)(1+\omega^2 r^2)^{1/2} z \tag{49}$$

Here H and Θ denote amplitude at the blade tip, and $a_j^{(b)}(r)$ and $a_k^{(t)}(r)$ denote the spanwise mode shapes of the j-th order bending and k-th order torsional vibrations. The natural mode shapes of a uniform cantilever beam are assumed.

In this paper an extensive parametric study is not attempted, but only a few numerical examples to demonstrate

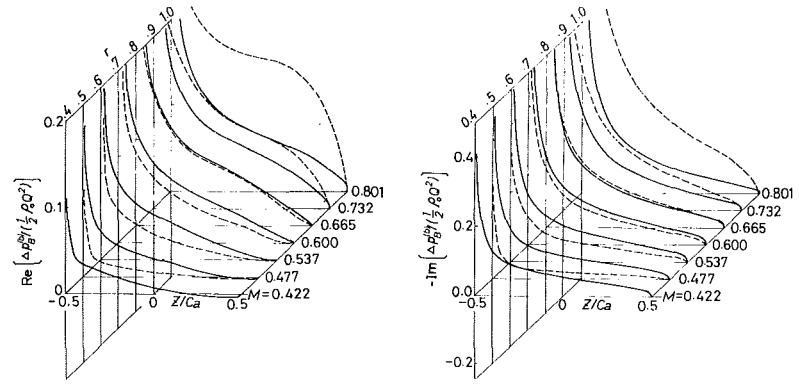

Fig. 7 Lifting pressure distributions due to the first-mode bending vibration in a subsonic flow: $h = 0.4$, $\omega = 2.4744$, $\lambda c_a = 0.2$, $\sigma/N = 0.2$, $N = 30$, $Nc_a = 2.0$, $M_a = 0.3$. M denotes the local relative Mach number; —— lifting surface theory, · · · · strip theory.

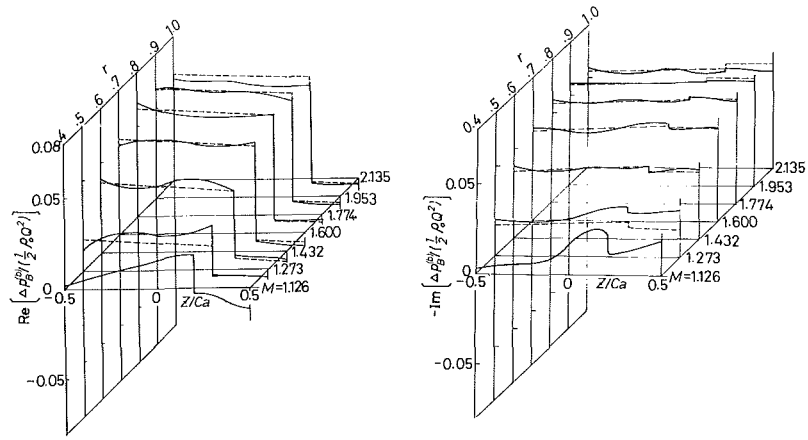

Fig. 8 Lifting pressure distributions due to the first-mode bending vibration in a supersonic flow: $M_a = 0.8$. Other conditions are same as in Fig. 7.

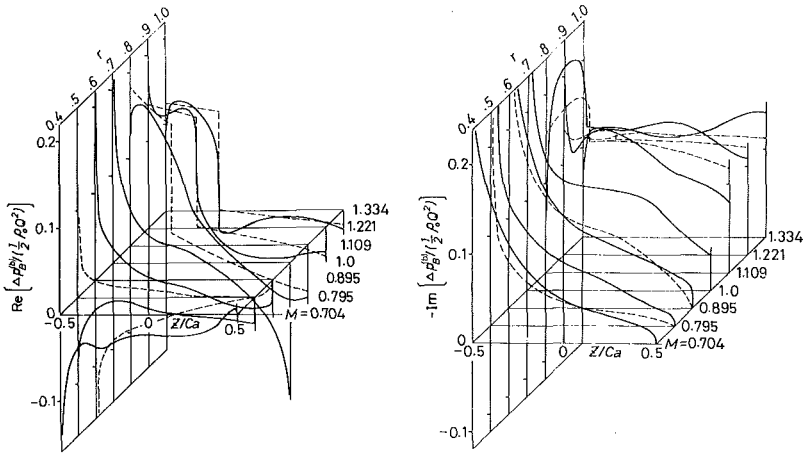

Fig. 9 Lifting pressure distributions due to the first-mode bending vibration in a transonic flow: $M_a = 0.5$. Other conditions are same as in Fig. 7.

the features of three-dimensional effects are presented. In all cases radial collocation stations, $L = 7$, and chordwise collocation stations, $I = 8$, are used. Computations were conducted on an electronic computer FACOM 230 M200 at the Computer Center of Kyushu University. In order to illustrate the three-dimensional effects results of the present lifting surface theory are compared with those of strip theory obtained by applying the two-dimensional linearized unsteady subsonic or supersonic cascade theory at each radial station.

Lifting Pressure Distributions. Figures 7, 8, 9 show the lifting pressure distributions for a first mode bending vibration of unit amplitude $H = 1$ in subsonic, supersonic, and transonic flows, respectively. Here Re[ ] and Im[ ] denote real and imaginary parts, respectively.

In subsonic flow the feature of the three-dimensional effect which makes the spanwise variation of aerodynamic forces less steep is clearly shown in Fig. 7. As was already pointed out by Namba [3], this effect is large since the predominant

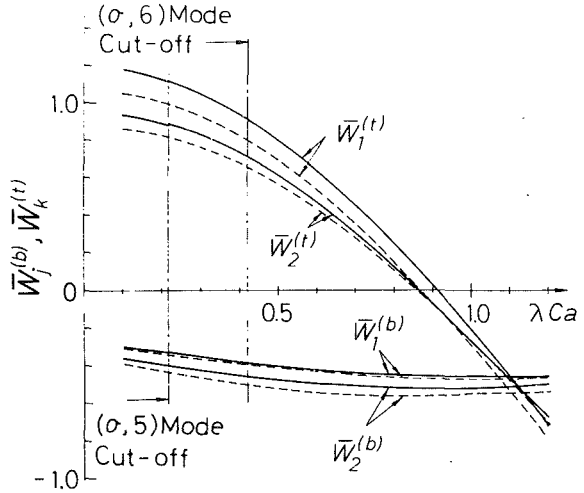

Fig. 10 Variation of the total aerodynamic works with the reduced frequency in a supersonic flow: $h = 0.4$, $\omega = 2.4744$, $N = 35$, $\sigma/N = 0.2$, $Nc_a = 1.8$, $M_a = 0.8$; —— lifting surface theory, · · · · strip theory

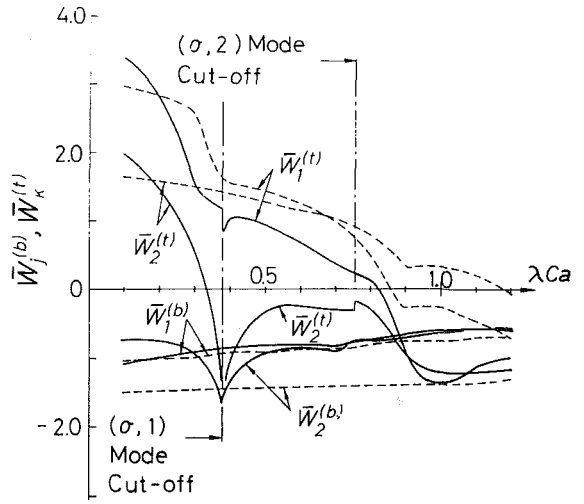

Fig. 11 Variation of the total aerodynamic works with the reduced frequency in a transonic flow: $Nc_a = 2.2$, $M_a = 0.48$. Other conditions are same as in Fig. 10.

acoustic modes are of cutoff state. The predominant acoustic modes are those in which the minimum circumferential wave number is equal to σ and radial mode shapes are close to the spanwise mode shape of the blade vibration. The acoustic field generated by the first- or second-mode blade vibration is in general dominated by acoustic modes of $(\sigma,0)$ and $(\sigma,1)$. Figure 7 illustrates the case where both modes are of cutoff state.

As shown in Fig. 8, three-dimensional effects are, in general, remarkably small in supersonic flow, where strip theory predicts lifting pressure distributions with excellent accuracy except near the hub. It should also be pointed out that in supersonic flow under conditions of interest for the flutter problem, the predominant acoustic modes are of cut-on state.

In the case of transonic flow, as shown in Fig. 9, the chordwise pressure profile at a subsonic or supersonic span station retains the features known from two-dimensional subsonic or supersonic flow theory respectively. However, the deviation of the lifting surface theory prediction from that of strip theory is substantial. The magnitude and chordwise profile of the blade surface pressure predicted by the lifting surface theory shows a continuous change with no singular behavior across the sonic span. On the other hand the lifting pressure predicted by strip theory shows divergent behavior across the sonic span.

Aerodynamic Work. The local aerodynamic work done on a blade surface per cycle, $W^*(r)$, is given by

$$W^*(r) = \frac{\pi}{2\lambda} r_T^{*2}(1+\omega^2 r^2)^{1/2} \int_{-c_a/2}^{c_a/2} [-i\lambda \bar{\eta}(r,z)\,\Delta p_B(r,z) + i\lambda \eta(r,z)\,\Delta \bar{p}_B(r,z)]\,dz \tag{50}$$

where $\bar{\eta}(r,z)$ and $\Delta\bar{p}_B(r,z)$ denote complex conjugates of $\eta(r,z)$ and $\Delta p_B(r,z)$, respectively. Let $W_j^{(b)}(r)$ and $W_k^{(t)}(r)$ denote the local aerodynamic works per unit span per cycle for the j-th mode bending and k-th mode torsional vibrations normalized by $\pi\rho_0 W_a^2 r_T^{*2} H^2$ and $\pi\rho_0 W_a^2 r_T^{*2}\Theta^2$, respectively. Furthermore total work coefficients, $\bar{W}_j^{(b)}$ and $\bar{W}_k^{(t)}$, are defined by

$$(\bar{W}_j^{(b)}, \bar{W}_k^{(t)}) = \int_h^1 (W_j^{(b)}(r), W_k^{(t)}(r))\,dr \tag{51}$$

In order to see how three-dimensional effects will affect flutter boundaries, variations of total unsteady aerodynamic works with the reduced frequency are demonstrated in Figs. 10 and 11.

For supersonic flow, as shown in Fig. 10, where the predominant acoustic modes $(\sigma,0)$ and $(\sigma,1)$ are of cut-on state for all frequencies, the blade vibrations are slightly destabilized by the three-dimensional effect. The effect is, however, generally small, and strip theory will give no substantial error in the prediction of flutter boundaries.

On the other hand, for transonic flow, as shown in Fig. 11, the total aerodynamic work predicted by the lifting surface theory shows a sharp decrease near the resonance states of the predominant acoustic modes. For the example in Fig. 11, this effect results in decreasing the critical reduced frequency of the second mode torsional vibration to $\lambda c_a \simeq 0.35$, which is much lower than the $\lambda c_a \simeq 1.2$ predicted by strip theory.

Conclusions

To predict unsteady loadings on a rotating annular cascade, a lifting surface theory applicable to all flow regimes, i.e., subsonic, supersonic and transonic, is developed. The method of finite radial acoustic order approximation is employed, and it has turned out not only to give a clear insight into the different features of the acoustic fields for the three flow regimes, but also to provide mathematical expressions advantageous to computational work. From some numerical examples the following conclusions are deduced.

For supersonic flow, three-dimensional effects on unsteady loadings are generally small, and strip theory predicts with good accuracy local loading distributions as well as total aerodynamic works.

In the case of transonic flow, three-dimensional effects are of substantial importance. The blade surface pressure predicted by lifting surface theory shows continuous transition across the sonic span, while the strip theory approximation breaks down near the sonic span. The aerodynamic work on vibrating blades shows sharp decrease near the resonance states of the predominant acoustic modes.

References

1 Lordi, J. A., and Homicz, G. F., "Linearized Analysis of the Three-Dimensional Compressible Flow Through a Rotating Annular Blade Row," *Journal of Fluid Mechanics*, Vol. 103, 1981, pp. 413–442.

2 Salaün, P., "Flutter Instabilities in an Annular Cascade with Supersonic Relative Flow," *ONERA. Publication* No. 1979-3.

3 Salaün, P., "Flutter Instabilities in an Annular Cascade," *Proceedings of IUTAM Symposium on Aeroelasticity in Turbomachines*, Paris, Oct. 1976, *Revenue Française de Mécanique*, Special issue, pp. 35–38.

4 Namba, M., "Lifting Surface Theory for Unsteady Flows in a Rotating

Annular Cascade," *Proceedings of IUTAM Symposium on Aeroelasticity in Turbomachines*, Paris, Oct. 1976, *Revue Française de Mécanique*, Special issue, pp. 39–46.

5 Namba, M., "Three-Dimensional Analysis of Blade Force and Sound Generation for an Annular Cascade in Distorted Flows," *Journal of Sound and Vibration*, Vol. 50, No. 4, 1977, pp. 479–508.

6 Namba, M., "Lifting Surface Theory for a Rotating Subsonic or Transonic Blade Row," *Aeronautical Research Council*, Great Britain, R & M 3740, Nov. 1972.

APPENDIX

The 'modal kernel function' $KT_m^*(r,\theta',z-\zeta)$ can be separated, in the same way as equation (35), into four parts as follows

$$KT_m = KT_m^{(SW)} + KTB_m^{(S)} + KTP_m^{(S)*} + KT_m^{R)} \tag{A1}$$

Each part is expressed as follows

$$KT_m^{(SW)}(r,\theta',z-\zeta) = -\frac{N}{8\pi}\beta_a^2\{1+\mathrm{sgn}(z-\zeta)\}e^{-i\lambda(z-\zeta)+i\sigma\theta'} \times \sum_{l=0}^{L-1} rR_l^{\{\infty\}}(r)B_{lm}^{\{\infty\}}\{\hat{\Omega}_l^{\{\infty\}}\}^2 \tag{A2}$$

$$KTB_m^{(S)}(r,\theta',z-\zeta) = \frac{N}{4\pi\beta_a^2}e^{ig}\sum_{l=l_\infty}^{L-1} rR_l^{\{\infty\}}(r)B_{lm}^{\{\infty\}} \times [F_{l+}e^{V_l\lambda|z-\zeta|}H^{(N,\sigma)}(\hat{\Omega}_l^{\{\infty\}}|z-\zeta|-i\phi) + F_{l-}e^{-V_l\lambda|z-\zeta|}H^{(N,-\sigma)}(\hat{\Omega}_l^{\{\infty\}}|z-\zeta|+i\phi) - i\lambda\{(\kappa_l^{\{\infty\}})^2/\hat{\Omega}_l^{\{\infty\}}\}\{e^{V_l\lambda|z-\zeta|}K^{(N,\sigma)}(\hat{\Omega}_l^{\{\infty\}}|z-\zeta|-i\phi) + e^{-V_l\lambda|z-\zeta|}K^{(N,-\sigma)}(\hat{\Omega}_l^{\{\infty\}}|z-\zeta|+i\phi)\}] \tag{A3}$$

$$KTP_m^{(S)*}(r,\theta',z-\zeta) = \frac{N}{4\pi\beta_a^2}e^{ig}\sum_{l=0}^{l_\infty-1} rR_l^{\{\infty\}}(r)B_{lm}^{\{\infty\}} \times \exp[-i\lambda|V_l(z-\zeta)|+i\sigma\{\theta'+(z-\zeta)A_l\}] \times [\beta_a^2|\hat{\Omega}_l^{\{\infty\}}|\{|\omega|-\mathrm{sgn}(z-\zeta)\beta_a^2|\hat{\Omega}_l^{\{\infty\}}|\} - \lambda(\kappa_l^{\{\infty\}})^2\{\mathrm{sgn}(\omega)/|\hat{\Omega}_l^{\{\infty\}}|\} \times (i\pi/N)ST^{(N,\sigma)}(\theta'+(z-\zeta)A_l)] \tag{A4}$$

$$KT_m^{(R)}(r,\theta',z-\zeta) = \frac{N}{4\pi\beta_a^2}r\sum_{j=0}^{L-1} R_j^{(0)}(r) \times (1/2)\{1+\mathrm{sgn}(z-\zeta)\}e^{-i\lambda(z-\zeta)}\sum_{\nu=-\infty}^{\infty} e^{in\theta'} \times \sum_{l=0}^{L-1}\{M_{lmj}^{(n)} - M_{lmj}^{(n)+} - 2(1-\delta_{\nu 0})B_{lm}^{\{\infty\}}B_{lj}^{\{\infty\}}\beta_a^4(\hat{\Omega}_l^{\{\infty\}})^2\} + \frac{N}{4\pi\beta_a^2}e^{ig}r\sum_{j=0}^{L-1} R_j^{(0)}(r)\sum_{\nu=-\infty}^{\infty} e^{in\Phi} \times \sum_{l=0}^{L-1}[M_{lmj}^{\{n\}}\exp(-\Omega_l^{\{n\}}|z-\zeta|) - (1-\delta_{\nu 0})B_{lm}^{\{\infty\}}B_{lj}^{\{\infty\}}\beta_a^2\exp(-\psi_l^{\{n\}}|z-\zeta|) \times \{\hat{\Omega}_l^{\{\infty\}}(i\omega\,\mathrm{sgn}(n)-\mathrm{sgn}(z-\zeta)\beta_a^2\hat{\Omega}_l^{\{\infty\}}) - (i\lambda/|n|)(\kappa_l^{\{\infty\}}/\beta_a)^2/\hat{\Omega}_l^{\{\infty\}}\}] \tag{A5}$$

Influence of Endwall Flow on Airfoil Suction Surface Midheight Boundary Layer Development in a Turbine Cascade

O. P. Sharma
Project Engineer.

R. A. Graziani
Project Engineer.

Pratt & Whitney Aircraft,
Commercial Products Division,
East Hartford, Conn. 06108

This paper presents the results of an analysis to assess the influence of cascade passage endwall flow on the airfoil suction surface midheight boundary layer development in a turbine cascade. The effect of the endwall flow is interpreted as the generation of a crossflow and a crossflow velocity gradient in the airfoil boundary layer which results in an extra term in the mass conservation equation. This extra term is shown to infuence the boundary layer development along the midheight of the airfoil suction surface through an increase in the boundary layer thickness and consequently an increase in the midheight losses, and a decrease in the Reynolds shear stress, mixing length, skin friction, and Stanton number. An existing two-dimensional differential boundary layer prediction method, STAN-5, is modified to incorporate the above two effects.

Introduction

Accurate knowledge of the airfoil surface heat loads and aerodynamic losses is essential for conducting designs and analyses of aircraft gas turbines. Turbine designers currently rely on empirical correlations of experimental rig data, analytical calculation methods, and limited engine data to guide the trade-off studies that eventually lead to a final design. The empirical correlations, usually obtained from cascade and rotating rig test data and the results of the analytical calculation techniques are subsequently modified to reflect the limited information deduced from real engine test data. This is because much of the experimental rig data is obtained for well-controlled, two-dimensional flow fields, where each parameter is investigated separately, but the complex interaction of all effects in the real turbine are neglected. Similarly, the analytical calculations are usually obtained from two-dimensional boundary layer prediction methods, and do not accurately account for the complex flow field and thermal environment of the gas turbine engine. As a consequence of this "building block" procedure in design systems, this procedure invariably leads to a conservative design with some inefficiency especially at off-design operating conditions.

There are good arguments why a designer is reluctant to rely heavily on heat transfer and aerodynamic information obtained from the analytical methods. As an example, although numerous calculation methods available in literature have been shown to compute the growth of laboratory generated two-dimensional boundary layers on either curved or flat surfaces, none of these methods have been demonstrated to consistently predict the development of both momentum and thermal boundary layer growth on turbine airfoils even in plane cascade configurations. It is not surprising, then, that a designer is reluctant to use information from such analytical methods in actual engine environments where the complex interaction of high turbulence level, radial pressure gradients, unsteadiness, rotation, and large temperature gradients are likely to influence the development of boundary layer flows to a significant extent.

Admittedly, the calculation of boundary layer growth on turbine airfoils is a formidable task. This is because the pressure and temperature gradients on turbine airfoil surfaces along with the small dimensions of the airfoil sections dictate low Reynolds number flows which result in transitional types of boundary layers over most of the airfoil surfaces. The problem is further complicated because typical gas turbine airfoils are highly cambered and operate in low aspect ratio configurations where the endwall secondary flows are likely to influence boundary layer development over most of the airfoil suction surface, even at midheight regions. The main objective of the present paper is to demonstrate that if the influence of endwall secondary flows on the midheight boundary layer development of realistic turbine airfoil geometries is properly accounted for, an available two-dimensional boundary layer calculation method [1] can be modified to obtain a much improved estimate of both momentum and thermal boundary layer growth.

Background. A number of attempts [5–7] have been made to calculate the boundary layer development over curved surfaces. An important objective of these investigations has been to develop a capability to predict the boundary layer development on turbomachine airfoils which are highly cambered. One of the simplest, yet physically realistic,

Contributed by the Gas Turbine Division of THE AMERICAN SOCIETY OF MECHANICAL ENGINEERS and presented at the 27th International Gas Turbine Conference and Exhibit, London, England, April 18–22, 1982. Manuscript received at ASME Headquarters December 10, 1981. Paper No. 82-GT-127.

analyses for turbulent boundary layer flows over curved surfaces has been proposed by Bradshaw [5]. He drew a simple analogy between the effect of curvature and that of buoyancy, the latter in the case of a heated shear layer, and predicted that the boundary layer mixing length in flows over a convex surface would be reduced while that over a concave surface would be increased. Through his analysis, Bradshaw demonstrated good agreement between experimental data and theoretical predictions for boundary layer skin friction and shape factor. Further extension of his analysis also indicates that a turbulent boundary layer over a convex surface would be thinner and that over a concave surface would be thicker when compared to the boundary layer over a flat surface. These predicted trends have been substantiated by experimental measurements in high aspect ratio two-dimensional curved channels [8, 9]. However, observations of turbulent boundary layer data in curved channels of moderate and low aspect ratios show exactly the opposite trend [10, 11, 12].

Similar results may be deduced from the experimental data in rotating radial channels. Application of Bradshaw's analysis for flows over a rotating radial surface (suction side) indicates that the mixing length would decrease and hence the boundary layer would be thinner when compared to the boundary layer over a flat stationary surface. This behavior is supported by experimental data from high aspect ratio rotating channels [13, 14] which show that the boundary layers over suction surfaces are thinner and those over pressure surfaces are thicker than the boundary layers over flat stationary surfaces. For lower aspect ratio rotating channels, however, opposite trends are again observed [15, 16].

Moore [16] proposed a model to explain the behavior of boundary layer flows on the pressure and suction surfaces of a rotating radial channel. According to this model, it is the cross-channel pressure gradient, generated by the Coriolis force in a rotating channel, that drives the low momentum endwall boundary layer fluid toward the suction surface of the channel. Moore also proposed a hypothesis for the flow in the corner regions of the endwall and pressure and suction surfaces. According to this hypothesis low momentum fluid directed towards the suction surface enters the suction surface boundary layer which results in increased loss on the suction surface over and above its two-dimensional value. Similarly, boundary layer fluid from the pressure surface migrates towards the endwall which results in lower losses on the pressure surface of the channel than expected in two-dimensional flow fields. Moore extended the two-dimensional boundary layer calculation method of Moses [21] for quasi-three-dimensional flows in a rotating channel and was able to obtain good estimates of the boundary layer flows in rotating radial impellers.

Sharma and Railly [22] applied Moore's analysis to rotating and stationary curved channels. They used Railly and Howard's [23] method to calculate the boundary layer development in the endwall regions, whereas for the growth of boundary layers on the pressure and the suction surfaces they used Moore's version of the Moses method. In addition Sharma and Railly also showed that the presence of cross flow on the pressure and suction surfaces of the rotating curved channels also causes change in mixing lengths over and above the changes proposed by Bradshaw [5]. Through their analysis the above authors were able to correctly estimate the boundary layer skin friction, shape factor, and momentum loss thickness for the data of Schubauer and Klebanoff [12] acquired in the midheight region of the convex surface in a stationary channel.

An alternate model to account for cascade endwall boundary layer cross flows on the airfoil midheight boundary layer development was proposed by Dunham [17]. He attributed increased loss at the airfoil midheight in a cascade to an axial velocity density ratio (AVDR) effect resulting from boundary layer growth in the endwall region. The AVDR effect (AVDR = (ρ *Va*) exit/(ρ *Va*) inlet) and the presence of boundary layers in the endwall region usually result in higher axial velocity in the exit plane of the cascade than at the inlet. However, when Dunham applied this model to the data of Shaalan [18], he had only limited success as shown in Fig. 1. Dunham obtained better agreement with the data when he used an AVDR value of 4.0 instead of 1.433, the latter value being obtained from the experimental data. This indicates

Nomenclature

CPT = total pressure coefficient, $2(Pt_i - Pt)/\rho U_i^2$
Cp = specific heat at constant pressure
H = half-height of the airfoil in a cascade
h = heat transfer coefficient
K = curvature of the airfoil surface
L = dissipation length
l = total length of the airfoil suction surface
P = static pressure
p = fluctuating static pressure
R = radius of curvature of the equivalent axisymmetric body
Ri = Richardson number
Re = Reynolds number based on momentum loss thickness
S = penetration height of the separation line on the airfoil suction surface
St = Stanton number based on local velocity
U,V,W = streamwise, normal, and transverse components of mean velocity
u,v,w = streamwise, normal, and transverse components of turbulence velocity
$\bar{u}^2,\bar{v}^2,\bar{w}^2$ = streamwise, normal, and transverse components of turbulence intensity
$-\overline{uv}$ = Reynolds shear stress in the streamwise-normal direction
$-\overline{wv}$ = Reynolds shear stress in the transverse-normal direction
x,y,z = streamwise, normal, and transverse distances

Greek Letters

β = constant defined in equation (13)
δ = boundary layer thickness
θ = boundary layer momentum loss thickness
ϵ = cross-flow angle
τ = shearing stress
ρ = density
μ = dynamic viscosity
ν = kinematic viscosity

Subscripts

∞ = indicates free stream condition
3D = three dimensional
e = edge of the boundary layer
i = inlet condition
k = curvature
te = trailing edge
w = wall

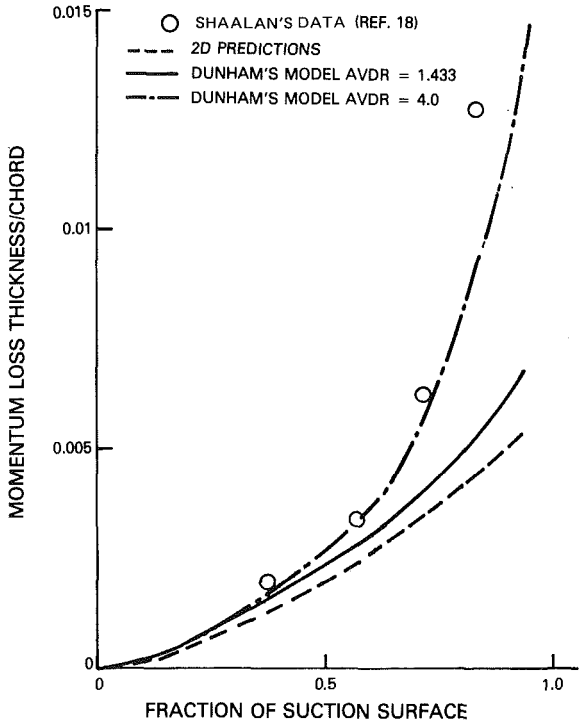

Fig. 1 Evaluation of AVDR effect to account for endwall flows on compressor airfoil suction surface midheight boundary layer development (replotted from Dunham [17])

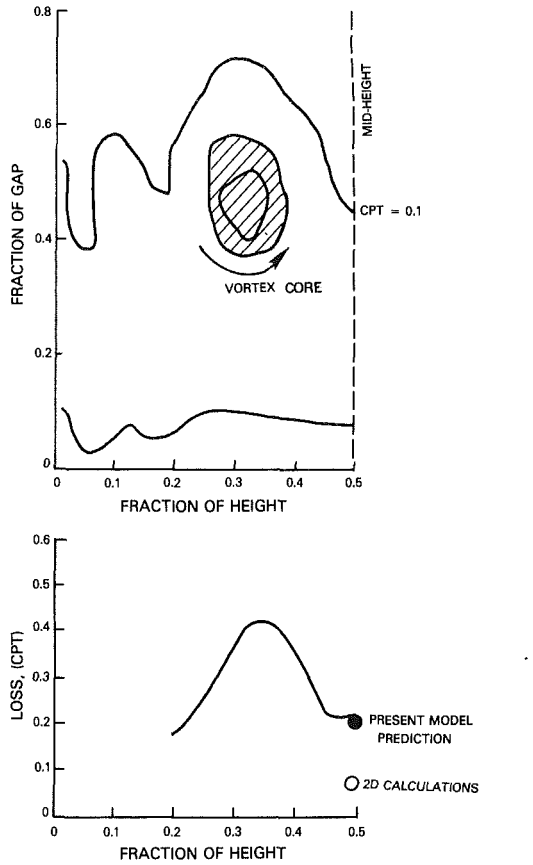

Fig. 2 Exit plane total pressure coefficient contours and gap averaged loss for the Langston et al. [2] test

that some mechanism other than the AVDR effect may be responsible for increased boundary layer thickness at the midheight of airfoils in cascades.

More recent investigations indicate the viscous flow development in a turbine cascade is more complex than in either a curved channel or a compressor cascade. Langston et al. [2] has shown that the inlet boundary layer entering a turbine cascade rolls into a horseshoe vortex that wraps around the leading edge of each airfoil. The pressure side leg of the horseshoe vortex travels across the passage to the suction side of the adjacent airfoil, and is reinforced by the new endwall boundary layer that is generated in the turbine passage. The combination of these two flows make up the passage secondary flow vortex. The axial velocity in the passage vortex is of the same order as the free stream velocity of the undisturbed flow. Thus, the presence of the passage vortex does not cause any appreciable blockage in the cascade passage which implies that AVDR effects are virtually absent in turbine cascades. Exit plane total pressure contours and gap-averaged loss values from the tests of Langston given in Fig. 2 show a very small region of constant loss in the midheight region of the cascade. Additional unpublished work conducted at Pratt & Whitney Aircraft by Langston included installation of a fence, similar to the ones used by Prumper [20], on the airfoil suction surface. The latter tests were conducted at the same test conditions and in the same test facility as described in the published investigations of Langston et al. Exit plane total pressure contours and gap-averaged loss with the fence installed, given in Fig. 3, show a larger area of almost constant loss in the midheight region of the cascade than observed with no fence. The magnitude of the midheight loss is also lower in Fig. 3 than in Fig. 2. It should also be noted that since midheight surface static pressure distributions on the airfoil surfaces were almost identical in these two investigations, the growth of a two-dimensional boundary layer would be expected to be the same in these two tests. These results demonstrate that: (*i*) viscous flow from the regions near the endwall on the suction surface migrated towards the midheight region of the cascade; (*ii*) installation of the fence on the airfoil surface reduced this migration; and (*iii*) the importance of this effect must be considered whenever cascade data is utilized to obtain information at midheight locations.

Graziani et al. [3] complemented Langston's study by conducting a detailed heat transfer investigation of the same cascade geometry in the same test facility. Graziani obtained data for two different cascade inlet boundary layer thickness to height ratios. In addition to heat transfer coefficient data, Graziani obtained flow visualization information on the airfoil and the endwall surfaces, and additional aerodynamic measurements of the exit flow fields. Figure 4 shows total pressure contours and gap-averaged loss for the lower value of inlet boundary layer thickness to height ratio from the investigation of Graziani. The data of Langston, plotted in Fig. 2, and the data of Graziani, plotted in Fig. 4, were obtained for the same test conditions except for the magnitude of the cascade inlet boundary layer thickness. A comparison of the regions of constant loss in Figs. 2 and 4 shows that a larger constant loss region resulted with the smaller cascade inlet boundary layer thickness. This indicates that the airfoil midheight loss is affected less with the smaller inlet boundary layer thickness.

A fair estimate of the magnitude of the endwall secondary flow that affects the midheight boundary layer development on the suction surface of an airfoil in a cascade can be obtained from flow visualization information on the airfoil suction surface. Airfoil suction surface flow visualization of the limiting streamlines, including the separation streamline, from the cascade tests of Langston et al. and Graziani et al. for thick (15 percent height) and thin (2 percent height) cascade inlet boundary layers are shown in Fig. 5. An im-

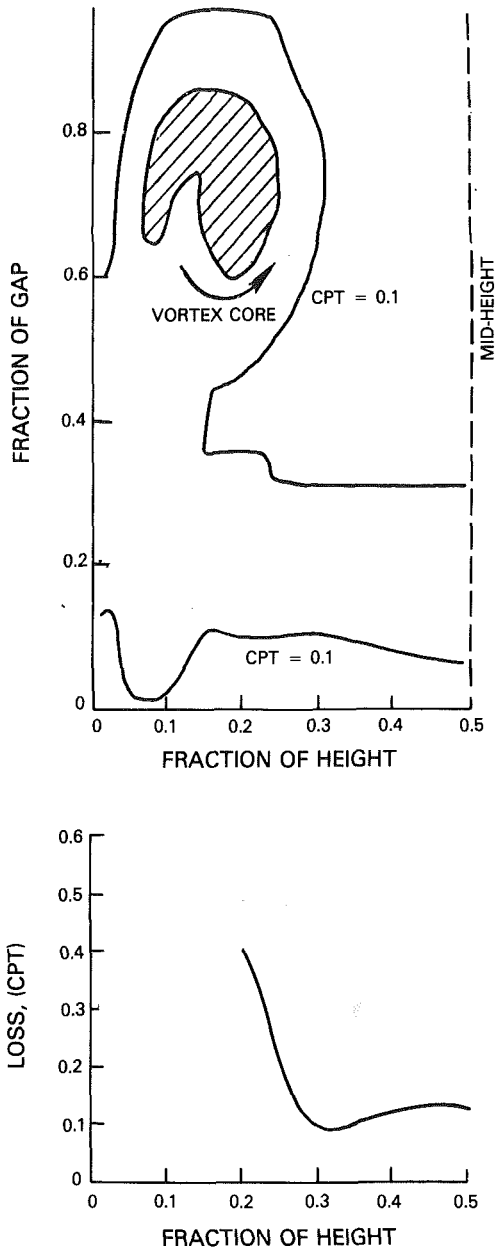

Fig. 3 Exit plane total pressure coefficient contours and gap averaged loss for the Langston's test with a fence installed on the airfoil suction surface

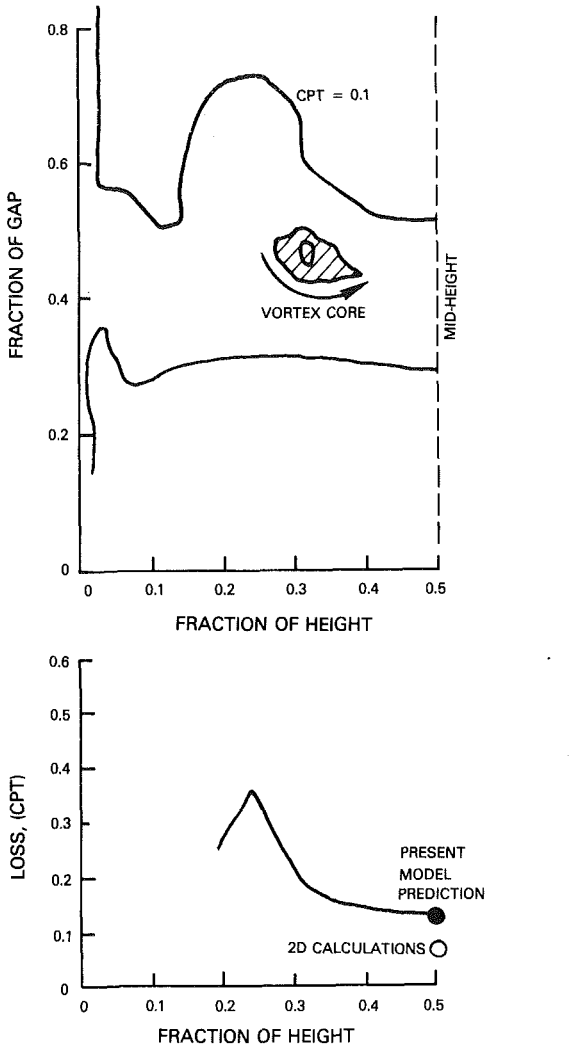

Fig. 4 Exit plane total pressure coefficient contours and gap-averaged loss for Graziani et al. [3] test

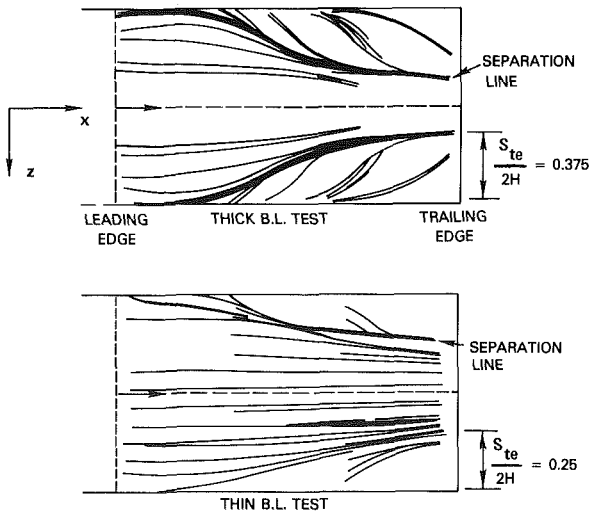

Fig. 5 Limiting streamline flow visualization on the airfoil suction surface from the tests of Langston et al. [2], thick inlet boundary layer and Graziani et al. [3], thin inlet boundary layer

portant feature to note is the larger penetration height of the separation streamline at the trailing edge for the thick inlet boundary layer case. It should also be pointed out that flow visualization acquired at Reynolds numbers other than the values presented in Fig. 5 indicated that Reynolds number variation had an insignificant effect on the distribution pattern of the airfoil suction surface limiting streamlines.

Collective evaluation of the information previously obtained from Figs. 2 and 4, and the separation line penetration height magnitudes from Fig. 5, indicate that when the magnitude of the endwall secondary flow vortex is large, the penetration height of the separation line is large, and so is the magnitude of the loss at the cascade midheight location. Consequently, penetration height of the separation line at the trailing edge of the suction surface of the airfoil can be used to estimate the size and the position of the endwall secondary flow vortex. This information may then be used to estimate the influence of endwall flow on the cascade midheight boundary layer development and hence provide an estimate of the loss.

Based on an endwall flow model formulated from the

results of the above data, the present work extends the aforementioned analysis of Sharma and Railly [22] to provide a reasonably accurate method for calculating midheight boundary layer development on the airfoil suction surface of turbine cascades. While the above analysis was limited to turbulent flows, the differential type of boundary layer calculation used in the present analysis is applicable to laminar, transitional, and turbulent boundary layer development. The present analysis utilizes the height of the separation streamline on the airfoil suction surface to give information for estimating the cross flow velocity profiles on the airfoil surface. Details of the theoretical treatment used in the present method are given below.

Theoretical Treatment. The theoretical equations governing the development of a boundary layer along the suction surface midheight of an airfoil in a cascade configuration, with endwall effects, are described in the first part of this section. It is assumed that the midheight of the airfoil is also the plane of symmetry. The flow along the plane of symmetry may be calculated in a manner similar to the flow developing over an axisymmetric body if a relationship can be established between the cross-flow velocity gradient and the radius of the hypothetical axisymmetric body. Such a relationship is proposed in the second part of this section. Also described in that part is a simplified formulation of the cross-flow velocity gradient as a function of the streamtube contraction and a relationship between the streamtube contraction and the penetration height of the separation streamline on the airfoil suction surface. The effects of the cross-flow velocity gradient and airfoil surface curvature on the Reynolds shear stress is described in the third part of this section, where it is proposed that a modified form of mixing length distribution should be used for calculating turbulent boundary layers developing under the influence of endwall flow effects. The final part of this section deals with the calculation of the onset and the extent of the transitional boundary layer regime.

Governing Equations. The conservation of momentum in the streamwise direction for a steady incompressible, three-dimensional turbulent boundary layer developing over a flat, stationary surface is given as

$$U\frac{\partial U}{\partial x}+V\frac{\partial U}{\partial y}+W\frac{\partial U}{\partial z}=-\frac{1}{\rho}\frac{dP}{dx}+\frac{1}{\rho}\frac{\partial}{\partial y}[\tau_{xy}+\tau_{zy}] \quad (1)$$

If the midheight of the suction surface of an airfoil in a cascade configuration is also the plane of symmetry of the flow, then at the plane of symmetry it can be assumed that $W = 0$ and $\tau_{zy} = 0$. Applying these assumptions to equation (1) and by substituting $\tau = \tau_{xy}$, the above equation reduces to:

$$U\frac{\partial U}{\partial x}+V\frac{\partial U}{\partial y}=-\frac{1}{\rho}\frac{dP}{dx}+\frac{1}{\rho}\frac{\partial \tau}{\partial y} \quad (2)$$

where

$$\tau=\mu\frac{\partial U}{\partial y}-\rho\overline{uv}$$

Equation (2) is essentially the same at the plane of symmetry as it is in two-dimensional flows. The equation governing the development of a thermal boundary layer for flows along the plane of symmetry takes a form similar to the momentum conservation equation and remains essentially the same as for two-dimensional flows.

The conservation of mass in a steady, incompressible, three-dimensional boundary layer flow is given by

$$\frac{\partial U}{\partial x}+\frac{\partial V}{\partial y}+\frac{\partial W}{\partial z}=0 \quad (3)$$

In two-dimensional flows $\partial W/\partial z = 0$. For calculating flows along the plane of symmetry, however, this extra term $\partial W/\partial z$ has to be accounted for. The treatment of this term adopted in the present procedure is described below.

Mass Conservation Equation at the Plane of Symmetry. It is emphasized here that although $W = 0$ at the plane of symmetry, $\partial W/\partial z$ is nonzero, the reason being the nonzero value of W away from the plane of symmetry.

It is assumed that W is a linear function of z, the plane of symmetry being located at $z = 0$ (Fig. 5). The form of the cross flow velocity is then taken as

$$W=-\epsilon_w\frac{U}{H-S}z \quad (4a)$$

where

H = distance from the endwall surface to the midheight of the cascade

S = distance of the endwall from the line describing the convergence of the flow (i.e., the approximate diameter of the endwall passage vortex defined by the 'separation line' in the airfoil suction surface as shown in Fig. 5)

$S = f(x)$

ϵ_w = cross-flow angle at the wall on the airfoil suction surface

$$=\frac{dS}{dx} \quad (4b)$$

The negative sign for W in equation (4) indicates that the overall mass in the boundary layer is greater than the two-dimensional value, due to the presence of the convergence effect on the midheight boundary layer.

Differentiating equation (4*a*) w.r.t. z and by assuming $\partial u/\partial z = 0$ (which is a reasonable assumption near the plane of symmetry) results in

$$\frac{\partial W}{\partial z}=-\epsilon_w\frac{U}{H-S} \quad (5)$$

Substitution of equation (5) in equation (3) results in the following expression for the mass conservation equation

$$\frac{\partial U}{\partial x}+\frac{\partial V}{\partial y}-\frac{\epsilon_w U}{H-S}=0 \quad (6)$$

Now, by way of comparison, the conservation of mass for boundary layers developing over axisymmetric bodies is written as

$$\frac{\partial UR}{\partial x}+\frac{\partial VR}{\partial y}=0 \quad (7)$$

where

r = radius of the axisymmetric body

If R is approximated by the following expression

$$R=\exp\left(-\int\frac{\epsilon_w}{H-S}dx\right) \quad (8)$$

then equation (7) takes on the same form as equation (6) and analytical results obtained for flows over axisymmetric bodies can be used to calculate the boundary layer development at the plane of symmetry.

Substituting for ϵ_w from equation (4*a*) in equation (8) leads to:

$$R=\exp\left(-\int\frac{dS/H}{1-S/H}\right)=1-\frac{S}{H} \quad (9)$$

The variation of S as a function of the air-foil suction surface length was obtained from flow visualization of the

airfoil suction surface limiting streamlines, notably the penetration height of the separation streamline.

A solution of equations (2), (7), and (9) may then be obtained by using any of the established procedures for calculating parabolic partial differential equations over axisymmetric bodies.

Structure of Turbulence at the Plane of Symmetry. In addition to the flow convergence effect influencing the mass conservation equation (equation (6)), as described above, this effect is also shown to influence the structure of turbulence in boundary layers.

Bradshaw [24] pointed out that the turbulence structure in boundary layers is strongly influenced by the extra rates of strain produced by curvature, rotation, and endwall flows. Sharma and Railly [22] showed that the effect of these extra rates of strain on the structure of turbulence in boundary layers generated by streamtube convergence and longitudinal surface curvature can be demonstrated through the use of the transport equation for Reynolds shear stress. This equation can be written as shown in Appendix A, as

$$U\frac{\partial -\overline{uv}}{\partial x}+V\frac{\partial -\overline{uv}}{\partial y}-\text{diffusion} \tag{10}$$

(Convection)

$$=-0.3\overline{uv}\frac{\partial U}{\partial y}-\overline{uv}\frac{\partial W}{\partial z}-KU(\overline{2u^2}-\overline{v^2})-0.3\frac{(-\overline{uv})^{3/2}}{L_o}$$

(Generation) (Dissipation)

Neglecting convection and diffusion of the Reynolds shear stress in the inner part of the boundary layer results in the following expression

$$-\overline{uv}\frac{\partial U}{\partial y}\left[1+\frac{10}{3}\frac{\partial W}{\partial z}\Big/\frac{\partial U}{\partial y}-\frac{10}{3}\frac{\overline{2u^2}-\overline{v^2}}{-\overline{uv}}KU\Big/\frac{\partial U}{\partial y}\right]=\frac{(-\overline{uv})^{3/2}}{L_o} \tag{11}$$

or $$\sqrt{-\overline{uv}}=L\frac{\partial U}{\partial y}$$

where $$L_o\left[1+\beta_{3D}\mathrm{Ri}_{3D}-\beta_k\mathrm{Ri}_k\right] \tag{12}$$

and $$\mathrm{Ri}_{3D}=\frac{\partial W}{\partial z}\Big/\frac{\partial U}{\partial y}$$

= gradient Richardson number due to the endwall flow effect

$$\mathrm{Ri}_k=2KU/\frac{\partial U}{\partial y}$$

= gradient Richardson number due to the presence of longitudinal surface curvature

$\beta_{3D}=10/3$

$$\beta_k=\frac{5}{3}\frac{\overline{2u^2}-\overline{v^2}}{-\overline{uv}}\simeq 9$$

($\overline{u^2}=-\overline{uv}/.3$, $\overline{v^2}=-\overline{uv}/.75$ ---according to McDonald-Fish [42]).

L = dissipation length

L_o = dissipation length for flow over flat surfaces in two dimensional flows.

For two-dimensional flows $\partial W/\partial z$ is zero, and for this condition equation (12) indicates that the dissipation length, which is of the same order as the mixing length in the inner part of the turbulent boundary layer, needs to be modified due to the effect of airfoil surface curvature. Bradshaw recommended that β_k be of the order of 7-10 for flows over convex stationary surfaces, which is in good agreement with the value 9 obtained in the present analysis. The above analysis shows that the effect of the streamtube contraction (representing the endwall flow effect) on the structure of turbulence can be obtained through the use of Ri_{3D} and β_{3D} and no empirical constant is required. Also, in the present case Ri_{3D} is negative and indicates a decrease in the length scale. A decrease in the dissipation or the mixing length would result in reduced Reynolds shear stress which in diffusing flows can be interpreted as a tendency towards separation.

Another important parameter that has a significant effect on the local structure of turbulence in boundary layers is the upstream history of the flow. Recent experimental studies conducted at Stanford University [25, 26] have shown that the influence of extra rates of strain produced by upstream wall curvature on two-dimensional turbulent boundary layers persist well beyond the end of the curvature region.

Although multiequation turbulence models [27-31] have the potential to automatically account for the upstream history effect, these sophisticated models have had only limited success in calculating boundary layers on turbine airfoils as shown by Daniels and Browne [32]. The calculation method described herein, which uses a simple mixing length model but with appropriate modifications to account for the recent findings as outlined above, show a significant improvement over previous methods. The effect of the upstream history on the mixing length was accounted for by using curvature and the ϵ_w values fifteen boundary layer thicknesses upstream of the calculation location.

Transition Model. Extensive experimental investigations [33, 34] have indicated that suction surfaces of turbine airfoils have extended regions of transitional flow. In order to accomplish the present objective of demonstrating the effect of endwall flows on airfoil midheight boundary layers a simple model was incorporated in an available boundary layer code (STAN-5) to facilitate calculations through the transitional region. The present transition model is similar to the one used by Gaugler [41] and is based on two correlations which give criteria for the onset of the transitional region and distribution of the intermittency factor in the transitional regime.

The modifications proposed in the above four subsections have been incorporated in the aforementioned boundary layer calculation method STAN-5. The theoretical predictions obtained from this method are compared with the experimental data of Graziani et al. [3], Langston et al. [2], and Dring et al. [4] and are described in the following section.

Comparison With Data. Only limited data is available in the published literature where measurements of both momentum and thermal boundary layer parameters were acquired in turbine cascades. The following sets of data were used in the present investigation to evaluate the above analysis, these being:

- Graziani et al. [3] data acquired with a thin inlet boundary layer for a large-scale, low-aspect ratio, high-turning linear cascade where measurements of airfoil surface heat transfer coefficient distribution, airfoil surface static pressure distribution, flow visualization information on the airfoil suction surface and the magnitude of the loss in the midheight region of the cascade in the exit plane were available.
- Langston et al. [2] data acquired in the aforementioned test facility for the same test conditions except with a thick inlet boundary layer to the cascade where measurements of boundary layer thickness near the trailing edge plane on the airfoil suction surface, flow visualization information on the

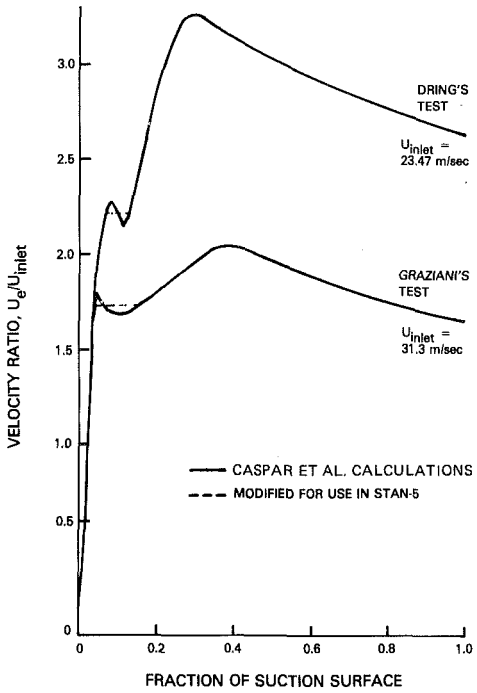

Fig. 6 Airfoil midheight free stream velocity distribution for the tests of Graziani et al. [3] and Dring et al. [4], both sets of velocity distributions obtained from Caspar et al. [43] calculations

airfoil suction surface and the magnitude of the loss in the midheight region of the cascade in the exit plane were available. Graziani's airfoil surface heat transfer coefficient distribution data, acquired at the same test conditions as Langston's thick boundary layer data, were used to obtain the Stanton number information.

- Dring et al. [4] data acquired in a 1-1/2 stage large scale, low aspect ratio rotating rig (with the rotor located at 65 percent axial chord downstream of the nozzle vane) where the measurements of the vane airfoil surface static pressure distributions and airfoil surface heat transfer distributions were available. Midheight loss for this test was obtained from the data published by Joslyn et al. [35]. Information about the airfoil suction surface flow visualization was obtained from unpublished tests conducted by Dring and his co-workers.

The free stream velocity distributions used to obtain the boundary layer calculations for the above data sets are shown in Fig. 6. These were acquired from the potential flow analysis of Caspar et al. [40] and were found to be in good overall agreement with the measured airfoil surface static pressure distributions, except in the leading edge overspeed region of the airfoil surface where detailed experimental data was unavailable. The calculations of the boundary layer growth with the predicted potential flow velocity distribution indicated separation of the laminar boundary layer in the leading edge region for all data sets. However, examination of the heat transfer data in the leading edge region of each test did not indicate turbulent or transitional reattachment of the flow. Thus, in the present investigation velocity distributions were faired as shown by dotted lines in Fig. 6 for each data set.

A comparison of the Stanton number data and theoretical predictions are shown in Figs. 7 and 8 for the tests of Graziani et al. for the thin and the thick inlet boundary layer test conditions and in Fig. 9 for the test of Dring et al. Two sets of predictions are shown, the dotted lines indicating results of two-dimensional calculations, whereas the solid lines indicate results of present calculations where the effect of endwall flows on airfoil midheight boundary layer development is

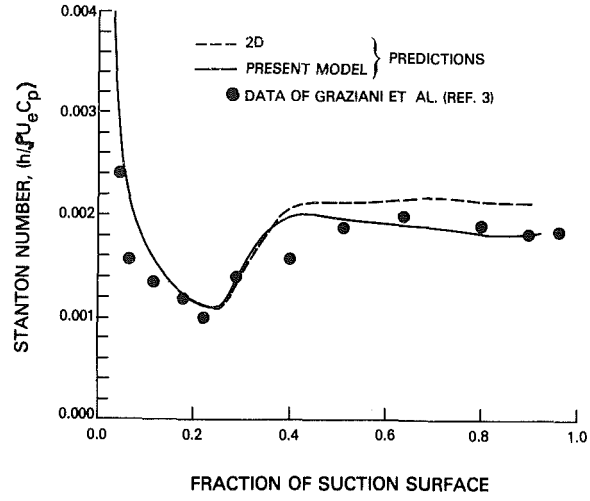

Fig. 7 Comparison of local Stanton number data of Graziani et al. [3] with theoretical predictions (thin inlet boundary layer test)

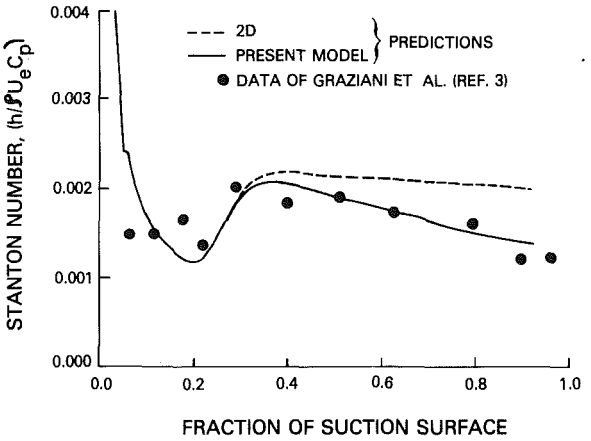

Fig. 8 Comparison of local Stanton number data of Graziani et al. [3] with theoretical predictions (thick inlet boundary layer test)

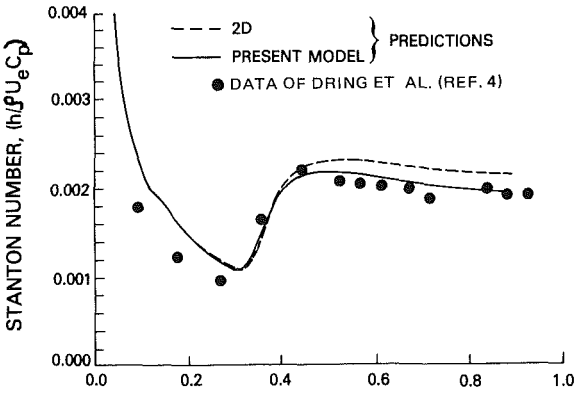

Fig. 9 Comparison of local Stanton number data of Dring et al. [3] with theoretical predictions (rotor located at 65 percent axial chord downstream of the stator)

accounted for. The present calculations show much better agreement with the data in the trailing edge region of the airfoil suction surfaces than the two-dimensional calculations.

Unfortunately, measurements of aerodynamic boundary layer parameters on the airfoil surfaces were not conducted in these tests. However, as previously stated, Langston et al. [2] have obtained detailed aerodynamic data in the same test

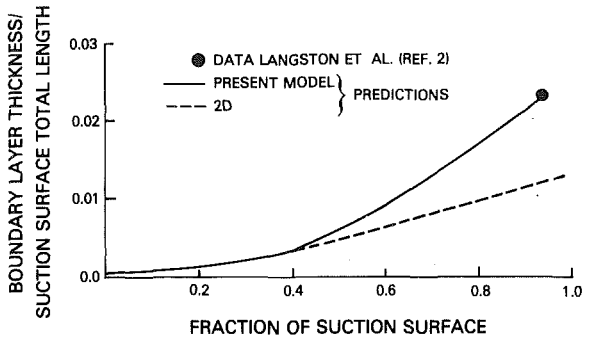

Fig. 10 Comparison of suction surface boundary layer thickness data of Langston et al. [2] with theoretical predictions

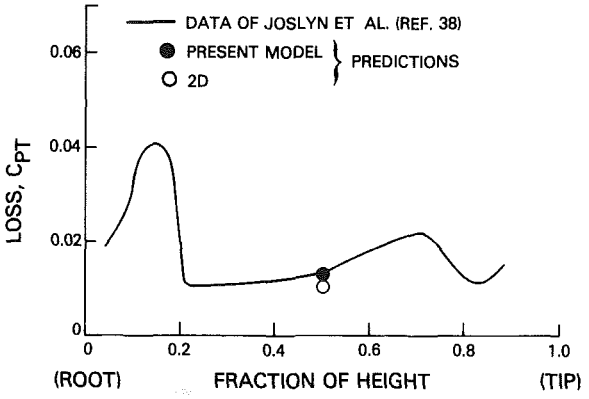

Fig. 11 Gap-averaged loss data of Joslyn et al. [35] and midheight loss predictions

facility and from that data the magnitude of the boundary layer thickness could be deduced for a location near the suction surface trailing edge. Calculated boundary layer thickness distributions obtained through the use of the two-dimensional and the present calculations for the Langston et al. test are shown in Fig. 10. Also shown in this figure is the measured boundary layer thickness data. The boundary layer thickness at the measurement location is almost twice as thick as the one predicted by the two-dimensional calculation. The present calculation shows excellent agreement with the data.

Theroetical calculations were also conducted to obtain an estimate of the cascade midheight loss by calculating the boundary layer development on the suction and pressure sides of the airfoil. These calculations were conducted for all of the above data sets, and the present analysis together with the mixing analysis of Stewart [38] were used to obtain the mixed out losses. Theoretical loss obtained for two-dimensional and the present calculations are shown in Figs. 2, 4, and 11 for each data set, respectively.

The theoretical midheight losses predicted by present calculations show good agreement with the measured data for these test conditions, whereas two-dimensional losses are much lower than the data. Losses obtained by two-dimensional calculations are shown by open symbols in the above figures and those obtained by present calculations are shown by solid symbols.

Conclusions

1 Airfoil suction surface boundary layers in turbine and compressor cascades are affected by endwall secondary flows, even in the midheight regions. This effect is evident in a comparison of measured data to predicted two-dimensional values for boundary layer thickness, heat transfer coefficients, and loss at the midheight of the airfoil in turbine cascades.

- Existing two-dimensional boundary layer calculation methods can underestimate the boundary layer thickness near the trailing edge of the airfoils in a low aspect ratio cascade by as much as 100 percent.
- Existing two-dimensional boundary layer calculation methods can overpredict Stanton number on the airfoil suction surface up to 75 percent as compared to measured data in cascades with large secondary flows.
- Existing two-dimensional boundary layer calculation methods can underestimate midheight boundary layer loss in the exit plane of low aspect ratio cascades by as much as 250 percent.

2 Axial velocity density ratio (AVDR) effect, in itself, is insufficient to explain the influence of endwall flows on the aerodynamics and heat transfer behavior on the suction sides of turbine/compressor cascades.

3 An existing two-dimensional differential boundary layer calculation method, STAN-5, modified to include a model which relates the endwall flow effect on the airfoil suction surface midheight boundary layer development to the size of the secondary flow vortex gives good agreement between experimental data and theoretical predictions.

4 Inclusion of secondary flow effects into the two-dimensional boundary layer prediction method is shown to influence the airfoil suction surface midheight boundary layer development in the following two ways:

- There is an increase in boundary layer thickness and consequently an increase in the midheight loss.
- There is a decrease in Reynolds shear stress, mixing length and Stanton number.

References

1 Crawford, M. E., and Kays, W. M., "STAN-5—A Program for Numerical Computation of Two Dimensional Internal and External Boundary Layer Flows," NASA CR-2742, 1976.

2 Langston, L. S., Nice, M. L., and Hooper, R. M., "Three-Dimensional Flow Within a Turbine Cascade Passage," ASME JOURNAL OF ENGINEERING FOR POWER, Jan. 1977, pp. 21-28.

3 Graziani, R. A., Blair, M. F., Taylor, J. R., and Mayle, R. E., "An Experimental Study of Endwall and Airfoil Surface Heat Transfer in a Large Scale Turbulent Blade Cascade," ASME JOURNAL OF ENGINEERING FOR POWER, Vol. 102, 1980, pp. 257-267.

4 Dring, R. P., Joslyn, H. D., Hardin, L. W., and Wagner, J. W., "Turbine Rotor Stator Interaction," Paper to be presented at the ASME Gas Turbine Conference, London, 1982.

5 Bradshaw, P., "An Analogy Between Streamline Curvature and Buoyancy in Turbulent Shear Flow," *J. Fluid. Mech.*, Vol. 36, 1969, pp. 177-191.

6 Wilcox, D. C., and Chambers, T. L., "Streamwise Curvature Effects on Turbulent Boundary Layers," AIAA Paper 76-356, San Diego, Calif.

7 Eide, S. A., and Johnston, J. P., "Prediction of the Effects of Longitudinal Wall Curvature and System Rotation on Turbulent Boundary Layers," Report No. MD-19, Department of Mechanical Engineering, Stanford University, California, 1974.

8 So, R. M. C., and Mellor, G. L., "An Experimental Investigation of Turbulent Boundary Layers Along Curved Surfaces," NASA CR-1940, 1972.

9 Mayle, R. E., Blair, M. F., and Kopper, F. C., "Turbulent Boundary Layer Heat Transfer on Curved Surfaces," ASME *Journal of Heat Transfer*, Vol. 101, No. 3, 1979, pp. 521-525.

10 Wattendorf, F. L., "A Study of the Effect of Curvature on Fully Developed Turbulent Flows," *Proc. Roy. Soc.*, 148A, 1935, pp. 565-598.

11 Eskinazi, S., and Yeh, H., "An Investigation on Fully Developed Turbulent Flows in a Curved Channel," *J Aero. Sci.*, Vol. 23, 1956, pp. 23-35.

12 Schubauer, G. B., and Klebanoff, P. S., "Investigation of Separation of the Turbulent Boundary Layer," NACA Rep. 1030, 1951.

13 Johnston, J. P., Halleen, R. M., and Lezius, D. K., "Effects of Spanwise Rotation on the Structure of Two Dimensional Fully Developed Turbulent Channel Flow," *J. Fluid Mech.*, Vol. 58, 1972, p. 533-557.

14 Johnston, J. P., "The Effects of Rotation on Boundary Layers in Turbomachine Rotors," Rep. MD-24, Thermosciences Division, Department of Mechanical Engineering, Stanford University, Calif., 1970.

15 Hill, P. G., and Moon, I. M., "Effects of Coriolis on the Turbulent Boundary Layer in Rotating Fluid Machines," Report No. 69, M.I.T. Gas Turbines Lab., 1962.

16 Moore, J., "A Wake and an Eddy in a Rotating, Radial Flow Passage,

Part I: Experimental Investigation, Part II: Flow Model," ASME JOURNAL OF ENGINEERING FOR POWER, 1973, pp. 205-219.
17 Dunham, J., "The Effect of Stream Surface Convergence on Turbomachine Blade Boundary Layers," *Aeronautical Journal*, Feb. 1974, pp. 90-92.
18 Shaalan, M. R. A., "The Stalling Performance of Compressor Cascades of Different Aspect Ratios," Ph.D thesis, Liverpool University, Liverpool, U.K., 1967.
19 Langston, L. S., "Effect of Prumper Fences on the Flow Distribution in a Low Aspect Ratio Turbine Cascade Passage," P&WA unpublished work.
20 Prumper, H., "Application of Boundary Layer Fences in the Turbomachinery," AGARDograph No. 164, DEc. 1972, pp. 311-331.
21 Moses, H. L., "A Strip Integral Method for Predicting the Behavior of Turbulent Boundary Layers," AFOSR-IFP Stanford Conference Thermosciences Division, Stanford University, Calif., 1968.
22 Sharma, O. P., and Railly, J. W., "Coriolis, Curvature and Endwall Effects on the Blade Boundary Layer in a Two-Dimensional Radial Impeller," Research Report No. 159, Department of Mechanical Engineering, University of Birmingham, Birmingham, U.K., 1977.
23 Railly, J. W., and Howard, J. H. G., "Velocity Profile Development in Axial Flow Compressors," *J. Mech. Eng. Sci.*, London, Vol. 4, 1962.
24 Bradshaw, P., "Effect of Streamline Curvature on Turbulent Flow," AGARDOgraph No. 169, 1973.
25 Simon, T. W., and Moffat, R. J., "Heat Transfer through Turbulent Boundary Layers—The Effect of Introduction of and Recovery from Convex Curvature," ASME Paper No. 79-WA/GT-10, 1979.
26 Gillis, J. C., Johnston, J. P., Moffat, R. J., and Kays, W. M., "Experimental Data and Model for the Turbulent Boundary Layer on a Convex, Curved Surface," NASA CR 3391, 1981.
27 Saffman, P. G., and Wilcox, D. C., "Turbulence Model Predictions for Turbulent Boundary Layers," *AIAA Journal*, Vol. 12, Apr. 1974.
28 Hanjalic, K., and Launder, B. E., "A Reynolds Stress Model of Turbulence and its Application to Thin Shear Flows," *J. Fluid Mech.*, Vol. 52, 1972, p. 4.
29 Arnal, D., and Michel, R., "Effect of Free Stream Turbulence on Turbulent Boundary Layers and on Boundary Layer Transition," EUROMECH 72, Boundary Layers and Turbulence in Internal Flows, University of Salford, Salford, U.K., Mar. 30-Apr. 1, 1976.
30 Wilcox, D. C., "Turbulence Model Transition Predictions for Blunt Body Flows," AFOSR-7R-74-1714, U.S. Air Force, July 1974.
31 Donaldson, C. duP., and Sullivan, R. D., "An Invariant Second Order Closure Model for Compressible Turbulent Boundary Layer on a Flat Plate," NASA CR-128172, June 1972.
32 Daniels, L. D., and Browne, W. B., "Calculations of Heat Transfer Rates of Gas Turbine Blades," *International Journal of Heat and Mass Transfer*, Vol. 24, No. 5, 1981, pp. 871-879.
33 Consigny, H., and Richards, B. E., "Short Duration Measurements of Heat Transfer Rate to Gas Turbine Rotor Blade," ASME Paper No. 81-GT-146, 1981.
34 Turner, A. B., "Local Heat Transfer Measurements on a Gas Turbine Blade," *Journal of Mechanical Eng. Science*, Vol. 13, 1971, pp. 1-12.
35 Joslyn, H. D., Sharma, O. P., and Dring, R. P., "Unsteady Three-Dimensional Aerodynamics," ASME Paper No. 82-GT-161, 1982.
36 Nash, J. F., "An Explicit Scheme for the Calculation of Three-Dimensional Turbulent Boundary Layers," ASME Paper 71-FE-19, 1971.
37 Bradshaw, P., "Outlook for Three-Dimensional Procedures," AFOSR-IFP Stanford Conference, Thermosciences Division, Stanford, University, Calif., 1968.
38 Stewart, E. L., "Analysis of Two-Dimensional Compressible Flow Loss Characteristics of Turbine Blades in Terms of Basic Boundary Layer Parameters," NACA TN 3515, 1955.
39 Nash, J. F., and Patel, V. C., "Three-Dimensional Turbulent Boundary Layers," Scientific and Business Consultants, Inc., Atlanta.
40 Caspar, J. C., Hobbs, D. E., and Davis, R. L., "The Calculation of Two-Dimensional Compressible Potential Flow in Cascades Using Finite Area Techniques," AIAA Paper 79-0007, Jan. 1979.
41 Gaugler, R. E., "Some Modifications to, and Operational Experience With, the Two-Dimensional, Finite-Difference, Boundary Layer Code, STAN-5," ASME Paper No. 81-GT-89, 1981.
42 McDonald, H., and Fish, R. W., "Practical Calculations of Transitional Boundary Layers," *International Journal of Heat and Mass Transfer*, Vol. 16, No. 9, 1972, 1729-1744.
43 Patankar, S. V., and Spalding, D. B., *Heat and Mass Transfer in Boundary Layers*, Intertext Books, London, U.K. 1970.

APPENDIX A

The Reynolds shear stress $(-uv)$ transport equation for three-dimensional steady boundary layer flow over curved surfaces may be written as follows, Nash and Patel [39],

$$\frac{D(-\overline{uv})}{Dt} + \overline{uv}\frac{\partial W}{\partial z} - \bar{v}^2\frac{\partial U}{\partial y} + \overline{wv}\frac{\partial U}{\partial z} + (2\overline{u^2} - \overline{v^2})KU$$

(Convection) (generation)

$$= -\overline{\frac{p}{\rho}\left(\frac{\partial v}{\partial x} + \frac{\partial u}{\partial y}\right)} + \frac{\partial}{\partial y}\overline{u\left(\frac{p}{\rho} + v^2\right)}$$

(redistribution) (diffusion)

$$- \nu\overline{(v\nabla^2 u + u\nabla^2 v)} \qquad \text{(A1)}$$

(dissipation)

For two-dimensional flows over flat surfaces, the above equation reduces to

$$\frac{D(-\overline{uv})}{Dt} = \bar{v}^2\frac{\partial U}{\partial y} - \overline{\frac{p}{\rho}\left(\frac{\partial v}{\partial x} + \frac{\partial u}{\partial y}\right)} + \frac{\partial}{\partial y}\overline{u\left(\frac{p}{\rho} + v^2\right)}$$

$$- \nu\overline{(\nabla^2 u + u\nabla^2 v)} \qquad \text{(A2)}$$

Bradshaw [37] and Nash [36] simplified the above equation in which the RHS of equation (A2) was approximated to

$$\bar{v}^2\frac{\partial U}{\partial y} - \overline{\frac{p}{\rho}\left(\frac{\partial v}{\partial x} + \frac{\partial u}{\partial y}\right)} + \frac{\partial}{\partial y}\overline{u\left(\frac{p}{\rho} + v^2\right)} \qquad \text{(A3)}$$

$$- \nu\overline{(v\nabla^2 u + u\nabla^2 v)} = 0.3\left[-\overline{uv}\frac{\partial U}{\partial y} - \frac{(-\overline{uv})^{3/2}}{L_o}\right] + \text{Diffusion}$$

Substituting equation (A3) in (A1) and assuming $W = 0$ and $\partial U/\partial z = 0$ results in the following equation:

$$U\frac{\partial(-\overline{uv})}{\partial x} + V\frac{\partial(-\overline{uv})}{\partial y} + \overline{uv}\frac{\partial w}{\partial z} + KU(\overline{2u^2} - \overline{v^2})$$

$$= 0.3\left[-\overline{uv}\frac{\partial U}{\partial y} - \frac{(-\overline{uv})^{3/2}}{L_o}\right] + \text{Diffusion} \qquad \text{(A4)}$$

D. M. Kercher
Gas Turbine Division.
Mem. ASME

R. E. Sheer, Jr.
Corporate Research and Development.

General Electric Company,
Schenectady, N.Y. 12345

R. M. C. So[1]
Department of Mechanical and Energy
Systems Engineering,
Arizona State University,
Tempe, Ariz.

Short Duration Heat Transfer Studies at High Free-Stream Temperatures

This paper describes short duration heat transfer measurements on a flat plate and a gas turbine nozzle airfoil at high free-stream temperatures. A shock tube generated the high-temperature and pressure air flow. Thin-film heat gages recorded the surface heat flux. The flat plate was tested both in the shock tube and in a shock tunnel placed aft of the tube. Shock tunnel tests on the nozzle airfoil measured the local heat transfer distribution. The flat plate free-stream temperatures varied from 830°R (460 K) to 3190°R (1770 K) for a $T_w/T_{T,g}$ temperature ratio of 0.17 to 0.64 at Mach numbers from 0.12 to 1.34. The nozzle measurements at a $T_w/T_{T,g}$ of 0.35 to 0.39 generally indicate that pressure (concave) surface heat transfer coefficients are high, whereas the suction (convex) surface shows much lower heat transfer coefficients than a turbulent flat-plate correlation.

Introduction

Coal-derived fuels and advanced cooling concepts will have an important application in future designs of heavy-duty combined-cycle power generation gas turbines. Maximum cycle efficiencies will require the highest turbine inlet temperature possible consistent with long-life structural integrity. To meet these requirements, General Electric Company is performing tests in critical gas turbine technology areas for the Department of Energy's High-Temperature Turbine Technology (HTTT) program [1, 2]. This program involves preliminary design of a water-cooled turbine called the Technology Readiness Vehicle (TRV). The TRV would feature a 73 MW output while operating on low-Btu coal-derived fuel at 2600°F (1427°C) firing temperature [3]. In the turbine section, the ability to predict the external heat transfer rates and distribution is an important ingredient in achieving the TRV airfoil's mechanical design life. A water-cooled composite-constructed first-stage nozzle has been designed and tested in a high-temperature and -pressure cascade at the reference design point [4]. The nozzle was designed for less than 1000°F (537°C) surface temperatures operating at maximum combustion gas temperatures of 3000°F (1649°C). The short duration shock tunnel heat transfer experimental program supports the first-stage nozzle design and test analysis. This investigation determined the effect that large gas-to-wall temperature differences have on the external heat transfer rates on a flat plate and the first-stage nozzle. A shock tube generated the high stagnation temperatures necessary to achieve the 0.17 to 0.64 range of wall-to-gas temperature ratios $T_w/T_{T,g}$ tested on the flat plate and 0.35 to 0.39 on the nozzle at 70 to 90°F (21 to 32°C) T_w.

Several types of experimental methods have been reported for measuring the heat transfer rates around a gas turbine airfoil. One of the early methods reported by Wilson and Pope [5] used embedded electrical heater strips where the normal direction of heat flow was reversed by raising the surface temperature higher than the mainstream gas temperature. More recent cascade investigations tested with the normal heat flow direction by pumping air through the airfoil [6] or individual channels [7] or by metering water through individual channels embedded in copper [8, 9]. A transient technique was used in [10] by rapidly shuttling the cascade into the hot primary gas. Most recently, short duration measurements have been conducted in a shock tunnel [11] and an isentropic light piston tunnel [12]. The present short duration technique utilizes the General Electric Corporate Research and Development shock tube facility to perform a low wall-to-gas temperature ratio heat transfer investigation on a flat plate and the TRV nozzle.

Graham [13] reviewed several flow phenomena which influence the airfoil heat transfer such as stagnation flow, curvature effects, flow unsteadiness and turbulence, accelerating and decelerating flow, secondary flow, body force effects, and transition and detransition processes. Each of the various experimental methods mentioned above may be well suited to study one or more of the above flow phenomena. The shock tunnel short duration method was selected for simulation of the wall-to-gas temperature ratio, T_w/T_g, because it accomplishes the primary purpose of measuring the airfoil centerline heat transfer rates and distribution in the most realistic situation possible for a two-dimensional airfoil. Since a cooled surface tends to stabilize a laminar boundary layer and delay transition to turbulent flow, the correct T_w/T_g and the normal direction of heat flow have special

[1] Formerly of Corporate Research and Development, General Electric Company.

Contributed by the Gas Turbine Division of THE AMERICAN SOCIETY OF MECHANICAL ENGINEERS and presented at the 27th International Gas Turbine Conference and Exhibit, London, England, April 18-22, 1982. Manuscript received at ASME Headquarters December 7, 1981. Paper No. 82-GT-129.

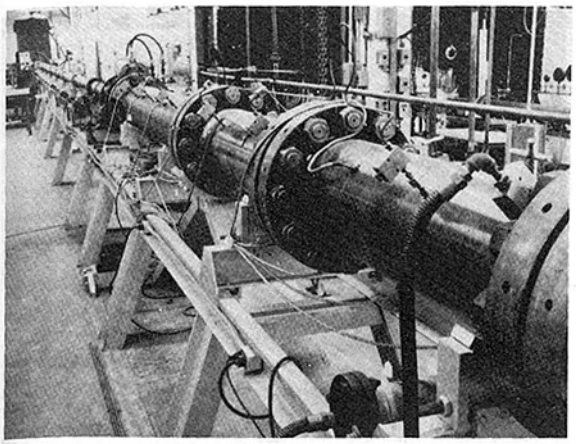

Fig. 1 Hypersonic shock tube heat transfer facility

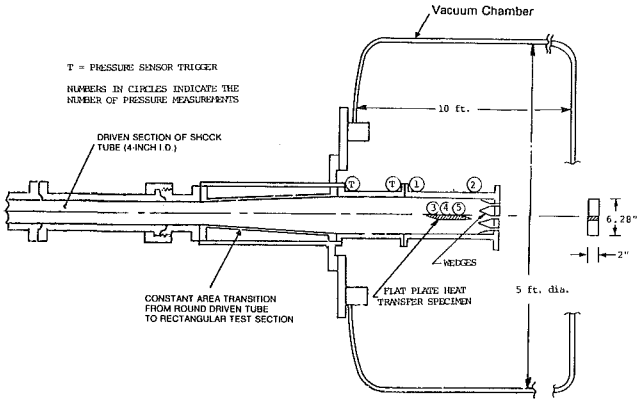

Fig. 2 Shock tube configuration and the flat-plate specimen

interest on the suction (convex) surface. The turbulence intensity is an unknown factor in the shock tube and tunnel experiments. Turbulence was not artificially generated or measured in the nozzle test; however, a flat plate test point was conducted with upstream turbulence grids. Another purpose of the heat transfer program was to determine the appropriate temperature for evaluation of fluid properties when reducing the measured nozzle data to Nusselt and Reynolds numbers. This was undertaken on the series of flat plate tests by matching the nondimensional data with an expected turbulent flat-plate correlation. The overall goal of these tests was to confidently extrapolate the shock tunnel lower temperature nozzle heat transfer data to the high-temperature design reference point in support of the water-cooled nozzle test and analytical design programs.

This paper describes the results of the experimental heat transfer program that has been conducted on a flat-plate specimen and the half-scale TRV constant pitch section nozzle airfoil in a cascade at the end of a shock tunnel. Shock tube technology and instrumentation have been used along with well-established transient test techniques and data analysis. The airfoil test results were used to partially validate and improve the confidence of a boundary layer prediction technique [14]. This paper concentrates on the heat transfer results and conclusions of the flat plate and nozzle, and makes comparisons with other investigations. For a discussion of the detailed analytical support of the test, heat, and pressure gage calibration and measurements, and support aeodynamic cascade tests, the reader is referred to [15] and [16].

Experimental Apparatus and Instrumentation

Figure 1 shows the hypersonic shock tube used to generate the high-temperature and -pressure airflow in this heat transfer investigation. It consists of a 6-in. (152-mm) i.d., 20-ft (6.1-m) long combustion driver section and a 4-in. (102-mm) i.d., 104-ft. (31.7-m) long driven section separated by a preset strength stainless steel burst diaphragm. At the end of the driven section, an instrumented test section containing a flat plate heat transfer specimen is attached directly to the driven section through a constant area transition piece from the 4-in. (102-mm) dia shock tube to the 2×6.28-in. (51×160-mm) rectangular test section shown in Fig. 2. The incident

Nomenclature[2]

C = nozzle airfoil chord length
C_p = specific heat
d_0 = nozzle throat width
E = voltage
h = heat transfer coefficient, equation (7)
H = blade height
I = current
k = thermal conductivity
L = airfoil chordwise surface length
M = Mach number
Nu_x = Nusselt number, hx/k
P = static pressure
Pr = Prandtl number, $C_p\mu/k$
$\dot{Q}$ = heat flux or rate
R = gas constant
Re_0 = nozzle upstream Reynolds number per inch, $\rho_\infty u_\infty/\mu_\infty$
$\mathrm{Re}_{x,\infty}$ = free stream Reynolds number, $\rho_\infty u_\infty x/\mu_\infty$
Re_x^* = Eckert's reference temperature Reynolds number, $\rho^* u_\infty x/\mu^*$
S = airfoil surface distance from leading edge stagnation point
t = time
T = temperature
T^* = Eckert's reference temperature, equation (2)
μ_∞ = free stream velocity
x = distance from stagnation point to heat gage
X_p = nozzle pressure ratio

Greek Symbols

α = thermal resistivity
γ = specific heat ratio
λ = running time coordinate
μ = micro, viscosity
ρ = density, P/RT
(τ) = time at steady-state heat flux

Superscripts

$*$ = fluid properties evaluated at Eckert's reference temperature
$'$ = shock tunnel conditions
$-$ = average

Subscripts

b = backing
f = film
g = gas
o = initial
p = airfoil pressure (concave) side
s = airfoil suction (convex) side
T = total
w = wall
x = length parameter
0 = free stream conditions upstream of nozzle cascade
1 = front of incident shock wave
5 = downstream of shock tube reflective shock wave
∞ = free stream static, free stream
r = recovery

[2] Conversion Factors for SI Units
(mm) = 25.4 (in.)
(m) = 0.3048 (ft)
(Pa abs) = 6895 (psia)
(K) = 0.555 (°R)
$(\mathrm{MW/m^2}) = 8.76 \times 10^{-4}$ ($\mathrm{BTu/ft^2\text{-}s}$)

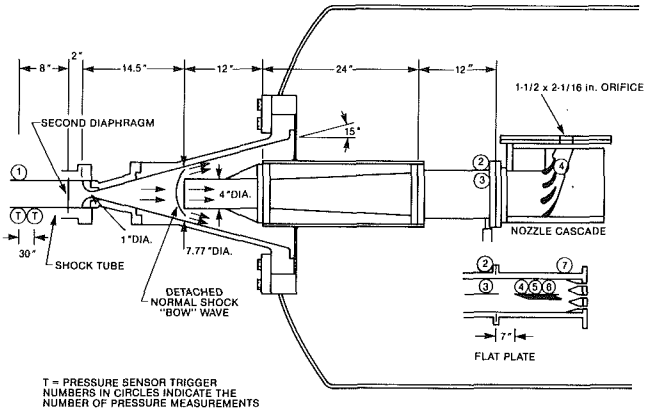

Fig. 3 Shock tunnel configuration with the flat-plate and nozzle cascade test section

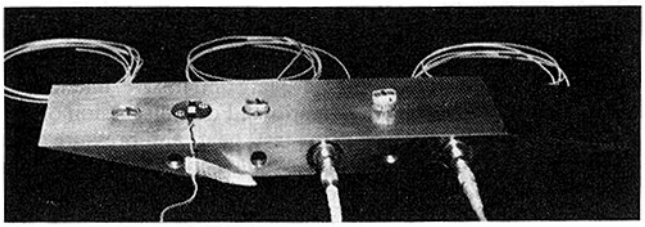

Fig. 4 Flat-plate heat transfer specimen

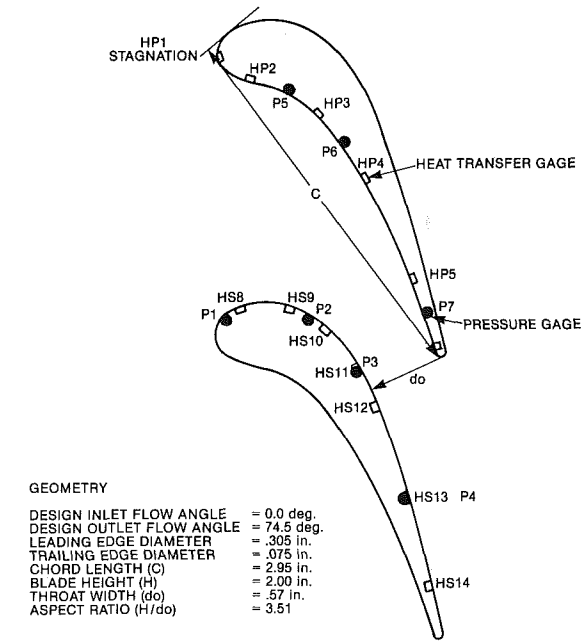

Fig. 5 Nozzle airfoil instrumentation locations and geometry

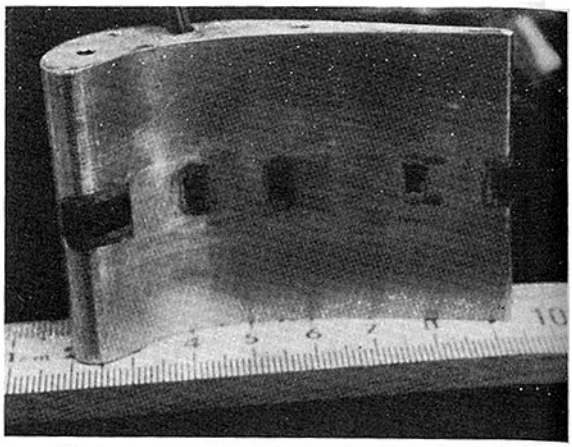

Fig. 6 Nozzle pressure surface heat transfer gages

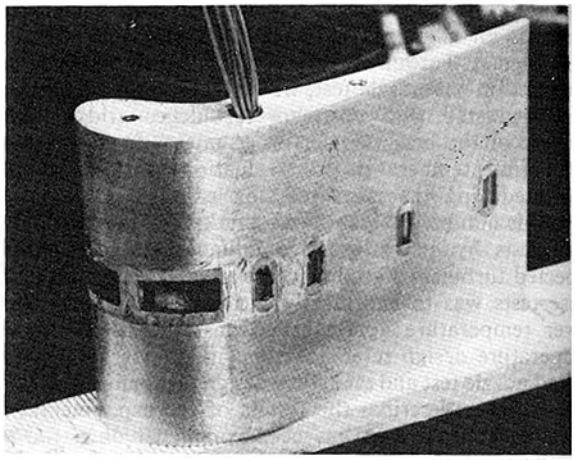

Fig. 7 Nozzle suction surface heat transfer gages

shock wave propagating down the driven section reflects from wedges shown downstream of the flat plate. This arrangement is referred to as the shock tube configuration since the mode of operation more closely resembles shock tube rather than shock tunnel operation. In the second or shock tunnel configuration (Fig. 3), the shock tube incident shock wave reflects off a primary converging-diverging nozzle with a 1-in. (25.4-mm) dia throat. A 4-in. (107-mm) dia duct is positioned inside the nozzle's diverging section at the 7.77-in. (197-mm) dia location. The test air expands through the nozzle, and a portion of this air passes through the transition section to the aft test section. The transition and test sections were designed to be used in either configuration, with existing hardware for the shock tunnel and with adapter pieces for the shock tube.

The instrumented flat-plate model shown in Fig. 4 was made of stainless steel, 2 in. (51-mm) wide by 9-in. (229-mm) long, with a sharp 15 deg angle leading edge, and a sharp trailing edge to minimize disturbances from the shock wave reflected from the downstream throat wedges. Three thin-film platinum heat transfer gages, one strain gage pressure transducer, and two quartz piezoelectric pressure transducers were installed along the centerline of the plate. Other pressure measurements were obtained upstream and downstream of the flat plate at locations on the test section shown in Figs. 2 and 3. Two quartz piezoelectric pressure transducers, shown in Figs. 2 and 3, were used as triggers to measure the incident shock wave velocity forward of the specimen. The sonic-throat wedges, shown behind the flat plate, control the test air Mach number through the test section. One set of wedges, consisting of three throats 0.43×2.0 in. (11×51 mm) each, was installed in both the shock tube and shock tunnel configuration to test at an airflow Mach number of 0.12. The other set of wedges, with throat dimensions of 1.36×2.0 in. (35×51 mm) was also installed in the shock tunnel configuration to test at an airflow Mach number of 0.41. A second diaphragm, shown in Fig. 3, was installed to achieve higher shock tube pressures for the shock tunnel tests. Monel diaphragms were used for the higher pressure tests, and aluminum was used for the lower pressures. Voltage output of the heat gages and pressure transducers were recorded by oscilloscopes and photographed for data analysis.

The nozzle test specimens are 1/2 scale, two-dimensional models of the TRV first-stage nozzle pitch section with

Table 1 Estimated uncertainties in instrumentations, calibration, and data analysis (odds of 20 to 1)

Item	% Uncertainty
Oscilloscopes	±1
Pressure gage calibration	±1
Heat gage dynamic calibration from the voltage trace	±2 to 4
Heat and pressure gage voltage trace readability	±2 to 4
Heat flux $\dot{Q}(t)$ equation (1) calculation	±5
$\dot{Q}(\tau)$ readability	±2 to 10
P_∞ during (τ)	±2
$T_{g,\infty}$ calculation during (τ)	±2
Mach number	±4

dimensions and airfoil contours shown in Fig. 5. The airfoils were milled from an aluminum block with the milling machine controlled by an optical follower which used a five times full-scale computer plot of the nozzle coordinates as a template. The surface finish obtained in this manner was approximately 32μin. (8×10^{-4} mm). Cavities were machined in the nozzle surfaces along the centerline and thirteen heat transfer gages and seven pressure transducers were installed on the suction and pressure surfaces at locations shown in Fig. 5. The thin-film heat transfer gages were mounted in epoxy flush with the surface of the flat plate and the nozzle airfoil pressure and suction surfaces shown in Figs. 6 and 7. These gages consist of a platinum strip approximately 250-Å thick by 3/64-in. (1.2-mm) wide by 3/16-in. (4.8-mm) long painted on a 1/8-in. (3.2-mm) thick Pyrex glass backing which had been ground and polished to conform to the model contours. A thin layer of silicone dioxide was evaporated over each gage surface to increase the abrasion resistance to the minute particles from the ruptured diaphragms. During the actual tests, a constant current of 50 milliamperes was applied to the gages which had room temperature resistances of 20 to 50 ohms.

A calibration constant for the thin-film backing material and thermal resistivity of the platinum, $\sqrt{(\rho c_p k)_b}/\alpha$, for each heat transfer gage was dynamically obtained in a calibration shock tube. The models with the gages installed were mounted in a plexiglass flat plate simulating a wall-mounting in a calibration shock tube. Shocks of $M=1.5$ to 3 at various pressures were used to obtain the calibration constant. With the dynamic calibration, the undefined quantities (such as the quality of the bond between the thin platinum film and the Pyrex backing material, the silicone dioxide coating, and the silver painted terminals) are included in this calibration constant. Each individual pressure gage was calibrated with a dead weight tested over a wide range of pressures. A more detailed calibration procedure is given in [15]. Estimated uncertainties in the heat and pressure gage calibration are given in Table 1 along with other individual uncertainties of the data analysis variables. A summary of the uncertainties in the data analysis final results in terms of Nu_x and Re_x will be discussed in the next section.

Test Description and Experimental Results

Shock Tube – Flat-Plate Tests. The purpose of the flat plate shock tube tests was to (*i*) determine if Mach number and high gas temperature have any effect on surface heat transfer; (*ii*) determine the effect of low wall-to-gas temperature ratios on the flat-plate heat transfer; and (*iii*) determine the appropriate temperature to use for evaluating the fluid properties in Nusselt and Reynolds number which best correlated the data against the turbulent flat plate equation. The appropriate temperature at which fluid

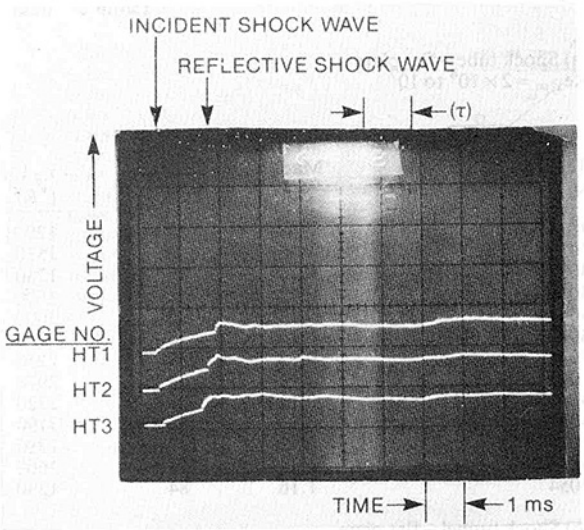

Fig. 8 Shock tube – flat-plate heat transfer gage measurements from test No. 3038

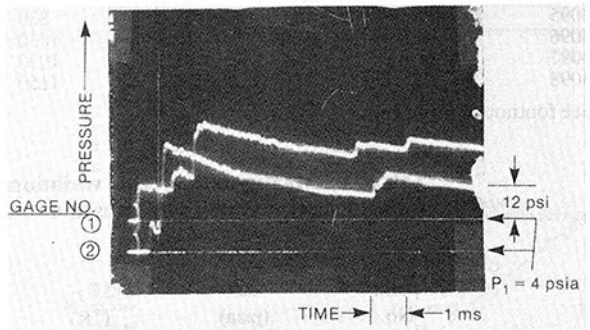

Fig. 9 Shock tube – flat-plate test section pressure gage measurements from test No. 3038

properties were evaluated would then be the temperature used for data reduction of the nozzle heat transfer test and eventual extrapolation to the nozzle design reference point using the conventional Nusselt and Reynolds number relationships.

Analysis of gas flow and temperature in the shock tube is based on well-established shock wave gas dynamics such as [16]. By placing the sonic-throat wedges at the end of the tube shown in Fig. 2, the incident shock wave reflects off the wedges, further increasing the pressure and temperature of the approaching test air and also reducing the velocity to the desired 0.12 Mach number behind the reflective shock wave. Transonic flow over the flat plate was accomplished by removing the wedges and computing the test air velocity imparted by the measured incident shock wave. The computed test air temperature was determined by the strength of the measured incident shock wave and the initial room temperature of the facility and whether the test was run in the reflective or straight-through mode. Because of the short test duration, the surface temperature of the specimen remained constant at room temperature. The incident shock wave Mach number was varied by preselecting the driver loading of hydrogen-oxygen-helium mixture and the predetermined strength of the burst diaphragm between the driver and driven tube. The measured test air pressure was a function of the initial evacuated air pressure in the driven tube and dump chamber and the strength of the incident shock wave. With the incident shock wave, Mach number varied between 1.7 and 4.2 and evacuated pressure between 0.5 and 14.6 psia (3.4 and 101 kPa), the test air temperature and pressure varied from 980 to 3190°R (544 to 1770 K) and 16 to 121 psia (110 to

Table 2 Flat-plate heat transfer results

(a) Shock tube – flat plate
$Re_{x,\infty} = 2 \times 10^4$ to 10^7

Test No.	Symbols (Figs. 11 and 12)	Mach No.	$\bar{P}(\tau)$ (psia)	$\bar{T}_{T,g}(\tau)$ (°R)	$T_w/\bar{T}_{T,g}$ (°R/°R)	$\dot{Q}(\tau)$ Btu/ft²-s heat gage HT1	HT2	HT3	Note
3036		1.08	23	1200	0.45	60	45	50	$x_{HT1} = 1.25$ in.
3037		1.25	16	1510	0.35	88	60	60	
3038		0.12	47	1280	0.42	20	20	20	$x_{HT2} = 3.25$ in.
3039		0.12	41	1600	0.33	30	23	25	
3041		0.12	28	3000	0.18	30	35	25	$x_{HT3} = 5.25$ in.
3042		0.12	74	980	0.54	24	16	20	
3044		0.12	37	2230	0.24	35	25	25	
3045		0.12	29	2970	0.18	30	20	25	5 mil trip
3046		0.12	26	2720	0.20	36	30	30	12 mil trip
3047		0.12	58	3190	0.17	55	45	50	10 mil trip
3049		0.12	119	1390	0.38	55	45	45	10 mil trip
3053		1.34	77	1660	0.32	260	220	250	
3054		1.16	84	1290	0.41	172	140	168	
(b) Shock tunnel – flat plate									
	(Fig. 15)								
3091		0.12	14.5	1890	0.28	4	8	8	
3093		0.12	15.0	1110	0.48	3	3.2	4	
3094		0.41	12.5	900	0.59	8	5	4.4	
3095		0.41	15.0	830	0.64	8	6.4	8	
3096		0.41	15.0	1030	0.51	11	6	8.4	
3097		0.41	13.5	1030	0.51	6	7.4	5	
3098		0.12	17.0	1150	0.46	7	4	4	turbulence grid

See footnote 2 for SI conversion factors.

Table 3 Maximum percent variations in Reynolds number and Nusselt number for variations in measured pressures and computed gas temperatures during $\dot{Q}(\tau)$ time period

Test point No.	ΔP (psia)	ΔT_{T_g} (°R)	$\frac{\Delta Re_x^*}{Re_x^*}$ (%)	$\frac{\Delta Nu_x^*}{Nu_x^*}$ (%)	Comments
		Shock tube – flat plate			
3038	+3.3	+22	+6.5	−3.0	HT2, Fig. 8, 9
	−1.7	−12	−3.4	+1.6	
3039	+6.7	+58	+14.0	−5.2	HT2, Fig. 10
	−3.6	−37	−8.4	+3.6	
		Shock tunnel – flat plate			
3096	+0.7	+12	+4.3	−2.3	HT1, Fig. 13, 14
	−0.6	−11	−3.8	+2.2	
		Shock tunnel – nozzle			
3099	0.0	0	0.0	0.0	HS13, Fig. 16
	−1.0	−13	−3.0	+1.3	
3100	+1.4	+23	+5.9	−2.8	HS10 Near P2, Fig. 17
	−0.8	−13	−3.4	+1.6	
3100	0.0	0	0.0	0.0	HS11, Fig. 18
	−0.8	−12	−3.0	+1.4	

See footnote 2 for SI conversion factors

834 kPa). This gave a range of 0.17 to 0.54 for $T_w/T_{T,g}$, 0.12 to 1.34 for Mach number, and 2×10^4 to 10^7 for free-stream Reynolds number (listed in Table 2). Four tests were conducted with leading edge boundary layer trips without any noticeable effect on the heat transfer results.

Photographs of each oscilloscope time-voltage signature from the heat and pressure gages provided the data to compute the heat rates and pressure variation during the test period. The three heat gages and two shock tube pressure gage oscilloscope traces are shown in Figs. 8 and 9 for a typical test point. On the left-hand side of the photographs are the calibration signals showing the intitial zero heat gage voltage and initial vacuum chamber pressure, P_1. The pressure measurements shown upstream and downstream of the flat plate were nearly the same values measured on the flat plate when superimposed on each other. All of the measured pressures decreased with time during the test period. Since the heat rates generally reached a steady-state value from 4 to 7 ms after the reflective shock wave passed the gage in a decreasing pressure environment, the calculated test air temperature was adjusted for the measured pressure by an adiabatic expansion process from the peak temperature and pressure computed from the shock wave gas dynamics developed in [16]. Because a steady-state analysis was conducted from data with environmental transient characteristics, a detailed evaluation was made of the highest and lowest variation on Reynolds and Nusselt numbers for each heat gage's measured pressure variation and computed gas temperature variation during the time period that steady-state heat flux $\dot{Q}(\tau)$ was evaluated. Examples of the data

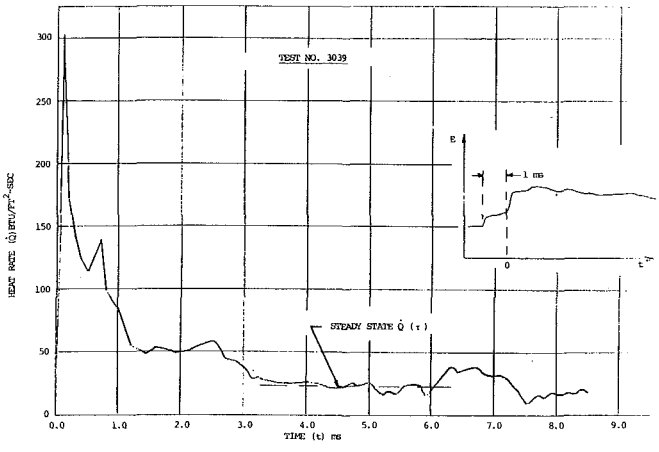

Fig. 10 Shock tube flat-plate heat rate history for gage HT2

variation, summarized in Table 3, generally show small percent variations in Re_x^* and Nu_x^* during the short (τ) time periods of approximately 2 to 3 ms. Pressure and temperature variations are included in the uncertainties in Table 1. These are incorporated in the final uncertainties of Re_x and Nu_x, which will be discussed near the end of this section.

These conclusions on the pressure variations in the shock tube flat measurements also pertain to the shock tunnel flat-plate and nozzle data to be discussed later. Their variations are also shown in the examples in Table 3.

The transient response of the heat flux gages was developed by Schultz [17] in the form used for this investigation as

$$\dot{Q}(t) = \frac{1}{\sqrt{\pi}} \frac{\sqrt{(\rho C_p k)_b}}{\alpha} \frac{1}{I_o R_o} \left[\frac{E(t)}{\sqrt{t}} + \frac{1}{2} \int_o^t \frac{E(t) - E(\lambda)}{(t-\lambda)^{3/2}} d\lambda \right] \quad (1)$$

where the constant $\sqrt{(\rho C_p k)_b}/\alpha$ for the thin-film backing material and thermal resistivity of the platinum was calibrated on each heat gage described in "Experimental Apparatus and Instrumentation." The computed steady-state heat flux $\dot{Q}(\tau)$ shown in Fig. 10 for the flat plate middle heat gage is typical of the other two gages and test runs. Flow Mach number, measured pressure, and the computed test air stagnation temperatures are listed along with the computed heat flux $\dot{Q}(\tau)$ in Table 2 and are the basis for the calculation of the gage heat transfer coefficient, Nusselt number, and Reynolds number. To select the appropriate temperature to evaluate the fluid properties in computing Nusselt and Reynolds numbers, four methods were evaluated [15]. In the first method for low heat flux and small gas-to-surface temperature differences, free-stream static temperature, T_∞, has previously been a reasonable temperature to evaluate the fluid properties in predicting heat transfer coefficient. For the second method at $T_w/T_g << 1.0$, Kays [18] suggested modifying the flat-plate equation by the ratio $(T_w/T_\infty)^{0.25}$ when T_∞ was used to evaluate fluid properties. The third method evaluated was suggested by Eckert [19] in the form of a reference temperature (or enthalpy)

$$T^* = 0.5(T_w + T_\infty) + 0.22(T_r - T_\infty) \quad (2)$$

where

$$T_r = T_\infty \left[1 + \sqrt[3]{Pr_\infty} \frac{\gamma - 1}{2} M_\infty^2 \right] \quad (3)$$

At low subsonic Mach numbers, T^* is also nearly identical to film temperature, $T_f = (T_w + T_\infty)/2$, which was suggested by [20]. The fourth method considered was to evaluate the thermal properties at T^* and density at T_∞. Nusselt and Reynolds numbers were computed using the above four

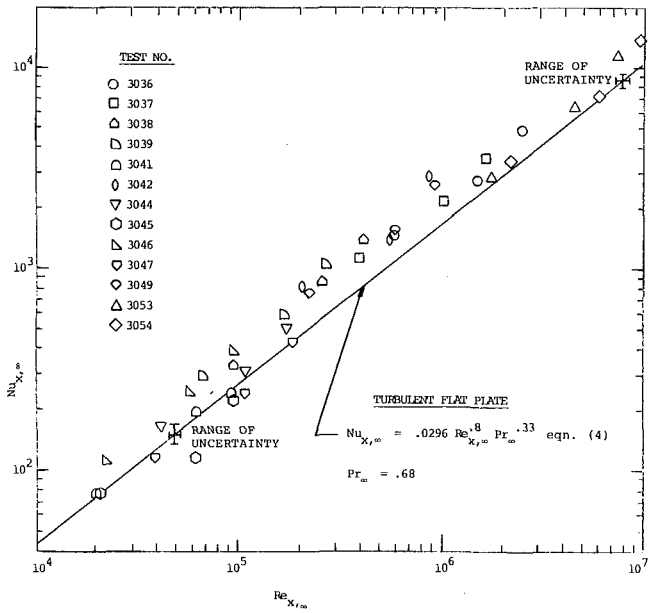

Fig. 11 Flat-plate heat transfer using T_∞ fluid properties

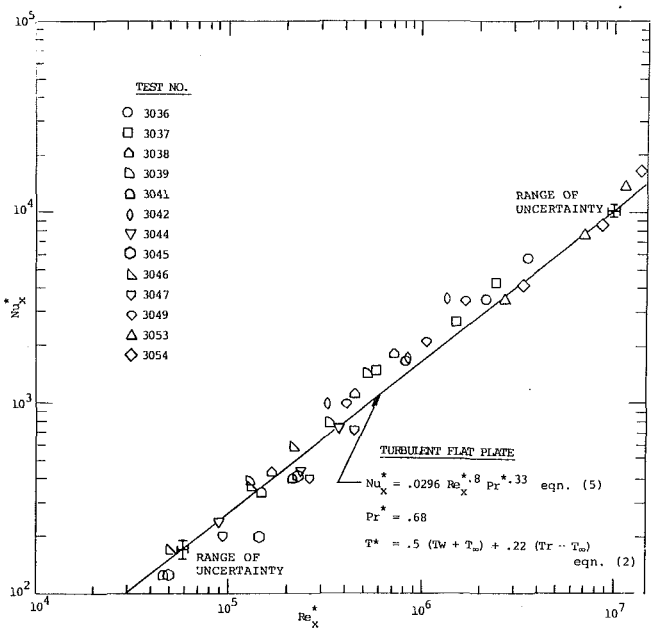

Fig. 12 Flat-plate heat transfer using T^* fluid properties

methods in evaluating fluid properties. Eckert's reference temperature was selected as the most appropriate temperature to evaluate fluid properties when comparisons were made of the computed Nusselt and Reynolds number against the classical turbulent flat plate correlation [15].

The first and third methods using T_∞ and T^* to evaluate fluid properties are plotted in Figs. 11 and 12 against the turbulent flat plate equation in the forms

$$Nu_{x,\infty} = 0.0296\, Re_{x,\infty}^{0.8}\, Pr_\infty^{0.33} \quad (4)$$

and

$$Nu_x^* = 0.0296\, Re_x^{*0.8}\, Pr^{*0.33} \quad (5)$$

where

$$\rho^* = P_\infty / RT^* \quad (6)$$

and

$$h = \frac{\dot{Q}(\tau)}{T_r - T_w} \quad (7)$$

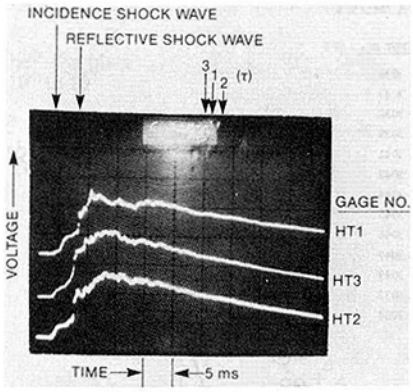

Fig. 13 Shock tunnel – flat-plate heat transfer gage measurements from test No. 3096

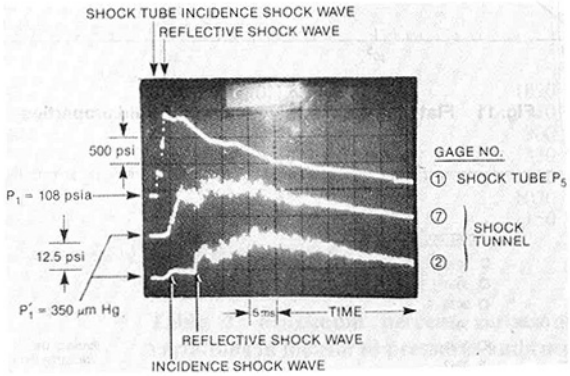

Fig. 14 Shock tube and tunnel test section pressure gage measurements from test No. 3096

This assumes the test results in some form should be characterized by the turbulent flat plate equation. Figure 11 shows that the test data correlated from T_∞ are generally higher than the flat-plate equation except at the lower Reynolds numbers. That is, if the flat-plate equation (4) was used to predict the heat transfer coefficients, it would generally underestimate the measured values. This increasing heat transfer at low T_w/T_g, shown in Fig. 11, is consistent with data from wall cooling of a subsonic turbulent tube in [20] and evaluation of flat-plate supersonic heat transfer data in [21]. There is some indication of transitional flow at the lower Reynolds numbers in Fig. 11, but since the Nusselt numbers are high this would imply a certain level of turbulence in the test air flow. Evaluating the thermal properties at T^* and density at T_∞ [15] did not improve the correlation shown in Fig. 11. Modifying the data in Fig. 11 by $(T_w/T_\infty)^{0.25}$ improved the agreement with the flat plate equation at $\mathrm{Re}_{x,\infty} > 2\times10^5$ but was somewhat lower at lower Reynolds numbers [15]. Using Eckert's reference temperature, T^*, in Fig. 12 gives the best agreement over the entire range of Reynolds numbers tested, and therefore it was selected as the most appropriate temperature to evaluate the thermal properties and density for low T_w/T_g heat transfer. Computed data uncertainties in Reynolds and Nusselt numbers using the method of [22] are shown in Figs. 11 and 12, based on the individual uncertainties in the instrumentation, calibration readability, variations, and data analysis summarized in Table 1. This indicates that the data analysis uncertainties vary between ±6 percent for Re_x and ±9 to 12 percent for Nu_x.

From the dimensionless group presentation of the data in Figs. 11 and 12, there is no indication that Mach number or free-stream gas temperature have any additional influence on

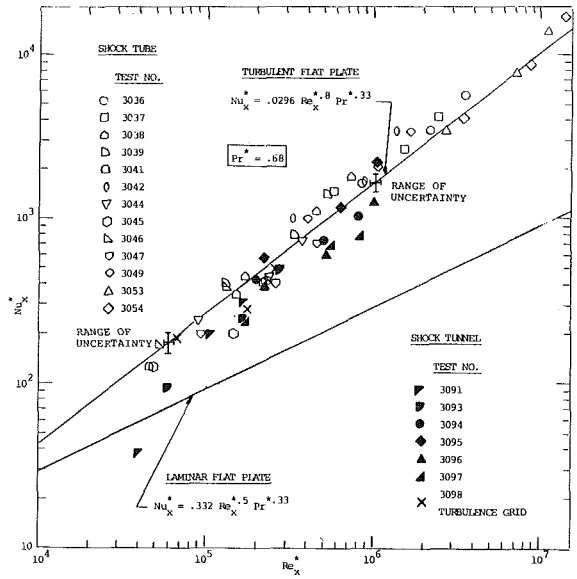

Fig. 15 Shock tube and tunnel flat-plate heat transfer comparison

surface heat transfer in the turbulent region aside from the minor influence Mach number has on computed T^* and its evaluation of fluid properties. This lack of detectable influence from Mach number on the cooled wall flat plate turbulent boundary layer heat transfer measurements is consistent with detailed data from [21]. Based on the above comparisons, Eckert's reference temperature was selected as the most appropriate temperature to use in reducing the TRV nozzle heat transfer data and eventual data extrapolation for predicting the heat transfer coefficients at the airfoil design reference point.

Shock Tunnel – Flat-Plate Tests. After the flat-plate test in the shock tube, the sonic-throat wedges were removed and the nozzle cascade was installed at the end of the tube. Preliminary tests showed that minute particles from the primary burst diaphragm were carried down the driven tube and lodged on the pressure surface of the nozzle airfoil. Since these particles could seriously affect the life of the thin-film gages and number of tests, the shock tube facility was modified to the shock tunnel configuration shown in Fig. 3.

To ensure the validity of the nozzle heat transfer results in the shock tunnel, the flat-plate specimen with two sets of sonic-throat wedges was tested to validate repeatability of the previous shock tube heat transfer results. Before firing the shock tube, the vacuum chamber was evacuated to as low as 150μm Hg while the shock tube was pressurized between the primary and secondary diaphragms up to 108 psia (745 kPa) with air at a dew point of $-80°$F ($-62°$C). The second diaphragm at the end of the driven section sets the pressure ratio across the primary diaphragm in the driver section for temperature and incident shock wave strength control. The second diaphragm also permits a higher initial pressure in the driven tube in order to achieve the desirable shock tube and shock tunnel pressures. The low vacuum chamber pressure of 150 to 350μm Hg helps attenuate a stable incident shock wave to the end of the shock tunnel. After ignition of the driver section and bursting of the primary diaphragm, the incident shock wave breaks the secondary diaphragm and reflects off the inlet of the primary converging-diverging nozzle, increasing the air temperature and increasing the pressure between 1000 and 2000 psia (6.9 to 13.8 MPa). Part of the air expands out the primary nozzle behind the nearly Mach 4 incident shock wave into the 4-in. (102-mm) i.d. duct at Mach 6.2, while the rest of the air spills into the dump chamber. The starting incident shock wave reflects off the wedges and

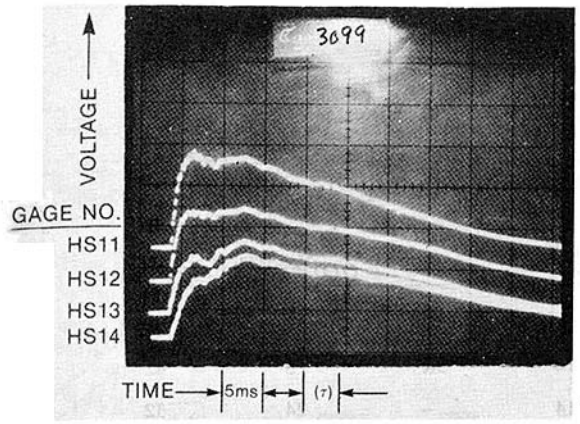

Fig. 16 Nozzle suction surface heat transfer gage measurements from test No. 3099

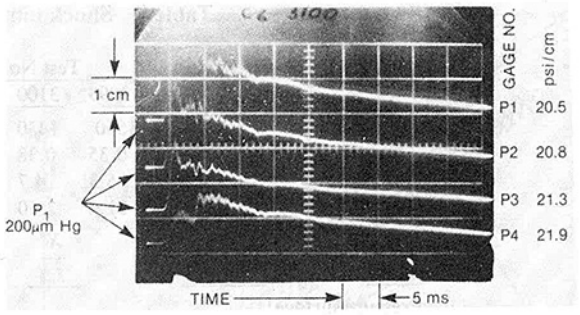

Fig. 17 Nozzle suction surface static pressure measurements from test No. 3100

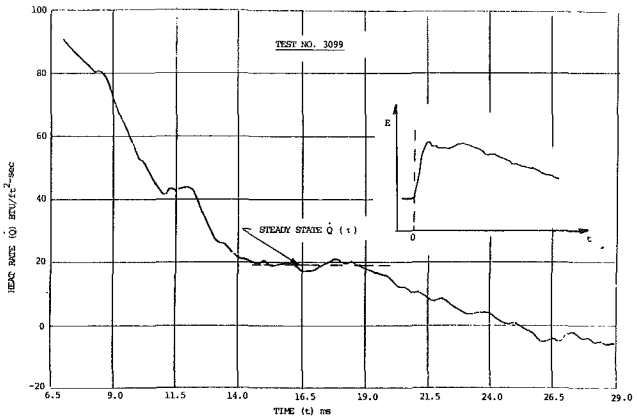

Fig. 18 Nozzle suction surface heat rate history for gage No. HS11

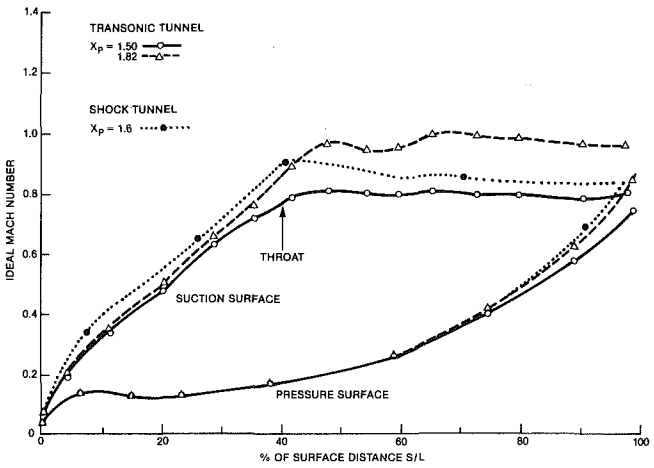

Fig. 19 Airfoil surface Mach number distribution

travels upstream to the inlet duct where a bow shock wave is formed. As the reflective shock moves upstream, it slows the approaching test air to subsonic velocity with its flow controlled by the sonic-throat area of the wedges. The test air, passing through the bow shock wave, is slowed to the subsonic velocity also controlled by the sonic throat area. The rest of the flow from the primary nozzle spills around the inserted duct into the dump chamber. Figure 13 shows the oscilloscope traces of the three heat gages' voltage outputs during a typical test. Regardless of the Mach number of the test air in the duct, the test time periods are 4 to 5 times longer than the shock tube tests. The computed heat fluxes reach steady-state $\dot{Q}(\tau)$ in 19 to 34 ms after the reflective shock wave passes the gage. The reflective shock wave gage response is shown as the "second-kick" on the left side of Fig. 13 after the incident shock wave "first-kick." Figure 14 shows typical measured pressures upstream and downstream of the flat plate, along with the shock tube pressure measurement. The measured pressure in the shock tube again decreases with time, and disturbances immediately propagate to the shock tunnel by expansion waves.

Results of the measured pressures and steady-state heat flux $\dot{Q}(\tau)$ along with computed air temperatures are also given in Table 2. $T_w/T_{T,g}$ ranged from 0.28 to 0.64. Turbulent grids consisting of $1/8 \times 1/8$-in. (3×3-mm) bars on 1/2-in. (13-mm) centers were incorporated in only one test. From the one turbulence intensity test point plotted in Fig. 15, there is an indication that only the front heat gage heat rate may have increased from the general trend of the other test data. The turbulent grids are capable of generating about 6 percent turbulence intensity from wind tunnel test measurements [15]. No change is indicated from the other two heat gages compared to the measurements without turbulent grids. General conclusions cannot be made about turbulence intensity effects on surface heat transfer based on this limited test result. The data comparison in Fig. 15 with the shock tube flat plate results based on Eckert's reference temperature in Nusselt and Reynolds numbers is generally good. At the lower Reynolds numbers, the shock tunnel data shows a transitional trend to a laminar boundary layer flow which would indicate a certain lack of turbulence in the test air compared to the shock tube. Data uncertainties in Nu_x and Re_x computed from Table 1 are ± 12 percent and ± 6 percent, respectively. The conclusion from these test results is that there is reasonable and valid comparison of the shock tunnel flat plate results with the shock tube data. Therefore, the shock tunnel test approach, data output, and computational methods should be valid for the nozzle airfoil heat transfer tests.

Shock Tunnel – Nozzle Tests. The nozzle cascade was installed in the shock tunnel as shown in Fig. 3. Operation of the tunnel is the same as described for the flat plate tests. The $1\text{-}1/2 \times 2\text{-}1/16$-in. ($38 \times 52$-mm) orifice behind the nozzle in the exhaust chamber controls the flow through the tunnel and cascade, while the nozzle throat area sets the inlet Mach number at 0.16. Typical nozzle airfoil suction surface heat gage and pressure voltage output is shown in Figs. 16 and 17. The incident shock wave reflects off the nozzle leading edge and results in a similar shock wave-flow sequence described in the flat plate tests section. The heat gage and pressure gage response on the left side of Figs. 16 and 17 are from the incident shock wave after the calibration zero signal. All pressures show a decreasing trend which is consistent with the shock tube pressure measurements and previous flat-plate test. Variations in pressure and computed temperature show insignificant variation in Nusselt and Reynolds numbers

Table 4 Shock tunnel – nozzle heat transfer results

	Test No.			
	3099	3100	3101	
	1560	1430	1400	$\bar{T}_{T,g}$(°R)
	0.35	0.38	0.39	$T_w/\bar{T}_{T,g}$(°R/°R)
	5.3	4.7	6.7	$Re_0(10^4)$
	31.0	25.0	35.0	$\bar{P}_0$(psia)

Heat gages	Pressure gages	$\frac{X}{L}$	Mach No.	$\dot{Q}(\tau)$ Btu/ft^{2}s		
Pressure surface						
HP1		0	0.16	–	–	–
HP2		0.1	0.14	30	6	42
	P5	0.2	–			
HP3		0.3	0.14	–	24	32
	P6	0.4	–			
HP4		0.5	0.21	34	26	16
HP5		0.8	0.48	37	60	24
	P7	0.9	0.67			
HP6		0.99	0.84	–	–	–
Suction surface						
	P1	0.075	0.35			
HS8		0.1	0.40	–	20	20
HS9		0.2	0.56	24	14	16
	P2	0.25	0.65			
HS10		0.3	0.74	29	16.5	21
HS11	P3	0.4	0.89	19.5	11	10
HS11	P3	0.4	0.89	19.5	11	10
HS12		0.5	0.88	23	22	17
HS13	P4	0.7	0.85	17	16	13
HS14		0.9	0.84	30	25	26

See footnote 2 for SI conversion factors.

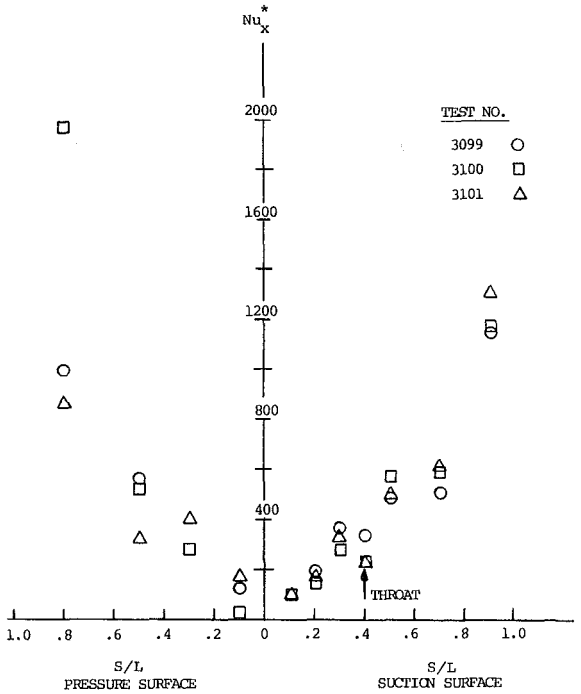

Fig. 20 Nozzle heat transfer distribution

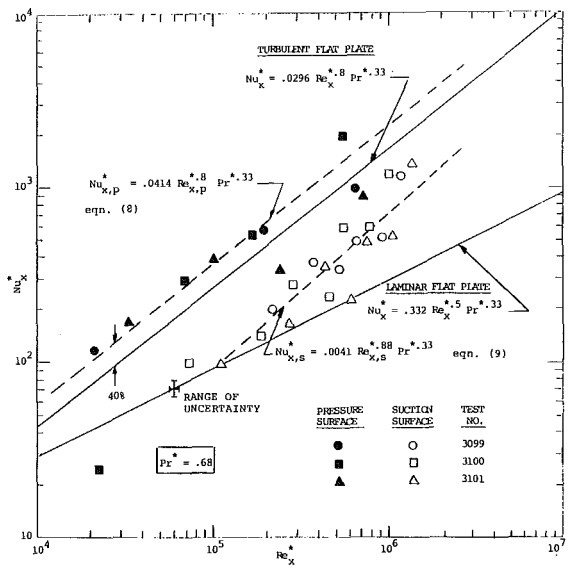

Fig. 21 Nozzle pressure and suction surface heat transfer

during (τ) from examples given in Table 3. Figure 18 shows a typical heat flux plot from equation (1) with steady-state $\dot{Q}(\tau)$ at about 15 to 18 ms after the incident wave initial response. The airfoil surface pressures were converted into local Mach numbers, plotted in Fig. 19, and compared with previous wind tunnel cascade results [15]. Two of the forward concave surface pressure gages recorded erroneously low static pressures typical of suction surface magnitude. A leak was suspected in the pressure gage tube assembly. The one concave trailing edge pressure gage and the four suction gages show good agreement with the wind tunnel aerodynamic cascade results. These results, indicating the nozzle operated at about 1.6 pressure ratio, were used to interpolate the Mach number at the heat gage location for calculation of the local Reynolds number. Table 4 lists pressure gage locations and measured Mach number, the interpolated heat gage location Mach number, and the computed steady-state heat fluxes, $\dot{Q}(\tau)$. The computed test air temperatures were between 1400 and 1560°R (777 and 867 K) for a wall-to-gas total temperature ratio of 0.35 to 0.39. The computed inlet Reynolds number is nearly constant for the three test points.

Figures 20 and 21 show the results of the data reduction in

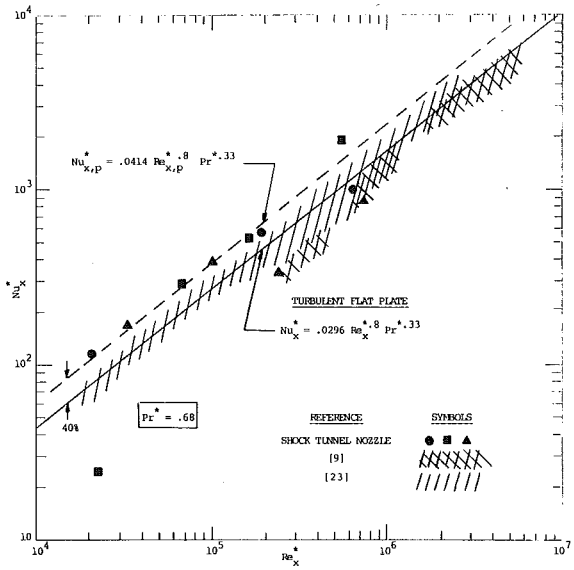

Fig. 22 Nozzle pressure surface heat transfer comparisons

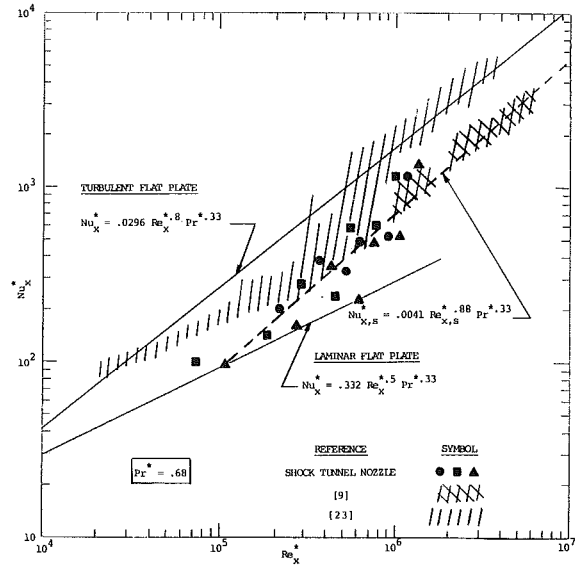

Fig. 23 Nozzle suction surface heat transfer comparisons

terms of Nusselt and Reynolds number. Figure 20 plots the local Nusselt number along the surface distance S/L. The data are somewhat scattered but repeatability is good on the suction surface in Fig. 20. Pressure surface results are generally higher than a turbulent flat-plate correlation, shown in Fig. 21, while the suction surface is characterized as transitional between laminar and turbulent. The generally high pressure surface heat transfer is attributed to a separation bubble calculated behind the leading edge [14], and is estimated to be 40 percent higher than turbulent flat plate using Eckert's reference temperature to evaluate the fluid properties where

$$\mathrm{Nu}^*_{x,p} = 0.0414\ \mathrm{Re}^{*\,0.8}_{x,p}\ \mathrm{Pr}^{*0.33} \tag{8}$$

The suction surface data is curve-fit in Fig. 21 as

$$\mathrm{Nu}^*_{x,s} = .0041\ \mathrm{Re}^{*\,0.88}_{x,s}\ \mathrm{Pr}^{*0.33} \tag{9}$$

The near-laminar to transitional heat transfer characteristics show reasonable agreement with the shock tunnel-nozzle suction surface boundary layer prediction techniques reported in [14]. Uncertainties in Re_x and Nu_x are computed to be ± 6 percent and ± 10 percent, respectively, in Fig. 21.

Results of the shock tunnel nozzle pressure surface heat transfer measurements in Fig. 22 are compared with steady-state nozzle cascade results using surface heater plates [23] and a single nozzle passage behind a combustor [9] using the calorimeter technique with metered water through channels surrounded by copper. Results from [9] and [23] are generally below or equal to the turbulent flat plate correlation compared to the generally higher shock tunnel nozzle results. There are many influences that contribute to the fact that heat transfer data are inconsistent from nozzle pressure surface test measurements. These influences range from the technique of measurement (local versus average measurements across the flow path scan and the T_w/T_g ratio) to the differences in nozzle geometry and aerodynamic characteristic of the velocity field. The destabilizing characteristic of the boundary layer from flow over a concave surface should itself be a significant factor that is influenced by the airfoil aerodynamics and geometry. These differences should emphasize and encourage the use and further development of boundary layer analytical techniques [14] to understand the influence factors and the heat transfer differences observed. This could result in more optimized airfoil cooling designs and improved nozzle structural integrity and cycle performance.

Figure 23 compares the suction surface results of [9] and [23] with the present shock tunnel results. While the transitional trends are generally the same up to the nozzle throat, there appears to be an earlier transition to turbulent heat transfer with [23] compared to the present results. This earlier transition may be the result of a destabilizing effect of the boundary layer caused by the reverse heat flow direction and $T_w/T_g > 1$ resulting from the heater plate measurement technique. This implies that the wall-to-gas temperature ratio is an important factor in duplicating the actual suction surface boundary layer and heat transfer characteristics. From these test results, it appears that large gas-to-wall temperature differences tend to stabilize the boundary layer on the suction surface and thus delay transition. The heat transfer results of [9] with a $0.25 < T_w/T_{T,g} < 0.35$ appear to support this conclusion since it shows excellent agreement with the trends of the shock tunnel measurements.

Nozzle Test Comparison

Applying the shock nozzle heat transfer results to the hot gas path test stand (HGPTS) water-cooled nozzle reference-design test conditions [4] indicates the shock tunnel airfoil average heat transfer coefficient is within 1 percent of the airfoil average heat transfer coefficient calculated from the water-cooled nozzle measured heat load at 2650 to 2700°F (1454 to 1482°C) firing temperature [24]. Lacking nozzle leading edge heat gage data from the shock tunnel tests, the leading edge heat transfer coefficient was computed from measured data in [23] and used in this HGPTS comparison along with the shock tunnel pressure and suction surface average coefficients from equations (8) and (9).

Conclusions

The application of short duration shock tube and shock tunnel technology using well-established transient testing techniques has determined the influence on flat plate and nozzle airfoil heat transfer from low wall-to-gas temperature ratios which simulate the design conditions of DOE's HTTT first-stage water-cooled nozzle. Eckert's reference temperature is the preferred method of evaluating fluid properties to account for the large gas-to-wall temperature differences and extrapolation of nozzle test data to the design conditions. Average airfoil heat transfer coefficients calculated from the short duration shock tunnel nozzle tests agree with HGPTS high-temperature cascade data analysis of water-cooled

nozzle test results. The successful results of the flat plate and nozzle tests support the validity of the short duration shock tunnel technique as a viable alternative to steady-state cascade heat transfer tests especially when low wall-to-gas temperature ratios are an important simulation factor for duplicating heat transfer results on turbine airfoils.

Acknowledgments

This investigation was supported by the Department of Energy under the High Temperature Turbine Technology Phase II Program, Contract Number DE-AC01-76ET-10340.

Significant contributions were made by Professor H. Nagamatsu, Rensselaer Polytechnic Institute; R. Mani, General Electric Corporate Research and Development; and J. C. Dudley, General Electric Gas Turbine Product Division. The authors appreciate their support.

References

1 Caruvana, A., et al., "System Status of the Water-Cooled Gas Turbine for the High Temperature Turbine Technology Program," ASME Paper No. 79-GT-39, Mar. 1979.

2 Horner, M. W., Cincotta, G. A., and Caruvana, A., "Test Verification of Water Cooled Gas Turbine Technology," ASME Paper No. 81-GT-66, Mar. 1981.

3 Caruvana, A., et al., "Design and Test of a 73-MW Water Cooled Gas Turbine," ASME Paper No. 80-GT-112, Mar. 1980.

4 Geiling, D. W., Chiu, R. P., and Klompas, N., "Mechanical, Thermal, and Hydraulic Design of a Composite Construction Water-Cooled Gas Turbine Nozzle," ASME Paper No. 81-JPGC-GT-3, Oct. 1981.

5 Wilson, D. G., and Pope, J. A., "Convective Heat Transfer to Gas Turbine Blade Surfaces," *Proc. Instn. Mech. Engrs.*, Vol. 168, No. 36, 1954, pp. 861-876.

6 Turner, A. B., "Local Heat Transfer Measurements on a Gas Turbine Blade," *Journal Mechanical Engineering Science*, Vol. 13, No. 1, 1971.

7 York, R. E., et al., "An Experimental Investigation of the Heat Transfer to a Turbine Vane at Simulated Engine Conditions," ASME Paper No. 79-GT-23, Mar. 1979.

8 Hosenfeld, H. G., and Schwerdtner, O. A. v., "Model Testing on Cooling of Gas Turbine Blades," *Siemen-Forsch-u Entwickl.-Ber. Bd. 8* (1979), Nr. 5.

9 Lilliquist, R. D., Eskesen, J. H., and DeLancey, G. J., "Heat Transfer Measurements on a Large-Scale Water Cooled Nozzle," General Electric TIS Report 76CRD044, May 1976.

10 Lander, R. D., Fish, R. W., and Suo, M., "The External Heat Transfer Distribution on Film Cooled Turbine Vanes," AIAA 72-9, Jan. 1972.

11 Dunn, M. G., and Stoddard, F. J., "Measurement of Heat Transfer Rate to a Gas Turbine Stator," ASME Paper No. 78-GT-119, Apr. 1978.

12 Consigny, H., and Richards, B. E., "Short Duration Measurements of Heat Transfer Rate to a Gas Turbine Rotor Blade," ASME Paper No. 81-GT-146, Mar. 1981.

13 Graham, R. W., "Fundamental Mechanisms that Influence the Estimate of Heat Transfer to Gas Turbine Blades," ASME Paper No. 79-HT-43, Aug. 1979.

14 So, R. M. C., et al., "A Two-Dimensional Boundary Layer Program for Turbine Blade Heat Transfer Calculations," ASME Paper No. 82-HT-93, Apr. 1982.

15 Kercher, D. M., Sheer, R. E., and Dudley, J. C., "Aerodynamic Cascades and Shock Tunnel Heat Transfer Investigations for Water Cooled Turbine Airfoils," General Electric TIS Report 81-GTD-042, July 1981.

16 Dudley, J. C., "Exact Analysis of Shock Tube Conditions for an Ideal Gas with Variable Specific Heats," General Electric TIS Report 81-GTD-043.

17 Schultz, D. L., and Jones, T. V., "Heat Transfer Measurements in Short Duration Hypersonic Facilities," *Agardograph*, No. 165, 1973.

18 Kays, W. M., *Convective Heat and Mass Transfer*, McGraw-Hill, New York, 1966.

19 Eckert, E. R. G., "Engineering Relations for Heat Transfer and Friction in High-Velocity Laminar and Turbulent Boundary-Layer Flow Over Surfaces with Constant Pressure and Temperature," ASME Paper No. 55-A-31, Nov. 1955.

20 Back, L. H., Cuffel, R. F., and Massier, P. F., "Laminar, Transition, and Turbulent Boundary-Layer Heat-Transfer Measurements with Wall Cooling in Turbulent Air Flow Through a Tube," ASME Paper No. 69-HT-8, Aug. 1969.

21 Hopkins, E. J., and Inouye, M., "An Evaluation of Theories for Predicting Turbulent Skin Friction and Heat Transfer on Flat Plate at Supersonic and Hypersonic Mach Numbers," *AIAA Journal*, Vol. 9, June 1971, pp. 993-1003.

22 Kline, S. J., and McClintock, F. A., "Describing Uncertainties in Single-Sample Experiments," *Mechanical Engineering*, Vol. 75, 1953, pp. 3-8.

23 Elovic, E., et al., "Supersonic Cascade Vane Heat Transfer Coefficient Data with and without Film Injection," General Electric TIS Report R71AEG202, 1971.

24 Horner, M. W., "High Temperature Turbine Technology Program Hot-Gas-Path Development Test—Part II (Testing)," DOE/General Electric Topical Report, DOE-ET-10340-132, Mar. 1982.

An Empirically Based Simulation Model for Heavy-Duty Gas Turbine Engines Using Treated Residual Fuel

J. C. Blanton
Mechanical Engineer,
Corporate Research and Development,
General Electric Company,
Schenectady, N.Y.
Assoc. Mem. ASME

W. F. O'Brien, Jr.
Professor,
Department of Mechanical Engineering,
Virginia Polytechnic Institute and State University,
Blacksburg, Va.
Mem. ASME

An empirically based engine simulation model was developed to analyze the operation of a heavy-duty gas turbine on ash-bearing fuel. The effect of the ash in the combustion products on turbine efficiency was determined employing field data. The model was applied to the prediction of the performance of an advanced-cooled turbine engine with a water-cooled first-stage nozzle, when operated with ash-bearing fuels. Experimental data from a turbine simulator rig were used to estimate the expected rates of ash deposit formation in the advanced-cooled turbine engine, so that the results could be compared with those for current engines. The results of the simulations indicate that the rate of decrease in engine power would be 32 percent less in the advanced-cooled engine with water cooling. An improvement in predicted specific fuel consumption performance was also noted, with a rate of increase of 38 percent for the advanced-cooled engine.

Introduction

The relative advantages and disadvantages of the gas turbine engine versus the Rankine steam engine are well known [1], and without considering fuel availability the gas turbine is the better choice for peak-load, electric power generating applications. As available supplies of light distillate petroleum fuels are diminished, increasing emphasis is being placed on fuels flexibility. The leading candidate alternative fuels are coal and residual fuel oil. Both of these are used successfully in Rankine steam engines, but to date only limited success has been obtained with gas turbine engines. Experience buring coal in gas turbines has been in general very poor, with erosion of turbine blades being the most serious obstacle [2, 3]. The use of gasified coal in combined cycles appears to offer the most promise [4, 5]. Experience burning residual fuel oil in gas turbines has been much better than with coal, and in some applications gas turbines are being operated with residual oil as the primary fuel [6]. There remain several unresolved problems, however, which compromise the operation of gas turbine engines using a residual fuel. Since it appears that clean distillate fuel oil and natural gas will soon no longer be available for use in electric power generation, it is quite possible that the future success of the heavy-duty gas turbine industry may well depend on the adaptation to alternative fuels.

The most serious unresolved problem encountered with the use of residual fuel oil in gas turbines is the depostion of solid ash material on the turbine gas path surface [6]. The manner in which these deposits affect the engine performance may be described by two separate variations in the turbine performance [7]. The first of these is a reduction in the mass throughflow capacity of the turbine resulting from the physical and aerodynamic blockage at the nozzle and rotor passage throats. The second effect is a reduction in the turbine efficiency (increased irreversibility) resulting from an adverse variation of the turbine aerodynamics.

A substantial amount of experimental research has been performed to investigate ash deposition in gas turbines. Most of this work has been carried out using so-called turbine simulator facilities [8, 9], which are attempts to simulate the environment in the first-stage nozzle passage of a gas turbine engine. Gas temperatures and hence throat velocities are matched to a full-scale turbine, but lower pressures are used and usually a simulated fuel is burned. The data obtained from turbine simulator tests may be used to calculate the rate at which the ash deposits produce a decrease in the mass throughflow capacity of the turbine nozzle. The extreme gas path conditions, however, prohibit the use of instrumentation necesary to obtain data relative to the cascade losses and hence the reduction in turbine efficiency.

To the user of a gas turbine engine, the most important operating parameters are the engine power output and the specific fuel consumption. The variation in these parameters may be predicted if the off-design characteristics of the engine are known, along with a knowledge of the decreases in turbine mass throughflow capacity and turbine efficiency resulting from the ash deposits. In this paper a model is described which has been developed to carry out the performance analysis for a gas turbine engine operating on an ash-bearing fuel. This model makes use of some of the existing turbine simulator data as well as some limited results of tests performed on full-scale engines in the field. The initial results are

Contributed by the Gas Turbine Division of THE AMERICAN SOCIETY OF MECHANICAL ENGINEERS and presented at the 27th International Gas Turbine Conference and Exhibit, London, England, April 18–22, 1982. Manuscript received at ASME Headquarters December 10, 1981. Paper No. 82-GT-139.

then extended to make predictions of the performance of a near-term, advanced-cooled gas turbine utilizing a water-cooled, first stage turbine nozzle.

Description of Model

The performance model used in this paper is a simplified version of a generalized model developed as part of an earlier, comprehensive investigation of ash deposit formation and removal in gas turbines [10]. The analysis is developed around a simplified gas turbine model shown in Fig. 1. In this model the turbine first-stage nozzle is considered separately from the rest of the turbine. A fraction of the compressor discharge air is extracted, bypasses the combustor, and re-enters the turbine as film and convective cooling air. Total-to-total efficiencies are used to characterize both the compressor and turbine, and losses in the compressor inlet and turbine exhaust are lumped into the efficiency of the respective components.

The procedure for determining the operating point for the gas turbine engine involves satisfying mass flow and pressure ratio compatibility between the compressor and turbine. In an electric power generating application, the engine speed remains constant (3600 rpm in the U.S.), and the engine power output is varied by changing the fuel flow and thus the turbine inlet temperature. The most common control scheme is to maintain the desired operating point by sensing the turbine exhaust temperature and varying the fuel flow to hold the temperature at some predetermined value. For an engine burning clean fuel at constant power output would be delivered. Changes in turbine characteristics resulting from ash deposits would, however, result in some different operating point and a lower power delivery.

The constant-speed, off-design point characteristics of the compressor and turbine were modeled using very simple approximations. A linear variation of compressor pressure ratio with mass flow was chosen, and a parabolic variation of compressor efficiency was used. This procedure provided flexibility in selecting the compressor mass flow coinciding with the maximum compressor efficiency. The turbine mass flow characteristic was assumed to be sufficiently steep (near-choking) so that a constant mass flow capacity was delivered at all operational pressure ratios for the clean turbine. The turbine efficiency was also assumed to be independent of pressure ratio. The following equations thus describe the compressor and turbine performance (property state points refer to stations on the schematic, Fig. 1):

$$\frac{(p_{02}/p_{01})}{(p_{02}/p_{01})_a} = 1 - a_i\left[\frac{(m_a\sqrt{T_{01}}/p_{01})}{(m_a\sqrt{T_{01}}/p_{01})_a} - 1\right] \tag{1}$$

$$\frac{\eta_c}{\eta_{c,\max}} = 1 - a_2\left[\frac{(m_a\sqrt{T_{01}}/p_{01})}{(m_a\sqrt{T_{01}}/p_{01})_{@\eta_{c,\max}}} - 1\right]^2 \tag{2}$$

$$\frac{m_p\sqrt{T_{03}}}{p_{03}} = a_3 \tag{3}$$

$$\eta_t = a_4 \tag{4}$$

Five variables in equations (1-4) are available for use in characterizing component off-design performance. The coefficient a_1 in equation (1) is the slope of the compressor mass flow characteristics. In equation (2), a_2 is related to the curvature of the compressor efficiency characteristic, and the compressor mass flow corresponding to the point of maximum efficiency is $(m_a\sqrt{T_{01}}/p_{01})_{@\eta_{c,\max}}$. The coefficients

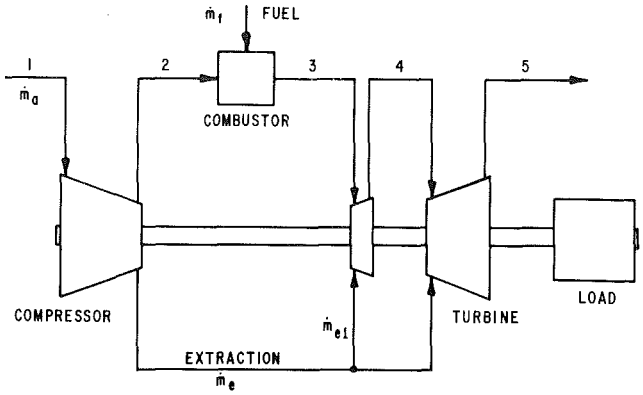

Fig. 1 Air-cooled combustion turbine engine schematic

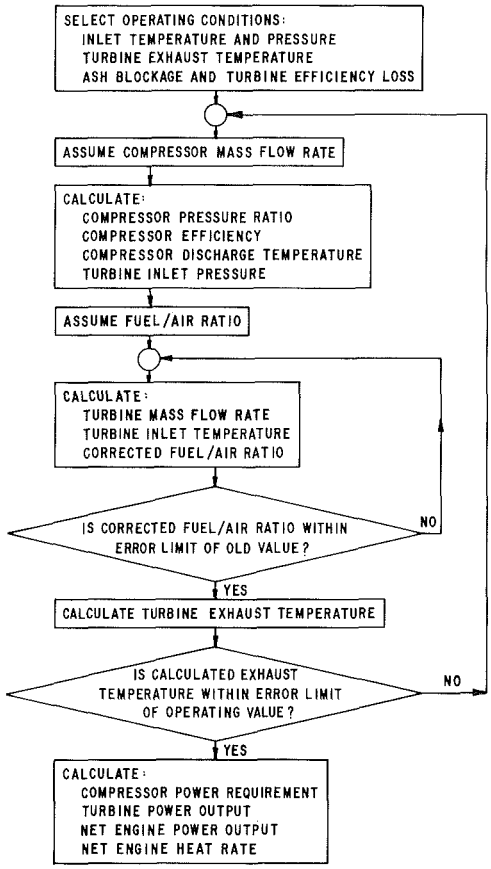

Fig. 2 Flowchart of combustion turbine engine analysis procedure

Nomenclature

a_k = coefficient in equations (1-4)
K_j = coefficients in equations (5-11)
m = mass flow rate
P_{oi} = stagnation pressure at station i
Q_{34} = heat transfer rate per unit mass in turbine nozzle
sfc = specific fuel consumption
T_{oi} = stagnation temperature at station i
t = time
η = total-to-total, isentropic or polytropic efficiency

Subscripts

a = air
c = compressor
d = at the design point
max = maximum
o = initial value
p = combustion products
t = turbine

Table 1 General electric MS7001B performance specifications

Inlet temperature	15°C (59°F)
Inlet pressure	1 atm
Shaft speed	3600 rpm
Air mass flow	245 kg/s (541 lb/s)
Compressor pressure ratio	9.4
Firing temperature	1010°C (1850°F)
Exhaust temperature	510°C (950°F)
General output	60,000 kW
Heat rate	11,740 kJ/kWh (11,130 Btu/kWh)

a_3 and a_4 in equations (3) and (4) may be lowered to account for reductions in turbine mass throughflow capacity and efficiency resulting from ash deposits.

A flowchart illustrating the complete analysis procedure used to obtain the engine operating point is shown in Fig. 2. A detailed description of the equations used in the analysis may be found in the Appendix of [10].

With the model thus developed capable of incorporating the effects of the ash deposits on the turbine performance and able to predict engine performance at off-design conditions, a suitable application was selected. A limited amount of operational data were available from two full-scale gas turbine engines, both of which were manufactured by the General Electric Company [11]. Both of these engines were model MS7001B units, capable of producing 60 MW of electrical output at full-rated ISO conditions. The first of these is operated by the Florida Power and Light Company at the DeBary site in central Florida. This unit is operated at the full-rated firing conditions on a residual fuel oil with relatively low contaminant levels and is used for peaking power only. The second unit is operated by the Alcoa Company at Paramaribo, Surinam, in northeastern South American. This unit is operated at slightly derated firing conditions on a relatively poor-grade residual, and is used in a baseload (continuous) application. Field tests were performed on each of these units, from which sufficient data were obtained to calculate the rate of decrease of the turbine mass throughflow capacity. In addition, the rate of decrease of engine power was also documented.

Recall that the required inputs to the engine simulation model are the rates of decrease of the turbine mass throughflow capacity and the turbine efficiency. The rate of decrease of engine power is the model output. In this particular case, the simulation may be used to determine the rate of decrease of turbine efficiency. From the field data, it was determined that the ratio of the rate of engine power loss to the rate of decrease in turbine mass throughflow capacity was approximately 2.5.[1] By examining various cases with different rates of turbine efficiency loss, the proper rate may be determined to yield this ratio.

A design-point cycle analysis was performed using the rated performance specifications of the MS7001B. These specifications are given in Table 1, and the assumptions underlying the cycle analysis and its results are given in Table 2. This analysis was necessary to determine the value of several of the coefficients in equations (1-4). The remaining unknown coefficients were a_1, a_2, $\eta_{c,\max}$, and $(\dot{m}_a\sqrt{T_0}/p_{01})_{@\eta_{c,\max}}$. Each of these terms relates to the off-design compressor performance characteristics. Several cases were examined to investigate the sensitivity of the simulation results to these variables. The coefficient a_1 in equation (1), which is the slope of the compressor pressure ratio characteristic, was assigned the values 2 and 4. The three terms in equation (2) are used to set the value of the maximum compressor efficiency and the mass flow at which this occurs. Two cases were investigated. In the first case, the maximum efficiency was assumed to be 90 percent and to occur at a mass flow rate of 3 percent below the design value. This yielded a value of a_2 equal to 40.74. In the second case, the maximum efficiency was taken to occur at the design point, and the same value of a_2 as above was used. A summary of the resulting four test cases is given in Table 3.

[1] Mr. H.vonE. Doering of the General Electric Company in Schenectady, N.Y., is gratefully acknowledged for his insights regarding the field experiments.

Table 2 MS7001B design point cycle analysis – assumptions and results

Assumptions	
Compressor isentropic efficiency	0.867
Combustor pressure drop	0.04 P_{02}
Turbine inlet temperature	1043°C (1910°F)
Fuel lower heating value	42,600 kJ/kg (18,320 Btu/lb)
Combustion efficiency	0.99
Results	
Fuel/air ratio	0.0189
Compressor discharge temperature	309°C (588°F)
Total turbine cooling air flow	0.094 $\dot{m}_{air}$
First-stage nozzle cooling air flow	0.047 $\dot{m}_{air}$
Rotor and generator loss	2560 kW
Turbine isentropic efficiency	0.974

Table 3 Test case summary

Case	a_1	$\eta_{c,\max}$	a_2	$\dfrac{[m_a\sqrt{T_{01}}/p_{01}]_d}{[m_a\sqrt{T_{01}}/p_{01}]_{@\eta_{c,\max}}}$
1	2	0.867	40.74	1.00
2	4	0.867	40.74	1.00
3	2	0.900	40.74	0.97
4	4	0.900	40.74	0.97

The turbine efficiency in the engine simulation model was assumed to decrease linearly with the decrease in turbine mass throughflow capacity according to the following relation:

$$\frac{\Delta a_4}{(a_4)_0} = \frac{K_1 \Delta a_3}{(a_3)_0} \tag{5}$$

As previously mentioned, the engine power output has been observed to vary linearly with the decrease in turbine mass throughflow capacity, or

$$\frac{\Delta P}{(P)_0} = \frac{K_2 \Delta a_3}{(a_3)_0} \tag{6}$$

where K_2 is approximately 2.5. A numerical investigation was undertaken to determine the value of K_1 which would yield a value of K_2 equal to 2.5 for the four test cases given in Table 3.

With the results of the MS7001B engine simulation yielding the rates of turbine efficiency loss for the various test cases, application to other geometrically similar engines may be attempted. One such case of current interest is the water-cooled turbine engine [12]. Although prototype application of the water-cooled gas turbine is intended for much higher turbine inlet temperatures, turbine simulator data are available for a water-cooled turbine nozzle operating at MS7001B conditions [8, 13], making a direct comparison possible. Consider, for example, an engine with a water-cooled first-stage turbine nozzle, with the remainder of the engine exactly the same as the MS7001B. The major thermodynamic difference between the water-cooled turbine engine and the MS7001B is that the water-cooled engine rejects heat in the first-stage nozzle rather than having cooling air added. For this comparison, the same turbine firing temperature (T_{04}) was used as in the MS7001B, and a polytropic turbine efficiency was incorporated into the analysis to account for the heat rejected. The magnitude of

the heat rejected was determined by scaling the results of turbine simulator tests [13] to account for Reynold's number and geometry differences. The remaining effect to be accounted for is how the ash deposits affect the heat transfer. A linear decrease in heat load was assumed of the form

$$\frac{\Delta Q_{34}}{(Q_{34})_0} = \frac{K_3 \Delta a_3}{(a_3)_0} \tag{7}$$

where a value of K_3 of 2.6 was determined from the turbine simulator experiments [10]. These data are shown in Fig. 3. With these modifications, the water-cooled turine engine simulation was performed, using the same off-design component performance characteristics as before. Each of the four cases in Table 3 was investigated, using the values of K_1 determined from the MS7001B simulations. The results yielded a value of the coefficient K_2 indicating how the engine power output varies with ash plugging in the turbine.

In actual engine operation the principal performance characteristic of interest is how the engine power varies with time. As previously mentioned, turbine simulator experiments yield rates of decrease of nozzle mass throughflow capacity of the form

$$\frac{\Delta a_3}{(a_3)_0} = K_4 \Delta t \tag{8}$$

If K_4 is known, the rate of power output decrease can then be determined by combining equations (6) and (8) to yield

$$\frac{\Delta P}{(P)_0} = K_2 K_4 \Delta t = K_5 \Delta t \tag{9}$$

Turbine simulator data are available for air- and water-cooled turbine nozzles at MS7001B firing conditions [8, 13], from which the respective values of K_4 can be determined. From the relative magnitudes of the coefficient product, K_5, a measure of estimated relative operational availabilities of the air- and water-cooled turbine engines is obtained.

The second operational characteristic, other then engine power output, which is of interest to the engine operator is the engine heat rate or specific fuel consumption. These parameters are indications of the overall efficiency of the engine and will increase during operation with residual fuels as the engine efficiency decreases. Choosing the specific fuel consumption as the parameter of interest, the rate of increase accompanying the decrease in turbine mass throughflow capacity may be expressed as

$$\frac{\Delta sfc}{(sfc)_0} = K_0 \frac{\Delta a_3}{(a_3)_0} \tag{10}$$

Using equations (8) to introduce time as the independent variable yields

$$\frac{\Delta sfc}{(sfc)_0} = K_4 K_0 \Delta t = K_7 \Delta t \tag{11}$$

The relative magnitudes of the coefficient, K_7, for the air-cooled turbine and water-cooled turbine engine simulations yield a second measure of the engine performance during operation with residual fuel oil.

Results and Discussion

The results of the numerical simulations of the air- and water-cooled gas turbine engines, discussed in the previous section, are summarized in Table 4. Four cases are considered, corresponding to the four types of compressor characteristics described in the previous section (see Table 3).

The results of the air-cooled turbine engine simulation are expressed in terms of the value of the coefficient, K_1, in the second column of Table 4. Recall that this term, defined by equation (5), is the coefficient of proportionality between the decrease in turbine mass throughflow capacity and the decrease in turbine efficiency. The values given in the table were found to result in a value of the coefficient, K_2, defined by equation (6), of 2.5. Note that the values of K_1 obtained in cases 1 and 2 were 0.68 and 0.74, respectively. The slightly larger value for case 2 results from the fact that the compressor mass flow rate is not decreased as much as case 1, and thus higher compressor efficiencies are maintained. The turbine efficiency must be lowered at a higher rate. In cases 3 and 4, the values of K_1 obtained were 0.88 and 0.86, respectively. The trend observed in cases 1 and 2 was reversed in these cases because reductions in compressor mass flow resulted in increasing rather than decreasing compressor efficiency. This result also accounts for the higher values of the coefficient, K_1, in case 3 and 4.

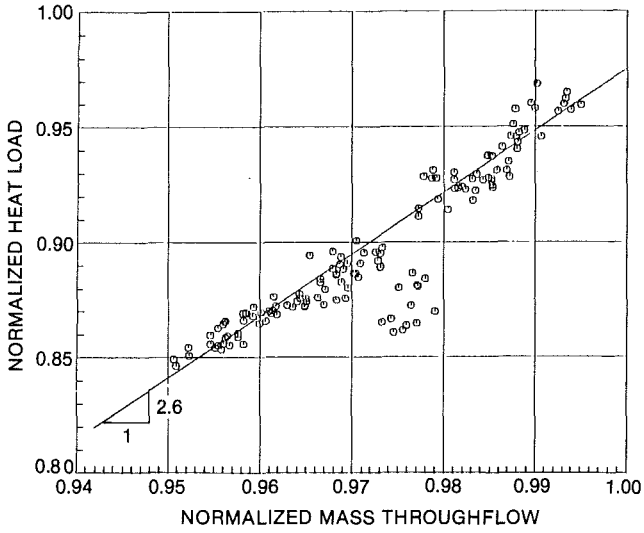

Fig. 3 Nozzle heat load variation with throat area correlation

Table 4 Engine Simulation Results

Case	K_1	$(K_2)_{wc}$	$\frac{(K_5)_{wc}}{(K_5)_{ac}}$	$\frac{(K_7)_{wc}}{(K_7)_{ac}}$
1	0.68	2.3	0.68	0.61
2	0.74	2.3	0.68	0.62
3	0.88	2.3	0.68	0.62
4	0.86	2.3	0.68	0.62

The values of the coefficient, K_1, obtained from the MS7001B simulation, indicate that the turbine efficiency decrease, required to obtain engine power loss rates observed in the field, is relatively insensitive to changes in the compressor performance characteristics.

The results of the water-cooled turbine engine simulation are expressed in terms of the coefficient, K_2, in the third column of Table 4. In this simulation, the same values of the coefficient, K_1, from the air-cooled turbine engine simulation were used. Recall that a value for K_2 of 2.5 was used in the air-cooled simulation. In cases 1 and 2, the value of K_2 obtained for the water-cooled turbine engine was 2.3, a value of 8 percent less than for the air-cooled engine. If the rates of turbine mass throughflow decrease resulting from ash deposits were the same for each engine, then the water-cooled turbine engine would be available for 8 percent greater time before a similar power loss is suffered. For cases 3 and 4 of the water-cooled turbine engine simulation, a value of the coefficient K_2 of 2.3 for each case was again obtained. These results seem to indicate that the rate of power decrease which would be observed in a water-cooled turbine engine, assuming equal amounts of ash deposits as in its air-cooled turbine counterpart, would be less by approximately 8 percent. Furthermore, this result appears to be insensitive to the off-design performance characteristics of the compressor.

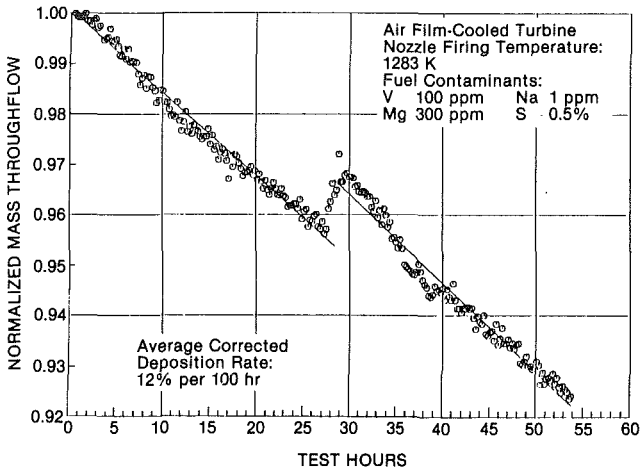

Fig. 4 Nozzle throat area history for test number 1

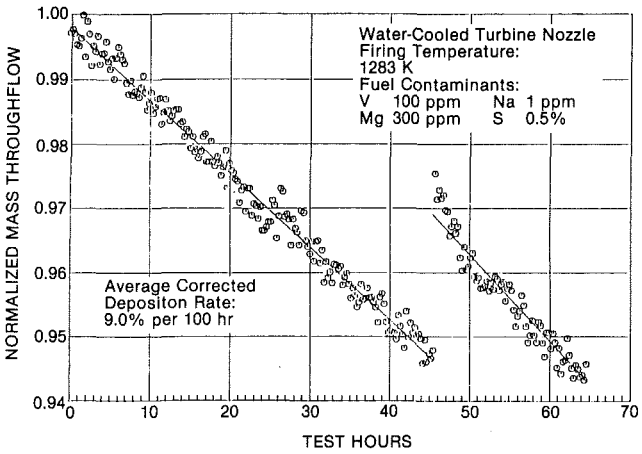

Fig. 5 Nozzle throat area history for test number 2

For a true comparison of the relative operational availabilities of the two engine types being investigated, time must be introduced as the independent variable through equation (8), and thus the magnitude of the coefficient, K_4. Turbine simulator data, taken at MS7001B firing conditions and corrected for nozzle throat widths, indicate that the coefficient, K_4, for the water-cooled turbine nozzle is 25 percent lower than for an air-cooled nozzle [10]. Data from these tests are shown in Figs. 4 and 5. A relative comparison may be obtained with these data of the time-availability coefficients, K_5, in equation (9). These coefficients are summarized in the fourth column of Table 4. The time availability of the water-cooled turbine engine is 32 percent greater than its air-cooled counterpart.

The specific fuel consumption comparison, again in terms of the relative magnitudes of the time-related coefficients, is summarized in column 5 of Table 4. The rate of increase in specific fuel consumption is decreased 38 percent to 39 percent with the water-cooled turbine. As before, these results are insensitive to the compressor characteristic.

Conclusions

An empirically-based engine simulation model has been developed to analyze the operation of gas turbine engines on ash-bearing fuel. This model was calibrated by applying it to an engine (MS7001B) with available field operational data. The model was then applied to a near-term, advanced-cooled turbine engine design consisting of a first-stage turbine nozzle with water cooling.

The results of the engine simulation indicate that the water-cooled turbine engine would operate for a 32 percent greater time period before experiencing the same output power loss as the air-cooled turbine engine. This increase is attributable to thermodynamic differences as well as to the lower rate of ash deposit formation. The rate of specific fuel consumption increase in the water-cooled turbine engine was 38 percent to 39 percent less than that of its air-cooled counterpart. In the case of either power output or fuel consumption calculations, the compressor performance model chosen had no effect on the final results.

From the engine simulation results, it is thus concluded that the water-cooled turbine engine would yield improved performance through both increased availability and lower specific fuel consumption.

References

1 Kaupang, B. N., "Why Gas Turbines?" Gas Turbine Reference Library Publication No. GER-3113, 1979, General Electric Company.

2 Mordell, D. L., and Foster-Pegg, R. W., "Test of an Experimental Coal-Burning Gas Turbine," ASME paper 55-A-158.

3 McKee, J. P., and Corey, R. C., "Bureau of Mines Coal-Fired Gas Turbine Research Project," *Combustion*, Apr. 1969, pp. 67–72.

4 Shah, R. P., and Corman, J. C., "Open Cycle Gas Turbine/Steam Turbine Combined Cycles with Synthetic Fuels from Coal," ASME paper 77-WA/Ener-9.

5 Strong, R. E., "Combined Cycles for Operation on Coal-Derived Fuels with High Temperature Combustion Turbines," ASME paper 77-WA/Ener-14.

6 Buckland, B. O., Kindl, F. H., and Lukas, H., "Worldwide Survey of Current Experience Burning Residual and Crude Oils in Gas Turbines," AF-1243, Technical Planning Study (TPS) 78-833, Dec. 1979, prepared by Encotech, Inc., for EPRI.

7 Pavri, R. E., and Hill, J. M., "Thermodynamics of Heavy Fuels Operations in Gas Turbine," ASME paper 80-GT-171.

8 Blanton, J. C., Durgin, G. A., and Palko, J. E., "Heavy Fuels Ash Deposit Formation and Removal in Water-Cooled High Temperature Gas Turbines," paper presented at ASME Gas Turbine Conference, London, England, Apr. 18–22, 1982.

9 Spengler, C. J., Lee, S. Y., and Young, W. E., "The Pressurized Passage, a Laboratory Rig for Gas Turbine Simulation," *Deposition and Corrosion in Gas Turbines*, edited by A. B. Hart and A. J. B. Cutter, John Wiley and Sons, 1973, pp. 294–330.

10 Blanton, J. C., "An Investigation of Residual Fuel Oil Ash Deposit Formation and Removal in Cooled Gas Turbine Nozzles," Ph.D. dissertation, Virginia Polytechnic Institute and State University, July 1981.

11 Hefner, W. J., and Lordi, F. D., "Progress in Heavy Fuels," Gas Turbine Reference Library Publication No. GER-3110A, General Electric Company, 1979.

12 Horner, M. W., Caruvana, A., Cohn, A., and Smith, D. P., "Near Term Application of Water Cooling," ASME paper 80-GT-159.

13 Blanton, J. C., and Durgin, G. A., "The Effect of Heavy Liquid Fuels Ash Deposition on Heat Transfer in a Water-Cooled Turbine Nozzle Sector," ASME paper 80-HT-15.

W. O. Afejuku
Nigerian National Petroleum Corporation,
Lagos, Nigeria

N. Hay

D. Lampard
Department of Mechanical Engineering,
University of Nottingham,
Nottingham, NG7 2RD,
United Kingdom

Measured Coolant Distributions Downstream of Single and Double Rows of Film Cooling Holes

A mass-transfer technique has been used to investigate experimentally the distribution of coolant from two rows of holes with independently varied blowing rates. Both staggered and in-line configurations were investigated for two injection angles and a range of row spacings. Detailed concentration distributions measured at and above the surface are presented and a possible mechanism to account for the large differences in behavior between staggered and in-line configurations is discussed.

Introduction

The film cooling of turbine blades and nozzle guide vanes usually requires the use of a succession of rows of film cooling holes. To assist in the development of film cooling systems, numerous experimental studies have been made, with attention being centerd on single row or full-coverage arrangements using multiple rows spaced at 10 hole dia or less. The urgent need to establish the dependence of the film cooling effectiveness upon a wide range of geometric and flow parameters for the purposes of thermal design optimisation of blades and vanes has resulted in the measurement of only the film cooling effectiveness by most investigators.

Recently, Bergeles et al. [1], [2], and [3] have shown that contemporary numerical flow calculation procedures permit the satisfactory calculation of effectiveness for shallow injection angles with low blowing rates for both a single row and two close-spaced rows of holes. The procedures are not so successful at high blowing rates or close to the cooling holes. The proper development and testing of such predictive schemes requires the existence of a body of experimental data relating to the coolant distribution above the surface, in addition to effectiveness data. As indicated in [3], the flow region immediately downstream of the injection point is particularly crucial in the modeling of the injection process.

In an earlier paper [4], the performance of a double row of discrete holes has been discussed in terms of the variation spanwise and area-averaged effectiveness with row spacing, injection angle and blowing rate. In the present paper, details are reported of the surface distribution of the coolant, and its distribution above the surface for both one and two rows of holes with the dual aims of the provision of data for program development and of giving a better insight into the local mixing and entrainment phenomena which determine the performance of a given film cooling geometry.

Experimental Techniques and Ranges of Parameters Studied

To simulate under isothermal conditions the injection of cold air into a hot gas stream, a mixture of Freon 12 with air was injected into an airstream. The proportions of Freon 12 and air in the injectant were chosen to give an injectant to mainstream density ratio of about 2, typical of turbine operating conditions.

Table 1 Main test parameters

Hole diameter, D	= 2.27 mm
Spacing to diameter ratio	= 3.0
Number of rows	= 2
Row spacings	= 10D, 20D, 30D, 40D
Injection angles	= 35 deg at both rows or 90 deg at both rows
Row configurations	= staggered or in-line (see Fig. 1)
Width of tunnel working section	= 381 mm
Injectant: mainstream density ratio ρ_j/ρ_∞	= 2.0
Mainstream velocity, u_∞	= 25 m/s
Blowing rate, M($\equiv \rho_j u_j/\rho_\infty u_\infty$)	= combinations of 0.5, 1, 2, 3 at the two rows
Boundary layer displacement thickness at the first row, δ^*/D	= 0.16
Pressure gradient	= zero

The injectant was introduced through long tubes set in a plate forming part of the flat floor of a wind tunnel. The tunnel wall boundary layer was bled off ahead of the first injecting row, and a trip wire was used to give a turbulent boundary layer. The thickness of the boundary layer was set by using a contoured roof in the tunnel to accelerate the flow over the boundary layer development section upstream of the injection point. At, and downstream of, the injection point, a zero pressure gradient condition was maintained. The plate containing the tubes could be traversed in a spanwise direction past an array of fixed tappings set in the tunnel floor. The concentration of Freon in samples drawn slowly through these tappings, or through an isokinetic sampling probe mounted on a traverse gear fixed to the tunnel roof, was measured using a thermal conductivity cell. High resolution mapping of the injectant distribution both at and above the surface could thus be carried out. The film cooling effectiveness was deduced from the Freon concentration in the samples drawn from the wall tappings relative to that in the injectant as described in [4].

A lateral (spanwise) traverse interval of 0.5 D was used for both measurements at and above the surface. For the surface

Contributed by the Gas Turbine Division of THE AMERICAN SOCIETY OF MECHANICAL ENGINEERS and presented at the 27th International Gas Turbine Conference and Exhibit, London, England, April 18-22. Manuscript received at ASME Headquarters December 11, 1981 Paper No. 82-GT-144.

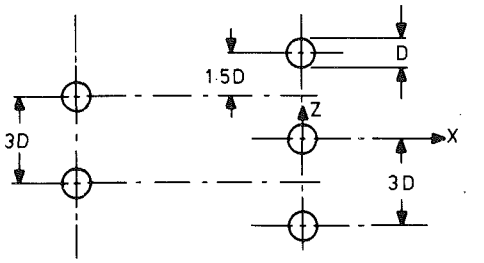

(a) staggered configuration

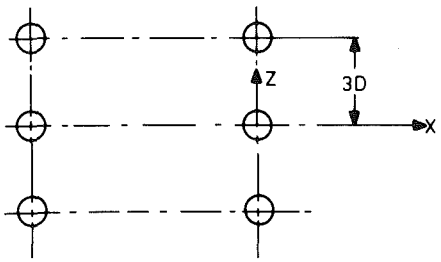

(b) in-line configuration

Fig. 1 Row configurations and coordinate system

measurements, the traverse commenced 1 D to one side of a hole centre and terminated at 2 D on the opposite side of the hole centre-line. For measurements above the surface, the range was 1.5 D either side of a hole centre, and vertical traverse increments commenced at 0.1 D and increased with distance from the surface.

Fuller details of the apparatus and techniques are given in [4] and [5]. Table 1 gives a summary of the test conditions and the range of parameters studied. Figure 1 shows the in-line and staggered row configurations used in the present investigations. Comparisons of the injectant distributions for the two configurations will be used to deduce explanation for the behaviour and interaction patterns of the injected flows.

Injectant Distribution Following Single Row Injection

Figure 2 shows surface concentration contours for 90 and 35 deg injection for the region up to 25 dia from the injection point at the relatively low nominal blowing rate, M, of 0.5. These contours have been produced by using a curve fitting routine with measured data as the input. Clear evidence is seen of the persistence of jet structures for considerable streamwise distances, as has previously been reported by Liess and Carnell [6] and by Foster and Lampard [7]. It is also evident that normal injection results in much faster mixing and consequent jet dilution than for shallow angle injection.

Measurements of the concentration within the cooling film made in the plane of the jet centreline, Fig. 3, indicate that the jet structure can still be present at streamwise distances of the order of 40 dia, the maximum spacing employed in the two-

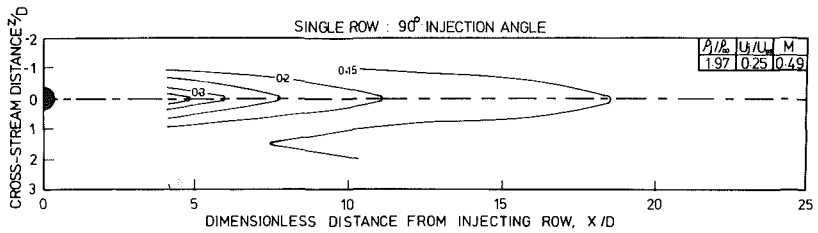

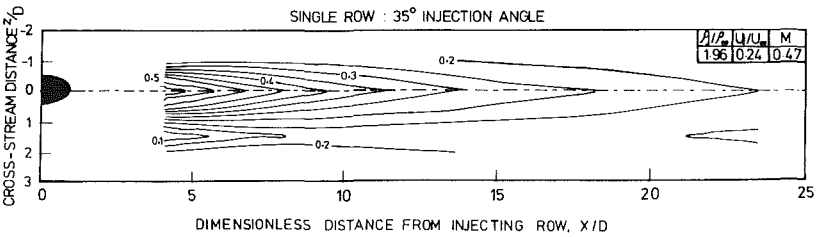

Fig. 2 Effect of injection angle on the surface concentration (effectiveness) distribution for a single row at $M = 0.5$

Nomenclature

c = concentration (by mass)
D = injection hole diameter
M = blowing rate, $\dfrac{\rho_j u_j}{\rho_\infty u_\infty}$
u = velocity
x = streamwise coordinate (measured from hole centre)
y = coordinate normal to surface
z = cross-stream (spanwise) coordinate
α = injection angle
δ^* = boundary layer displacement thickness
ρ = density

Subscripts

up = value at upstream row
down = value at downstream row
c = value along centre-line ($z = 0$)
j = jet (injectant)
w = wall ($y = 0$)
∞ = freestream

row studies of the present work. Film nonuniformity as determined by the peakiness of the concentration profiles is seen to increase with decreasing injection angle and with increasing blowing rate. It is certain that jet lift-off will have occurred at the higher nominal blowing rate of 2.0, and this has resulted in the presence of a pronounced peak at some distance from the surface in the concentration distribution for 35 deg injection.

The presence of jet structures in the film produced by the upstream row of holes will clearly affect the mixing of any coolant injected into the film from any subsequent row of holes. The relative configuration of the holes in the two rows, the blowing rates, the row separation, and the injection angle might all be expected to result in changes in the mixing at, and downstream of, the second row. Some of the gross effects, and their implications from the design standpoint, have been discussed by the authors in an earlier paper [4]. In particular, it was noted that a staggered configuration gave markedly superior spanwise averaged effectiveness to an in-line configuration for shallow injection angles, high blowing rates, and small row spacings, all of which the single row results above would indicate as leading to strong film nonuniformity approaching the second row.

Injectant Distribution Following Injection Through Two Rows

Comparison of Surface Distributions for In-line and Staggered Configurations. Figure 4 compares the relative concentration, c_w/c_j, distributions in the surface downstream of the second row for staggered and in-line configurations. The row spacing is the smallest used in the present investigation – 10 dia – and the nominal blowing rates at the upstream and downstream rows are 3 and 0.5, respectively. The combination of the shallow injection angle (35 deg) with the high upstream blowing rate implies that the upstream film will be highly nonuniform. Despite this, the contours are similar in form to that of a single row, Fig. 2, with similar peak relative concentrations, c_w/c_j, of around 0.6 being recorded in all cases. Inspection of the region between the holes, $z/D=1.5$, close to the injection point, $x/D=5$, does, however, reveal a significant difference. For single row injection, the relative concentration falls to less than 0.1, while the corresponding levels for in-line and staggered two row configurations are 0.2 and 0.3, respectively.

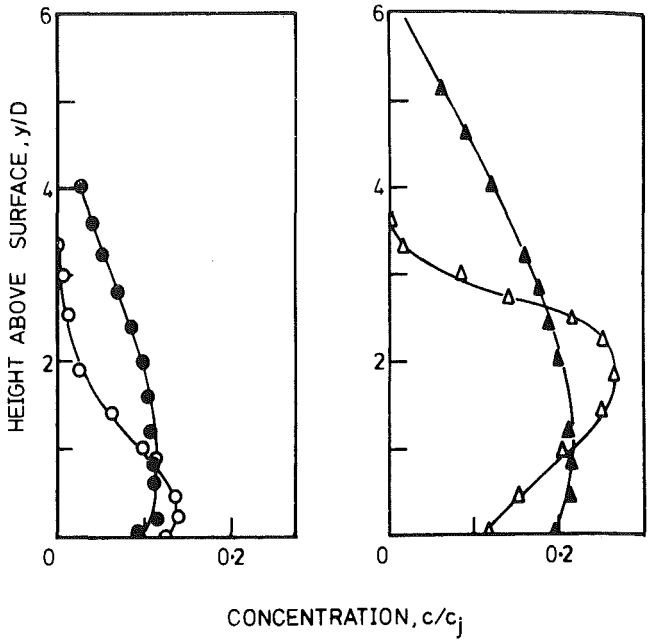

	α	$\frac{\rho_j}{\rho_\infty}$	$\frac{U_j}{U_\infty}$	M	$\frac{X}{D}$
○	35°	2·03	0·25	0·51	38·3
●	90°	1·97	0·24	0·48	
△	35°	1·98	0·99	1·97	
▲	90°	2·01	1·01	2·03	

Fig. 3 Effect of blowing rate and injection angle variations on the centerline concentration distribution above the surface for single row injection

These increased levels in the region between the jets from the second row result in a reduction of the jet dilution further downstream. On the jet centerline between $x/D=20$ and 25 the relative concentration for a single row at 35 deg is around 0.2 (Fig. 2), whereas for two rows in the in-line configuration (Fig. 4) it is 0.25 and, for the staggered configuration, in excess of 0.3.

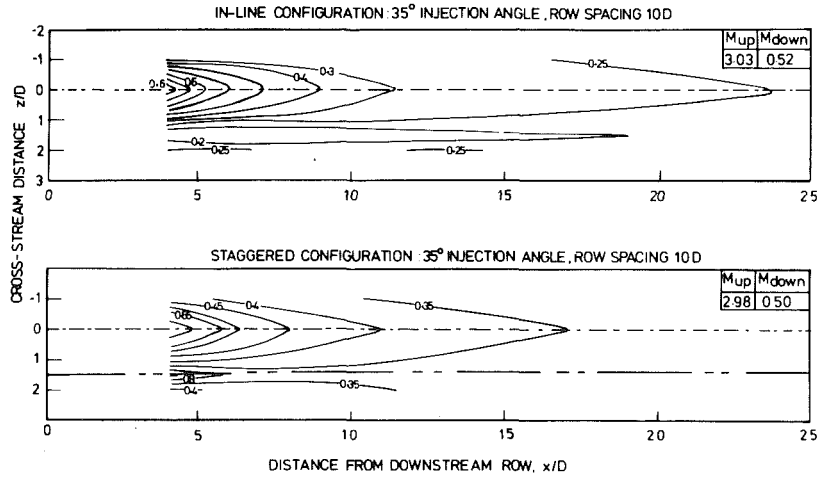

Fig. 4 Comparison of surface concentration (effectiveness) distributions for in-line and staggered configurations at a row spacing of 10 dia

Evidently the staggered configuration results in enhanced levels not only in the interhole regions of the second row, but also in the regions beneath the jets from the second row except very near the injection point.

Injectant Distribution Above the Surface. Traverses to measure relative local concentrations above the surface were made in the plane $x/D=4.09$ and also the plane $z/D=0$, on the centreline of a hole in the downstream row.

Figure 5 shows contours of relative concentration for 35 deg injection angle and a row spacing of 10 dia with nominal blowing rates of 0.5 and 1.0 at upstream and downstream rows, respectively. Under these conditions, the jets from the upstream row should remain attached to the surface, and Fig. 2 indicates that the peak surface relative concentration level arising from these jets at the traverse location would be around 0.2 to 0.25. This is seen to correspond to the level at $z/D=1.5$ for the staggered configuration. The level in this interhole region for the in-line configuration of between 0.1 and 0.2 is typical of the corresponding region for the single row (Fig. 2). Although the peak levels recorded for the two configurations were identical, the extent of the region of maximum concentration is greatest for the in-line case, and the jet structure is clearly stronger. No structure relating to the upstream jets is discernible for either configuration.

It can be concluded that, for the in-line configuration, the upstream jet provides a measure of shielding for the downstream resulting in less vertical and lateral diffusion than for the staggered configuration.

Changing the injection angle to 90 deg at both rows (Fig. 6) results in a much thicker film for both configurations with broadly the same characteristics as for the 35 deg injection case discussed above, see Fig. 6. The level between the holes is, however, rather higher in both cases than that indicated as arising from the upstream row of holes. This is a consequence of the faster mixing resulting from the increased injection angle which has caused a tendency towards coalescence of the downstream jets. The peak relative concentration levels in the jets have also been considerably reduced by this mechanism.

It is interesting to note that the in-line configuration is approaching lift-off conditions rather more closely than the staggered configuration. It may be that lift-off is inhibited in the latter case by enhanced lateral mixing arising from the upstream jets in the inter-hole spaces.

Effect of Blowing Rate and Row Spacing Variation. As noted in [4], the effectiveness distribution downstream of the second row depends on the blowing rate at that row, the blowing rate at the upstream row, and the row separation in a complex fashion. If the upstream blowing rate and row separation are such that the film approaching the downstream row has achieved a good degree of two-dimensionality, then the effectiveness downstream of the second row will become independent of the relative arrangement of the holes in the two rows.

The region immediately downstream of the second row is most sensitive to upstream conditions. An examination of the behaviour in this region will therefore be used to infer the controlling mechanisms.

Figure 7 presents measured concentration distributions above the surface in the plane of a downstream hole centreline at $x/D=4.09$. The distribution for a single row injecting at a blowing rate of 2 is also shown for comparison. In every case, the peak concentration occurs well away from the surface indicating that the jets from the downstream row have lifted off.

Looking first at the staggered configuration with a row spacing of 10 dia, it is seen that the concentration peak for an upstream blowing rate of 0.5 is considerably further from the surface than that for a single (downstream) row. Increasing the blowing rate to 1 produces a shift back towards the

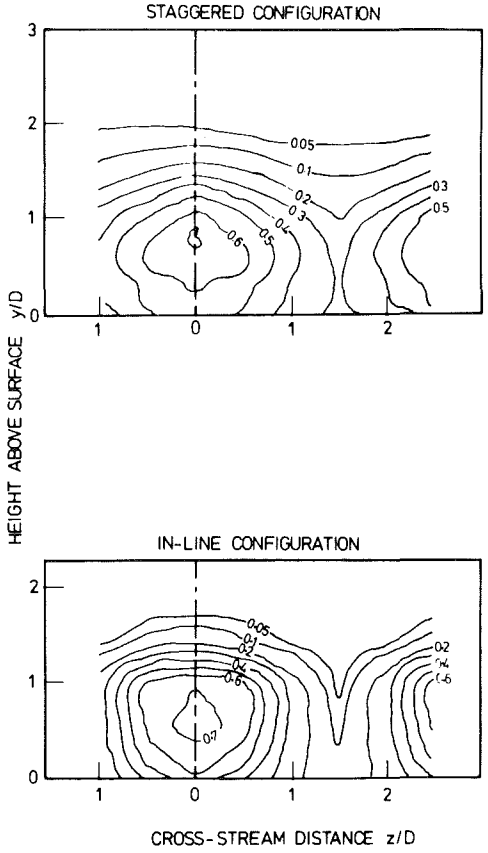

Fig. 5 Effect of row configuration on the concentration distribution above the surface at $x/D=4.09$ (35 deg injection; $M_{up}=0.5$; $M_{down}=1$)

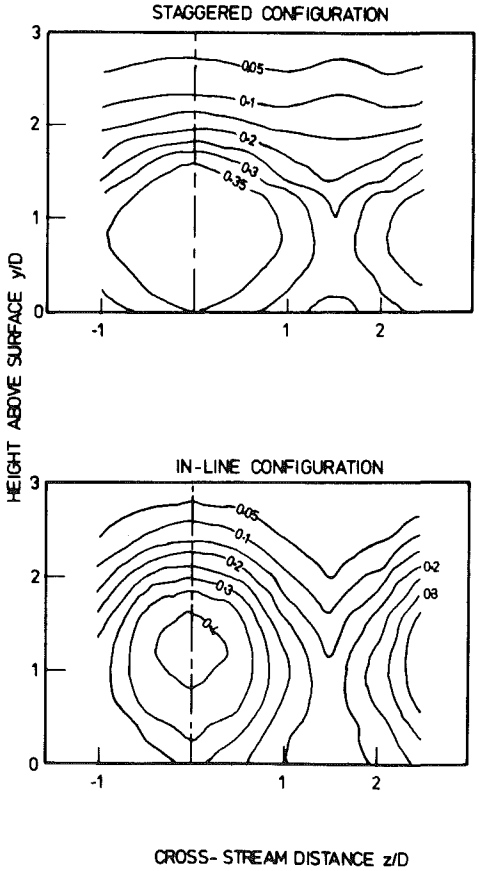

Fig. 6 Effect of row configuration on the concentration distribution above the surface at x/D = 4.09 (90 deg injection; $M_{up}=0.5$; $M_{down}=1$)

surface. At the same time, a progressive increase in the concentration close to the wall occurs as the upstream blowing rate increases from zero.

Bergeles et al. [3] inferred that the upstream jets may help to keep the downstream jets on the surface at high blowing rates, when considering the performance of two staggered rows spaced at 3.5 dia. Jabbari and Goldstein [8] have also noted greatly improved performance relative to a single row under similar conditions.

The inward movement of the concentration peak with increasing upstream blowing rate seems in accordance with these observations, but the higher trajectories relative to single row injection warrant some explanation.

It seems probable that it is the momentum distribution within the approaching upstream film that controls the downstream jet trajectory. For the present work, a density ratio of injectant to mainstream of 2 has been used, and consequently a blowing rate of 0.5 gives a corresponding momentum flux ratio of one-eighth. At the 0.5 blowing rate, therefore, the film approaching the downstream row will have considerably less momentum than the boundary layer approaching the single row operating alone. Moreover, pockets of low momentum will exist in the film in the regions between the downstream jets. An increase in the jet penetration above that observed for a single row is therefore to be expected.

Increasing the upstream blowing rate to 1 decreases the momentum deficit in the film resulting in an inward movement of the downstream jets. The progressive increase in wall concentration seen with increasing upstream blowing rate can be explained by entrainment of fluid from the upstream film into the region beneath the downstream jets. It should be noted that for high upstream blowing rates the concentration in the film will increase with distance from the wall. It is therefore possible for a rise in effectiveness above that given by the upstream row to occur beneath the downstream jets if they draw in fluid from the region above the wall.

Turning now to the concentration distributions for the in-line configuration with 10 dia row spacing, it is seen that at an upstream blowing rate of 0.5, the concentration peak remains at the same distance from the surface as for a single row. An increase in the blowing rate to 1 leads to a movement of the peak away from the wall. The wall concentration is seen first to increase, then decrease.

The disparate behaviour of the in-line and staggered configurations can be reconciled if it is argued that it is momentum of the flow between the downstream jets that controls their trajectory. For the in-line configuration, very low concentrations occur in these gaps when the upstream blowing rate is 0.5 (see Fig. 5), indicating the predominance of the mainstream flow with its associated high momentum. The jet trajectory is therefore close to that of an isolated row.

As noted earlier, the upstream jets seem to form a sheath around the downstream for the in-line configuration. When the upstream blowing rate is increased, the jet structure approaching the downstream row increases in cross section and the 'sheaths' from adjacent jets coalesce, filling the gaps between the downstream rows with relatively low momentum fluid. The downstream jets therefore lift off, and the peak concentration now occurs at a distance from the wall similar to that for the staggered configuration.

The filling of the interhole space with low momentum fluid from the upstream row could account also for the relatively poorer resistance to lift-off of the in-line configuration seen in Fig. 6. With the 90 deg injection angle, a more diffuse jet is obtained at any given blowing rate than with the 35 deg angle. Consequently, the gaps between the holes of the downstream row become blocked by the low momentum fluid at a lower upstream blowing rate.

Finally, for the larger row spacings shown in Fig. 7 (40 dia for the staggered, and 30 dia for the in-line configuration) an

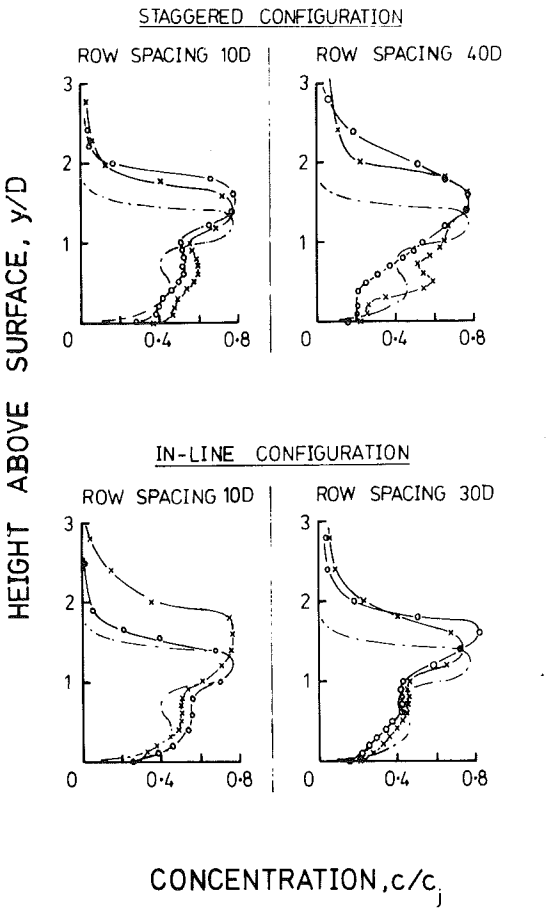

Fig. 7 Centerline concentration distributions above the surface at $x/D = 4.09$ at a downstream blowing rate, $M_{down} = 2$. (Injection angle 35°; – o – $M_{up} = 0.5$, $M_{down} = 2$; – x – $M_{up} = 1$, $M_{down} = 2$ – · – single row, $M_{down} = 2$)

outward movement of the concentration peak of about the same magnitude occurs for both configurations. With the increased development lengths available, the upstream film becomes much more uniform. It will be much thicker and have a larger momentum deficit than the boundary layer which would exist in its absence. Jet penetrations above those seen for the single row are therefore not unexpected. A small inward shift occurs for the in-line configuration as the upstream blowing rate is increased from 0.5 to 1. For the staggered configuration, the peak appears to remain at the same level. However, there is a considerable change in the profile shape beneath the peak, and comparison of the profiles above the peak does indicate that this may be masking an inward shift similar to that for the inline configuration.

Concluding Remarks. Measured concentration distributions at and above a flat surface with two rows of injecting holes have been presented for a range of geometric and flow conditions. Strong differences have been shown to result from the use of staggered and in-line configurations.

It is tentatively suggested that the momentum flux in the upstream film in the zones between the downstream holes plays a crucial role in the control of the trajectory of the jets from the downstream row. An increased momentum flux reduces the tendency to lift-off, and, when lift-off occurs, results in a lower trajectory.

These observations help to explain the excellent film cooling performance at high blowing rates reported for two close-spaced staggered rows by Jabbari and Goldstein [8] and Bergeles et al. [3]. It is also in accordance with the earlier conclusion of the present authors [4] that, where different

blowing rates are used at the two rows, the best cooling performance is obtained by applying the highest at the upstream row.

Acknowledgments

This work was supported by a grant from the Science Research Council and carried out in the Department of Mechanical Engineering at Nottingham University. The financial support and the use of the facilities are gratefully acknowledged.

References

1 Bergeles, G., Gosman, A. D., and Launder, B. E., "The Prediction of Three-Dimensional Discrete-Hole Cooling Processes—1: Laminar Flow," ASME *Journal of Heat Transfer*, Vol. 98, 1976, p. 379.

2 Bergeles, G., Gosman, A. D., and Launder, B. E., "The Turbulent Jet in a Cross-Stream at Low Injection Rates: a Three-Dimensional Numerical Treatment," *Numerical Heat Transfer*, Vol. 1, 1978.

3 Bergeles, G., Gosman, A. D., and Launder, B. E., "Double-Row Discrete-Hole Cooling: an Experimental and Numerical Study," ASME JOURNAL OF ENGINEERING FOR POWER, Vol. 102, 1980, p. 498.

4 Afejuku, W. O., Hay, N. and Lampard, D., "The Film Cooling Effectiveness of Double Rows of Holes," ASME JOURNAL OF ENGINEERING FOR POWER, Vol. 102, 1980, p. 601.

5 Afejuku, W. O., "Superposition of Cooling Films," Ph.D. thesis, University of Nottingham, 1977.

6 Liess, C. and Carnell, J., "Application of Film Cooling to Gas Turbine Blades," *High Temperature Turbines*, AGARD CP 73-71, 1971, pp. 23.1-23.9.

7 Foster, N. W. and Lampard, D., "The Flow and Film Cooling Effectiveness Following Injection Through a Row of Holes," ASME JOURNAL OF ENGINEERING FOR POWER, Vol. 102, 1980, p. 584.

8 Jabbari, M. Y. and Goldstein, R. J., "Adiabatic Wall Temperature and Heat Transfer Downstream of Injection Through Two Rows of Holes," ASME JOURNAL OF ENGINEERING FOR POWER, Vol. 100, 1978, p. 303.

blowing rates are used at the two rows, the best cooling performance is obtained by applying the highest at the upstream row.

Acknowledgments

This work was supported by a grant from the Science Research Council and carried out in the Department of Mechanical Engineering at Nottingham University. The financial support and the use of the facilities are gratefully acknowledged.

References

1 Bergeles, G., Gosman, A. D., and Launder, B. E., "The Prediction of Three-Dimensional Discrete-Hole Cooling Processes—1: Laminar Flow," ASME *Journal of Heat Transfer*, Vol. 98, 1976, p. 379.

2 Bergeles, G., Gosman, A. D., and Launder, B. E., "The Turbulent Jet in a Cross-Stream at Low Injection Rates: a Three-Dimensional Numerical Treatment," *Numerical Heat Transfer*, Vol. 1, 1978.

3 Bergeles, G., Gosman, A. D., and Launder, B. E., "Double-Row Discrete-Hole Cooling: an Experimental and Numerical Study," ASME JOURNAL OF ENGINEERING FOR POWER, Vol. 102, 1980, p. 498.

4 Afejuku, W. O., Hay, N. and Lampard, D., "The Film Cooling Effectiveness of Double Rows of Holes," ASME JOURNAL OF ENGINEERING FOR POWER, Vol. 102, 1980, p. 601.

5 Afejuku, W. O., "Superposition of Cooling Films," Ph.D. thesis, University of Nottingham, 1977.

6 Liess, C. and Carnell, J., "Application of Film Cooling to Gas Turbine Blades," *High Temperature Turbines*, AGARD CP 73-71, 1971, pp. 23.1-23.9.

7 Foster, N. W. and Lampard, D., "The Flow and Film Cooling Effectiveness Following Injection Through a Row of Holes," ASME JOURNAL OF ENGINEERING FOR POWER, Vol. 102, 1980, p. 584.

8 Jabbari, M. Y. and Goldstein, R. J., "Adiabatic Wall Temperature and Heat Transfer Downstream of Injection Through Two Rows of Holes," ASME JOURNAL OF ENGINEERING FOR POWER, Vol. 100, 1978, p. 303.

DISCUSSION

G. E. Andrews[1]

The technique of using Freon and air mixtures to simulate a density difference which in practice arises from a temperature difference has implications for hole size and coolant pressure loss. The technique essentially allows the velocity and densiy of the coolant air to be varied independantly, whereas in practice density and velocity variations are directly linked. The test conditions of the author are presumably aimed at a simulation of actual conditions similar to a coolant temperature of 700K and a mainstream gas temperature of 1400K. For these temperatures Table 2 compares the engine velocity and coolant hole pressure loss parameters with the rig simulation of these engine conditions. For the same blowing rate the large differences in mainstream velocities and coolant jet efflux velocities could result in significant differences in turbulent mixing.

[1] Department of Fuel and Energy, University of Leeds, LEEDS LS2.9JT., U.K.

Table 2

	Rig simulation			Equivalent engine conditions		
M	U_∞	U_j	$\left(\frac{\Delta P}{P}\right)_j$	U_∞	U_j	$\left(\frac{\Delta P}{P}\right)_j$
	m/s	m/s	%	m/s	m/s	%
0.5	25	6.3	0.05	117	29	0.21
1	25	12.5	0.18	117	58	0.85
2	25	25.0	0.73	117	117	3.39
3	25	37.5	1.64	117	175	7.63

The wall pressure loss ($\Delta P/P$) has been calculated, assuming a unity discharge coefficient for the long tube used. For practical wall hole geometries, the C_D would be lower, and for the same blowing rate the pressure loss would be higher. We have found that the wall pressure loss, and hence coolant hole size, is a very significant parameter in wall cooling effectiveness.

Closure

The discussor raises three points: namely, how to specify the blowing parameter, the fact that density and velocity are coupled in the real situation, and the effect of absolute velocity on mixing.

Taking the first point, in the paper the blowing parameter is defined as $\rho_c u_c / \rho_\infty u_\infty$ *at exit from the hole*. The use of wall pressure drop is appropriate where hole feed and hole geometry are also being modeled as is usual in the combustor situation. With our definition, the coolant hole pressure loss is already included. The fact that the hole pressure loss is different in the rig so that in the equivalent engine conditions will not affect the film cooling situation since the blowing parameter is matched at exit from the hole.

In the case of turbine blades and vanes, the supply conditions to successive rows may differ. This means that velocities and densities at the two rows are not necessarily coupled as the discussor implies. For these reasons, we have not attempted the precise simulation of any particular real case, but rather have preferred to set the hole exit conditions and to use a single density ratio which is typical of turbine conditions. The intention is, as explained in the paper, to provide data for testing computer predictions, and to shed some light on the flow mechanisms which control the mixing of the coolant jets and mainstream flow.

Addressing the last point, since the velocity and density ratios, and mainstream Reynolds number based on the injection hole diameter are similar to those encountered in turbines, we would not expect the mixing observed in the rig to differ significantly from that occurring under turbine conditions.

An Investigation of Ingress for an "Air-Cooled" Shrouded Rotating Disk System With Radial-Clearance Seals

U. P. Phadke

J. M. Owen

School of Engineering and Applied Sciences,
University of Sussex,
England

In order to model the flow between an air-cooled gas turbine rotor and its stationary casing, a simple isothermal plane rotating disk and stator are used. In tests reported earlier, the cavity between the rotor and stator was sealed by a stationary cylindrical shroud, and the dimensionless minimum amount of "coolant," $C_{w,\,min}$, necessary to prevent a radial inflow (or ingress) of "hot gas" through the axial clearance between the shroud and the rotor, was determined. In the current tests, a number of seals with a radial clearance between the cylindrical shroud and the rotor are tested. Unlike their axial-clearance counterparts, radial-clearance seals can exhibit a pressure-inversion effect, where the pressure inside the cavity increases, rather than decreases, with increasing rotational speed. Using pressure measurements and flow visualization, correlations showing the variation of $C_{w,\,min}$ with clearance ratio and rotational Reynolds number are presented, and it is shown that—under equivalent conditions—a seal with a radial clearance can be much more effective than one with an axial clearance.

1 Introduction

In recent years, the quest for improved performance has led to great interest in the study of disk sealing and cooling air systems of gas turbines. The disk cooling air must not only remove the heat conducted into the disk from the blades but must also prevent the ingress of hot gas into the cavity between the disk and its stator. Bayley and Owen [1] used a plane disk rotating close to a plane stator to model the more complex geometry of an air-cooled gas turbine rotor; the axial clearance between the rotor and stator was restricted at the outlet by means of a cylindrical shroud fitted to the stator. From pressure measurements for gap ratios of $G = 0.06$, 0.12, 0.18 ($G \equiv s/r_{o,R}$, s being the axial clearance between the disk, of radius $r_{o,R}$, and its stator) and shroud axial clearance ratios of $G_{ca} = 0.0033$, 0.0067 ($G_{ca} \equiv s_{ca}/r_{o,R}$, s_{ca} being the axial clearance between the disk and the shroud), they found that the minimum dimensionless flow rate required to prevent ingress, $C_{w,\min}$, could be estimated by

$$C_{w,\min} = 0.61\, G_{ca}\, \mathrm{Re}_\theta \qquad (1)$$

where $C_w \equiv \dot{m}/\mu r_{o,R}$ and $\mathrm{Re}_\theta = \rho\omega r_{o,R}^2/\mu$, $\dot{m}$ being the coolant mass flow rate, and ω the rotational speed of the disk.

Owen and Phadke [2] studied the sealing behaviour of a similar rotor-stator system, incorporating an axial clearance between a shrouded stator and rotor (seal A, fig. 1), for clearance ratios in the range $0.0025 < G_{ca} < 0.04$ for a fixed gap ratio of $G = 0.1$. From detailed pressure measurements and flow visualization, they obtained the following generalised correlation for $C_{w,\min}$, the minimum dimensionless mass flow rate to prevent ingress:

$$C_{w,\min} = 0.14\, G_{ca}^{\,0.66}\, \mathrm{Re}_\theta \qquad (2)$$

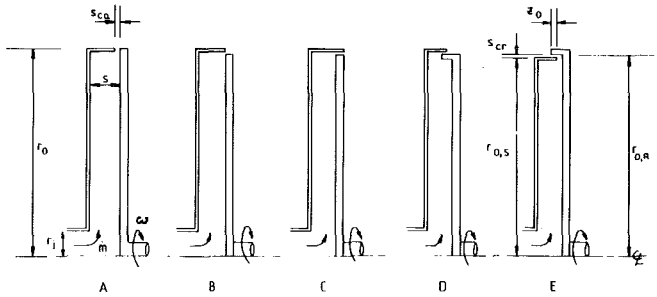

Fig. 1 Schematic diagram of rotor-stator seal configurations

Although the rotor-stator system incorporating an axial-clearance shroud provides a simple model, in real gas turbines the seals can have quite complicated geometries, utilizing radial clearances between the stationary and rotating components. In the present investigations, several different rotor-stator seals with radial clearances between cylindrical shrouds on both the rotor and the stator are studied; the different seal configurations tested are shown in Fig. 1.

These tests were conducted, as were the earlier tests, in the absence of an external axial flow, which occurs in an actual gas turbine. The object is to provide detailed information on which to base later tests using an external flow to simulate mainstream gas flow. The effects of external flow on these seal geometries will be discussed in subsequent papers.

The experimental apparatus is described in section 2.

Contributed by the Gas Turbine Division of THE AMERICAN SOCIETY OF MECHANICAL ENGINEERS and presented at the 27th International Gas Turbine Conference and Exhibit, London, England, April 18–22, 1982. Manuscript received at ASME Headquarters December 11, 1981. Paper No. 82-GT-145.

Pressure measurements and the determination of ingress are discussed in sections 3 and 4, respectively.

2 Experimental Apparatus

Figure 1 shows the different radial seal configurations tested. The various geometries were obtained by using different peripheral shrouds on both the rotor and the stator. The stator, with a nominal diameter (the actual diameter, for both the rotor and the stator, depended on the type of seal being used) of 378 mm, was made from perspex of 10 mm thickness and supported by four radial struts of aluminum 12.7 mm wide and 19.05 mm deep. The peripheral shrouds, with different axial widths, were made from 2 mm thick perspex and were secured to the stator by a retaining ring. Annular spacers were used between the stator and the shroud to provide the required stator diameter for each configuration.

The stator was instrumented with static pressure taps (0.25 mm dia) on four orthogonal radii. On the test radius, taps were located at radial positions of 65.5, 80.5, 95.5, 110.5, 125.5, 140.5, 155.5, 175.5, 180.5, 185.5 mm. On the other three radii, which were used to test axisymmetry of the flow, taps were located at radial positions of 80.5, 110.5, 140.5, 180.5 mm. For seals B and C, the stator shrouds were also instrumented with static taps at axial distances of 3.5, 7.5, 11.5, 15.5 mm from the free edge of the shroud. The pressure measurements were made with a Mercury M10 electromanometer (resolution 0.05 mm W.G.) incorporating an auto-zero facility.

Air, at flow rates up to $C_w = 2\text{x } 10^4$, was fed to the center of the stator via a pipe of 38 mm inside dia and length 1.2 m. The air was supplied from a Secomak centrifugal fan driven by a 1.5-kW motor and was metered, with an accuracy of 3 percent, by an Annubar differential pressure flow meter.

A "sandwich" construction was used for the rotor, with a perspex shroud being clamped between two tapered duralumin disks. The outside diameter of both disks was 360 mm, and the required working diameter (nominally 378 mm) was achieved by addition of the appropriate shroud. Several different shrouds were used in order to obtain the required rotor-edge configurations. Each shroud was clamped between the outer edges of the disks by means of twelve equispaced bolts. The shrouds, which were 5 mm thick, were individually machined from a cast perspex cylinder. The estimated radial growth at the outer radius of the rotor was approximately 0.05 mm at the maximum speed tested (4000 rev/min).

Both the disks were of composite construction; each duralumin disk was pressed onto a tapered central mild steel hub, and the hubs were bolted to a driving flange on the main drive-shaft. The rotating disk assembly could be driven at speeds up to 4000 rev/min ($\text{Re}_\theta \simeq 10^6$) by a 1.9 kW variable-speed electric-motor, and the speed was measured by a 60-pole disk and magnetic transducer in conjunction with an electronic timer-counter. The rotational speed, which could be measured to one rev/min, was steady to within 1 percent.

Four different radial-clearance seals (seals B to E in Fig. 1) were investigated; they are described below:

(i) Seal B consisted of a shrouded stator with a radial clearance, s_{cr}, between the shroud, of outer radius, $r_{o,S}$, and the rotor, of outer radius, $r_{o,R}$. For this shroud, the axial overlap, z_o, was zero.

(ii) Seal C was similar to seal B but the overlap ratio, $H(H \equiv z_0/r_{0,R})$ was 0.032 (that is, $z_0 = 6$ mm).

(iii) Seal D consisted of a shrouded stator overlapping a shrouded rotor ($r_{o,S} > r_{o,R}$) with an overlap ratio of $H = 0.01$.

(iv) Seal E consisted of a shrouded rotor overlapping a shrouded stator ($r_{o,R} > r_{o,S}$) with an overlap ratio of $H = 0.01$.

For each of these shrouds, the radial clearance ratio was variable with $G_{cr} = 0.0025$, 0.005 and 0.01 ($G_{cr} \equiv s_{cr}/r_{o,R}$). At the smallest clearance ratio, the maximum reduction in radial clearance, due to rotor growth, was estimated to be less than 10 percent of the nominal clearance. For all tests, the gap ratio was kept constant at $G = 0.1$.

For flow visualization, the air was seeded with oil particles (approximately 1 μm dia) from a Concept smoke-generator. The smoke was introduced either at the inlet of the fan (this will be referred to as "central seeding") or at the periphery of the seals (this will be referred to as "peripheral seeding") through a toroidal pipe with a series of holes at 9 deg angular intervals. A 4W Spectra-Physics 164 Argon-ion laser, operating in the all-line mode, was used to provide "slit illumination" in an r-z plane, through the central axis of the cavity. Further details, and photographs of flow visualization, can be found in reference [2].

3 Pressure Measurements

3.1 Radial Presssure Distributions. Using the M10 electromanometer, pressures on the test radius and on the orthogonal radii were measured for the four radial seals with $G = 0.1$, $G_{cr} = 0.0025$, 0.005 and 0.01. Pressure distributions at six values of rotational speed and four values of flow

Nomenclature

a,b = constants in theoretical model
$C_p \equiv (p-p_a)/1/2\rho V^2$ = pressure coefficient
$C_w \equiv \dot{m}/\mu r_{o,R}$ = mass flow coefficient
$G \equiv s/r_{o,R}$ = gap ratio
$G_{ca} \equiv s_{ca}/r_{o,R}$ = axial clearance ratio
$G_{cr} \equiv s_{cr}/r_{o,R}$ = radial clearance ratio
$H \equiv z_0/r_{o,R}$ = overlap ratio
$\dot{m}$ = coolant mass flow rate
p = static pressure
$p^* \equiv 10^3(p-p_a)/p_a$ = dimensionless pressure drop
p^*_{in} = ingress-predicting pressure
r = radial distance from disc centre line
$\text{Re}_\theta \equiv \rho\omega r^2_{o,R}/\mu$ = rotational Reynolds number
s = axial gap between rotor and stator
s_{ca} = axial clearance between shrouded stator and rotor
s_{cr} = radial clearance between stator shroud and rotor or rotor shrouds
$V = \dot{m}/2\pi\rho r_0 s_{ca}$ = average velocity at outlet of rotor-stator cavity
z = axial distance measured from stator face
z_0 = axial overlap between stator shroud and rotor or rotor shrouds
μ = fluid viscosity
ρ = fluid density
ω = disc angular velocity

Subscripts

0 = outer radius
R = rotor
S = stator
a = ambient conditions
min = minimum value

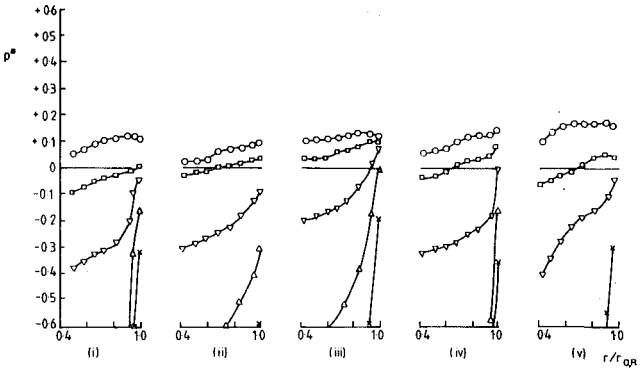

Fig. 2 The effect of rotational Reynolds number on the radial distribution of pressure for C_w = 2950 for the five seals; G_{ca}, G_{cr} = 0.01.

Symbol : ○ □ ▽ △ X
$Re_\theta/10^6$: 0.0 0.4 0.6 0.8 1.0

(i) seal A; (ii) seal B; (iii) seal C; (iv) seal D; (v) seal E.

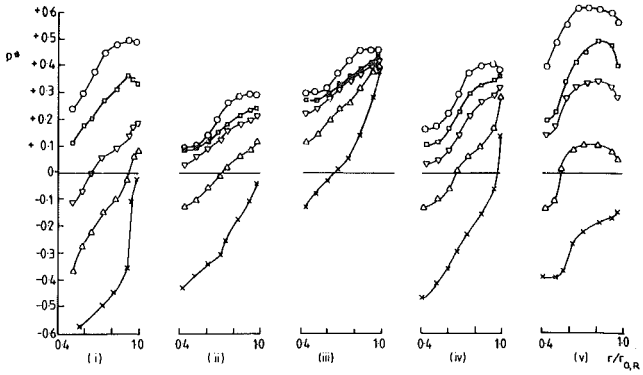

Fig. 3 The effect of rotational Reynolds number on the radial distribution of pressure for C_w = 5940 for the five seals; G_{ca}, G_{cr} = 0.01.

Symbol : ○ □ ▽ △ X
$Re_\theta/10^6$: 0.0 0.4 0.6 0.8 1.0

(i) seal A; (ii) seal B; (iii) seal C; (iv) seal D; (v) seal E.

rate were obtained in each case. The measurements on the orthogonal radii confirmed that, for all seals tested, the flow was axisymmetric to within 2 percent under all conditions.

In Fig. 2, the effect of rotational speed on the variation of dimensionless pressure difference, p^* (where $p^* \equiv 10^3(p - p_a)/p_a$, p_a being the ambient pressure outside the cavity) with the radius ratio, $r/r_{0,R}$, is shown for the four radial seals with G_{cr} = 0.01 and C_w = 2950. The distribution for the axial clearance seal A with G_{ca} = 0.01 (obtained in reference [2]) is also plotted for comparison. At this relatively low flow rate, there are only small differences between pressure levels for the five seals. It should be noted that, for all seals, the pressure level at any radius decreases with increasing rotational speed. However, for a given rotational speed, the pressure level at the edge of the cavity appears to be highest for seal C, suggesting it would be the most efficient seal.

Figure 3 shows the equivalent pressure distributions for the higher flow rate of C_w = 5940. The trends seen in Fig. 2 are now clearly visible. For seal C, at the outer edge of the cavity, the effect of rotation on the pressure level is much weaker than for the axial seal. Seals B and D would also, on this evidence, be more effective than the axial seal A. Seal E is the only one of the four radial seals which does not show this reduced sensitivity to rotational speed near the outer radius of the cavity.

The difference between the seals can be seen quite distinctly in Fig. 4, for C_w = 11,900. Whereas seals A and E show the expected monotonic decrease in pressure with increasing Re_θ, seals B, C and D show reversals of this trend, with the pressure actually increasing with rotational speed! For seal C, this "pressure-inversion" phenomenon can be seen for all values of $r/r_{o,R}$. For seal D, the pressure first falls with increasing speed, as expected, and then starts to increase as the rotational speed is increased further. For seal B, the inversion is strongest near the outer edge of the cavity. Comparing Figs. 2, 3, and 4 shows the gradual trend towards the pressure-inversion, for seals *B*, *C*, and *D*, with increasing coolant flow rate. It is also worth noting that this inversion is strongest where the degree of overlap of the radial-clearance seal is highest, and only occurs when the stationary shroud overlaps the rotor or a rotating shroud. Qualitatively similar distributions were also obtained for G_{ca}, G_{cr} = 0.005 and 0.0025, although the pressure-inversion effect appeared to get weaker as the clearance ratio was decreased.

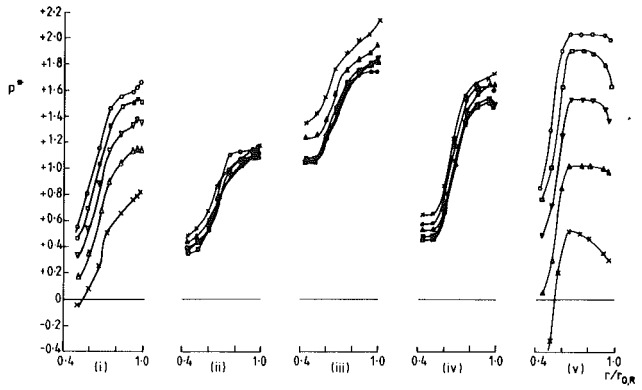

Fig. 4 The effect of rotational Reynolds number on the radial distribution of pressure for C_w = 11,900 for the five seals; G_{ca}, G_{cr} = 0.01.

Symbol : ○ □ ▽ △ X
$Re_\theta/10^6$: 0.0 0.4 0.6 0.8 1.0

(i) seal A; (ii) seal B; (iii) seal C; (iv) seal D; (v) seal E.

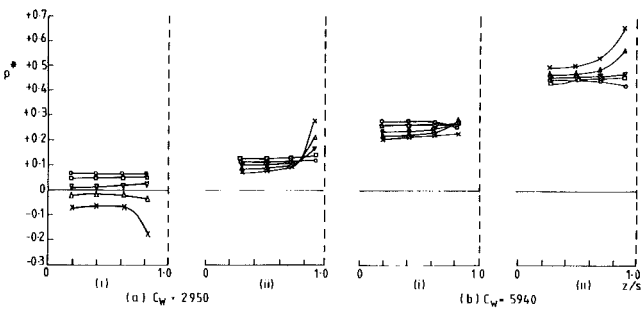

Fig. 5 The effect of rotation on the axial variation in static pressure along the stator shroud for radial clearance seal; G_{cr} = 0.01.
(i) seal B (H = 0); (ii) seal C (H = 0.032)

Symbol : ○ □ ▽ △ X
$Re_\theta/10^6$: 0.0 0.4 0.6 0.8 1.0

····· Inner face of rotor

3.2 The "Pressure-Inversion" Effect. In order to investigate the pressure-inversion phenomenon, the variation static pressure along the stator shroud was measured for seals B and C for values of G_{cr} = 0.0025, 0.005 and 0.01. Figure 5 shows how, for G_{cr} = 0.01, the use of an overlapping seal (seal C) produces a strong pressure-inversion effect in the vicinity of the seal. The strength of this inversion clearly increases with coolant flow rate. For C_w = 2950, the inversion only occurs for values of $z/s > 0.7$; for C_w = 5940, the inversion can be clearly seen for all values of z/s. For seal B, a weak inversion for $z/s > 0.7$ can only be seen for C_w = 5940.

At least one of three possible mechanisms was considered to be responsible for the inversion effect.

(i) Referring to Fig. 1, the coolant flow, which for the radial-clearance seals leaves axially, could interact with the free disk flow which is pumped radially outwards on the back face of the rotor. Additional tests were conducted with seals B and C in which the shrouds were extended axially, on the free disk side, to steer the free disk flow away from the seal. No significant difference in the results was observed using these wide shrouds. This, and the absence of the pressure inversion effect for seal E, led to the conclusion that the effect was not caused by free disk pumping.

(ii) Even in the absence of an axial flow, the outer cylindrical surface of the rotor will develop a boundary layer when the disk is rotating. For the radial-clearance seals B, C, and D, the axial flow of coolant could interact with this rotating cylindrical boundary layer; for seals A and E, no such interaction is possible.

(iii) Owing to the large centrifugal forces on the rotor surface, the coolant boundary layer can be turned through 90 deg in Seals D and E with little or no separation from the inner surface of the rotor. However, referring to Fig. 1(D), as the flow is turned through a further 180 deg in seal D, the centrifugal forces will tend to increase the separation from the outer surface of the rotating shroud. This separation, which will occur in seals B, C, and D, but not in E, is likely to increase the exit losses, and the pressure drop would be higher.

It is probable that a combination of (ii) and (iii) above results in the observed pressure-inversion effect. How this effect influences the sealing characteristics is discussed in the next section.

4 Determination of Ingress

At low rotational speeds and low flow rates, where clear flow visualization was possible, the flow structure inside the cavity, when a radial-clearance seal was fitted, was similar to that observed in reference [2]. At high flow rates, where pressure-inversion could occur, flow visualization was not possible. Peripheral seeding was used to obtain estimates of $C_{w,\min}$ (the minimum dimensionless flow rate necessary to prevent ingress) for $G_{cr} = 0.01$, and values obtained in this way were in close agreement with those obtained by the pressure technique described below.

In reference [2] a simple theoretical model developed for the axial-clearance seal gave

$$C_p = a - b(G_{ca}\,\mathrm{Re}_\theta / C_w)^2 \qquad (3)$$

where $C_p \equiv (p - p_a)/\tfrac{1}{2}\rho V^2$ (V being the average radial velocity at the seal outlet) and a and b are constants. It was argued that ingress occurs when $C_p < 0$; and the value of $C_{w,\min}$ based on $C_p = 0$, was determined from linear regression of equation (3) for different values of G_{ca}. Although the tests showed that $C_{w,\min} \propto \mathrm{Re}_\theta$, the G_{ca} variation was found to be nonlinear.

For some of the radial-clearance seal tests discussed below, there was some evidence of nonlinear Re_θ behaviour at the higher rotational speeds. Instead of correlating the results according to equation (4*a*), it was decided to estimate $C_{w,\min}$ from individual cross-plots of p^*_{in} versus Re_θ. For these tests, p^*_{in} was the dimensionless pressure measured at $r/r_{o,R} = 0.975$ for shrouds A, B, C and D, and at $r/r_{o,R} = 0.955$ for shroud E.

Figure 6 shows the cross-plots of p^*_{in} versus Re_θ, for several values of C_w, for the five seals with $G_{ca} = G_{cr} = 0.01$. The pressure-inversion effect can be clearly seen for shrouds B, C and D, which require higher values of Re_θ, compared with seals A and E, before p^*_{in} becomes negative. Seal C, which has the greatest overlap, appears to be the most effective if $p^*_{\mathrm{in}} = 0$ is used as the criterion to determine $C_{w,\min}$.

Figure 7 shows the variation of $C_{w,\min}$, based on both the flow visualization and the pressure criteria, for the five seals

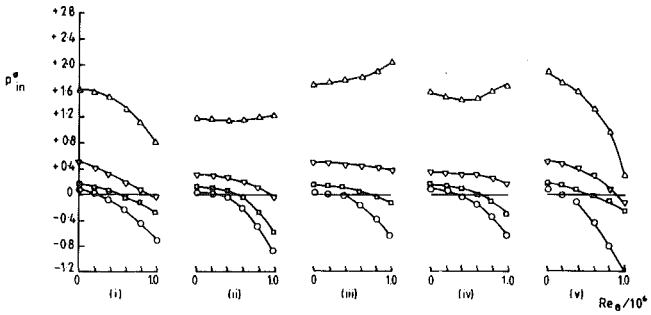

Fig. 6 The effect of C_w on the variation of p^* i_n with Re_θ for the five seals; G_{ca}, G_{cr} = 0.01.
(i) seal A; (ii) seal B; (iii) seal C; (iv) seal D (v) seal E.
Symbol : ○ □ ▽ △
C_w : 1490 2950 5940 11,900

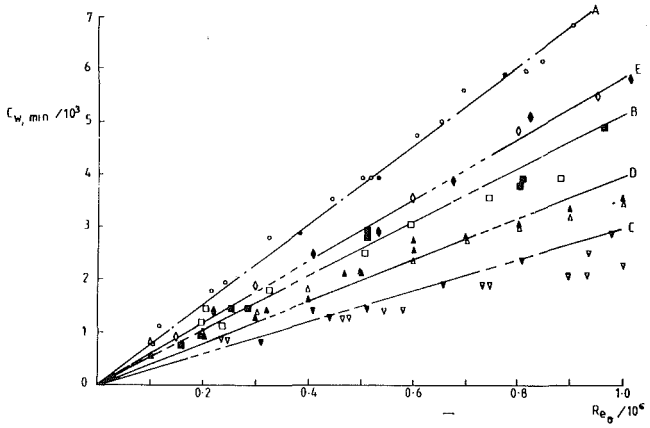

Fig. 7 The variation of $C_{w,\,\min}$ with Re_θ based on flow visualization and the pressure criterion for the five seals; G_{ca}, G_{cr} = 0.01.
Seal type : A B C D E
Flow visualization : ○ □ ▽ △ ◇
Pressure measurement : ● ■ ▼ ▲ ◆

with $G_{ca} = G_{cr} = 0.01$. It can be seen that the estimates of $C_{w,\min}$ based on the cross-plot pressure criterion are in good agreement with the values determined from flow visualization. Assuming a linear variation of $C_{w,\min}$ with Re_θ, the pressure data were correlated using least-squares linear regressions; these correlations are also shown in Fig. 7, and the values are given in Table 4.1. It should be pointed out that the correlation for the axial-clearance seal, seal A, based on the cross-plot criterion was intermediate between the two pressure correlations, and close to the flow visualization correlation, given in reference [2].

From Fig. 7, it can be seen that seal C is, indeed, the most effective seal. There is also some indication from the results for seals C and D that, at the higher values of Re_θ, the estimated values of $C_{w,\min}$ are smaller than the linear $C_{w,\min}$ versus Re_θ relationship would suggest. This observation is consistent with the fact that the pressure-inversion effect increases with increasing C_w and the correlations for the overlapping radial-clearance seals C and D are probably conservative at high values of Re_θ.

Figure 8 shows the variation of $C_{w,\min}$, based on the cross plot pressure criterion, for the five seals with $G_{ca} = G_{cr} = 0.005$. Although the order-of-merit is the same as that for $G_{cr} = 0.01$, with seal C being the "best" and seal A being the "worst", the differences are much smaller. The effect of clearance ratio is greater for the axial-clearance seal than it is for the radial-clearance seals.

For $G_{ca} = G_{cr} = 0.0025$, Fig. 9 shows that, based on the pressure criterion, seal C is still the most effective, but seal A now shows a slightly superior performance to the other radial-clearance seals, which all exhibit a similar behaviour. Flow

visualization was not practicable at this clearance ratio, or at G_{cr} = 0.005, and the pressure correlations for all clearance ratios are presented in Table 4.1

5 Conclusions

Flow visualization and pressure measurements have been used to study the performance of four radial-clearance seals in a rotor-stator rig with a gap ratio of G = 0.1, seal clearance ratios of G_{cr} = 0.0025, 0.005 and 0.01, overlap ratios up to H = 0.032, and rotational Reynolds numbers up to $Re_\theta = 10^6$. For the radial-clearance seals where the stationary shroud overlaps the rotor, a pressure-inversion effect was observed where the pressure inside the cavity, between the rotor and stator, increases, rather than decreases, with increasing rotational speed. The inversion effect occurs at high flow rates and increases in strength with increasing shroud overlap.

For G_{cr} = 0.01, the estimation in ingress using flow visualization was in good agreement with that estimated from a cross-plot pressure criterion. For this clearance ratio, and for G_{cr} = 0.005, the four radial-clearance seals required less coolant to prevent ingress than that required for an axial-clearance seal, and the amount of coolant required decreased with increasing overlap ratio. The effect of reducing the clearance ratio was less marked on the radial-clearance seals than it was on the axial-clearance seal, and at G_{cr} = 0.0025 the latter showed slight superiority over three of the four radial-clearance seals. The radial-clearance seal with the greatest overlap was superior for all clearance ratios tested.

Acknowledgments

The authors would like to thank GEC Gas Turbines Limited and Ruston Gas Turbines Limited, U.K., and Sulzer Brothers, Switzerland, for sponsoring the work described in this paper.

References

1 Bayley, F. J., and Owen, J. M., "The Fluid Dynamics of a Shrouded Disk System With a Radial Outflow of Coolant," ASME JOURNAL OF ENGINEERING FOR POWER, Vol. 92, 1970, p. 335.

2 Owen, J. M., and Phadke, U. P., "An Investigation of Ingress for a Simple Shrouded Rotating Disk System with a Radial Outflow of Coolant," Paper No. 80-GT-49, 25th ASME Gas Turbine Conference, New Orleans, 1980.

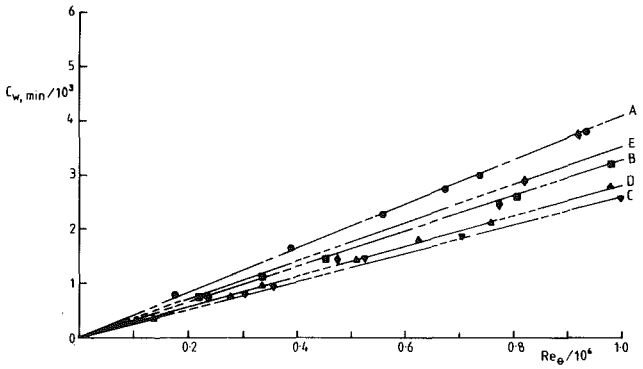

Fig. 8 The variation of $C_{w,\,min}$ with Re_θ based on the pressure criterion for the five seals; G_{ca}, G_{cr} = 0.005.
Seal type : A B C D E
Symbol : ● ■ ▼ ▲ ◆

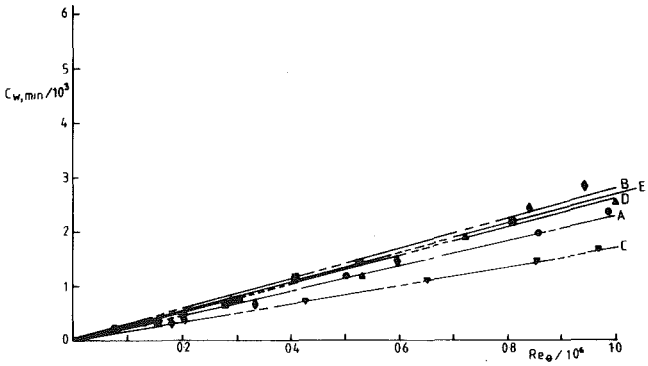

Fig. 9 The variation of $C_{w,\,min}$ with Re_θ based on the pressure criterion for the five seals; G_{ca}, G_{cr} = 0.0025.
Seal type : A B C D E
Symbol : ● ■ ▼ ▲ ◆

Table 1 Comparison of $C_{w,min}/Re_\theta$ for the five seals

	$C_{w,min}/Re_\theta$		
G_{cr},G_{ca}	0.0025	0.005	0.01
Seal A	0.0023	0.0041	0.0076
Seal B	0.0028	0.0033	0.0052
Seal C	0.0017	0.0026	0.0030
Seal D	0.0026	0.0028	0.0040
Seal E	0.0027	0.0035	0.0059

visualization was not practicable at this clearance ratio, or at $G_{cr} = 0.005$, and the pressure correlations for all clearance ratios are presented in Table 4.1

5 Conclusions

Flow visualization and pressure measurements have been used to study the performance of four radial-clearance seals in a rotor-stator rig with a gap ratio of $G = 0.1$, seal clearance ratios of $G_{cr} = 0.0025$, 0.005 and 0.01, overlap ratios up to $H = 0.032$, and rotational Reynolds numbers up to $Re_\theta = 10^6$. For the radial-clearance seals where the stationary shroud overlaps the rotor, a pressure-inversion effect was observed where the pressure inside the cavity, between the rotor and stator, increases, rather than decreases, with increasing rotational speed. The inversion effect occurs at high flow rates and increases in strength with increasing shroud overlap.

For $G_{cr} = 0.01$, the estimation in ingress using flow visualization was in good agreement with that estimated from a cross-plot pressure criterion. For this clearance ratio, and for $G_{cr} = 0.005$, the four radial-clearance seals required less coolant to prevent ingress than that required for an axial-clearance seal, and the amount of coolant required decreased with increasing overlap ratio. The effect of reducing the clearance ratio was less marked on the radial-clearance seals than it was on the axial-clearance seal, and at $G_{cr} = 0.0025$ the latter showed slight superiority over three of the four radial-clearance seals. The radial-clearance seal with the greatest overlap was superior for all clearance ratios tested.

Acknowledgments

The authors would like to thank GEC Gas Turbines Limited and Ruston Gas Turbines Limited, U.K., and Sulzer Brothers, Switzerland, for sponsoring the work described in this paper.

References

1 Bayley, F. J., and Owen, J. M., "The Fluid Dynamics of a Shrouded Disk System With a Radial Outflow of Coolant," ASME JOURNAL OF ENGINEERING FOR POWER, Vol. 92, 1970, p. 335.

2 Owen, J. M., and Phadke, U. P., "An Investigation of Ingress for a Simple Shrouded Rotating Disk System with a Radial Outflow of Coolant," Paper No. 80-GT-49, 25th ASME Gas Turbine Conference, New Orleans, 1980.

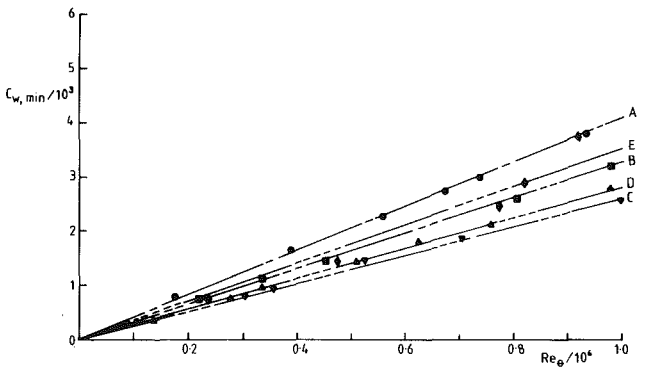

Fig. 8 The variation of $C_{w,\,min}$ with Re_θ based on the pressure criterion for the five seals; $G_{ca}, G_{cr} = 0.005$.
Seal type : A B C D E
Symbol : ● ■ ▼ ▲ ◆

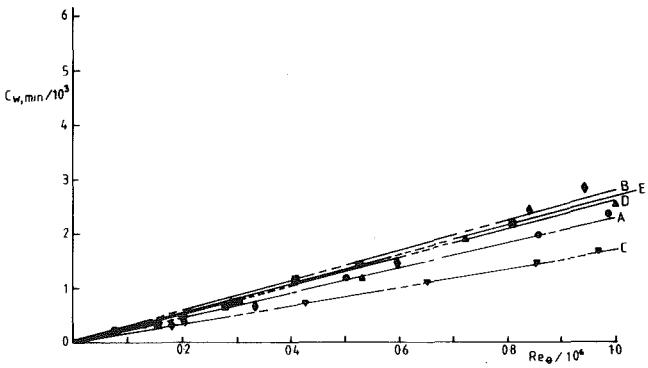

Fig. 9 The variation of $C_{w,\,min}$ with Re_θ based on the pressure criterion for the five seals; $G_{ca}, G_{cr} = 0.0025$.
Seal type : A B C D E
Symbol : ● ■ ▼ ▲ ◆

Table 1 Comparison of $C_{w,min}/Re_\theta$ for the five seals

	$C_{w,min}/Re_\theta$		
G_{cr}, G_{ca}	0.0025	0.005	0.01
Seal A	0.0023	0.0041	0.0076
Seal B	0.0028	0.0033	0.0052
Seal C	0.0017	0.0026	0.0030
Seal D	0.0026	0.0028	0.0040
Seal E	0.0027	0.0035	0.0059

DISCUSSION

D. A. Campbell[1]

In discussing the pressure inversion effect observed with seal C, the authors conclude that it was not caused by pumped flow on the free side of the disk. Before accepting this, we should perhaps examine other relevant data to see if we should, in fact, expect a significant effect from this cause.

The static pressure drop across the seal gap can be obtained from the author's Fig. 5, using the pressure measurement nearest the disk. From this and the flow rate a discharge coefficient, C_D, can be calculated.

Some error is possible from the assumption that the pressure is measured in the plane of the disk, i.e. at the seal entrance; in fact, the measurement plane is slightly upstream of the entrance and the discharge coefficient will therefore be underestimated in the static case. A discharge coefficient from [3] has therefore been assumed for the seal with no pumping effect. The Reynolds number for axial flow is very low but it is assumed that the Reynolds number for tangential flow of about 10,000 will give turbulent conditions when rotating.

To separate the inlet and exit pressure losses, the exit discharge coefficient without pumping effect is assumed to be about 0.95, and taking the overall discharge coefficient of 0.66, an entry loss coefficient can then be calculated.

The radial velocity, $V_{r,max}$, on the free disk is about 0.1 ωR [4] and is used to calculate the exit flow velocity ratio, $V/V_{r,max}$. Reference [5] gives data for air outlets to a fast moving stream. Figure 9 (for a Mach number of 0.7) of [5] on the following page shows the effect as a function of $m/\rho VA$ (which is equivalent to $V/V_{r,max}$), where V is the continuity-derived velocity through the seal. The exit discharge coefficients can be read from this graph for the two flow levels. At the lower flow level there is a marked drop in discharge coefficient.

In conjunction with the overall discharge coefficient these exit coefficients can be used to calculate an entry loss coefficient for the rotating case. This shows a large increase at both flow levels.

At the lower flow levels associated with the possibility of ingress, the effect of the free disk flow is thus probably quite important. This emphasizes the need to design all test rig features with careful reference to actual or proposed turbine

[1] Section Leader, Internal Air Systems, Rolls-Royce Ltd., Derby, U.K.

seal designs. The authors are to be congratulated on the progress made in this direction by this work, but further work is needed to cover some important features.

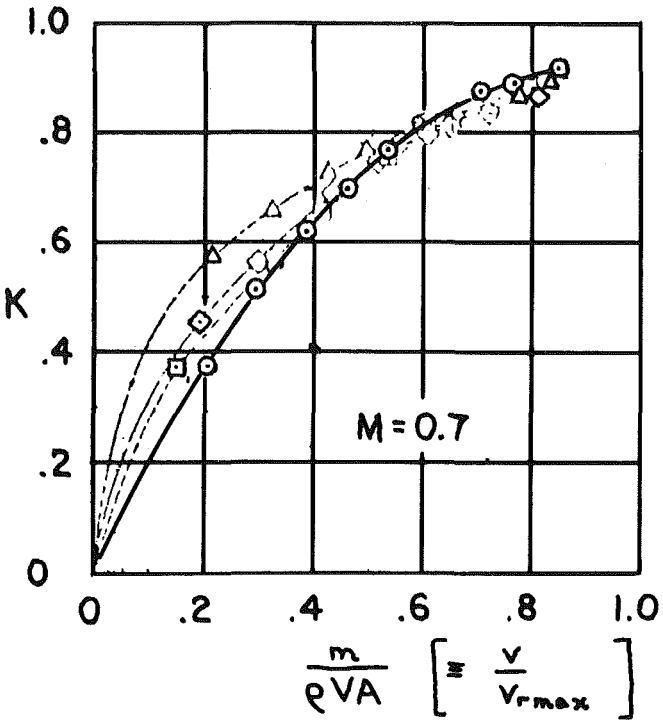

Table 2 Seal type C "pressure inversion" effect: $G_{cr} = 0.01$

Re_θ	0		10^6	
C_w	2950	5940	2950	5940
$C_{w,min}$ (flow visualisation)			≃ 2200	
$p^*/10^3$	0.12	0.43	0.28	0.66
$\therefore C_D$	0.61	0.64	0.45	0.55
Re in clearance, axial flow	940	1980	940	1980
C_D [3]	0.66			
Expected exit, C_D, without pumped flow effect			0.95	
Equivalent exit loss coefficient			1.11	
$\therefore$ Entry and friction loss coefficient			1.19	
$V/V_{r,max}$ for exit flow			0.44	0.89
Exit C_D [5]			0.68	0.92
Equivalent exit loss coefficient			2.16	1.18
$\therefore$ Entry and friction loss coefficient			2.78	2.12

Further References

3 Bell, K. J., and Bergelin, O. P., "Flow Through Annular Orifices," ASME *Transactions*, Vol. 79, 1957, p. 593.

4 Dorfman, L. A., *Hydrodynamic Resistance and the Heat Loss of Rotating Solids*, Oliver and Boyd, Edinburgh, 1963.

5 Dewey, P. E., and Vick, A. R., "An Investigation of the Discharge and Drag Characteristics of Auxilliary Air Outlets Discharging into a Transonic Stream." NACA Report TN 3466, 1955.

Authors' Closure

We should like to thank Mr. Campbell for his discussion; in the light of this, we have conducted a similar one-dimensional analysis for seal C over the entire range of clearance ratios, coolant flow rates, and rotational speeds for which experimental data are available. It should be emphasized that one-dimensional analyses are fraught with problems: discharge coefficients are calculated using Bernoulli's equation, but in this problem the rotor introduces an indeterminate work term; the choice of the upstream reference plane affects the results; the influence of the tangential velocity is indeterminate.

Making similar assumptions to those of Mr. Campbell, and using the data of Dewey and Vick [5], it is possible to show that crossflow (from the "free-disk pumping" on the back face of the rotor) can affect the exit loss from the seal. However, although the crossflow exit loss increases with increasing Re_θ, so does the total loss (which was calculated for seal C using the one-dimensional model); the ratio of crossflow exit loss to total loss actually decreases with increasing Re_θ. At $Re_\theta = 10^6$, the estimated ratio of this exit to total loss was less than 0.3 for virtually all the data.

In the preceding calculation, the authors (like Mr. Campbell) assumed that the crossflow velocity, created by the free disk pumping, was equal to the *maximum* radial velocity in the free disk boundary layer. Even so, the above results suggest that the increase in total loss with increasing Re_θ (the so-called pressure inversion effect) cannot be caused solely, or mainly, by free disk pumping. In fact, if the crossflow velocity is assumed equal to the *average* radial velocity in the free disk boundary layer, then the effect of crossflow on exit loss is, according to the data of Dewey and Vick, even smaller.

As stated in section 3 of this paper, the authors found that the pressure inversion effect also occurred in seal D, in which the crossflow from the free disk face was displaced from the seal outlet. Additional tests were also conducted for those radial-clearance seals in which the rotating shrouds were extended axially (for a distance of 15.1 mm) on the free disk side "to steer the free disk flow away from the seal"; a strong pressure inversion effect was still observed. For all these reasons, the authors conclude that this effect was not caused by free disk pumping.

Unbalance Response Analysis of a Complete Turbomachine

N. Klompas
General Electric Company,
Gas Turbine Division,
Schenectady, N.Y. 12345
Mem. ASME

A new method is derived to calculate unbalance response of a complete turbomachine, including mount asymmetry, disk flexibility, and fluid-film bearing anisotropy by utilizing conventionally obtained stiffness coefficients for the rotor and stator. Formulation through the coordinates whirl and whip is in real variables with only eight equations per bearing. Whereas the stator is usually ignored, sample analysis illustrates possible strong influence of casing flexibility. Coordinate transformations to enhance visualization and verification of the solution are shown.

Introduction

Current analytical methods for turbomachine dynamics analysis offer the gas turbine designer either a complicated solution of the rotor mounted on pedestals – the science of rotor dynamics analysis has become very sophisticated – or an oversimplified solution of the complete system. It will be shown analytically, and is evident from the occurence of vibration problems in gas turbines, that neither choice is adequate. Therefore, derivation of a suitable method for system analysis is presented.

The method outlined for application to aircraft engines in references [1] and [2] is extended to account for anisotropic response of journal bearings. The principal feature of this method is the use of unconventional coordinates, called whirl and whip, to account for gyroscopic effects, even with flexible disks, in a set of stiffness, or influence, coefficients which represent the response of the rotor to deflections at the bearings. The final equations of motion are expressed in terms of the necessary eight components of deflection at each bearing. The conventional Cartesian coordinates would involve gyroscopic cross-coupling which precludes these deflections from being treated as independent variables in such equations. Therefore, the whirl and whip coordinates allow the response of structures to be determined independently by whatever means are available, including the possible use of test data.

The present paper organizes such structural and the corresponding bearing film coefficients into the final equations of motion and completes the solution. Because the coordinates used are nonorthogonal, repeatability of the solution with the reference frames rotated 90 deg automatically verifies most of the analysis. With the solution transformed to different coordinates, complete verification can be obtained independently.

Therefore, this new method would allow the design engineer to integrate his structural analysis or test data into calculation of the overall machine dynamics. The advent of finite element analysis broadens his ability to obtain the necessary stiffness coefficients for very complex structures. Reliance on specialized rotor dynamics computer programs which often cannot accurately simulate even the rotor alone could be eliminated. Recognition of limitations in simulating the construction of a rotor in current rotor dynamics analyses is found in the technical literature. Darlow et al. [3] and Bannister [4] describe methods to obviate some of these limitations.

Whereas similar analyses in the technical literature usually employ functions of complex variables in sophisticated mathematical processes, the present analysis is performed in simple steps which can be visualized by the engineer. Also, illustrations of sophisticated theory in the literature usually omit features often influential in dynamic behavior of turbomachines. For example, Li and Gunter [5] omit gyroscopic effects and the effects of mount asymmetry.

The possible strong influence of disk flexibility, which is accounted for in the present method, has been demonstrated by Hagiwara et al. [6]. They analyzed and tested a rotor with an impeller which would usually be considered rigid, because even before correction for rotational stiffening it had a resonant frequency 14 percent above the frequency of excitation at the calculated critical speed. Nevertheless, they demonstrated reduction of 20 percent in the critical speed and significant impeller vibratory stress.

Theory

Whirl and Whip Coordinates. This analysis is an extension of that described in references [1] and [2] for systems with squeeze-film dampers. The key feature is the use of unconventional coordinates to avoid cross-coupling of gyroscopic moments in two planes. A pair of coordinate dimensions, called whirl and whip, are the magnitudes associated with the corresponding pair of reference vectors. Whirl is associated with a unit vector contained in a rotating plane with fixed reference to unbalance. Whip is associated with an oscillating vector which is the projection of the whirl vector into a stationary reference plane. These vectors coincide at 180 deg intervals when the rotating plane passes the stationary whip reference plane. A second pair of whirl and whip coordinates defined by the pair of vectors in a whirl plane 90 deg ahead of the unbalance reference plane and in the

Contributed by the Gas Turbine Division for publication in the Journal of Engineering for Power. Manuscript received by the Gas Turbine Division May 13, 1982.

same whip plane accommodate asymmetric and nonconservative response of fluid-film bearings. The two pair of coordinates will be called primary and secondary, respectively.

Stiffness Coefficients and Unbalance Forces. It is necessary first to obtain dynamic stiffness coefficients for the rotor and stator at each bearing. Since each of these coefficients is derived from forced response in one plane of an axisymmetric structure, methods for obtaining them are available. Those for the stator, in particular, might best be obtained experimentally if a suitable model should exist. The increasing use of finite element analysis should find suitable application in determining stiffnesses of complex components. Such stiffnesses could be integrated into an overall analysis using simpler simulation as in the Prohl method. Therefore, the necessary coefficients will be defined without recommendations for their calculation.

Subscripts designate a bearing force as one of a set which must be applied at each bearing of a rotor or the stator to constrain the deflections at all bearings to zero except to impress one component at one bearing to a value of 1. Therefore, a subscripted force is equivalent to a particular stiffness coefficient. The first pair of subscripts designate, in order, the reference coordinates of the force and the impressed deflection. The second pair designate, in order, the bearing at which the force applies and the bearing at which a deflection of 1 is impressed.

Stiffness coefficients representing response of the stator which is assumed axisymmetric and mounted elastically on a stationary foundation through structures of different stiffness in the horizontal and vertical planes are defined as follows:

F^S_{rrij} designates whirl forces associated with whirl deflection. The whirl mount stiffnesses are those normal to the plane designated whip. The calculation to impress deflection at a bearing yields at each mount a whip force, if translational stiffnesses are not equal in the two planes, and moment, if rotational stiffnesses are not equal, which must be assumed to constrain the response to the whirl coordinate.

F^S_{ssij} designates whip forces associated with whip deflection. The mount stiffnesses in the whip plane are used and response is contained in the whip coordinate.

F^S_{srij} designates whip forces associated with whirl deflection. Whip deflections are constrained to zero at all bearings and the mount stiffnesses in the whip plane are used. These bearing forces produce the whip forces and moments necessary to satisfy the conditions assumed in calculation of F^S_{rrij}. Therefore, the opposites of those forces and moments are applied externally at each mount. The force applied at each mount is $y_r(C_h - C_v)$ and the moment is $y_r'(D_h - D_v)$. Positive direction for force or moment is such as to resist the corresponding deflection or slope.

Response of a rotor is similarly represented by forces at each bearing as follows:

F^R_{ssij} designates the whip forces associated with whip deflection. With the assumption of significant gyroscopic effects only due to thin disks, the effective gyroscopic moment at a disk is $-y_s' c^- (2\Omega\omega + \Omega^2) I_D/g$ with the usual sign convention where positive gyroscopic moment acts to resist angular displacement of the disk. The calculation to impress deflection at a bearing yields a set of whirl moments which must be assumed acting at each disk to constrain the response to the whip coordinate.

F^R_{rrij} designates the whirl forces due to whirl deflection. The gyroscopic moment at each disk is $y_r'\ c^+ (2\Omega\omega - \Omega^2) I_D/g$. All forces and moments are contained in the whirl coordinates.

F^R_{rsij} designates whirl forces due to whip deflection. Whirl deflections are constrained to zero at all bearings and the whirl gyroscopic moments are accounted for at each disk. These bearing forces produce the whirl moments necessary to satisfy the condition assumed in calculation of F^R_{ssij}. Therefore, the opposite of these moments are applied externally to each disk. This moment at each disk is

$$y_s'\{c^- (2\Omega\omega + \Omega^2) + c^+ (2\Omega\omega - \Omega^2)\} I_D/2g$$

Unbalance loading is represented by a set of forces at the bearings of the rotor driving the vibration:

F_{ui} designates the forces due to unbalance in the primary whirl reference plane. Calculation of these forces is identical to that of F^R_{rsij}, except that the external loading is due to unbalance. Moments due to disk skew can readily be included in the loading. Components of unbalance which do not project into one plane are accommodated in the secondary whirl reference plane.

Nomenclature

B = bearing damping coefficient, lb s/in (N s/m)
$\bar{B}$ = bearing damping coefficient relative to rotated axes, lb s/in (N s/m)
C = translational stiffness at mount lb/in (N/m)
c^+ = magnification factor for forward whirl, dimensionless
c^- = magnification factor for backward whirl, dimensionless
D = rotational stiffness at mount, lb in/rad (Nm/rad)
F = force at bearing, lb (N)
$\bar{F}$ = force at bearing relative to rotated axes, lb (N)
g = acceleration due to gravity, in/s^2 (m/s^2)
I_D = diametral moment of inertia of disk, lb in^2 (N m^2)
K = bearing spring coefficient, lb/in (N/m)
$\bar{K}$ = bearing spring coefficient relative to rotated axes, lb/in (N/m)
t = time, s
U = unbalance, lb in (N m)
W = work in one cycle, lb in (N m)
x = deflection along x-axis, in (m)
y = deflection along y-axis or in plane of reference, in (m)
y' = slope in plane of reference, dimensionless
$\bar{y}$ = deflection in plane of reference relative to rotated axes, in (m)
α = orientation angle of ellipse axes, rad
Δt = time increment, defined by equation (4), s
ϕ = phase angle, rad
Ω = angular velocity of whirl, rad/s
ω = angular velocity of spin, rad/s
θ = angle relative to reference plane, rad

Subscripts

a = along ellipse axis rotated through α from x-axis
b = along ellipse axis rotated through α from y-axis
i,j = dummy indices
h = horizontal
r = whirl
s = whip
u = due to unbalance
v = vertical
x = along x axis
y = along y axis

Superscripts

F = bearing fluid film
R = rotor
S = stator
$*$ = in coordinates 90 deg ahead of primary reference
$+$ = forward whirl
$-$ = backward whirl

Bearing Stiffness and Damping Coefficients. The hydrodynamic forces of a bearing fluid film are conventionally represented as four spring coefficients, K_{ij}, and four damping coefficients, B_{ij}, where the subscripts refer to the two Cartesian coordinates, usually the x-coordinates along the horizontal axis and the y-coordinate along the vertical axis. When these coordinates are defined by oscillating unit vectors which are projections into each plane of the primary and secondary whirl vectors, the force due to deflection of the shaft relative to the bearing housing is expressed by the equations

$$\begin{aligned} F_x &= K_{xx}x + K_{xy}y^* - \Omega B_{xx}x^* + \Omega B_{xy}y \\ F_y &= -K_{yx}x^* + K_{yy}y + \Omega B_{yx}x - \Omega B_{yy}y^* \\ F_x{}^* &= K_{xx}x^* - K_{xy}y + \Omega B_{xx}x + \Omega B_{xy}y^* \\ F_y{}^* &= K_{yx}x + K_{yy}y^* - \Omega B_{yx}x^* + B_{yy}y \end{aligned} \tag{1}$$

where components transmitted by the film to resist shaft deflection by reaction against the housing are positive. Also, rotation of the reference vectors is in the positive direction as defined by conventional polar coordinates.

To apply to the present analysis these coefficients are transformed to whip and whirl coordinates by the equations

$$\begin{aligned} K_{rr} &= K_{yy} - \Omega B_{yx} \\ K_{ss} &= K_{xx} + \Omega B_{yx} \\ K_{rs} &= -\Omega B_{yx} \\ K_{sr} &= K_{xx} - K_{yy} + \Omega(B_{yx} + B_{xy}) \\ B_{rr} &= K_{yx} + \Omega B_{yy} \\ B_{ss} &= -K_{yx} + \Omega B_{xx} \\ B_{rs} &= K_{yx} \\ B_{sr} &= -K_{xy} - K_{yx} + \Omega(B_{xx} - B_{yy}) \end{aligned} \tag{2}$$

where the whip plane is through the x-axis. If the whip plane is through the y-axis, the subscripts x and y should be interchanged, and the sign of each coefficient with a subscript of both x and y should be reversed. It should be noted that the new damping coefficients, which relate to forces 90 deg ahead of the associated displacements, are based on displacements rather than velocities as for the conventional coordinates. These coefficients are multiplied by the corresponding components of the relative deflection to produce components of force. This multiplication is applied in equations (3) below.

Final Equations of Motion. With the complete system simulated by the stiffness coefficients and the fluid-film coefficients, the unbalance forces are satisfied by a set of equilibrium equations at the bearings. Four components of force must be simultaneously satisfied by eight independent components of deflection at each bearing. Therefore, each component of force yields two equations; one equates the rotor and stator forces, and the other equates the rotor and fluid-film forces. The number of equations is eight times the number of bearings; they are:

$$\begin{aligned} &F^R_{rrij}y^R_{rj} + F^R_{rsij}y^R_{sj} - F^S_{rrij}y^S_{rj} = -F_{ui} \\ &F^R_{ssij}y^R_{sj} - F^S_{srij}y^S_{rj} - F^S_{ssij}y^S_{sj} = 0 \\ &F^R_{rrij}y^R_{rj} + F^R_{rsij}y^R_{sj} - \delta_{ij}\{K_{rrj}(y^R_{rj} - y^S_{rj}) \\ &\qquad + K_{rsj}(y^R_{sj} - y^S_{sj}) - B_{rrj}(y^{R*}_{rj} - y^{S*}_{rj}) \\ &\qquad - B_{rsj}(y^{R*}_{sj} - y^{S*}_{sj})\} = -F_{ui} \\ &F^R_{ssij}y^R_{sj} - \delta_{ij}\{K_{srj}(y^R_{rj} - y^S_{rj}) + K_{ssj}(y^R_{sj} - y^S_{sj}) \\ &\qquad - B_{srj}(y^{R*}_{rj} - y^{S*}_{rj}) - B_{ssj}(y^{R*}_{sj} - y^{S*}_{sj})\} = 0 \\ &F^{R*}_{rrij}y^{R*}_{rj} + F^{R*}_{rsij}y^{R*}_{sj} - F^{S*}_{rrij}y^{S*}_{rj} = -F^*_{ui} \\ &F^{R*}_{ssij}y^{R*}_{sj} - F^{S*}_{srij}y^{S*}_{rj} - F^{S*}_{ssij}y^{S*}_{sj} = 0 \\ &F^{R*}_{rrij}y^{R*}_{rj} + F^{R*}_{rsij}y^{R*}_{sj} - \delta_{ij}\{K_{rrj}(y^{R*}_{rj} - y^{S*}_{rj}) \\ &\qquad + K_{rsj}(y^{R*}_{sj} - y^{S*}_{sj}) + B_{rrj}(y^R_{rj} - y^S_{rj}) \\ &\qquad + B_{rsj}(y^R_{sj} - y^S_{sj})\} = -F^*_{ui} \\ &F^{R*}_{ssij}y^{R*}_{sj} - \delta_{ij}\{K_{srj}(y^{R*}_{rj} - y^{S*}_{rj}) + K_{ssj}(y^{R*}_{sj} - y^{S*}_{sj}) \\ &\qquad + B_{srj}(y^R_{rj} - y^S_{rj}) + B_{ssj}(y^R_{sj} - y^S_{sj})\} = 0 \end{aligned} \tag{3}$$

where the conventional summation of expressions with repeated index applies, and δ_{ij} is the Kronecker delta which takes a value of 1 if $i=j$ and 0 if $i \neq j$. These are the final equations of motion which yield the response of the system. Any desired resultant such as force, moment, slope, or deflection is obtained in the two pair of whirl and whip coordinates by back-substitution into the analyses of the stiffness coefficients and the unbalance forces.

Transformation of Solution to Orbits. The four components of any resultant may be transformed into elliptical coordinates which are represented as the dimensions of an ellipse and a phase angle. If the resultant transformed is deflection, the ellipse represents the orbit. The following derivation of this transformation will, for simplicity, relate to orbits. However, it should be recognized that the same transformation can be used for other desired quantities as, for example, the effective gyroscopic moment of a disk.

Deflection is obtained as the four components y_r, y_s, y_r^*, y_s^*. If a new whirl reference plane is selected at the angle $\tan^{-1}(y_s^*/y_s)$ ahead of the primary whirl reference plane, the transformed coordinates are $\bar{y}_r$, $\bar{y}_s$ and $\bar{y}_r^*$, $\bar{y}_s^*$ with $\bar{y}_s^* = 0$. An expression for the distance from the center to the deflected position represented by the transformed coordinates is written as a function of $\Omega\Delta t$, the angle of rotation of the new primary whirl plane from the whip plane in the time increment Δt. An angle where the derivative of this expression is zero represents an axis of the ellipse. Algebraic simplification of the derivative set to zero yields the equation

$$(\sin\Omega\Delta t \cos\Omega\Delta t)/(\cos^2\Omega\Delta t - \sin^2\Omega\Delta t) = -\bar{y}_r^*/(2\bar{y}_r + \bar{y}_s) \tag{4}$$

The deflected positions calculated for whirl angles of $\Omega\Delta t$, the first solution of equation (4) where $|\Omega\Delta t|$ is at the minimum and $\Omega\Delta t + \pi/2$, the second solution, define the components of deflection, y_a and y_b, respectively, along the axes of the ellipse as illustrated in Fig. 1. The orientation angle of the ellipse axes is designated α. The component, y_a, is on the axis displaced by α from the whip plane. The phase angle as illustrated is

$$\phi = \Omega\Delta t - \tan^{-1}(y_s^*/y_s) - \alpha \tag{5}$$

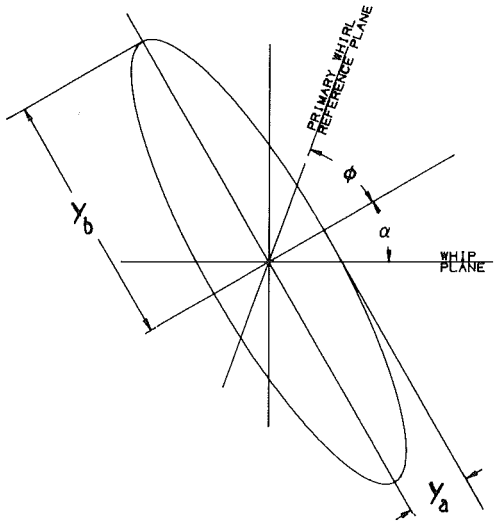

Fig. 1 Nomenclature of orbit dimensions

and represents the location of the original whirl primary reference plane at the instant of the deflected position defined by the dimension y_a. Therefore, the phase angle is the lag angle in relation to the unbalance reference plane of the deflection on an axis of the ellipse and on the side designated by the sign of the appropriate component y_a or y_b.

If the signs of the two components are the same, the motion in the orbit is forward; if the signs are opposite, the motion is backward. The results do not automatically fall in a consistent pattern of quadrants which would enhance visualization. Therefore, if it should be desired to limit the range of phase angle to 180 deg, a simple transformation may be performed by adding or subtracting 180 deg from any value calculated to be outside the range. At the same time, the signs of y_a and y_b should be reversed to preserve the location on each axis referenced by the phase angle. Also, if 90 deg should be added or subtracted from the orientation angle to attain consistency, the values of y_a and y_b should be interchanged. The resulting components will be described as vertical and horizontal where the corresponding ellipse axis deviates by the orientation angle from vertical and horizontal, respectively.

Verification of Analysis. Since the whirl and whip coordinates are nonorthogonal, the analysis presents an automatic verification of the solution assuming given coefficients for the structures and the bearings and given unbalance forces. Rotation of the reference axes 90 deg to repeat a solution is verification of the bearing coordinate transformations, the formulation and solution of the final equations, the back-substitution and the transformation to elliptical coordinates.

A second simple analysis, which includes verification of unbalance forces, will be derived. It consists of calculating the work done by the unbalance forces on the system and the work absorbed by the bearings in one cycle, which must be equal.

It is convenient to introduce additional new coordinates to perform the verification calculations. These coordinates also are unconventional and will be called forward and backward whirl. They are defined by two outwardly directed unit vectors; the forward whirl vector is identical to the whirl vector, and the backward whirl vector is also identical, except its direction or rotation is reversed. These two rotating vectors are phased to coincide in the whip plane. Transformation from the whirl and whip coordinates is shown using deflection as example by equations

$$y^+ = y_r + (y_s/2)$$
$$y^- = y_s/2 \tag{6}$$

These coordinates will be found very useful because they are orthogonal, eliminate coupling at disks, and are easily visualized. Transformation to Cartesian coordinates is also useful and is illustrated for the whip plane selected through the x-axis by these equations

$$x = y_r + y_s$$
$$y = y_r \tag{7}$$

Calculation of the work done by unbalance loading is very simple when the new orthogonal coordinates are used. For example, if a particular unbalance, U, is applied at an angle, θ, in the direction of rotation from the primary whirl reference plane, the work done per cycle is

$$W_u = 2\pi U y^+ \sin(\phi+\theta)\Omega^2/g \tag{8}$$

where positive unbalance is due to eccentricity of a weight in the positive direction. For couple unbalance due to disk skew, positive due to positive initial shaft slope, the forward component of slope is substituted for deflection and the sign is reversed.

Coordinate transformation can make calculation of the work absorbed by a bearing relatively simple. The orbit of the shaft relative to the housing is obtained as the difference in deflections

$$y^F = y^R - y^S \tag{9}$$

resulting in the four components

$$y_r^F, y_s^F, y_r^{F*}, y_s^{F*}$$

which are then transformed to the elliptical coordinates to obtain the components

$$y_a^F, y_b^F, \alpha^F, \phi^F$$

The bearing coefficients are then transformed to a new reference frame which coincides with the axes of the ellipse by the equations

$$\begin{aligned}
\bar{K}_{xx} &= K_{xx}\cos^2\alpha + K_{yy}\sin^2\alpha + (K_{xy}+K_{yx})\cos\alpha\sin\alpha \\
\bar{K}_{yy} &= K_{yy}\cos^2\alpha + K_{xx}\sin^2\alpha - (K_{xy}+K_{yx})\cos\alpha\sin\alpha \\
\bar{K}_{xy} &= K_{xy}\cos^2\alpha - K_{yx}\sin^2\alpha + (K_{yy}-K_{xx})\cos\alpha\sin\alpha \\
\bar{K}_{yx} &= K_{yx}\cos^2\alpha - K_{xy}\sin^2\alpha + (K_{yy}-K_{xx})\cos\alpha\sin\alpha \\
\bar{B}_{xx} &= B_{xx}\cos^2\alpha + B_{yy}\sin^2\alpha + (B_{xy}+B_{yx})\cos\alpha\sin\alpha \\
\bar{B}_{yy} &= B_{yy}\cos^2\alpha + B_{xx}\sin^2\alpha - (B_{xy}+B_{yx})\cos\alpha\sin\alpha \\
\bar{B}_{xy} &= B_{xy}\cos^2\alpha - B_{yx}\sin^2\alpha + (B_{yy}-B_{xx})\cos\alpha\sin\alpha \\
\bar{B}_{yx} &= B_{yx}\cos^2\alpha - B_{xy}\sin^2\alpha + (B_{yy}-B_{xx})\cos\alpha\sin\alpha
\end{aligned} \tag{10}$$

with the superscript on α omitted. These transformed coefficients are in turn transformed by equations (2) to obtain the damping coefficients

$$\bar{B}_{rr}, \bar{B}_{ss}, \bar{B}_{rs}, \bar{B}_{sr}$$

The corresponding deflection components referenced to the ellipse axes are obtained by transforming y_a^F and y_b^F to $\bar{y}_r^F$ and $\bar{y}_s^F$ by equations (7);

$$\bar{y}_r^{F*} \text{ and } \bar{y}_s^{F*} \text{ are zero.}$$

The damping coefficients are multiplied by the appropriate components of deflection across the film to yield the damping forces associated with orbit across the film:

$$\begin{aligned}
\bar{F}_r^{F*} &= \bar{B}_{rr}\bar{y}_r^F + \bar{B}_{rs}\bar{y}_s^F \\
\bar{F}_s^{F*} &= \bar{B}_{sr}\bar{y}_r^F + \bar{B}_{ss}\bar{y}_s^F
\end{aligned} \tag{11}$$

With these force and deflection components transformed to forward and backward whirl coordinates by equations (6) the work done by the shaft on the film in one cycle is

$$W^F = 2\pi(\bar{F}^{F*+}\bar{y}^{F+} + \bar{F}^{F*-}\bar{y}^{F-}). \tag{12}$$

The forward and backward whirl coordinates can also provide simple analysis to verify rotor response. It is necessary to transform the solution which is first obtained in two pair of whirl and whip coordinates into the corresponding two pair of backward and forward whirl coordinates by application of equations (6). If only orbits are available, or if it is desired to verify the transformation of the results to elliptical coordinates, the required forward and backward whirl components may be obtained by the equations

$$\begin{aligned}
y^+ &= \{(y_a+y_b)/2\}\cos\phi \\
y^- &= \{(y_a-y_b)/2\}\cos(\phi+2\alpha) \\
y^{*+} &= -\{(y_a+y_b)/2\}\sin\phi \\
y^{*-} &= -\{(y_a-y_b)/2\}\sin(\phi+2\alpha)
\end{aligned} \tag{13}$$

where the transformation is shown for deflection. The process of verification then becomes that of calculating the response of the rotor in each plane, where no coupling between planes exists. Deflections at the bearings obtained from the overall solution are impressed to calculate independent solutions in each plane. Gyroscopic effects are independent because only steady precession is represented by each solution. The ef-

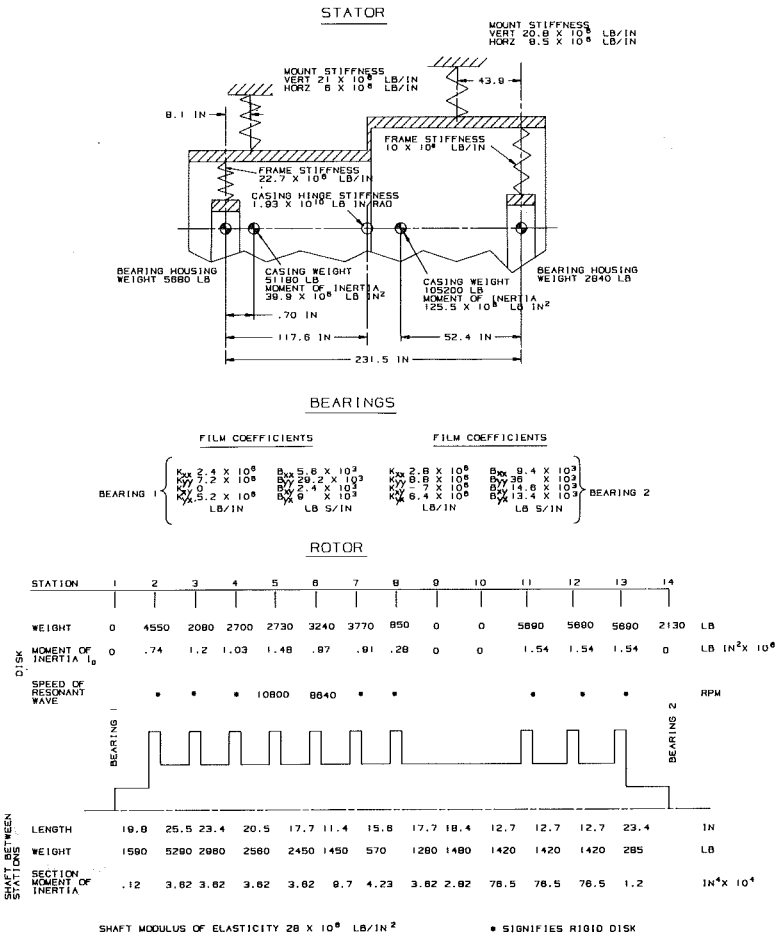

Fig. 2 Model of sample analysis; conversion factors: (m) = (in.) × 2.54 × 10^{-2}, (m^4) = ($in.^4$) × 4.162 × 10^{-7}, N = (lb) × 4.448, (N/m) = (lb/in) × 1.751 × 10^2, (N/m^2) = ($lb/in.^2$) × 6.895 × 10^3, (Nm^2) = (lb $in.^2$) × 2.870 × 10^{-3}, (Ns/m) = (lb s/in.) × 1.751 × 10^2, (Nm/rad) = (lb in./rad) × .1130

fective gyroscopic moments at the disks are expressed for forward and backward whirl as for calculation of F^R_{rrij} and F^R_{ssij}, respectively. Forces at the bearings due to motion of the rotor are obtained. The corresponding forces due to response of the bearing fluid films are also calculated. Although the coefficients transformed by equations (2) may be used in conjunction with the whirl and whip deflections across the films, equations (1) provide independence from the calculations used in the overall solution. Therefore, the orbits across the films are transformed to Cartesian coordinates by equations (13), (6), and (7), and the forces are calculated by equations (1). Transformation of the forces by equations (7) and (6) should yield forces equal to those calculated for the rotor.

The forces due to stator motion are also best calculated in Cartesian coordinates to avoid coupling of mount reactions. Again, an equal set of forces must be obtained to secure verification.

The back calculation of bearing forces due to motion of a rotor and the stator provides also results to verify assumptions used to calculate the response of these structures. Since these results are obtained in uncoupled planes, only elementary principles are necessary to determine if the elastic response and the dynamic loading are compatible. Also, relative magnitudes of different effects can be calculated to explain system behavior.

Sample Analysis

The model used for sample analysis is defined in Fig. 2 and is a simulation of a possible large two-bearing gas turbine. The casings are assumed rigid except for an elastic hinge which represents the typical bulkhead at the juncture between the compressor and the combustor casings. This simple assumption of casing flexibility is considered realistic. The rotor is flexible and two flexible disks are intended to simulate groups of compressor stages. The remaining five compressor disks and the three turbine disks are assumed rigid. The bearing coefficients are typical and, for convenience, are assumed constant.

The stator stiffness coefficients were calculated directly from equations of motion for the system of rigid bodies and springs. Rotor stiffness coefficients and unbalance forces were calculated by the Prohl method as described in reference [1]. Magnification factors representing effects of disk flexibility were assumed by analogy to the simple system of a weight mounted on a spring. The design parameters of the model were selected to illustrate substantial sensitivity to the stiffness of the casing hinge. Design speed is 3600 rpm.

Figure 3 illustrates the response of the complete machine to an unbalance due to an eccentric weight at station 7 which is near the shaft center. To save space the vertical axis is inclined across the page. All orbits are plotted to the same scale as they appear in planes perpendicular to the axis of the machine. Arrows show the direction of motion in each orbit and of the unbalance. Phase angle associated with each orbit is shown by a dotted line extending from the center and a small circle on the intersection of the orbit with one of the axes. The dotted line indicates the location of the unbalance at the instant of location in orbit on the center of the small circle. The dif-

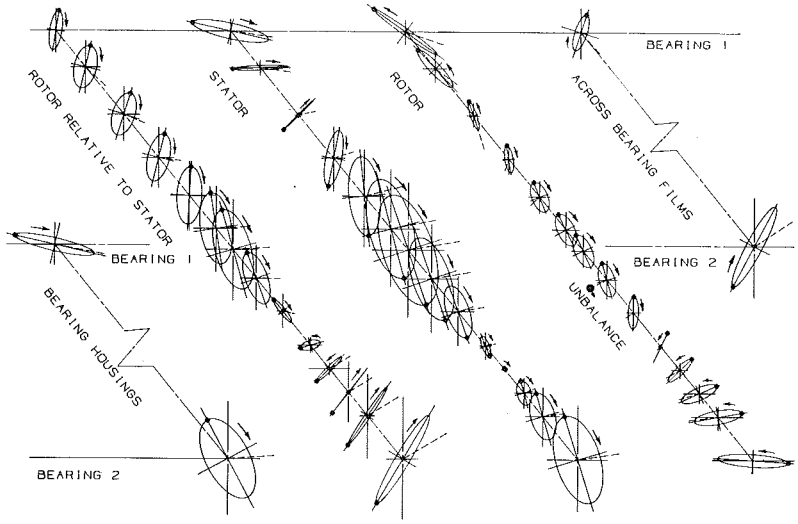

Fig. 3 Response of complete system to eccentric weight at station 7 plotted as orbits

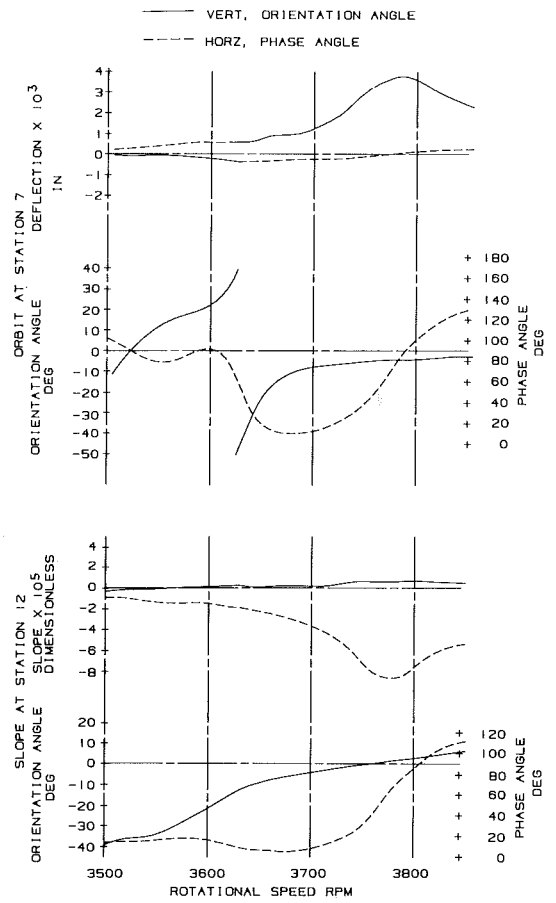

Fig. 4 Variation with speed of two representative rotor orbits due to eccentric weight at station 7; unbalance = 16 lb in.; conversion factors: (m) = (in) × 2.54 × 10^{-2}, (Nm) = (lb in) × .1130

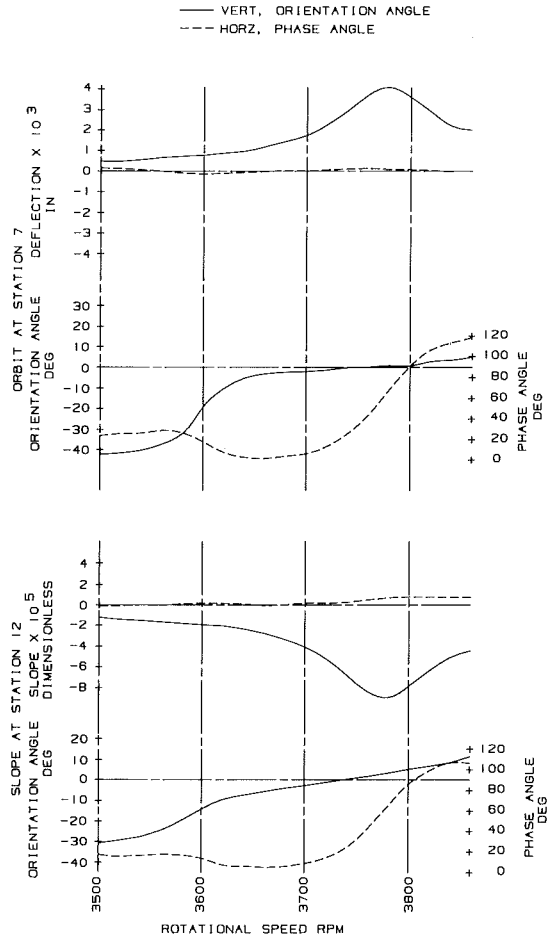

Fig. 5 Variation with speed of two representative rotor orbits due to disk skew at station 12; unbalance = 800 lb in.^{2}; conversion factors: (m) = (in) × 2.54 × 10^{-2}, (Nm^2) = (lb in.^{2}) × 2.870 × 10^{-3}

ficulty of representing graphically the four dimensional results can be seen. Therefore, the illustrations to follow will reduce the amount of information shown.

The dimensions of two orbits which represent rotor response as deflection at station 7 and slope at station 12 are plotted in each of Figs. 4 and 5 for a speed range of 3500 rpm to 3850 rpm. The unbalance represented by Fig. 4 is the same as that illustrated in Fig. 3; couple unbalance due to disk skew at station 12 is represented by Fig. 5. The resulting moment applied to the disk is positive due to disk skew corresponding to positive initial shaft slope. The influence of casing hinge stiffness is illustrated by Fig. 6. The orbit dimensions shown in Fig. 4 are plotted at design speed for a range of hinge stiffness.

Verification of the analyses was attained at several points

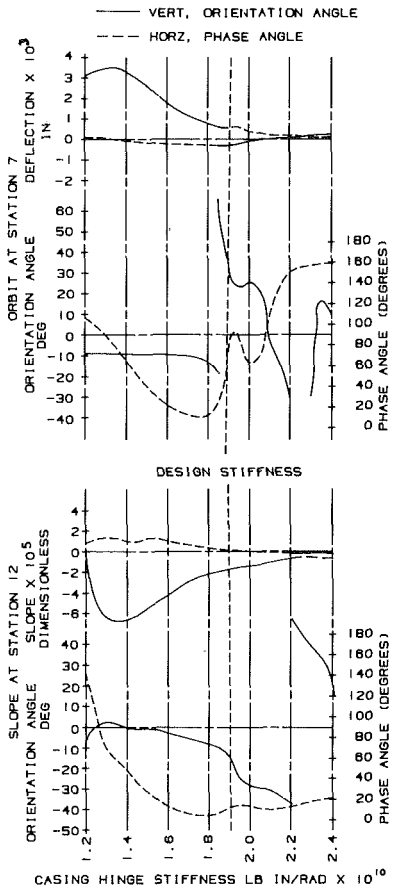

Fig. 6 Effect of casing stiffness on two representative orbits due to eccentric weight at station 7; couple unbalance = 16 lb in.; rotational speed = 3600 rpm; conversion factors: (m) = (in.) x 2.54 x 10^{-2}, (Nm) = (lb in.) x .1130, (N/m/rad) = (lb in./rad) x .1130

Table 1 Summary of verification by comparison of work due to unbalance with work dissipated; conversion factors: (m) = (in.) x 2.54 x 10^{-2}, (Nm) = (lb in.) x .1130, (Nm^2) = ($lb\ in.^2$) x 2.870 x 10^{-3}

			UNBALANCE AT 3600 RPM	16 LB IN AT STATION 7	800 LB IN^2 AT STATION 12
DEFLECTION ACROSS BEARING FILM	BEARING 1	VERT X10^4 IN		2.015	1.843
		HORZ X10^4 IN		-6.222	-5.775
		ORIENTATION ANGLE DEG		-17.67	-14.83
	BEARING 2	VERT X10^4 IN		-2.647	1.449
		HORZ X10^4 IN		14.977	-9.882
		ORIENTATION ANGLE DEG		-27.51	-30.21
IN PLANE OF UNBALANCE DEFLECTION		VERT X10^4 IN		-2.788	
		HORZ X10^4 IN		5.850	
		PHASE ANGLE DEG		91.44	
SLOPE		VERT X10^6 DIMENSIONLESS			-20.010
		HORZ X10^6 DIMENSIONLESS			1.120
		PHASE ANGLE DEG			11.94
		WORK IN ONE CYCLE LB IN		5.7	3.6

by rotation of coordinates 90 deg and by calculating the work due to unbalance and that dissipated in one cycle. Results of these work comparisons for the design point with the two unbalance conditions assumed in the solutions plotted in Figs. 3 and 4 are summarized in Table 1.

The response of the rotor and the stator at these two conditions was also verified. The orbits across the bearing

Table 2 Summary of verification by comparison of film, shaft, and housing forces; conversion factors: (N) = (lb) x 4.448, (m) = (in.) x 2.54 x 10^{-2}, (Nm) = (lb in.) x .1130, (N/m^2) = ($lb\ in.^2$) x 2.870 x 10^{-3}

			UNBALANCE AT 3600 RPM	16 LB IN AT STATION 7	800 LB IN^2 AT STATION 12
DEFLECTION ACROSS BEARING FILM	BEARING 1	VERT X10^4 IN		2.015	1.843
		HORZ X10^4 IN		-6.222	-5.775
		ORIENTATION ANGLE DEG		-17.67	-14.83
		PHASE ANGLE DEG		59.35	38.37
	BEARING 2	VERT X10^4 IN		-2.647	1.449
		HORZ X10^4 IN		14.977	-9.882
		ORIENTATION ANGLE DEG		-27.51	-30.21
		PHASE ANGLE DEG		151.39	13.67
SHAFT DEFLECTION AT BEARING	BEARING 1	VERT X10^4 IN		-12.955	-13.175
		HORZ X10^4 IN		-1.124	-1.865
		ORIENTATION ANGLE DEG		-35.52	-16.31
		PHASE ANGLE DEG		16.97	4.90
	BEARING 2	VERT X10^4 IN		-11.690	-9.039
		HORZ X10^4 IN		-2.114	1.094
		ORIENTATION ANGLE DEG		-3.775	-11.74
		PHASE ANGLE DEG		2.84	14.93
BEARING HOUSING DEFLECTION	BEARING 1	VERT X10^4 IN		-13.541	14.988
		HORZ X10^4 IN		2.204	-3.022
		ORIENTATION ANGLE DEG		-12.86	-3.79
		PHASE ANGLE DEG		2.36	174.44
	BEARING 2	VERT X10^4 IN		7.212	9.886
		HORZ X10^4 IN		-14.417	-10.403
		ORIENTATION ANGLE DEG		28.20	-11.72
		PHASE ANGLE DEG		65.74	174.72
FORCE TRANSMITTED BY FILM LB	BEARING 1	FORWARD, IN PHASE WITH UNBALANCE		-18.0	152.0
		BACKWARD, IN PHASE WITH UNBALANCE		-1635	-1604
		FORWARD, 90 DEG AHEAD OF UNBALANCE		-406	-543
		BACKWARD, 90 DEG AHEAD OF UNBALANCE		235	-87
	BEARING 2	FORWARD, IN PHASE WITH UNBALANCE		-775	-1355
		BACKWARD, IN PHASE WITH UNBALANCE		286	-248
		FORWARD, 90 DEG AHEAD OF UNBALANCE		-870	-105
		BACKWARD, 90 DEG AHEAD OF UNBALANCE		-1788	-794

BACKWARD AND FORWARD REFERENCE VECTORS COINCIDE WHEN PASSING HORIZONTAL AXIS

fluid films and the orbits of the shaft and housings at the bearings were used to calculate the forces at the bearings. The forces due to rotor and stator motion were obtained by repeating the calculations used to obtain the overall solution. The forces due to response of the films were calculated by equations (1). Equal forces were obtained form each of the three calculations; the results are summarized in Table 2. Also, spot back calculations showed that elastic compatibility and equilibrium were attained.

Discussion

Behavior of the system analyzed is too complex to be adequately described by the conventional definitions of critical speed and modal response. The design casing stiffness does indeed show a critical speed at approximately 3800 rpm. Here the response tends toward the maximum in all its components, the form of the response tends to be independent of the unbalance and a 90 deg phase angle of the orbit associated with either type of unbalance at any station occurs in a narrow speed range. No other such critical speed is found in the range down at least to 2400 rpm. However, in reality it would be necessary to compensate for bearing coefficient variation with speed to derive such a conclusion. There are, however, two other speeds where a 90 deg phase angle arises in response to the unbalance at station 7. It is the response near the second of these speeds that is illustrated in Fig. 3.

It is possible that the unbalance, which simulates thermal

bow, might cause vibration despite the remoteness from the recognized critical speed. Although response of the shaft itself is low, there is a magnification in the stator. Transmission of vibration through the bearings is heightened when the phase angle of the bearing housings approaches 90 deg. In the example illustrated, this condition is seen at bearing 2. Also, the critical speed is sensitive to the casing stiffness. It is seen from Fig. 6 that reducing the casing hinge stiffness to 1.3×10^{10} lowers the critical speed to 3600 rpm. Similar conditions to those described above for 3800 rpm are indicated.

It should be of interest that the response can contain a mixture of forward and backward orbits. However, transition from one direction to another occurs smoothly with one component passing through zero. Such continuity is to be expected from a system which is significantly influenced by gyroscopic effects; the elementary analogy of independent motion in the horizontal and vertical planes is not adequate, because it implies that gyroscopic moment jumps due to one plane passing through resonance affect only the motion in that plane.

It obviously is impossible to draw general conclusions on the effects of any particular feature in a complex turbomachine as the gas turbine represented by the sample analysis. However, it is hoped to illustrate that dynamic analysis of the complete system is prudent and possible. Although strong influence of the stator is illustrated to show that conventional analysis of the rotor and bearings alone is not adequate, each machine may possess sensitivity to different features. Such features can be identified by analysis even though the reasons for the particular sensitivity may be difficult to relate to the characteristics of the individual components comprising the system. However, coordinate transformation of the overall results can explain the interactions involved in a particular effect.

Although it is, unfortunately, not possible to provide the design engineer with a guide to particular effects, the method of analysis presented is simple enough for him to devise his own analysis. This simplicity also lends the method to accounting for nonlinear effects. For instance, reference [2] discusses possible application to nonlinear fluid films. It concludes that nonlinear jumps due to squeeze-film dampers might be predicted. Li and Gunter [5] also discuss such a jump.

Simulation of a flexible bladed disk by analogy to the simple spring-weight would be correct if its flexing comprises only a single mode form which is not affected by the speed of spin. However, precise simulation may also be expressed as forward and backward magnification factors. These factors would depend on the relative speed between whirl and spin and the speed of spin.

Summary and Conclusions

A method for analyzing unbalance response of a complete turbomachine, accounting for mount asymmetry, fluid-film bearing anisotropy and disk flexibility, was derived and sample analyses were presented for a hypothetical large two-bearing gas turbine. The method permits the design engineer to utilize tests and/or independent analyses to characterize critical structures of the system. The overall analysis is simple; it requires solution of only eight simultaneous equations for each bearing in the machine. It provides for identification of any characteristics to which the system is sensitive.

Coordinate transformations which reduce the results of the overall analysis to independent planes were derived and discussed. These transformations provide for independent verification of results by application of only elementary principles and should enhance visualization and understanding of any perplexing system behavior.

Sample analyses showed that the conventional practice of treating the rotor and bearings alone is not adequate; the characteristics of the stator can affect the overall response to unbalance. Also, they showed that response to unbalance is not necessarily uniform, and variations of unbalance should be considered.

The engineer is offered the ability to obtain dynamic solution of an entire turbomachine and to visualize, interpret, and verify the results. Interpretation would allow comparison of the results with specific design objectives. For example, vibratory stresses in bladed disks may be calculated. Such ability should improve accepted design practice.

References

1 Klompas, N., "Significance of Disk Flexing in Viscous-Damped Jet Engine Dynamics," ASME JOURNAL OF ENGINEERING FOR POWER, Oct. 1978, pp. 647–654.

2 Klompas, N., "Blade Excitation by Elliptical Whirling in Viscous-Damped Jet Engines," JOURNAL OF ENGINEERING FOR POWER, Apr. 1981, pp. 326–330.

3 Darlow, M. S., et al., "Extension of the Transfer Martix Method for Rotor Dynamic Analysis to Include a Direct Representation of Conical Sections and Trunnions," ASME *Journal of Mechanical Design*, Jan. 1980, pp. 122–129.

4 Bannister, R. H., "Methods for Modelling Flanged and Curvic Couplings for Dynamic Analysis of Complex Rotor Construction," ASME *Journal of Mechanical Design*, Jan. 1980, pp. 130–139.

5 Li, D. F., and Gunter, E. J., "Component Mode Synthesis of Large Rotor Systems," ASME Paper No. 81-GT-147, to be published in ASME JOURNAL OF ENGINEERING FOR POWER.

6 Hagiwara, N., et al., "Analysis of Coupled Vibratory Response in a Rotating Flexible Shaft-Impeller System," ASME *Journal of Mechanical Design*, Jan. 1980, pp. 162–167.

W. G. Steltz[1]
Advisory Engineer,
Steam Turbine-Generator Division.

P. K. Lee
Senior Research Scientist,
Physical and Inorganic Chemistry Department,
Research and Development Center.

W. T. Lindsay, Jr.
Consulting Scientist,
Chemical Sciences Division,
Research and Development Center.
Westinghouse Electric Corporation,

The Verification of Concentrated Impurities in Low-Pressure Steam Turbines

The problem of corrosion-assisted low-pressure blade failures is discussed from the water chemistry and aerothermodynamic viewpoints. The physical chemistry of particular steam impurities existing in low-pressure steam turbines is reviewed with special applicability to blade path steam conditions. The interaction of the turbine expansion line with the salt solution zone has been verified by field testing which has, for the first time, demonstrated the existence of concentrated impurities within the low pressure turbine blade path. In addition, the existence of low levels of moisture as measured by an optical moisture probe offers strong evidence that the expansion process in low-pressure steam turbines takes place, on the average, in thermodynamic equilibrium, at least in the vicinity of the saturated vapor line.

Introduction

Corrosion-assisted cracking has been experienced in many steam turbine units, varying from those used in plants with drum type steam generators operating at less than 2000 psi (13.8 MPa) upward through the pressure scale to plants with supercritical once-through steam generators. As a recognized industry-wide problem, many programs are underway to study the fundamental causes of material failures in steam environments.

A significant problem area of turbine material corrosion involves the transport of corrosive impurities throughout the steam turbine cycle. It is essential to determine the identity of the corrosive species, their sources in the plant water/steam cycle, the mechanism of their transport and deposition during the expansion cycle, and the modes of attack on turbine materials by the significant corrodents.

These several investigative programs form a broadly based effort spanning many disciplines. Included in this effort are the fracture analysis of failed turbine blades, the metallurgical testing of turbine materials in corrosive environments, the determination of steam and water purity in operating units, the physical and chemical characteristics of water, water treatment additives, and corrosive substances, and the analysis of the thermochemical mechanisms that cause deposition of corrodents on turbine parts.

This paper will describe the several aspects of these programs dealing with water chemistry and the analysis of the mechanisms controlling corrodent deposition within steam turbines. The physical chemistry of steam impurities is reviewed and particular evaluation of their interaction with the turbine blade path expansion line is discussed. The first experimental detection of concentrated impurities in low-pressure turbine blade path steam is described in detail, further test programs are described, and finally, conclusions are drawn.

Table 1 Summary of ASME turbine survey

	Drum type	Once-through	Total
Number of units reviewed	64	31	95
Percent of units with cracks	15	42	
Percent of units with pitting	15	39	
Percent of units with fouling	29	19	

Table 2 Summary of ASME turbine survey cracks with drum type units

	Phosphate[a] treatment	Volatile treatment
Number of units	55	9
Percent of units with cracks	14	25

[a]Coordinated phosphate control

Corrosion-Assisted Failure Experience in Field Turbines

Many interactive factors control the mechanisms of stress corrosion and corrosion fatigue. In some instances of blade cracking it is impossible to identify their separate effects. As an all-inclusive descriptive term, it is usually advisable to characterize the problem as a corrosion-assisted failure.

A significant factor in the occurrence of corrosion-assisted blade failures is the type of steam generator supplying the turbine system. The conventional drum type boiler and the once-through supercritical steam generators differ fundamentally in the type of water treatment chemicals utilized. The all-volatile treatment employed in all once-through boilers is sometimes used in drum type boilers, but, more usually, low-phosphate water treatment is used in drum type

[1]Currently affiliated with Power Dynamics, Inc., Broomall, Pa. 19008

Contributed by the Gas Turbine Division and presented at the ASME Winter Annual Meeting, Washington, D.C., November 15–20, 1981. Manuscript received by the Gas Turbine Division, June 18, 1982.

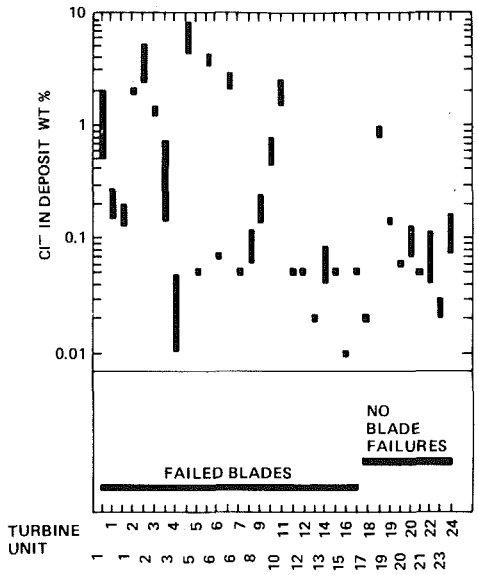

Fig. 1 Deposit analyses for Cl^- from penultimate blades of twenty-four Westinghouse fossil low-pressure turbines. Range indicates average to maximum values.

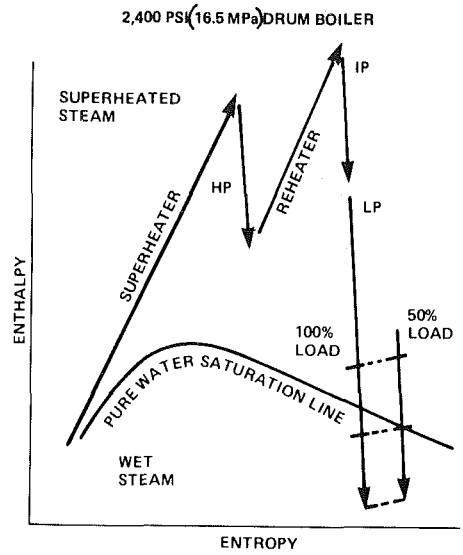

Fig. 2 Simplified Mollier diagram showing turbine expansion lines at 100 and 50 percent load

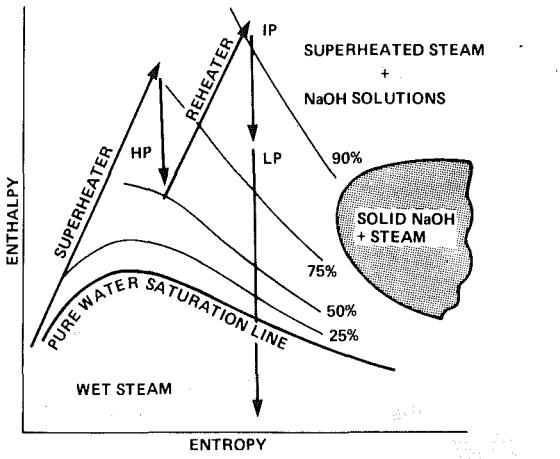

Fig. 3 Simplified Mollier diagram showing turbine expansion lines and sodium hydroxide liquid phase concentrations

boilers. A recent survey sponsored by the ASME Committee on Water for Thermal Power Systems evaluated 95 boiler-turbine systems; these 95 were comprised of 31 once-through and 64 drum type boilers [1]. These results are summarized in Tables I and II.

Although these survey results consistently indicate that corrosion-assisted turbine failures are more prevalent in boiler systems which utilize all-volatile water treatment, other significant factors such as the use and maintenance of polishers and the transfer of undesirable chemical species throughout the turbine cycle could also have a profound influence on turbine blading distress.

A substance which contributes significantly to material corrosion is sodium chloride. Figure 1 shows the weight percent of chloride in deposits taken from twenty-four fossil low-pressure turbine elements, some of which have been inspected more than once [2]. The units are classified in the lower portion of the figure into a group that has had blade failures, and a group that has operated without blade problems.

Chloride is considered to be a primary turbine material corrodent, as is substantiated by the units which have experienced failures generally having a high fraction of chloride in their deposits.

While chloride is considered to be a primary factor in corrosion-assisted cracking, other chemical species have also been shown to contribute to turbine corrosion. These species include sulfate, caustic, and dissolved oxygen. The sodium ion itself is not considered to be corrosive, but is usually the charge compensating cation found in deposits with the anions mentioned above.

Physical Chemistry Aspects of Impurities in Steam

The purpose of a behavior study of impurities in steam turbines is to develop understanding, quantification, and the prediction of their behavior in order to control and ameliorate their undesirable effects on turbine materials. Concentrations of the minor constituents, which exist at levels from parts per million (ppm) down to parts per billion (ppb), are transformed into higher local concentrations. Detailed calculations of the equilibrium fluid composition involving some important volatile substances can now be performed [3] as most of the data needed for this purpose is available.

The characteristics of nonvolatile contaminants are quite different from the volatiles normally used in water treatment. Two substances are of considerable concern to the turbine designer. The first is sodium hydroxide, which has probably damaged more turbines than any other single contaminant. Caustic contamination of steam can occur in a number of different ways. It can be caused by improper regeneration of condensate polishers, by chemistry upsets in phosphate-treated boilers, or by poor steam separation in drum boilers that are being deliberately treated with low-level free caustic.

Plotted on the Mollier diagram of Fig. 2 are expansion lines for steam passing through a fossil fueled turbine system with a 2400 psi (16.5 MPa) drum boiler. A part of the LP expansion line for 50 percent load is shown to the right, where it can be seen how the dry-to-wet transition location (the saturated vapor line) shifts to a different location in the turbine at reduced load. Solutions of sodium hydroxide can be very concentrated with substantially elevated boiling points, so they can exist in the superheated steam region. Lines showing sodium hydroxide concentrations of 25 to 90 percent are shown in the Mollier diagram of Fig. 3. These concentrated solutions cover almost all the region traversed by the steam expansion line. It is only in the wet region, near the outlet of the low pressure turbine, where the sodium hydroxide concentration becomes so dilute as to be non-corrosive.

The second contaminant of great significance is sodium chloride. Salt is a very common contaminant of steam, and its

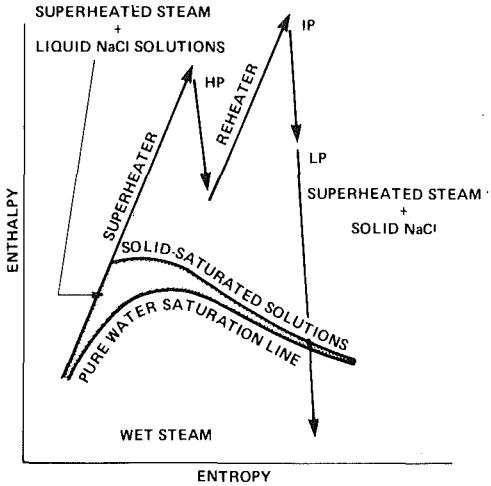

Fig. 4 Simplified Mollier diagram showing turbine expansion lines and sodium chloride liquid solution zone

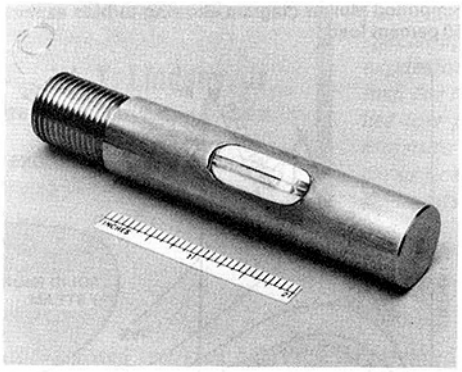

Fig. 5 Typical conductance sensor

concentrated solutions have been shown to cause pitting, corrosion fatigue, and stress corrosion cracking. The thermodynamic properties of sodium chloride are quite different from those of sodium hydroxide, as it has a more limited solubility. The same Mollier diagram and the same expansion lines for a 2400 psi (16.5 MPa) drum boiler turbine system are shown in Fig. 4. The shaded zone is the only region where concentrated salt solutions are stable. Above the shaded zone, only pure dry sodium chloride is stable in superheated steam. Below the zone in the wet region, salt contamination becomes so dilute as to be without much corrosive significance. A similar band of salt solution stability exists for other compounds that are moderately soluble in water.

The upper boundary of the shaded zone is the three-phase boundary at which steam, solid sodium chloride, and liquid solutions saturated with sodium chloride coexist. The position of the three-phase boundary for other salts depends on the boiling point elevation of their solid-saturated solutions. With sodium chloride, the concentration is approximately 28 weight percent at the condition where the low-pressure fossil turbine expansion line crosses this boundary (at about 220°F (104°C)) and is essentially 0 percent at the equilibrium saturated vapor line.

The important feature is that corrosively significant solutions of sodium chloride, and solutions of other salts with limited maximum boiling points, are thermodynamically stable within one stage of the low-pressure turbine.

In summary, solutions of sodium chloride and other moderately water soluble salts are stable only in a narrow band near the liquid-vapor saturation line, whereas solutions of sodium hydroxide and similarly highly soluble compounds can exist in the entire superheated steam region. Thus, in a steam turbine, this means that the corrosive effects of sodium

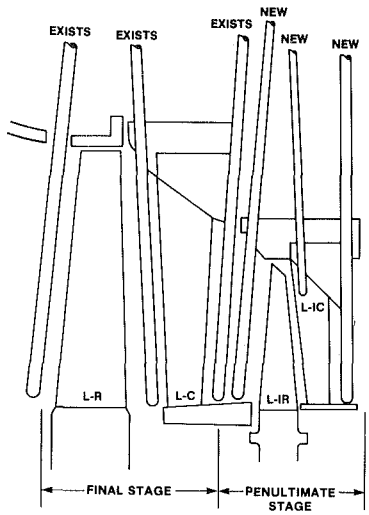

Fig. 6 Transverse probe locations at Encina No. 4, San Diego Gas and Electric Company

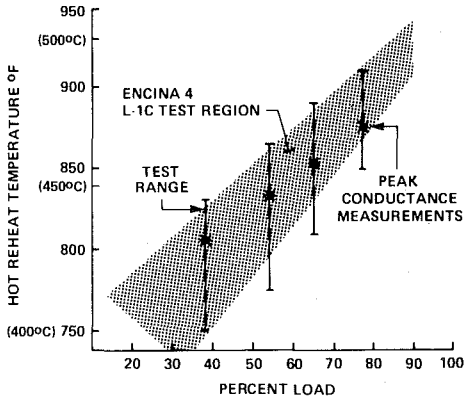

Fig. 7 Encina No. 4 test plan for conductance measurements at the inlet to L-1C

chloride are very localized, while those of sodium hydroxide can occur anywhere, depending on the level of contamination.

Field Verification of Concentrated Impurities Within Low-Pressure Steam Turbines

A key factor pertaining to the cause and effect of impurities in blade path steam is the determination of the physical processes which concentrate these impurities into corrosive solutions. Development activities led to a field test program for verification of the existence of the "salt solution zone" phenomenon in operating turbines.

A measurement device capable of immersion in the blade path steam was conceived as a "surface conductance probe" and designed, developed, and constructed at the Research and Development Center. A typical conductance sensor, which is attached to a long support barrel to form a complete probe, is shown in Fig. 5. The sensing element itself consists of two parallel platinum electrodes spaced less than a millimeter apart, held in place and separated by an insulating block of MACOR[1]. The electrical signal developed by the sensor is affected by the conductance of a fluid film deposited on the insulating surface between the two electrodes. The conductance, in turn, depends on the chemical species comprising the fluid; in the case of pure water, very low levels of conductance are developed. On the other hand, ionizable dissolved impurities increase the conductance by orders of magnitude. Laboratory calibration of several probes at the

[1] Trademark of Corning Glass Works.

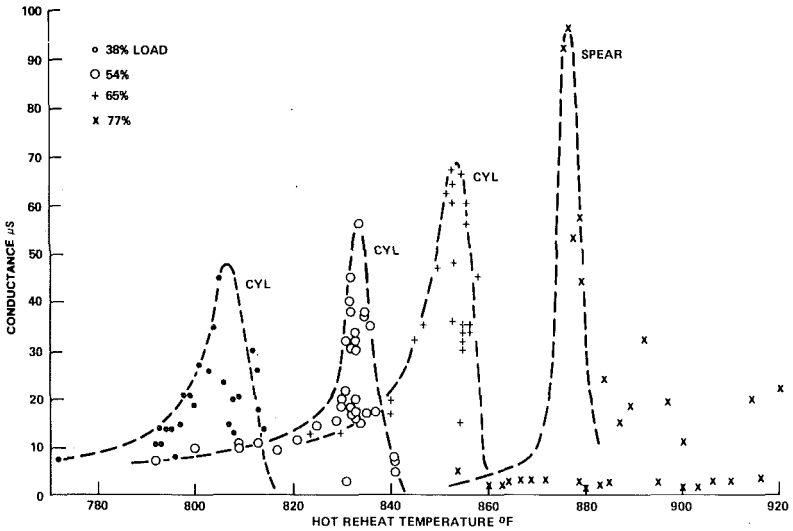

Fig. 8 Electrical conductance data taken at Encina No. 4

Research and Development Center prior to their use in field turbines verified high sensitivity to small amounts of electrolytes.

Figure 6 indicates the location of probe guides in the low pressure turbine of Encina No. 4, a phosphate treated drum boiler unit of the San Diego Gas and Electric Company. The locations marked "NEW" supplemented existing probe locations. In effect, three measurement planes were available: before, in the middle of, and following the penultimate stage. All three locations were fitted with conductance probes of several designs.

The physical location yielding the pertinent results reported herein is the L-1C inlet location. It was this location which could be controlled in such a manner as to control movement across the saturation line from wet to superheated steam and vice-versa.

The test plan, Fig. 7, describes the desired loads and range of hot reheat temperature required to effect the movement of the saturation line. The region of interest is shown as the shaded area labeled L-1C test region. This region is consistent with the predicted "salt solution" zone of Fig. 4. The test loads were limited by the pressure level existing at the plane of measurement, i.e., atmospheric pressure corresponded to about 75 percent load. Actual test points, denoted by asterisks, indicate the location of pertinent conductance data collected during the test program.

At the lowest load, specific points were initially run with steam conditions at their wettest state. Higher values of hot reheat temperature were then established. Indications from the conductance probe located at the L-1C inlet appeared at a nominal level and increased until the probe's environment became superheated steam. The probe output then dramatically dropped to essentially a zero conductance indication. By ramping the hot reheat temperature slowly downward, a distribution of conductance readings emerged. These were substantiated by succeeding up and down ramps. Very careful control of the boiler (drum type) operation was achieved by the several operators assisting in the test program.

The results of the conductance probe(s) measurements are shown in Fig. 8. At each load, as a function of hot reheat temperature, distinct conductance peaks were observed; these were established, and verified, by the up and down ramping of the hot reheat temperature. These observed changes in conductance levels with steam temperature indicate the presence of contaminated condensed water on the conductance probe's surface.

The conversion of the location of the conductance peaks at

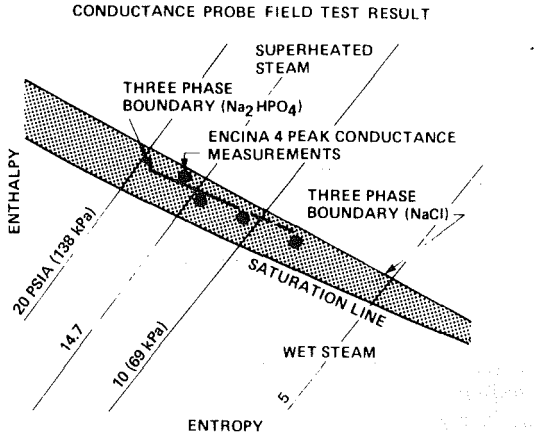

Fig. 9 Simplified Mollier diagram showing location of peak conductance measurements at Encina No. 4

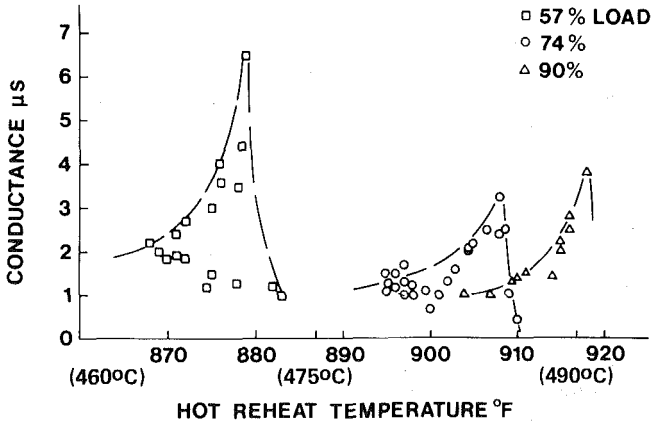

Fig. 10 Electrical conductance data taken at Big Brown No. 2

the four loads has been made to the Mollier diagram of Fig. 9. Heat balance calculations were made for the unit operating conditions consistent with the individual test points. The locus of local steam conditions, compatible with these conductance peaks, is a line of nearly constant superheat. This line is essentially parallel to the maximum concentration line defining the predicted upper limit of the sodium chloride solution zone.

In addition to surface conductance measurements in the low pressure turbine blade path steam, samples were taken of the

Table 3

Blade height %	Average droplet diameter $d \times 10^6$m	Moisture content %
17 (near rotor blade hub)	–	–
29	2.48	0.3
76 (near rotor blade tip)	0.17	0.5

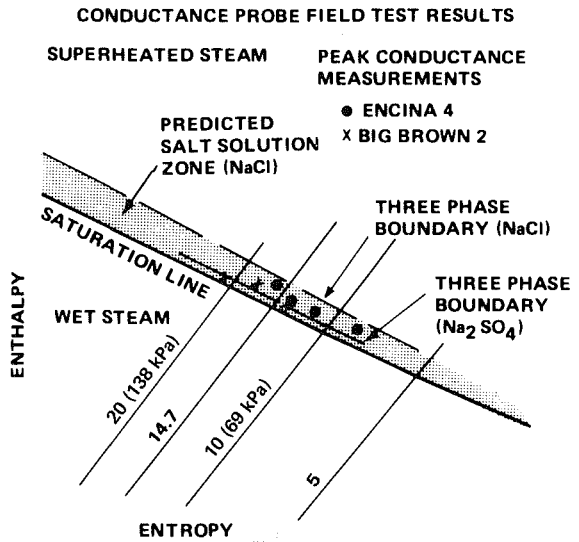

Fig. 11 Simplified Mollier diagram showing location of peak conductance measurements at Big Brown No. 2 and Encina No. 4

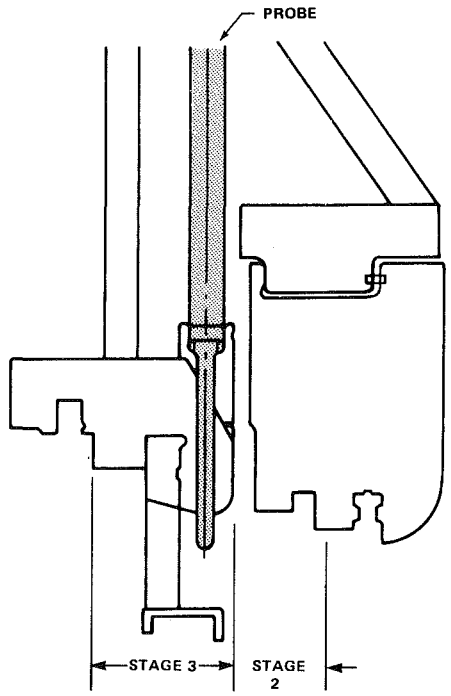

Fig. 12 Conductance probe location at Turkey Point No. 4, Florida Power and Light Company

crossover steam through a sampling tube identical to that used in a steam purity continuous analyzer program [2] in order to determine the chemical species existing in the superheated steam prior to its entry to the blade path. The samples taken from Encina No. 4 showed that phosphate and sodium were the main contaminant species. The three-phase boundary for a sodium phosphate salt (Na_2HPO_4) is shown by the dotted line in Fig. 9. The conductance peak locations are closer to this line than they are to the sodium chloride three-phase boundary.

The observation of conductance peaks at steam conditions with a significant amount of superheat can result only from coverage of the probe insulator surface with a film of a substantially concentrated solution of an electrically conducting substance that is essentially nonvolatile. It could be postulated that such a film could be created by condensation of moisture on an initially contaminated surface, or by some effect of adsorbed moisture or capillary condensation on the properties of the insulator surface. However, the reproducibility of the observations after exposure of the probe to the washing effects of wet steam and the result of laboratory tests of probe response to static (non-contaminating) conditions effectively rule out such explanations for the observations. The most probable cause of these effects is the deposition on the probe of water soluble contaminants that were present in the turbine steam.

We believe that these measurements are the first to be taken directly from a field unit to demonstrate experimentally the existence and location of turbine operating regions where concentrated contaminated solutions exist.

During the course of these experiments, measurements were made of the moisture content and the corresponding average droplet diameter. The locations chosen during these tests were at the L-R exit position in Fig. 6 (the turbine blade path exhaust) the L-1R exit, and the L-1C inlet. The results of pertinence to the conductance probe measurements, are those obtained at the L-1C inlet location. These moisture measurements were made using a multiple wavelength optical probe [4] developed for steam turbine applications.

Moisture measurements were made only at the 65 percent load condition at a reheat temperature of approximately 850°F (454°C), the operating conditions coincident with the peak of the conductance probe response curve, Fig. 8. Table 3 describes the results of these moisture measurements. In the near tip region (i.e., the outer diameter) of the inlet to this stationary blade row, where the conductance probe was situated, moisture contents on the order of 0.5 percent were observed. As the conductance probe was situated at a larger diameter than the 76 percent location of Table 3, the inherent blade path radial energy variation undoubtedly produced higher local enthalpy conditions than that sensed by the moisture probe. Although precisely corresponding measurements of moisture and conductance were not made, extremely low levels of moisture were sensed quite close to the conductance probe's location.

Further Field Verification Testing

Since these initial tests were run in the summer of 1979, three other units were fitted with appropriate probe guides and tested. Two of these units were also fossil units. Conductance peaks were observed in all fossil test programs.

The second fossil unit tested was Big Brown No. 2 of the Texas Utilities Generating Company which is a once-through unit equipped with condensate polishers. The corresponding electrical conductance data for Big Brown No. 2 are presented in Fig. 10. The loci of these peaks have been converted to local steam conditions and are located on the Mollier diagram of Fig. 11. Steam samples indicated the presence of low levels of sulfates and sodium at the low pressure turbine inlet. The "x" symbols on Fig. 11 are close to the three-phase boundary for sodium sulfate solutions, suggesting that a nearly saturated solution of sodium sulfate formed on the surface conductance probe. Data from the third fossil unit tested, Centralia No. 2 of the Pacific Power and Light Company, produced similar characteristics but test data clarity precluded exact quantification.

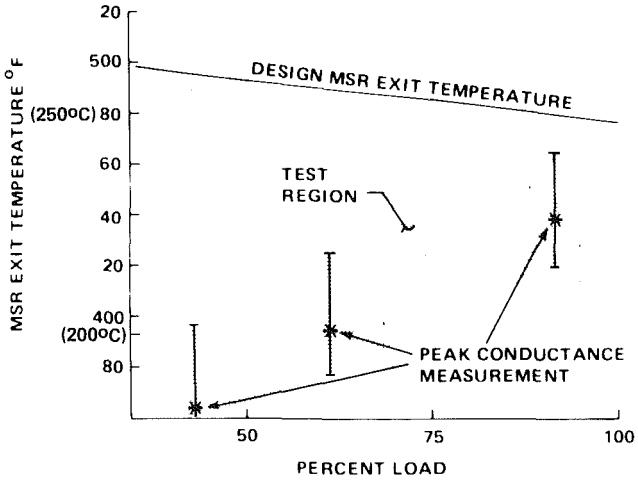

Fig. 13 Turkey Point No. 4 test plan for conductance measurements between disks number 1 and 2

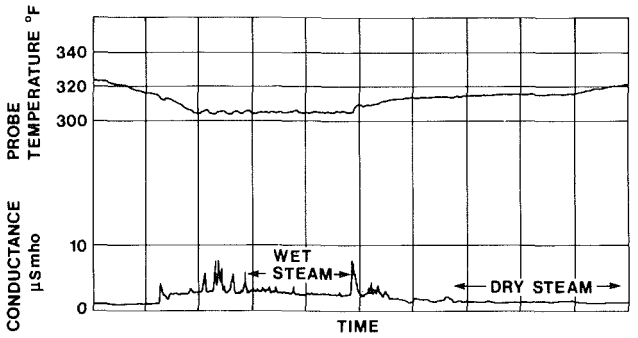

Fig. 14 Electrical conductance and thermocouple traces at Turkey Point No. 4

The First Nuclear Unit Verification Test

The fourth test program was the first to be performed on a nuclear unit, Turkey Point No. 4 of the Florida Power and Light Company. This is a pressurized water reactor system operating with all volatile treatment, consisting of ammonia and hydrazine additions to the feedwater. Two probes were installed at different circumferential locations in the space between stages number 2 and 3 of a low pressure turbine element, Figure 12. These probes were installed during a startup while the turbine was on turning gear. As the blade path pressure at this location is on the order of 80 psia (552 KPa) at full load, the probes were designed to be semipermanent, that is, once installed they would not be removed until the unit came down or until load was reduced to 20 percent or lower.

During the test program, an automatic recorder was employed to sense and document the signal generated by one of the conductance probes. In effect, two signals were recorded: (*i*) the signal from the conductance sensor, and (*ii*) steam temperature as sensed by a thermocouple adjacent to the conductance sensor.

The test program for this nuclear unit required control of the steam temperature entering the low-pressue turbine element. This was effected by control of the steam flow rate entering the reheater tube bundle of the moisture separator reheaters (MSR's) supplying the low pressure turbine. The desired test region is indicated in Fig. 13 with the actual test lines superimposed.

Typical results from the surface conductance probe and its thermocouple are presented in Fig. 14 as a function of time. The lower trace is the conductance sensor's output while the upper trace is that of the thermocouple.

In this instance, which is typical of data collected in this

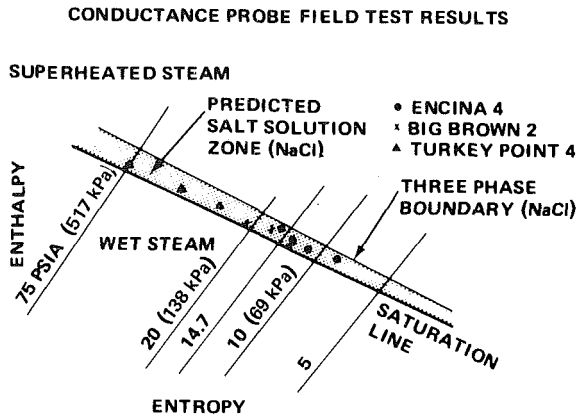

Fig. 15 Simplified Mollier diagram showing location of peak conductance measurements at Turkey Point No. 4, Big Brown No. 2, Encina No. 4

manner, the unit was operated along a load line of Fig. 13 while the MSR outlet temperature was varied. Initially, the MSR temperature was high enough to maintain the probe's local temperature in the superheated region and above the "salt solution zone." As MSR temperature is reduced, the probe temperature also reduces and the conductance sensor responds to the formation of solutions of concentrated contaminants. Increases in conductance level occur within a very narrow range of temperature change. The unsteady character of the sensor's response is thought to be due to the variation in liquid film thickness and extent surrounding the platinum-sensing elements.

As the MSR outlet temperature is further reduced, the probe output reduces to an essentially steady level typical of the conductance of nearly pure water as the blade path steam conditions move further into the wet steam region. A reversal of the process results in the trace on the right-hand side of the figure – an increase of steam conditions from the wet region through the concentrated contaminant zone and into the superheated zone. The probe responds in a similar manner and upon becoming superheated, its response falls to a minimal level.

A similar conversion of the local steam conditions compatible with these observed conductance peaks results in the additional points on the Mollier diagram of Fig. 15. In this instance, the maximum pressure level is 75 psia (517 KPa), approximately a fourfold increase over the maximum pressure levels encountered in the fossil unit test programs.

The most likely salt contaminant of the steam during the testing period at Turkey Point No. 4 is sodium chloride, since measurable amounts of both sodium and chloride were present in the steam generator blowdown water. The location of the conductance peak on Fig. 15 is very close to the pure water equilibrium saturated vapor line and far removed from the three-phase boundary for sodium chloride. This indicates that a relatively dilute solution of the salt condensed on the surface conductance probe, corresponding to a very low concentration in the steam.

Conclusions

In summary, this paper has dealt with the chemistry and aerothermodynamic aspects of steam as it pertains to the general problem of corrosion-assisted blade failures. The interaction of the steam turbine expansion line with the salt solution zone has been verified by field testing which has, for the first time, demonstrated the existence of concentrated impurities within the low-pressure turbine blade path.

This phenomenon has been observed in each turbine tested to date including three fossil units and a single nuclear unit.

These units represent three different physical designs installed by four different utilities located throughout the United States. The boiler systems delivering steam to these turbines include both once-through and drum type fossil boilers; the nuclear unit was of the pressurized water reactor type. Water treatment techniques varied between units and included phosphate treated subcritical drum type boilers, all volatile treated supercritical once-through boilers, and the all volatile water treatment of the nuclear steam supply system. Regardless of these variations, the observed results and conclusions are the same.

In the unit in which moisture measurements were obtained in conjunction with electrical conductance measurements, a relationship was observed between the two measurement sets. Very slight, but measurable amounts of moisture were sensed by the moisture probe when turbine operating conditions were held in the immediate vicinity of the conductance peak. These droplets were generally less than 2.5×10^{-6} m in diameter and the indicated moisture content less than or equal to 0.5 percent.

These findings also support the contention that steam flowing in low-pressure steam turbines tends to approximate equilibrium conditions. These moisture measurements made in the vicinity of the equilibrium saturated vapor line, albeit with some experimental uncertainty, have been made under local steam conditions ranging up to 75 psia (517 KPa) and at local Mach numbers from 0.5 to 0.8. The possibility of local supersaturation of the steam flow in expanding turbine passages cannot be dismissed, as hosts of laboratory data confirm this phenomenon. These current findings indicate that in the flow spaces between blade rows, steam tends toward the equilibrium state, that is, "on the average," steam tends to follow the equilibrium characteristics defined by many publications in this area. It is quite logical that equilibrium and nonequilibrium flow processes coexist in steam turbines. Local conditions within nozzles or rotating blade rows generally experience very high rates of expansion, conducive to subcooling and delay in achieving equilibrium conditions.

Some degree of uncertainty must be assigned to these test data and to their implications. For example, tests of this type in power plant installations utilizing delicate and sophisticated instruments and electronic systems must be coordinated with plant operations and to some degree depend on the accuracy of plant operational instruments. The final determination of local steam conditions surrounding the surface conductance probe depends on these operating parameters by way of turbine cycle heat balance calculation procedures.

The exact chemical species responsible for the conductance probe response were not measured and are, of course, a source of speculation. These important factors have yet to be resolved; they have, however, prompted continued activity in this area and are significant links in the chain relating the corrosion phenomena to steam turbine reliability.

Acknowledgments

The authors wish to express their appreciation to the Westinghouse Electric Corporation for permission to publish this paper and to certain individuals without whom these results could not have been achieved, especially L. D. Smith, S. Anderson, and W. Snyder.

References

1 Gabrielli, F., and Grabowski, H. A., "Steam Purity at High Pressures-System Considerations," presented at the Joint Power Generation Conference, 1979.

2 Peterson, S. H., Bellows, J. C., Pensentadler, D. F., and Hickam, W. M., "Steam Purity Monitoring for Turbine Corrosion Control: A Total Plant Survey," International Water Conference, 1979, Paper No. IWC-79-26.

3 Lindsay, Jr., W. T., "Behavior of Impurities in Steam Turbines," *Power Engineering*, Vol. 83, No. 5, 1979.

4 Wyler, J. S., and Desai, K. J., "Moisture Measurements in a Low Pressure Steam Turbine Using a Laser Light Scattering Probe," ASME H00108, 1977.

A Thermodynamic Efficiency Concept for Heat Exchange Devices

L. C. Witte

N. Shamsundar

Heat Transfer/Phase Change Laboratory,
Department of Mechanical Engineering,
University of Houston,
Houston, Texas 77004

A thermodynamic efficiency based on the second law of thermodynamics is defined for heat exchange devices. The efficiency can be simply written in terms of the mean absolute temperatures of the two fluids exchanging heat, and the appropriate environment temperature. It is also shown that for a given ratio of hot to cold inlet temperatures, the efficiency and effectiveness for particular heat exchange configurations are related. This efficiency is compared to second-law efficiencies proposed by other authors, and is shown to be superior in its ability to predict the effect of heat exchanger parameter changes upon the efficiency of energy use. The concept is applied to typical heat exchange cases to demonstrate its usefulness and sensitivity.

Introduction

The continued rise in the cost of energy has made it imperative to augment the usual heat flow analyses for power plants, refineries, chemical plants, and other energy intensive industries by adding analyses of available energy flow and device irreversibilities. The reclamation of what was formerly "waste heat" by using additional, or more efficient, equipment has become not only economically feasible, but sometimes essential. The chemical process industry, in particular, has shown considerable ingenuity and foresight in putting waste heat recovery into practice.

Much of the available energy loss in process plants is immediately traceable to devices such as boilers, evaporators, chillers, heaters, etc., all of which are heat exchangers, even though their design, purpose and mode of operation may vary considerably. That a heat exchanger is irreversible (in the thermodynamic sense) is well recognized, and many students of thermodynamics will name the heat exchanger as their first example of an irreversible device. A good discussion of the concepts of irreversibility and available energy is presented by Haywood in [1].

It is a simple matter to calculate the irreversibility of a heat exchanger with known specifications. This number, however, is not adequate for the designer and plant manager, who have to weigh several alternatives in equipment selection and operation. For their purposes, a relative figure of merit that is meaningful, useful as a discriminant, easy to calculate, and independent of equipment size is necessary. This figure of merit should also agree with well-known facts about the effect on the irreversibility of varying the heat exchanger parameters.

The two definitions most encountered in the literature are based on the available energy concept, but both fail to satisfy the criteria that were set out above. The first, proposed by Moran [2], Neilson and Crawford [3], and by Ahern [4], defines the efficiency as the ratio of the increase in the availability of the cold fluid to the decrease in the availability of the hot fluid. The second definition of the efficiency, also given by Moran [2], is the ratio of the outflow to the inflow of available energy. Both these definitions have the drawback of using a quantity in the denominator that is not directly fixed by the duty of the heat exchanger. The first definition gives uniformly low efficiencies for all types of heat exchangers; it is pessimistic and cannot be used to compare alternative heat exchanger designs. The second definition seems sound at first sight but, as will be shown in the Analysis section, behaves unacceptably as the effectiveness of the heat exchanger for a specified heat duty is raised. Obviously, a properly defined thermodynamic efficiency would show an increase when the temperatures of the two fluids are brought closer.

The definition proposed in this paper is only slightly different from the second definition given above, and overcomes the drawbacks just stated. The influence of the heat exchanger parameters on this efficiency is established, the superiority of this efficiency to other definitions is demonstrated, and the application of the concept is illustrated.

The term efficiency is used in this paper exclusively with reference to the second law of thermodynamics. It should not be confused with concepts such as boiler efficiency, etc., which are related to the first law of thermodynamics. Our work will be restricted to heat exchangers that operate under adiabatic conditions, that is, with negligible heat losses; consequently, their first-law efficiency is always unity.

Analysis

One way of defining an efficiency related to the second law of thermodynamics is to conceptually devise an ideal system that performs the same function as the actual system, but in a reversible way, and to form the ratio of two comparable quantities between the systems. In devising the reversible

Contributed by the Power Division for publication in the JOURNAL OF ENGINEERING FOR POWER. Manuscript received by the Power Division July 21, 1982.

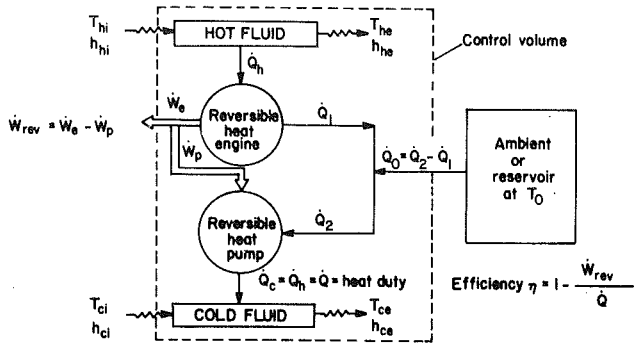

Fig. 1 Diagram showing reversible system that meets same duty as heat exchanger

system, one has to be careful not to alter the operating parameters of the heat exchanger. In particular, the heat removal from the hot fluid, the heat addition to the cold fluid, and the inlet and outlet temperatures should be left intact. Such a reversible system is shown in Fig. 1.

The hot fluid supplies $\dot{Q}_h$ to the reversible heat engine, rejects $\dot{Q}_1$ to a large reservoir at temperature, T_0, and produces $\dot{W}_e$ as work. The heat pump absorbs $\dot{Q}_2 (> \dot{Q}_1)$ from the same reservoir, takes in a part, $\dot{W}_p$, of the engine work, and pumps $\dot{Q}_c$ into the cold fluid. The units are sized such that $\dot{Q}_h = \dot{Q}_c = \dot{Q}$, the heat duty of the heat exchanger.

The irreversibility of a heat exchanger may be attributed to not exploiting the capability for extracting work by interposing a heat engine between the hot and cold sides. The ratio of this unextracted work to the heat transfer represents inefficiency; consequently, our definition of thermodynamic efficiency is

$$\eta \equiv 1 - \dot{I}/\dot{Q} = 1 - \dot{W}_{rev}/\dot{Q} \tag{1}$$

which is similar to the second definition of Moran [2], except that $\dot{Q}$ in the denominator has replaced the availability inflow.

The definition of equation (1) is based on the following reasoning. By definition, the irreversibility rate $\dot{I} = \dot{W}_{rev} - \dot{W}_{act}$; $\dot{W}_{act}$ is zero in a heat exchanger, so that $\dot{I} = \dot{W}_{rev}$. According to the second law, $\dot{I} \geq 0$ and $\dot{W}_{rev} < \dot{Q}$, so that the efficiency lies between zero and unity.

To show that the efficiency just defined is independent of the size of the heat exchanger, as well as for use in examples later, the quantities $\dot{I}$ and $\dot{Q}$ are written in terms of the inlet and exit conditions. The laws of thermodynamics applied to the control volume shown in Fig. 1 yield the following

$$\text{I Law: } \dot{Q}_o = \dot{W}_{rev} + (\dot{m}\Delta h)_h + (\dot{m}\Delta h)_c \tag{2}$$

$$\text{II Law: } \dot{Q}_o/T_o = (\dot{m}\Delta s)_h + (\dot{m}\Delta s)_c \tag{3}$$

The application of the first law of thermodynamics to the hot and cold sides separately shows that

$$\dot{Q} = -(\dot{m}\Delta h)_h = (\dot{m}\Delta h)_c \tag{4}$$

so that equation (2) becomes

$$\dot{Q}_o = \dot{W}_{rev} \tag{5}$$

The second law applied to the actual heat exchanger gives $(\dot{m}\Delta s)_h + (\dot{m}\Delta s)_c \geq 0$; from equation (3), it follows that $\dot{Q}_o$ cannot be negative, and η cannot exceed unity. Therefore, the efficiency is given by

$$\eta = 1 - \dot{Q}_o/\dot{Q} = 1 - T_o[(\dot{m}\Delta s)_h + (\dot{m}\Delta s)_c]/\dot{Q}$$

But

$$(\dot{m}\Delta s)_h/\dot{Q} = -(\dot{m}\Delta s)_h/(\dot{m}\Delta h)_h = -\Delta s_h/\Delta h_h,$$

$$(\dot{m}\Delta s)_c/\dot{Q} = (\dot{m}\Delta s)_c/(\dot{m}\Delta h)_c = \Delta s_c/\Delta h_c$$

Thus,

$$\eta = 1 - T_o[-(\Delta s/\Delta h)_h + (\Delta s/\Delta h)_c]$$

In the last equation, the ratio $\Delta h/\Delta s$ may be interpreted as the mean absolute temperature of the fluid since, at constant pressure,[1]

$$\frac{\Delta h}{\Delta s} = \frac{\int dh}{\int ds} = \frac{\int dh}{\int dh/T} = \bar{T} \tag{6}$$

Then, the efficiency becomes a function only of temperatures, given by

$$\eta = 1 + T_o/\bar{T}_h - T_o/\bar{T}_c \tag{7}$$

This simple formula, along with the definition of equation (1), is the central result of this paper. The formula immediately yields qualitative results such as the following by mere inspection.

(*i*) The efficiency increases as the hot and cold fluids are brought closer in temperature. In the limit when the temperatures are equal – for example, in a very large counterflow heat exchanger – the efficiency approaches unity.

(*ii*) The efficiency increases as the absolute temperatures are raised while maintaining a fixed temperature difference.

(*iii*) The efficiency decreases as the ambient temperature T_o increases.

(*iv*) The formula is characteristically thermodynamical, showing no effect whatsoever of the details of the heat exchanger used for a given set of temperatures.

Relation Between Efficiency and Effectiveness

The efficiency formula just developed is more useful if the effect of the heat transfer area on the efficiency is assessed, since both increase together. Larger area implies higher equipment cost, and higher efficiency implies lower operating cost, so that a compromise is necessary to fix the design

[1] The effect of the pressure loss due to friction has been ignored. Usually the effect of this pressure loss on Δs and Δh is negligible.

Nomenclature

A = heat exchanger area
$\dot{A}$ = rate of flow of available energy
C = thermal capacity = $\dot{m}c_p$
c_p = specific heat
h = enthalpy
$\dot{I}$ = rate of irreversibility production
$\dot{m}$ = mass flow rate
NTU = number of transfer units, NTU = UA/C_{min}
R = ratio of thermal capacities = C_c/C_h
S = entropy
T = absolute temperature
$\bar{T}$ = log-mean absolute temperature, equation (6)
$\dot{Q}$ = heat transfer rate
U = overall heat transfer coefficient
$\dot{W}$ = work rate
η = thermodynamic efficiency, equation (1)
η_1, η_2 = alternative thermodynamic efficiencies, equations (11) and (13)
ϵ = heat exchanger effectiveness

Subscripts

act = actual
c = cold
e = exit, engine
h = hot
i = inlet
o = surroundings
p = heat pump
rev = reversible
1 = heat engine
2 = heat pump

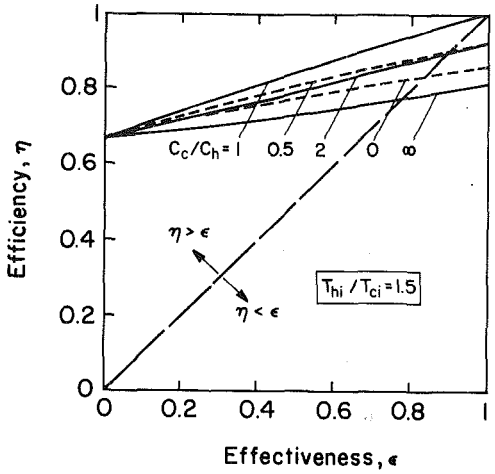

Fig. 2 Plot of thermodynamic efficiency against heat exchanger effectiveness, $T_{hi}/T_{ci} = 1.5$

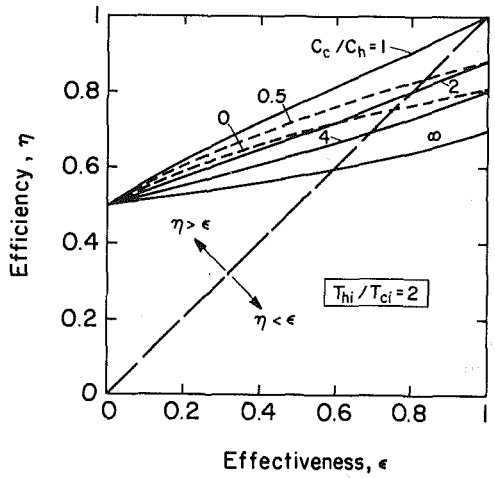

Fig. 3 Plot of thermodynamic efficiency against heat exchanger effectiveness, $T_{hi}/T_{ci} = 2$

values. However, the relation between efficiency and area depends on the type of heat exchanger, heat transfer coefficients, etc. Consequently, instead of the area, a quantity that reflects the extent of the heat transfer surface is used that yields quantitative results which are not restricted to any type of heat exchanger. This quantity is the heat exchanger effectiveness, ϵ, which, for a particular type of heat exchanger, is a function of (*i*) the number of transfer units (NTU), which is proportional to the area of the heat transfer surface, and (*ii*) the capacity ratio $R = (\dot{m}c_p)_c/(\dot{m}c_p)_h$. Charts and formulae relating ϵ, NTU, and R are the standard tools of the heat exchanger designer.

To continue the development, it is assumed that the heat exchanger fluids remain single-phase or two-phase between inlet and outlet, i.e., part single-phase, part two-phase flow is not allowed. In addition, it is assumed that the specific heats are independent of temperature. Both of these assumptions are routinely used in obtaining the ϵ-NTU-R relationships for exchangers. With c_p constant, equation (6) becomes

$$\bar{T} = \frac{\int dh}{\int dh/T} = \frac{\int dT}{\int dT/T} = \frac{T_e - T_i}{ln(T_e/T_i)} = T_i \frac{T_e/T_i - 1}{ln(T_e/T_i)} \tag{8}$$

so that $\bar{T}$ is a log-mean absolute temperature. Thus, from the inlet and exit temperatures of both fluids and T_o, the efficiency could be calculated. The outlet temperatures, however, would depend on the heat exchanger design, whereas the inlet temperatures are almost always specified. Consequently, the outlet temperatures are replaced, using ϵ and R as follows.

For $R < 1$, the cold fluid has the smaller capacity rate, and

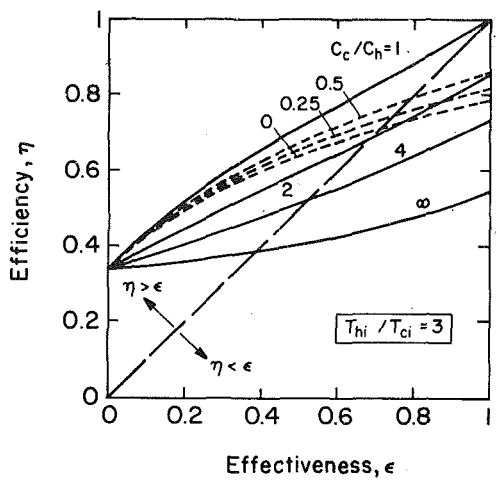

Fig. 4 Plot of thermodynamic efficiency against heat exchanger effectiveness, $T_{hi}/T_{ci} = 3$

$$\epsilon = \frac{T_{ce} - T_{ci}}{T_{hi} - T_{ci}} = \frac{T_{ce}/T_{ci} - 1}{T_{hi}/T_{ci} - 1} = \frac{1}{R} \frac{1 - T_{he}/T_{hi}}{1 - T_{ci}/T_{hi}} \tag{9}$$

Similarly, for $R > 1$,

$$\epsilon = \frac{T_{hi} - T_{he}}{T_{hi} - T_{ci}} = \frac{1 - T_{he}/T_{hi}}{1 - T_{ci}/T_{hi}} = R \frac{T_{ce}/T_{ci} - 1}{T_{hi}/T_{ci} - 1} \tag{10}$$

Using values for ϵ, R and T_{hi}/T_{ci}, the T_e/T_i ratios for calculating the mean temperatures from equation (8) are found, and substituted into equation (7) to obtain the efficiency.

One comment to be added concerns the appropriate reservoir temperature, T_o. Usually, the cold fluid is air or water and differs little from T_o in temperature. Consequently, in the absence of a specified T_o, it is suggested that T_o be set equal to T_{ci}. This is adopted in the rest of the paper.

It is helpful at this stage to express the alternative efficiencies proposed by other authors in terms of the mean temperatures and to develop the relations between the different efficiencies. Moran's first definition is

$$\eta_1 \equiv (\Delta \dot{A})_{\text{cold fluid}}/(-\Delta \dot{A})_{\text{hot fluid}} \tag{11}$$

By a calculation similar to that given for η, it is found that

$$\eta_1 = (1 - T_o/\bar{T}_c)/(1 - T_o/\bar{T}_h) \tag{12}$$

From equation (12), the problem with this definition of efficiency is apparent: in many heat exchangers, the coolant is close to ambient temperature, and the numerator of the RHS of equation (12) is very small, causing η_1 to be near zero.

The second definition found in the literature for the efficiency is

$$\eta_2 \equiv \dot{A}_{out}/\dot{A}_{in} = 1 - \dot{W}_{rev}/\dot{A}_{in} \tag{13}$$

which is to be compared to our equation (1). The two efficiences are related by

$$(1 - \eta_2) = (1 - \eta)\dot{Q}/\dot{A}_{in} \tag{14}$$

The behavior of the efficiencies η and η_2 with changes in effectiveness, heat capacity ratio, and inlet temperatures will now be discussed using plots of efficiency, and illustrated with examples.

Results

To illustrate the usefulness of the formulae derived above and to throw additional light on the effect of the parameters ϵ, R, and T_{hi}/T_{ci} on the efficiency, results for several practical cases are presented. Plots of efficiency against effectiveness for various combinations of parameters are shown in Figs. 2–4. These were obtained from equations (7) through (10). In

each of these figures, full lines are used for cases with $R = C_c/C_h > 1$, dashed lines for $R < 1$. A diagonal line joining the corners of the plot is also shown by long dashes, to help compare efficiency values to effectiveness values. Figure 2 has $T_{hi}/T_{ci} = 1.5$, which pertains to most liquid-liquid, liquid-air, and gas-air heat exchangers. Because of the moderate temperature difference range involved, the efficiency is high and not very sensitive to changes in the effectiveness or the ratio, R. Figure 3 with $T_{hi}/T_{ci} = 2$ corresponds to most economizers, air preheaters, waste heat recovery units, etc. This is followed by Fig. 4 with $T_{hi}/T_{ci} = 3$, which is the range in which exhaust coolers, medium pressure steam boilers, primary loop to secondary loop heat exchangers of pressurized water reactors, etc. operate. As the ratio T_{hi}/T_{ci} goes up, the thermodynamic efficiency not only goes down, but becomes more sensitive to changes in ϵ and R at a time when the "efficiency" of the surfaces in transferring heat has considerably increased. The salient points to be made from the figures are as follows.

(*i*) Increased effectiveness always achieves an increase in efficiency. The efficiency and the slope, $d\eta/d\epsilon$, increase as the capacity ratio, R, approaches unity. As the temperature ratio, T_{hi}/T_{ci}, increases, the efficiency decreases and $d\eta/d\epsilon$ increases.

(*ii*) The highest efficiency is obtained when the capacity rates are equal. When the capacity rates are not equal, better efficiency is obtained when the hot fluid has the larger capacity. In contrast to the effectiveness, which is unaffected by interchanging C_c and C_h, the efficiency is strongly dependent on which of the two is greater. An example of the effect of this is that boilers and evaporators ($R = \infty$) are inherently less efficient thermodynamically than condensers ($R = 0$).

(*iii*) The thermodynamic efficiency reaches the maximum value of unity when the capacity rates are equal and the effectiveness is equal to unity. Thus, an infinitely large counterflow heat exchanger has an efficiency of unity. The minimum value of efficiency is equal to T_{ci}/T_{hi}, and is approached as the effectiveness approaches zero, regardless of the value of the capacity ratio, R.

(*iv*) For small temperature differences, the efficiency is generally high and does not change much as the effectiveness and the size of the heat exchanger are varied. When the temperature difference is large, however, the efficiency is quite sensitive to changes in the effectiveness. Consequently, in design calculations with large T_{hi}/T_{ci}, competing effects of η and ϵ on the lifetime cost must be taken into account.

Next, for a comparison of the efficiency defined here to the alternative efficiency to be made, the alternative efficiency η_2 is plotted against effectiveness for the case of $T_{hi}/T_{ci} = 1.5$ in Fig. 5. The variation of η_2 with effectiveness is drastically different from that of η. Whereas the latter increases with effectiveness always, as is desirable, the alternative efficiency η_2 decreases to a minimum, and then increases. This nonmonotonic behavior and the early decrease in η_2 makes the alternative definition unsuitable for system evaluation. The explanation of this unexpected failure of a seemingly proper definition is as follows. For fixed inlet temperatures, increasing the effectiveness increases the heat transfer, $\dot{Q}$, and the efficiency η, while maintaining $\dot{A}_{in}$ constant. In equation (14), then, $\dot{Q}$ increases and $(1 - \eta)$ decreases as the effectiveness is increased. Consequently, their product can either decrease or increase. When the effectiveness (and efficiency η) is low, the increase in $\dot{Q}$ overcomes the decrease in $(1 - \eta)$ and causes $(1 - \eta_2)$ to increase, thus reducing η_2. In contrast, for larger ϵ, this trend reverses, because the efficiency η is high and $(1 - \eta)$ is a small quantity.

Increasing the area of a heat exchanger results in the temperature differences between the hot and cold fluid reducing throughout the exchanger. This should result in a decrease in irreversibility of heat transfer, thus giving a higher η_2 with an increase in ϵ. But Fig. 5 shows that η_2 is decreased as ϵ is increased.

It is clear that our definition of η meets all of the criteria that were set out before, while the traditional definitions fail to do so.

As noted earlier, the efficiency is not directly influenced by the type of the heat exchanger. For studying heat exchanger performance, it may be advantageous to combine the above

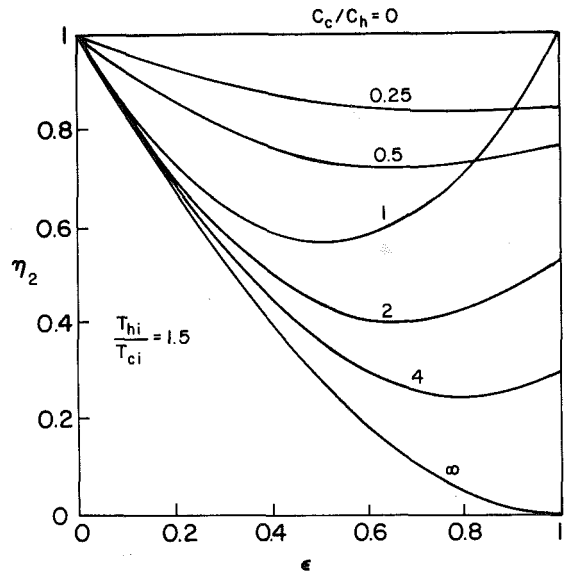

Fig. 5 Plot of thermodynamic efficiency, η_2, against heat exchanger effectiveness, $T_{hi}/T_{ci} = 1.5$

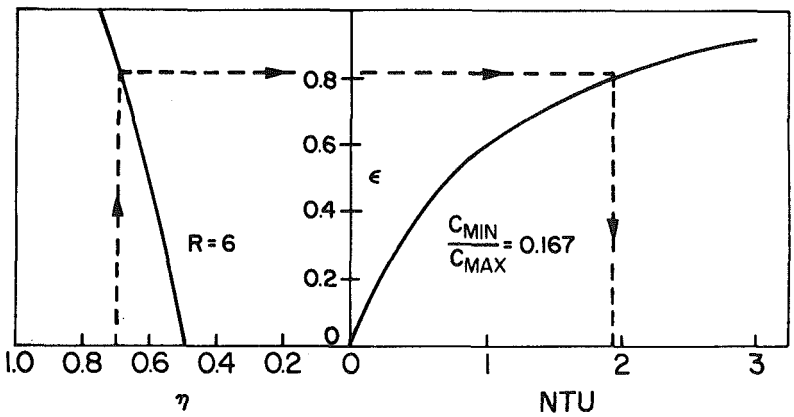

Fig. 6 Diagram illustrating relations between efficiency, effectiveness and number of transfer units for example 1

figures with the appropriate effectiveness-NTU charts which are contained in most heat transfer texts, such as in [5]. This will be illustrated by the following example.

Example 1: A waste heat recovery unit uses stack gases at 600K, C_h = 50kW/K, to heat water from 300K to 350K. Design a crossflow unit with a thermodynamic efficiency of at least 0.7, given that U = 15W/m^{2}K.

$$R = C_c/C_h = (T_{hi} - T_{he})/(T_{ce} - T_{ci})$$
$$\geq (T_{hi} - T_{ci})/(T_{ce} - T_{ci}) = 6, T_{hi}/T_{ci} = 2.$$

With R = 6, from the plot of η against ϵ, $\epsilon \approx 0.8$ and, from the ϵ-NTU chart, at $C_{\min}/C_{\max}$ = 1/6, NTU $\approx$ 1.93; therefore, A = 6434 m^2. The exit temperature of the gas is $T_{he} = T_{hi} - \epsilon(T_{hi} - T_{ci})$ = 360K, which represents a 10K terminal difference. The above calculation procedure is compactly shown in the diagram of Figure 6.

The concept of efficiency is also useful in showing the effects of exchanger performance degradation. For example, the effects of fouling on the overall heat transfer coefficient, U, can be readily determined through a reduction in efficiency. Example 2 shows this effect.

Example 2: A shell-and-tube process heater with one shell pass and two tube passes uses condensing steam at 150°C to heat a light organic liquid from 10°C to 40°C. The thermal capacity of the liquid is 35 kW/°C, and the overall heat transfer coefficient U is 1.5 kW/m^2.°C at start-up. After a period of operation, fouling reduces the coefficient U to 1 kW/m^2.°C. To meet the required duty, the steam temperature (and pressure) has to be raised. Find the effect of this on the effectiveness and efficiency of the heater.

Initially, ϵ = (40-10)/(150-10) = 0.21. From equation (8), $\bar{T}_h$ = 423 K, $\bar{T}_c$ = 298 K. Thus, the initial efficiency is 1 − 283/298 + 283/423 = 0.72. From the appropriate ϵ-NTU chart, NTU = 0.24.

After fouling, the NTU has dropped to (0.24) (1/1.5) = 0.16, which results in an effectiveness of ϵ = 0.15. To obtain this effectiveness, the steam temperature will have to be (40-10)/0.15 + 10 = 210°C. With this steam temperature, $\bar{T}_h$ = 483 K, $\bar{T}_c$ being unchanged, and the efficiency becomes 1 − 283/298 + 283/483 = 0.64.

	T_{steam}	NTU	Effectiveness	Efficiency
Before fouling	150°C	0.24	0.21	0.72
After fouling	210°C	0.16	0.16	0.64

The results are summarized in the above table, and show the effect of fouling on effectiveness and efficiency. Both of these decrease significantly as a result of the increased steam temperature used to counteract fouling. The important effect here is the loss in efficiency, because it will relate directly to the increase in the cost of supplying the higher pressure steam.

Concluding Remarks

The thermodynamic efficiency based on the second law of thermodynamics, as defined in this paper, is a simple way of gauging the efficacy of energy usage. Application of the concept to widely divergent heat exchanger cases shows that it can be used as a discriminant between different strategies of heat exchange. When used with the traditional tools of heat exchanger design and costing, it can provide the designer with an awareness of the effect of a particular design not only on capital costs but operating costs as well.

Thermoeconomic studies of systems containing heat exchangers generally treat the system as a whole rather than isolating individual components as is done in this paper. However, the second-law efficiency of a component is a valuable concept in that it allows the contribution of the component to the irreversibility of the system to be calculated. In turn, the cost penalty associated with the system irreversibilty can be estimated and a program for minimizing this cost by improving the system parameters can be undertaken.

This paper presents one of the tools for performing thermoeconomic studies for design of new energy systems, or for the consideration of replacement of "inefficient" heat exchangers in operating systems, as done by Fehring and Gaggioli [6]. The use of this tool in thermoeconomic analyses will be the subject of subsequent papers.

Acknowledgment

The authors are indebted to Professor John Lienhard for his insightful and stimulating discussion of both the appropriate form for the efficiency expression and its potential usefulness.

References

1 Haywood, R. W., "A Critical Review of the Theorems of Thermodynamic Availability, with Concise Formulations," *Journal of Mechanical Engineering Science*, Vol. 16, 1974, pp. 160-173 and 258-267.

2 Moran, M. J., *Availability Analysis: A Guide to Efficient Energy Use*, Prentice-Hall, Englewood Cliffs, N.J., 1982, p. 100.

3 Nielson, J. H., and Crawford, R. A., "Efficiencies of Thermodynamic Processes," *Journal of Physics D*, Vol. 5, 1972, pp. 28-42.

4 Ahern, J. E., *The Exergy Method of Energy Systems Analysis*, Wiley-Interscience, New York, 1980, pp. 66-73.

5 Lienhard, J. H., *A Heat Transfer Textbook*, Prentice-Hall, Englewood Cliffs, N.J., 1981, pp. 92-97.

6 Fehring, T. M., and Gaggioli, R. A., "Economics of Feedwater Heater Replacement," *ASME* JOURNAL OF ENGINEERING FOR POWER, 1977, pp. 482-489.

Measurement of Aerodynamic Work During Fan Flutter

A. P. Kurkov
National Aeronautics and Space Administration,
Lewis Research Center,
Cleveland, Ohio 44135

Stationary high-response pressure and displacement measurements are used to describe the flutter characteristics of the first fan-rotor of a turbofan engine. Flutter occurred at part speed and at high incidence. Several forward and backward traveling waves were identified in a predominantly torsional flutter mode. Positive aerodynamic work contribution was confined to the region close to the leading edge and was mainly due to modes corresponding to forward traveling waves of nodal diameters in the range 3 to 5.

Introduction

Stall flutter constitutes one of the least tractable aeroelastic problems in turbomachinery. Experimental data are therefore needed to establish the values of parameters controlling the flutter. For the purpose of assessing theoretical models, it is important to also include more detailed results related to the variation of physical quantities along the blade chord.

The experimental data on the full scale rotors in the past were generally confined to the description of the steady-state conditions in flutter or flutter onset. The experimental data are further complicated by the fact that stall flutter in rotors is usually mistuned. That is, the vibratory amplitude and interblade phase angle distributions are nonuniform. In such a case a flutter mode can be viewed as a superposition of several nodal diameter modes with different amplitudes and phases [1].

The interpretation of mistuned flutter experiments can be greatly enhanced by the use of stationary instrumentation. Recently a method of analysis was presented [2] which allows one to deduce the unsteady force acting on a blade element from measurements made by using a casing-mounted static presure transducer. The phase angle of the unsteady pressure was measured relative to the displacement phase for each nodal diameter mode that significantly contributed to flutter. The tip displacements were measured independently by means of two fiber optics probes mounted in the casing. In reference [2] results were presented only for the leading edge pressure port. In the present paper complete unsteady pressure results are presented for five chordwise positions. To reduce random error, the pressure and displacement data were independently vectorially averaged. An attempt was also made to deduce aerodynamic work during flutter for each component flutter mode.

In these experiments flutter occurred at about 65 percent of the design speed and at a high positive incidence. The relative Mach number was 0.795, the reduced frequency based on the blade chord was 1.8, and the rotor inlet static pressure and temperatures were 10.82 N/cm^2 and 168.8° C, respectively. The flutter mode was predominantly above shroud torsion. The flutter boundaries were reported previously [3] (test point 125).

Contributed by the Power Division and presented at the ASME Winter Annual Meeting, Washington, D.C., November 15-20, 1981. Manuscript received by the Power Division May 5, 1982.

Experimental Measurements

Figure 1 illustrates the axial position of the measurement ports relative to the rotor blade. In this figure the optical displacement ports are shown circumferentially close to the pressure ports for convenience only. Actually these ports were about 10 blade pitches apart from each other.

Only a brief description of measurement procedures and subsequent data processing is given since a detailed description is available [2, 4, 5]. Both pressure and displacement data were recorded on magnetic tapes and subsequently digitized for further processing on a minicomputer. In addition to these data two reference pulses were recorded, the 1E and the 38E, which corresponded to the blade passing frequency. The 1E pulse was common on all tapes and was used to trigger the acquisition of digital data. This permitted blade identification in the relative frame of reference. The 38E pulse was used as a reference for computation of tangential displacements. As the blades swept optical ports, a light beam was reflected from the blade tips and conducted to a photomultiplier by means of a fiber optics bundle. A voltage spike was generated every time a blade passed an optical port. The position of this spike relative to the 38E reference pulse provided an indication of the instantaneous position of a blade in flutter.

On playback of the data tapes it was essential that the rate of digitization be sufficiently high. For the displacement data this was necessary in order to be able to resovle the blade motion. For the pressure data the high digitizing rate was necessary in order to capture the unsteady pressure difference across the blade. Both these objectives were met by digitizing at a rate of 10,295 points per revolution or the equivalent of about 270 points per blade passage. Extensive use of peripheral storage devices was made to store the digitized data for further processing on a minicomputer.

Pressure transducers were calibrated prior to each run. Calibrations were fairly consistent except for the transducer at port 4 (Fig. 1). Therefore another transducer at the same axial location but at a different circumferential position was used instead. In the data analysis an allowance was made for the difference in the sampling time due to the different circumferential location of this transducer.

Analysis of the Displacement Data

The displacement data and, as seen later, the pressure data

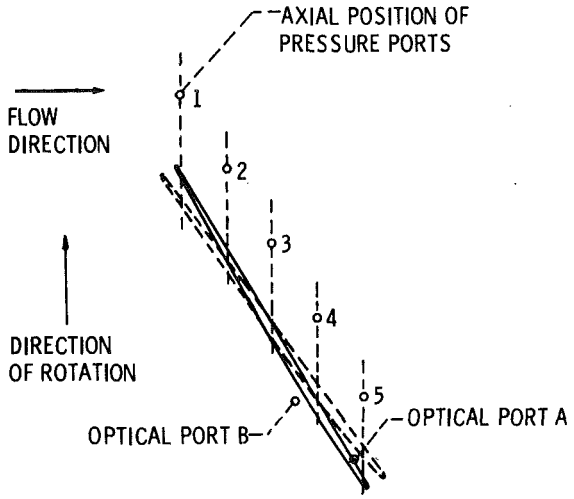

Fig. 1 Location of measurement ports

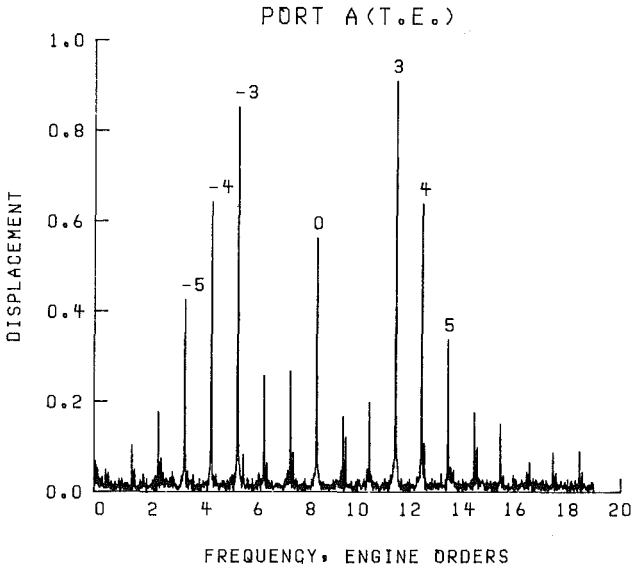

Fig. 2 Displacement-amplitude spectrum, port A, 1 unit = 3.267×10^{-3} radians (average of four FFT's)

can be analyzed in two ways. One method is to sort the sampled data into groups so that each group includes samples from a particular blade only. As each blade is sampled only once per revolution, the flutter frequency in the resulting spectrum is folded in the range 0 to 1/2 E. (Note that the true flutter frequency was 8.45 E.)

In the other method spectral analysis is performed on the data set that includes samples from all blades in the order in which they pass the measurement port. The sampling rate is now equal to the number of blades, (i.e., 38E, which is sufficiently high to prevent data aliasing). The overall spectrum (Fig. 2), clearly exhibits all the nodal diameters that contribute to flutter vibration. This can be seen by transforming the expression for unsteady displacement, D, in the rotating frame of reference

$$D = \sum_{i=1}^{38} A_i \cos(\omega_f t - \Phi i + \psi_i)$$

into a stationary frame as viewed by the displacement sensor [2],

$$D = \sum_{i=1}^{38} A_i \cos[(\omega_f + \omega_r i)t + \psi_i]$$

In these expressions the summation is carried out over all

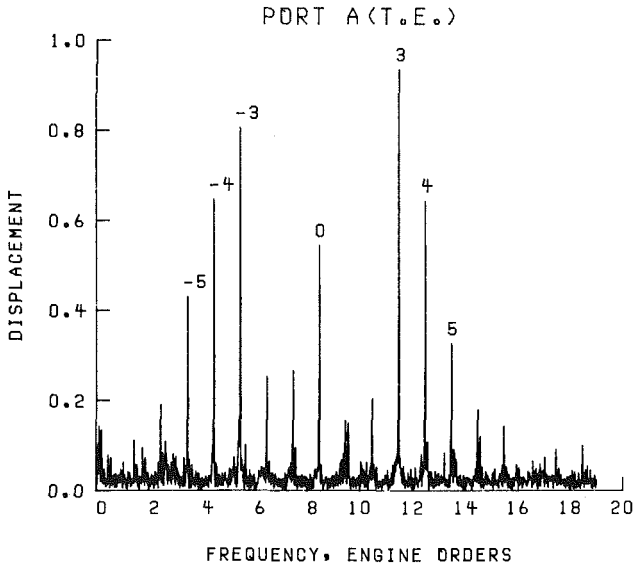

Fig. 3 Displacement-amplitude spectrum, port A, single FFT

nodal diameters i; ω_f and ω_r represent flutter and rotational frequencies, respectively; t denotes time; Φ, the angular coordinate oriented in the direction of rotation; and ψ_i, the phase angle for the ith nodal diameter.

The analysis in this paper was based on the overall spectrum. Individual blade spectra were only used to obtain phase angles for the reference blade. This was essential for the vector averaging of Fourier transforms and also for the correlation of the displacement and the differential pressure spectra. The procedure for doing this is described in detail in the Appendix. Only four transforms were averaged; nevertheless, as shown in Figs. 2 and 3, a significant improvement in the signal-to-noise ratio was achieved.

The displacement amplitudes are expressed in digitized units for convenience. In terms of angular displacement one unit corresponds to 3.267×10^{-3} radian. This constant was used later in the definition of the work coefficient.

In the derivation of angular displacement [2] it was assumed that there is no contribution to the tangential displacement due to chordwise bending. The justification for this was provided by visual observation of the stroboscopic image of the blade tip during flutter [5].

Analysis of the Pressure Data

The important difference between the displacement and pressure data is that the displacement data are essentially discrete whereas pressure data are continuous. Therefore, to obtain a spectrum corresponding to a particular point on the blade surface, one has to perform vectorial superposition of all pressure waves associated with the flutter frequency. However, it is also possible to locate the blades first in the digitized data string and then collect only the points that correspond to a desired blade surface location. This amounts to discretization of the pressure data. One can now analyze pressures in a similar way as displacements, that is, either in terms of individual blade spectra (sampling rate 1E) or in terms of the overall spectrum (sampling rate 38E). For reasons already mentioned the overall spectrum analysis is used in this paper.

Note that, as a result of the sampling procedure for the pressure data, there exists an interaction between the steady and unsteady pressure fields [2]. This interaction has to be taken into account during the interpretation of the results.

The blade surfaces in the digitized data string were located from the average steady-state distribution. Figure 4 illustrates

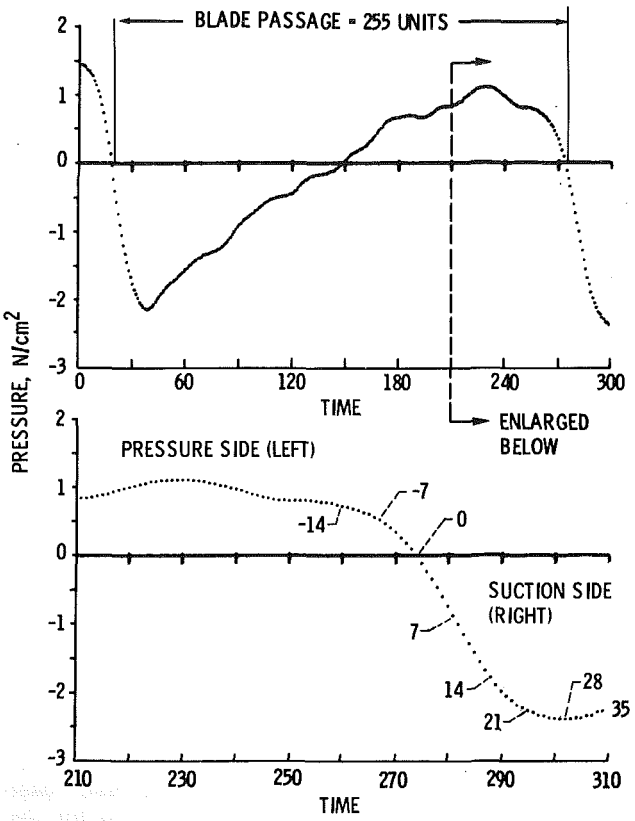

Fig. 4 Steady-state pressure distribution; port 1, 1 unit = 1/(10295E)

this procedure. The steady-state pressures in this figure were obtained by averaging instantaneous pressures over 66 revolutions. The time scale is expressed in digitized time units. In terms of distance traversed by a blade tip each unit represents 1/10, 295 fraction of a revolution. The steep pressure gradient region is presented with expanded horizontal scale in the lower part of the figure. The points are marked in this part of the figure according to their positions relative to the zero crossing. These points corresponded to the locations where the unsteady pressures were sampled for every blade passage. Prior to the unsteady pressure sampling the steady-state pressure component was removed from the data.

Points on the left side of the steep gradient region such as 0 and -7 are associated with the pressure side of the blade, and points such as 14 and 21 on the right side of the gradient region are associated with the suction side.

The interaction of the steady and unsteady pressure fields is proportional to the product of the steady-state pressure gradient and the blade displacement [2]. Therefore, by forming an unsteady pressure difference such as $P_{14} - P_0$, the contribution due to the interaction will be minimized because the pressure gradients for points 0 and 14 are approximately equal and because the displacements for suction and pressure surfaces are the same.

It was shown [2] that a consistent phase angle is obtained for the pressure difference regardless of the choice of two points forming the difference, provided their slopes are about equal. However, the amplitude varies roughly in proportion to the distance between two points in the steep gradient region. It is therefore desirable to select these points near the edges of the gradient region. Upon considering the steady-state distributions at other chordwise locations as well, it was decided to form suction-pressure side differences based on the separation distance of twenty-one digitized units.

Note that the interaction between the steady and unsteady pressure fields is inconsequential for the computation of the work per cycle since it is only the pressure component that is

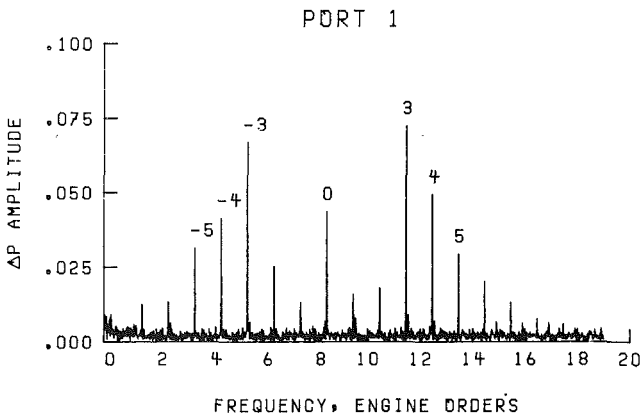

Fig. 5 Differential pressure spectrum, port 1 (average of four FFT's)

out of phase with the displacement that contributes to the work.

The analysis of the pressure data at ports 2 to 5 closely paralleled the analysis for the leading-edge port 1 [2]. However, because of a smaller steady-state pressure differential across the blade and the higher noise level at ports 4 and 5, the blades could not be reliably located from the steady-state distribution. Therefore the blades were actually located by using the averaged displacement pulse data. For the chordwise position 4, port B data were used; and for position 5, port A data were used.

Figures 5 to 8 present the linear spectra of the differential pressure amplitudes at different chordwise positions. In these figures, pressures were made dimensionless by using the inlet dynamic head. Figures 5 and 6 illustrate the gain in the signal-to-noise ratio achieved by averaging at the leading-edge pressure port. Similar gains were achieved at other chordwise positions.

The subtraction involved in obtaining the difference spectra in Figs. 5 to 8 was carried out in the frequency domain. Prior to the subtraction, a small correction was applied to the individual spectra that form the difference. This correction accounted for a nonsimultaneous sampling of pressure at two points involved in the difference.

Comparison of Figs. 5, 7, and 8 with Fig. 2 indicates that the pressure amplitudes for the different component modes for ports 1 and 2 are in roughly the same relative proportions as the corresponding angular displacement amplitudes.

Results

In the interpretation of results obtained with stationary pressure instrumentation, one of the key problems is the determination of the blade suction and pressure surface positions. There is no assurance that the choice for the blade surface positions made in the previous section is optimum. The unsteady results in this section are therefore presented not only for the chosen blade surface positions but also for the region covering about one-fifth of the blade passage in the vicinity of each blade. This allows one to revise the choice for the blade surface positions and also to examine the sensitivity of the results to this choice. Ultimately the object is to compute the modal contribution to the unsteady work at each port location.

Figures 9 and 10 illustrate the spatial change in phase of the unsteady pressure in the vicinity of the blade. The horizontal scale is expressed in units corresponding to the distance traversed by a blade tip during the interval of time between two successive digital points. From Fig. 4 it can be seen that there are about 255 units for the particular blade passage. On the average the number of units per blade passage was 270.

The starting point for the top curve was selected arbitrarily, and the starting points for successive curves below were

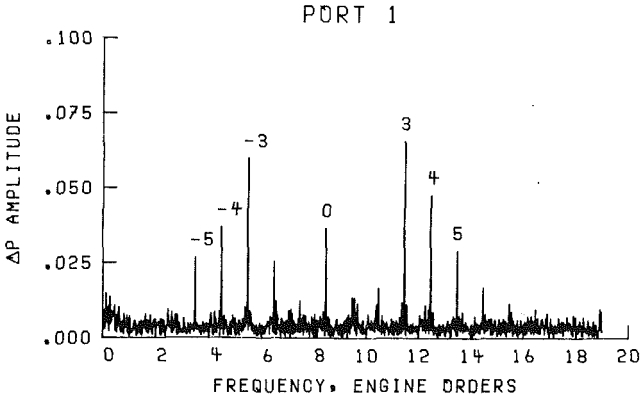

Fig. 6 Differential pressure, port 1, single FFT

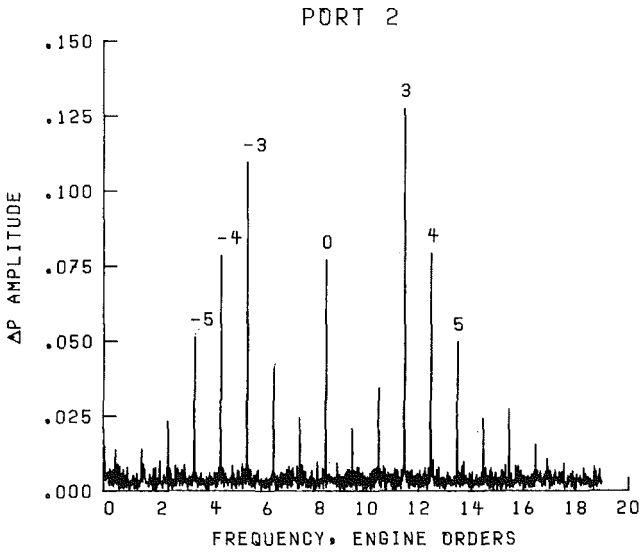

Fig. 7 Differential pressure spectrum, port 2 (average of four FFT's)

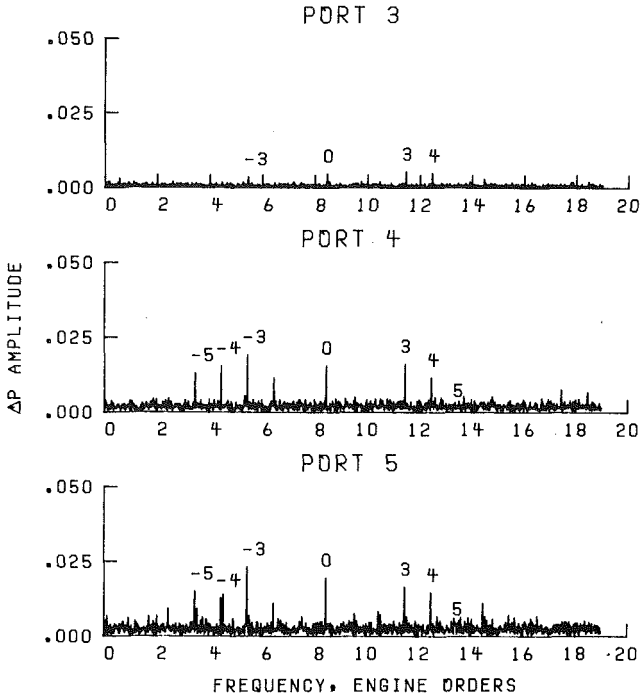

Fig. 8 Differential pressure spectra, ports 3, 4, and 5 (average of four FFT's)

displaced downward by increments of 40 deg. The absolute phase angles have therefore no meaning and only the spatial change in phase is significant. The corresponding nodal diameters were marked on the right of each curve.

The first point for each curve in Fig. 9 for port 1 corresponds to point −14 in the steady-state distribution (Fig. 4). The adjacent points in Fig. 9 are plotted in the same order as in Fig. 4. Points 0 and 21 in Fig. 4, which were selected to represent the locations of pressure and suction surfaces for the spectrum in Fig. 5, were marked in the top curve in Fig. 9, port 1, as P and S, respectively. Equivalent points for other ports in Figs. 9 and 10 were marked identically. They correspond to the locations of pressure and suction surfaces for the different spectra in Figs. 7 and 8. The amplitudes for port 3 were too small for the determination of phase angles.

Note that the spatial distribution of the instantaneous phase of flutter in Figs. 9 and 10 is obtained by a preselection of spatially different sets of points in the input for spectral analysis. Because the sampling rate is 38E, the spectrum for each point in these figures extends only to 19E. In itself therefore any one of the spectra cannot describe the spatial variation in phase in the blade passage. It is the collection of all the spectra and the knowledge of their origin (relative to the zero crossing) that makes it possible to describe the spatial variation in phase.

The points plotted in Figs. 9 and 10 represent a vector average of four Fourier transforms, each corresponding to 62 revolutions. Because the results in these figures include samples from all the blades, the change in phase in Figs. 9 and 10 can be considered representative for all blades rather than for a single blade.

The spatial change in phase between points P and S ranges between 94 and 170 deg for port 1 and between 135 and 167 deg for port 2. Note that based on theoretical considerations this change in phase would be expected to be 180 deg. Ideally, the interval between points P and S should include all the phase angle change across the blade and exclude any change that occurs away from the blade surfaces. It appears that these conditions are most nearly approached for port 2. Although most of the change of phase is bracketed by points P and S for port 1, some perturbations of these positions may be desirable.

The change in phase between points P and S for ports 4 and 5 is much less consistent than for ports 1 and 2. For example, for port 4, the spatial change in phase is fairly small for nodal diameters 3 and 4 and fairly large for nodal diameters −5, −4, −3, and 0. The phase angles for nodal diameter 5 could not be reliably determined because the amplitudes were too small (Fig. 8).

As already mentioned, the blade location could not be reliably determined from the steady-state distribution for ports 4 and 5 because of the noise and relatively small pressure difference between the suction and pressure surfaces. Blade spacing derived from displacement data was used as a sampling interval for obtaining results in these figures, and the pressure-suction interval was taken to be the same as in the previous figure.

Note that the phase angle results in Figs. 9 and 10 are affected by the blade motion as discussed previously. However, at the ends of the pressure-suction interval (i.e., points P and S), the effect should be small because of the smaller steady-state pressure gradients in these regions. Also, this effect should be small for ports 4 and 5 because of the smaller pressure gradients and a higher level of data randomness at these locations.

It is usual practice in flutter studies to resolve the pressure into two components, one in phase and the other out of phase with the displacement. Because of the frequently employed complex representation, the former is usually termed a real component and the latter an imaginary component. It can be shown that only the imaginary component contributes to the work integrated over one flutter cycle. The imaginary

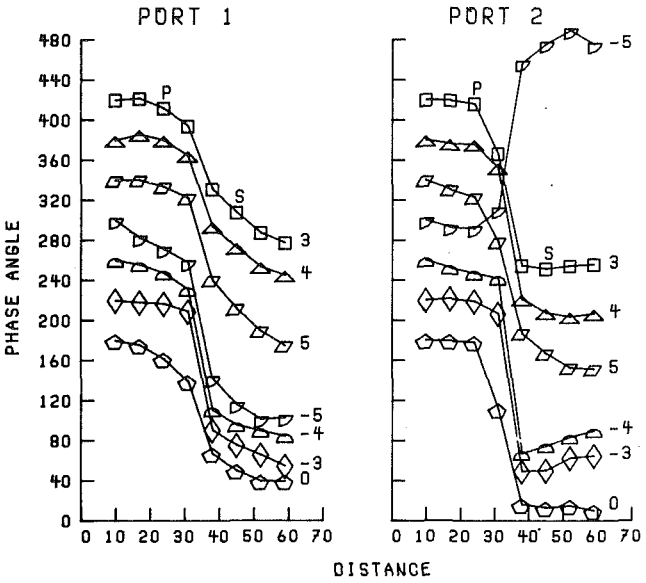

Fig. 9 Spatial variation of pressure phase, ports 1 and 2

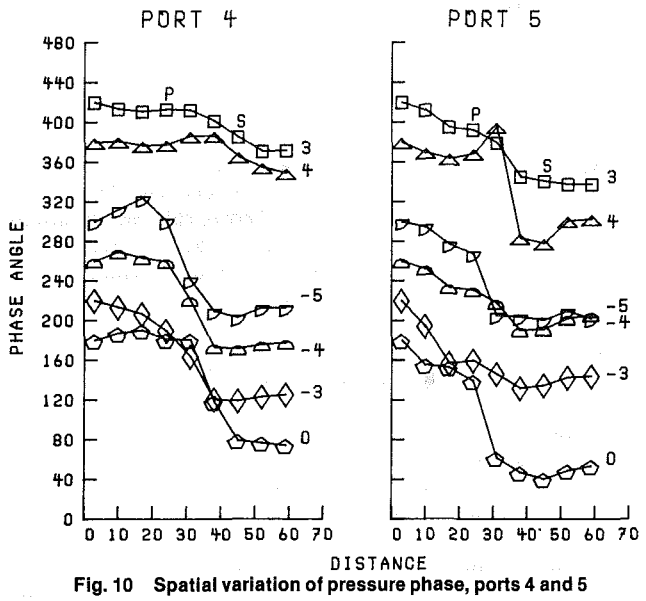

Fig. 10 Spatial variation of pressure phase, ports 4 and 5

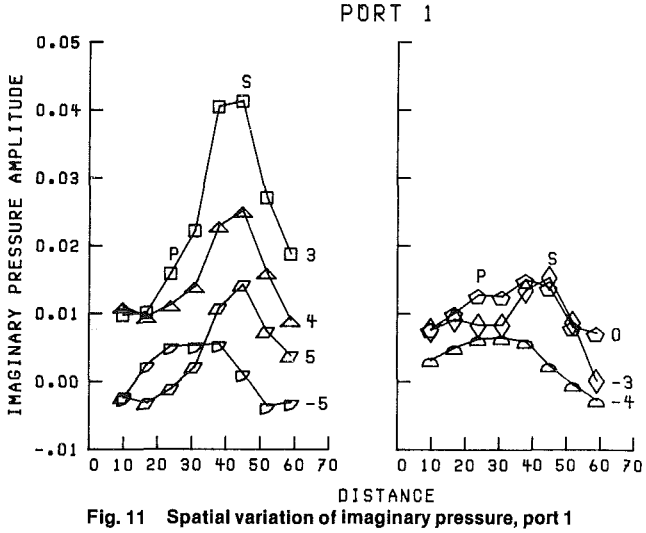

Fig. 11 Spatial variation of imaginary pressure, port 1

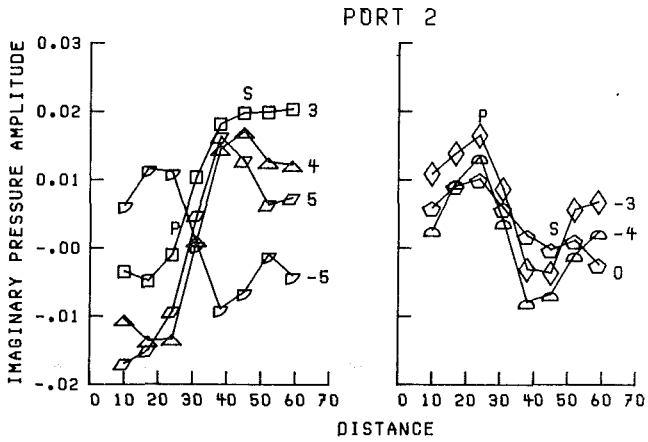

Fig. 12 Spatial variation of imaginary pressure, port 2

component is also free from the contribution due to blade motion. It appears desirable therefore to plot the distribution of this component of the pressure in the vicinity of the blade.

Note that each mode contributes independently to the work per cycle. This is a direct consequence of the orthogonality of the modes associated with each nodal diameter.

Figures 11 to 14 present the imaginary pressure distribution. The positions of points in these figures correspond directly to the positions of points in Figs. 9 and 10. The difference between points S and P is proportional to the modal work per cycle at the particular port location. A positive suction-pressure surface difference results in a positive work contribution for ports 1 and 2 and negative work for ports 4 and 5. As in Figs. 5 to 8, pressures were made dimensionless by using the inlet dynamic head.

An interesting result in Fig. 11 for the leading edge port is a rather steep spatial variation of the imaginary pressure on the suction side of the blade. This variation makes the location of the suction surface very critical. Considering that nodal diameters 3, 4, and 5 contribute most of the positive work, it appears that the suction surface is close to the optimal location. Some variation in the imaginary pressure amplitude is also evident on the suction side of the blade in Fig. 12 for port 2, although it is less pronounced. All the negative nodal diameter modes in this figure contribute to negative work (i.e., positive damping).

The imaginary pressure component distribution for ports 4 and 5 appears to be nearly monotonic. All modes generate a negative contribution to work. Again, the imaginary pressures for the fifth nodal diameter could not be determined reliably because of small amplitudes.

The work per cycle for each mode for the four ports is presented in Table 1, and the phase angles between the differential pressures and displacements in Table 2. The angles in this table were defined so that the positive angle implies positive work and conversely. Strictly, therefore, the angles are between the suction-pressure, ΔP, and the angular displacement ahead of the torsional axis and between the pressure-suction, ΔP, and the angular displacement behind the axis.

To compute the local contribution to the work at each location, the port area assignments had to be made. This was accomplished by dividing the chord into five sections so that the section boundaries were located midway between the adjacent ports. Pressure distribution in each section was assumed to be uniform and equal to the local port pressure. The line of action of the force was assumed to pass through the centroid of the section. Although this scheme appears crude, the sparse measurement port coverage does not seem to justify a more elaborate approach using the interpolation methods. The moment for each chordwise section was calculated by assuming that the torsional axis is located at 44 percent of the chord [2]. The work in Table 1, C_w, was

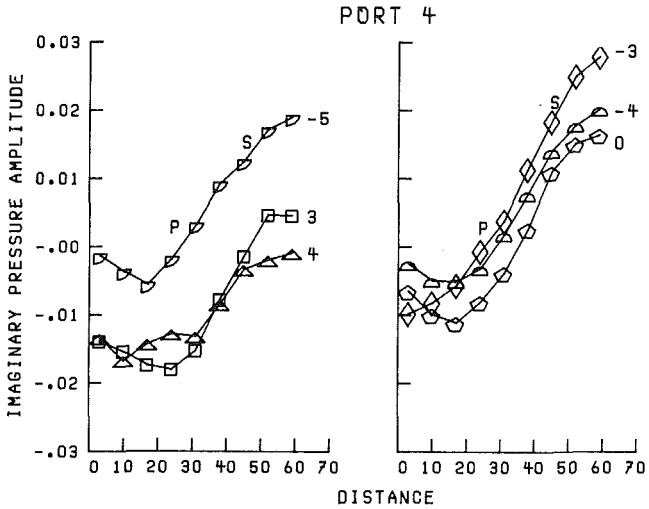

Fig. 13 Spatial variation of imaginary pressure port 4

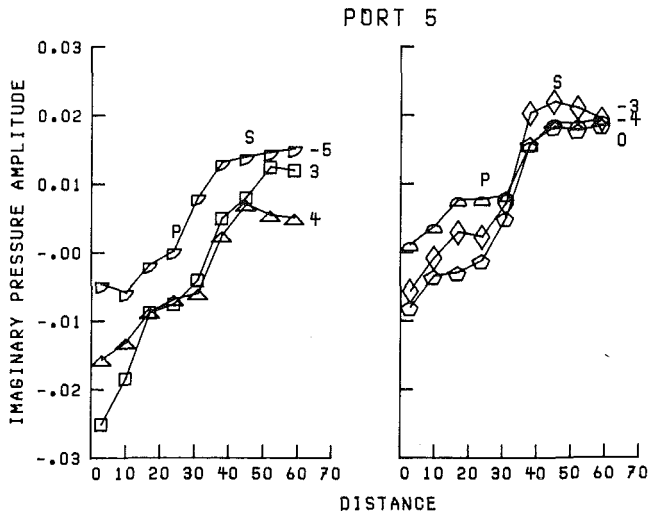

Fig. 14 Spatial variation of imaginary pressure port 5

nondimensionalized by using a product of the inlet dynamic head, the square of the chord, and the constant A_Θ^2. The quantity A_Θ is the angular displacement in radians per digitized unit of displacement, $A_\Theta = 3.267 \times 10^{-3}$. Numerically, it is nearly equal to the angular displacement for nodal diameter 3, Fig. 2. For this nodal diameter then, C_w is numerically equivalent to, and of opposite sign of, Carta's [6, 7] damping coefficient and a $2\pi^2$ multiple of Whitehead's [1] imaginary moment coefficient.

The main positive contribution to the work is for nodal diameters 3, 4, 5, and −3 at port 1 and for nodal diameters 3, 4, and 5 at port 2. The column on the right presents the total contribution to the work for each location. Despite the relatively small differential pressure amplitudes at ports 4 and 5 (Fig. 8), the apparent negative contribution to work in this area exceeds by a large margin the positive contribution at ports 1 and 2. The main reason for this is the much larger absolute phase angles between the differential pressure and the displacements (Table 2).

To examine whether or not the work balance could be improved by a different choice of pressure and suction surface locations, the contribution to work at each port was calculated for a pair of points at 17 and 45 units and also for a pair of points at 24 and 38 units in Figs. 11 to 14. For the former, the contributions to work for ports 1 to 4 were respectively 2.72, 0.60, −5.94, and −4.57, and for the latter the contributions were 2.17, 0.06, −3.20, and −3.59. The influence of the axis position was also examined. Accepting a 6 percentage point error in the axis position and shifting it to the midchord position resulted in a work contribution at each port of 2.24, 0.17, −3.68, and −3.35. The P and S points for this iteration were located as in Figs. 9–14.

A factor that should be considered in the explanation of the negative work balance is the accuracy of the phase angles, particularly at the trailing edge where the amplitudes are small. In the Appendix the phase angle error for ports 4 and 5 is estimated to be ±30 deg except for −5 and 0 nodal diameter modes for which the estimate is ±60 deg. Considering the absolute magnitude of phase angles in Table 2, it is apparent that even in the extreme error case none of the signs of the phase angles would be reversed. Also, it appears unlikely that the magnitudes of corrections would be sufficient to offset the negative work balance.

Two other possibilities remain that may explain the negative value for the total work. One is that the largest pressure amplitudes and phase angles are achieved someplace between the two leading-edge ports and that, therefore, the positive work contribution at the leading edge is underestimated. However, in view of the fairly large work imbalance, it seems unlikely that this alone could offset the excess of the negative work. The other possibility, which is thought to be more plausible, is that the work contribution at the two rear ports (4 and 5) is largely due to the variation in a separated region away from the blade surface and not across the blade.

Note that the contribution to the work at the trailing edge would also violate the Kutta-Joukowski condition. Measurements [8] conducted at a reduced frequency considerably higher than that used in the present study indicate that this is unlikely because of the low camber of the airfoil tip section.

At this time it appears, therefore, that the contribution at ports 4 and 5 should not be included in the work balance. Blade-mounted pressure instrumentation would be necessary to obtain definite quantitative results in this region.

It should be noted that in the calculation of the work per cycle and in the above discussion the spanwise variations were ignored. However, there remains a possibility that the work is positive at other spanwise positions and that over the whole span of the blade the total work is positive. Future studies would have to be specifically designed to document the spanwise variation of stability.

The one source that may cause the spanwise variation of velocity at the tip are the end-wall effects. These effects would tend to decrease velocity at the tip and therefore increase the incidence and the reduced frequency. The former is a destablizing effect and the latter tends to stabilize the system.

Stability analysis for this test point, which includes blade mistuning, was performed in reference [9]. Both the aerodynamic and mechanical coupling between the blades were considered. Aerodynamic coefficients were calculated based on the zero incidence flat-plate airfoil analysis [10]. With blade mistuning present the system was found to be stable. For a tuned system unstable behavior was predicted for the −7 nodal diameter mode. This was shown to be due to the "acoustic resonance" [11]. It appears that in order to predict the unstable behavior for the positive nodal diameters, a more sophisticated aerodynamic analysis is needed. Another stability analysis for this test point based on a semiempirical approach is presented in reference [3].

The results obtained here in many respects resemble the results obtained in a stationary cascade experiment [6, 7], despite the large difference in the reduced frequencies. (Based on the blade chord, the reduced frequencies in [6, 7] were 0.074 to 0.384). As in the present investigation the leading-edge contribution to aerodynamic work was found to be dominant in these references. Furthermore, the differential

Table 1 Distribution of aerodynamic work

Position	Nodal diameter							Sum
	3	4	5	-5	-4	-3	0	
	Dimensionless work C_w							
1	1.252	0.494	0.303	-0.091	-0.134	0.329	0.033	2.186
2	0.799	0.847	0.342	-0.314	-0.541	-0.742	-0.247	0.145
4	-1.197	-0.494	-----	-0.478	-0.864	-1.317	-0.858	-5.208
5	-0.951	-0.614	-----	-0.391	-0.477	-1.150	-0.742	-4.325

Table 2 Differential pressure phase relative to displacement phase

Position	Nodal diameter						
	3	4	5	-5	-4	-3	0
	Phase angle, deg						
1	20.2	16.2	29.9	-7.3	-5.3	6.0	1.4
2	9.2	24.8	26.1	-19.6	-14.6	-10.7	-7.3
4	-112.2	-139.7	----	-103.9	-103.8	-107	-96.3
5	-76.5	-89.4	----	-107.5	-117.5	-60.1	-85.2

pressure at the trailing edge appeared to converge to 0, particularly for a positive interblade phase angle. This reinforces previous reasoning regarding the interpretation of the ΔP measurement at locations 4 and 5. The phase angle between the differential pressure and the angular displacement for this condition ranged from about 10 to 30 deg at the leading edge, and this is in agreement with the values in Table 2. The phase could not be evaluated beyond the midchord position because of small amplitudes. However, extrapolating the chordwise phase variation beyond the midchord and redefining the phase consistent with Table 2 would lead to large negative phase angles in this region. Qualitatively this is the same trend observed in Table 2. The unstable behavior was, in general, confined to the positive interblade phase angles, and this again agrees with the present observations. Interestingly, the second harmonic contribution to the pressure at the leading edge observed in these references was absent in the present investigation.

Conclusions

Following are the main conclusions derived from a fan-flutter test using stationary pressure and displacement measurements:

1 A positive contribution to the aerodynamic work was concentrated near the leading edge.

2 The largest contribution to aerodynamic work was due to modes corresponding to nodal diameters of 3, 4, and 5. The modes corresponding to 0, −3, −4, and −5 nodal diameters contributed either a negative or a small positive work.

3 The contribution to the aerodynamic work at the rear of the blade could not be determined conclusively with stationary pressure measurements.

4 Near the leading edge there exists a steep spatial variation in the phase angle across the blade. Depending on the mode, it ranges between 94 and 107 deg.

5 The phase angle between the differential pressure and the angular displacement for the modes which contribute to positive work ranges between 1.4 and 30 deg.

6 The differential pressure amplitudes for different component modes near the leading edge were in the same relative proportions as the corresponding angular displacement amplitudes.

7 Vectorial averaging of pressure and displacement spectra is essential for a quantitative determination of phase relationships.

References

1 Whitehead, D. S., "Torsional Flutter of Unstalled Cascade Blades at Zero Deflection," R M-3429, Aeronautical Research Council, England, 1966.

2 Kurkov, A. P., "Flutter Spectral Measurements Using Stationary Pressure Transducers," *Measurement Methods in Rotating Components of Turbomachinery*, ASME JOURNAL OF ENGINEERING FOR POWER, Vol. 103, No. 2, Apr. 1981, pp. 461-467.

3 Jeffers, J. D., May, A., and Deskin, W. J., "Evaluation of a Technique for Predicting Stall Flutter in Turbine Engines," PWA-FR-9620, Pratt & Whitney Aircraft, West Palm Beach, Fla., Feb. 1978. (NASA CR-135423, 1978.)

4 Kurkov, A., and Discus, J., "Synthesis of Blade Flutter Vibratory Patterns Using Stationary Transducers," ASME Paper No. 78-GT-160, Apr. 1978.

5 Nieberding, W. C., and Pollack, J. L., "Optical Detection of Blade Flutter," ASME Paper No. 77-GT-66, Mar. 1977.

6 Carta, F. O., and St. Hilaire, A. O., "Experimentally Determined Stability Parameters of a Subsonic Cascade Oscillating Near Stall," ASME JOURNAL OF ENGINEERING FOR POWER, Vol. 100, No. 1, Jan. 1978, pp. 111-120.

7 Carta, F. O., and St. Hilaire, A. O., "Effect of Interblade Phase Angle and Incidence Angle on Cascade Pitching Stability," ASME Paper No. 79-GT-153, Mar. 1979.

8 Fleeter, S., "Trailing Edge Conditions for Unsteady Flows at High Reduced Frequency," *AIAA Journal*, Vol. 18, No. 5, May 1980, pp. 497-503.

9 Srinivasan, A. V., and Kurkov, A., "Effects of Mistuning on Blade Torsional Flutter," presented at *Fifth International Symposium on Air-breathing Engines*, Feb. 16-21, 1981, Bangalore, India, NASA CR-165137, 1980.

10 Smith, S. N., "Discrete Frequency Sound Generation in Axial Flow Turbomachines," R M-3709, Aeronautical Research Council, England, 1971.

11 Whitehead, D. S., "The Effect of Compressibility on Unstalled Torsional Flutter," R M-3754, Aeronautical Research Council, England, 1974.

12 Singleton, R. C., "On Computing the Fast Fourier Transform," *Communications of the ACM*, Vol. 10, No. 10, Oct. 1967, pp. 647-654.

APPENDIX

To correlate the data recorded on different tapes, it was essential to start digitization at an identical instant in time. This was achieved by using the time code reader and the 1E reference pulse [2]. The time code reader searched for a particular time instant selected in advance. Upon reaching this instant the digitization started at the first following 1E pulse. However, because the time code was not recorded on the displacement data tape, displacements were evaluated relative to blade 1, and the strain-gage phase for that blade (at a selected 1E pulse) was used as the absolute phase angle for the displacement of blade 1.

Pressure, P, and displacement, D, can be expressed as [2]:

$$P,D = \sum_{i=1}^{38} A_i^{P,D} \exp\{j[\omega_f t - (\Phi_i - \Phi_1)i + \psi_i]\}$$

where the summation is carried over all nodal diameter modes. Here the time, t, is referenced to a particular 1E reference pulse, and the angular coordinate Φ is measured relative to blade 1.

The phase angles, ψ_i, are given by

$$\psi_i^D = \phi_i^D + \frac{37}{38} 2\pi i - \frac{0.45}{38} 2\pi \frac{\omega_f}{\omega_r} + \phi_i^S - \left(-\frac{37.45}{38} 2\pi \frac{\omega_f}{\omega_r} + \phi_1^D\right)$$

$$\psi_i^P = \phi_i^P + \frac{9}{38} 2\pi i - \frac{0.97}{38} 2\pi \frac{\omega_f}{\omega_r}$$

In these expressions, ϕ_i's are the ith nodal diameter phase angles measured relative to the first blade-associated sample in the respective input data for spectral analysis. These corresponded to blade 38 for displacements and to blade 10 for pressures. The second terms in these expressions account for the position of blade 1 relative to these blades, and the third terms account for the time delay between the occurrence of the 1E pulse and the time these blades are under the respective sensors. The term ϕ_1^S is the phase of the blade 1 strain gage, and ϕ_1^D is the phase of the displacement of blade 1 referenced to the first time this blade appears under the sensor. This term was evaluated from the aliased 1/2 E spectrum associated with this blade. The term preceding ϕ_1^D in parentheses accounts for the time between the occurrence of the 1E pulse and the time blade 1 is under the sensor.

When averaging data vectorially, it is important to choose a correct reference phase. It is convenient to consider the difference $\psi_i^P - \psi_i^D$ since it is a fundamental property. The following pairs of phase angles will appear in this difference:

$$\phi_i^P - \phi_1^S \text{ and } \phi_i^D - \phi_1^D$$

It is therefore convenient to reference the pressures to ϕ_1^S and the displacements to ϕ_1^D prior to the vectorial averaging. Once average pressures and displacements are obtained, the phase difference $\psi_i^P - \psi_i^D$ corresponding to the average spectrum is computed. Before the averaging, the phase of each individual Fourier transform was corrected to account for non-simultaneous sampling of points which were spatially apart. The Singleton algorithm [12] was used to obtain the Fourier transforms. The number of points in the input data set in this algorithm can be arbitrary rather than only a power of 2 as in typical fast Fourier transforms. This allows the selection of an integral number of revolutions and approximatley an integral number of cycles in the input data set. As a result, each nodal diameter peak in the spectrum is very nearly concentrated in the single-frequency line. The spectra in Figs. 2, 3, and 5 to 8 were obtained in such a way. Therefore each peak in these figures corresponds very nearly to the true amplitude. The number of revolutions in the input data for Figs. 2 and 3 was 65 and for Figs. 5 to 8, 62, The number of samples per revolution was 38 (i.e., equal to the number of blades).

To evaluate the phase difference $\phi_i^P - \phi_1^S$ needed in the computation of average pressure spectra, it would be necessary to use engine order sampling for strain-gage data with the same total number of revolutions and total number of samples per revolution as were used for the pressure spectra. To effect this type of sampling procedure for strain-gage data would require a digitization rate beyond the available range because these data were recorded at much lower speed and hence on playback the speed reduction ratio was limited. Instead, the interpolation between frequency lines was used to evaluate the absolute phase angles corresponding to the exact flutter frequency for both pressure and strain-gage data.

Previously [2] the square window was used mainly because of the availabilty of the interpolation formula for this window. However, Braun of NASA Lewis recently derived the interpolation formula for the Hanning window, so that it could also be applied. The Hanning window proved to be advantageous especially for pressure data. Therefore, all quantitative analysis as well as the results in Figs. 9 to 14 were obtained with this window.

If f_u denotes the frequency of the dominant frequency line, f_g the exact flutter frequency, and β the frequency bin spacing, then the interpolation fraction v is defined by

$$v = (f_g - f_u)/\beta, -1/2 \le v \le 1/2$$

This fraction can be computed from the spectrum by using the amplitude ratio $R = A_u/A_{u\pm1}$ where A_u is the dominant amplitude and $A_{u\pm1}$ is the next largest amplitude; that is,

$$v \approx \pm \frac{2-R}{1+R}$$

Here the minus sign is used when $A_{u+1} < A_{u-1}$. The amplitude at the true frequency is given by

$$A_g \approx \frac{2(1-v^2)\sin(2\pi v/N)}{A_h \sin(\pi V)} A_u, A_h = \frac{2}{N}\sqrt{\frac{8}{3}}$$

and the phase angle Θ_g by

$$\Theta_g \approx \phi_u - \pi v$$

Here N denotes the number of points, A_h is the normalization constant, and ϕ_u, is the phase angle for the dominant frequency line. In the expression for A_g the approximation

$$\left[\frac{\tan(\pi v/N)}{\tan(\pi/N)}\right]^2 \approx v^2$$

was made.

Some indication of the accuracy of the phase angles can be obtained by computing v for each nodal diameter mode in the spectrum. Ideally, as a result of the sampling procedure, v should be constant for all peaks. In practice, v varied between 0.192 and 0.224 for the displacement data. Considerably larger variations in v were encountered for the pressure data. Excluding from the considerations the nodal diameters 5 and -5 at the leading edge, and in addition the 0 nodal diameter at the trailing edge, v varied between -0.05 and -0.18 at the leading edge and between -0.25 and 0.10 at the trailing edge. If the mentioned nodal diameters were included, the range for v would about double. Therefore the phase results for these nodal diameters are somewhat questionable. From Figs. 5 to 8 it can be seen that these nodal diameters correspond to the lowest amplitudes.

With this qualification one can expect an error in the pressure phase angle within the range ± 12 deg at the leading edge and ± 30 deg at the trailing edge. It should be noted, however, that because of the larger absolute phase difference $\psi_i^P - \psi_i^D$ at the trailing edge (Table 2), the accuracy there is not as critical as at the leading edge.

The estimates for variations in v were obtained for the average spectra; for the single transforms variations in v would be considerably larger. It was concluded therefore that the data averaging was essential.

For the results presented in Table 2 an effective average v was assumed for all pressure ports. This is likely to improve somewhat the accuracy of the pressure phase angles. The accuracy of the displacement phase angles is estimated to be ± 30 deg for all nodal diameters.

Journal of Engineering for Power

Discussion

Acoustic Control of Dilution-Air Mixing in a Gas Turbine Combustor[1]

J. A. C. Kentfield.[2] The authors are to be congratulated on identifying a technique which shows promise in controlling unwanted temperature nonuniformities in the flow leaving a typical gas turbine type combustor. However, by applying the acoustic stirring to the dilution air the control is applied so late in the flow process that its influence must be somewhat restricted. Do the authors feel that potentially more effective uses of acoustic stirring can be made by applying the technique to the secondary and possibly even the primary zones? Is there some expectation that this could result in a reduction of combustion length? In fact, a single relatively large-scale vortex ring is, it would appear from flow visualization evidence [1], primarily responsible for the mixing occurring in typical valveless pulse-combustors. In a sense this can be regarded, by analogy with classical steady flow combustors, as an application of strong acoustical stirring in a primary zone.

It seems, to this discussor, that self-contained fluidic or fluid-mechanical methods of generating the required signals must be developed before acoustic stirring can be accepted as a practical proposition. Possibly an attach-separate flow situation can be contrived to generate vortex rings periodical. Another alternative, which does not appear to require totally new technology, would utilize fluidic oscillators. It is envisaged that in such a system each oscillator would apply a signal, alternately, to two or more of the air ports in the flame tube. Perhaps it would be possible to incorporate, in the spirit of the present work, self-oscillating slot-nozzles such as those described by Viets [2]? This involves substituting, for the periodic vortex-ring generation of the present system, a somewhat different, laterally oscilalting flow pattern. This concept has been shown to be very effective in promoting mixing and presumably, because of its nonsteady nature, it can also be expected to be effective in stirring the general surroundings.

Yet another possibility for a simple self-contained system without external drive could, perhaps, be based on so-called hypermixing nozzles. Nozzles of this type have been developed to promote rapid mixing in short length ejectors intended for thrust augmentation applications [3]. In hypermixing nozzles it appears that strong, continuous vortices are formed with their axes aligned with the flow. Again, this is quite a different flow pattern from that used by the authors and one which does not take advantage of periodic nonsteady flow phenomena and is not, therefore, strictly an acoustic control method.

It can be asked, do the authors forsee any difficulties with their system with respect to the deliberate tailoring of combustor exit temperature profiles to achieve, for example, a relatively low temperature in the region of the blade roots? Presumably gross biasing of this type should still be attainable by appropriate adjustment of the dilution air ports in the flame tube.

It seems that whilst a very interesting start has been made on investigating the potentials of acoustic stirring much more work is required before the subject can be said to have been explored comprehensively.

References

1 Kentfield, J. A. C., "Valveless Pulse-Combustors With Multiple Inlets," *Proceedings, Sympsoium on Pulse-Combustion Applications*, Paper No. 2, Gas Research Institute, Atlanta, Mar. 1-3, 1982.

2 Viets, H., "Flip-Flop Jet Nozzle," *AIAA Journal*, Vol. 13, No. 10, Oct. 1975, pp. 1375-1379.

3 Bevilaqua, P. M., "Evaluation of Hypermixing for Thrust Augmenting Ejectors," *AIAA Journal of Aircraft*, Vol. 11, No. 6, June 1974, pp. 348-354.

A. A. Putnam.[3] Both my comments have to do with vortex shedding, which the authors touch on in their Fig. 9. Since I could not find a comment on the duct diameter or area where these vortics occur, I could not compute the Strouhal number, i.e., DF/V, and resolve my questions.

Recently, we studied the acoustics of the flow in a duct, in which an upstream signal was imposed in a manner similar to that indicated in the paper. We measured both the transmitted and reflected acoustic energy from the exit. The minimum energy loss from the signal (considering both the transmission and upstream reflection) was at a constant Strouhal number, independent of Mach number. Away from the optimum frequency, increasing Mach number increases the loss. This would seem to indicate the proper frequency could trigger strong discrete vortices with a minimum of energy input. Have the authors observed a similar phenomenon, and, if so, what was the critical Strouhal number?

A second question is related to pioneer work by Dr. Lockwood, reported in several places. In studies of pulse combustion vertical lift devices many years ago, Lockwood found that strong aspiration effects occurred with pulsed jets used with augmenters. Pulsing a jet between two augmenters resulted in more effective aspiration than using a single steady jet. His observations lead me to believe the use of augmenters in a like manner might lead to even more mixing than with the drivers alone. Have the authors given any consideration to this possibility?

[1] By P. J. Vermeulen, J. Odgers, and V. Ramesh, published in the October 1982 issue of the ASME JOURNAL OF ENGINEERING FOR POWER, Vol. 104, No. 4, pp. 844-852.

[2] Professor, Department of Mechanical Engineering, University of Calgary, Calgary, Alberta, Canada.

[3] Fuels and Combustion Section, Battelle-Columbus Laboratories, Columbus, Ohio 43201. Fellow ASME

Authors' Closure

The discussers' comments are most interesting and informative, and specific replies are as follows:

J. A. C. Kentfield. The application of the technique to the dilution zone was preferred because it promised quick success. However, we recognized early on that application of the technique within the primary zone might promote more effective stirring processes resulting in improved combustion efficiency and hence less need for a secondary zone. This might therefore shorten the combustion length and that of the overall combustor.

It is readily agreed that the present method of flow modulation is not practical and that other more practical methods must be developed. In fact, work on fluidic or fluid-mechanical methods is already underway, and the drawing of our attention to the work of Viets and Bevilaqua may prove to be invaluable.

Regarding the tailoring of combustor exit temperature profiles for, say, cool temperatures at the turbine blade roots, we do not forsee difficulties with the present technique since the trimming experiment described in the paper could easily be "inverted." Thus, instead of driving two dilution ports by the No. 3 loudspeaker, the dilution ports diametrically opposite could have been driven (with rig modification), thereby raising the hot spot temperature and reducing the temperature in the region at 9 o'clock. The "no-drive" "radial" temperature profile shown in Fig. 8 would therefore be accentuated towards an even more pronounced hot tip-cool root distribution.

A. A. Putnam. The dilution ports are 19.6-mm dia, giving a Strouhal number of 0.21 at the low air mass flow rate and 0.12 at the high air mass flow rate. We have not observed any evidence for a critical Strouhal number largely because of a preocupation with the mismatched driving system. However, the observation is an important one and will be considered in our future work.

The possibility of using Lockwood type augmenters is a new idea to us, but it would be difficult to apply to an existing combustor design and would raise flow path problems. The mixing behaviour of such augmented pulsed jet flows may very well be superior to those undergoing only acoustic modulation and may be worthwhile considering in future developments.